Mineralogic and Petrologic Studies of Archaean Metamorphic Rocks from West Greenland, Lunar Samples, and the Meteorite Kapoeta

Thesis by

Robert F. Dymek

In Partial Fulfillment of the Requirements

for the Degree of

Doctor of Philosophy

California Institute of Technology

Pasadena, California

1977

(Submitted May 18, 1977)

ACKNOWLEDGEMENTS

Professor A. L. Albee has provided me with the freedom and opportunity to become involved in several research projects during my tenure as a graduate student. This is reflected in the triptych nature of my dissertation, which evolved with his enthusiastic support. I extend my thanks to him, and also to Professor G. J. Wasserburg, for encouraging me to pursue this broad-based research program. The intensity with which they approach their own work has been an inspiration to me, and I am pleased to have had the opportunity to be associated with them. Their forthright criticisms, albeit frustrating at times, forced me to reconcile many of my not so solid ideas with the data and observations in hand. I thank them for their patience in these matters.

Much of my learning has occurred through discussions with colleagues and fellow students over the last five years. I extend my thanks in particular to Drs. A. J. Gancarz and J. C. Huneke for their contributions in relation to the study of lunar samples and meteorites, and to Ms. Jo Laird and Mr. T. C. Labotka for their assistance with problems related to metamorphic rocks and the microprobe.

All of the analytical data presented in this thesis were acquired with the Caltech electron microprobe which is under the skilled supervision of Mr. A. A. Chodos. Without his careful maintenance of the microprobe laboratory, this work could never have been completed.

I would also like to thank my co-authors of the papers in Parts II and III for allowing me to include these articles in my thesis. Pergamon Press has granted me written permission to reproduce them herein in unmodified form.

This research has been supported by grants from the National Science Foundation (GP-28027, GA-31729, DES-75-03417) and the National Aeronautics and Space Administration (NGL-05-002-188, NGL-05-002-338). Although the work presented in Part I is based on studies of samples collected during the summer of 1973 under the auspices of the NSF-funded "Project Oldstone," some of the conclusions were made possible by examination of material supplied to me at a later time by the Geological Survey of Greenland (GGU), and by examination of samples collected during the summer of 1975 during which I was supported by GGU in the field. The microprobe laboratory has been developed through the generous support of the National Science Foundation, the Jet Propulsion Laboratory, and the Union Pacific Foundation.

ABSTRACT

In Part I of this thesis, petrographic and electron microprobe data are reported for samples from a series of high-grade Archaean gneisses, collected on Langø, an island in the northwest corner of the Godthåb District of West Greenland. Rocks with a wide variety of bulk compositions occur that all preserve evidence for two distinct episodes of metamorphic mineral growth. Syn- to post-tectonic hornblende-granulite grade metamorphism (MI) was followed by post-tectonic amphibolite grade metamorphism (MII) at a later time. In potassium feldspar-bearing gneisses, MI assemblages, in addition to quartz and plagioclase are: garnet + biotite (brown) ± sillimanite; cordierite + biotite (brown) ± sillimanite; and biotite (brown). In potassium feldspar-free gneisses, MI assemblages, in addition to quartz and plagioclase are: cordierite + garnet + biotite (brown); and orthopyroxene + biotite (brown) ± cordierite. As a result of MII, cordierite and garnet have been replaced by kyanite + biotite (green). Brown biotite is Ti-rich (>1.0 wt % TiO_2), whereas green biotite is Ti-poor (≲1.0 wt % TiO_2), and an examination of biotite analyses suggests that Ti is incorporated in that mineral via a vacancy-forming substitution. In mafic rocks, MI assemblages include various combinations of hornblende (green-brown) + clinopyroxene ± orthopyroxene ± garnet ± biotite, with plagioclase and rarely quartz. However, garnet and clinopyroxene do not occur together. As a result of MII, pyroxene has been replaced by calcic amphibole that differs in color (pale green to blue green) and composition (Na, K, Al, Ti are lower; Si, Mg, Fe^{3+} are higher) from the

MI varieties. MI hornblende and plagioclase have an extremely large compositional range, which correlate with one another in terms of Al/(Al+Si) and Na/(Na+Ca), and suggest that their compositions are controlled by rock composition, and not by metamorphic grade at these conditions.

The composition of coexisting pyroxenes, the position of the kyanite-sillimanite boundary, and the composition of garnet (cores) and cordierite constrain the pressure and temperature for MI to lie between ∿7-8 kb and ∿700-800°C. Temperatures calculated from Fe-Mg partitioning between garnet (rims) and MII biotite suggest ∿450°C for MII, and the occurrence of kyanite would indicate a pressure of 3-4 kb for this temperature. The MI event can be ascribed with certainty to regional metamorphic-magmatic activity at ca. 2.8 AE (Black et al., 1973), whereas MII may correspond to regional heating during the emplacement of the Qôrqut Granite at ca. 2.5 AE (Baadsgaard and Collerson, 1976), or to a regional thermal event at ca. 1.6 AE identified in isotopic studies (Pankhurst et al., 1973).

The pressure and temperature estimated for MI imply a thermal gradient of ca. 30°C/km, and a minimum crustal thickness of 20 km at the time of metamorphism. The petrologic characteristics of MI are similar to medium-P facies series metamorphism found in younger orogenic belts, and nothing "unique" can be ascribed to this Archaean metamorphic event, based on the presently-available data and observations.

Parts II and III of this thesis are a series of published papers that involve mineralogic and petrologic studies of Apollo 15, 16, and 17 lunar samples and the meteorite Kapoeta.

TABLE OF CONTENTS

PART I:

Mineralogic and Petrologic Studies of High-Grade Polymetamorphic Archaean Gneisses from Langø, West Greenland.

CHAPTER 1

I. INTRODUCTION

A. Prologue

In the last several years, the early history of the earth and the nature of its lower crust have been the subject of intense study (Windley, 1976; Moorbath, 1977). Ancient Archaean rocks, whose ages overlap the time of lunar magmatic activity, have now been reported from most of the world's Precambrian cratons. Such rocks can yield important information on the early chemical and thermal evolution of the crust, and provide a critical test for the basic geological principle of uniformitarianism.

Studies of xenoliths in diatremes throughout the world suggest that granulite grade assemblages predominate in the lower crust. However, the small numbers of such samples make detailed systematic investigation difficult.

A large proportion of the world's Precambrian cratons are comprised of granulite grade gneisses (Oliver, 1969; Clifford, 1974). Thus, through uplift and erosion, such areas provide a "window" to deep crustal rock types.

This work is concerned with a sequence of Archaean granulite grade gneisses from West Greenland, and will address itself in part to the two issues outlined above.

B. West Greenland Archaean

Approximately 90% of the West Greenland Archaean craton is comprised of a series of complexly-deformed, migmatitic quartzofeldspathic gneisses that appears to be derived from suites of calc-alkaline intrusive rocks. Within the Godthåb District (Fig. 1-1), two major groups of gneisses with different ages have been identified in the field (McGregor, 1973). The stratigraphically older group, the Amîtsoq gneisses, has yielded isotopic ages of ca. 3.7 AE by a variety of techniques (Moorbath et al., 1972; Baadsgaard, 1973; Gancarz and Wasserburg, in press). The stratigraphically younger group, the Nûk gneisses, has yielded isotopic ages of ca. 2.8 AE (Moorbath and Pankhurst, 1976; Baadsgaard and Collerson, 1976).

Scattered throughout these gneisses are areas of metamorphosed mafic volcanic rocks, and pelitic and aluminous metasedimentary rocks collectively known as the Malene Supracrustals (McGregor, 1973). These are stratigraphically older than the Nûk gneisses, but their age relative to the Amîtsoq gneisses is ambiguous in the field. However, reconaissance U-Pb studies on zircons separated from samples of the Malene Supracrustals in one small locality yield ages of ∿2.6 to 2.9 AE which are distinctly younger than that of the Amîtsoq gneisses (Baadsgaard and Collerson, 1976).

This entire gneiss-supracrustal sequence was subjected to widespread regional metamorphism at ca. 2.8 AE (Black et al., 1973) that was in part coincident with the formation of the igneous parents of the Nûk gneiss, and locally reached granulite grade. A detailed discussion of the geochronologic/lithostratigraphic relationships in this area can

Figure 1-1: Generalized map illustrating the position of the Archaean craton of West Greenland and localities therein. The area mapped by McGregor (1973), in which the chronology of the area is worked out in detail, and the area mapped by Berthelsen (1960) are indicated.

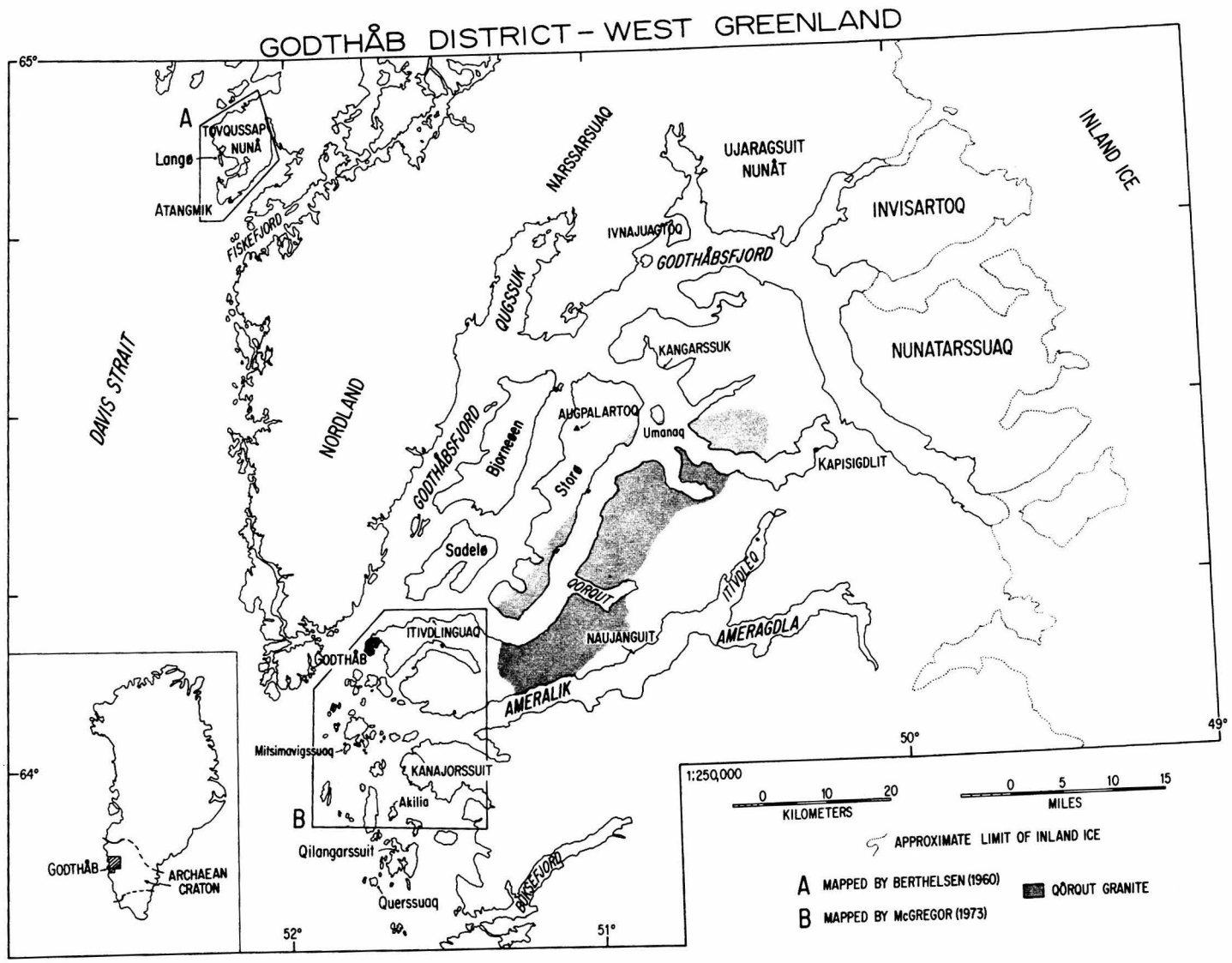
GODTHÅB DISTRICT – WEST GREENLAND
65°
A
TOVQUSSAP NUNÅ
Langø
ATANGMIK
FISKEFJORD
NARSSARSUAQ
UJARAGSUIT NUNÅT
INLAND ICE
INVISARTOQ
IVNAJUAGTOQ
GODTHÅBSFJORD
QUGSSUK
DAVIS STRAIT
KANGARSSUK
NUNATARSSUAQ
NORDLAND
AUGPALARTOQ
Umanaq
GODTHÅBSFJORD
Bjørneøen
Store
KAPISIGDLIT
Sadelø
QÔROUT
ITIVDLEQ
ITIVDLINGUAQ
GODTHÅB
NAUJANGUIT
AMERAGDLA
AMERALIK
Mitsimavigssuaq
KANAJORSSUIT
Akilia
B
Qilangarssuit
Querssuaq
BUKSEFJORD
64°
52°
51°
50°
49°
GODTHÅB
ARCHAEAN CRATON
1:250,000
0 10 20
KILOMETERS
0 5 10 15
MILES
APPROXIMATE LIMIT OF INLAND ICE
A MAPPED BY BERTHELSEN (1960)
B MAPPED BY McGREGOR (1973)
QÔROUT GRANITE

be found in McGregor (1973), Bridgwater et al. (1974), and Bridgwater et al. (1976).

Despite the tremendous recent interest in this area, engendered for the most part by the discovery of the ancient Amîtsoq gneisses, very little attention has been paid to the petrologic aspects of the lithologies exposed there. A knowledge of phase assemblages and mineral-chemical relationships in these gneisses would increase substantially our understanding of metamorphic processes that operated during this segment of the Archaean. In addition, a knowledge of the physical conditions accompanying metamorphism will help to constrain models for the early evolution of the crust.

I have, therefore, initiated a project to examine in detail the variations in metamorphic conditions throughout the Godthåb District, with emphasis on the Malene Supracrustals. The results reported here represent the first phase of that study.

The area selected for study was Langø, a small island in the NW corner of the Godthåb District that forms part of a complex dome structure at Tovqussaq. It was mapped in detail by Berthelsen (1960), hence the geological relationships are largely known.

In summary, the main purpose of this project is threefold:

1) increase our knowledge of the geological evolution of West Greenland;
2) increase our understanding of granulite grade metamorphism; and
3) increase our understanding of the early evolution of the earth.

CHAPTER 2

II. GEOLOGIC SETTING

A. Tovqussap Nuna

The region of Tovqussap Nuna (= Tovqussaq Land) (see Fig. 1-1) is a typical Precambrian high-grade migmatitic gneiss-pyribolite terrain. Berthelsen (1960) mapped the region in detail and recognized eight lithostratigraphic units that could be traced continuously over a large area, together with small bodies of syn- to post-tectonic pyroxene diorite. A simplified version of a portion of Berthelsen's map is given in Figure 2-1, and general descriptions of these lithologies are presented in Table 2-1. The persistent nature of these gneiss units allowed Berthelsen to outline the presence of a dome structure centered near Tovqussaq Mountain, and a number of folded synforms and antiforms surrounding the dome. The Tovqussaq structure is one of a series of domes and basins that formed throughout the Archaean craton of West Greenland during the waning stages of prolonged extensive deformation approximately 2800 m.y. ago (Bridgwater et al., 1976).

On the basis of detailed fabric analyses, Berthelsen (1960) recognized four distinct phases of deformation that led to the development of the structures observed at Tovqussaq, and culminated in widespread granulite-grade metamorphism.

The first phase - Midterhoj - was characterized by NW-SE trending, subhorizontal isoclinal folds of large dimension (>5 km) and was inferred to have occurred under low P-T conditions. The second phase - Smalledal - was characterized by plastic deformation associated with

Figure 2-1: Generalized geological map of the area around Tovqussaq Mountain showing concentric arrangement of the eight principal lithostratigraphic units that comprise the Tovqussaq structure (modified from Berthelsen, 1960).

GEOLOGY OF A PORTION OF TOVQUSSAP NUNÂ *

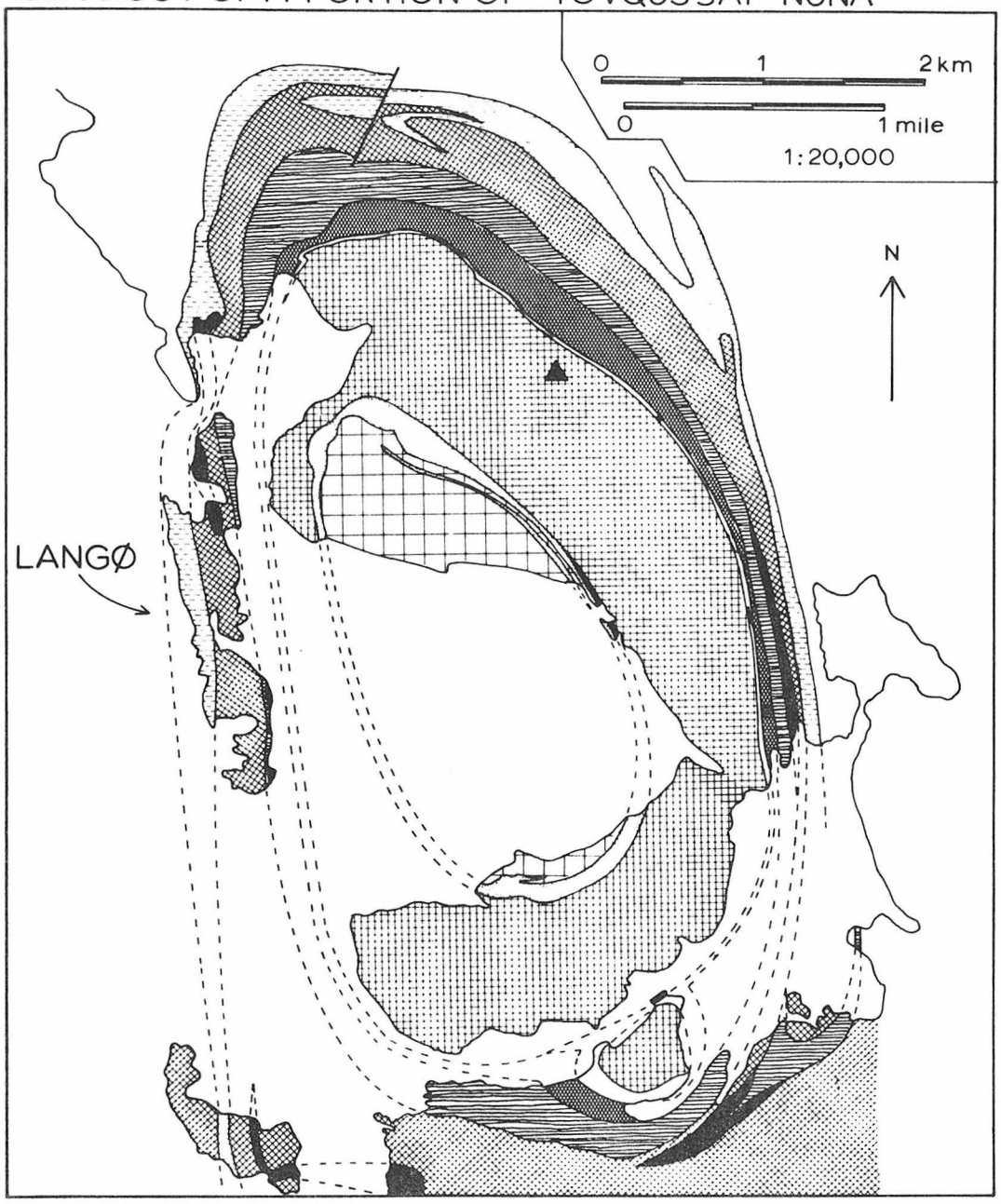

Central Dome
Little Pyribolite
2nd Intermediate Layer
Interior Pyribolite
1st Intermediate Layer
Pas Pyribolite
Frame Layer
Great Pyribolite
Pyroxene Diorite
▲ Tovqussaq Mountain (524 meters)

*(adapted from Berthelsen, 1960)

TABLE 2-1: BRIEF DESCRIPTIONS OF
PRINCIPAL LITHOLOGIES AT TOVQUSSAQ*

1. Central Dome (core rock): Medium-to coarse-grained, greenish-brown to purple, homogenous quartz diorite gneiss characterized by nebulitic shearfolds. It grades outward into pale granodioritic to granitic gneiss. The latter types separate the core from enclosing pyribolite.
2. Interior Pyribolite: Medium to coarse-grained, black to greenish, banded mafic gneiss comprised of pyroxene, hornblende and plagioclase that enclose meter size blocks of ultramafic rock locally. Comformable layers of pyroxene diorite are present.
3. Frame Layer: Medium to coarse-grained brown to pale, layered quartzofeldspathic gneisses that range from biotite-bearing types to orthopyroxene-bearing types. Garnet occurs locally in all lithologies. Some layers are characterized by abundant inclusions of anorthositic rocks and/or rafts of pyribolite. Most of the gneisses are migmatitic, and the contact with the inner pyribolite is agmatitic.
4. Little Pyribolite: Similar to 2.
5. 1st Intermediate Layer: Fine-to medium-grained pale biotite granodioritic gneiss. Contacts with surrounding pyribolite units are sharp and appear to have been the locus of fault movement.
6. Great Pyribolite: Medium-to coarse-grained mafic gneiss characterized by intercalations of pyroxene diorite, calc-silicate layers, and abundant pods of ultramafic rocks. Gneiss ranges from highly banded to homogenous.
7. 2nd Intermediate Layer: In northern and eastern portion of dome, this unit is a medium-grained pale biotite granodioritic gneiss containing scattered conformable layers of pyribolite. In south, it is a medium-grained pale quartz diorite gneiss containing various combinations of orthopyroxene, hornblende, and biotite; conformable pods and layers of garnet-biotite gneiss and pyribolite also occur here. The western portion is a quartz dioritic to granodioritic gneiss that contains layers of pyribolite, garnet-biotite-sillimanite gneiss, calc-silicate bands, and cordierite-bearing hypersthene gneiss; pyribolite layers enclose pods of ultramafic rocks.
8. Pas Pyribolite: Ranges from homogenous banded mafic gneiss that contains pods of ultramafic rocks locally on the northern and eastern part of the dome to a mixed pyribolite-hypersthene-biotite dioritic gneiss on the west portion of the dome. This western mixed gneiss contains conformable layers of calc-silicate rock, red-colored nodular-weathering hornblende pyroxenite, and some scattered rafts of anorthositic rocks.
9. Pyroxene Diorites: These include syntectonic coarse-grained rocks that range from foliated types conformable with enclosing pyribolite to massive, semi-concordant to trangressive bodies that appear to be late to post-tectonic intrusions.

* Modified from Berthelsen (1960).

NE-SW trending recumbent folding that led to the development of nappes. Extensive migmatization accompanying amphibolite grade metamorphism set up conditions that brought about the diapiric rise of the core gneisses to form the Tovqussaq dome at this time. The Pakitsøq phase was characterized by refolding along SE- to S-plunging folds under conditions of granulite grade metamorphism. Berthelsen (1960) suggested that these three phases represent parts of the same prolonged orogenic cycle accompanied by progressive metamorphism up to granulite grade. Near the conclusion of deformation, small bodies of pyroxene diorite were emplaced.

The last phase of deformation - Posthumous - had only negligible effect upon the earlier-formed structures. It resulted in retrograde metamorphism, emplacement of microcline pegmatites, local shear folding, and the formation of mylonites. The Posthumous phase clearly developed over an extended period of time and over a wide range of conditions, since, for example, plastic shear folding and brittle failure associated with the formation of mylonites, seem to imply quite different stress regimes.

B. Langø

Langø is a small, elongate island (∿1/2 x 3 km), characterized by low elevations, low relief, and excellent exposure (Fig. 2-2). It occurs along the Western flank of the Tovqussaq dome and is oriented parallel to the strike of the three main lithostratigraphic units that comprise it (Fig. 2-1). Berthelsen (1960) mapped Langø in considerable

Figure 2-2: Aerial photograph of a portion of Tovqussap Nuna looking East across Langø, the low-lying island in the foreground. The center of the dome structure is on the southern slope of Tovqussaq Mountain, in the upper left of this view.

detail (1:4,000), and a somewhat simplified version of his map is illustrated in Figure 2-3.

The Pas Pyribolite exposed on Langø ranges from a homogeneous, layered hornblende-pyroxene-plagioclase gneiss (Figure 2-4A) to a mixed rock series consisting of biotite grandioritic gneiss containing cm to meter size layers of pyribolite (Figure 2-4B). Thicker (up to 50 m) layers of concordant biotite grandiorite gneiss are also present. A ∿10 meter wide band of calc-silicate rock crops out along the center of this unit, and conformable layers consisting of elongated pods of red-colored, nodular-weathering hornblende orthopyroxenite also occur. A few of the pyribolite layers are garnet-bearing.

The 2nd Intermediate Layer includes distinct conformable horizons of biotite grandodioritic gneiss, hypersthene-bearing tonalitic gneiss, garnet "granulite" (=garnet-biotite-sillimanite gneiss), and pyribolite. The NE-SW trending contact between the garnet granulite horizon and the hypersthene gneiss horizon near Nordnor is related to intense tight folding associated with a plunging synform (Berthelsen, 1960). A few scattered meter-sized calc-silicate layers are also present in the northern portion of the 2nd Intermediate Layer, and the southernmost exposure of garnet granulite contains enclaves and layers of a characteristic red-weathering cordierite-orthopyroxene gneiss. The pyribolite horizons habitually contain scattered inclusions of hornblende peridotite.

The pyroxene diorite near Nordnor is a massive equigranular coarse-grained hornblende-pyroxene-plagioclase rock that is unfoliated but displays a faint lineation locally. All exposed contacts are sharp

Figure 2-3: Geologic sketch map of the principal lithologic units exposed on Langø.

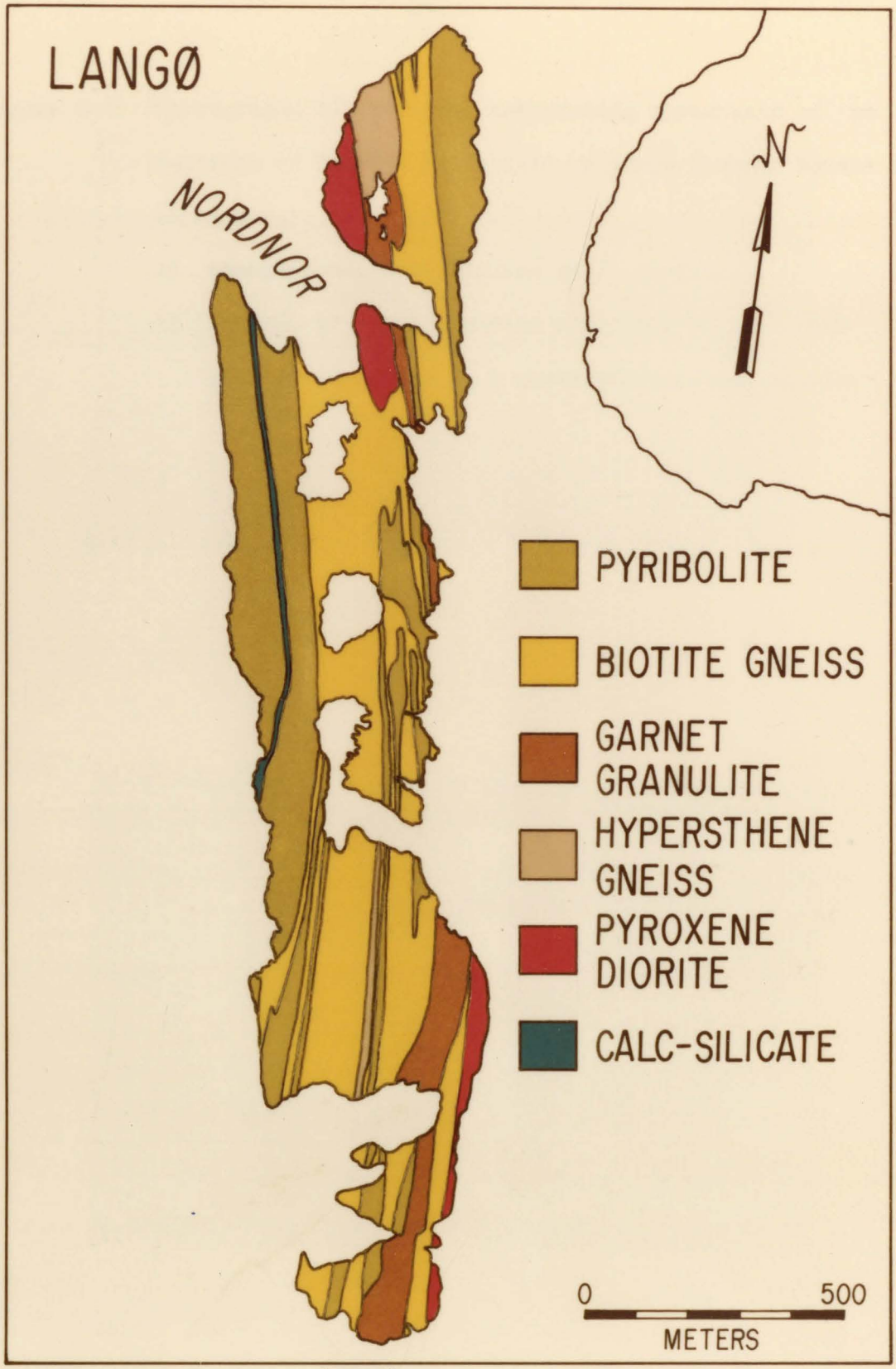

Geology by A. Berthelsen (1960)

Figure 2-4: Photographs illustrating contrasting appearance of two outcrops of the Pas Pyribolite on Langø (hammer handle is 40 cm long).

A) Homogeneous, dark layered mafic gneiss.

B) Folded, migmatitic gneiss comprised of thin dark pyribolite layers in a quartzofeldspathic matrix.

Figure 2-4A

Figure 2-4B

and underformed but the diorite is locally discordant to the surrounding gneisses. It contains abundant angular meter-size and smaller gneiss inclusions, mainly pyribolite, that are largely unaffected by the diorite, although a biotite selvage was observed around one. Apophyses of the diorite extend into the gneiss, and small pockets of presumably late-stage pegmatitic material with bladed biotite (up to 10 cm long) are present. The overall features of the Nordnor diorite suggest that it is a post tectonic minor intrusion, although Berthelsen (1960) indicated that it was of replacement origin based on the similarity in the orientation of fold axes between inclusions in the diorite and surrounding gneiss.

The Great Pyribolite is a black massive to layered hornblende-pyroxene plagioclase gneiss that locally contains garnet-bearing layers. A few conformable layers of small ultramafic pods were observed and a pyroxene diorite horizon crops out along its entire length. This diorite is much paler than, and has been deformed along with, the enclosing pyribolite. The latter relationship contrasts this diorite with the one near Nordnor.

Although only three of the eight principal lithostratigraphic units that comprise Tovqussap Nuna occur on Langø, the variations within these three units are similar to the total range observed in the lithologies throughout the area. This becomes apparent upon reading Berthelsen's thin section descriptions which also serve to bring out the polymetamorphic nature of the rocks. The fact that the gneisses are layered on a scale that ranges from cm to tens of meters allows one to sample a variety of rock compositions at each locality.

This lithologic variation, the complex nature of the samples described by Berthelsen, the good exposure and favorable physiographic features made Langø a prime target for detailed sampling for petrologic study prior to the onset of field work during the summer of 1973. Consequently, a comprehensive suite of 69 samples was collected on Langø, and augmented in part by material supplied courteously by the Geological Survey of Greenland.

CHAPTER 3

III. PETROGRAPHY

A. Introductory Statement

For the purpose of understanding the metamorphic evolution of Langø, the various samples have been classified according to observed mineral assemblages, and divided into eight groups. A tabulation of modal mineralogies and the corresponding petrographic group are given in Appendix I, and locations of the samples are illustrated in Figure 3-1. Rather than presenting petrographic descriptions of individual samples, the features of each group are summarized as a whole in this section. In addition, a limited amount of compositional data are presented where it is considered relevant to the description. A detailed discussion of mineral chemistry is given in Chapter 4. Note that the few samples of ultramafic rocks that were collected are not included in the presentation here.

Throughout the text, constant emphasis will be placed on the polymetamorphic character of the samples. The first episode of metamorphic mineral growth will be referred to as "primary" or "MI", and the second episode of metamorphic mineral growth will be referred to as "secondary" or "MII".

B. Potassium Feldspar Gneisses

1. General Overview

These are typically fine- to medium-grained leucocratic rocks in which the amount of quartz and feldspar generally exceeds 90%. The

Figure 3-1: Sketch map of Langø illustrating locations where samples were collected (compare with Fig. 2-3).

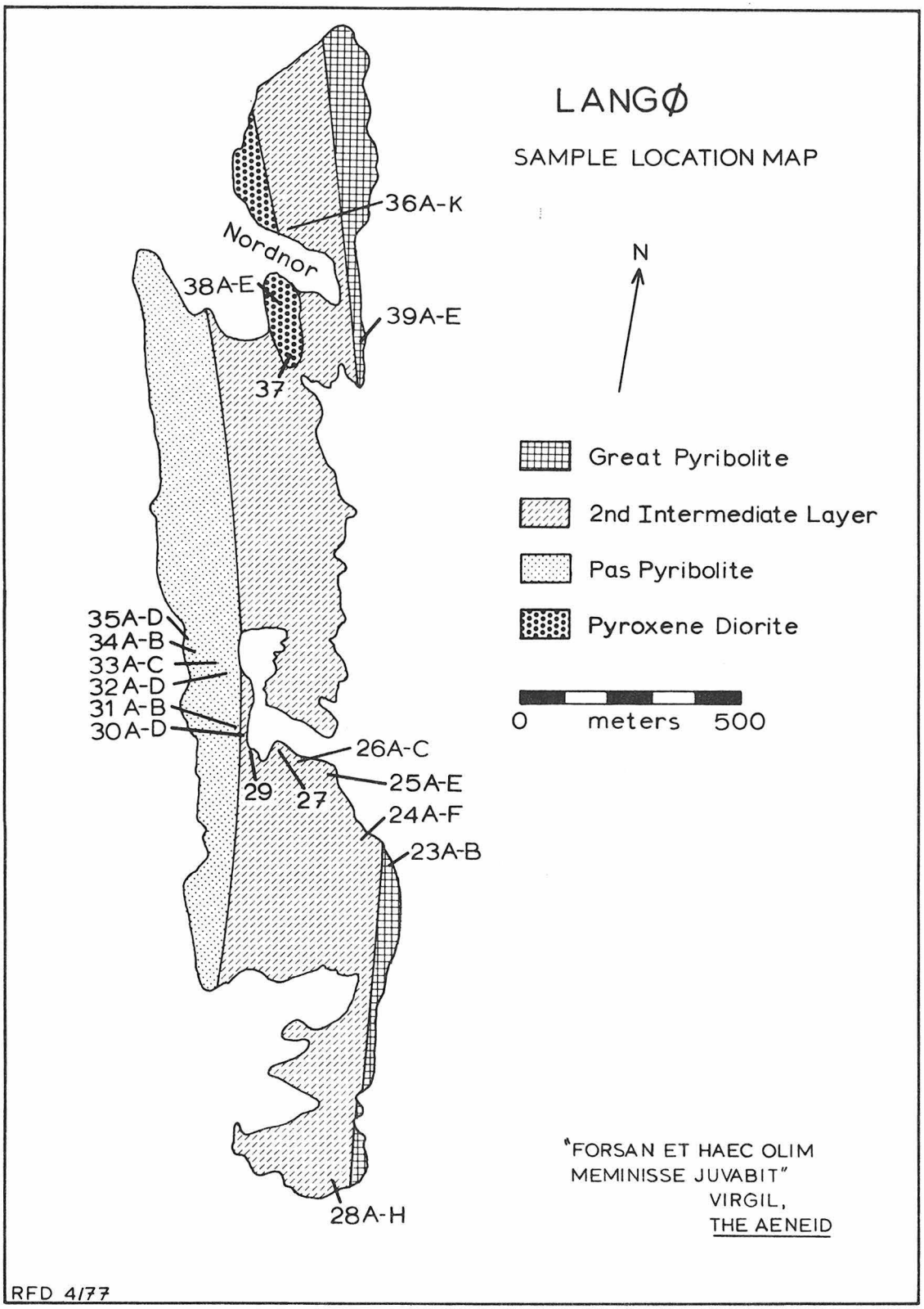
LANGØ
SAMPLE LOCATION MAP
N
Great Pyribolite
2nd Intermediate Layer
Pas Pyribolite
Pyroxene Diorite
0 meters 500
36A-K
Nordnor
38A-E
39A-E
37
35A-D
34A-B
33A-C
32A-D
31 A-B
30A-D
26A-C
25A-E
24A-F
23A-B
29
27
28A-H
"FORSAN ET HAEC OLIM
MEMINISSE JUVABIT"
VIRGIL,
THE AENEID
RFD 4/77

samples were collected from various layers within the biotite gneiss and garnet granulite lithologies. Variations in the modal abundances of quartz, plagioclase, and potassium feldspar indicate that the samples range from tonalite through granodiorite to adamellite, but no petrogenetic implications should be inferred from this.

Several percent biotite occurs in all samples, and scattered cm-size crystals of burgundy-colored garnet are present in a few. Very fine-grained, fibrous sillimanite is found along foliation planes in garnet-bearing samples, and traces of kyanite, white mica, ilmenite, magnetite, hematite, chlorite, zircon, and apatite have been observed in thin section. Relic cordierite has been identified in one sample, but no orthopyroxene has been found, although its former presence can be inferred on the basis of textural criteria to be discussed shortly. Although it is difficult to ascertain the nature of the protolith of these samples, the overall fine grain size and highly aluminous and siliceous compositions suggest that these gneisses may be derived from a series of felsic volcanic rocks and/or pelitic sediments.

2. Petrography and Mineralogy

The texture of these gneisses ranges from lepidoblastic to granoblastic, and is characterized by irregularly-shaped, sutured grain boundaries among quartz, feldspar, and biotite (Figure 3-2A). Foliation, where observed, is marked by the parallel alignment of grains of biotite and/or sillimanite. Quartz also shows preferential orientation locally, but the feldspars tend to be randomly oriented.

Figure 3-2: Photomicrographs of textural features in potassium feldspar gneisses (A, B - transmitted cross-polarized light; C, D - transmitted, plane-polarized light; all bar scales = 100 μm).

A) Typical texture of potassium feldspar gneiss. Note smooth to irregular grain boundaries, strain bands in quartz, and grid twinning in microcline (sample 24D).

B) Antiperthite consisting of patches of alkali feldspar in a plagioclase host (24D).

C) Tabular, dark-brown and TiO_2-rich biotite. These are grains of primary biotite that are aligned parallel to the foliation in the sample (27).

D) Aggregate of pale greenish-brown, TiO_2-poor secondary biotite. These are intergrown with quartz and radiate from a "nucleus" of magnetite (36B).

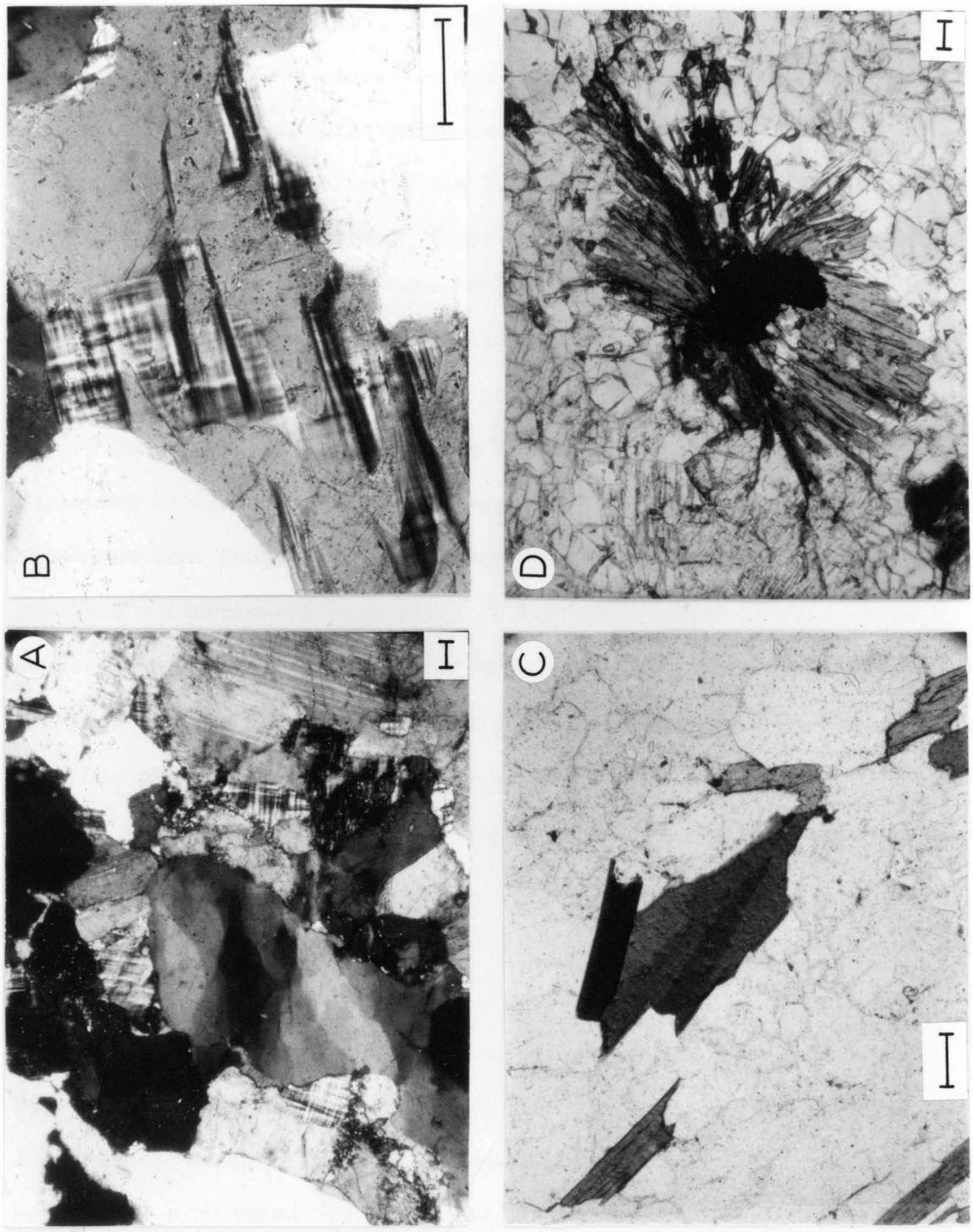
B
D
A
C

Mosaicism and recrystallization of the quartz and feldspars have resulted in widespread reduction in average grain size, although the extent to which these processes occurred varies tremendously from sample to sample. A relic polygonal, granulite-like texture with straight to slightly-curved grain boundaries and 120^{o} triple junctions is present in a few samples. There appears to be an overall transition from a coarse polygonal texture, to mortar texture, to finer-grained recrystallized material. In addition, most samples preserve evidence for two episodes of mafic mineral growth.

Quartz ranges from elongate lobate grains that parallel the foliation to irregularly-shaped, ameoboid grains with local tiny apophyses that project outwards between feldspar grain boundaries. Undulose extinction is ubiquitous in the quartz, and is related to subparallel or approximately orthogonal sets of strain bands (Fig. 3-2A). The resultant mosaicism coupled with minor to extensive recrystallization has produced smaller strain free subgrains in these areas. Boundaries with adjacent feldspars are locally granulated and recrystallized in addition.

Plagioclase has only a limited range in composition to ($An_{14.9}Ab_{84.2}Or_{0.9}$ to $An_{21.0}Ab_{78.1}Or_{0.9}$), and occurs as subequant to irregularly-shaped grains that locally show a preferred orientation. Most are simply twinned (albite and pericline), although untwinned varieties do occur. In addition, most grains are optically homogeneous, but grains with symmetrical or undulose extinction are present. Bent twin lamellae and the formation of subgrains by recrystallization of larger ones also occur.

Some of the plagioclase in these samples is distinctly antiperthitic (Figure 3-2B). The form of the exsolved alkali feldspar phase ranges from regularly-distributed, rounded to elongated μm-sized and larger blebs to irregularly-shaped patches and stringers that comprise up to half of the feldspar. The latter are more appropriately termed "mesoperthite". Rare aggregates of an unidentified, colorless, μm-size acicular Al-rich phase occur along some plagioclase grain boundaries.

In addition to the above, potassium feldspar also occurs as large subequant to irregularly-shaped grains similar in size to the quartz and plagioclase, and as smaller interstitial grains that locally partly surround and embay plagioclase. The position of much of this interstitial potassium feldspar suggests that it formed via granular exsolution from the plagioclase.

The potassium feldspar is commonly perthitic, as indicated by the presence of tiny submicron, elongate blebs that have a refractive index higher than the host. Aggregates of an acicular colorless mineral, similar to those associated with plagioclase, occur along potassium feldspar grain boundaries.

Most of the potassium feldspar, including the exsolved blebs in plagioclase, display spindle/grid twinning characteristic of microcline (Fig. 3-2A, 2B). However, some of the interstitial alkali feldspar is apparently untwinned and may be orthoclase. If this interstitial alkali feldspar did in fact originate by granular exsolution from plagioclase, then the observations suggest that unmixing in the feldspars was developed on an extensive scale prior to the monoclinic (orthoclase) - triclinic (microcline) inversion. There is only a small

range in the composition of the potassium feldspar ($Ab_{11.5}Or_{88.5}$ to $Ab_{4.0}Or_{96.0}$), and no differences were detected among large grains, blebs in plagioclase, and interstitial grains.

Biotite is the principal mafic mineral in the potassium feldspar gneisses and shows a range in texture, color, and composition. The most common occurrence is as dark mahogany-brown, Ti-rich (up to 4.5 wt % TiO_2) stubby to elongate grains that tend to delineate the foliation in these samples (Figure 3-2C). In those samples in which the quartz-feldspar grain boundaries are sutured, the contacts with biotite tend to be irregular also. Brown to green biotite also occurs in parallel to rarely vermicular intergrowth with quartz that tend to radiate from a "nucleus" of magnetite (Figure 3-2D). Potassium feldspar is not present in the intergrowth. These intergrowths are randomly-oriented and crosscut the pre-existing foliation. Hence, they are post-tectonic and are interpreted to represent the breakdown products of pre-existing orthopyroxene that formed by the reaction:

$$Opx + Kf + Fluid \rightleftarrows Bio + Qtz + Mt.$$

Green, Ti-poor ($\lesssim$0.5 wt % TiO_2) biotite occurs as rims around garnet, or along fractures in the garnet where in both cases it is typically intergrown with kyanite and quartz. Potassium feldspar is absent from these intergrowths. The petrographic features suggest that the following reaction has taken place:

$$Gar + Kf + Fluid \rightleftarrows Bio + Ky + Qtz.$$

In a few rare instances, biotite grains have been replaced along cleavage planes by dark green chlorite.

Biotite ranges in Mg-value* from 0.49 to 0.81, with the maximum variation in a single sample being approximately half this amount. Without exception those "secondary" biotites that formed by the breakdown of garnet or inferred to have formed from orthopyroxene (or corderierite, see below) are more Mg-rich than "primary" biotites. In addition, biotite that occurs in samples with either garnet, sillimanite or kyanite are more aluminous (17.8-20.6 wt % Al_2O_3) than those that occur by themselves (15.8-17.8 wt % Al_2O_3).

The garnet is pale brownish-pink, and occurs typically as rounded, resorbed porphyroblasts up to 1 cm across. Nearly every garnet is surrounded completely by intergrowths of brown kyanite and green biotite as indicated above (Figure 3-3A, 3C). The garnet contains small (5-50 μm) inclusions of tabular brown biotite, quartz, plagioclase, and rarely sillimanite. The quartz inclusions are sometimes arranged in a circular pattern suggesting rotation of the garnet during growth.

The garnet is predominantly almandine - pyrope, and is low in CaO (0.6-1.1 wt %) and MnO (1.8-3.9 wt %). The total measured range in Mg-value (.18-.37) is about twice that in an individual sample. All garnet grains are zoned slightly, being more Fe-rich on the rim than in the core.

In one sample (24C), an aggregate of polygonal grains comprised of yellow, isotropic material occur in association with garnet (Figure 3-3B). These are interpreted to be altered cordierite. The yellow material ("pinite"?) is identical to that observed in less altered

---

*Mg-value = cations Mg/(Mg + Fe + Mn)

Figure 3-3: Photomicrographs of textural features in potassium feldspar gneisses (transmitted, plane-polarized light; all bar scales - 100 μm).

A) Intergrown kyanite-green biotite-quartz (top) replacing garnet (bottom) (24C).

B) Polygonal aggregate comprised of yellow isotropic material that appears to be pseudomorphous after cordierite. Needles along previous grain boundaries are kyanite (24C).

C) Close-up view of MII kyanite-green biotite intergrowth shown in A (24C).

D) Layer of primary (MI) grains of prismatic sillimanite; secondary (MII) kyanite, associated with garnet (see A) occurs elsewhere in this sample. Note elongate brown (MI) biotite grain in contact with sillimanite (24D).

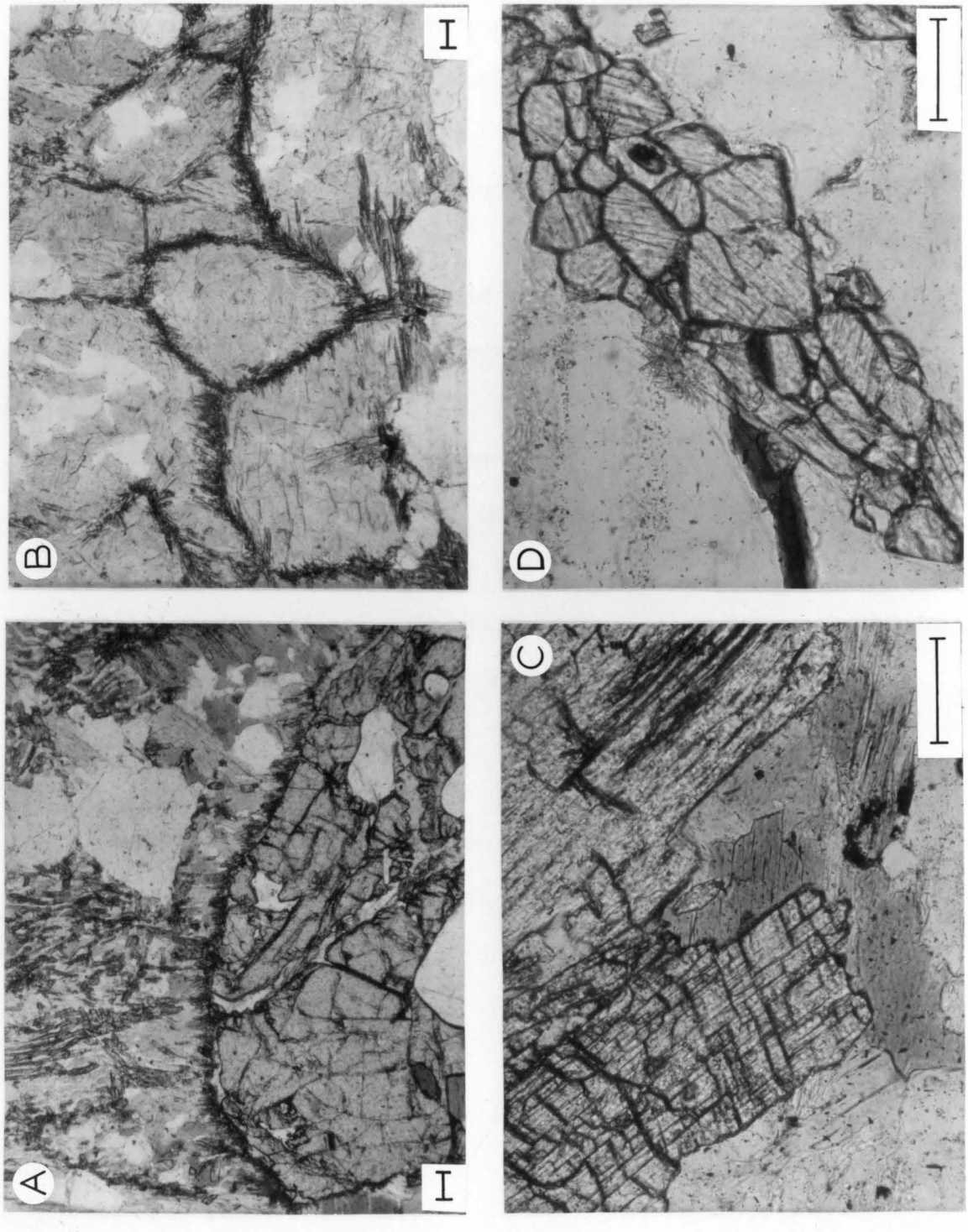
B
I
D
A
I
C

cordierite from other samples (e.g., 35861-1). It appears as if the "cordierite" had been in textural equilibrium with garnet.

This cordierite in 24C is surrounded by intergrowths of fine-grained green biotite and brown kyanite that had grown into and replaced the cordierite prior to alteration. The petrographic features suggest that the following reaction, analogous to the one inferred for garnet, occurred:

$$\text{Cordierite} + \text{Kf} + \text{Fluid} \rightleftarrows \text{Biotite} + \text{Kyanite} + \text{Qtz}.$$

Since no cordierite is actually preserved, its composition could not be determined.

Sillimanite is a rare yet important constituent of the potassium feldspar gneisses. It is acicular to stubby in habit with a prismatic cross-section, and is restricted in its occurrence to a few layers that are parallel to the foliation in the samples (Figure 3-3D). Sillimanite has been observed in contact with biotite and garnet, and occurs as inclusions in garnet. However, its relationship to cordierite is unclear.

In those samples that contain both sillimanite and kyanite, the two Al_2SiO_5 polymorphs have not been observed in contact. Thus, kyanite has grown later than and separate from sillimanite. The sillimanite is, however, locally replaced at its margins by a pale-brown isotropic material.

Fe-Ti oxides occur as anhedral subequant to elongate interstitial grains and include the assemblages: magnetite, ilmenite, ilmenite-magnetite, and ilmenite-hematite. The latter is restricted to garnet-free samples only and may be related to late stage oxidation. In

addition to forming the nuclei of the radiating green biotite-quartz intergrowths, magnetite granules occur at the margins of some brown biotite flakes.

Muscovite occurs as very minor late-stage interstitial grains where it replaces potassium feldspar and/or plagioclase. However, muscovite has never been observed in contact with sillimanite or kyanite in these samples.

3. Summary

The potassium feldspar gneisses on Langø are relatively simple rocks that preserve evidence for two episodes of mineral growth. The first produced the phases: biotite ± garnet ± cordierite ± sillimanite ± hypersthene (?), in which the biotite tends to be dark brown and Ti-rich; the second yielded biotite + quartz ± kyanite, in which the biotite tends to be pale green and Ti-poor. Emphasis should be placed on the occurrence of sillimanite as a primary phase and kyanite as a secondary phase.

C. Orthopyroxene Gneisses

1. General Overview

These are fine- to coarse-grained rocks that range from dark, layered types to pale rather homogeneous gneisses. The samples were collected from "hypersthene gneiss" units and from enclaves within the "garnet granulite" lithology on Langø. The samples are characterized megascopically by brown-weathering orthopyroxene, gray to white plagioclase, colorless to blue transluscent quartz, black biotite, and rare grains of dark gray, greasy-lustred cordierite. The layering

and foliation are related to the tendency for quartz and biotite to become concentrated in certain layers. Orthopyroxene locally forms porphyroblasts up to 2 cm across. Sillimanite occurs in these samples, but was not detected in hand specimen. Traces of talc, kyanite, rutile, zircon, and apatite were observed in thin section. The former presence of alkali feldspar is inferred from certain textural features seen in thin section.

The orthopyroxene-biotite ± cordierite gneisses probably represent higher grade equivalents of orthoamphibole-biotite ± cordierite gneisses that form an integral portion of the Malene Supracrustals elsewhere within the Godthåb District (McGregor, 1973; Dymek, unpublished). It is difficult to ascertain the nature of the protolith of the orthopyroxene gneisses, but since the orthoamphibole-cordierite gneisses appear to be metasedimentary rocks, the units on Langø may also be paragneisses.

2. Petrography and Mineralogy

The samples are characterized for the most part by a coarse polygonal texture marked by smooth grain boundaries and 120° triple junctions among the constituent minerals (Figure 3-4A, 4B). However, cordierite-bearing samples have rather extensively-developed sutured grain boundaries. The orthopyroxene gneisses do not display the large degree of mosaicism and strain-induced recrystallization so apparent in the potassium feldspar gneisses.

Foliation, which is apparent in hand specimen, is marked in thin section by variations in the proportions of light and dark minerals, as

Figure 3-4: Photomicrographs of texturial features in orthopyroxene gneisses (A, B, C - transmitted, cross-polarized light; D - transmitted plane-polarized light, all bar scales = 100 μm.).

A) Polygonal, equigranular mosaic of plagioclase (center, left), quartz (bottom, center), and orthopyroxene (top, right). Note smooth grain boundaries and 120° triple junctions (28A).

B) Polygonal, equigranular mosaic of cordierite (pale gray, unfractured) and orthopyroxene (dark gray with fractures). Note polysynthetic twinning in cordierite grain in top right hand corner of photo (28F).

C) Plagioclase grain with vermicular inclusions of quartz (28H).

D) Optically-continuous grain of orthopyroxene (P), the center of which is replaced by an intergrowth of brown biotite and quartz (28H).

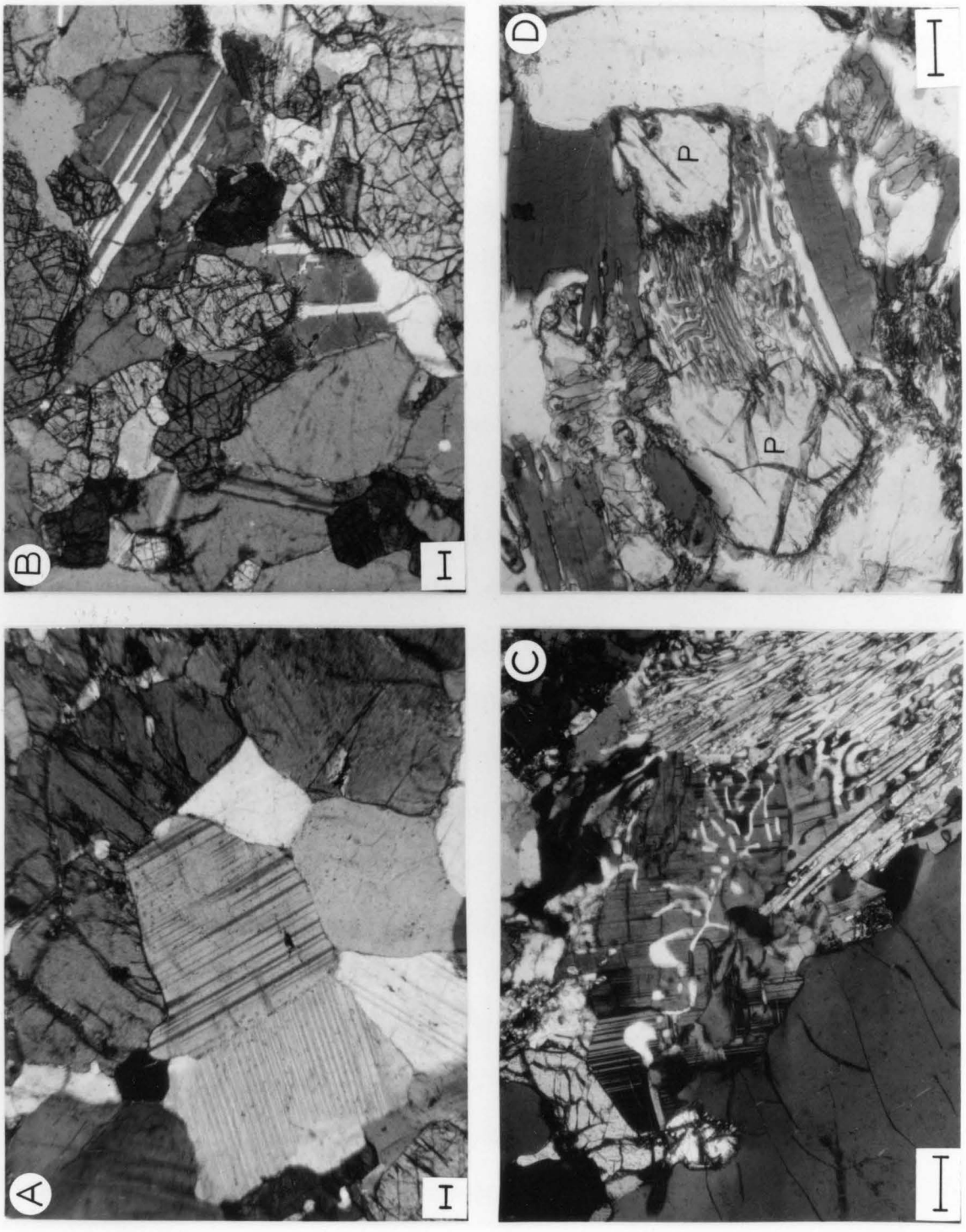
A
B
C
D
P
P

most phases do not appear to have a preferred orientation. Quartz however locally forms lenticles oriented parallel to the banding. These primary textures have been modified rather extensively in some samples by secondary mineral reactions that have produced a variety of mineral intergrowths.

The principal occurrence of quartz is as rounded to lobate grains that may be elongated parallel to the foliation, as mentioned above. Undulose extinction and strain features, although present, are not developed on an extensive scale. However, in sample 35861-1, strain induced mosaicism and minor recrysallization is a prominent feature in the quartz grains.

The secondary occurrences of quartz include parallel to vermicular intergrowths with biotite, vermicular intergrowth with plagioclase (myrmekite, Figure 3-4C), and vermicular intergrowths with cordierite. The first type is clearly related to the replacement of orthopyroxene, whereas the origin of the latter two types is not clear.

Plagioclase occurs as subrounded to slightly elongated grains that are simply twinned (albite and pericline) and optically homogenous. Rare bent twin lamellae and composite, "broken" grains that formed from pre-existing larger ones have been observed. The plagioclase in 35861-1 and 35861-2 is locally antiperthitic.

The range in measured composition for six samples is $An_{23.8}Ab_{74.7}Or_{1.5}$ to $An_{36.2}Ab_{63.1}Or_{0.8}$. Most grains are homogeneous chemically, but slight reverse zoning ($\lesssim$2 mole % An) is present locally. The range in composition in each sample tends to be small (<4 mole %

An), but in 35861-1, plagioclase with compositions $\sim An_{25}$ and $\sim An_{35}$ occur in separate layers.

Several types of biotite occur in the orthopyroxene gneisses as indicated by a range in textures and to some extent composition. Dark mahogany brown Ti-rich biotite (1.4-4.8 wt % TiO_2) occurs as stubby to blocky to acicular grains that tend to parallel the foliation. In three samples (28A, 28C, 28H) these contain inclusions of sillimanite (Figure 3-5D).

Brown biotite (1.4-2.7 wt % TiO_2) also occurs in parallel to vermicular intergrowth with quartz, replacing orthopyroxene and cordierite (Figure 3-4D). Kyanite occurs with the biotite and quartz associated with cordierite.

Elongate green biotite (0.6-1.0 wt % TiO_2), also intergrown with quartz (and rarely magnetite) replaces orthopyroxene (Figure 3-5A). Finally, pale-green biotite (<0.1 wt % TiO_2), intergrown with kyanite and quartz, replaces cordierite.

The total range in the measured Mg-value of the biotite is 0.69-0.88, with the variation in a single sample approximately one-third of this amount. The "secondary" biotite, which replaces orthopyroxene and cordierite, tends to be slightly more Mg-rich than "primary" biotite. The measured Al_2O_3-contents range from 15.4 to 19.4 wt %, with green biotite associated with kyanite being the most aluminous.

Orthopyroxene occurs as anhedral blocky grains that form rare porphyroblasts up to 3 cm across, irregularly shaped grains with embayed margins, and fine-grained ($\leq$10 μm) granules. The latter two

Figure 3-5: Photomicrographs of textural features in orthopyroxene gneisses (transmitted plane-polarized light; A, B-bar scale = 100 μm; C, D-bar scale = 50 μm).

A) Single crystal of orthopyroxene replaced by acicular grains of green biotite. Note contrast between this texture and that in Fig. 3-4D.

B) Single crystal of cordierite with turbid margins caused by very fine-grained MII kyanite needles that grow inward from the grain boundary. Biotite (B) also replaces cordierite here (28H).

C) Close-up of MII kyanite needles in cordierite grain shown in B. The other mineral shown here is quartz (28H).

D) Sillimanite (S) inclusions in biotite. Note ragged appearance of smaller grains (28H).

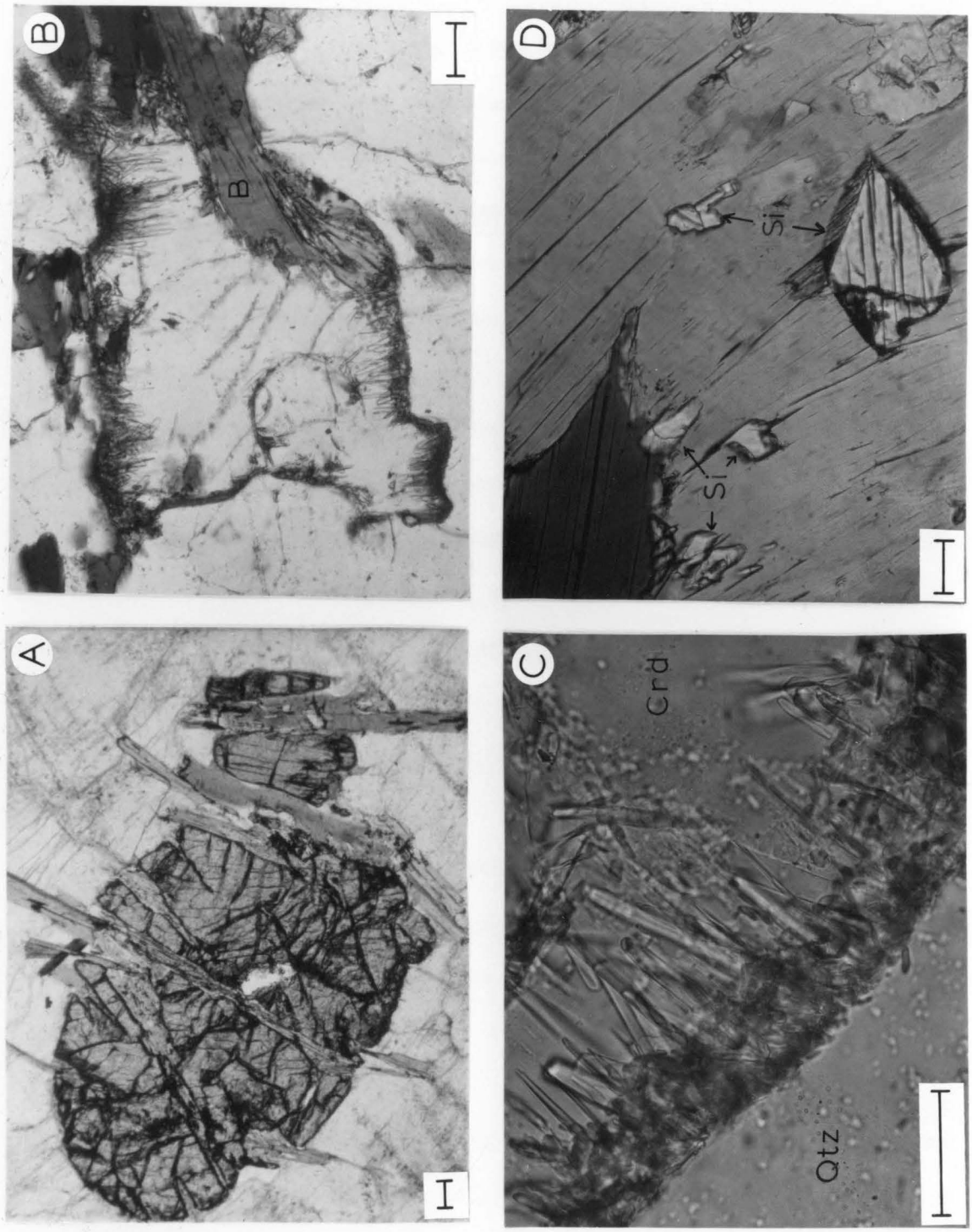
A
B
B
C
Crd
Qtz
D
Si
Si

textures are a consequence of secondary mineral reactions that produced biotite and quartz (Figure 3-4D, 5A). The inferred reaction is:

$$Opx + Kf(?) + Fluid \rightleftarrows Bio + Qtz.$$

In some samples, orthopyroxene contains euhedral to subhedral biotite inclusions, and at the same time is demonstrably replaced by biotite along its margins. All orthopyroxene grains show some degree of pleochroism from deep pink to pale red-brown to greenish-brown. Cores in some grains tend to be more intensely-colored than rims.

A very small percentage (<1) of the orthopyroxene has been altered to a very fine-grained, greenish-yellow, apparently isotropic material. This "uralitization" seems to have occurred before any of the secondary mineral reactions mentioned above. Local, minor alteration to talc occurs in samples 28A and 28B, and the orthopyroxene in sample 28C has a few grains of an elongate, colorless euhedral phase developed along fractures and grain boundaries. Although this mineral could not be identified positively, its morphology and occurrence suggest that it is anthophyllite.

The measured Mg-values of the orthopyroxene range from .65-.82, with the maximum variation in a single sample being .05. All the pyroxenes have an extremely low Ca-content (<.12 wt % CaO), but are relatively aluminous (3.8-8.1 wt % Al_2O_3), with cores containing more Al than rims.

Cordierite may occur as rounded to irregularly-shaped isolated single grains, or in elliptical clusters of polygonal grains that are probably the recrystallized remnants of larger single crystals. The cordierite is quite easily identified by the presence of one or more of

the following features: yellow pleochroic halos around zircon inclusions (indigo in cross-polarized light); complex interpenetrating twins (Fig. 3-4B); and dark turbid margins (Fig. 3-5B).

These turbid margins are related to the presence of minute (<5 μm wide) sheaves and needles of densely-packed kyanite (Figure 3-5C). This feature is similar to secondary gedrite-kyanite intergrowths described by Vernon (1972), except that no gedrite has been identified in any of the samples from Langø.

The presence of a low-Al_2O_3 phase seems to be required here, since cordierite should break down by a reaction of the type:

Cordierite + Fluid → Kyanite + Gedrite + Quartz.

X-ray diffraction studies of various mineral separates have so far yielded negative results with respect to the identification of gedrite. However, in sample 35861, kyanite-green biotite intergrowths replace cordierite, and in samples 28B and 28H, kyanite-brown biotite intergrowths replace cordierite in addition to ones that do not contain biotite. Thus, the replacement of cordierite may occur by the reaction:

Cordierite + Fluid + Kf(?) → Kyanite + Biotite,

with the biotite nucleating away from the cordierite in some cases. The extent to which cordierite is replaced by these intergrowths ranges from virtually complete to nil, even within a single thin section.

Most grain contacts between cordierite and orthopyroxene, as well as between cordierite and biotite, tend to be smooth. Hence, even though a given cordierite grain may be replaced extensively, the original smooth boundary with orthopyroxene (or biotite) is preserved. There is no evidence for cordierite-orthopyroxene incompatibility on Langø, and

where biotite is involved in the replacement of cordierite, this biotite formed during a second period of mineral growth. These observations indicate that the breakdown of cordierite was a complex process.

The cordierite is very magnesian (Mg-value = .88-.95), and the measured alkali contents are exceedingly small (Na_2O <0.05 wt %). No chemical zonation was detected in any of the grains that were analyzed.

Sillimanite occurs as tabular to elongate grains with a prismatic cross section in association with cordierite in sample 35861, and as inclusions in biotite in samples 28C and 28H (Figure 3-5D). Some of the sillimanite inclusions in biotite have ragged margins and appear resorbed. This feature may indicate that the sillimanite in 28B, 28C and 28H is a relic phase related to the assemblage sillimanite-cordierite-biotite prior to the appearance of orthopyroxene in these samples. Sample 35861 does in fact contain the assemblage sillimanite-cordierite-biotite.

Kyanite occurs as a secondary mineral replacing cordierite (Figure 3-5B and 5C). In general, kyanite and sillimanite are not in contact. However, in sample 35861 previous cordierite-sillimanite grain boundaries are now separated by a thin selvage of kyanite needles. The kyanite grows into and replaces the cordierite, with sillimanite retaining its euhedral, prismatic form, apparently being unaffected by the growth of the kyanite.

The only oxide phase observed in the orthopyroxene gneisses is rutile. It occurs as blocky interstitial grains up to 100 μm across and as tiny (<10 μm) granules scattered throughout primary biotite in

samples 28A, 28B, 28C, and 28H. Pyrite is a rare accessory phase in samples 28D and 28E.

3. Summary

The orthopyroxene gneisses are complex rocks that show petrographic evidence for multiple episodes of mineral growth. The assemblages (including quartz + plagioclase): orthopyroxene-biotite, orthopyroxene-cordierite-biotite, and cordierite-sillimanite-biotite formed during MI or the primary stage of mineral growth. During MII or the secondary stage, orthopyroxene was replaced by biotite + quartz, and cordierite was replaced by kyanite or kyanite + biotite. As was the case with the potassium feldspar gneisses, the first episode of mineral growth in the orthopyroxene gneisses is characterized by sillimanite, whereas the second episode produced kyanite.

D. Pyribolite Gneisses

1. General Overview

These are medium- to coarse-grained, dark-colored, relatively homogeneous to layered gneisses collected from the Pas Pyribolite, the Great Pyribolite, and pyribolite horizons in the 2nd Intermediate Layer. They are characterized in hand specimen by brown orthopyroxene, black hornblende and clinopyroxene, and gray to white plagioclase. Quartz was observed only in cross cutting veinlets.

The layering is due to differences in the relative amounts of mafic minerals and plagioclase in adjacent layers, whereas homogenous types tend to have a "salt and pepper" textured appearance. Those layers that are virtually pure hornblende, pyroxene or plagioclase tend to be

slightly coarser-grained than the rest of the sample, which accentuates the banding. Small amounts of ilmenite, magnetite, biotite, and secondary quartz and amphibole, as well as traces of apatite and zircon were observed in thin section. Rare grains of rutile occur in one sample (35C).

Some of the cm-scale layering that is present may be related to original variations in plagioclase and mafic mineral content, and this certainly seems to be the case for meter-size layers. Elsewhere in the Godthåb District banded amphibolites, not unlike some on Langø, result from extensive deformation of pillow structures. The absence of these or any other "primary" textural features in the pyribolite gneisses on Langø, makes it difficult to infer the nature of their protolith. However, the compositions of these rocks would indicate that they represent predominantly a series of highly-metamorphosed mafic volcanic rocks. The fact that the mafic minerals tend to be Mg- and/or Ca-rich might also indicate a calcareous component in the protolith.

2. Petrography and Mineralogy

The samples are all characterized by an extremely well-preserved coarse polygonal texture with smooth grain boundaries and 120° triple junctions among pyroxene, hornblende, plagioclase (Figure 3-6A and 6B). Some of the larger grains of pyroxene have bent cleavages, but the samples are in general remarkably devoid of evidence of strain. Many mineral grains tend to be slightly elongate parallel to the foliation.

Samples from the Great Pyribolite and the 2nd Intermediate Layer display rather extensive development of secondary quartz - Ca-amphibole coronas around grains of pyroxene. However, these coronas are absent

Figure 3-6: Photomicrographs of textural features in pyribolite gneisses (A, B, C - transmitted, plane-polarized light; D - transmitted cross-polarized light; all bar scales - 100 μm).

A) Polygonal, mostly equigranular intergrowth of plagioclase (white), hornblende (dark gray), and orthopyroxene and clinopyroxene (pale gray). Note smooth grain boundaries and 120^{o} triple junctions (30).

B) Subhedral to anhedral hornblende grains with exsolved Fe-Ti oxide grains concentrated at grain boundaries (39E).

C), D) Plagioclase grain comprised of irregularly-shaped blebs with composition An_{70-75} in a host with composition An_{55-60}. This texture may be related to exsolution associated with the Huttenlocher solvus (24E).

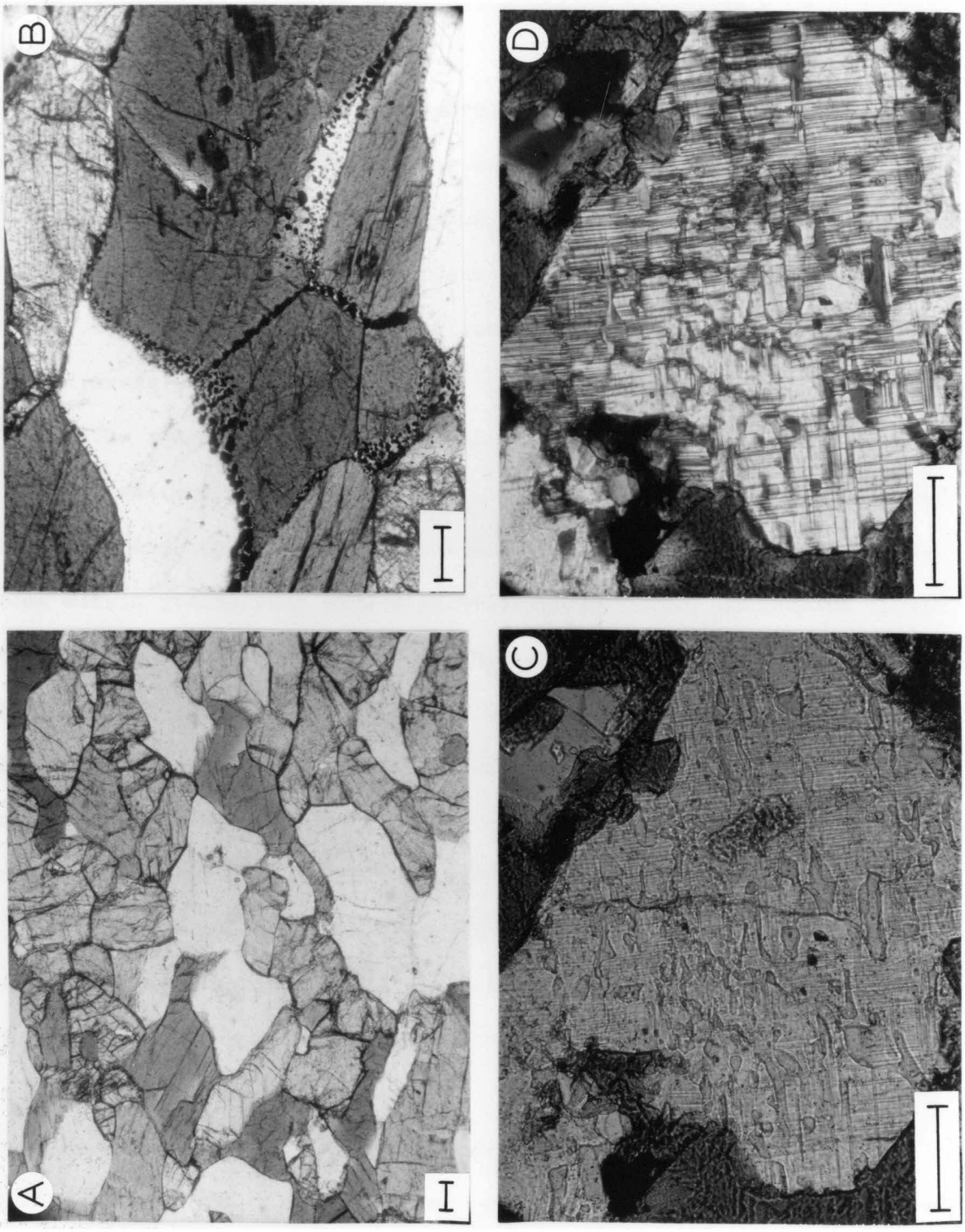
B
D
A
C

from samples collected within the Pas Pyribolite. In the latter, Ca-amphibole replaces portions of pyroxene grains producing a patchwork texture.

Plagioclase occurs as anhedral subrounded to slightly elongate grains with simple twinning (albite and pericline). The plagioclase in all samples may contain inclusions of pyroxene and hornblende, and itself occur as tiny inclusions within these phases. Optical zoning is typical of the plagioclase with extinction zones being parallel to boundaries with adjacent grains of pyroxene.

The measured range in composition in the nine samples studied in detail is extremely large ($An_{32.8}Ab_{65.7}Or_{1.5}$ to $An_{79.0}Ab_{20.7}Or_{0.3}$), and reverse zoning, typically <3 mole % An, occurs. In sample 24E, compositions within grains that show highly-irregular patchy extinction apparently fall in two groups: An_{48} to An_{60} and An_{71} to An_{79}. The more calcic varieties occur as rounded to elongate blebs (<5-40 μm wide) within the more sodic host (Figure 3-6C, 3-6D). Such textural features suggest an exsolution origin and the compositions are appropriate for the Huttenlocher immiscibility gap (Huttenlocher, 1942; Nissen, 1971).

Core compositions in other samples range from An_{32} to An_{60}, with the range within an individual specimen being $\lesssim$3 mole % An. However, in sample 35B, homogenous plagioclase with compositions An_{36}, An_{43}, and An_{60} occur in three distinct layers. (Pyroxene and hornblende compositions are also different in these three layers.)

Orthopyroxene, clinopyroxene or both are present in all samples in this group. They occur as anhedral, untwinned grained (Figure 3-6A) that only rarely display exsolution lamellae. Orthopyroxene forms rare

porphyroblasts up to 1 cm across in some samples (e.g., 23B, 35C). The pyroxene in most samples tends to be elongate in the plane of the foliation. Some grains contain exsolved, oriented platelets and rods of ilmenite (?).

In samples from the Great Pyribolite and 2nd Intermediate Layer, most pyroxene grains are surrounded by spectacular coronas comprised of green Ca-amphibole (Figure 3-7A). The amphibole typically occurs in vermicular intergrowth with quartz (Figure 3-7B), and may contain blocky grains of magnetite and ilmenite in addition. The extent to which these amphibole coronas develop varies tremendously, even within a single thin section, but they always occur only along previous pyroxene-plagioclase grain boundaries.

In samples from the Pas Pyribolite, patches within some of the clinopyroxene grains have been replaced by green Ca-amphibole and quartz. This type of replacement also occurs along the margins of pyroxene grains, but the coronas seen in the other samples are absent here.

The petrographic features involving the replacement of pyroxene by Ca-amphibole suggest that the following "retrograde" reaction has occurred:

$$\text{Pyx} + \text{Plag} + \text{Fluid} \rightarrow \text{Ca-amph} + \text{Qtz}.$$

Orthopyroxene is strongly pleochroic from green to pink, with cores of some grains being more intensely-colored than rims. It is uniformly low in Ca-content (0.2 to 1.0 wt %), and contains only small amounts of Al_2O_3 (0.2 to 2.9 wt %), with cores being more aluminous than rims. There is a very large range in Mg-value, with measured compositions being $Wo_1En_{77}Fs_{22}$ to $Wo_1En_{52}Fs_{47}$.

Figure 3-7: Photomicrographs of textural features in pyribolite gneisses (transmitted plane-polarized light; all bar scales = 100 μm).

A) Orthopyroxene (top) and clinopyroxene (lower right) mantled by coronas of secondary Ca-amphibole (39E).

B) Close-up of boundary between clinopyroxene (P) and secondary amphibole (A); note oriented oxide inclusions in pyroxene and vermicular quartz inclusions in amphibole (39E).

C) Primary grains of euhedral tabular biotite intergrown with hornblende and pyroxene (pale gray) and plagioclase (white) (23B).

D) Grain of bladed secondary biotite (B) that crosscuts orthopyroxene (bottom left) and hornblende (top left) (25D).

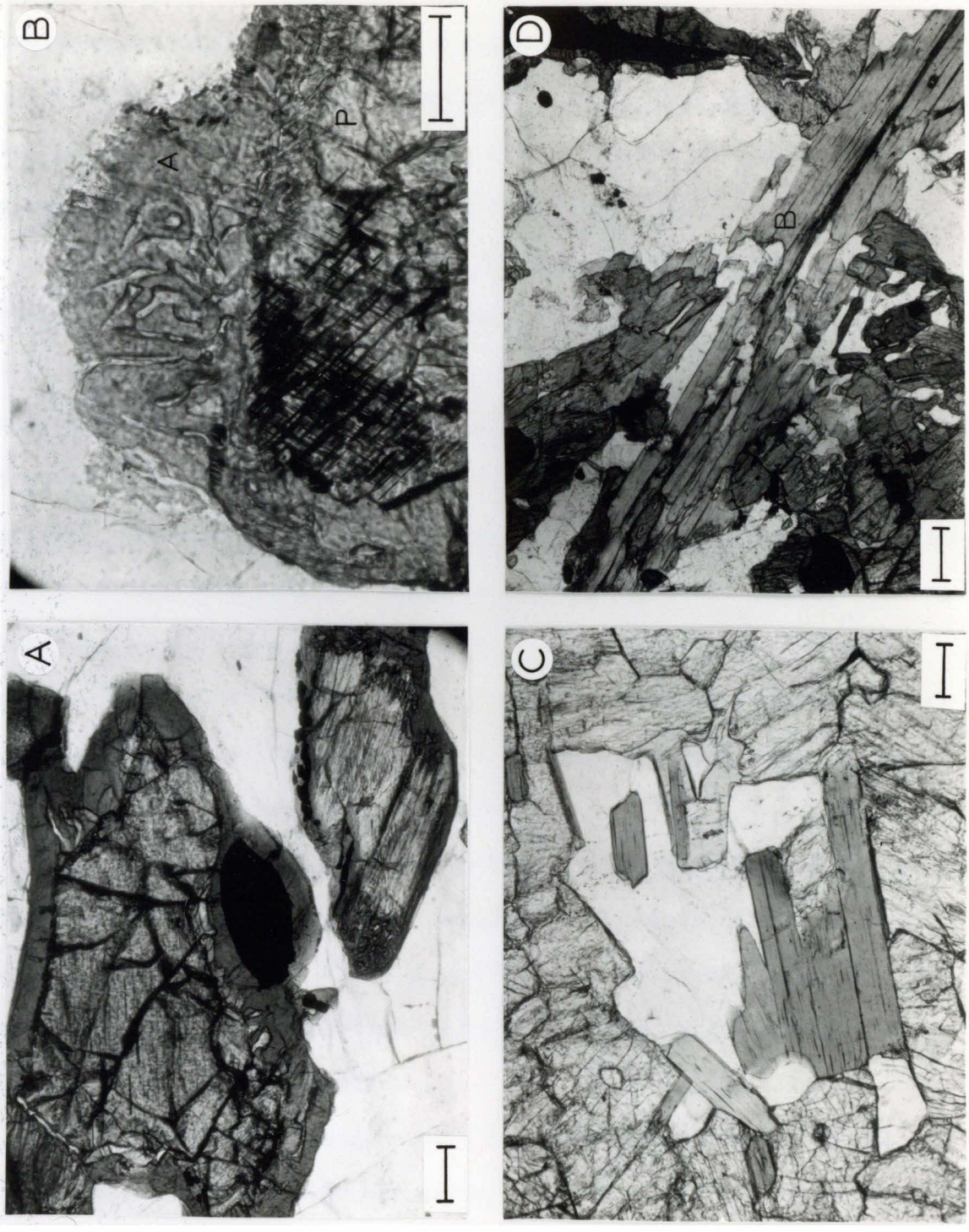
B
A
P
D
B
A
C

Clinopyroxene is faintly pleochroic in shades of pale green, and there are no observable differences in color between cores and rims. Ca-contents are high (21.1-24.3 wt % CaO), and decrease slightly with decreasing Mg-value. Measured compositions range from $Wo_{48}En_{47}Fs_5$ to $Wo_{46}En_{35}Fs_{19}$. The Al_2O_3 - contents range from 0.6 to 3.6 wt %, with cores being slightly more aluminous than rims.

Primary hornblende ranges from euhedral grains with a diamond-shaped cross-section to anhedral grains elongate in the plane of the foliation. Some samples contain cm-size clusters of hornblende grains that may represent the recrystallized remnants of larger single crystals. Exsolved oriented platelets of ilmenite occur scattered throughout many grains. Ilmenite also occurs as tiny granules that in some samples tend to be concentrated near the edges of single hornblende grains or along hornblende-hornblende grain contacts (Figure 3-6B). Pleochroism is strong, with colors ranging from greenish-brown to olive green to very dark green. Cores tend to be more darker-colored than rims. A few simple (100) twins have been observed.

The contents of Ca (10.5-12.8 wt % CaO), Al (10-14 wt % Al_2O_3) and Ti (1.5-3.0 wt % TiO_2) are high, with cores being slightly more Ti- and Al-rich than rims. The higher Ti-content of cores is probably the cause of the darker coloration. There is a very large variation in measured Mg-values (0.52-0.90).

Secondary hornblende occurs intergrown with tiny (1-10 μm) blebs of quartz as narrow continuous coronas around pyroxene, and as irregular patches within, or at the margins of, pyroxene grains where it replaces that phase (Figure 3-7A, 7B). In some samples, the secondary hornblende

surrounds small (25-100 μm) grains of ilmenite and magnetite in addition to pyroxene (Fig. 3-7A). Pleochroism in the secondary hornblende is strong, but the color is very different from primary amphibole, ranging from pale green to blue green to grass green. Ca-contents are similar to those in the primary hornblende, but Al_2O_3- and TiO_2-contents (8-10 wt % and 0.2-1.5 wt % respectively) are lower.

Biotite occurs as pleochroic pale to dark brown plates that tend to be aligned in the plane of the foliation. These appear to be in textural equibrium with pyroxene and primary hornblende (Figure 3-7C). There is a large range in Mg-value of the biotite (0.59 to 0.85). Measured Al_2O_3- and TiO_2-contents range from 14.0 to 15.7 and 2.4 to 6.0 wt % respectively. In a few samples, secondary green to brown biotite, intergrown with quartz, replaces orthopyroxene (Figure 3-7D). These have a higher Mg-value (0.87) and higher Al_2O_3-content ($\sim$16.5 wt %), but a lower TiO_2-content ($\sim$0.65 wt %) than primary brown biotite.

Ilmenite-magnetite represents the most common Fe-Ti oxide assemblage in the pyribolite gneisses, with magnetite-ilmenite-hematite (24E) and ilmenite-rutile (35B) occurring in one sample each. The hematite in 24E occurs as lamellae in ilmenite, and may be related to late stage oxidation, rather than conditions existing at the peak of metamorphism. TiO_2- contents of ilmenite always exceed 48 wt %, and calculated Fe_2O_3-contents are less than 5 wt %. The TiO_2-contents of magnetite are always less than 0.5 wt %, indicating only very small amounts of ulvöspinel substitution. Cr_2O_3-contents of the magnetite are generally less than 1 wt %, but values as high as 8 wt % were found, indicating a large range in chromite content.

Small amounts of sulfides, apatite and zircon occur dispersed throughout the samples, as well as some secondary carbonate. No epidote, sphene, chlorite or white mica have been observed.

3. Summary

The pyribolites represent a series of foliated gneisses that are homogenous to layered on a cm scale and characterized by a polygonal-granular equilibrium texture. A primary assemblage consisting of plagioclase, hornblende (green-brown), and pyroxene is present in all samples. Various degrees of subsequent retrograde reaction between plagioclase and pyroxene produced a secondary assemblage consisting of hornblende (blue-green) and quartz. Hence, the pyribolite gneisses, like the potassium feldspar gneisses and the orthopyroxene gneisses, preserve petrographic evidence for two episodes of mineral growth. It is important to note that the pyribolites contain hornblende that is in textural equilibrium with pyroxene, and hornblende that demonstrably replaces pyroxene.

A gap in the composition of plagioclase between $\sim An_{60}$ and $\sim An_{70}$ in sample 24E may be related to unmixing associated with the Huttenlocher solvus.

E. Garnet Pyribolite Gneisses

1. General Overview

Within the pyribolite gneisses on Langø are a few discontinuous cm-size layers that contain conspicuous red garnet. There appears to be more hornblende and correspondingly less pyroxene in these garnet-bearing layers, but otherwise they are virtually identical to the garnet-free

("ordinary") pyribolites, being medium- to coarse-grained layered mafic gneisses.

The garnet porphyroblasts range up to 2 cm in maximum dimension, and are irregular in form, i.e., they are lenticular and appear flattened in the plane of the foliation. In thin section, plagioclase, hornblende, orthopyroxene, biotite, ilmenite, magnetite, and green hercynitic spinel are found in addition to garnet. Clinopyroxene does not occur with garnet, and the formation of secondary hornblende by reaction between pyroxene and plagioclase has not occurred in the garnet-bearing layers, in contrast to the "ordinary" pyribolites. The fact that the garnet pyribolite forms lenses or layers within "ordinary" pyribolite suggests that they are simply a compositional variant of the latter, and are derived from a similar mafic volcanic protolith.

2. Petrography and Mineralogy

Except for the presence of irregularly-shaped, inclusion-rich garnet porphyroblasts, the overall texture of the garnet pyribolites is quite similar to the "ordinary" pyribolites, and consists of medium to coarse anhedral grains that form an equigranular polygonal mosaic. In sample 33C, which contains no pyroxene, the garnet, although quite irregular in overall shape, has smooth boundaries with hornblende and plagioclase, and is in apparent textural equilibrium with these phases (Figure 3-8A). In samples 39A, 39D, and 33B, which do contain pyroxene, the garnet tends to have jagged boundaries, and appears to be relic. Garnet contains inclusions of hornblende, plagioclase, biotite, hercynitic spinel, ilmenite, magnetite, and rarely pyroxene. The

Figure 3-8: Photomicrographs of textural features in garnet pyribolites (A, B, C - transmitted, plane-polarized light; C - transmitted cross-polarized light; bar scales in A, B, C = 100 μm; bar scale in D = 50 μm).

A) Contact between hornblende (H) and garnet with faceted boundary (G). Grains of plagioclase (white), biotite (B), magnetite (M), and hercynitic spinel (S) are also shown (33C).

B) Stringers of orthopyroxene emanating from edge of garnet grain. Hornblende, which occurs as inclusions in garnet is absent from the area of orthopyroxene and plagioclase (white), but reappears beyond this area (top left) (33B).

C) Complex plagioclase grains illustrating sharp optical discontinuity between cores ($\sim An_{50-60}$) and rims ($\sim An_{70-85}$) (33B).

D) Close-up of core-rim boundary in one of the plagioclase grains shown in C; note the presence of tiny submicron spindles that project from boundary between core (right) into rim (left). This spindle texture may be evidence for spinodal decomposition in the plagioclase, and the overall complex features displayed here and in Fig. 3-8C suggest the presence of the Huttenlocher solvus. (c.f., Figures 3-6C and 6D) (33B).

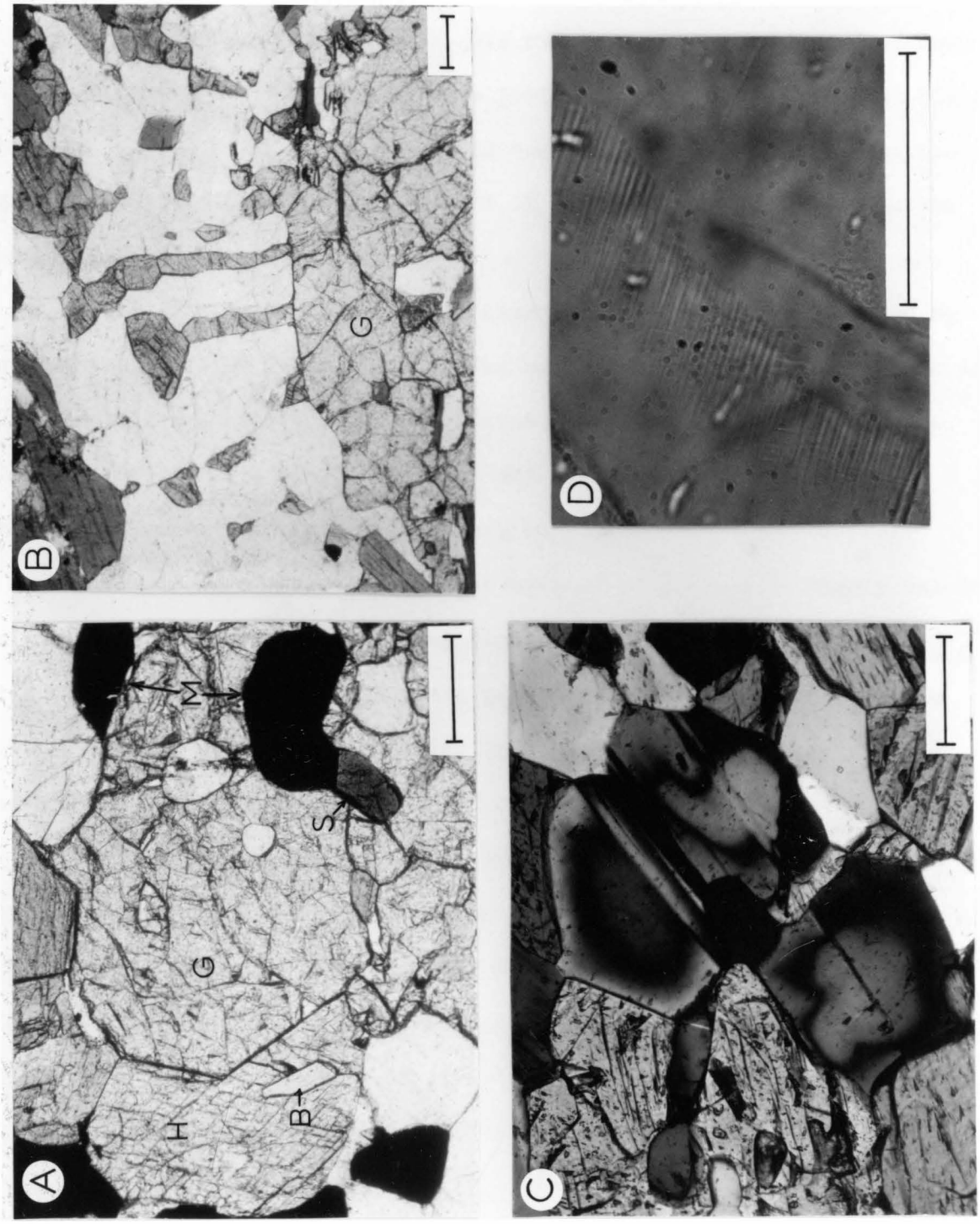
A
M
S
G
H
B
B
G
C
D

orthopyroxene that is present in the vicinity of garnet tends to occur as curvilinear blebs that project outward from the garnet boundary (Figure 3-8B). The area in which this pyroxene occurs is devoid of hornblende, whereas hornblende reappears just beyond where the pyroxene blebs terminate. The petrographic features suggest that the prograde reaction: ga + hbl $\rightleftarrows$ opx + plag has taken place in samples 39A, 39D, and 33B, but not in 33C.

The garnet is predominantly almandine - pyrope with measured Mg-values ranging from 0.21 to 0.40. The maximum variation in any sample is 0.10 and all grains are zoned, with rims being more Fe-rich than cores. CaO- and MnO-contents are small (<3.5 and <1.5 wt % respectively) and show no systematic variation from core to rim.

Plagioclase shows only slight optical zoning and is highly calcic, with measured compositions ranging from $An_{83.0}Ab_{16.8}Or_{0.2}$ to $An_{95.4}Ab_{4.6}Or_{0.0}$. The most calcic plagioclase occurs in the pyroxene-free sample (33C), and the range in composition in each garnet bearing layer is <5 mole % An.

Hornblende in the garnet pyribolites is dark green to green brown, and similar in form, but somewhat different in composition from that in the "ordinary" pyribolites. The range in Mg-values is less (0.60-0.72), and the Al_2O_3-contents are distinctly higher (14.1-16.4 wt % Al_2O_3). The orthopyroxene is likewise more aluminous (2.5 to 3.5 wt % Al_2O_3), and also has a more restricted range in Mg-value (0.63-0.72) than in ordinary pyribolites.

In samples 33B, 39A, and 39D brown biotite occurs only as small tabular inclusions in garnet, whereas in 33C it is also present throughout

the rest of the sample. The biotite tend to be more aluminuous (16.0-17.9 wt % Al_2O_3) and have a higher Mg-value (0.73-0.81) than in "ordinary" pyribolites. Ti-contents however are similar (2.3-3.9 wt % TiO_2).

Green hercynitic spinel is characteristic of the garnet pyribolite (Figure 3-8A). It occurs as rounded 10-100 μm grains dispersed throughout the sample (33C), or as inclusions in garnet (33B, 39A, 39D). It always occurs either adjacent to or surrounded by magnetite. Mg-values range from 0.45 to 0.55, and Cr-, Zn-, and calculated Fe^{3+}-contents are small. The occurrence and composition of magnetite and ilmenite is similar to that in "ordinary" pyribolites.

The plagioclase in garnet-free layers immediately adjacent to garnet-bearing layers is highly unusual, and consists of zoned cores ($An_{49.2}$ to $An_{61.4}$), separated by a marked optical discontinuity from more calcic rims with a range in composition ($An_{70.3}$ to $An_{89.9}$) (Figure 3-8C). A traverse across a typical grain demonstrates that the center of the core has composition $\sim An_{52}$ that changes continuously outward to $\sim An_{60}$. At the optical boundary, the composition "hops" to $\sim An_{70}$, with rim compositions changing continuously outward to $\sim An_{85}$. The cores tend to have irregular shapes that conform to the outline of grain boundaries with adjacent pyroxene and/or hornblende, although Figure 3-5D does not illustrate this feature well.

The origin of these complex plagioclase grains is problematic. There are no secondary amphibole coronas around pyroxene in their vicinity, hence the compositional variation does not appear to be related to "retrograde" plagioclase-pyroxene reaction. In addition, zoning

patterns of this type do not occur even where there is extensive replacement of pyroxene by secondary amphibole.

The prograde reaction: garnet + hornblende → opx inferred in these samples should yield calcic plagioclase as a product. Thus, the calcic rims may represent plagioclase formed as a consequence of this reaction, and the fact that rim compositions approach the composition of plagioclase near to garnet would support such an interpretation.

The compositional gap between core and rim in these samples is virtually identical to the one observed in 24E, where it appears that immiscibility related to the Huttenlocher solvus is present. Hence, it might be that the complex features in these plagioclase grains are related to reaction zoning as a consequence of the formation of orthopyroxene, in which the composition of the plagioclase changed continuously, and a compositional discontinuity resulted when the Huttenlocher solvus was encountered. This type of core-rim relationship is similar to those described for the peristerite solvus in lower grade rocks (Anderson, 1977). Here, the boundary between core and rim is marked typically by an array of extremely fine-grained spindles (Fig. 3-8D). Such a texture is suggestive of spinodal decomposition (Cahn, 1962), which complicates the relationships even further.

3. Summary

In general, the garnet pyribolites are very similar to "ordinary" pyribolites except for the presence of garnet and absence of clinopyroxene. They appear to represent a transition from an original assemblage of garnet + hornblende + plagioclase + spinel (e.g., 33C) to

orthopyroxene-bearing types (e.g., 33B, 39A, 39D) by the prograde reaction gar + hbl → opx. The lack of any retrograde reaction between plagioclase and pyroxene to yield secondary amphibole stands in marked contrast to "ordinary" pyribolites.

The occurrence of very anorthite-rich (i.e., aluminous) plagioclase, aluminous spinel, and aluminous hornblende emphasize the high Al-content of the garnet-bearing specimens. Mg-values of the hornblende and pyroxene are higher than those in many of the "ordinary" pyribolites. These features suggest that a high aluminum rather than high iron content has stabilized garnet in these samples. An additional interesting feature is the inferred occurrence of the Huttenlocher immiscibility gap in plagioclase from garnet-free layers in these samples.

F. Biotite-Rich Pyribolite Gneisses

1. General Overview

These are gray-green rocks collected from layers within the garnet granulite and biotite gneiss lithologies on Langø. The three samples studied include a medium-grained homogenous equigranular layered gneiss containing abundant green clinopyroxene (24B), a medium-grained gneiss with biotite-rich and pure quartz layers in it (36J), and a coarse-grained gneiss containing conspicuous pink orthopyroxene and pale green amphibole porphyroblasts up to 1.5 cm long (28I). These types of rocks were called "biotite pyriclasites" (= pyroxene-plagioclase rock) by Berthelsen (1960), and thin sections of two of his samples (35817 and 35861-3) were kindly provided for study by the Geological Survey of Greenland (GGU).

In thin section, it can be seen that virtually all of the amphibole is secondary. Primary hornblende is either not present (24B, 36J, 35861-3), or occurs in only very small amounts (<1%) as rare inclusions in pyroxene (28I, 35817) or surrounded by secondary amphibole (35817). Abundant quartz and plagioclase, in addition to pyroxene and amphibole, and trace amounts of rutile, zircon, apatite, and scapolite also occur.

The near absence of primary hornblende, and the presence of abundant modal quartz and biotite, serve to distinguish these samples from the "ordinary" pyribolites. There is nothing obvious in the field occurrence, mineral chemistry, or petrography which indicates what the nature of the protolith of these samples may have been.

2. Petrography and Mineralogy

These samples are extremely complex texturally, as evidenced by reaction relations between pyroxene and amphibole, and vermicular intergrowths of quartz-biotite, quartz-plagioclase, and quartz-amphibole. However, these features are all "secondary," and have been superimposed on a pre-existing polygonal intergrowth of plagioclase, pyroxene, quartz, and biotite. Quartz occurs in discrete layers or in lenticular pods, that, along with pyroxene and biotite, are elongate in the plane of the foliation.

A few grains of clear, twinned plagioclase occur as subrounded, equant to slightly elongated inclusions within pyroxene. These are apparently unzoned, and have only a slight range in measured composition from grain to grain ($An_{52.2}Ab_{47.1}Or_{0.7}$ to $An_{55.4}Ab_{43.6}Or_{1.0}$).

Plagioclase elsewhere in these samples has a variety of forms ranging from subequant to slightly-elongate to rounded and irregular. The latter type has its form dictated by adjacent boundaries with pyroxene or biotite. Although most of this plagioclase is clear and inclusion-free, the cores of some grains contain μm-size quartz blebs and/or have a faint yellow color. Core compositions are $An_{49.7}Ab_{49.8}Or_{0.5}$ to $An_{68.4}Ab_{31.3}Or_{0.3}$ with the more-calcic analyses from grains with either quartz inclusions or with yellow color. All grains studied show some degree of reverse zoning. Rim compositions range from $An_{53.8}Ab_{45.7}Or_{0.5}$ to $An_{86.8}Ab_{13.1}Or_{0.1}$.

Some of the clear plagioclase is surrounded by a vermicular intergrowth of quartz and yellow plagioclase. The boundary between core and rim tends to be marked by a pronounced optical discontinuity, in addition to the textural change (Figure 3-9A, 9B). This feature is best developed in sample 36J, where in one grain, cores have measured compositions $An_{63.3}Ab_{36.4}Or_{0.3}$ to $An_{67.4}Ab_{32.2}Or_{0.4}$, and the yellow plagioclase in the "overgrowth" ranges from $An_{75.2}Ab_{24.6}Or_{0.2}$ to $An_{81.3}Ab_{18.6}Or_{0.1}$. Although these compositions are appropriate for the Huttenlocher gap, plagioclase compositions in all samples from this group range from An_{50} to An_{86}, with several analyses in the range An_{67} to An_{75}.

All the pyroxene in these samples is incipiently to extensively replaced by either pale green amphibole, pale brown biotite, or both. Where pyroxene is replaced by amphibole, the latter forms a continuous rim that ranges from a few microns thick to cases where the pyroxene occurs as ragged relics in mm-size grains of amphibole (Figure 3-9C).

Figure 3-9: Photomicrographs illustrating textural features in biotite pyribolites (A, D - transmitted, plane-polarized light; B, C - transmitted, cross-polarized light; all bar scales = 100 μm).

A), B) Complex plagioclase grain comprised of a zoned core ($\sim An_{63-67}$) separated by a sharp optical discontinuity from a rim of vermicularly-intergrown quartz and plagioclase with composition ($\sim An_{75-81}$). These features may be related to a compositional gap associated with the Huttenlocher solvus (36J).

C) Grain of relic orthopyroxene surrounded by tremolitic hornblende containing biotite inclusions (24B).

D) Orthopyroxene grain replaced by biotite-quartz intergrowth (36J).

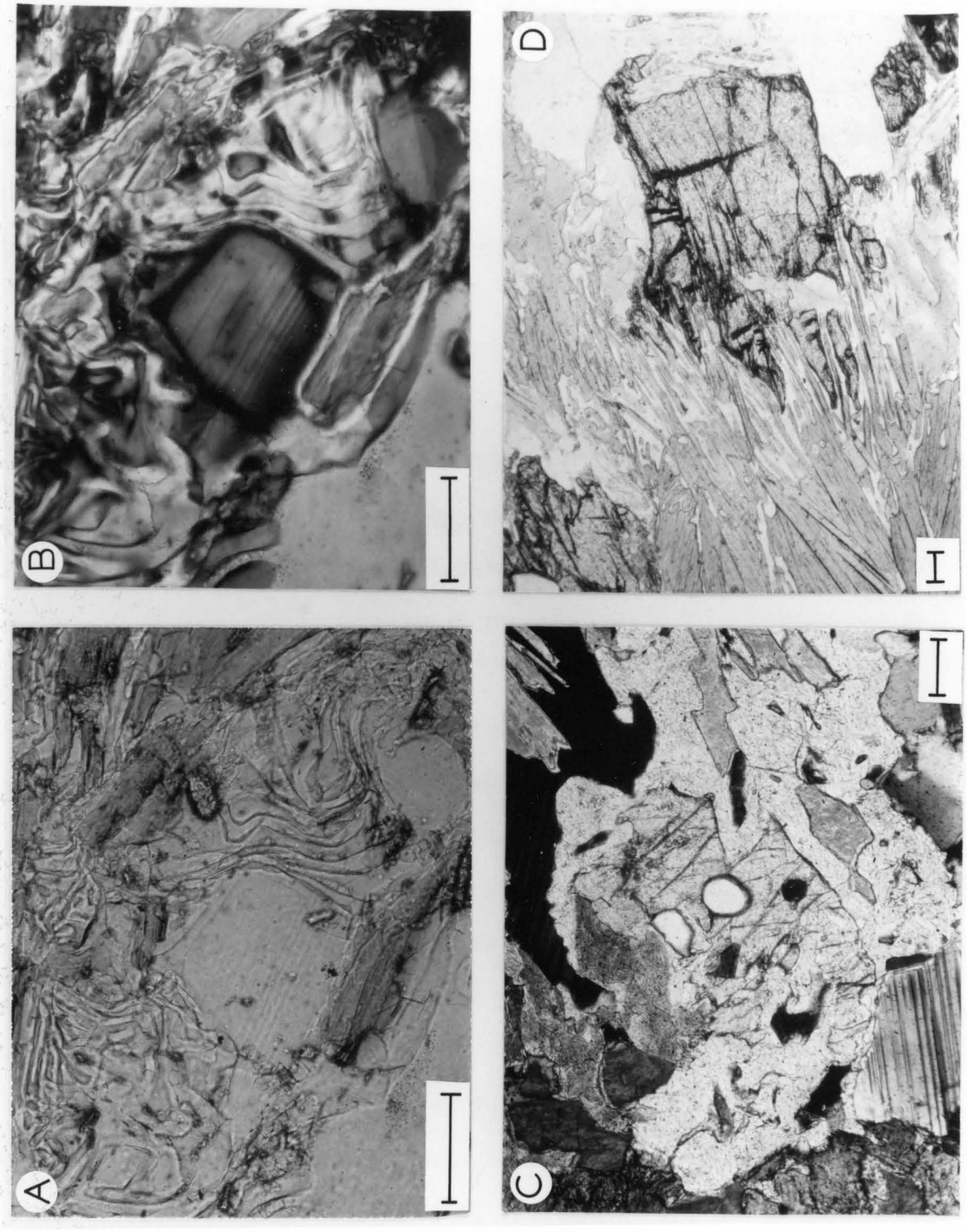
B
D
A
C

Where pyroxene is replaced by biotite, the latter forms vermicular to parallel intergrowths with quartz that consume pyroxene along grain boundaries (Figure 3-9D) leaving tiny relics behind as the replacement works its way inward. These features suggest that the following reactions have occurred:

$$\text{Pyx} + \text{Plag} + \text{Fluid} \rightarrow \text{Amph} + \text{Qtz}, \text{ and}$$

$$\text{Pyx} + \text{Kf(?)} + \text{Fluid} \rightarrow \text{Biotite} + \text{Qtz},$$

with both ortho- and clinopyroxene involved in the first reaction, and apparently only orthopyroxene in the second.

Other features present in pyroxene include kink bands, exsolution lamellae, and simple (100) twinning. These features are best developed in 28I where the combination of exsolution and twinning results in the herringbone structure characteristic of inverted pigeonite (Poldervaart & Hess, 1951).

Orthopyroxene is very pale brown and only faintly pleochroic. It is low in Ca-content (<0.3 wt % CaO), highly-magnesian, and has a very narrow range in measured composition ($Wo_1En_{89}Fs_{11}$ to $Wo_1En_{84}Fs_{15}$). Clinopyroxene ranges from colorless to very pale green. It has a high Ca-content (23.5 - 24.5 wt % CaO), and like the orthopyroxene, is highly magnesian and has only a narrow range in composition ($Wo_{48}En_{47}Fs_5$ to $Wo_{48}En_{49}Fs_3$).

The pale green amphibole in these samples locally contains abundant blebby inclusions of quartz. Chemically, the amphibole is high in CaO (12.5-13.3 wt %), low in Al_2O_3 (2.0-6.9 wt %), and is very magnesian (Mg-values - 0.89-0.94). Hence the compositions approach that of tremolite.

The tremolite tends to be associated with previous pyroxene-plagioclase grain boundaries, with the plagioclase near the secondary amphibole being reversely zoned in some cases. These features suggest that the amphibole was formed by the reaction:

Pyx + Plag-1 + Fluid → "Tremolite" + Qtz + Plag-2.

The production of a more calcic plagioclase and quartz probably explains the vermicular quartz-plagioclase intergrowths discussed above.

In sample 35817, the secondary amphibole replaces darker green primary amphibole in addition to pyroxene. The compositions of these darker green cores were not determined, but amphibole inclusions in pyroxene in sample 28I have 7.6 wt % Al_2O_3 and an Mg-value of 0.89.

Biotite is strongly pleochroic from brown to pale yellow brown, and occurs as elongate to stubby plates that for the most part are aligned parallel to the foliation in the sample. The ends of the biotite grains tend to be jagged, especially where they touch quartz or plagioclase. Al_2O_3- and TiO_2-contents range from 14.5 to 15.8 and 0.9-3.1 wt % respectively. The range in Ti-content in a given sample is smaller than the total range recorded, and those biotite analyses with the highest Ti-content are from rutile-bearing specimens. The biotite is quite magnesian, and has only a small range in measured Mg-values (0.88-0.93).

Although the vast majority of the biotite appears "primary", some grains near the pyroxene in samples 28I and 36J occur in parallel to vermicular intergrowth with quartz, and are often associated with tremolite, as mentioned above (Figure 3-6D). These biotite grains, like the amphibole, may be secondary, having formed by the reaction:

Opx + Fluid (+ Kf) → Biotite + Qtz.

However, unlike the potassium feldspar gneisses, and orthopyroxene gneisses, where "primary" and "secondary" biotite can be distinguished on the basis of TiO_2-content, in these samples there is no correlation between petrographic occurrence and composition.

Rutile occurs as equant to elongate subhedral grains (<1.0 mm) interstitial to pyroxene and plagioclase. Apatite occurs as subrounded single grains or in elliptical clusters of polygonalized grains. The latter may represent recrystallized larger single crystals. Scapolite is present in samples 35817 and 35861-3, and occurs as anhedral polygonal grains that appear to be in textural equilibrium with plagioclase. The scapolite has a high sulfur content (4.3-5.6 wt % SO_3), and low contents of F and Cl (<0.05 wt %).

3. Summary

The biotite-rich pyribolites are unique rocks that differ from other pyribolites on Langø by the presence of abundant quartz and biotite, the near absence of primary hornblende, and the uniformly high Mg-value of the mafic minerals. The occurrence of scapolite in 35861-3 is also a distinguishing feature. However, they are similar to the other pyribolites in that they display evidence for two episodes of mineral growth: a prograde assemblage of pyroxene and plagioclase, and a retrograde assemblage characterized by the formation of secondary amphibole.

G. Calc-Silicate Gneisses

1. General Overview

Two samples from Langø contain the assemblage clinopyroxene-plagioclase-sphene-scapolite and are termed "calc-silicate" rocks to

distinguish them from the other lithologies studied. Sample 33A was collected from a several meter thick layer termed "diopside-quartz rock" by Berthelsen (1960) that crops out continuously along half the length of the Pas Pyribolite. It is a layered gneiss with coarse-grained, nearly monomineralic layers of gray quartz, up to ∿1 cm thick, which alternate with medium-grained layers comprised of subequal amounts of pale green clinopyroxene and gray plagioclase. Sample 36I was collected from a thin layer within pyribolite from the 2nd Intermediate Layer on northern Langø. It is a medium-grained, layered gneiss with nearly monomineralic layers of dark green clinopyroxene up to 5 mm thick that alternate with layers comprised of subequal amounts of clinopyroxene and white plagioclase.

In thin section, in addition to quartz, plagioclase, and clinopyroxene, small amounts of sphene, scapolite, biotite, hornblende, ilmenite, magnetite, calcite, and molybdenite were also identified. These are the only samples from Langø in which sphene occurs. The hornblende, ilmenite, magnetite, calcite, molybdenite and some of the scapolite are secondary.

The association of these scapolite- and molybdenite-bearing calc-silicate rocks with pyribolite is similar to the association of sharn rocks with amphibolite in the area around Godthåb (McGregor, 1973). These amphibolites appear to be derived in part from mafic pillow lavas, whereas the sharn rocks appear to be derived from selvages between pillows. Although it is possible to infer a similar origin for the rocks on Langø by analogy with those to the south, there are no features in the calc-silicate rocks on Langø that bear on the nature of their protolith.

2. Petrography and Mineralogy

The prominent layering observed in hand specimen is marked in thin section by layering in which the grain size is a function of the modal mineralogy of each layer. For example, in layers that are dominated by either quartz, plagioclase, or clinopyroxene, these phases tend to be rather coarse (1-5 mm), with single grains of quartz up to at least 2 cm in length (i.e., they extend across the entire width of the thin section), whereas the phases that occur in minor abundance in these layers are smaller (<1 mm). In layers with "mixed" mineralogy, the grain sizes of all phases are similar (∿0.5 mm).

Quartz and locally clinopyroxene tend to have a preferred orientation parallel to the layering, whereas the other minerals are randomly-oriented and form a more or less equigranular polygonal mosaic characterized by ubiquitous 120° triple junctions and smooth grain boundaries. These calc-silicate rocks display the best developed "equilibrium" texture of any of the samples from Langø (Figure 3-10A).

Primary quartz is a principal constituent of sample 33A where it occurs as elongate elliptical-shaped grains that display some undulose extinction related to polygonalization and recrystallization. A few inclusions, up to 5 mm long, of subrounded to elliptical shaped clinopyroxene are present in the quartz (Fig. 3-10B). Primary quartz has not been identified in sample 36I, but both samples contain trace quantities of secondary quartz associated with the replacement of clinopyroxene by hornblende.

Plagioclase occurs as anhedral polygonal grains that are extremely well-twinned (albite and pericline). In sample 33A, primary plagioclase

Figure 3-10: Photomicrographs illustrating textural features in samples of calc-silicate gneiss. (A, B - transmitted, plane-polarized light; C, D - transmitted, cross-polarized light; all bar scales - 100 μm).

A) Polygonal equigranular intergrowth of clinopyroxene (dark gray) and plagioclase (white); note smooth grain boundaries and 120° triple junctions (36I).

B) Lenticular grains of clinopyroxene (pale gray) enclosed in quartz (white) (33A).

C) Equilibrium texture among clinopyroxene (C), scapolite (S) and plagioclase (P) (36I).

D) Irregularly-shaped optically-continuous grain of scapolite (bright white) replacing plagioclase; note anastamosing form of scapolite (33A).

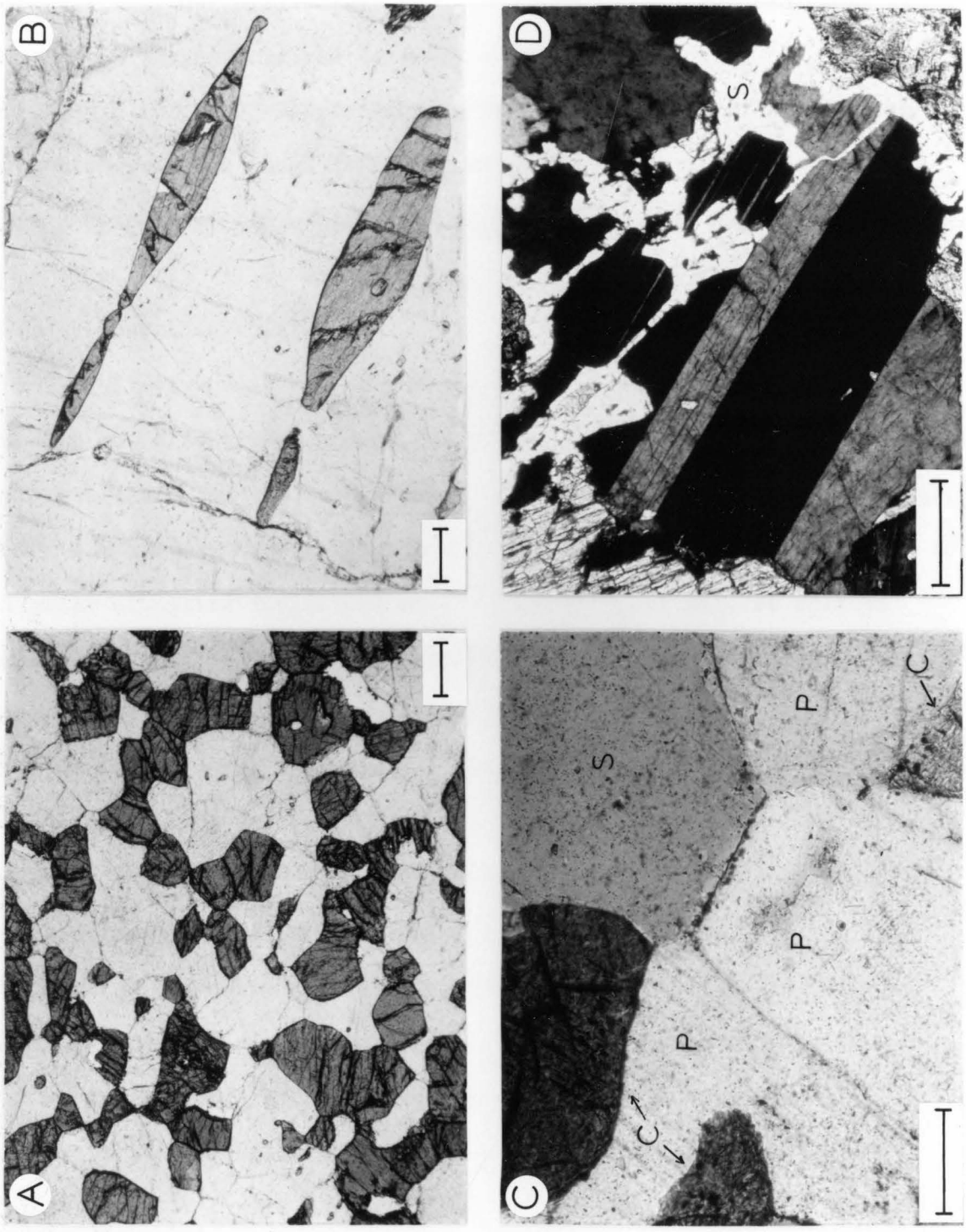
B
D
S
A
C
S
P
P
P
C
C

has only a narrow range in composition ($An_{77.8}Ab_{21.9}Or_{0.3}$ to $An_{81.3}Ab_{18.5}Or_{0.2}$), but plagioclase occurring near secondary hornblende is distinctly less calcic and reversely zoned ($An_{56.1}Ab_{43.1}Or_{0.8}$ to $An_{43.7}Ab_{55.3}Or_{1.0}$). Plagioclase in 36I is extremely calcic, and has only a very narrow range in composition even where it occurs with secondary hornblende ($An_{93.4}Ab_{6.6}$ to $An_{95.8}Ab_{4.2}$). The high anorthite content (i.e., high Al_2O_3 and low SiO_2) may be related to the absence of primary quartz in this sample.

Clinopyroxene ranges from subequant polygonal grains to subrounded and slightly elongated types. In sample 33A, some of the clinopyroxene grains in the quartz-rich layers are extremely elongate (e.g., 0.4 x 5.0 mm) and have an eliptical form (Figure 3-10B). Subrounded to slightly elongated inclusions of plagioclase ($\lesssim$0.1 mm), as well as exsolved granules (<10 μm) and oriented platelets of ilmenite are present. The latter feature is better developed in sample 36I where, in addition, some of the exsolved ilmenite granules have been expelled from the pyroxene and occur at grain boundaries. In both samples, such granular exsolution of ilmenite is best displayed where the clinopyroxene is replaced by hornblende.

The clinopyroxene in these calc-silicate samples is the most intensely colored of any observed on Langø, and is pleochroic from yellow-green to blue-green. CaO-contents are uniformly high (22.7-23.7 wt %), and similar to those in other samples. The Al_2O_3- and Cr_2O_3- contents (up to 5.71 and 1.14 wt % respectively) are the highest values measured for any clinopyroxene from Langø. In addition, the clinopyroxene tends to be the most iron-rich, and in both samples the

range in Mg-value is quite large ($Wo_{48.7}En_{36.7}Fs_{14.6}$ to $Wo_{50.0}En_{26.9}Fs_{23.1}$). Most of the chemical variation detected in pyroxene in these samples occurs from grain to grain and layer to layer, as zoning within individual grains is limited to decreases in Al_2O_3-content and slight increases in Mg-value from core to rim. An optical absorption spectrum obtained for the clinopyroxene in sample 33A indicates that the deep green color is related to the high content of Cr^{3+} (G. R. Rossman, personal communication).

Pale-green to blue-green pleochroic hornblende replaces clinopyroxene in both samples. The hornblende occurs in irregularly-shaped patches within the pyroxene and/or at the margins of certain grains where it may be associated with secondary calcite, quartz, ilmenite, and magnetite. The hornblende does not form the spectacular coronas found in the pyribolite gneisses. Al_2O_3-contents of this secondary hornblende range from 5.1 to 8.1 wt %, and Mg-values from 0.68 to 0.75. Hence, chemically this hornblende is similar to the secondary amphibole in the pyribolites.

Sphene occurs as subrounded elongate grains (up to 2 mm long) that are bright orange. In some places, especially where the sphene is included in clinopyroxene, fractures (expansion cracks?) radiate outwards from the sphene.

Dark-brown to pale-brown pleochroic biotite is present in sample 33A, and occurs as irregularly-shaped corroded grains ($\lesssim$0.2 mm) near pyroxene that is being replaced by hornblende. Measured TiO_2-contents are high (4.9-5.7 wt %) whereas Al_2O_3-contents are low (13.7-14.3 wt %). There is only a narrow range in measured Mg-value (0.62-0.65). It is not

clear whether the biotite is primary or secondary, although its high TiO_2-content suggests that it is primary.

Calcite with rather high contents of MgO, FeO and MnO (up to 2.7, 2.2, and 1.1 wt % respectively) forms irregularly shaped grains that locally appear to be participating in the replacement of the clinopyroxene. Ilmenite occurs as larger (up to 0.5 mm) grains that replace sphene. These are characterized by high MnO-contents (1.5-4.9 wt %). In addition to the tiny granules associated with pyroxene (which were too small to analyze), ilmenite is also present in those areas where pyroxene is replaced by hornblende. Here, magnetite with 3.1 wt % Cr_2O_3 was observed in one area of sample 33A.

Scapolite occurs as large (up to 1 mm) anhedral grains that are in textural equilibrium with plagioclase (Figure 3-10C), smaller ($\sim$0.5 mm) anhedral grains that appear to replace plagioclase, irregularly-shaped grains (0.1-0.3 mm) associated with secondary hornblende, and as anastamosing, veinlet-like grains up to 2 mm long that crosscut plagioclase, pyroxene, and quartz (Figure 3-10D).

The Ca-content of the scapolite is high (18.1-21.0 wt % CaO), whereas SO_3-, F-, and Cl-contents are low (<1.9, <0.2, and <0.05 wt % respectively). The low analytical totals (95-97 wt %) indicate a high carbonate content.

The recent experimental work of Newton and Goldsmith (1975) and Goldsmith (1976) indicates that anorthite + calcite reacts to form scapolite at high temperature (800-900^{o}C). The complex petrographic relationships between scapolite and plagioclase (and calcite) may

represent the arrested prograde breakdown of plagioclase + calcite to form scapolite.

3. Summary

The two samples classified as "calc-silicate rocks" are characterized by a primary assemblage of calcic plagioclase, clinopyroxene, sphene, and scapolite. The formation of secondary hornblende indicates that these samples, like the other types described, display evidence for two episodes of metamorphic mineral growth. As in the pyribolites, pyroxene was a stable phase in the first event, and unstable during the second.

H. Diorite

1. General Overview

Six samples were collected from a small body of intrusive diorite near Nordnor. Five of these are massive, medium-grained rocks comprised of subequal amounts of mauve to gray plagioclase and black mafic minerals. The latter occur locally in larger cm-size clots. These samples all have an igneous-looking hypidiomorphic granular texture, and although they are unfoliated, there is a faint yet noticeable alignment of the mafic minerals.

Sample 38C is a strongly lineated rock comprised of ∿10% plagioclase and ∿90% mafic minerals that was collected from a pyribolite inclusion in the diorite; it will not be considered further here. The field occurrence and other pertinent features of the diorite have been outlined in Chapter 2 (p. 18).

2. Petrography and Mineralogy

It becomes apparent upon examination of the thin sections of the diorite that the grain size is in fact considerably smaller than it appears in hand specimen. The large 3-5 mm plagioclase and mafic mineral "crystals" are actually aggregates of smaller (∿1 mm) anhedral grains. Thus, the original igneous texture has been modified by extensive recrystallization so that the samples now consist of polygonal grains with smooth boundaries and 120° triple junctions. However, some igneous features are preserved such as rare subhedral, tabular inclusions of plagioclase in pyroxene. Further recrystallization has resulted in the development of sutured grain boundaries, particularly in sample 38D.

It is difficult to distinguish pyroxene from hornblende in the hand samples. In thin section, the mafic mineral assemblages that occur are: hornblende (38A, 38B); hornblende - clinopyroxene (38D); and hornblende - clinopyroxene - orthopyroxene (37, 38C). The former presence of pyroxene in samples 38A and 38B can be inferred from talc pseudomorphs enclosed in hornblende in 38B, and secondary hornblende-quartz intergrowths in both. Other minerals identified in thin section include biotite, ilmenite, cummingtonite, apatite, zircon and white mica.

As in the other mafic rocks on Langø, pyroxene is partly replaced by secondary hornblende. However, in contrast to the other samples, primary hornblende in the diorite is likewise partly replaced here by intergrowths of bladed secondary hornblende and cummingtonite. The occurrence of cummingtonite and extensive replacement of primary hornblende are features unique to the diorite.

As indicated above, plagioclase occurs in aggregates of anhedral 1-2 mm grains and as rare subhedral to anhedral (∿0.1-1.0 mm) inclusions in pyroxene and hornblende. Most grains are well-twinned (albite, carlsbad-albite, pericline) and show some degree of optical zoning. The latter is characterized by patchy to regular, concentric extinction that may or may not conform to boundaries with adjacent mafic minerals. There does not appear to be any correlation between extinction irregularities in the plagioclase and chemical zoning; i.e., grains that are strongly zoned optically are chemically homogenous. The range in measured compositions is $An_{42.5}Ab_{56.2}Or_{1.3}$ to $An_{34.7}Ab_{64.2}Or_{1.1}$, with slight (≲2 mole % An) reverse or normal zoning present.

Large (up to 3 mm) grains of anhedral pink pleochroic orthopyroxene occur intergrown with primary hornblende. Measured CaO- and Al_2O_3-contents are low (<0.4 and 0.7 to 1.3 wt % respectively), and there is virtually no variation in measured Mg-values ($Wo_{<1}En_{66}Fs_{33}$).

Clinopyroxene is pale green and occurs as either small (∿0.5 mm) rounded grains intergrown with primary hornblende, or as larger relic grains (up to 2 mm across) that are now converted almost entirely to secondary amphibole. The CaO-content (∿22.4 wt %) is high, the Al_2O_3-content (1.8-2.5 wt %) is low, and there is almost no variation in Mg-value ($Wo_{47}En_{40}Fs_{13}$).

Primary hornblende is strongly pleochroic from green brown to dark green, and occurs as subhedral to anhedral grains (∿0.5-2.0 mm) that in a few cases display simple (100) twins. Some of the hornblende grains contain innumerable μm-sized and smaller particles of ilmenite (?). These inclusions tend to be absent from the edges of each crystal,

whereas the cores are nearly opaque (Figure 3-11A). In samples 38A and 38B, the primary hornblende is replaced by paler secondary amphiboles.

The Ca-contents of the primary hornblende are uniformly high (11.3-12.5 wt % CaO) and there is only a slight range in Mg-values (0.64-0.71). However, there is a considerable range in Al-content (9.6-12.5 wt % Al_2O_3), with cores being more aluminous than rims.

There are five distinct textural types, and two distinct compositional types, of secondary amphibole in the diorite. Pale-green to blue-green amphibole occurs as irregularly-shaped to bladed grains intergrown with quartz that replace clinopyroxene, as isolated euhedral to subhedral grains with vermicular quartz inclusions, as bladed grains intergrown with quartz that replace primary hornblende (Figure 3-11B), as tiny (μm size and smaller) granules intergrown with quartz and plagioclase (?) that replace primary hornblende (Figure 3-11C), and as thin ($\lesssim$50 μm wide) rims around orthopyroxene (Fig. 3-11D). The range in composition of these secondary amphiboles is quite large (12.0-12.7 wt % CaO; 3.2-9.2 wt % Al_2O_3; Mg-value = 0.72-0.80), and overlaps in part that of the primary hornblende. There is no apparent correlation between the composition of these secondary calcic amphiboles and their occurrence.

Very pale green, polysynthetically-twinned secondary cummingtonite (3.0-3.3 wt % CaO; 0.8-1.1 wt % Al_2O_3; Mg-value = 0.69) is intergrown with the secondary calcic amphibole that replaces primary hornblende. The diorite is the only rock type on Langø that contains cummingtonite, or in which extensive replacement of primary hornblende occurs.

Figure 3-11: Photomicrographs illustrating textural features in samples of pyroxene diorite (transmitted, plane-polarized light; all bar scales = 100 μm).

A) Several grains of hornblende with opaque oxide inclusion-rich cores, and clear rims; note oxide granules along grain boundaries (37).

B) Pale-green MII Ca-amphibole with tiny quartz inclusions (right) replacing darker MI hornblende (left) (38B).

C) Thin rim of MII Ca-amphibole surrounding large orthopyroxene grain (37).

D) Intergrowth of tiny micron-size granules of MII Ca-amphibole, quartz, and plagioclase (?) replacing MI hornblende (38D).

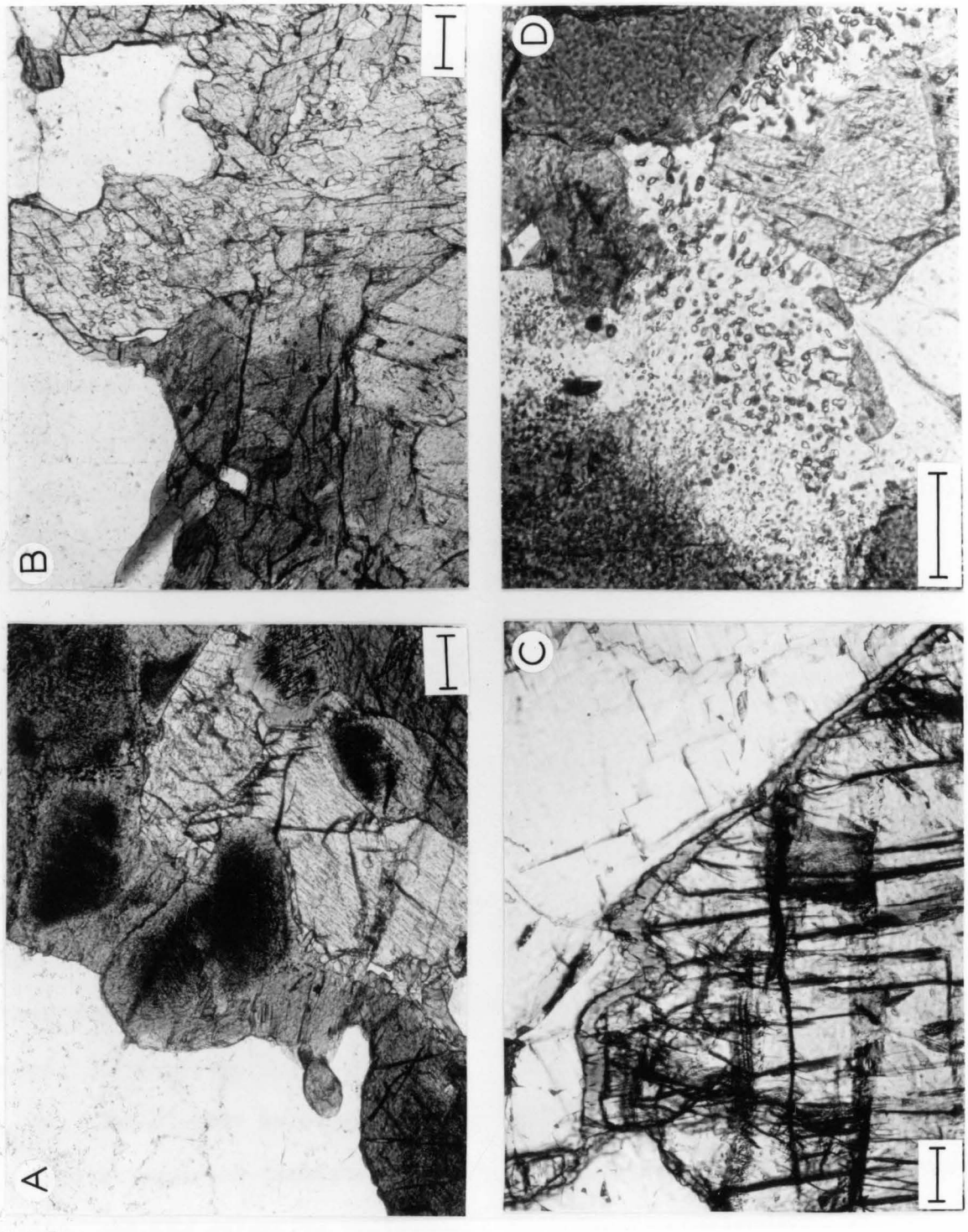
B
D
A
C

The petrographic features indicate that the following retrograde reactions have occurred:

$$\text{Pyx} + \text{Plag} + \text{Fluid} \rightarrow \text{Hbl}_2 + \text{Qtz}, \text{ and}$$

$$\text{Hbl}_1 \rightarrow \text{Hbl}_2 + \text{Cumm} + \text{Qtz}.$$

Biotite is pleochroic from dark to pale brown, and occurs as tabular to acicular grains up to 0.5 mm long intergrown with pyroxene and primary hornblende, and locally appear to replace them. The few analyses obtained for the biotite serve to distinguish "primary" from "secondary" types (14.4 to 15.4 vs ∿15.6 wt % Al_2O_3; 3.2 to 5.3 vs ∿1.1 wt % TiO_2; Mg-value = 0.63 to 0.71 vs ∿0.74). Rare grains of ilmenite with low calculated Fe_2O_3- contents (<2.5 wt %), zircon, and apatite are also present.

3. Summary

The samples of diorite from Nordnor have a primary mineral assemblage of pyroxene, plagioclase and hornblende, and a secondary assemblage of quartz and amphibole. Thus, like the other lithologies on Langø, the diorite preserves evidence for two episodes of metamorphic mineral growth. However, in contrast to the other rock types on Langø, the diorite has not suffered the complex sequence of deformation. Hence. these observations indicate that metamorphism outlasted deformation on Langø.

The diorite is similar mineralogically to the pyribolite gneisses. It is distinguished from the latter by the presence of secondary cummingtonite, and the extensive replacement of primary hornblende.

CHAPTER 4

IV. COMPARATIVE MINERALOGY

A. Introductory Statement

One of the principal objectives of this study was to outline the detailed variations in the chemical composition of minerals from a variety of host rocks in a high-grade metamorphic complex. Consequently, considerable effort was spent in acquiring electron microprobe analyses of all the principal minerals in each sample.

Several samples from each petrographic group discussed in Chapter 3 have been analyzed. Such a procedure should permit a separation of the effects of bulk composition from those of metamorphic grade. However, as emphasized throughout Chapter 3, all the samples preserve evidence for two episodes of mineral growth, and hence are polymetamorphic. Therefore, it is imperative that the compositions of the primary minerals, which formed during prograde hornblende granulite grade metamorphism, be distinguished from the compositions of secondary minerals that formed during subsequent amphibolite grade metamorphism.

In this section, the results of these analyses are presented in summary form for each major mineral group. Where appropriate, primary minerals are referred to as MI, and secondary minerals as MII. The analytical techniques employed in this study are discussed in Appendix II, and individual analyses are tabulated in Appendix III. The latter can be obtained upon request for the cost of reproduction.

B. Alkali Feldspar

Alkali feldspar is an uncommon mineral in the samples studied and occurs only in the potassium feldspar gneisses. However, the former presence of small amounts of alkali feldspar in other lithologies may be inferred from certain petrographic features (c.f. Chapter 3).

Alkali feldspars were analyzed for Na, Mg, Al, Si, K, Ca, Ti, Fe*, and Ba, and the resultant analyses normalized to: Total Cations = 5.0. The mineral formula is taken to be $(K_{1-x}Na_x)\ AlSi_3O_8$, with measured compositions falling in the range: $(K_{.87-.96}Na_{.04-.11})\ AlSi_3O_8$. This observed range of K/(K + Na) may be due in part to the fact that much of the alkali feldspar is perthitic, and the relatively large beam diameter used for analysis ($\sim$25 μm) overlapped adjacent lamellae of K- and Na-phases. The measured Al/Si does not deviate significantly from 1/3.

BaO is the only other oxide present in substantial amounts (0.4-1.3 wt %), with the contents of CaO (<0.13 wt %) and FeO (<0.11 wt %) uniformly low; MgO and TiO_2 are near or below their respective detection limits ($\lesssim$0.05 wt %). The compositions of the alkali feldspar are illustrated in Figure 4-1 in terms of atomic K-Na-Ca. There is nothing remarkable about these compositions, and they are similar to analyses reported for alkali feldspars in other high-grade metamorphic terranes (Smith, 1974).

C. Plagioclase Feldspar

Plagioclase feldspar is the most common mineral in the samples studied and forms an important constituent of each lithology on Langø.

---

* Total iron as FeO in all cases.

Figure 4-1: Compositions of alkali and plagioclase feldspar in terms of atomic K-Na-Ca. The tie line connects the compositions of the two feldspars that occur in the potassium feldspar gneisses. The bar along the plagioclase sideline indicates the position of the gap in plagioclase compositions associated with the Huttenlocher solvus. Note that some analyses fall within this gap.

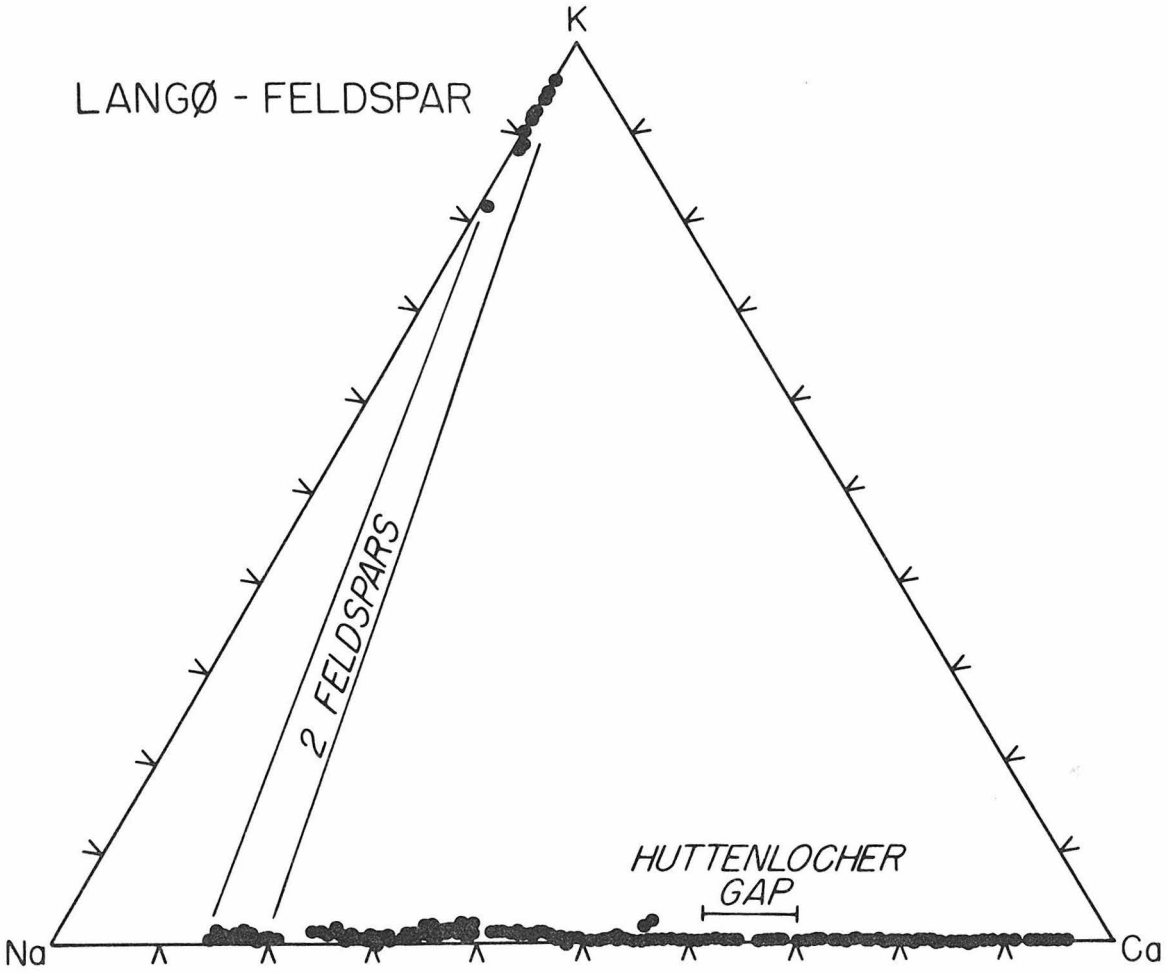
LANGØ - FELDSPAR
K
Na
Ca
2 FELDSPARS
HUTTENLOCHER
GAP

It was analyzed for Na, Mg, Al, Si, K, Ca, Ti, Fe, and Ba, and the resultant analyses normalized to: Total Cations = 5.0. The general mineral formula is taken to be (Na_xCa_{1-x}) $(Al_{2-x}Si_{2+x})$ O_8, with measured compositions falling in the range $(Na_{0.04-0.89}Ca_{0.11-0.96})$ $(Al_{1.11-1.96}$ $Si_{2.04-2.89})$ O_8.

K_2O is present in small but generally measurable amounts (<0.05-0.43 wt %). Most analyses yield concentrations in the range 0.05-0.20 wt %, and the higher values are probably related to submicroscopic anti-perthitic exsolution. Although BaO (<0.05-0.31 wt %), FeO (<0.05-0.28 wt %), MgO (0.05-0.27 wt %), and TiO_2 (<0.05-0.14 wt %) have a wide range in concentration, most values are <0.10 wt %. The higher values for FeO, MgO and TiO_2 may be related to cryptic inclusions of mafic minerals and/or caused by secondary fluorescence from adjacent phases.

Compositions of all the analyzed plagioclase are illustrated in Figure 4-1 in terms of atomic K-Na-Ca. Two important features should be emphasized. First, there is a tremendous range in Na/(Na + Ca) that spans nearly the entire compositional range from albite to anorthite, and second, there is a slight yet systematic increase in K-content as Na/(Na + Ca) increases.

Also shown in Figure 4-1 is the position of the compositional gap (Huttenlocher solvus) identified in plagioclase from samples 25E, 33B, and 39A. The fact that analyses of plagioclase from other samples lie in this region could be caused by a failure to unmix, unmixing at different temperatures, or unmixing on a scale that is too small to be resolved with the microprobe.

Figure 4-2: Compositions of all analyzed plagioclase grains in terms of cations Ca and Si. Note that, within error, the analyses lie along a line from anorthite to albite, and appear stoichiometric.

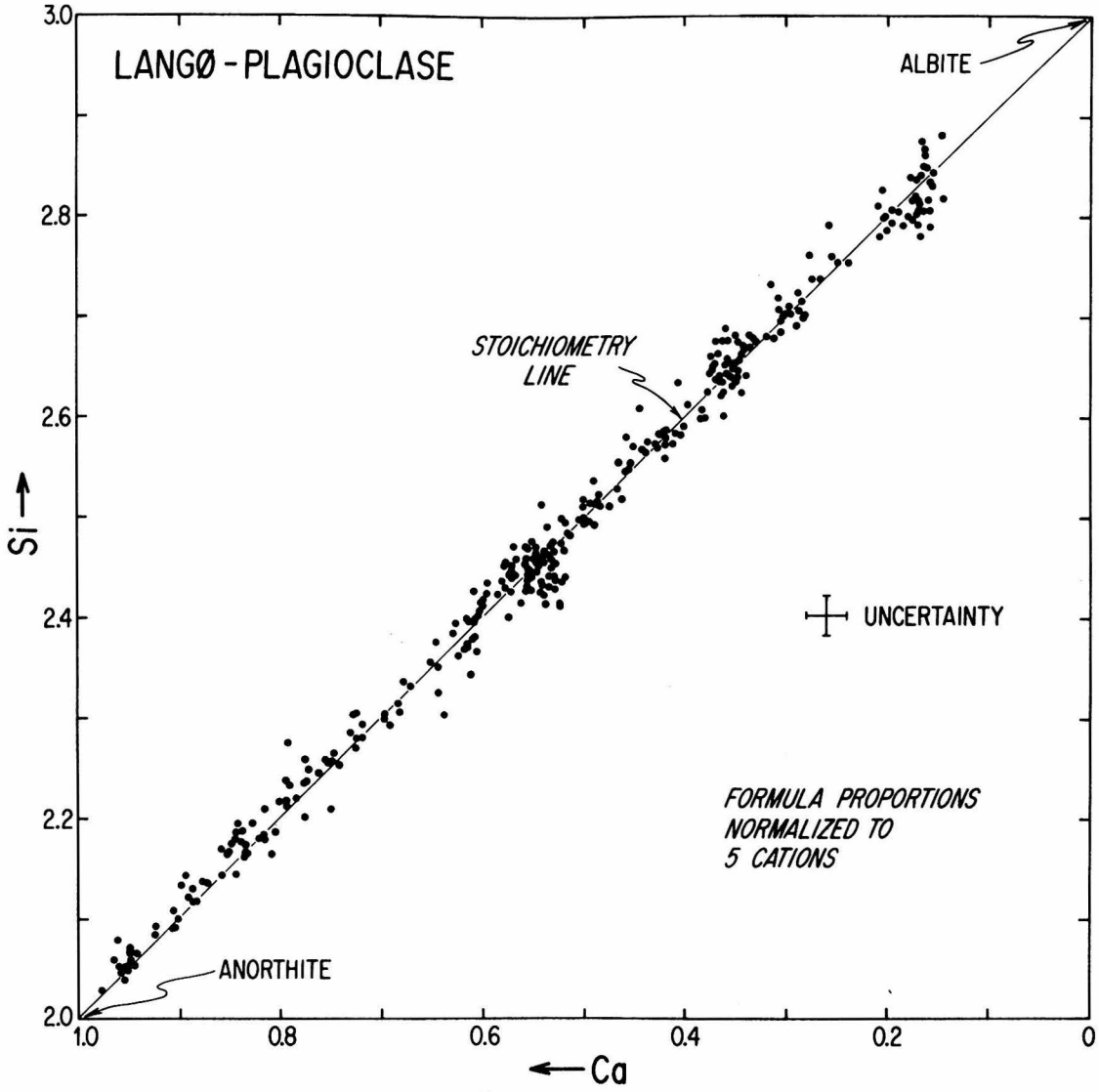
LANGØ - PLAGIOCLASE
ALBITE
STOICHIOMETRY LINE
UNCERTAINTY
FORMULA PROPORTIONS NORMALIZED TO 5 CATIONS
ANORTHITE
Si
Ca
3.0
2.8
2.6
2.4
2.2
2.0
1.0
0.8
0.6
0.4
0.2
0

Ca and Si in all the analyzed plagioclase from Langø are illustrated in Figure 4-2. Note that the data cluster about a line connecting albite (Ca = 0, Si = 3) and anorthite (Ca = 1, Si = 2), and thus appear stoichiometric within analytical error. This relationship is in marked contrast to lunar plagioclase, which is not stoichiometric, i.e., their compositions lie above the An-Ab line indicating excess Si (Weill et al., 1970; Crawford, 1973). The few systematic investigations of terrestrial plagioclase indicate both adherence to, and departures from stoichiometry (c.f., Smith, 1974). Clearly, more data and observations are needed to elucidate the factors that govern stoichiometry in plagioclase (e.g., Longhi et al., 1976).

Figure 4-3 also illustrates Ca and Si in plagioclase from Langø, on which are outlined the compositional fields for primary (MI) plagioclase in each lithology. These data represent the compositions of plagioclase that are interpreted to have formed at hornblende granulite grade.

The fact that each lithology appears to have its own distinctive compositional range suggests that plagioclase compositions in these samples are a function of Na/Ca and Al/Si in the host rock, and independent of metamorphic grade. This observation stands in contrast to lower grades of metamorphism where plagioclase composition does seem to be related to metamorphic grade (Miyashiro, 1974). The data from Langø thus establish the great range in plagioclase composition attainable at high metamorphic grade.

D. Calcic Amphibole

Primary hornblende comprises up to 65 volume % of the ordinary pyribolites, garnet pyribolites, and the diorite. Its dark green to

Figure 4-3: Diagram illustrating the compositional fields for analyses of primary (MI) plagioclase from the various lithologies on Langø. Note the large overall range in plagioclase composition and the fact that plagioclase from each lithology has a more restricted range in composition. The latter suggests that plagioclase composition is controlled by the Al/Si and Na/Ca of the host rock, and not by metamorphic grade, which is the same for all samples.

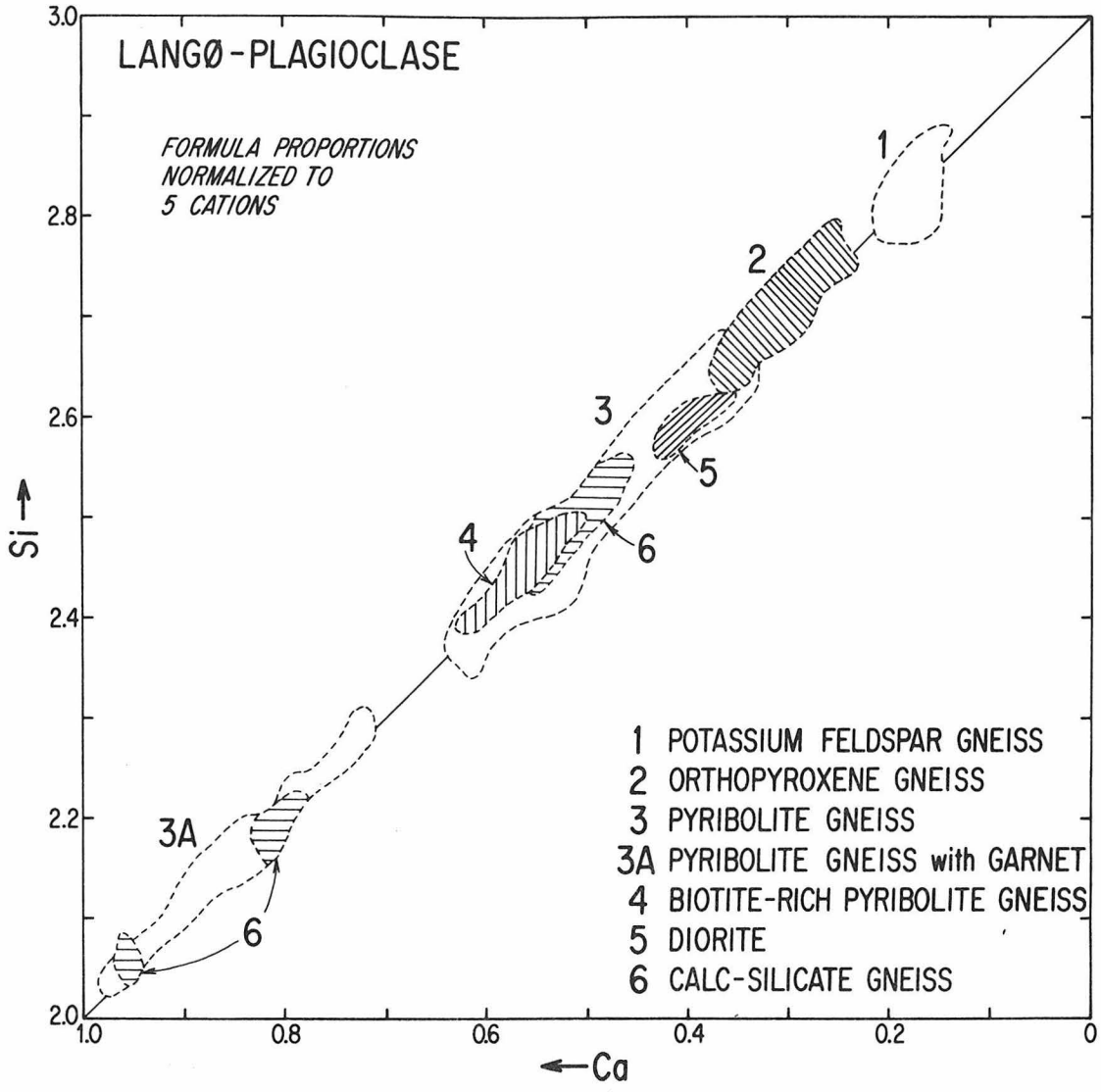
LANGØ - PLAGIOCLASE
FORMULA PROPORTIONS
NORMALIZED TO
5 CATIONS
Si
Ca
3.0
2.8
2.6
2.4
2.2
2.0
1.0
0.8
0.6
0.4
0.2
0
1
2
3
3A
4
5
6
1 POTASSIUM FELDSPAR GNEISS
2 ORTHOPYROXENE GNEISS
3 PYRIBOLITE GNEISS
3A PYRIBOLITE GNEISS with GARNET
4 BIOTITE-RICH PYRIBOLITE GNEISS
5 DIORITE
6 CALC-SILICATE GNEISS

green brown pleochroism is similar to that described in other high-grade gneiss terranes. Secondary, pale-green to blue green actinolitic hornblende, which formed by reaction between pyroxene and plagioclase, occurs in the pyribolites, biotite pyribolites, calc-silicate gneisses, and diorite. The presence of two differently-colored and texturally distinct types of calcic amphibole in many of these samples provides some of the best petrographic evidence for the polymetamorphic nature of the gneisses on Langø.

Amphiboles were analyzed for Na, Mg, Al, Si, K, Ca, Ti, Cr, Mn, Fe, F and Cl. The general mineral formula is taken to be: $A\ (X_2\ Y_5)\ ^{VI}(Z_8)\ ^{IV}O_{22}\ (OH, F, Cl)_2$, where A = Na + K; X = Ca, Na, (Fe^{2+}); Y = Mg, Fe^{2+}, Al, Ti, Cr, Fe^{3+}, Mn; and Z = Si, Al. Normalization of microprobe analyses of amphibole present a problem that is exacerbated by the presence of substantial amounts of Fe^{3+}, in addition to the fact that both Na and Fe^{2+} may occur in two different cation sites. Three normalization schemes were used:

1) Total Cations - (Na + K) = 15.0, which allocates all the Na to the "A" site, and sets 2.0-Ca = Fe^{2+} in X (i.e., M(4));
2) Total Cations - (K) = 15.0, which allocates all the Na to the M(4) site, and sets 2.0-Na-Ca = Fe^{2+} in X (i.e., M(4));
3) Total Cations - (Ca + Na + K) = 13.0, which allocates all the Fe^{2+} to Y, sets $Na^{M(4)}$ = 2.0-Ca, and sets $Na^{A} = Na^{Total} - Na^{M(4)}$.

The amount of Fe^{3+} was estimated from charge deficiency assuming a theoretical maximum of 46.00. The amount of Fe^{3+} calculated in this way, and the relative amounts of Na^{A} and $Na^{M(4)}$, although they are estimates in each case, can provide constraints on the legitimacy of the three

different normalizations. However, the choice of which normalization scheme seems "best" is at times quite arbitrary.

For all analyses of primary amphibole, normalization 2 was rejected since it yielded $(Na + Ca)^{M(4)} > 2.0$, which is impossible, and indicated that most, if not all, the iron was present as Fe^{3+}, which is unlikely. The data for normalization 1 indicated that almost all the iron occurred as Fe^{2+}. Since wet chemical analyses of amphibole indicate the presence of substantial Fe^{3+}, normalization 1 was also rejected. In addition, total positive charge calculated using normalization 1 exceeds 46.00 in some cases. This suggests that some of the Na occurs in the M(4) site, whereas normalization 1 constrains Na to occur in the A-site only. Normalization 3 provided the most satisfactory results, and the data illustrated in the accompanying figures for compositions of MI calcic amphibole are based on that scheme.

The compositional data for MII calcic amphibole are based on all three normalizations, with 1 and 2 chosen for the most alkali-poor types. It should be pointed out that the choice of normalization does not change the trends or relative positions of any data points, it merely shifts the positions slightly.

It seems instructive to discuss the compositional variations of calcic amphiboles in terms of deviations from the ideal formula for tremolite $[(\square)^{A}\ (Ca_2Mg_5)^{VI}(Si_8)^{IV}O_{22}(OH, F, Cl)_2)]$, using the following well-documented substitutional mechanisms:

1) Glaucophane, $(Na^{+} + Al^{3+})^{VI} \rightleftarrows (Ca^{2+} + Mg^{2+})^{VI}$;

2) Edenite, $(Na^{+} + K^{+})^{A} + (Al^{3+})^{IV} \rightleftarrows (\square)^{A} + (Si^{4+})^{IV}$; and

3) Tschermakite, $(Al^{3+})^{VI} + (Al^{3+})^{IV} \rightleftarrows (Mg^{2+})^{VI} + (Si^{4+})^{IV}$.

In addition, substantial amounts of simple Fe^{2+}-Mg^{2+} substitution also occur.

The occurrence of glaucophanitic amphiboles in high-P facies series assemblages (Ernst et al., 1970) indicates that substitution 1) is favored by increases in pressure. The fact that the edenite content of calcic amphibole tends to increase rather uniformly with increased metamorphic grade (Wiseman, 1934; Shido and Miyashiro, 1959; Bard, 1970; Graham, 1974; and others) suggests that substitution 2) is favored by increases in temperature. Raase (1974) has suggested that substitution 3) may be favored by pressure, but the data are complicated by Fe^{3+}, and also consistent with temperature-related increases in metamorphic grade.

The above statements concerning the relative importance of the three substitutions are based primarily on studies of the variation in the composition of calcic amphibole with progressive metamorphism. How variations in rock composition affect these substitutions at a uniform metamorphic grade are not well understood. Hence, considerable effort has been devoted to documenting the variations in the chemical compositions of the two generations of calcic amphibole in the samples from Langø.

There is a tremendous range in both the major and minor element composition of Ca-amphibole in the samples studied. These data are summarized in Table 4-1, and the petrogenetic implications of this compositional range (columns 1 and 2), with particular emphasis on the difference between primary (MI) and secondary (MII) amphibole compositions

Table 4-1: Compositional Data For Calcic Amphiboles From Langø.

	1.	2.	3.	3A.	4.	4A.
SiO_2	40.6-50.0	44.9-56.4	43.6	6.382	48.2	6.884
Al_2O_3	7.50-16.4	2.01-10.7	11.9	2.062	8.19	1.378
Cr_2O_3	<0.05-1.28	<0.05-0.58	<0.05	0.000	0.05	0.005
TiO_2	0.34-2.63	<0.05-1.06	1.10	0.122	0.27	0.029
MgO	10.8-19.1	12.7-22.5	13.05	2.851	15.64	3.330
FeO*	5.71-16.3	2.64-14.8	12.60	1.545	10.97	1.311
MnO	<0.05-0.36	<0.05-0.54	0.30	0.037	0.52	0.063
CaO	11.3-12.6	11.9-13.3	12.0	1.878	12.0	1.833
Na_2O	1.15-2.25	0.18-1.21	1.28	0.363	0.77	0.215
K_2O	0.21-1.61	0.12-1.10	1.17	0.219	0.52	0.095
F	<0.05-0.33	<0.05-0.64	0.11	0.052	<0.05	-----
Cl	<0.05	<0.05	<0.05	-----	<0.05	-----
Mg-value	0.541-0.849	0.611-0.938		0.643		0.707
$Mg/MgFe^{2+}Mn$	0.608-0.961	0.686-0.979		0.742		0.856
			Fe^{2+}	0.954		0.495
*Total iron as FeO			Fe^{3+}	0.591		0.816
			$\frac{Fe^{2+}}{Fe^{Total}}$	= 0.617		0.378

1. Compositional range of primary (MI) Ca-amphibole.
2. Compositional range of secondary (MII) Ca-amphibole.
3. Primary Ca-amphibole in sample 24E.
3A. Formula proportions for 3.
4. Secondary Ca-amphibole in sample 24E.
4A. Formula proportions for 4.

(columns 3 and 4), are discussed in the following paragraphs. The two analyses listed in the Table are representative of each type.

Figure 4-4 illustrates cations Ca and Ti vs (Na + K) in all primary and secondary amphibole analyses*. As can be seen in the diagram, the amphiboles are quite calcic (1.74-1.98 cations Ca/formula), which limits the Na-content of the M(4) site to less than 0.26 cations/formula in all cases. Thus, there is only a small amount of glaucophane substitution, in contrast to high pressure hornblende associated with eclogites for example (Machatschki and Walitzi, 1962).

Note that, although there is quite a large range in their Ti- and alkali-contents, MI amphibole is consistently more Ti-rich and alkalic than MII amphibole. The data in Figure 4-4 thus illustrate a major distinguishing feature between the higher grade, primary (MI), calcic amphiboles, and lower grade, secondary (MII) calcic amphiboles. The data of Engel and Engel (1962) and Binns (1965), which indicate that Ti and (Na + K) in calcic amphibole from mafic rocks increase with increasing metamorphic grade, are consistent with the conclusions reached here.

The A-site occupancy (Na + K) and Al-contents of the Ca-amphiboles are illustrated in Figures 4-5 and 4-6. These data emphasize that MI amphibole contains distinctly more (Na + K), Al^{IV} and Al^{VI} than MII amphibile, although there is considerable overlap in terms of Al^{VI}.

---

* The three analyses of cummingtonite from sample 38B are not included in this discussion.

Figure 4-4: Diagram illustrating cations Ca and cations Ti plotted against cations (Na+K) for all analyses of calcic-amphibole from Langø. Note the uniformly high Ca-contents of all analyses, and the fact that primary (MI) amphibole tends to contain more Ti and more (Na+K) than secondary (MII) amphibole.

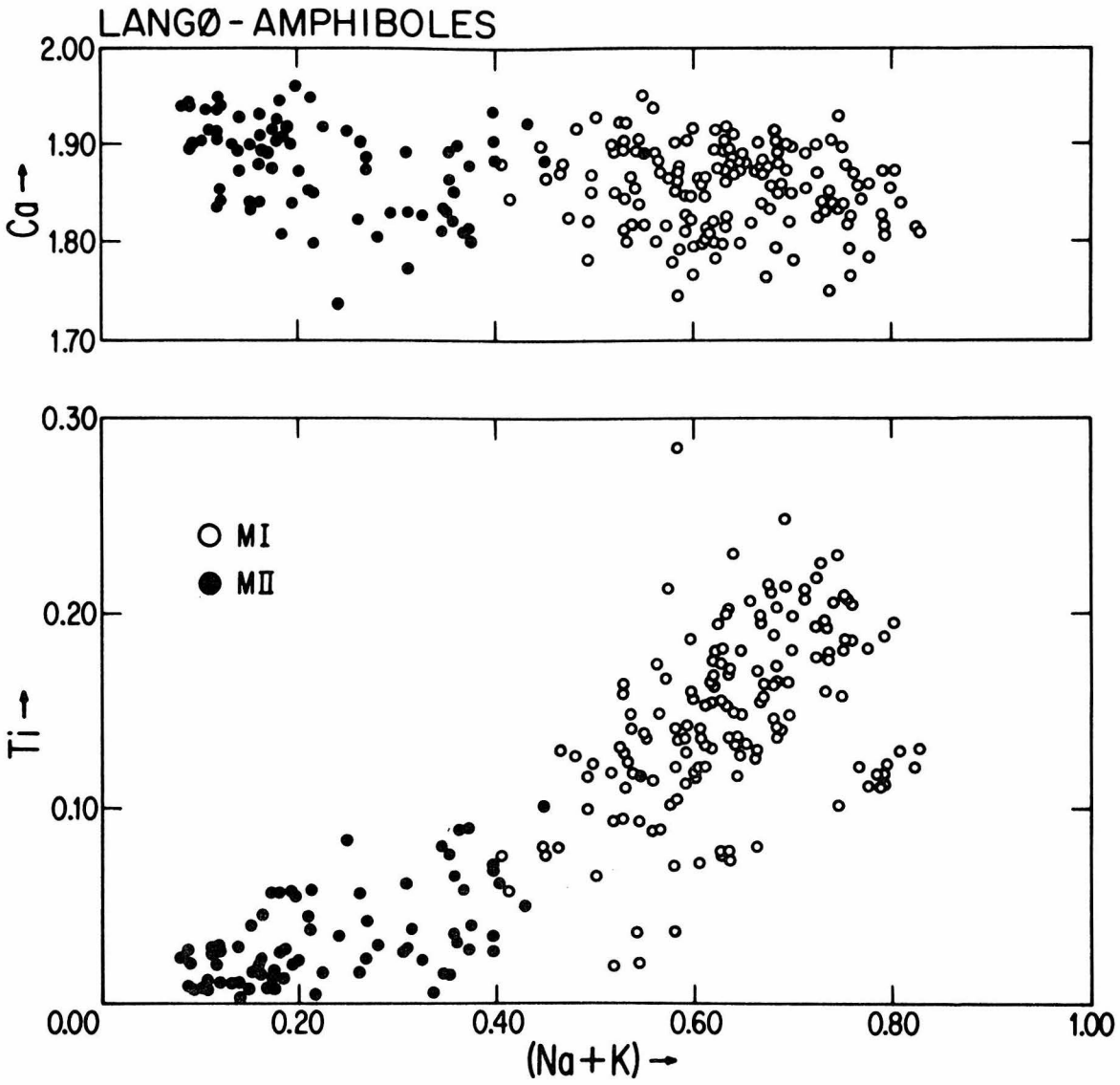
LANGØ - AMPHIBOLES
2.00
1.90
1.80
1.70
Ca →
0.30
0.20
0.10
0.00
Ti →
O MI
● MII
0.20
0.40
0.60
0.80
1.00
(Na+K) →

Figure 4-5: Diagram illustrating occupancy of the A-site [cations (Na+K)] plotted against the content of tetrahedrally-coordinated aluminum (cations Al^{IV}) in all analyses of Ca-amphibole from Langø. Note that primary (MI) amphibole contains more alkalis in the A-site, and is more aluminous than secondary (MII) amphibole. Note also that MI-amphibole with garnet contains more alkalis and Al^{IV} than the other MI amphiboles. No amphibole analyses may plot above the line from tremolite to edenite, and this "forbidden zone" is marked with an appropriate logo.

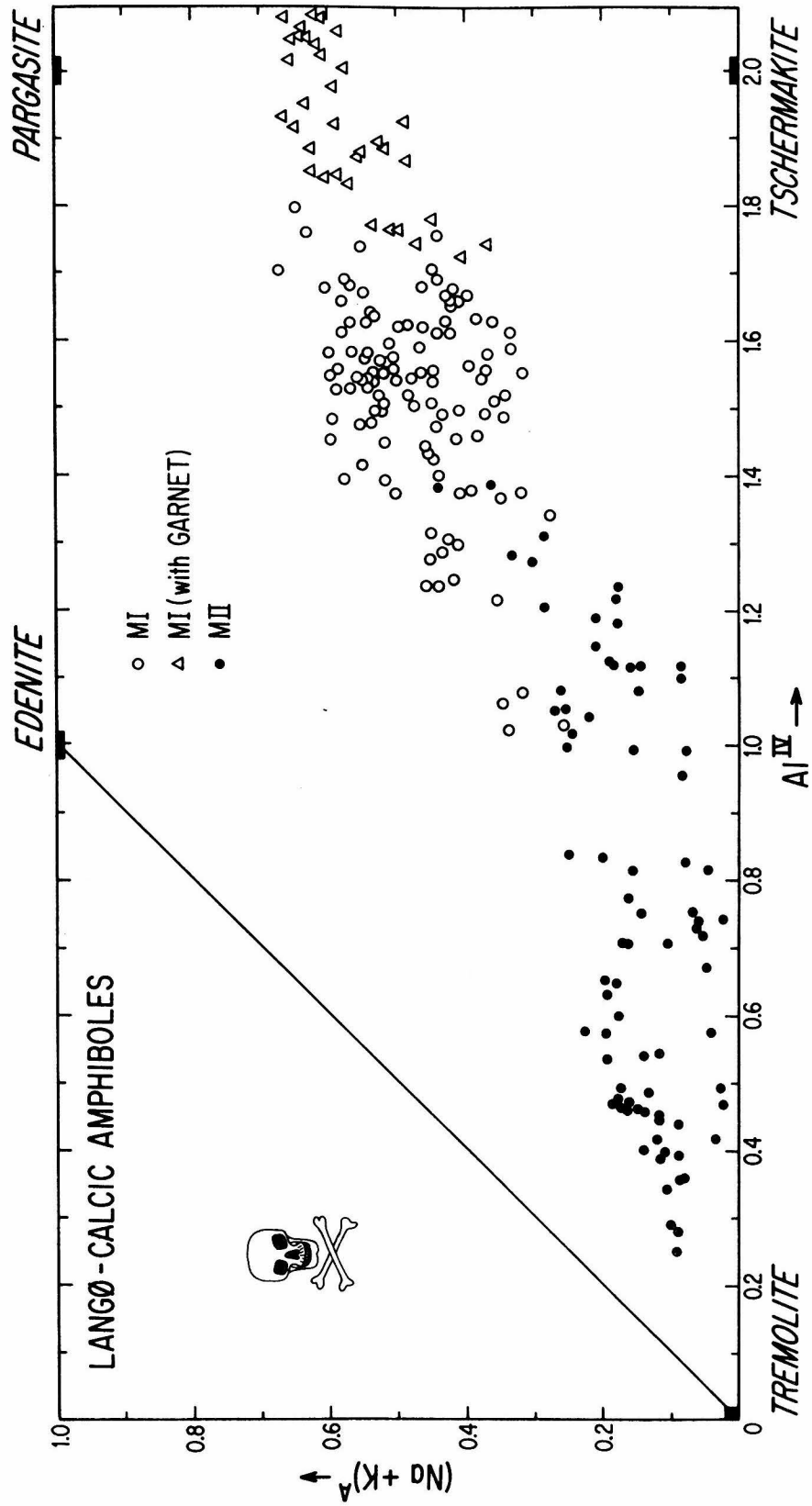
PARGASITE
EDENITE
TREMOLITE
TSCHERMAKITE
LANGØ-CALCIC AMPHIBOLES
MI
MI (with GARNET)
MII
$(Na+K)^A \rightarrow$
$Al^{IV} \rightarrow$
0
0.2
0.4
0.6
0.8
1.0
1.2
1.4
1.6
1.8
2.0

Figure 4-6: Diagram illustrating occupancy of the A-site [cations (Na+K)] plotted against the content of octahedrally-coordinated aluminum (cations Al^{VI}) in all analyses of Ca-amphibole from Langø. Note that primary (MI) amphibole contains more alkalis in the A-site, and is more aluminous than secondary (MII) amphibole, although there is considerable overlap in terms of Al^{VI}. Note also that MI amphibole with garnet, although it contains the most alkalis, has an Al^{VI}-content similar to the other MI amphiboles.

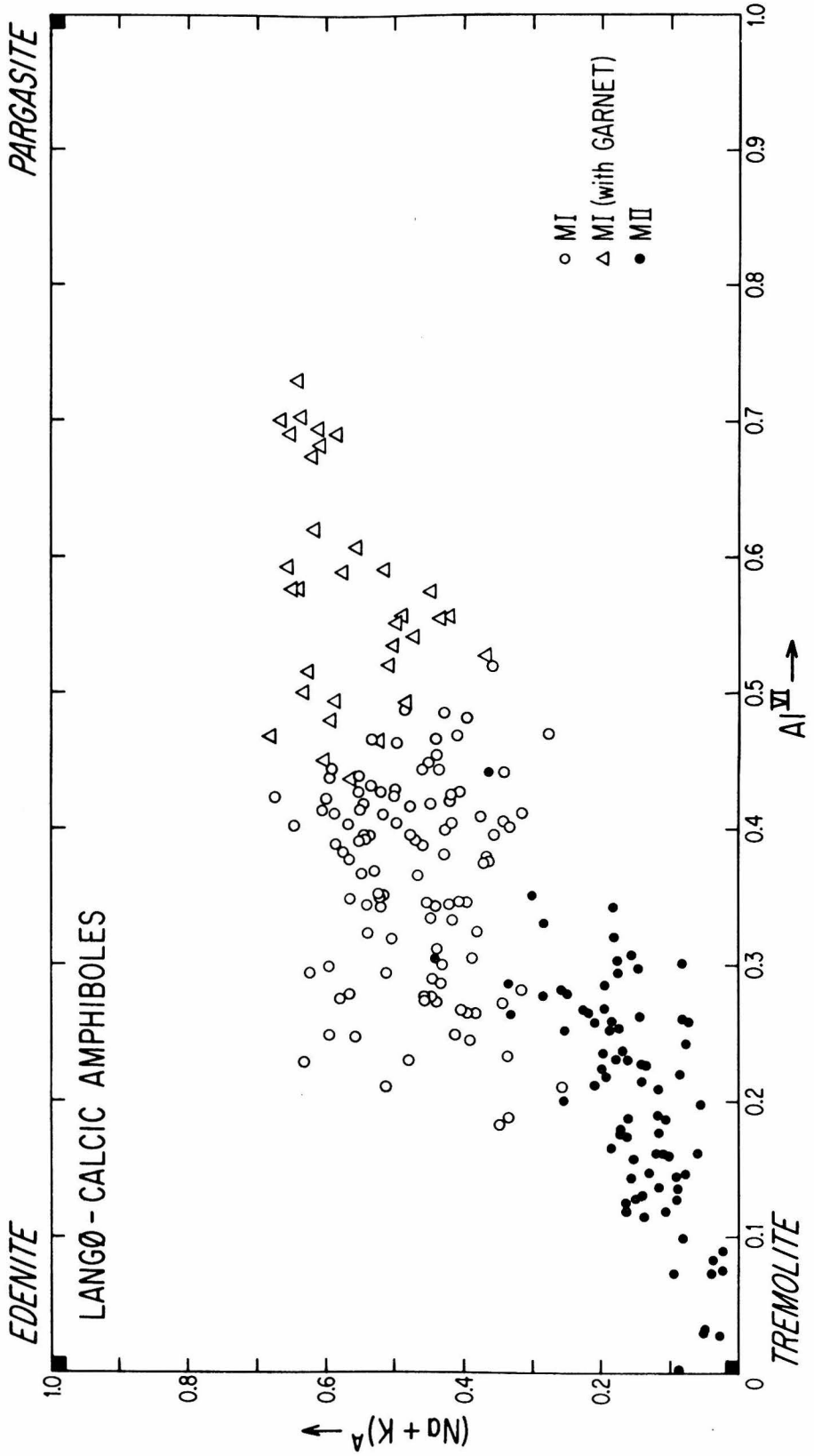
PARGASITE
EDENITE
TREMOLITE
LANGØ - CALCIC AMPHIBOLES
MI
MI (with GARNET)
MII
$(Na + K)^A \rightarrow$
$Al^{VI} \rightarrow$
1.0
0.8
0.6
0.4
0.2
0
0.1
0.2
0.3
0.4
0.5
0.6
0.7
0.8
0.9
1.0

Note also that amphibole occurring with garnet is the most aluminous of all.

$(Na + K)^A$ increases as Al^{IV} increases, indicating substantial edenite substitution. However, the fact that the data fall well away from the 1:1 line drawn from tremolite to edenite in Figure 4-5, indicates that a large amount of Al^{IV} is not balanced by cations in the A-site. There does not appear to be any correlation between $(Na + K)^A$ and Al^{VI} in MI amphibole, but these do seem to vary sympathetically in MII amphibole (Figure 4-6).

Figure 4-7 illustrates Al^{VI}-Al^{IV} variation in amphibole from Langø. As indicated previously, MI amphiboles are more aluminuous than MII amphiboles, and amphiboles that coexist with garnet are the most aluminous of all. The overall combined increase of Al-content across this diagram is consistent with the tschermakite substitution discussed previously.

The fact that the data do not lie along a 1:1 line, and are enriched substantially in Al^{IV}, indicates that a large portion of Al^{IV} is not balanced by Al^{VI}. An "excess" of Al^{IV} still remains even when that associated with the edenite substitution is taken into account. These data indicate that an additional substitutional mechanism must balance Al^{IV}.

Examination of the analyses (c.f., Table 4-1, columns 3A and 4A) indicates that both primary and secondary amphiboles contain substantial amounts of Fe^{3+}. This Fe^{3+} in VI-fold coordination, together with the smaller amounts of Ti^{4+} and Cr^{3+}, balance exactly the "excess" Al^{IV}.

Figure 4-7: Diagram illustrating the range of Al_2O_3-content in Ca-amphibole from Langø in terms of cations Al^{IV} and cations Al^{VI}. Note that primary (MI) amphibole is distinctly more aluminous than secondary (MII) amphibole, and amphibole associated with garnet is the most aluminous of all. The diagonal line represents the limit of Al^{VI}-contents observed in amphibole analyses as compiled by Leake (1965).

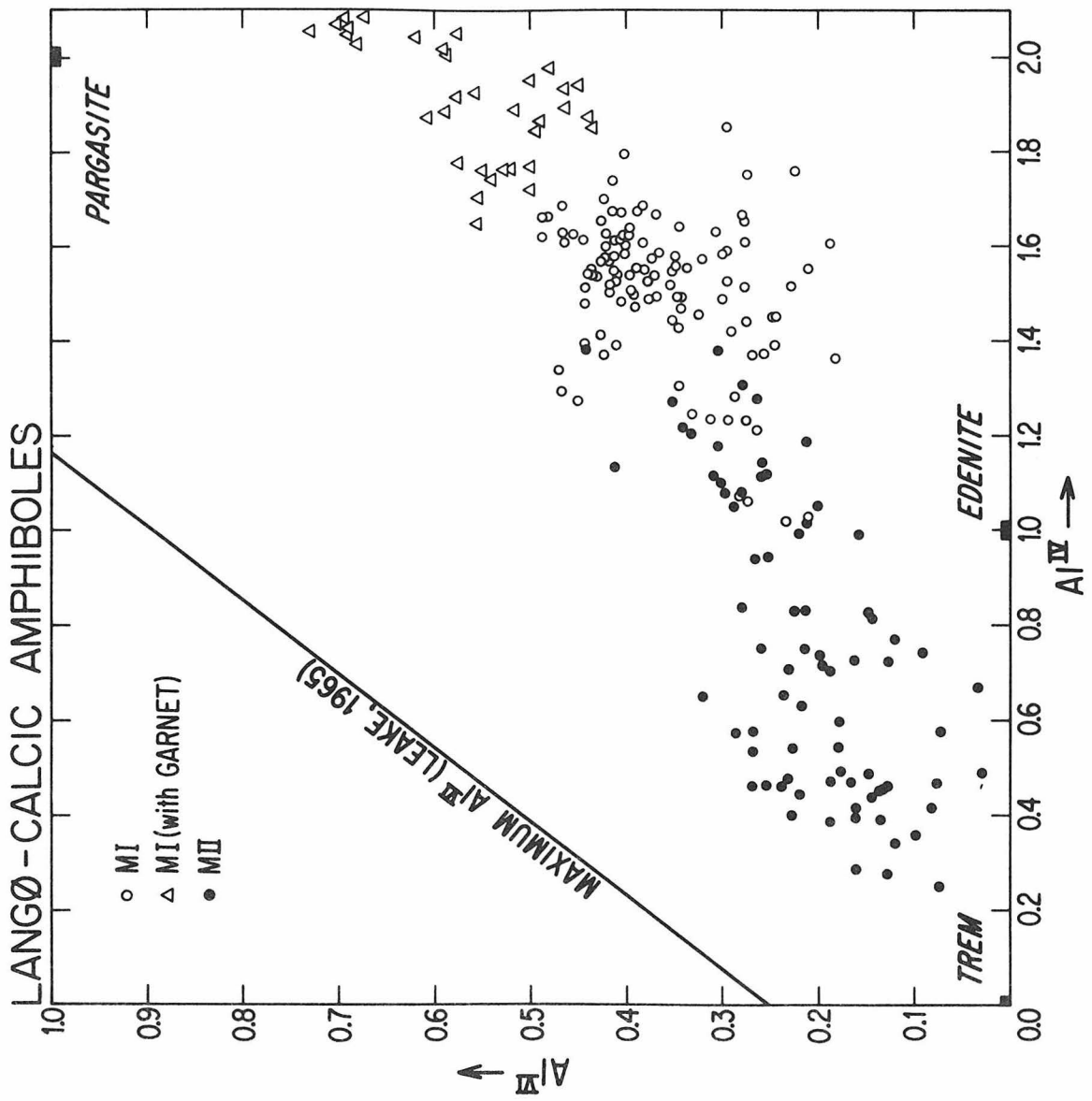
LANGØ - CALCIC AMPHIBOLES
PARGASITE
EDENITE
TREM
MAXIMUM Al^{VI} (LEAKE, 1965)
MI
MI (with GARNET)
MII
Al^{VI} ←
Al^{IV} →
1.0
0.9
0.8
0.7
0.6
0.5
0.4
0.3
0.2
0.1
0.0
0.2
0.4
0.6
0.8
1.0
1.2
1.4
1.6
1.8
2.0

These data suggest that in calcic amphibole, Fe^{3+} substitutes for and behaves precisely like Al^{3+}.

As mentioned previously the two amphibole analyses shown in Table 4-1 are typical of the MI and MII types. In addition to the features associated with their contents of Na, Al, Si, K, Ca and Ti discussed above, their Fe^{2+}- and Fe^{3+}-contents merit comment. The analysis of the MI amphibole shown in column 3A indicates that less than half its iron is Fe^{3+}, whereas in the MII amphibole (column 4A) more than half the iron is Fe^{3+}. This relationship, that MII amphibole tends to be enriched in ferric iron relative to MI amphibole, is another feature that distinguishes the two types chemically.

Figure 4-8 illustrates cations Mg and Si in the amphibole. It appears as if the Mg-content increases as Si increases (or Al^{IV} decreases). A plot of $Mg/(Mg + Fe^{2+})$ vs. $Al/(Al + Si)$ indicates a similar trend. These data suggest that the Tschermakite substitution is predominantly $(Mg^{2+})^{VI} + (Si^{4+})^{IV} \rightleftarrows (Al,Fe^{3+})^{VI} + (Al^{3+})^{IV}$, and that Mg/Fe^{2+} in Ca-amphibole is in part related to the contents of both Al and Si. Hence, any study that attempts to investigate Fe-Mg partitioning between Ca-amphibole and another phase should take into consideration the relationship between Mg/Fe, Al, and Si. Ray and Sen (1970) have, in fact, demonstrated that $K_{D_{Fe/Mg}}^{Hbl-Cpx}$ increases as Al^{IV} in hornblende increases. The principal conclusion that can be drawn from all of the above data is that the range in composition of MI and MII Ca-amphibole is related to variations in rock composition, and independent of metamorphic grade. However, the difference between MI and MII <u>is</u> related to differences in metamorphic grade.

Figure 4-8: Diagram illustrating cations Mg and cations Si in Ca-amphibole from Langø. Note that primary (MI) amphibole tends to have a smaller content of both Mg and Si than secondary (MII) amphibole. Note also that a decrease in Si corresponds to an increase in Al^{IV}.

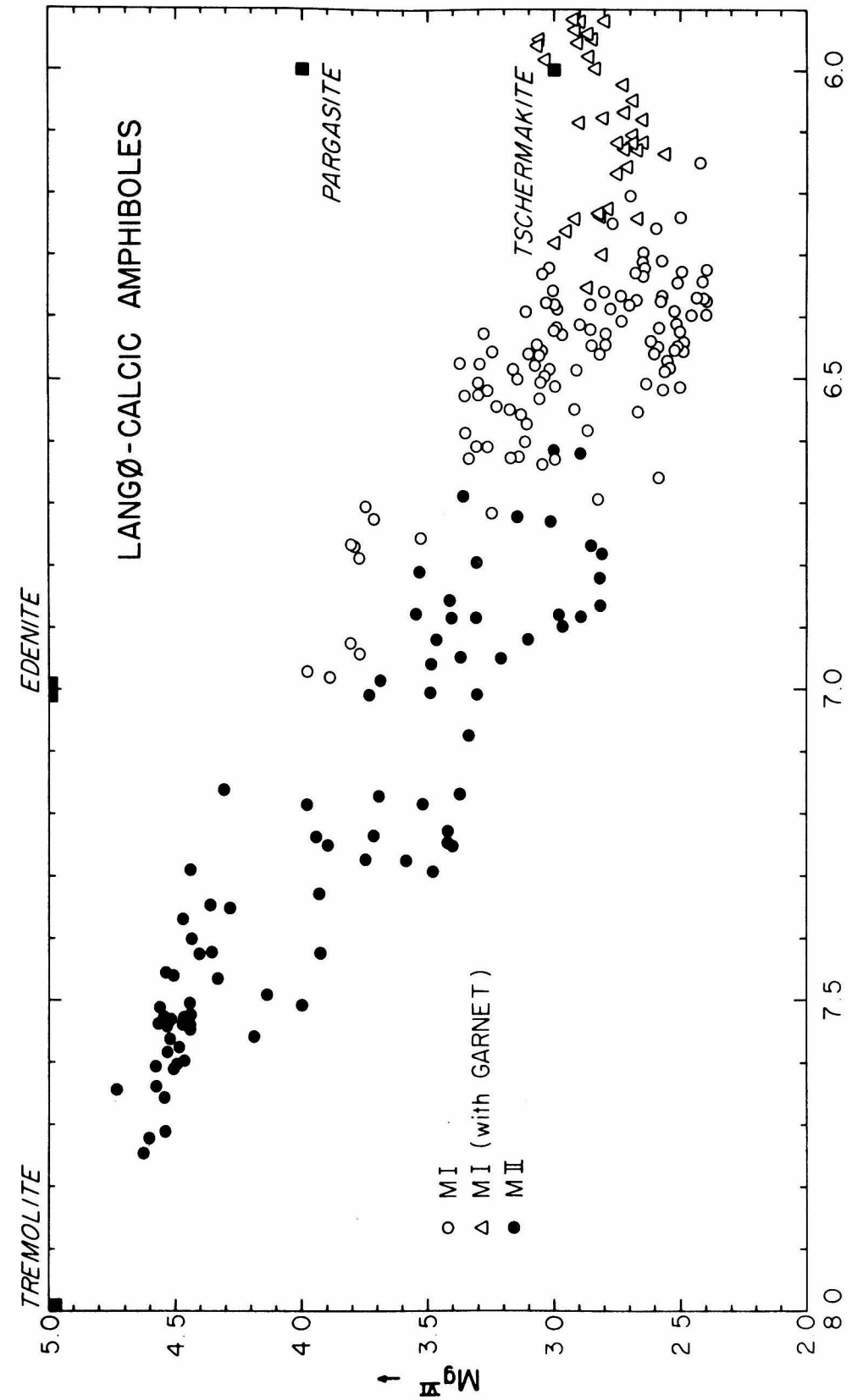
LANGØ-CALCIC AMPHIBOLES
TREMOLITE
EDENITE
PARGASITE
TSCHERMAKITE
○ MI
△ MI (with GARNET)
● MII
Mg^VI →
← Si^IV
5.0
4.5
4.0
3.5
3.0
2.5
2.0
8.0
7.5
7.0
6.5
6.0

All samples that contain MI Ca-amphibole on Langø also contain plagioclase, and the relationship between chemical changes that occur simultaneously in both phases is not well understood, particularly in high-grade metamorphic rocks (Leake, 1965). Figure 4-9 illustrates atomic Na/(Na + Ca) and Al/(Al + Si) in hornblende plotted against mole % anorthite [Ca/(Ca + Na + K)] in coexisting plagioclase. The detailed chemical variations in each phase have already been discussed, where emphasis was placed on the wide range in composition observed in each phase.

The data plotted in Figure 4-9 represent only MI amphibole and plagioclase. The plotted points are the average for each phase in one area in a particular sample, and the bars indicate the compositional range observed in that area. The dashed lines connect the compositions of the calcic and sodic plagioclase associated with the Huttenlocher gap.

Note that both Na/(Na+Ca) and Al/(Al+Si) in hornblende tend to increase as the anorthite content of plagioclase increases. This corresponds to a sympathetic relationship between Al/(Al+Si) in both phases, and an antithetic relationship between Na/(Na+Ca). This contrast is explainable in terms of the differing ways in which Na, Ca, Al and Si are incorporated in plagioclase and hornblende.

Ca in hornblende is nearly constant (Figure 4-4) so that an increase in the ratio Na/(Na+Ca) is predominantly an increase in Na-content. An increase in the ratio Al/(Al+Si) represents both an increase in Al and a decrease in Si. These changes correspond to the edenite substitution: $[(Na)^{A} + (Al)^{IV} \rightleftarrows (\square)^{A} + (Si)^{IV}]$, as discussed previously.

Figure 4-9: Diagram illustrating atomic Al/(Al+Si) and atomic Na/(Na+Ca) in primary (MI) hornblende plotted against the anorthite content [atomic Ca/(Ca+Na+K)] of adjacent primary (MI) plagioclase. The length of the bars represents the range in composition in each area, the data points represent the average composition of the phases in each area, and the dashed lines connect the compositions of co-existing plagioclase in grains with the Huttenlocher intergrowth (see text for discussion).

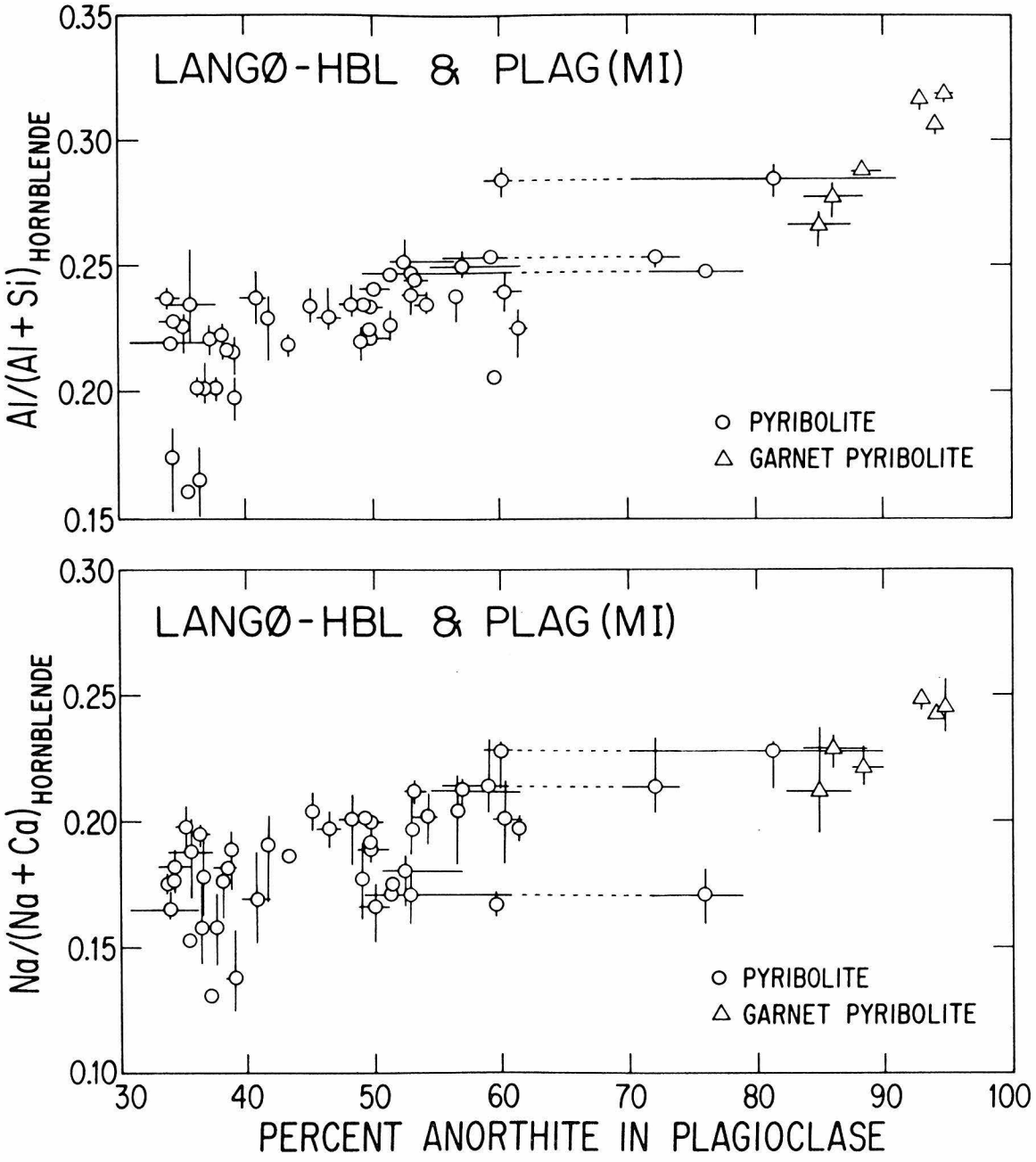
LANGØ-HBL & PLAG(MI)
Al/(Al + Si)HORNBLENDE
0.35
0.30
0.25
0.20
0.15
PYRIBOLITE
GARNET PYRIBOLITE
LANGØ-HBL & PLAG(MI)
Na/(Na + Ca)HORNBLENDE
0.30
0.25
0.20
0.15
0.10
30
40
50
60
70
80
90
100
PERCENT ANORTHITE IN PLAGIOCLASE
PYRIBOLITE
GARNET PYRIBOLITE

In plagioclase, Ca and Al both increase as Na and Si decrease corresponding to substitution of anorthite ($CaAl_2Si_2O_8$) for albite ($NaAlSi_3O_8$).

Thus the data in Figure 4-9 reflect an increase in the Al-content of both plagioclase and hornblende that is probably related to increases in the Al_2O_3-content of the host rock. The fact that the most aluminous hornblende and the most aluminous plagioclase occur with garnet supports this conjecture. Na happens to increase along with Al in hornblende by virtue of the edenite substitution, whereas Na in plagioclase decreases as Al increases due to the anorthite-albite substitution.

These data indicate clearly that under conditions of hornblende granulite grade metamorphism, the compositions of plagioclase and hornblende are correlated over the range $\sim An_{30}$ to $\sim An_{100}$. This observation, together with the data on the compositions of both Ca-amphibole and plagioclase,

of plagioclase or amphibole compositions alone, or relationships between amphibole and plagioclase compositions, as an indicator of metamorphic grade, unless the compositional variation at a uniform metamorphic grade is known.

E. Pyroxene

Orthopyroxene, clinopyroxene, or both occur in all the lithologies on Langø except for the potassium feldspar gneisses where only relic orthopyroxene was observed. The presence of pyroxene in these samples forms the basis for classifying the earlier metamorphism (MI) at granulite grade. In addition, there is abundant petrographic evidence that pyroxene became unstable with respect to the growth of new, lower grade minerals

during a later metamorphism (MII). In the various pyribolites, diorite, and calc-silicate gneisses, ortho- and/or clinopyroxene was replaced locally by hornblende, whereas in the orthopyroxene gneisses and biotite pyribolites, it was replaced by biotite-quartz intergrowths.

Pyroxene was analyzed for Na, Mg, Al, Si, Ca, Ti, Cr, Fe and Mn, and the resultant analyses normalized to: Total Cations = 4.0. The mineral formula is taken to be $(Ca, Fe^{2+}, Mg)_2 Si_2O_6$, but some analyses deviate substantially from this composition, especially with respect to Fe^{3+}, Mn, and Al.

The amount of Fe^{3+} was estimated from calculated charge deficiency, assuming a theoretical maximum of 12.0. Calculated values for Fe^{2+}/Fe^{Total} ($\sim$0.9 in orthopyroxene and $\sim$0.7 in clinopyroxene) are rather constant over a considerable range of $Mg/(Mg+Fe^{Total})$ (0.52 to 0.89). It is thus apparent that clinopyroxene concentrates Fe^{3+} relative to orthopyroxene.

The MnO-content of the pyroxene on Langø ranges from <0.05 to 1.78 wt %, with the concentration in orthopyroxene generally higher than in clinopyroxene. Although MnO in the pyroxene tends to increase as FeO increases, the data scatter considerably (Figure 4-10), and do not follow the simple pattern related to igneous processes displayed by FeO and MnO in lunar and certain meteoritic pyroxene (Dymek et al., 1976).

The Al_2O_3-content of the pyroxene ranges from 0.67 to 8.1 wt %, with the highest values found in orthopyroxene associated with cordierite. For any given lithology, the clinopyroxene tends to be enriched in Al relative to orthopyroxene.

Al^{VI}-Al^{IV} variation in the pyroxene is illustrated in Figure 4-11. As can be seen in the diagram, most of the pyroxene has substantially

Figure 4-10: Diagram illustrating wt % MnO and wt % FeO (i.e., total iron) in pyroxene from Langø. The lack of a straight line correlation is in marked contrast to that discovered for pyroxene in lunar samples and the meteorite Kapoeta (Dymek et al., 1976). Consideration of calculated Fe^{2+} and Fe^{3+} does not reduce the scatter in the data. The data for the Langø samples probably reflect original heterogeneities in the distribution of iron and manganese in the protolith of these metamorphic rocks.

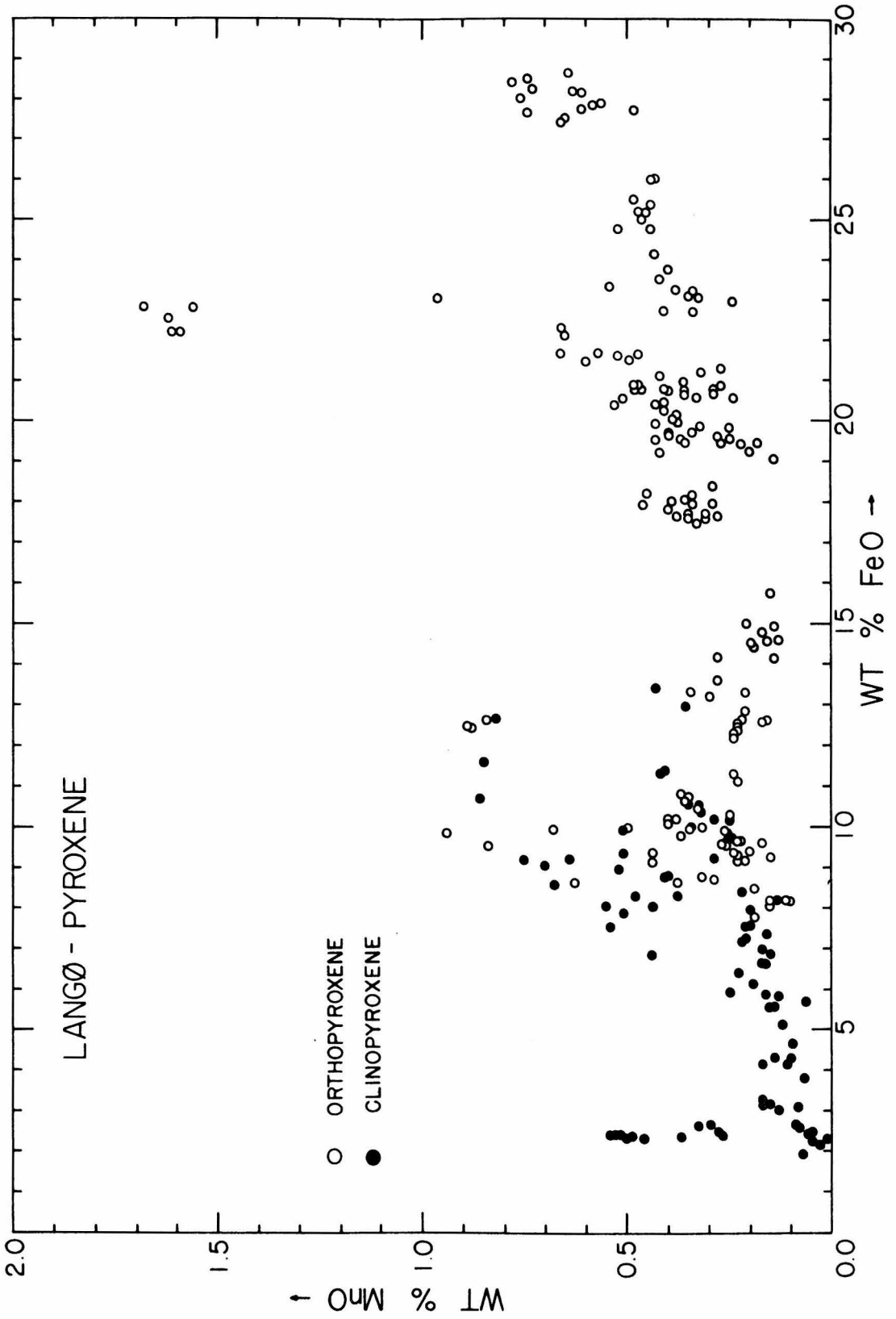
LANGØ - PYROXENE
○ ORTHOPYROXENE
● CLINOPYROXENE
WT % MnO →
WT % FeO →
0.0
0.5
1.0
1.5
2.0
5
10
15
20
25
30

Figure 4-11: Diagram illustrating the Al_2O_3-contents of pyroxene in samples from Langø in terms of cations Al^{VI} and cations Al^{IV}. Note that, with only a few exceptions, the pyroxene is enriched in Al^{IV} relative to Al^{VI}. Note also that in a given lithology, clinopyroxene tends to be more aluminous than orthopyroxene, although orthopyroxene that occurs with cordierite is the most aluminous pyroxene observed in any of the samples.

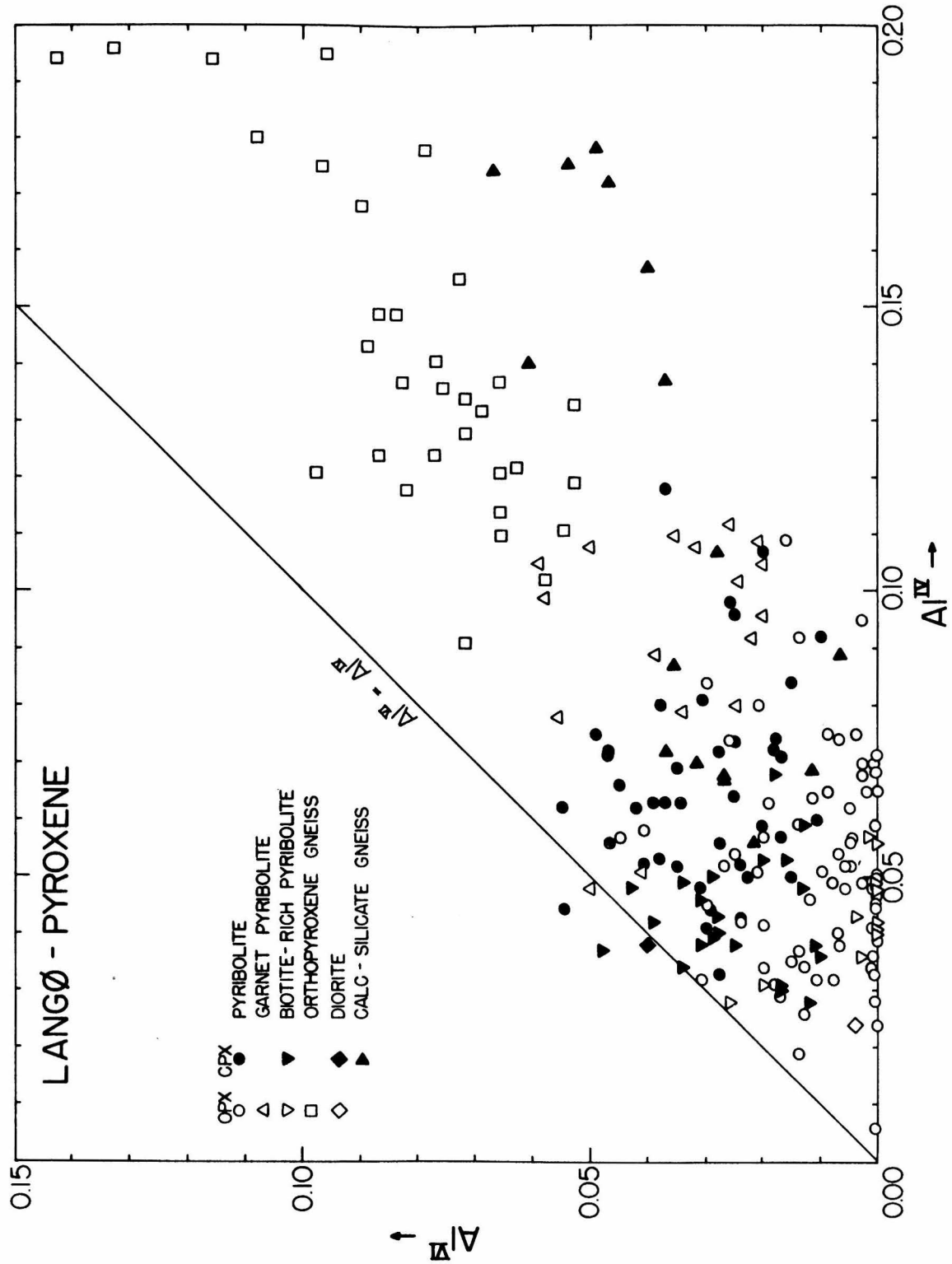
LANGØ - PYROXENE
CPX
OPX
PYRIBOLITE
GARNET PYRIBOLITE
BIOTITE-RICH PYRIBOLITE
ORTHOPYROXENE GNEISS
DIORITE
CALC-SILICATE GNEISS
$Al^{VI} = Al^{IV}$
Al^{VI} →
Al^{IV} →
0.00
0.05
0.10
0.15
0.20

more tetrahedral than octahedral aluminum. This observation indicates that the substitutional mechanism: $(R^{2+})^{VI} + (Si^{4+})^{IV} \rightleftarrows (Al^{3+})^{VI} + (Al^{3+})^{IV}$ would not balance the large amounts of Al^{IV} present in the pyroxene even after allocating Al^{IV} to form the end-members $R^{2+}TiAlAlO_6$ and $R^{2+}CrAlSiO_6$. However, examination of the analyses indicates that there is sufficient calculated Fe^{3+} to balance the "excess" Al^{IV} as the end-member $R^{2+}Fe^{3+}AlSiO_6$. Hence, Fe^{3+} in pyroxene substitutes for and behaves like Al^{3+}, as was shown for Ca-amphibole.

The concentration of Na_2O is distinctly lower in orthopyroxene ($\lesssim$0.06 wt %) than in clinopyroxene (0.18-0.81 wt %). However the low overall Na-content indicates that the clinopyroxene from Langø bears no relationship to omphacite found in high pressure eclogites.

There is some overlap in the TiO_2- and Cr_2O_3-contents, but the amounts are generally higher in clinopyroxene (TiO_2: <0.05-0.51 vs. <0.05-0.35 wt %; Cr_2O_3: <0.05-1.14 vs. <0.05-0.31 wt %). The highest Cr_2O_3-contents occur in clinopyroxene from the calc-silicate gneisses.

Figure 4-12 illustrates pyroxene compositions in terms of atomic Ca-Mg-Fe+Mn. (This is not a pyroxene quadrilateral, since minor element end-members are not considered). Mg-values range from 0.52 to 0.89 in the orthopyroxene and 0.53 to 0.95 in the clinopyroxene. The latter are highly calcic ($\sim$22 to 24 wt % CaO) and, except for those analyses from clinopyroxene in the calc-silicate samples, the Ca-content tends to decrease slightly as Fe/Mg increases. The orthopyroxene contains very little CaO (<1.0 wt %), but note that the orthopyroxene from orthopyroxene gneisses is slightly less calcic (<0.1 wt % CaO) than the others.

Figure 4-12: Compositions of pyroxene from Langø illustrated in terms of cations Ca, Mg, and Fe+Mn. Note the wide range of observed compositions, the uniformly high Ca-contents of clinopyroxene, and the uniformly low Ca-contents of orthopyroxene.

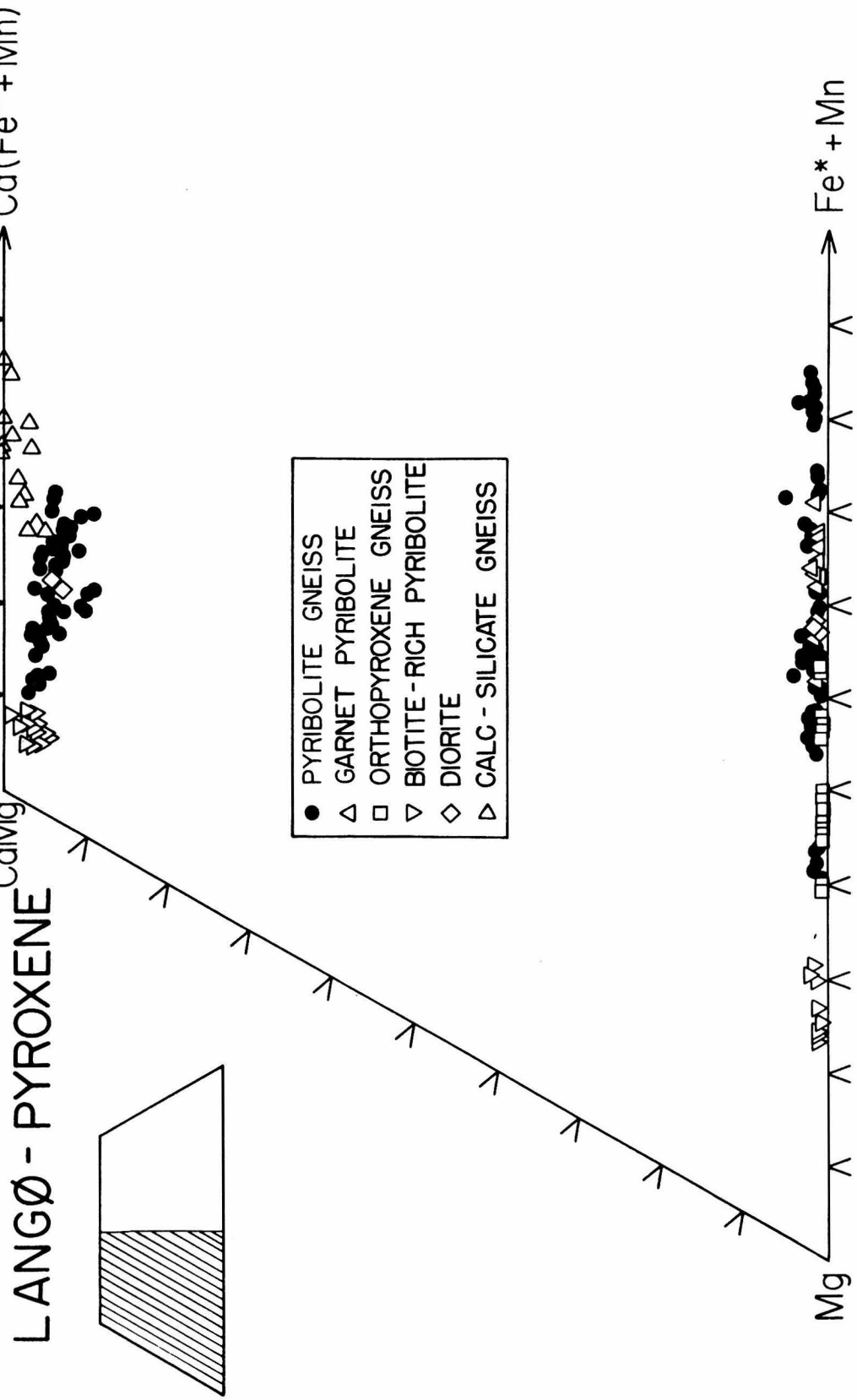
LANGØ - PYROXENE
Ca(Fe* + Mn)
CaMg
Mg
Fe* + Mn
PYRIBOLITE GNEISS
GARNET PYRIBOLITE
ORTHOPYROXENE GNEISS
BIOTITE-RICH PYRIBOLITE
DIORITE
CALC - SILICATE GNEISS

Compositions of coexisting ortho- and clinopyroxene are illustrated in Figure 4-13. The position and orientation of the tie lines are similar to those reported in other granulite terranes, and the average K_D ($=[Mg/Fe]_{opx}/[Mg/Fe]_{cpx}$) is 0.54, identical to that calculated for pyroxene pairs in other granulites (Kretz, 1961). Individual values for K_D range from .47 to .65 and tend to increase as the Mg-value in the clinopyroxene decreases, as noted by Fleet (1974).

Equilibration temperatures were calculated from Mg-Fe partitioning between orthopyroxene and clinopyroxene using the computer program PYXTEMP (Hewins, 1975), which is based on the empirical geothermometer of Wood and Banno (1973). The results ranged from 764° to 930°C (avg = 831°C) with all iron as Fe^{2+}, and from 779° to 951°C (avg = 817°C) using calculated Fe^{2+} and Fe^{3+}. There are no apparent correlations between the calculated temperatures and K_D, $(Fe/Mg)_{opx}$, or $(Fe/Mg)_{cpx}$.

Comparison of the Ca-contents of the ortho- and clinopyroxene with the experimentally-determined limbs of the pyroxene quadrilateral (Lindsley et al., 1974) suggests equilibration temperatures below 810°C, distinctly lower than those calculated from Fe-Mg partitioning. Lindsley (written communication, 1976) has indicated that the Wood-Banno empirical geothermometer fails to yield equilibration temperatures consistent with those actually used in carefully reversed experimental runs. The inadequacy of the Wood-Banno model is probably due to the fact that it was calibrated using high temperature (1200°C-1300°C) experimental data which cannot be extrapolated to lower temperatures.

Figure 4-13: Diagram illustrating tie-lines connecting the compositions of coexisting orthopyroxene and clinopyroxene in samples from Langø. Also illustrated are the compositions of coexisting pyroxenes equilibrated at 810°C (Lindsley et al., 1974). A comparison between the experimental work and the analyses of the pyroxene from Langø indicates equilibration temperatures of <810°C for the latter.

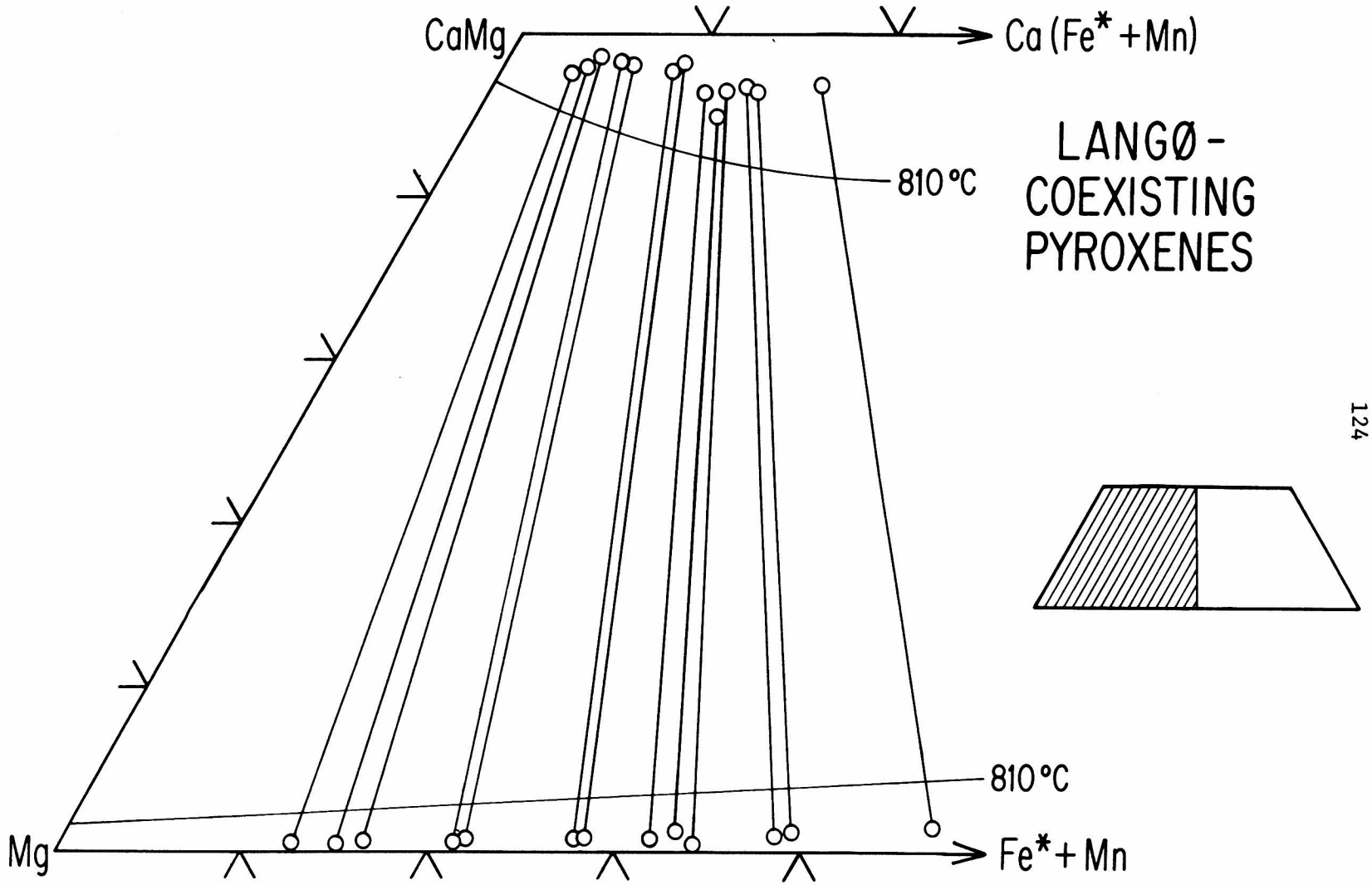
CaMg
Ca (Fe* + Mn)
810 °C
LANGØ -
COEXISTING
PYROXENES
810 °C
Mg
Fe* + Mn

F. Biotite

Biotite is present in most of the samples studied, its content ranging from negligible to ∿50 volume %. Many of the samples contain biotite grains with different colors and/or textures, which indicates at least two episodes of mineral growth.

All grains of green biotite are secondary (MII) and characterized by low Ti-content (<0.05-1.1 wt % TiO_2). In the same samples, primary (MI) biotite is brown and Ti-rich (∿1.5-6.0 wt % TiO_2). Green biotite can replace primary brown biotite, hornblende, pyroxene, cordierite, or garnet.

Secondary (MII) brown, Ti-rich (∿2-4 wt % TiO_2) biotite can also occur, and replaces pyroxene, hornblende, or cordierite. Thus the color and Ti-content of biotite do not necessarily discriminate between primary (MI) and secondary (MII) types.

Biotite has been analyzed for Na, Mg, Al, Si, K, Ca, Ti, Mn, Fe, Zn, F and Cl, and the analyses normalized to: Total Cations - (K+Na+Ca) = 7.0. The general mineral formula is taken to be: $(K)^{XII}(Fm_3)^{VI}(AlSi_3)^{IV}O_{10}(OH, F, Cl)_2$. The normalization procedure assumes full occupancy of the VI- and IV-fold sites, but permits vacancies in the XII-fold (alkali) site.

The contents of MnO and ZnO are generally very low (<0.10 wt % each), and CaO is below its detection limit (<0.03 wt %). The substitution of Na for K is likewise small (<0.05 cations Na). However, there are two significant departures from the idealized formula given above: the number of Al+Si cations/formula is always greater than 4, indicating

substantial Al^{VI} in addition to Al^{IV}, and the number of Ti cations/formula ranges up to 0.34 (= 6.0 wt % TiO_2).

There is a very large range in Mg-value of the biotite (0.49-0.93) that appears to be related to the nature of the host rock. As can be seen in Figure 4-14, biotite from potassium feldspar gneisses tends to be the most Fe-rich, whereas that in biotite pyribolite gneisses is the most Mg-rich. Also, for a given lithology, secondary biotite is more magnesian than primary biotite. The shift towards higher Mg-values accompanying the formation of secondary biotite is related in part to the growth of secondary magnetite that concentrates the iron. Also evident in Figure 4-14 is the lack of any apparent correlation between Mg-value and either Al^{IV} or Al^{VI}.

Chemical analyses of biotite from high grade metamorphic rocks by classical methods indicate modest contents of Fe_2O_3. Since iron is determined only as FeO with the microprobe, the amount of Fe^{3+} in the biotite analyses presented here is an unknown quantity. In general, the Fe^{3+}-content of any mineral can be estimated by calculating a total positive charge (with all iron as Fe^{2+}) and allowing the charge deficiency from a theoretical maximum to be equal to the number of Fe^{3+} atoms. Such a procedure works quite well on analyses of pyroxene and amphibole, for example.

However, with but a few exceptions, the total positive charge calculated for the analyses of biotite from Langø always exceeds the theoretical maximum of 22.00, assuming a full complement of 2 (OH + F + Cl). A charge excess may be caused by the presence of vacancies, in which case the analyses are normalized to a larger number of cations

Figure 4-14: Diagram illustrating the composition of biotite in samples from Langø in terms of atomic Mg/(Mg+Fe+Mn) versus cations Al^{IV} and Al^{VI}. No apparent correlation exists between Mg-value and Al-content.

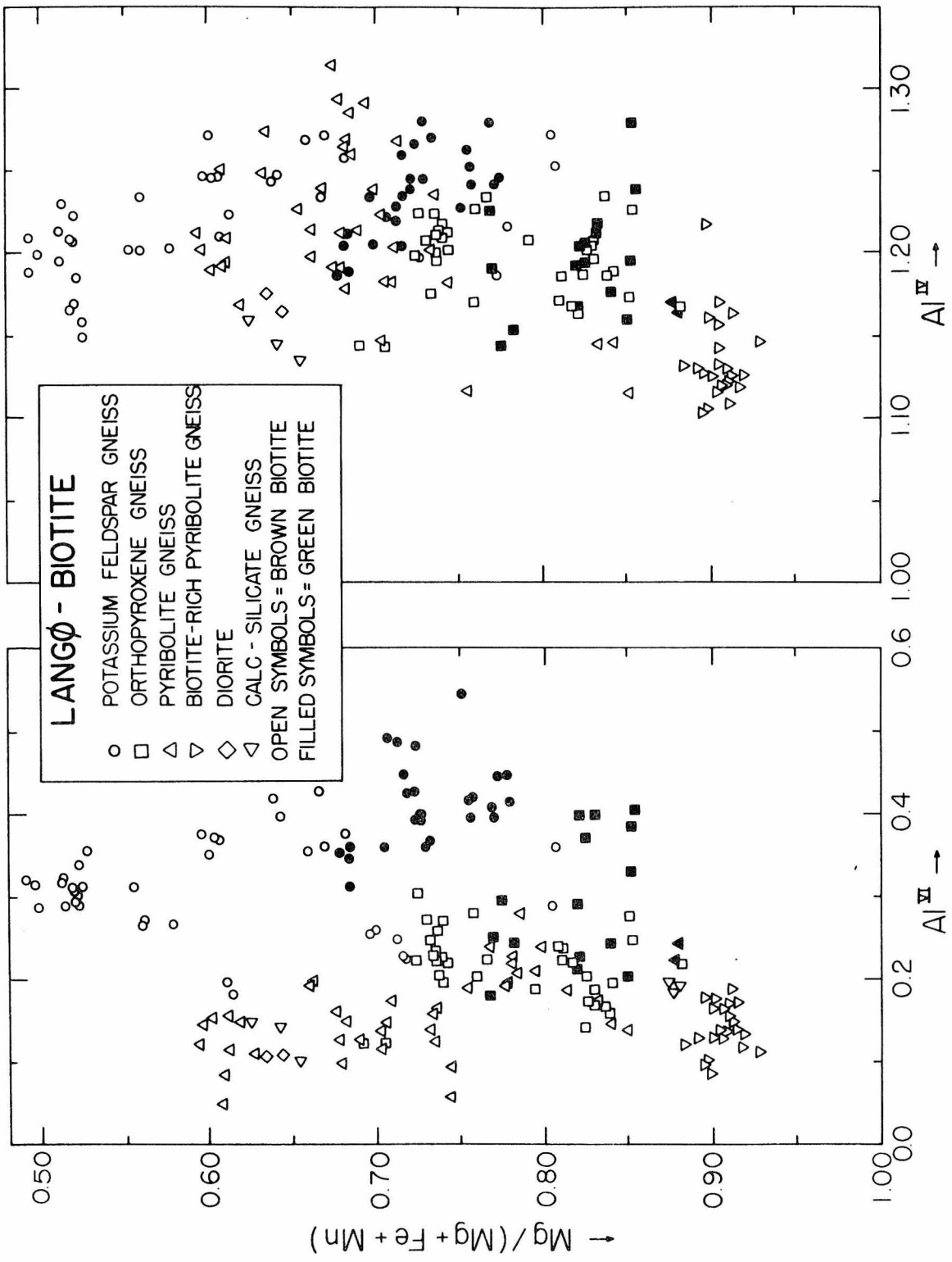
LANGØ - BIOTITE
POTASSIUM FELDSPAR GNEISS
ORTHOPYROXENE GNEISS
PYRIBOLITE GNEISS
BIOTITE-RICH PYRIBOLITE GNEISS
DIORITE
CALC - SILICATE GNEISS
OPEN SYMBOLS = BROWN BIOTITE
FILLED SYMBOLS = GREEN BIOTITE
Mg / (Mg + Fe + Mn)
0.50
0.60
0.70
0.80
0.90
1.00
AlIV
0.00
0.2
0.4
0.6
1.00
1.10
1.20
1.30

than is actually present, hence a charge excess is "created" by the normalization procedure used. Alternatively there may be no vacancies, and the charge excess is balanced by a deficiency in (OH+F+Cl).

The (K+Na)-content of the XII-fold site is always less than 1, thus indicating the presence of vacancies in that position. However, there is no correlation between the charge excess and occupancy of the XII-fold site. Hence, the charge excess does not appear to be related to cation deficiency there.

Since Σ (Al+Si) >4.0 in all cases, it appears as if the IV-fold site is filled, and neither vacancies nor charge excess can be attributed to it.

The only cations present in substantial amounts in octahedral coordination are Mg, Fe, Ti and Al. It is logical to suspect that, if vacancies occur here, they are related to the incorporation of Al^{3+} and/or Ti^{4+} rather than simple Mg-Fe substitution.

There is an excellent correlation between charge excess and Ti-content in biotite (Figure 4-15), and the fact that the data cluster about the line: Charge excess = 2Ti, suggests that the vacancy-forming substitution:

$$(Ti^{4+})^{VI} + (\square)^{VI} = (2R^{2+})^{VI}, \text{ is operative*.}$$

---

* Other possible mechanisms for Ti substitution in biotite have been considered and rejected. These include:

a) $R^{2+} + Ti^{4+} \rightleftarrows 2Al^{3+}$. This is analogous to the well-documented $R^{2+}TiAl_2O_6$ substitution in pyroxene, which maintains charge balance, but does not produce a charge excess. (Footnote continued pg. 132.)

Figure 4-15: Diagram illustration cations Ti and calculated total positive charge for analyses of biotite in samples from Langø. The theoretical maximum positive charge is 22.00, and note that nearly all the analyses yield a charge excess. The fact that the data cluster about the line: Charge Excess = 2 Ti, suggests that Ti is incorporated in biotite by means of a vacancy-forming substitution. Note also that analyses of biotite from potassium feldspar gneisses have a charge excess that is typically larger than analyses of biotite from other lithologies. (See text for discussion).

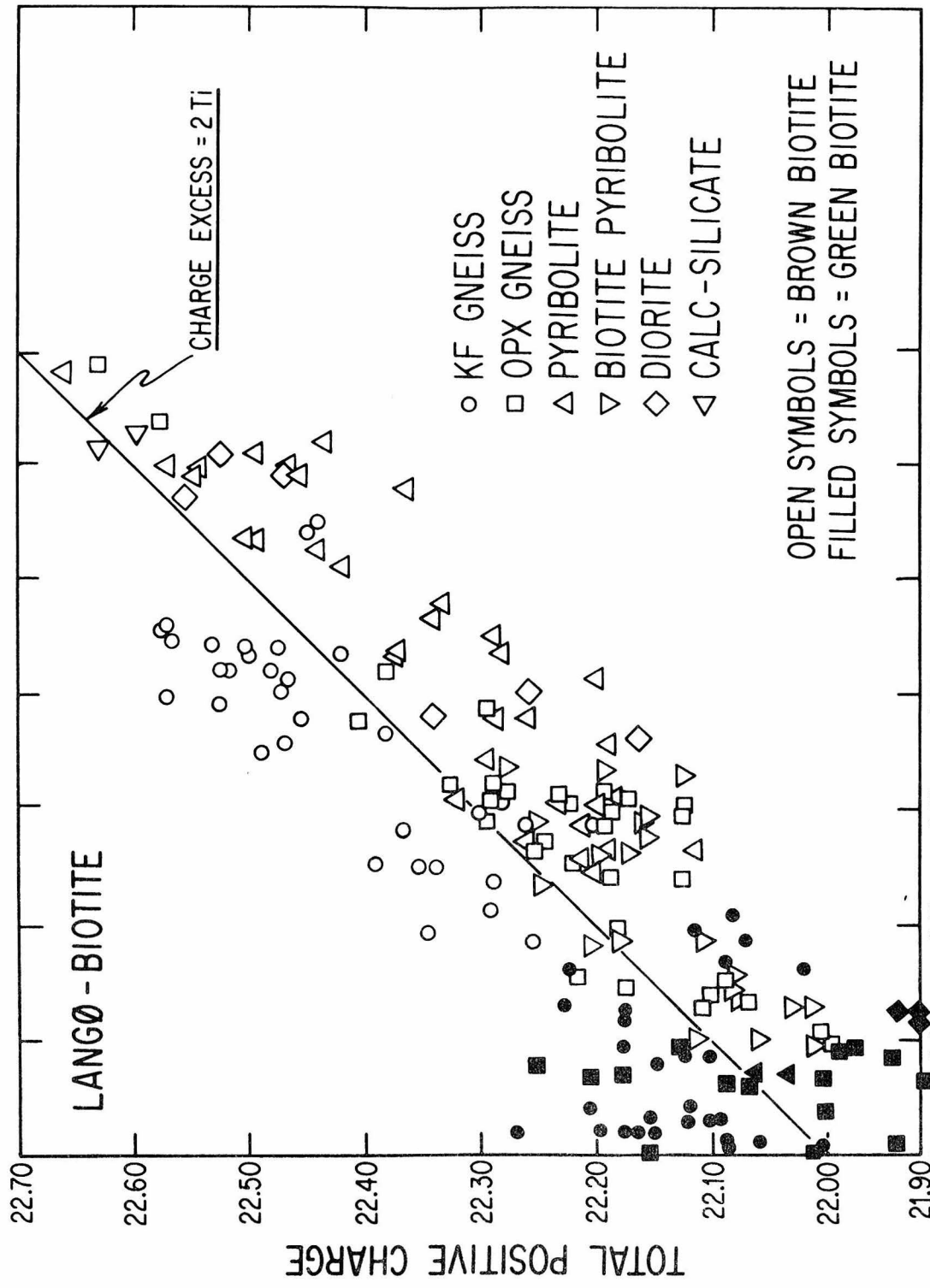
LANGØ-BIOTITE
CHARGE EXCESS = 2 Ti
KF GNEISS
OPX GNEISS
PYRIBOLITE
BIOTITE PYRIBOLITE
DIORITE
CALC-SILICATE
OPEN SYMBOLS = BROWN BIOTITE
FILLED SYMBOLS = GREEN BIOTITE
TOTAL POSITIVE CHARGE
22.70
22.60
22.50
22.40
22.30
22.20
22.10
22.00
21.90
0
0.05
0.10
0.15
0.20
0.25
0.30
0.35
Ti

Dahl (1969, 1970) presented data in support of this substitution, but did not illustrate any correlations with charge excess.

Figure 4-16 illustrates Ti-content and Mg/Fe in biotite. The data suggest that as Mg/Fe increases, the Ti-content decreases. However the analyses of biotite from biotite pyribolites are inconsistent with such a relationship, and any effects related to Fe^{3+} (which would change Mg/Fe) are unknown.

---

b) $(R^{2+})^{VI} + (2Si^{4+})^{IV} \rightleftarrows (Ti^{4+})^{VI} + (2Al^{3+})^{IV}$. This substitution was discussed by Foster (1960), and more recently by Guidotti et al., (in press). Like a), it maintains charge balance but does not produce a charge excess.

c) $Ti^{4+} + 2O^{2-} \rightleftarrows R^{2+} + 2(OH)^{-}$. This substitution seems to be the only alternative to the Ti-vacancy substitution, since it not only maintains charge balance, but also provides for an octahedral charge excess. It explains Ti-substitution in clinohumite rather well, where there is a corresponding correlation between Ti-content and (OH+F) deficiency (Jones et al., 1969). Recently, Takeda and Ross (1975) have proposed this substitution in relation to ferric iron-rich oxybiotite from a rhyodacite ash flow. However, an examination of the biotite analyses indicates no correlation between Ti-content and (OH+F+Cl). Hence, this mechanism also seems unimportant.

Figure 4-16: Diagram illustrating cations Ti and atomic Mg/Fe for analyses of biotite in samples from Langø. Note that in biotite from potassium feldspar gneisses, orthopyroxene gneisses, and pyribolite gneisses, the Ti-content tends to decrease as Mg/Fe increases.

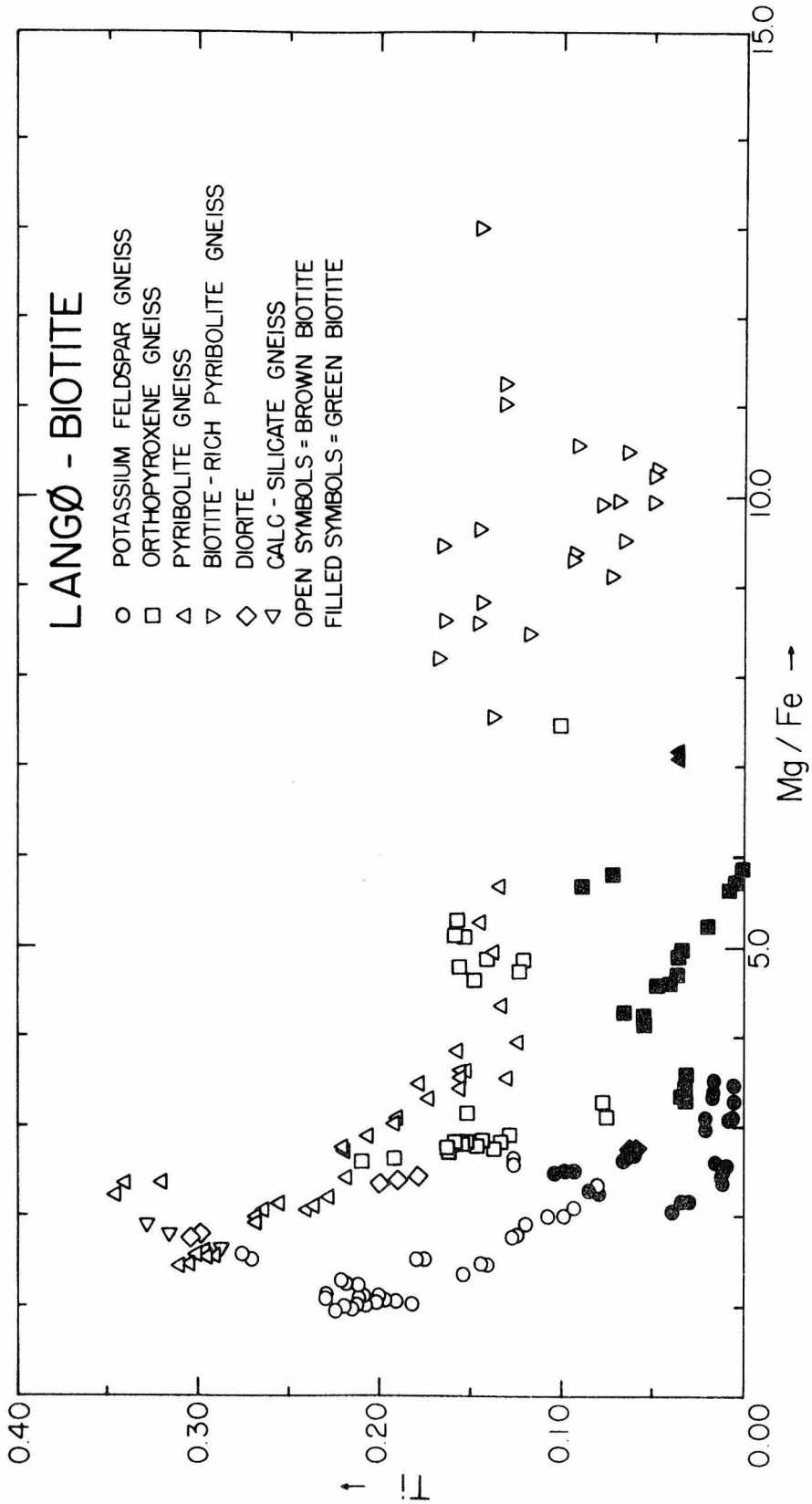
LANGØ - BIOTITE
POTASSIUM FELDSPAR GNEISS
ORTHOPYROXENE GNEISS
PYRIBOLITE GNEISS
BIOTITE - RICH PYRIBOLITE GNEISS
DIORITE
CALC - SILICATE GNEISS
OPEN SYMBOLS = BROWN BIOTITE
FILLED SYMBOLS = GREEN BIOTITE
Ti →
0.40
0.30
0.20
0.10
0.00
5.0
10.0
15.0
Mg / Fe →

Figure 4-17 illustrates Al^{IV} and Al^{VI} in biotite from Langø. Note that a large number of data points plot above the line for theoretical Al^{VI}-Al^{IV} variation and have "excess" Al^{VI}. Note also that, on the average, analyses of biotite from potassium feldspar gneisses have more Al^{VI} than analyses of biotite from pyribolite gneisses.

This pattern of increasing Al^{VI} can be correlated with the data in Figure 4-15 for total positive charge and Ti-content of the biotite. In Figure 4-15, the line: Charge Excess = 2Ti, represents the maximum allowable charge excess associated with the Ti-vacancy substitution. Any Fe^{3+} present in the biotite will lower the calculated charge from this line. Note, however, that many biotite analyses plot above the line in Figure 4-15, and thus have a charge excess that exceeds that accounted for by the Ti-vacancy substitution. In particular, note that nearly all of the analyses of biotite from potassium feldspar gneisses, which have the most Al^{VI} (Figure 4-17), plot above the line in Figure 4-15. The presence of this additional charge excess suggests that incorporation of large amounts of Al^{VI} in biotite requires the formation of additional VI-fold vacancies by the dioctahedral-trioctahedral substitution: $2R^{3+} + \square \rightleftarrows 3R^{2+}$.

One additional point should be made with respect to Ti and Al^{VI} in biotite. Figure 4-15 illustrates quite emphatically that the Ti-contents of biotite from Langø are in general quite large. The Ti-content of biotite tends to increase with increasing metamorphic grade, and substantial amounts of Ti occur typically in only high-grade biotite (Miyashiro, 1974). Low-grade Ti-poor biotite can be quite Al-rich (Dymek, unpublished; Labotka, personal communication) and characterized by large

Figure 4-17: Diagram illustrating the Al_2O_3-content of biotite in terms of cations Al^{IV} and cations Al^{VI}. Note that many of the biotite analyses have Al^{VI}-contents greater than that permitted by simple Al^{VI}-Al^{IV} substitution among the theoretical biotite end-members.

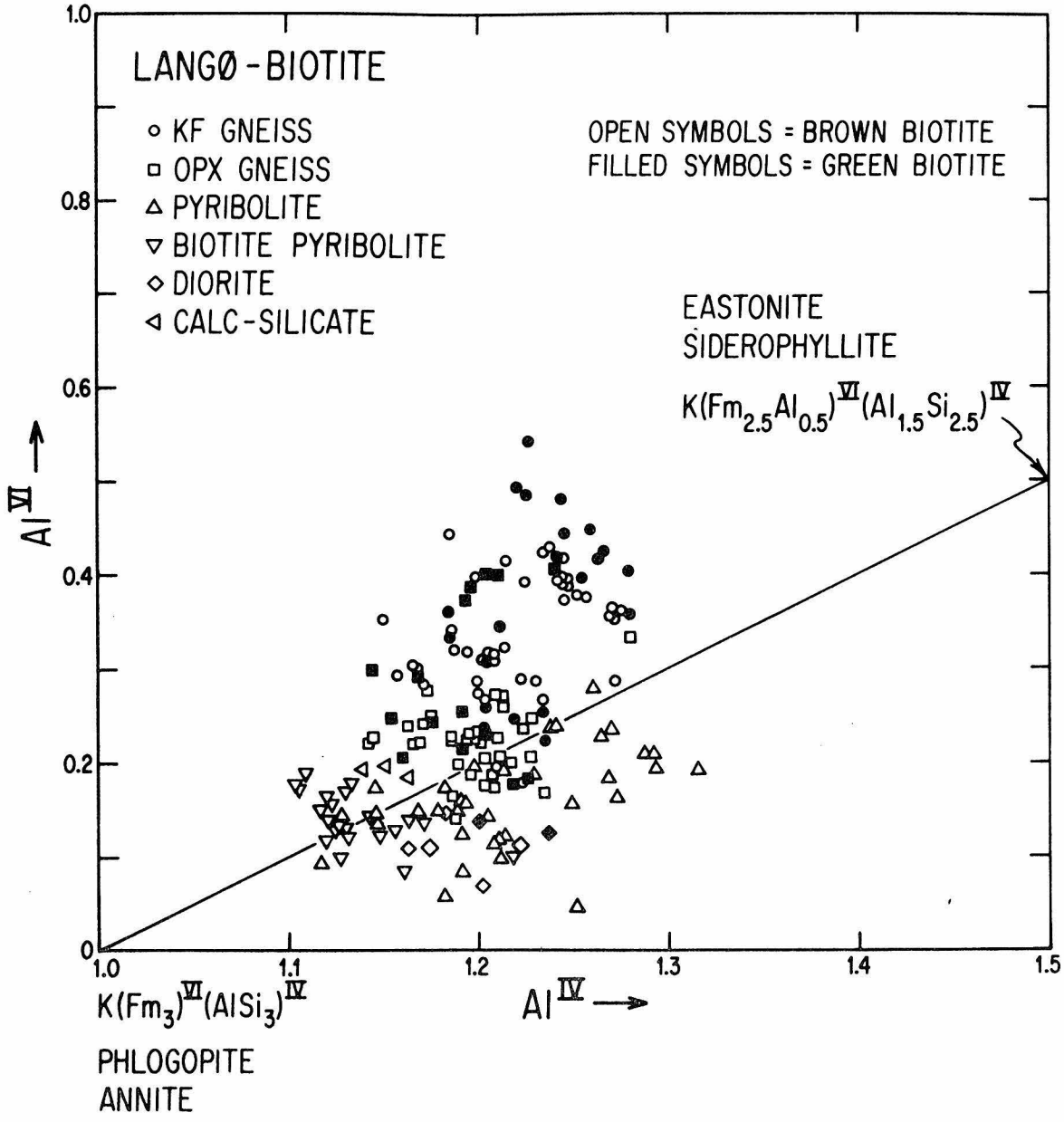
LANGØ - BIOTITE
KF GNEISS
OPX GNEISS
PYRIBOLITE
BIOTITE PYRIBOLITE
DIORITE
CALC-SILICATE
OPEN SYMBOLS = BROWN BIOTITE
FILLED SYMBOLS = GREEN BIOTITE
EASTONITE
SIDEROPHYLLITE
$K(Fm_{2.5}Al_{0.5})^{VI}(Al_{1.5}Si_{2.5})^{IV}$
Al^{VI}
Al^{IV}
$K(Fm_3)^{VI}(AlSi_3)^{IV}$
PHLOGOPITE
ANNITE
1.0
0.8
0.6
0.4
0.2
0
1.0
1.1
1.2
1.3
1.4
1.5

amounts of Al^{VI}-related vacancies. These tend to "swamp out" the Ti-vacancy substitution, and the latter would be observed only under exceptional circumstances in low-grade rocks.

The data presented here suggest that the normalization procedure for biotite that was used is inappropriate. Calculations indicate that if biotite analyses are normalized to: Total Cations - (Na+K+Ca) + Ti = 7, which "removes" the effect of Ti-related vacancies, then minimum Fe^{3+} can be estimated from the resultant charge deficiency, or minimum Al^{VI}-related vacancies from charge excess. Since both ferric iron and vacancies appear to occur together, the normalization of microprobe analyses of biotite still remains a problem.

G. Garnet

Dark pink to burgundy-colored garnet is present in a few of the pyribolite gneisses and is a characteristic mineral in most of the potassium feldspar gneisses. In both lithologies it was apparently unstable, breaking down to kyanite + biotite via a retrograde reaction in the potassium feldspar gneisses, and reacting with hornblende to form orthopyroxene via a prograde reaction in the pyribolite gneisses.

The garnet was analyzed for Mg, Al, Si, Ca, Ti, Cr, Mn and Fe, and the resultant analyses normalized to: Total Cations = 8.0. The general formula is taken to be: $(Mg, Ca, Mn, Fe^{2+})_3 (Si, Fe^{3+})_2 Si_3 O_{12}$, and the garnet analyses conform very closely to this.

TiO_2-and Cr_2O_3-contents of garnet in the potassium feldspar gneisses are uniformly low (<0.05 wt %), but in the pyribolite gneiss their concentrations range to higher values (0.08 and 0.65 wt %

respectively). The number of Si cations/formula ranges from 2.93-3.02, Al cations/formula ranges from 1.90-2.03, and Fe^{3+} calculated from stoichiometric considerations is <0.05 cations/formula.

Figure 4-18 depicts garnet compositions in terms of atomic Mg-Ca-Fe-Mn. The garnet from pyribolite gneisses is distinctly more calcic than that from potassium feldspar gneisses (3.7 to 5.4 vs. 0.6-1.1 wt % CaO), whereas those in potassium feldspar gneisses are slightly more Mn-rich (1.3 to 3.9 vs. 0.9-1.9 wt % MnO). The range in Mg-value is similar in both garnet groups (∿16 mole %), but those in the potassium feldspar gneisses are slightly more Fe-rich. Each garnet grain analyzed was slightly zoned, becoming more Fe-rich from core to rim.

The compositions of the garnet from Langø are similar to those reported from other high-grade metamorphic terranes in that they are more magnesian and less calcic than those found at lower grade (Binns, 1969; Miyashiro, 1974).

H. Cordierite

Cordierite is a rare mineral in the samples studied. It occurs in five of the orthopyroxene gneisses where it comprises up to 30 volume percent of the sample. In addition, altered cordierite has been identified in one of the potassium feldspar gneisses (24C).

The cordierite was analyzed for Na, Mg, Al, K, Ca, Ti, Mn and Fe, and normalized to: Total Cations = 11 - (K+Na+Ca). This normalization procedure assigns all the (Na+K+Ca) to the channels in the cordierite structure (Goldman et al., in press). The oxide totals (96.5-99.5 wt %) indicate that substantial H_2O is present, which is also assigned to the channels (Goldman et al., in press).

Figure 4-18: Compositions of garnet in samples from Langø illustrated in terms of atomic Fe - Ca - Mg - Mn. The length of the bar corresponds to the Mn-content as indicated in the figure.

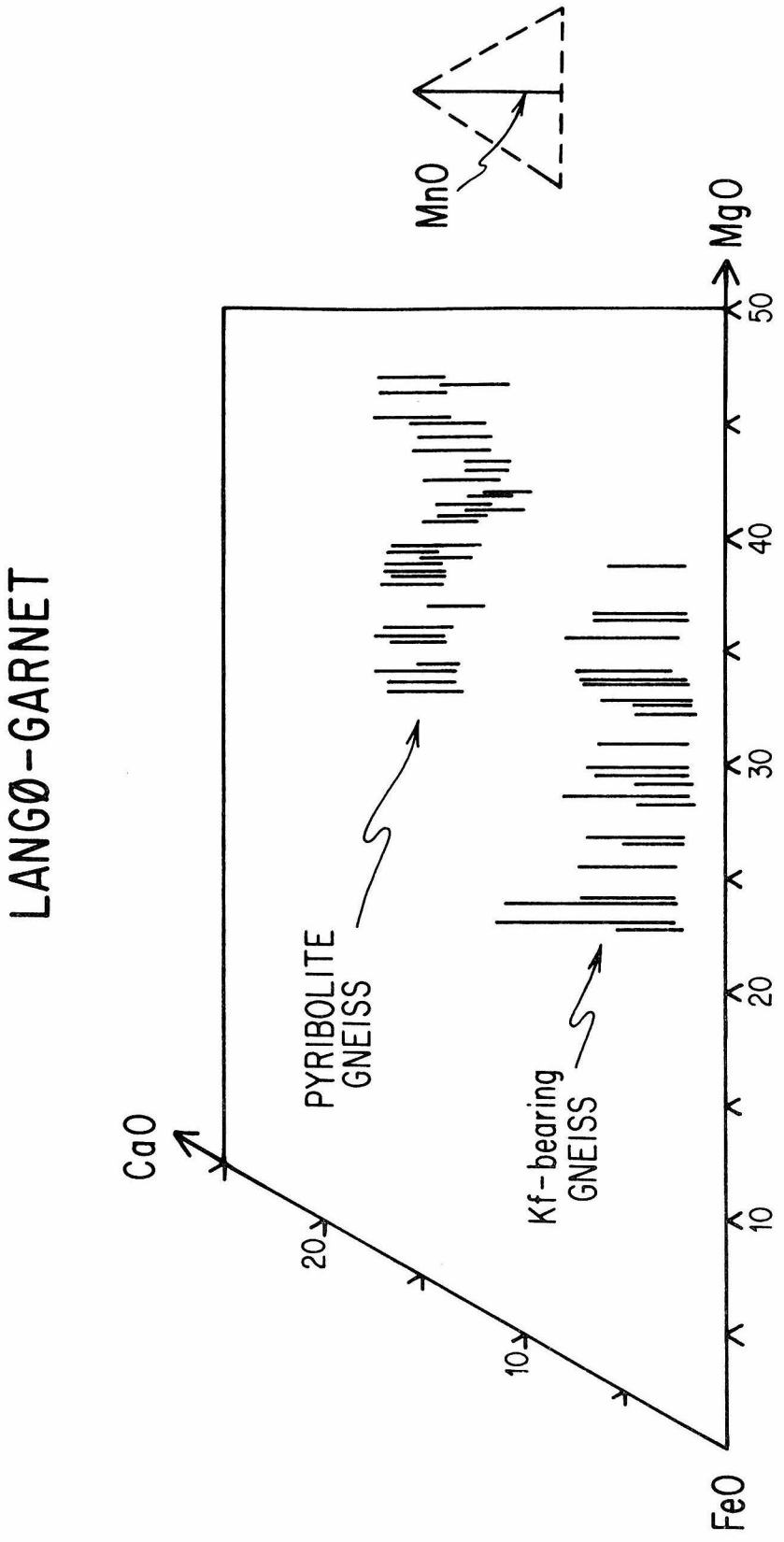
LANGØ-GARNET
MnO
MgO
CaO
FeO
PYRIBOLITE GNEISS
Kf-bearing GNEISS
10
20
10
20
30
40
50

CaO and K_2O were not detected (<0.03 and <0.05 wt % respectively) and the contents of Na_2O, MnO and TiO_2 are small (<0.10, <0.40 and 0.09 wt % respectively). Thus, the cordierite is virtually pure $(Mg,Fe)_2Al_4Si_5O_{18}$.

The cordierite is highly magnesian, with measured Mg-values ranging from 0.88 to 0.95. Zoning was not detected. Such compositions are characteristic of cordierite from granulite grade gneisses (Wynne-Edwards and Hay, 1963).

I. Sillimanite and Kyanite

Prismatic sillimanite occurs as a primary mineral in some of the potassium feldspar gneisses, and as relic inclusions in biotite in some orthopyroxene gneisses. Secondary, acicular to blocky kyanite replaces garnet and cordierite in the potassium feldspar gneisses and cordierite in the orthopyroxene gneisses.

Both minerals were analyzed for Na, Al, Si, K, Ti and Fe, and normalized to: Total Cations = 3.0. Na and K were not detected, and Ti is at or near its detection limit (<0.07 wt % TiO_2). Iron is the only element present in substantial amounts (0.75-1.11 wt % in sillimanite; 0.40-0.93 wt % in kyanite). Stoichiometry considerations indicate that all the iron occurs as Fe^{3+}.

The Fe-content of aluminosilicates was studied by Albee and Chodos (1969) who reported similar values for coexisting Al_2SiO_5 polymorphs. In the samples studied from Langø, the Fe-contents of sillimanite and kyanite that occur in the same thin section are virtually identical, even though these phases formed at distinctly different times. Hence,

differences in minor element content cannot explain the occurrence of both sillimanite and kyanite, as was also indicated by Albee and Chodos (1969).

J. Fe-Ti Oxides

Small amounts of the Fe-Ti oxide minerals are present in most of the samples studied, and include the assemblages: ilmenite; magnetite; ilmenite-magnetite; rutile; rutile-ilmenite; hematite-ilmenite-magnetite; and hematite-ilmenite. These were analyzed for Mg, Al, Si, Ti, Cr, Mn, Fe, Zn, Zr, and Nb. Ilmenite and hematite were normalized to: Total Cations = 2.0; magnetite to: Total Cations = 3.0; and rutile to: Total Cations = 1.0. The content of Fe_2O_3 in each phase was calculated from stoichiometry considerations.

Minor elements in the Fe-Ti oxide minerals have a large, apparently nonsystematic, range in abundance, except that certain elements tend to be concentrated in different phases. Ilmenite concentrates MnO (0.24-4.91 wt %) and has low abundances of Nb_2O_5 ($\leq$0.15 wt %), ZrO_2 ($\leq$0.08 wt %), ZnO ($\leq$0.22 wt %), and Cr_2O_3 ($\leq$0.49 wt %). The Mg-value in ilmenite ranges from <0.01-0.05. Calculated Fe_2O_3-contents are 1.5 to 8.9 wt %, with the higher values found in grains associated with hematite.

Magnetite concentrates Cr_2O_3 (up to 8.2 wt %), whereas the other oxides have low abundances (Nb_2O_5 and ZrO_2 <0.05 wt % each; ZnO $\leq$ 0.18 wt %; MnO $\leq$0.21 wt %; MgO $\leq$0.17 wt %). Of particular significance is the low TiO_2-content of the magnetite ($\leq$0.31 wt %).

Hematite has a large range in TiO_2-content (8.4-12.5 wt %), but the higher values were measured in hematite lamellae found in complex grains of hemoilmenite. The contents of MgO (≤0.08 wt %), MnO (≤0.26 wt %), ZnO (≤0.09 wt %), Cr_2O_3 (≤0.24 wt %), ZrO_2 (≤0.06 wt %), and Nb_2O_5 (≤0.09 wt %) are small.

Rutile concentrates Nb_2O_5 (up to 0.80 wt %), but is virtually pure TiO_2, as indicated by the low contents of FeO (≤0.43 wt %), MnO (≤0.05 wt %), MgO (<0.05 wt %), Cr_2O_3 (≤0.57 wt %) and ZrO_2 (≤0.22 wt %).

Compositions of the Fe-Ti oxide minerals are illustrated in Figure 4-19 in terms of FeO, TiO_2, and calculated Fe_2O_3. Schematic tie lines that connect analyses of coexisting phases are also shown.

Magnetite has an exceedingly small compositional range and coexists with ilmenite with a somewhat larger range in composition. These phases occur as discrete grains adjacent to one another and not in lamellar intergrowth.

Coexisting ilmenite and hematite, on the other hand, do occur in lamellar intergrowth, in which each lamella contains smaller lamellae of the other phase. Hence, the measured compositions of coexisting ilmenite and hematite are not necessarily representative of the actual phase compositions, although special care was taken when acquiring these data. Similar problems are associated with the ilmenite-hematite-magnetite assemblage as the hematite and ilmenite are intergrown here also. It is possible that the presence of hematite is related to late-stage oxidation, although it is not clear what petrographic criteria can be used to judge this.

Figure 4-19: Compositions of the Fe-Ti oxide minerals in samples from Langø illustrated in terms of weight percent FeO - Fe_2O_3 - TiO_2. The Fe_2O_3-contents of the various minerals have been calculated from stoichiometry considerations.

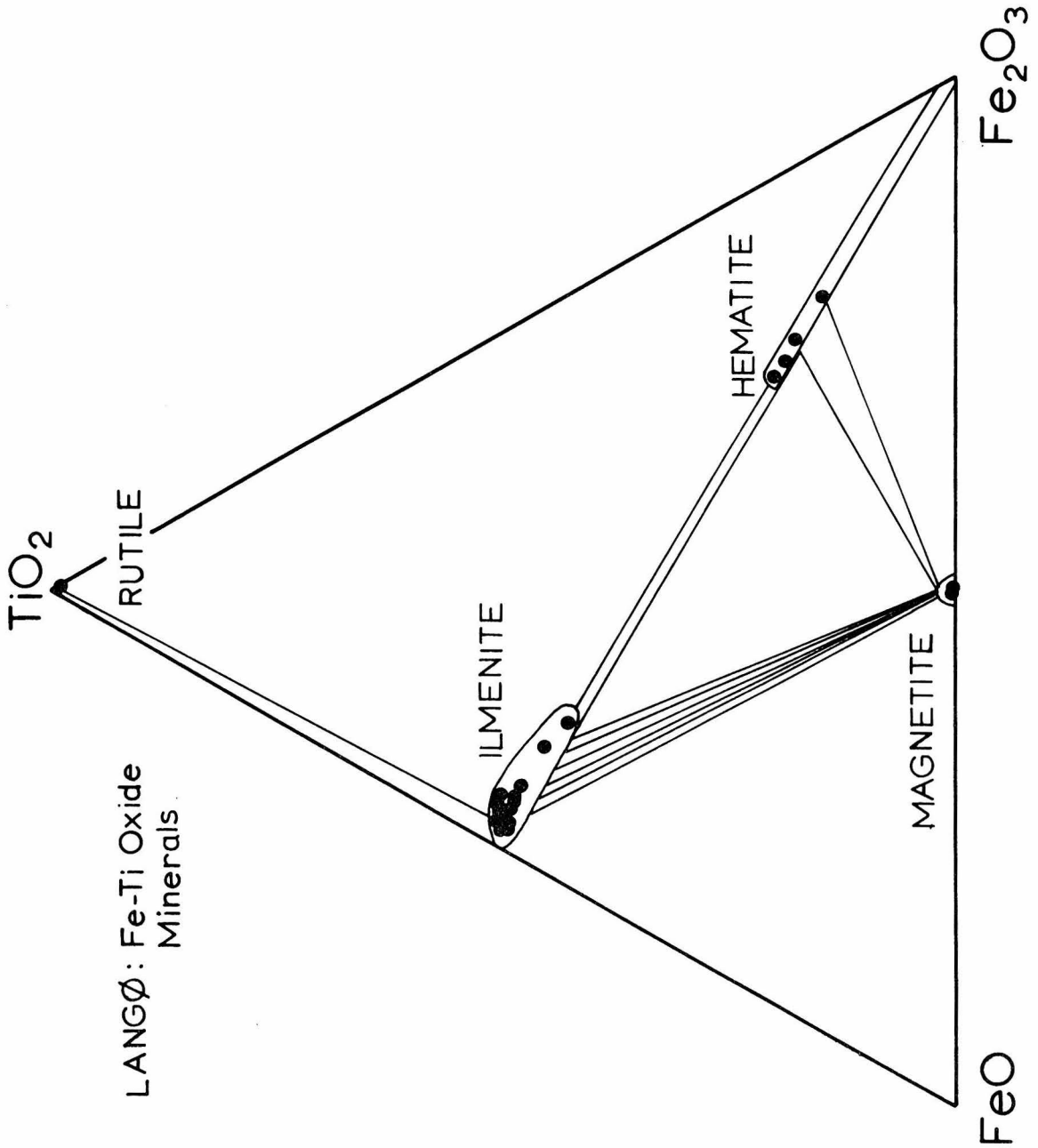
LANGØ: Fe-Ti Oxide Minerals
TiO2
RUTILE
ILMENITE
HEMATITE
MAGNETITE
Fe2O3
FeO

Lindsley (1962, 1963, 1965) has investigated phase relations among the Fe-Ti oxides as a function of temperature and oxygen fugacity. This work demonstrated that the assemblages ilmenite-hematite and ilmenite-hematite-magnetite cannot coexist stably at the same T and f_{O_2} with the assemblage rutile-ilmenite and, in general, with magnetite-ilmenite, despite the apparent topologic compatibility inferred from Figure 4-19. Rumble (1973) has emphasized that ambient f_{O_2} must have been higher in the hematite-bearing assemblages.

Since the samples have experienced at least two episodes of metamorphic mineral growth, the fact that the Fe-Ti oxide minerals may have equilibrated over a range of T and f_{O_2} is not surprising. It is important to note that the low temperature oxidized assemblages, rutile-magnetite and rutile-hematite do not occur. This constrains f_{O_2} to lie nearer to the N-NO (nickel metal-nickel oxide) buffer curve than to the H-M (hematite-magnetite) buffer curve (Rumble, 1976). The Ti-content of magnitite coexisting with ilmenite indicates final equilibration temperatures below 500°C (Buddington and Lindsley, 1964).

K. Scapolite

Scapolite is present in both calc-silicate gneiss samples (33A and 36I), and in biotite pyribolite samples 35817 and 35861-3. As noted in Chapter 3, the status of the scapolite is problematic, for in the same thin section it occurs in textural equilibrium with plagioclase and elsewhere demonstrably replaces plagioclase (c.f., Figure 3-10C, 10D). Only a cursory investigation of the scapolite and its relationship to plagioclase was undertaken, and these preliminary results are reported here.

Scapolite was analyzed for Na, Mg, Al, Si, K, Ca, Ti, Mn, Fe, Ba, Sr, S, F and Cl and the resultant analyses normalized to: Total Cations = 16.0 and Σ (Si+Al) = 12.0. The latter normalization, suggested by Evans et al. (1969), yielded less satisfactory charge balance and stoichiometry than the former. Hence, the data reported here are presented according to the total cation normalization scheme, although the differences between the two normalizations are slight and probably insignificant. The difference between the analytical total and 100% was assumed to be CO_2, since H_2O (or OH) does not appear to be present in scapolite (Evans et al., 1969).

The analyses were recalculated to theoretical end-members according to the following scheme: F and Cl were allocated to NaF and NaCl; MgO, FeO, BaO and SrO were grouped with CaO; SO_3 and CO_2 were allocated to $CaSO_4$ and $CaCO_3$; K_2O was allocated to $KAlSi_3O_8$; the remaining Na_2O and CaO were allocated to $NaAlSi_3O_8$ and $CaAl_2Si_2O_8$. This procedure yielded either small excesses or deficiencies in Al and Si, which were $\lesssim$0.5% in each case, and deemed insignificant.

The minor element content of the scapolite is small. TiO_2 and SrO were not detected (<0.05 wt %), and the contents of BaO ($\leq$0.08 wt %), MnO ($\leq$0.09 wt %), and K_2O ($\leq$0.08 wt %) are near their respective detection limits. Somewhat larger amounts of FeO ($\leq$0.17 wt %) and MgO ($\leq$0.29 wt %) are present, but these may be related to the presence of μm-sized dark inclusions that are quite abundant locally in some scapolite grains.

The major element composition of the scapolite is very close to mizzonite ($NaCa_3Al_5Si_7O_{24}CO_3$; Orville, 1975); with Na/(Na+Ca) ranging from 0.15 to 0.27 and only minor sulfate substituting for carbonate.

However, in sample 35861-3, nearly half of the carbonate is replaced by sulfate. The scapolite contains between 17.3 and 20.9 wt % CaO, and Cl is below its detection limit (<0.05 wt %), although slightly larger amounts of F seem to occur ($\leq$0.18 wt %). It is typical of granulite grade scapolite to be Ca-rich, contain some sulfate, and be nearly Cl-free (Lovering and White, 1969). The data illustrated in Figure 4-20 are similar to other natural occurrences of scapolite from high-grade gneisses (Evans et al., 1969).

Despite the narrow range in scapolite composition, it occurs with plagioclase that ranges from An_{46} to An_{96}. The An-content of the plagioclase seems to be independent of Na/(Na+Ca) in scapolite. For plagioclase with compositions between An_{78} and An_{96}, $Na/(Na+Ca)_{scap} > Na/(Na+Ca)_{plag}$, for less calcic plagioclase $Na/(Na+Ca)_{scap} < Na/(Na+Ca)_{plag}$ (Figure 4-21). These relationships are consistent with the experimental work of Orville (1975, Fig. 6) who showed that at fixed pressure and temperatures (750°C, 4Kb in his experiment), Cl-free scapolite with only a small range in composition coexists with plagioclase that ranged from An_{39} to An_{85}.

Goldsmith (1976) has shown that a reaction of the type: Plagioclase + Calcite $\rightleftarrows$ Scapolite would have a steep slope on a P-T diagram, and can be nearly independent of pressure. Pure meionite (3 anorthite $1CaCO_3$) would break down to anorthite + calcite below 850°C in the pressure range 0-10 kb (P_T = Ps). Addition of Na to the system would shift the reaction to lower temperature.

The fact that the compositions of scapolite and plagioclase in samples 33A and 36I are quite similar to those synthesized at 750°C and

Figure 4-20: Diagram illustrating weight percent CaO and weight percent (F+Cl) for analyses of scapolite in samples from Langø. The diagonal line drawn on the figure represents the variation in the composition of natural scapolite as indicated by Evans et al. (1969).

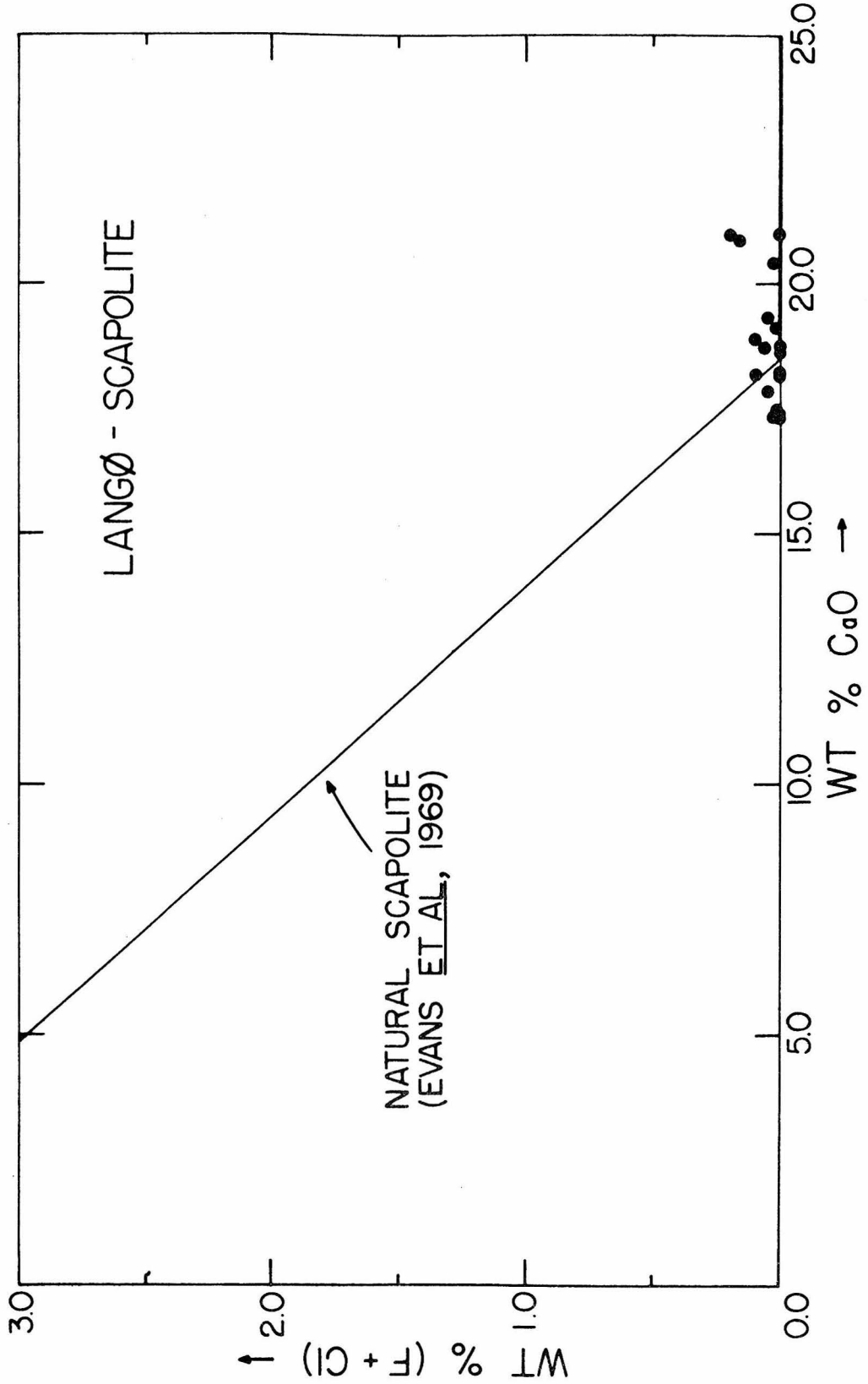
LANGØ - SCAPOLITE
NATURAL SCAPOLITE
(EVANS ET AL, 1969)
WT % (F + Cl) →
WT % CaO →
0.0
1.0
2.0
3.0
5.0
10.0
15.0
20.0
25.0

Figure 4-21: Diagram illustrating atomic Na/(Na+Ca) in coexisting scapolite and plagioclase in samples from Langø. Note that there is no apparent correlation in the compositions of these phases.

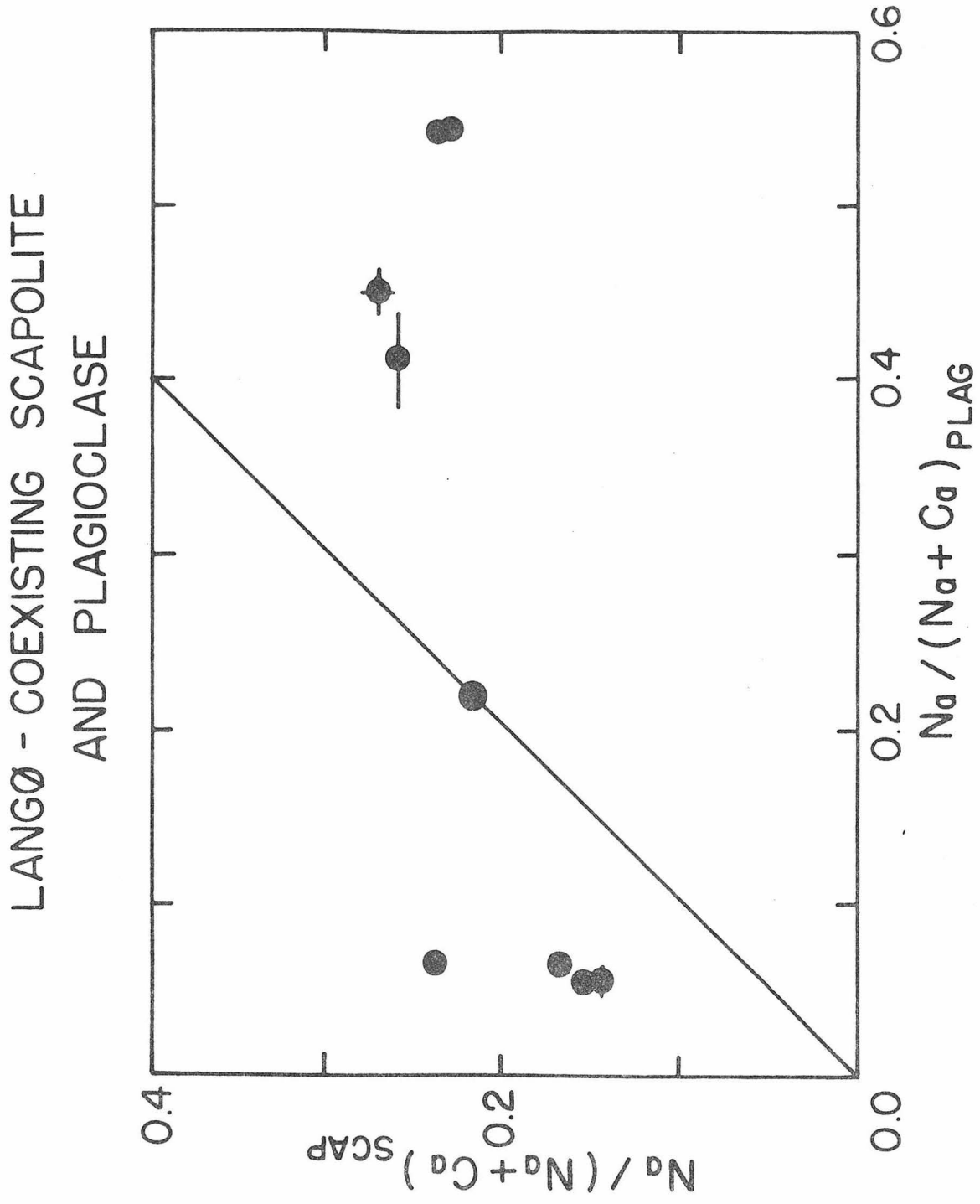
LANGØ - COEXISTING SCAPOLITE
AND PLAGIOCLASE
0.4
0.2
0.0
0.2
0.4
0.6
$Na_D / (Na_D + Ca_D)_{SCAP}$
$Na / (Na + Ca)_{PLAG}$

4kb (Orville, 1975) suggests that this temperature may represent a close approximation to the actual equilibration temperature. However, the complicated petrographic relationships between scapolite and plagioclase, together with the presence of small amounts of calcite of uncertain paragenesis, would make such a temperature estimate tentative at best.

L. Sphene

A few grains of bright orange sphene occur in calc-silicate samples 33A and 36I. These appear to have formed and been stable during the first episode of mineral growth (MI), but were replaced locally by ilmenite during the second episode of mineral growth (MII).

Sphene was analyzed for Mg, Al, Si, Ca, Ti, Mn, Fe, Ce and F, and normalized to: Total Cations = 3.0. The analyses indicate that it is nearly pure $CaTiSiO_5$, as the contents of minor elements are small. Al_2O_3 (0.67-1.73 wt %), FeO (0.40-1.36 wt %) and MnO (0.08-0.63 wt %) are the principal impurities, and stoichiometry considerations indicate that they substitute for TiO_2. The contents of MgO and Ce_2O_3 are below their detection limits (<0.04 wt %), but the fluorine content ranges up to 0.48 wt %.

M. Muscovite

A few rare grains of coarsely-crystalline white mica replace the feldspars in the potassium feldspar gneisses. These were analyzed for Na, Mg, Al, Si, K, Ca, Ti, Fe, Zn, F and Cl and normalized to: Total Cations - (Na+K+Ca) = 6.0. The mineral formula is taken to be: $(K)(Al_2)^{VI}(Si_3Al)^{IV}O_{10}(OH,F,Cl)_2$.

The contents of MnO, ZnO, and CaO are near or below their detection limits (<0.06 wt %), but there is a rather large range in TiO_2-content (<0.05-0.68 wt %). Charge considerations indicate that most of the iron (1.7-3.2 wt % FeO) occurs as Fe^{3+}, probably substituting for Al in octahedral coordination. This observation, together with the low MgO-content (0.6-1.5 wt %) and only slight Si-excesses (i.e., Si cations exceed the theoretical 3 only up to a maximum of 3.12), indicates only a small "phengite" substitution [$(Mg, Fe)^{VI} + (Si)^{IV} \rightleftarrows (Al)^{VI} + (Al^{IV})$].

The paragonite content is likewise small (0.11-0.16 wt % Na_2O; Na/(Na+K) = 0.015-0.022) and similar to that in muscovite from the K-feldspar-sillimanite zone in NW Maine (Guidotti and Sassi, 1976). Thus, although the muscovite is retrograde or secondary, it appears to have formed at a high metamorphic grade.

N. Chlorite

Chlorite is exceedingly rare in the samples from Langø, and occurs in only three of the thin sections used for the microprobe study. In 25E and 28H, dark green to pale green pleochroic chlorite replaces biotite along cleavages, whereas in 36H pale green chlorite is associated with retrograde muscovite.

The chlorite was analyzed for Na, Mg, Al, Si, Ca, Ti, Cr, Mn, Fe, Zn, F and Cl, and normalized to: Total Cations - (Na+Ca) = 10.0. The general mineral formula is taken to be: $(Mg, Fe, Al)_6^{VI} (Si, Al)_4^{IV} O_{10} (OH, F, Cl)_8$.

The contents of Na_2O and Cr_2O_3 are very small (<0.10 and <0.07 wt % respectively), but there is a considerable nonsystematic variation in

the contents of the other minor elements: CaO (0.08-0.30 wt %); TiO_2 (0.21-1.63 wt %); MnO (0.06-1.48 wr %); and ZnO (<0.05-0.18 wt %). Mg-values range from 0.58 to 0.62, and chlorite that occurs with muscovite is distinctly more aluminous than that which occurs with biotite (22.0-22.6 vs. 13.8-18.6 wt % Al_2O_3).

CHAPTER 5

V. PHASE EQUILIBRIUM CONSIDERATIONS

A. Introductory Statement

As indicated in Chapter 3, the samples collected on Langø have a variety of mineral assemblages characteristic of the hornblende-granulite grade of metamorphism. The compositions of these minerals were discussed in detail in Chapter 4. Here, an attempt will be made to correlate phase assemblages and compositions via various chemographic representations. Such an approach provides one possible way to test for chemical equilibrium, since partitioning of major elements between co-existing phases can be scrutinized, and assemblages evaluated in terms of the Gibbs Phase Rule.

No claim is made that the minerals, as they are manifested in the samples now, represent equilibrium phase assemblages. The presence of reaction textures due to polymetamorphism attests to the lack of overall equilibrium. The main purpose of the following exercise, then, is to determine whether useful information can be obtained from the observed MI assemblages. It is remarkable that self-consistent patterns do in fact emerge from the data.

B. Graphical Analysis

One of the most useful applications of the Gibbs Phase rule to the study of geological systems has been in terms of the graphical representation and analysis of mineral assemblages. Ternary ACF and AKF diagrams (Eskola, 1915) portray rather well mineral relationships

in a variety of rock types over a range of metamorphic conditions. However, these diagrams suffer from the fact that FeO and MgO, which are important non-identical components in many rock-forming minerals, are combined, and any effects related to their variation are ignored or remain undiscovered. Thompson (1957) subsequently demonstrated how the AKFM tetrahedron can be used to understand changes in mineral assemblages accompanying increases in pressure and temperature during progressive metamorphism of Ca-poor metasedimentary rocks. This method projects mineral compositions from muscovite (KAl_3O_5) onto the plane AFM. Hence, the effects of variation in Fe/Mg and Al/(Fe+Mg) on the observed assemblage at a given metamorphic grade can be evaluated. Robinson and Jaffee (1970) discussed a similar type of projection from plagioclase in the tetrahedron ACFM. Modified forms of both of these projection tetrahedra were utilized in the analysis of MI mineral assemblages from Langø.

1. AKFM

The tetrahedron AKFM (Al_2O_3-K_2O-FeO-MgO) was used to understand phase assemblages observed in both potassium feldspar gneisses and orthopyroxene gneisses. These samples can be described in terms of the following oxide components: Na_2O, MgO, Al_2O_3, SiO_2, CaO, TiO_2, Cr_2O_3, Cr_2O_3, MnO, FeO, Fe_2O_3, P_2O_5, BaO, ZrO_2 and H_2O. The MI phases observed in these samples include: alkali feldspar, apatite, biotite, cordierite, garnet, ilmenite, magnetite, orthopyroxene, plagioclase feldspar, rutile, sillimanite, and zircon. The MII biotite and kyanite, as well as late

stage chlorite, hematite, muscovite and talc need not be considered in the interpretation of primary phase assemblages.

In order to understand the relationship among the Fe-Mg-Al silicate minerals, the following sequence of simplifying assumptions were made (c.f., Thompson, 1957; Korzhinskii, 1960), in order to construct a thermodynamically valid diagram (Greenwood, 1975):

a) The components Cr_2O_3, MnO, BaO, P_2O_5, and ZrO_2 occur in either trace amounts in the major phases, or cause the appearance of a trace phase such as apatite and zircon. Similarly, Na_2O, CaO, TiO_2 and Fe_2O_3 occur in small amounts in major phases (e.g., CaO in garnet, TiO_2 in biotite), or cause the appearance of the phases plagioclase, ilmenite, rutile and magnetite. These components do not appear to affect the stability relations of any of the Mg-Fe-Al silicate phases, and the chemical potential of each of these components is assumed fixed throughout the system.

b) SiO_2 is a major component of the principal phases and variations in μ_{SiO_2} could affect their stability relations. However, the presence of quartz in all the samples indicates that $a_{SiO_2} = 1$. Changes in the abundance of SiO_2 will merely alter the amount of quartz present, and will not change the mineral assemblage.

c) Biotite contains substantial H_2O, and differences in μ_{H_2O} could control the presence or absence of that phase. Thompson (1955) emphasized that, although geological systems may be closed with respect to the chemical potentials of most components forming the solid phases, they may be open with respect to the chemical potential of some volatile constituents, notably H_2O. Hence, if μ_{H_2O} is controlled external to

the system, much like pressure and temperature, then an additional degree of freedom will result. It may be assumed that μ_{H_2O} was constant, but not necessarily equal to unity. Also, μ_{H_2O} may have been controlled by the presence of a fluid phase, but that fluid phase need not have been pure H_2O to satisfy this constraint.

d) The remaining four components (Al_2O_3-K_2O-FeO-MgO) define the tetrahedron AKFM, in which lie the compositions of the Fe-Mg-Al silicate phases of interest. By projecting the compositions of these phases from $KAlO_2$ (the composition of potassium feldspar in this system) onto the plane Al_2O_3-FeO-MgO (AFM) (Barker, 1961), phase relations among biotite, cordierite, garnet, orthopyroxene, and sillimanite can be portrayed.

In summary, for such a projection to be valid thermodynamically, quartz and potassium feldspar must be present in all assemblages, the composition of potassium feldspar must be fixed (which it is, c.f., Chapter 4), and μ_{H_2O}=constant. In the AFM projection, application of the phase rule indicates that a three phase field is invariant, and phase compositions are fixed at constant P, T, μ_{H_2O} for a range of rock compositions; and a two phase field is univariant, and the compositions of the phases can differ at constant P, T, μ_{H_2O} depending on the composition of the rock.

The resultant AFM projections for potassium feldspar gneisses are illustrated in Figure 5-1, and for orthopyroxene gneisses in Figure 5-2. In both figures, solid lines connect primary (MI) mineral assemblages and dashed lines secondary (MII) mineral assemblages. In

Figure 5-1: Projection from potassium feldspar onto the plane AFM in the tetrahedron AKFM illustrating phase assemblages and compositions in potassium feldspar gneiss samples. Additional phases include quartz, plagioclase, ilmenite, magnetite, apatite, and zircon. For the compositions of garnet illustrated, C = core and R = rim. For the compositions of biotite illustrated, open symbols are MI and filled symbols are MII.

LANGØ - AFM PROJECTION FOR POTASSIUM FELDSPAR GNEISSES

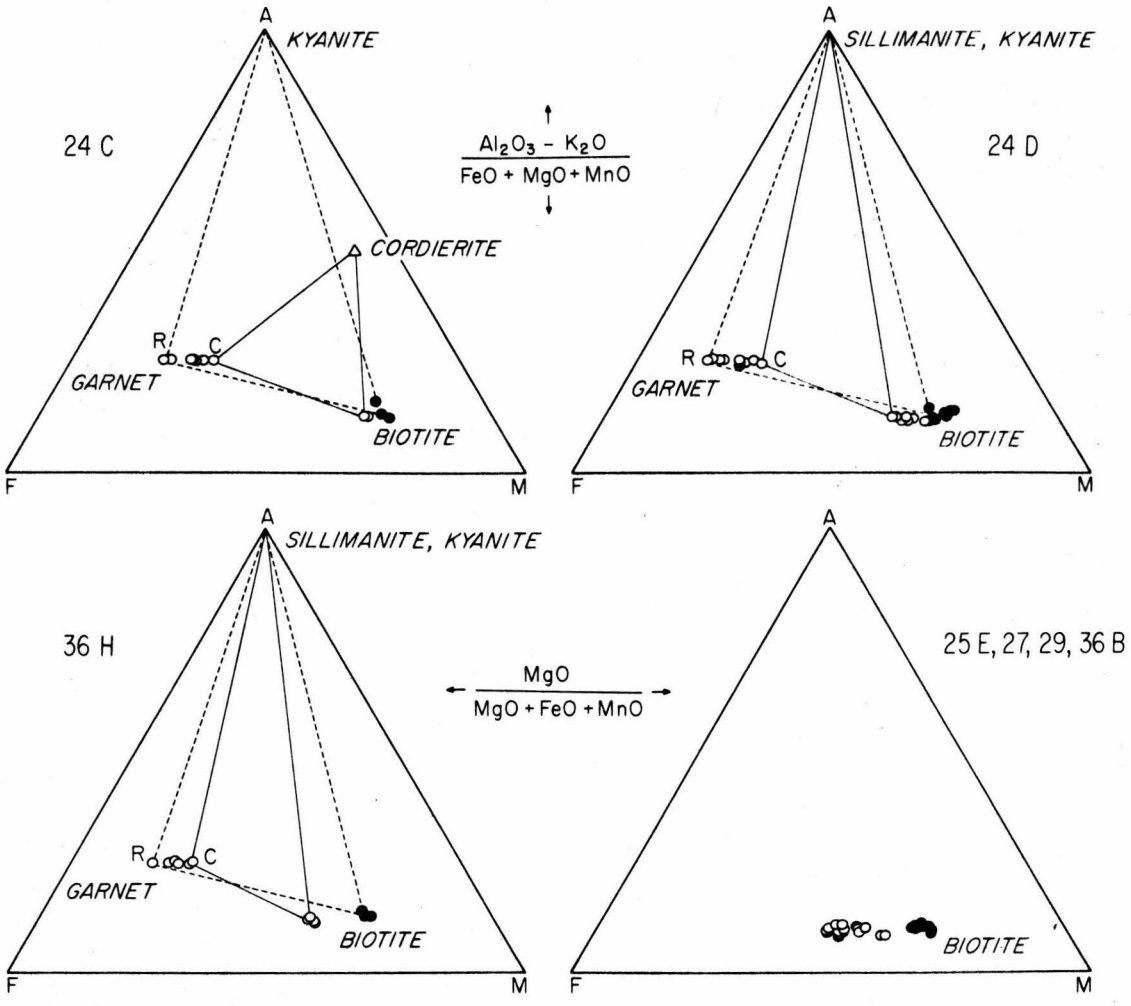

Figure 5-2: Projection from potassium feldspar onto the plane AFM in the tetrahedron AKFM illustrating phase assemblages and compositions in orthopyroxene gneiss samples. Additional phases include quartz, plagioclase, rutile, apatite, and zircon. For the compositions of biotite illustrated, open symbols are MI and filled symbols are MII.

LANGØ - AFM PROJECTION FOR ORTHOPYROXENE GNEISSES

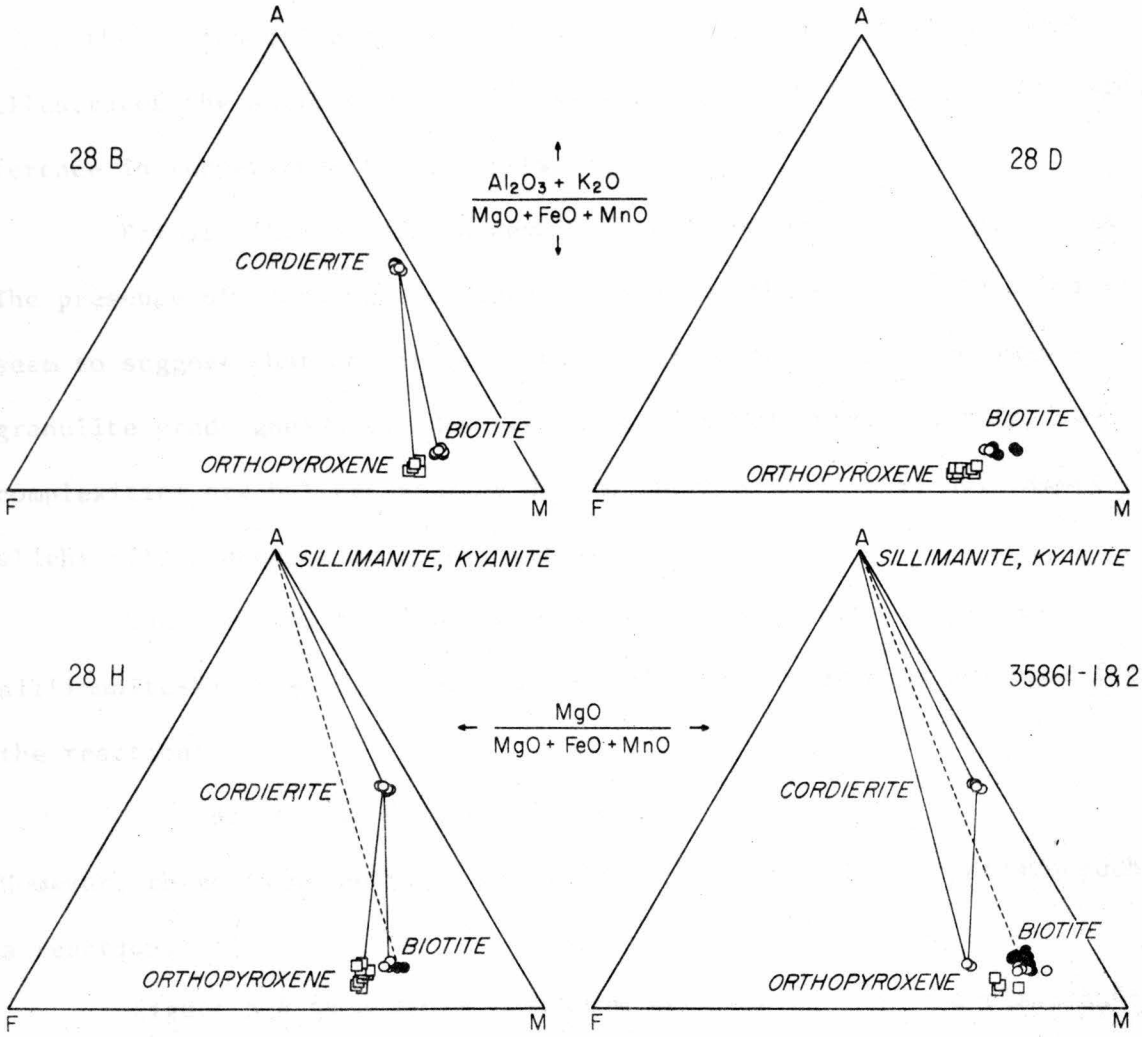

Figure 5-1A, the composition of cordierite is inferred, due to the fact that the cordierite in that particular rock is completely altered. All other data points represent actual phase compositions. Note that in Figure 5-1, tie lines connecting garnet cores with primary (MI) biotite cross those connecting garnet rims and secondary (MII) biotite. This illustrates the shift of $K_{D_{Fe-Mg}}^{Gar-Bio}$ between MI and MII, suggesting a difference in temperature for those two events.

Primary (MI) mineral assemblages are summarized in Figure 5-3A. The presence of crossing tie lines and shifted three phase fields might seem to suggest that no simple topology exists for these hornblende-granulite grade gneisses. However, as will be discussed shortly, these complexities are not necessarily due to incompatibilities, but rather slight differences in bulk composition.

The crossing tie line between garnet-cordierite in 24C and sillimanite-biotite in 24D and 36H could be interpreted as evidence for the reaction:

$$\text{Bio} + \text{Sill} \rightleftarrows \text{Cord} + \text{Gar} + \text{Kf}.$$

However, there is no petrographic evidence that would substantiate such a reaction.

Figure 5-4 is a projection from sillimanite onto the plane K_2O-FeO-MgO, which illustrates that the four-phase assemblages sillimanite-garnet-biotite-potassium feldspar and sillimanite-cordierite-biotite-potassium feldspar can coexist with the four-phase assemblage sillimanite-garnet-cordierite-biotite. When quartz is present, these three five phase fields are invariant at fixed P, T, and μ_{H_2O}. It follows then that the three three-phase fields: cordierite-biotite-potassium feldspar,

Figure 5-3: A) AFM diagram illustrating summary of phase relations shown in Figures 5-1 and 5-2. Note crossing tie lines and shifted three-phase fields.

B) AFM diagram illustrating phase relations in only those samples in which the presence of potassium feldspar is manifest.

C) AFM diagram illustrating phase relations in those samples in which the presence of potassium feldspar was inferred from petrographic features. Note that the three-phase assemblages garnet-cordierite-sillimanite and garnet-cordierite-orthopyroxene are compatible with those observed.

LANGØ - OBSERVED PHASE ASSEMBLAGES

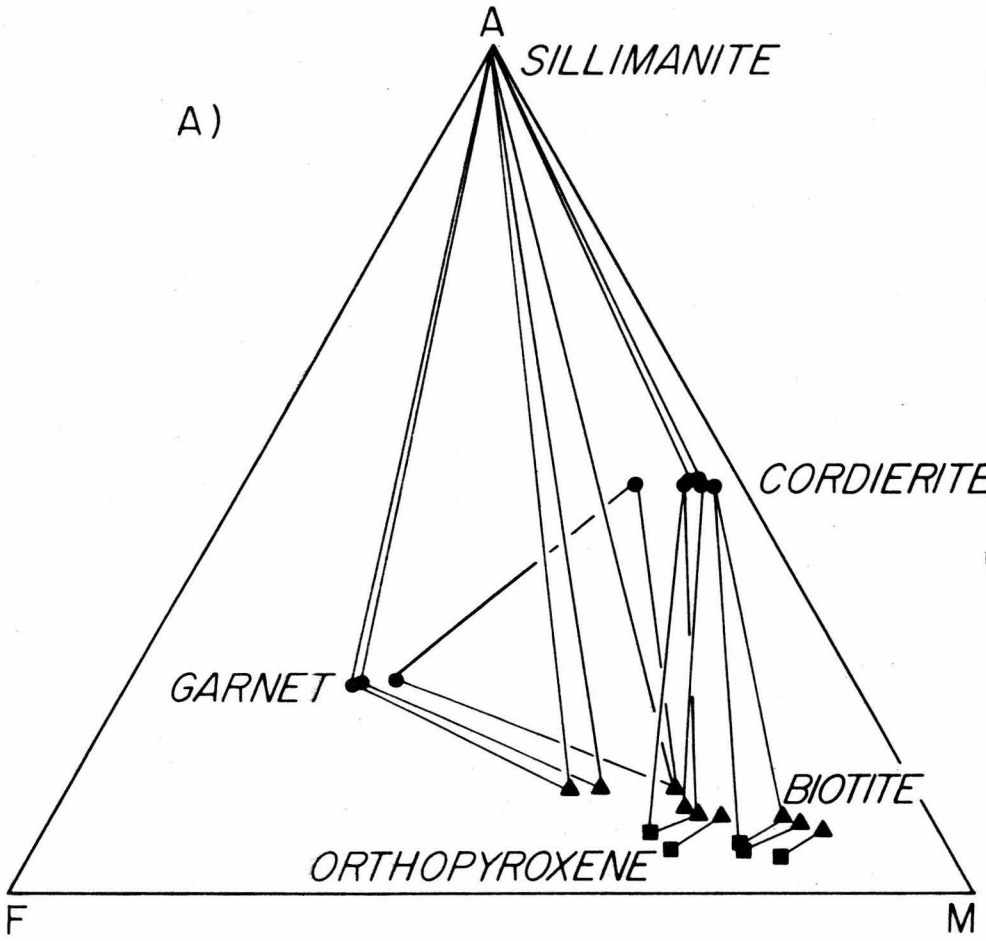

B) + QTZ
Kf
PLAG
ILM
Mt

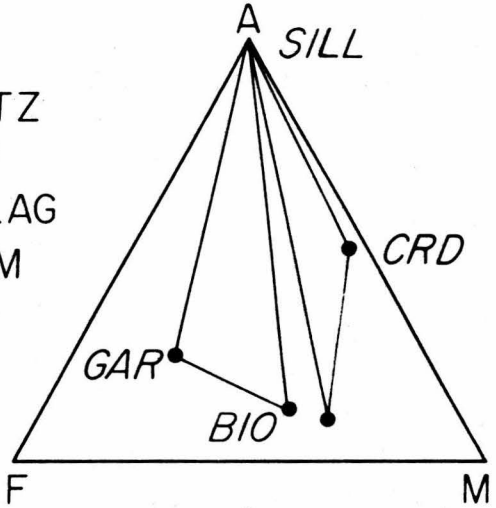

C) + QTZ
BIO
PLAG
RUT

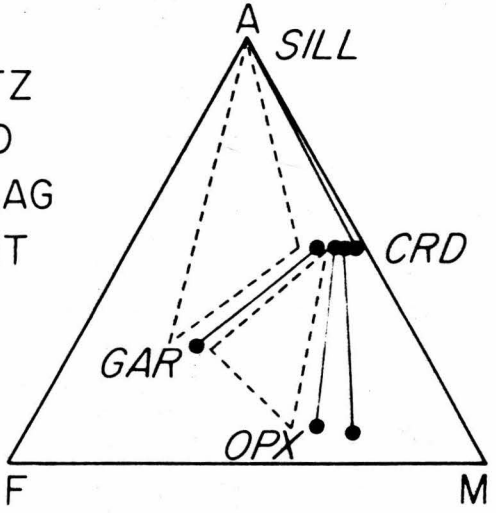

Figure 5-4: Projection from sillimanite onto the plane KFM (K_2O - FeO - MgO) in the tetrahedron AKFM. Note that the potassium feldspar-free assemblage garnet-cordierite-biotite-sillimanite can coexist with the potassium feldspar-bearing assemblages biotite-garnet-sillimanite-potassium feldspar and biotite-cordierite-sillimanite-potassium feldspar.

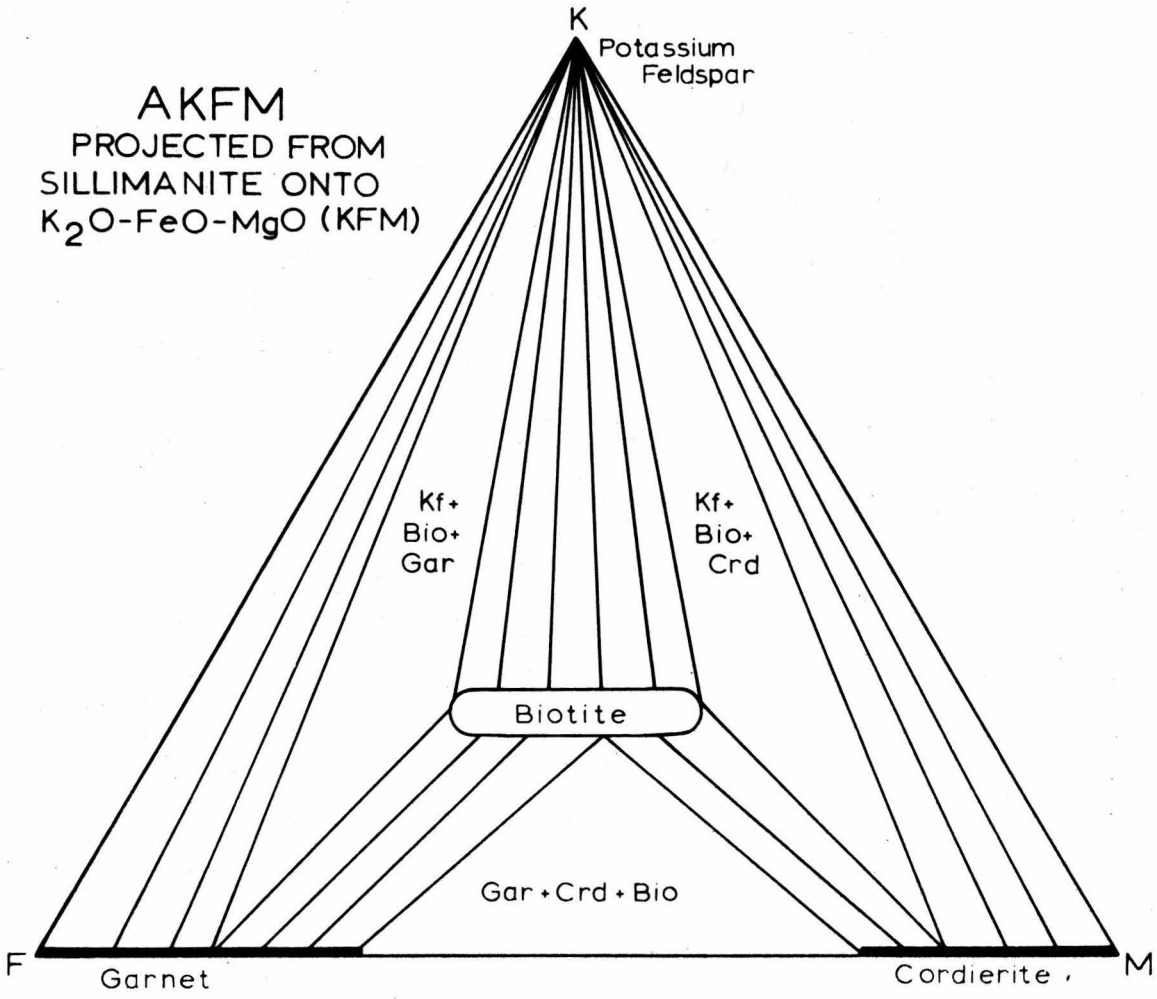
AKFM
PROJECTED FROM
SILLIMANITE ONTO
K_2O-FeO-MgO (KFM)
K
Potassium
Feldspar
Kf+
Bio+
Gar
Kf+
Bio+
Crd
Biotite
Gar+Crd+Bio
F
Garnet
Cordierite
M

cordierite-garnet-biotite, and garnet-biotite-potassium feldspar, with quartz as a fourth phase in each would all be univariant. Although a small amount of potassium feldspar occurs in sample 24C, none is present in the immediate vicinity of the garnet and cordierite. Hence the assemblage garnet-cordierite-biotite-quartz is compatible with the assemblage garnet-biotite-sillimanite-potassium feldspar-quartz, as indicated by the relationships in Figure 5-4.

The second apparent inconsistency in Figure 5-3A is caused by the occurrence of two compositionally-distinct three-phase fields involving cordierite-biotite-orthopyroxene in samples 28B and 28H, which overlap phase fields from other samples. If the projection is valid, the phase rule prohibits the juxtaposition of two such three phase fields, unless they formed at different P, T, and μ_{H_2O}*, which seems unlikely since they were collected from the same outcrop approximately 1 meter apart. Recall that in Chapter 3, it was indicated that potassium feldspar does not actually occur in the orthopyroxene gneisses, but rather was inferred due to reaction textures involving the replacement of orthopyroxene (c.f., Figure 3-3). It is entirely possible that the potassium required to account for the replacement of orthopyroxene by secondary biotite was introduced in an aqueous fluid,

---

*The occurrence of two three-phase fields for garnet-biotite-sillimanite in Figure 5-1, is related to the presence of chemical zoning in each phase. Tie lines were drawn between the most magnesian garnet core, and the most iron-rich biotite. They could just as well be drawn to be exactly coincident.

and no potassium feldspar ever existed in these samples. If this were the case then the assemblage cordierite-biotite-orthopyroxene is univariant, and in the AKFM projection used, it would be represented by a series of tie triangles.

Another projection in the tetrahedron AKFM might elucidate the above. If one considers the ternary $KAlO_2$-Al_2O_3-FmO (Figure 5-5), then the orthopyroxene gneisses might be envisioned as having compositions on the right hand side, or K-poor side, of the sillimanite-biotite join, and tie-lines to potassium feldspar from orthopyroxene would not be possible. Hence, projecting the phase assemblages in orthopyroxene gneisses from potassium feldspar does not result in a thermodynamically valid projection.

A third set of crossing tie-lines is associated with the assemblage cordierite-biotite-sillimanite present in a portion of 35861-1. Since this sample has trace amounts of potassium feldspar scattered throughout, it might be more appropriately grouped with the potassium feldspar gneisses.

If the phase assemblages are regrouped by plotting the cordierite-sillimanite-biotite assemblage from 35861-1 with the potassium feldspar gneisses (Figure 5-3B), and by plotting the cordierite-garnet-biotite assemblage from 24C with the orthopyroxene gneisses (Figure 5-3C), then the topologic inconsistencies are removed. Figures 5-3B and 5-3C represent mineral assemblages formed at hornblende-granulite grade of metamorphism in relatively K-rich and K-poor paragneisses on Langø. An important observation that should be emphasized

Figure 5-5: Ternary Al_2O_3 - FeO+MgO - $KAlO_2$ diagram which illustrates that the presence of biotite may prevent orthopyroxene-bearing assemblages from coexisting with potassium feldspar.

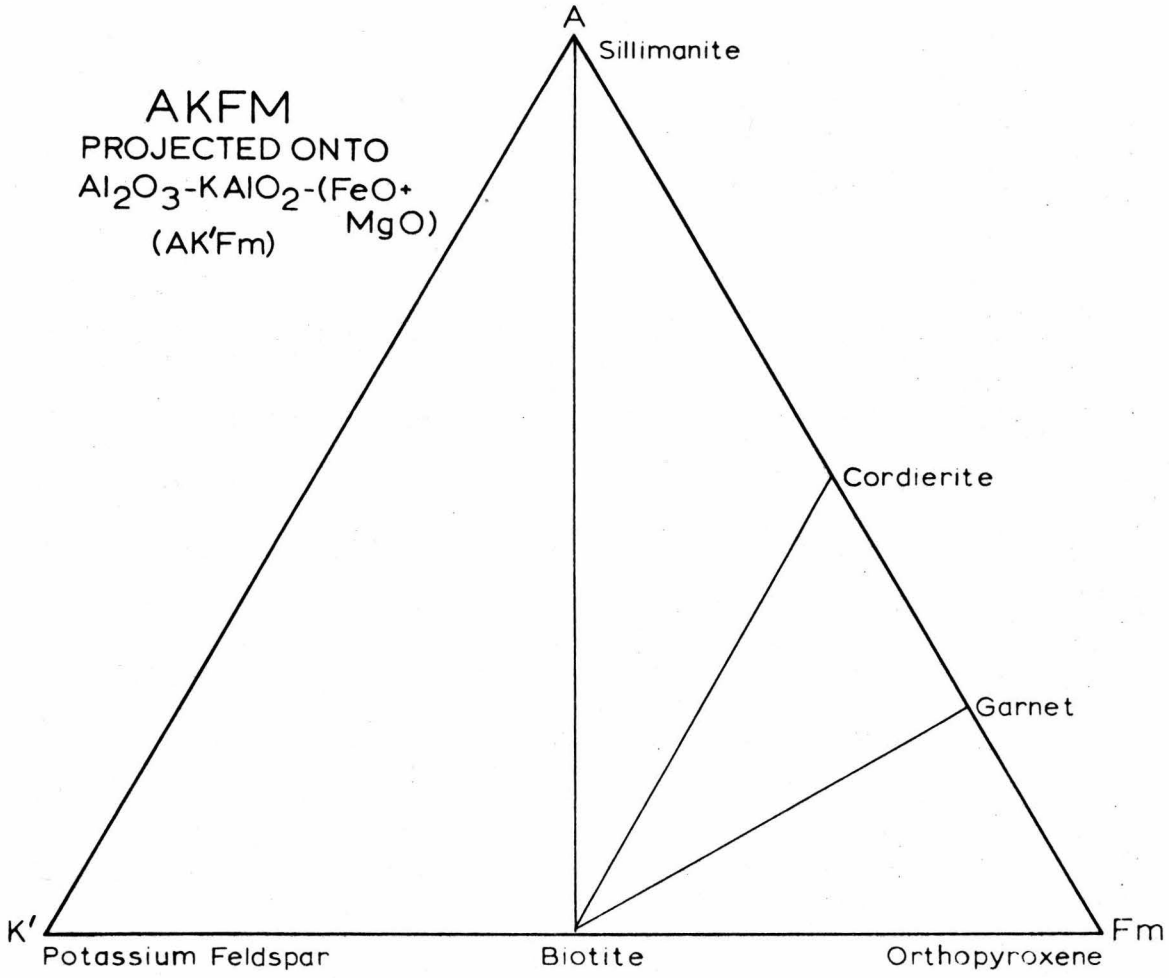
A
Sillimanite
AKFM
PROJECTED ONTO
Al_2O_3-$KAlO_2$-(FeO+MgO)
(AK'Fm)
Cordierite
Garnet
K'
Fm
Potassium Feldspar
Biotite
Orthopyroxene

is that the assemblages biotite-sillimanite-garnet, cordierite-garnet-biotite, and cordierite-orthopyroxene-biotite can coexist at the same metamorphic grade. Also, as can be seen in Figure 5-3C, the assemblages cordierite-garnet-sillimanite-biotite and cordierite-garnet-orthopyroxene-biotite would occur in rocks of appropriate composition.

2. ACFM

The tetrahedron ACFM was used to analyze phase assemblages observed in the various pyribolite gneisses, the diorite, and the calc-silicate gneisses. For the sake of completeness, orthopyroxene gneiss samples 28B, 28D, and 28H were also included in this analysis. The oxide components are the same as those considered for AKFM, and include: Na_2O, MgO, Al_2O_3, SiO_2, K_2O, CaO, TiO_2, Cr_2O_3, MnO, FeO, Fe_2O_3, P_2O_5, BaO, ZrO_2, CO_2, and H_2O. The MI phases include: apatite, biotite, clinopyroxene, cordierite, garnet, hercynitic spinel, hornblende, ilmenite, magnetite, orthopyroxene, plagioclase feldspar, rutile, scapolite, sphene, and zircon. Secondary amphibole, kyanite, chlorite, biotite, and hematite are not considered.

The simplifying assumptions are the following:

a) The components Cr_2O_3, MnO, BaO, and ZrO_2 occur in either trace amounts in the major phases, or cause the appearance of a trace phase such as apatite and zircon. Similarly, K_2O, TiO_2, and CO_2 occur in small amounts in major phases (e.g., K_2O in hornblende) or cause the appearance of an additional phase such as biotite, ilmenite, scapolite and sphene. The chemical potentials of all these components are assumed to be fixed throughout the system and they do not appear to affect the

stability relations of the other principal Ca-Mg-Fe-Al silicate minerals.

b) The principal effect of the component Fe_2O_3 is to stabilize magnetite. However, Fe^{3+} occurs in substantial quantities in hornblende (and pyroxene) where, as indicated in Chapter 4, it "behaves" like Al^{3+}. Hence Fe_2O_3 is grouped with Al_2O_3.

c) SiO_2 is a major component of the principal phases (except spinel), and variations in μ_{SiO_2} could affect their stability relations. The presence of quartz in the orthopyroxene gneisses, in the biotite pyribolites, and in one of the calc-silicate gneisses (33A) indicates that $a_{SiO_2}=1$. Changes in the abundance of SiO_2 in these lithologies should merely alter the amount of quartz present. Quartz does not occur as a primary mineral in the diorite, the other calc-silicate gneiss (36J), the garnet pyribolites, and most of the "ordinary" pyribolites. Thus, although SiO_2 can be eliminated as a determining component in some samples, this assumption may be false for others and lead to an additional degree of freedom.

d) The chemical potential of H_2O is assumed to be fixed at a constant value.

e) The remaining five components define two tetrahedra, Al_2O_3+Fe_2O_3- CaO - FeO - MgO and Al_2O_3+Fe_2O - Na_2O - FeO - Mgo, which can be combined into one ACFM tetrahedron that was used in this study: Al_2O_3+Fe_2O_3- CaO+Na_2O - FeO - Mgo. This tetrahedron describes the compositions of the silicate phases of interest: clinopyroxene, cordierite, garnet, hercynitic spinel, hornblende, and orthopyroxene.

Compositions of these phases were projected from the composition of plagioclase [$(CaO+Na_2O)$. Al_2O_3] onto a plane parallel to the AC side of the tetrahedron passing through the line FM, as indicated in Figure 5-6. Such a projection in this system has the advantage over a ternary projection because in the latter clinopyroxene projects at $-\infty$. In addition, this projection expands the area in which hornblende and pyroxene plot, and any slanting tie line indicates Fe-Mg fractionation between coexisting phases.

For this projection to be valid thermodynamically, the projection phases quartz and plagioclase must be present everywhere, and the plagioclase composition must be identical in all assemblages (Greenwood, 1975). These two constraints are not met, since quartz tends to be absent in the pyribolite samples, and the composition of plagioclase ranges from $\sim An_{25}$ to $\sim An_{95}$. However, the fact that CaO and Na_2O can mix in almost all proportions in plagioclase, may make this last caveat not as severe as it seems. Further discussion of this point will be presented shortly.

Compositions of the various minerals in projection are illustrated in Figure 5-7, where the data are grouped by lithologic type. There is quite a large range in the compositions of all the phases involved, and the compositional field for hornblende is expanded somewhat owing to the uncertainties involved in estimating its Fe^{3+}-content. Note however, that the compositions of hornblende occurring with garnet project into a field which distinguishes them from the other hornblende analyses. The compositions of orthopyroxene form a loop that conforms

Figure 5-6: Diagram illustrating the method of construction and projection in the ACFM tetrahedron used in this study.

PROJECTION SCHEME IN THE TETRAHEDRON ACFM

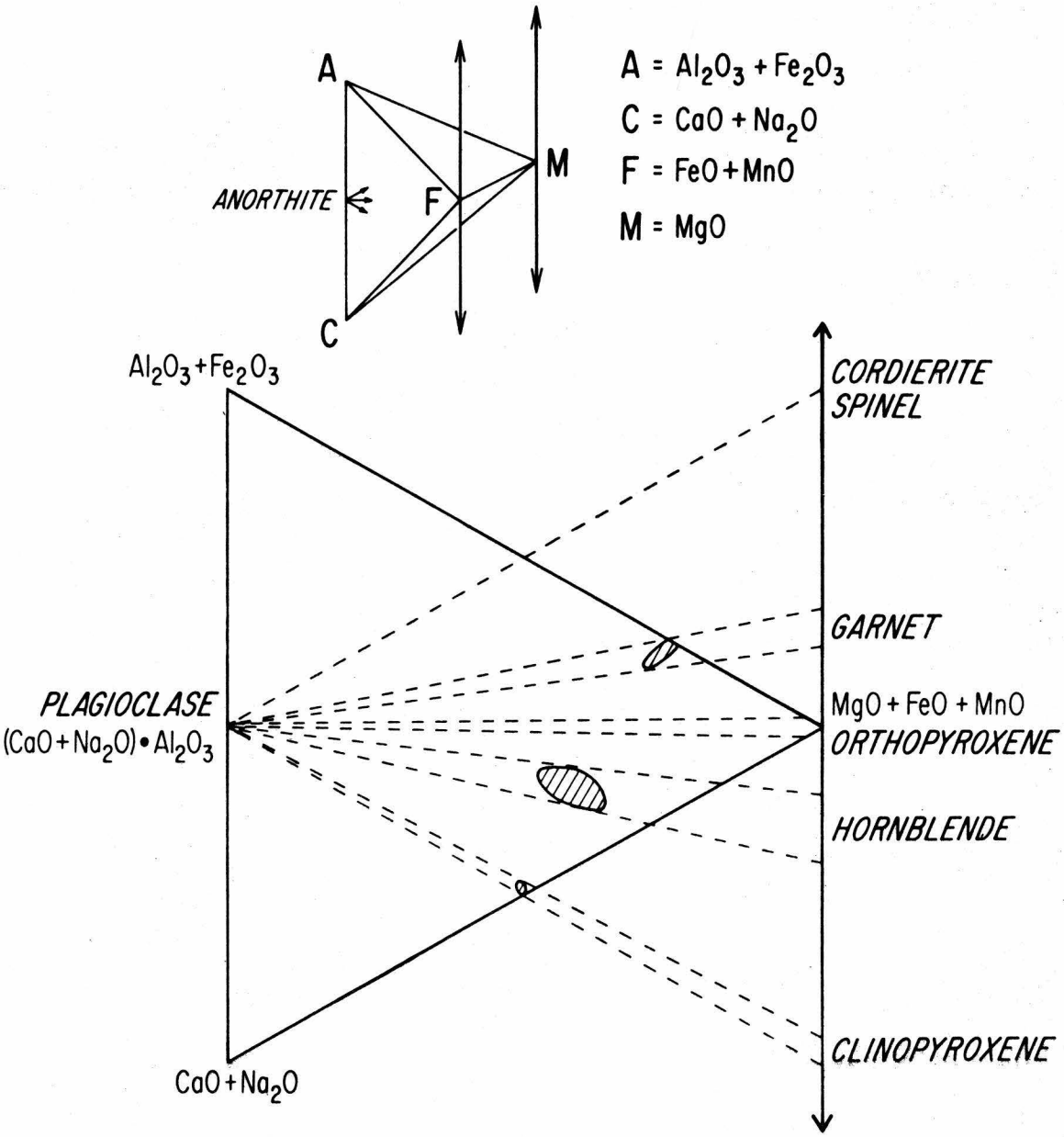

Figure 5-7: ACFM projection of phase compositions in various samples from Langø.

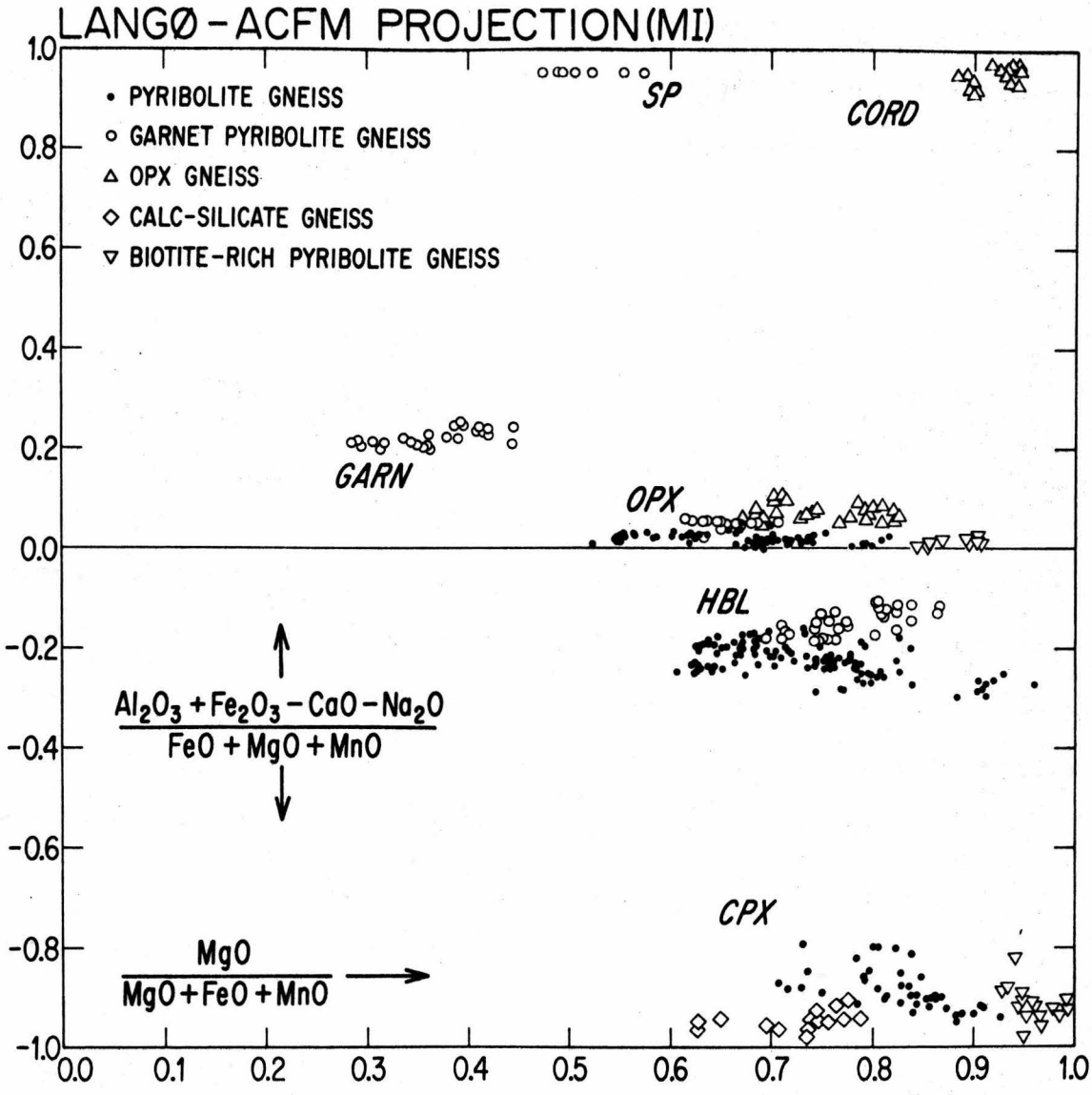
LANGØ - ACFM PROJECTION (MI)
• PYRIBOLITE GNEISS
○ GARNET PYRIBOLITE GNEISS
△ OPX GNEISS
◇ CALC-SILICATE GNEISS
▽ BIOTITE-RICH PYRIBOLITE GNEISS
SP
CORD
GARN
OPX
HBL
CPX
$\frac{Al_2O_3 + Fe_2O_3 - CaO - Na_2O}{FeO + MgO + MnO}$
$\frac{MgO}{MgO + FeO + MnO}$
1.0
0.8
0.6
0.4
0.2
0.0
-0.2
-0.4
-0.6
-0.8
-1.0
0.0
0.1
0.2
0.3
0.4
0.5
0.6
0.7
0.8
0.9
1.0

to its assemblage, with those analyses from cordierite- and garnet-bearing samples being slightly more aluminous than those that coexist with hornblende and/or clinopyroxene. The projection also serves to illustrate that hornblende and orthopyroxene that coexist with garnet have higher Mg-values than many analyses from garnet-free samples. Clinopyroxene from the calc-silicate samples projects into a field distinct from those in pyribolites, consistent with its slightly different bulk composition (c.f., Figure 4-17). Note that both the clinopyroxene and orthopyroxene from biotite pyribolite samples have the highest Mg-values.

Schematic tie lines that connect the average composition of coexisting phases in several of the samples are illustrated in Figure 5-8. Because of the large number of pyribolite samples analyzed, only a select few are shown in the figure. These were chosen to span the entire compositional range observed. The similarity in the orientation of tie lines in a given assemblage indicates fairly constant Fe-Mg partitioning, and is consistent with the assemblages equilibrating at the same grade of metamorphism.

The maze of crossing tie lines and multiple three-phase tie triangles appears confusing. Note that all of the complexities are related to tie lines emanating to or from hornblende, and if this phase were eliminated from the system, say by complete breakdown to pyroxene + plagioclase, then a topology similar to that illustrated in Figure 5-9 would result. Hence, the complications with the projection appear to be related to hornblende.

Figure 5-8: ACFM projection for samples from Langø illustrating schematic tie lines connecting observed phase assemblages.

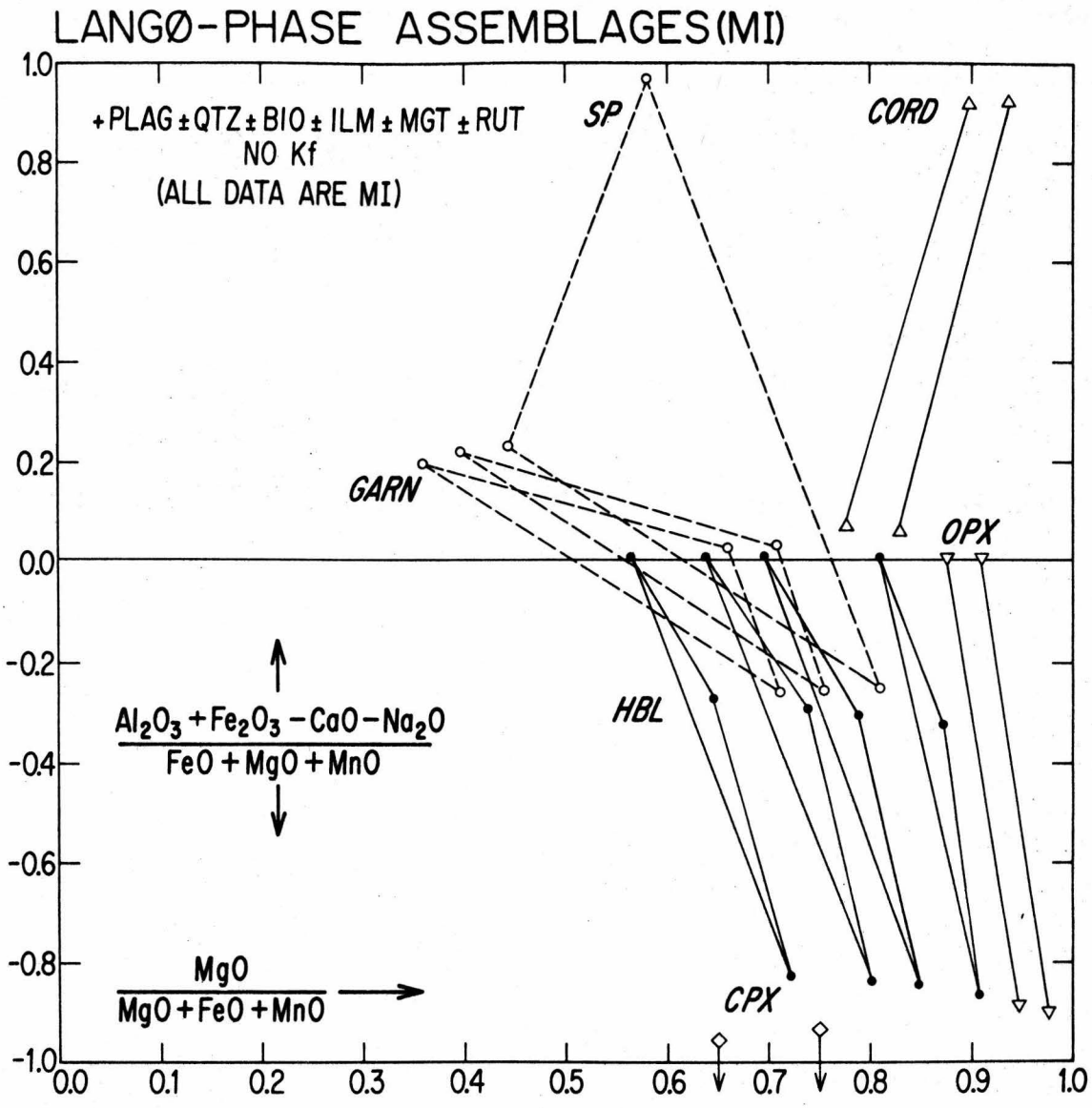
LANGØ-PHASE ASSEMBLAGES(MI)
+PLAG ± QTZ ± BIO ± ILM ± MGT ± RUT
NO Kf
(ALL DATA ARE MI)
SP
CORD
GARN
OPX
HBL
CPX
$\frac{Al_2O_3 + Fe_2O_3 - CaO - Na_2O}{FeO + MgO + MnO}$
$\frac{MgO}{MgO + FeO + MnO}$
1.0
0.8
0.6
0.4
0.2
0.0
-0.2
-0.4
-0.6
-0.8
-1.0
0.0
0.1
0.2
0.3
0.4
0.5
0.6
0.7
0.8
0.9
1.0

Figure 5-9: ACFM projection illustrating hypothetical hornblende-absent granulite-grade phase assemblages based on analysis of samples from Langø. The position of a possible three-phase tie triangle involving garnet-clinopyroxene-orthopyroxene is also shown.

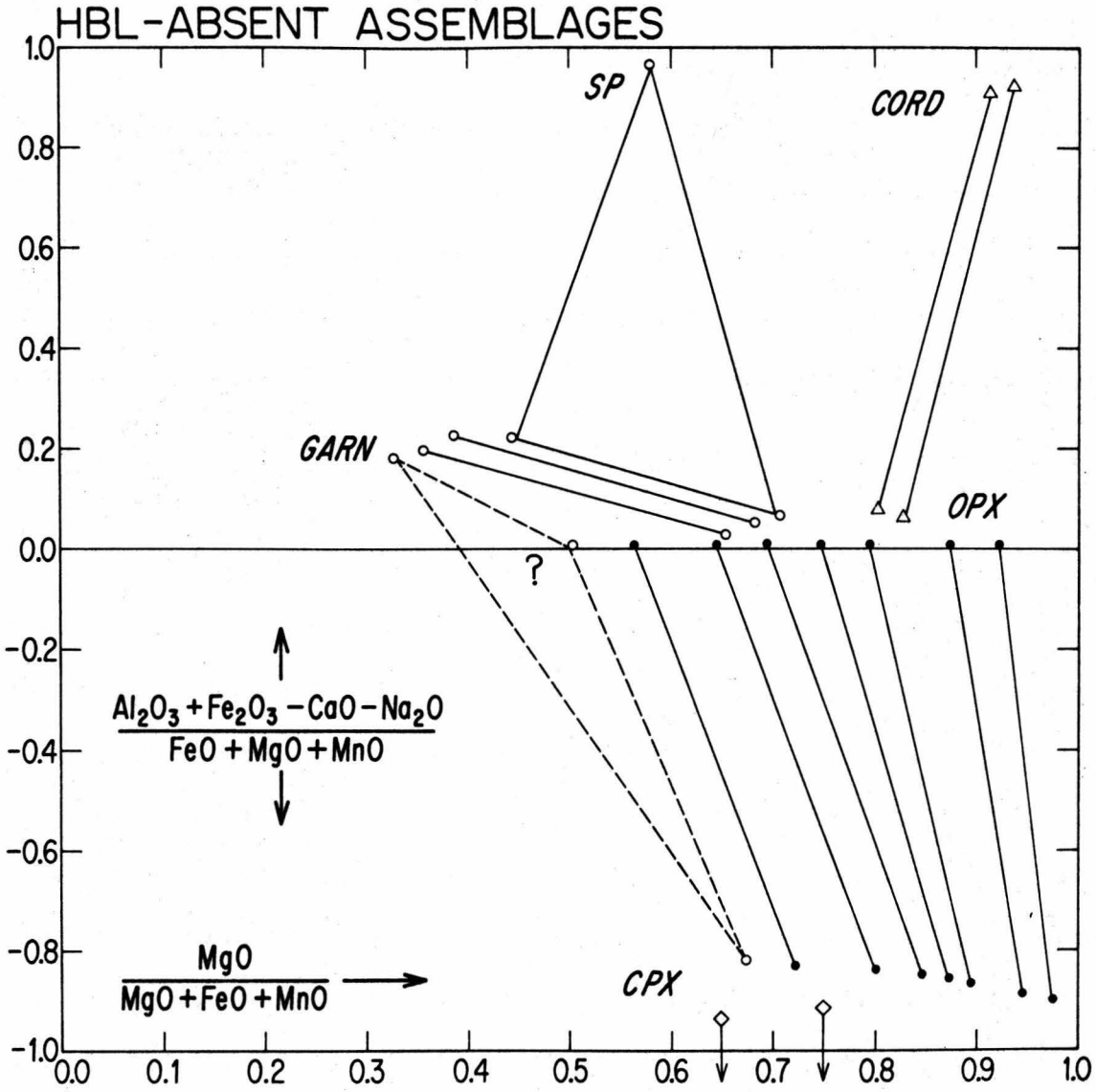
HBL-ABSENT ASSEMBLAGES
SP
CORD
GARN
OPX
?
CPX
$\frac{Al_2O_3 + Fe_2O_3 - CaO - Na_2O}{FeO + MgO + MnO}$
$\frac{MgO}{MgO + FeO + MnO}$
1.0
0.8
0.6
0.4
0.2
0.0
-0.2
-0.4
-0.6
-0.8
-1.0
0.0
0.1
0.2
0.3
0.4
0.5
0.6
0.7
0.8
0.9
1.0

Each four phase assemblage plagioclase-hornblende-orthopyroxene-clinopyroxene, plagioclase-hornblende-orthopyroxene-garnet and plagioclase-hornblende-garnet-spinel that are represented as the three phase tie triangles in Figure 5-8 are from quartz-free samples. The phase rule requires that these assemblages be univariant, and the projection is consistent with this. The assemblages represented by the two phase fields cordierite-orthopyroxene and orthopyroxene-clinopyroxene (orthopyroxene gneisses and biotite pyribolites respectively) occur with both plagioclase and quartz, and are also consistent with the phase rule. Hence, the complications in this projection seem explicable in part by variations in μ_{SiO_2}.

Another factor that may contribute to the added degree of freedom is the presence of Na_2O in hornblende. Since hornblende is the only mafic mineral represented in Figure 5-8 that contains appreciable Na_2O, it cannot be coplanar with pyroxene and garnet, even in projection. Combining Na_2O with CaO assumes that these components substitute freely for one another, which is certainly true for plagioclase. However, in hornblende, practically all of the Na is incorporated in the vacant A-site, and does not substitute for Ca in the M(4) site (c.f., Chapter 4). Hence, Na-substitution may also explain the additional degree of freedom associated with the hornblende-bearing assemblages.

The above statements concerning SiO_2 and Na_2O may be combined into a model that attempts to explain the topologic complexities observed in these granulite grade gneisses. An original amphibolite grade assemblage of $hornblende_1$ + plagioclase + quartz reacts to a

higher grade assemblage of hornblende$_2$ + orthopyroxene + clinopyroxene + plagioclase. Pyroxene contains more SiO_2 than hornblende, and quartz is consumed by this reaction. The hornblende$_2$ is more aluminous, and more sodic due to the edenite substitution. The chemical data given in Chapter 4, indicate that as hornblende becomes more aluminous and sodic, its silica content decreases. In summary then, the data suggest that the formation of pyroxene, which is high in SiO_2 relative to hornblende, causes the hornblende to become more sodic and more aluminous, and quartz is exhausted before the reaction to pyroxene can go to completion. The fact that Na/(Na+Ca) and Al/(Al+Si) in coexisting hornblende and plagioclase are nicely correlated (c.f., Figure 4-22) is consistent with this interpretation. This analysis implies that the two five-phase invariant assemblages quartz-plagioclase-orthopyroxene-clinopyroxene-hornblende and quartz-plagioclase-orthopyroxene-hornblende-garnet should be observed at some other conditions of P, T, and μ_{H_2O}.

The ACFM projection that is presented here, although complicated, does serve to illustrate the nature of the assemblages and the consistent Fe-Mg-Al partitioning among the phases. The projection illustrates that cordierite-bearing rocks occur with hornblende-pyroxene rocks, but not with garnet-clinopyroxene assemblages at the metamorphic grade on Langø.

C. Summary

Mineral assemblages observed in a wide variety of lithologies sampled on Langø were portrayed graphically in a series of AKFM and ACFM projection tetrahedra. The resultant phase assemblage diagrams, although complex, seem to be internally consistent.

The topologies outlined in Figures 5-3B, 5-3C, and 5-7 thus establish a series of phase assemblages that can coexist under the conditions of hornblende-granulite grade of metamorphism. It is important to determine at what temperature and pressure these assemblages formed, and this topic is discussed in the concluding chapter.

CHAPTER 6

VI. DISCUSSION

A. Introduction

The presentation so far has concentrated on the details of the petrographic and mineral-chemical features in the samples from Langø, and how these can be used to interpret phase relations in granulite grade metamorphic rocks. In this section, these data will be synthesized in an attempt to understand some aspects of the evolution of the West Greenland Archaean and the Archaean crust in general.

B. Polymetamorphism

The petrographic observations presented in Chapter 3 clearly establish the polymetamorphic nature of the samples from Langø. Evidence was presented for two distinct episodes of metamorphic mineral growth, which is preserved in samples with a variety of bulk compositions. The first event (MI) occurred at hornblende granulite grade, and the second event (MII) occurred at amphibolite grade.

In the potassium feldspar gneisses and orthopyroxene gneisses, sillimanite formed during MI, whereas kyanite formed during MII. In mafic rocks, pyroxene and green-brown hornblende formed during MI, and pyroxene became unstable during MII with respect to the growth of secondary green calcic amphibole.

The data presented in Chapter 4 indicate that minerals common to both MI and MII, such as calcic amphibole and biotite, tend to have different compositions. It was also demonstrated in Chapter 4 that large differences in the compositions of MI amphibole, plagioclase,

biotite, and pyroxene occur at the same metamorphic grade, and reflect variations in the compositions of the host rock. The same appears to be true for MII amphibole.

All the mineral reactions that characterize MII, which include the replacement of pyroxene by amphibole or biotite, and the replacement of garnet and cordierite by kyanite + biotite, are hydration reactions. Such reactions developed sporadically, even on the scale of a single thin section, and would seem to require the ingress of a water-rich fluid at a later time. However, phases such as staurolite, chlorite*, epidote, muscovite*, pyrophyllite etc. were not formed suggesting that MII on Langø was a relatively high-grade event.

The question arises then, as to whether MII phases developed as a consequence of reaction between MI phases and fluids produced during prograde dehydration reactions. If this were the case, then MII should be regarded as simple "retrogression" that occurred during crustal cooling following the peak of metamorphism. Hence, whereas MI can be assigned with confidence to the major episode of orogenic activity at ca. 2.8 AE (Black et al., 1973), which affected the entire West Greenland Archaean craton at that time, it is not clear whether MII corresponds to any recognizable geological event.

Two other important pieces of information should be considered here. First, approximately 80 km. to the SE of Langø (Figure 1-1), in the south-central portion of the Godthåb District, is a complex ca. 2.5

---

* Although a few grains of these phases do occur, they are exceedingly rare and unimportant.

AE old (Baadsgaard and Collerson, 1976) quartz monzonite intrustion termed the Qôrqut Granite (McGregor, 1973). The field relationships and Rb-Sr isotopic characteristics of the Qôrqut Granite (Moorbath and Pankhurst, 1976) indicates that it formed by extensive melting of older quartzofeldspathic gneisses. Since the emplacement of the Qôrqut Granite seems to require reheating at a time later than MI, then MII may be a consequence of this reheating event.

Secondly, Pankhurst et al. (1973) reported Rb-Sr isotopic data for biotite separated from ca. 3.7 AE Amîtsoq Gneiss, in which there seemed to be evidence for a "regional thermal event" at ca. 1.6 AE. Such an event might also be the cause of MII.

Isotopic studies on some of the samples from Langø might elucidate this problem, since 1.6 AE should be resolvable from 2.8 AE, although the 2.5 AE event associated with the Qôrqut Granite may not be. Petrographic study of samples of the Malene Supracrustals throughout the Godthåb District (Dymek, unpublished) also indicate the presence of a small amount of secondary mineral growth in these rocks. This includes replacement of pyroxene and hornblende by epidote + actinolite, replacement of cordierite by staurolite + cholorite, and reaction between orthopyroxene and cordierite to yield gedrite. As was the case on Langø, these secondary reactions are developed sporadically. However, the pervasive character of these secondary mineral reactions suggests that MII is an event that must be identified more clearly and reckoned with in interpreting the evolution of the Godthåb District.

The growth of secondary minerals is reported in samples from many metamorphic terranes throughout the world, and commonly ignored.

Recognition of such phenomena as being a consequence of polymetamorphism, and not simply "retrogression", may provide an added insight into the interpretation of local geological history.

C. Physical Conditions of Metamorphism

One of the primary objectives of metamorphic petrology is to outline the physical conditions that act to form a group of mineral assemblages. Once phase assemblages and compositions are known, pressure and temperature can be estimated by comparison with the appropriate experimental systems, or calculated from thermodynamic data.

1) MI: In Chapter 5, chemographic relationships among the various MI mineral assemblages were discussed, and an internally consistent set of topologies constructed for this hornblende-granulite grade metamorphism. Thus, despite the complexities associated with polymetamorphism, it appears that meaningful information can be obtained from the observed, primary (MI) mineral assemblages.

The assemblages have been compared to the appropriate experimental work, and the results are illustrated in Figure 6-1. There are a sufficient number of useful assemblages to constrain the pressure and temperature of the first metamorphism (MI) to lie between $\sim$6.6-8.3 Kb and $\sim$675-810^{o}C.

The presence of primary sillimanite in samples from two lithologies indicates that MI assemblages crystallized in the stability field of that mineral. The coexistence of potassium feldspar and sillimanite indicates that MI occurred beyond the stability limit of muscovite + quartz. The fact that the quartzofeldspathic gneisses are migmatitic

suggests that MI occurred at a temperature greater than that of the onset of partial melting in the "granite" system.

Experimentally-determined curves for the stability relations of the aluminosilicate minerals (Holdaway, 1971), the reaction muscovite + quartz $\rightleftarrows$ potassium feldspar + aluminosilicate + vapor (Althaus et al., 1970; Storre, 1972), and the onset of melting in the system Ab-Or-Q-H_2O (Tuttle and Bowen, 1958) are illustrated in Figure 6-1. The position of curve 1, which represents the kyanite-sillimanite boundary, is reasonably well-established and should be approximately correct as shown in the diagram. Curve 3, which represents the maximum stability of muscovite + quartz, is valid for the specific condition that $P_{H_2O} = P_T$ ($a_{H_2O} = 1$). Fluid inclusion studies (Touret, 1971; Hollister and Burruss, 1976) suggest that the fluid in high grade metamorphic rocks is not pure H_2O. Hence, curve 2 would shift towards lower temperatures under the condition that $P_{H_2O} < P_T$ ($a_{H_2O} < 1$). Curve 2, which represents the onset of anatexis is valid as shown for $P_{H_2O} = P_T$ ($a_{H_2O} = 1$), and for plagioclase with the composition of pure albite. The presence of the anorthite component in plagioclase and $P_{H_2O} < P_T$ ($a_{H_2O} < 1$) would shift curve 3 towards higher temperatures.

The presence of sillimanite rather than kyanite indicates that curve 2 could not be depressed by more than $\sim 75^\circ$ above 5 Kb to $\sim 640^\circ C$. A corresponding shift of curve 3 would increase the temperature where curves 2 and 3 would intersect. Considering the uncertainties involved, $650^\circ C$ should represent a reasonable minimum temperature for MI, constrained primarily by the presence of sillimanite.

Figure 6-1: Diagram illustrating estimated pressure and temperature during the two metamorphic events on Langø. The P and T for MI are constrained to lie within the hachured area, whereas the P and T for MII appear to lie within the stippled area. The appropriate reaction curves are labeled. Temperatures calculated from Fe-Mg partitioning between garnet and biotite are based on the method of Thompson (1976) (see text for discussion).

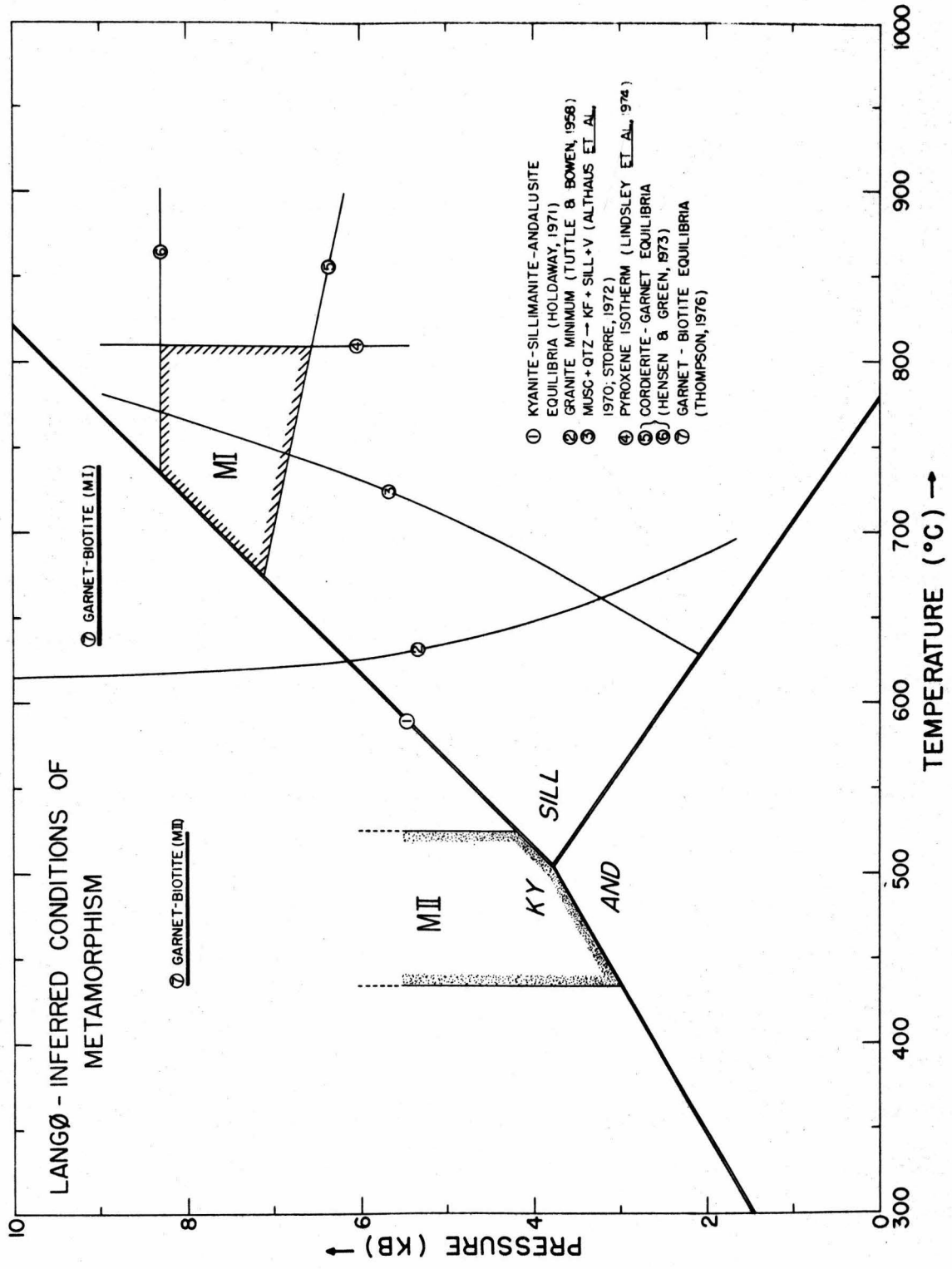
LANGØ - INFERRED CONDITIONS OF METAMORPHISM
PRESSURE (KB) →
TEMPERATURE (°C) →
MII
MI
KY
SILL
AND
⑦ GARNET-BIOTITE (MII)
⑦ GARNET-BIOTITE (MI)
① KYANITE-SILLIMANITE-ANDALUSITE EQUILIBRIA (HOLDAWAY, 1971)
②③ GRANITE MINIMUM (TUTTLE & BOWEN, 1958) MUSC+QTZ → KF+SIL+V (ALTHAUS ET AL. 1970; STORRE, 1972)
④ PYROXENE ISOTHERM (LINDSLEY ET AL. 1974)
⑤⑥ CORDIERITE-GARNET EQUILIBRIA (HENSEN & GREEN, 1973)
⑦ GARNET-BIOTITE EQUILIBRIA (THOMPSON, 1976)

The maximum temperature for MI is constrained by the compositions of coexisting pyroxenes to be less than 810°C. A detailed discussion of this has been presented in Chapter 4.

Temperatures calculated from Fe-Mg partitioning between garnet cores and primary biotite range from 630°-740°C, based on a comparison with the data presented by Thompson (1976). This range in calculated temperatures, although complicated somewhat by uncertainties in the thermodynamic model (see Thompson 1976, p. 425-430 for discussion), is interpreted to be caused by the presence of Fe-Mg zoning in both garnet and biotite due to polymetamorphism. Such zoning would shift the calculated temperatures to lower values. In addition, it is not clear whether the highest grade cores were analyzed in each case. Therefore, the maximum temperature calculated by this method (740°C) probably represents the best approximation to the actual temperature during MI using this method.

Hensen and Green (1973) have shown experimentally that Fe/Mg in coexisting garnet and cordierite are sensitive to variations in pressure during metamorphism. However, utilization of their data requires the presence of the three phase assemblages garnet-cordierite-sillimanite or garnet-cordierite-orthopyroxene, neither of which have been observed on Langø. Nevertheless, the occurrence of the two phase assemblages garnet-cordierite (24C) and cordierite-orthopyroxene (28B, 28H) implies that the three-phase assemblages mentioned above are stable on Langø in rocks of the appropriate bulk composition, as indicated in Figure 5-3C. Hence, the measured compositions of garnet and cordierite can be used to bracket the pressure during MI.

An examination of Figure 5-3C indicates that a garnet which is slightly more Mg-rich than the one that coexists with cordierite in 24C would occur in the assemblage garnet-cordierite-orthopyroxene. Thus, the most-magnesian garnet composition in 24C will define the minimum pressure, and the corresponding isopleth from Hensen and Green (1973) is illustrated in Figure 6-1 as curve 5.

Similarly, a cordierite that is slightly more Fe-rich than the ones that occur with orthopyroxene in 28B and 28D would occur in the assemblage garnet-cordierite-orthopyroxene. Thus, the most iron-rich cordierite in 28B will define the maximum pressure, and the corresponding isopleth from Hensen and Green (1973) is illustrated in Figure 6-1 as curve 6.

In summary the pressure and temperature of MI are constained by the compositions of cordierite and garnet, the Ca-contents of coexisting pyroxenes, and the position of the kyanite-sillimanite boundary curve to lie within the hachured area in Figure 6-1. It is interesting to note that the average temperature (750°C) is in agreement with the postulated equilibration temperature of plagioclase and scapolite (c.f., Chapter 4).

Wells (1976) has recently reported on the physical conditions during this 2.8 AE metamorphism for samples collected from the Buksefjord region, which overlaps the southwest corner of the Godthåb District, approximately 125 km south of Langø (Fig. 1-1). He presented estimates for pressure and temperature during the 2.8 AE (i.e., MI) metamorphic event based on thermodynamic calculations for two sets of mineral assemblages. The first set of assemblages, which included combinations of cordierite-gedrite-staurolite-garnet-sillimanite, yielded an average

calculated pressure and temperature of ∿7 Kb and ∿630°C respectively. The second set of assemblages included hornblende-orthopyroxene-clinopyroxene-garnet, and the calculations yielded an average pressure and temperature of ∿10.5 Kb and ∿810°C respectively.

The absence of pyroxene in the first set of assemblages indicates that they formed at a lower metamorphic grade than those on Langø, and the calculated P and T are in agreement with this inference. The presence of garnet + clinopyroxene in the second set of assemblages from Buksefjord indicates that they formed at a higher grade than those on Langø, and the calculated P and T are likewise in agreement.

These three data sets are illustrated in Figure 6-2, which emphasizes the intermediate nature of the metamorphic conditions on Langø relative to the two localities in the Buksefjord area. This diagram also summarizes what is currently known concerning the range of P and T during the 2.8 AE metamorphism in the Archaean craton of West Greenland.

2) MII: The presence of secondary kyanite in two lithologies on Langø indicates that MII occurred in the stability field of that mineral. Equilibration temperatures calculated from Fe-Mg partitioning between garnet (rims) and secondary (MII) biotite intergrown with kyanite yield values of 425-525°C. This large temperature range is probably related to the presence of Fe/Mg zoning in both garnet and biotite, as in the case of MI.

Such temperatures in the presence of kyanite necessitate pressures greater than 3-4 Kb (Figure 6-1). The fact that secondary amphibole, which occurs with plagioclase, has an exceedingly small content of

Figure 6-2: Summary diagram illustrating variations in physical conditions of metamorphism during the 2.8 AE event in West Greenland based on the conclusions reached in this study and the results reported by Wells (1976).

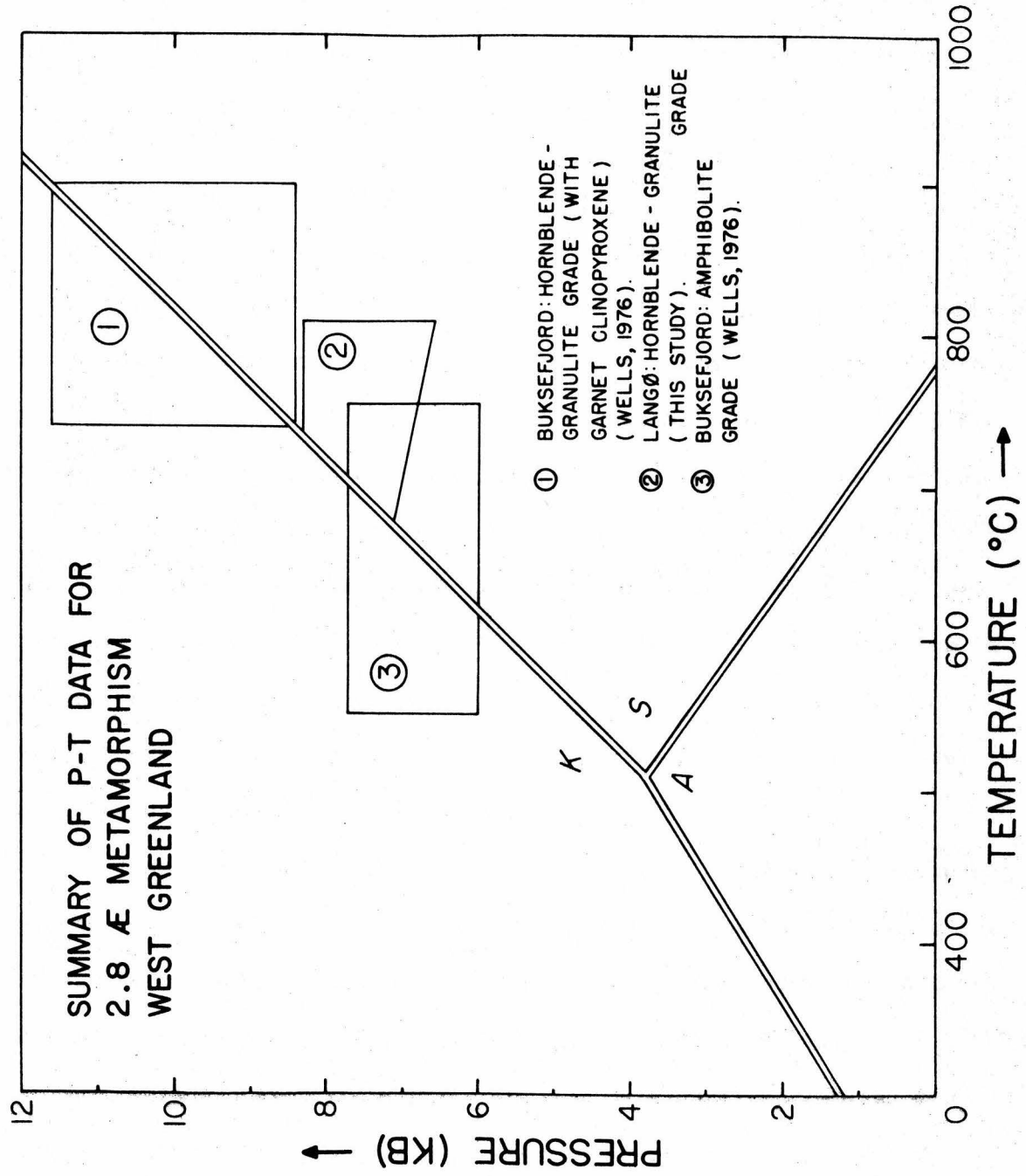
SUMMARY OF P-T DATA FOR
2.8 Æ METAMORPHISM
WEST GREENLAND
① BUKSEFJORD: HORNBLENDE - GRANULITE GRADE (WITH GARNET CLINOPYROXENE) (WELLS, 1976).
② LANGØ: HORNBLENDE - GRANULITE GRADE (THIS STUDY).
③ BUKSEFJORD: AMPHIBOLITE GRADE (WELLS, 1976).
K
S
A
PRESSURE (KB) →
TEMPERATURE (°C) →
0
400
600
800
1000
2
4
6
8
10
12

of the glaucophane component (c.f., Chapter 4) would imply low to moderate P at this temperature, and values greater than 5-6 Kb seem highly unlikely. However, there does not appear to be a more precise way to define the maximum pressure during MII.

D. Implications and Conclusions

In conclusion, the principal results of this study need to be reiterated. Most importantly, the occurrence of two metamorphic events on Langø has been documented in detail both from a mineral-chemical and petrographic point of view. The first event (MI) occurred at ∿7.5 Kb ∿750°C whereas the second event (MII) occurred at ∿475°C and ≳3-4 Kb.

The estimated P and T for MI imply a thermal gradient of ∿30°C/km. This thermal gradient, and the observed mineral assemblages, are similar to those inferred for moderate-P facies series metamorphism in younger orogenic areas such as the Dalradian (c.f., Miyashiro, 1974). Hence, nothing "unique" can be ascribed to the 2.8 AE Archaean metamorphism as it is manifested on Langø.

However, the estimated P and T for MI on Langø merely represent a single point on a P-T trajectory during regional metamorphism in this area. Before any comprehensive description of this metamorphism can be offered, samples from the rest of the Godthåb District have to be studied. As was mentioned in the introduction, the work described herein represents the first phase of a large scale study to investigate this problem.

Regarding such problems as the evolution of the continental crust over time, the pressure estimated for Langø would require a crustal thickness of >20 km at 2.8 AE [>30 km if Wells (1976) data are included], assuming that the samples studied are truly supra-crustal in origin.

Since the crust in Precambrian shield areas is presently ∿30 km thick, this would imply that at least 20 km of erosion would be necessary to expose the metamorphosed rocks on Langø, and that a ∿50 km thick crust was present in this area at 2.8 AE. A crustal thickness of this magnitude is similar to that found or inferred for younger orogenic belts.

If one assumes a crude 2:1 ratio between crustal thicknesses in orogenic belts and non-orogenic areas, then the stable continental crust at 2.8 AE may have been as thick as 25 km. Clearly these issues are ripe for speculation, but estimation of pressure and temperature from mineral assemblages preserved in ancient metamorphic rocks provide the only way of measuring Archaean geotherms in such complex terranes. Data of this kind constrain severely any and all models for crustal evolution.

AMEN.

REFERENCES

Albee A.L. and Chodos A.A. (1969) Minor element content of coexistent Al_2SiO_5 polymorphs. Amer. J. Sci., 267, 310-316.

Albee A.L. and Ray L. (1970) Correction factors for electron probe microanalysis of silicates, oxides, carbonates, phosphates, and sulfates. Anal. Chem., 42, 1408-1414.

Althaus E., Nitsch K.H., Karotke E., and Winkler H.G.F. (1970) An experimental re-examination of the upper stability limit of muscovite plus quartz. N. Jb. Miner. Abh., 121, 325-336.

Anderson J.R. (1977) The polymetamorphic sequence in the Paleozoic rocks of Northern Vermont: A new approach using metamorphic veins as petrologic and structural markers. Ph. D. thesis, California Institute of Technology, 622 pages.

Baadsgaard H. (1973) U-Th-Pb dates on zircons from the early Precambrian Amîtsoq Gneiss, Godthaab District, West Greenland. Earth Planet. Sci. Lett., 19, 22-28.

Baadsgaard H. and Collerson K.D. (1976) U-Pb geochronology in the Godthaabsfjord area, West Greenland and the Saglek area, Labrador. Geol. Soc. Amer. Abstr. with Prog., 8, 760.

Bard J.P. (1970) Composition of hornblendes formed during the Hercynian progressive metamorphism of the Aracena metamorphic belt (SW Spain). Contr. Min. Pet., 28, 117-134.

Barker F. (1961) Phase relations in cordierite-garnet-bearing Kinsman quartz monzonite and the enclosing schist, Lovewell Mountain Quadrangle, New Hampshire. Am. Miner., 46, 1166-1176.

Bence A.E. and Albee A.L. (1968) Empirical correction factors for the electron microanalysis of silicates and oxides. J. Geol., 76, 382-403.

Berthelsen A. (1960) Structural studies in the Precambrian of Western Greenland. II Geology of Tovqussap Nunâ. Medd. om Grønland, 123, 1-223.

Binns R.A. (1965) The mineralogy of metamorphosed basic rocks from the Willyama Complex, Broken Hill District, New South Wales. Part I. Hornblendes. Min. Mag., 35, 306-326.

Binns R.A. (1969) Ferromagnesian minerals in high-grade metamorphic rocks. In: Geol. Soc. Australia, Sp. Publ. #2, 323-332.

Black L.P., Moorbath S., Pankhurst R.J., and Windley B.F. (1973) $^{207}Pb/^{206}Pb$ whole rock age of the Archaean granulite facies metamorphic event in West Greenland. Nature, Phys. Sci., 244, 50-53.

Bridgwater D., McGregor V.R., and Myers J.S. (1974) A horizontal tectonic regime in the Archaean of Greenland and its implications for early crustal thickening. Precambrian Res., 1, 179-197.

Bridgwater D., Keto L., McGregor V.R., and Myers J.S. (1976) Archaean gneiss complex of Greenland. In: Geology of Greenland, p. 20-75, Geological Survey of Greenland, Copenhagen.

Buddington A.F. and Lindsley D.H. (1964) Iron-titanium oxide minerals and synthetic equivalents. J. Petrology, 5, 310-357.

Cahn J.W. (1962) On spinodal decomposition in cubic crystals. Acta Met., 10, 179-183.

Champion D.E., Albee A.L., and Chodos A.A. (1975) Reproducibility and operator bias in a computer controlled system for quantitative electron microprobe analysis. Proc. 10th Nat. Conf. on Electron Probe Analyses. Las Vegas, Nev., 55.

Chodos A.A., Albee A.L., Gancarz A.J., and Laird J. (1973) Optimization of computer controlled system for quantitative electron microprobe analysis. Proc. 8th Nat. Conf. on Electron Probe Analyses. New Orleans, La., 45.

Clifford T.N. (1974) Review of African granulites and related rocks. Sp. Pap. Geol. Soc. Amer. #156, 49 pages.

Crawford M.L. (1973) Crystallization of plagioclase in mare basalts. Proc. Fourth Lunar Sci. Conf., Geochim. Cosmochim Acta, Suppl. 4, 1, 705-717.

Dahl O. (1969) Irregular distribution of iron and magnesium among coexisting biotite and garnet. Lithos, 2, 311-322.

Dahl O. (1970) Octahedral titanium and aluminum in biotite. Lithos, 3, 161-166.

Dymek R.F., Albee A.L., Chodos A.A., and Wasserburg G.J. (1976) Petrography of isotopically-dated clasts in the Kapoeta howardite and petrologic constraints on the evolution of its parent body. Geochim. Cosmochim. Acta, 40, 1115-1130.

Engel A.E.J. and Engel C.G. (1962) Hornblendes formed during progressive metamorphism of amphibolites, Northwest Adirondack Mountains, New York. Bull. Geol. Soc. Amer., 73, 1499-1514.

Ernst W.G., Seki Y., Onuki H., and Gilbert M.N. (1970) Comparative study of low-grade metamorphism in the California Coast Ranges and the Outer Metamorphic Belt of Japan. Mem. Geol. Soc. Amer. #124, 276 pages.

Eskola P. (1915) On the relations between the chemical and mineralogical composition in the metamorphic rocks of the Orijarvi region. Bull. Comm. Geol. Finlande, 44, 109-145.

Evans B.W., Shaw D.M., and Haughton D.R. (1969) Scapolite stoichiometry. Contr. Min. Pet., 24, 293-305.

Fleet M.E. (1974) Mg, Fe^{2+} site occupancies in coexisting pyroxenes. Contr. Min. Pet., 47, 207-214.

Foster M.D. (1960) Interpretation of the composition of trioctohedral micas. U.S.G.S. Prof. Paper 354-B, 48 pages.

Gancarz A.J. and Wasserburg G.J. (in press) Initial Pb of the Amîtsoq Gneiss and a 4.47 "Age of the Earth". Geochim. Cosmochim. Acta.

Goldsmith J.R. (1976) Scapolites, granulites, and volatiles in the lower crust. Bull. Geol. Soc. Amer., 87, 161-169.

Goldman D.S., Rossman G.R., and Dollase W.A. (in press) Channel constituents in cordierite. Amer. Miner.

Graham C.M. (1974) Metabasite amphiboles of the Scottish Dalradian. Contr. Min. Pet., 47, 165-185.

Greenwood H.J. (1975) Thermodynamically valid projections of extensive phase relations. Amer. Miner., 60, 1-8.

Guidotti C.V. and Sassi F.P. (1976) Muscovite as a petrogenetic indicator mineral in pelitic schists. N. Jb. Miner. Abh., 127, 97-142.

Guidotti C.V., Cheney J.T., and Guggenheim S. (in press) Distribution of titanium between coexisting muscovite and biotite in pelitic schists from northwestern Maine. Amer. Miner.

Hensen B.J. and Green D.H. (1973) Experimental study of the stability of garnet and cordierite at high pressures and temperatures. III. Synthesis of experimental data and geological applications. Contr. Min. Pet., 38, 151-166.

Hewins R.H. (1975) Pyroxene geothermometry of some granulite facies rocks. Contr. Min. Pet., 50, 205-209.

Holdaway M.J. (1971) Stability of andalusite and the aluminum silicate phase diagram. Amer. J. Sci., 271, 97-131.

Hollister L.S. and Burruss R.C. (1976) Phase equilibria in fluid inclusions from the Khtada Lake metamorphic complex. Geochim. Cosmochim. Acta, 40, 163-175.

Huttenlocher H. (1942) Beiträge zur Petrographie des Gesteinzuges Ivrea Verbano I. Allgemeines. Die gabbroiden Gesteine von Anzola. Schw. Miner. Petr. Mitt., 22, 326-366.

Jones N.W., Ribbe P.H., and Gibbs G.V. (1969) Crystal chemistry of the humite minerals. Amer. Miner., 54, 391-411.

Korzhinskii D.S. (1960) Physiochemical Basis of the Analysis of the Paragenesis of Minerals (translated from Russian). Consultants Bureau, Inc., New York, 142 pages.

Kretz R. (1961) Some applications of thermodynamics to coexisting minerals of variable composition. Examples: orthopyroxene-clinopyroxene and orthopyroxene-garnet. J. Geol., 69, 361-387.

Leake B.E. (1965) The relationship between composition of calciferous amphibole and grade of metamorphism. In: Controls of Metamorphism, W.S. Pitcher and G.W. Flinn, eds., 299-318.

Lindsley D.H. (1962) Investigations in the system $FeO-Fe_2O_3-TiO_2$. Carnegie Inst. of Washington, Year Book 61, 100-106.

Lindsley D.H. (1963) Fe-Ti oxides in rocks as thermometers and oxygen barometers. Carnegie Inst. of Washington, Year Book 62, 60-66.

Lindsley D.H. (1965) Iron-titanium oxides. Carnegie Institute of Washington, Year Book 64, 144-148.

Lindsley D.G., King H.E., Jr., and Turnock A.C. (1974) Compositions of synthetic augite and hypersthene at 810°C. Application to pyroxenes from the lunar highlands. Geophys. Res. Lett., 1, 134-136.

Longhi J., Walker D., and Hays J.F. (1976) Fe and Mg in plagioclase. Proc. Lunar Sci. Conf. 7th, 2, 1281-1300.

Lovering J.F. and White A.J.R. (1969) Granulitic and eclogitic inclusions from basic pipes at Delegate, Australia. Contr. Min. Pet., 21, 9-52.

McGregor V.R. (1973) The early Precambrian gneisses of the Godthåb district, West Greenland. Phil. Trans. R. Soc. Lond. A., 273, 343-358.

Machatschki K. and Walitzi E.M. (1962) Hornblenden aus Eklogiten und Amphiboliten der südlichen Koralpe. Tschmer. Min. Petr. Mitt., 8, 140-151.

Moorbath S. (1977) The oldest rocks and the growth of continents. Sci. Amer., 236, #3, 92-104.

Moorbath S., O'Nions R.K., Pankhurst R.J., Gale N.H., and McGregor V.R. (1972) Further rubidium-strontium age determinations on the very early Precambrian rocks of the Godthåb district, West Greenland. Nature Phys. Sci., 240, 78-82.

Moorbath S. and Pankhurst R.J. (1976) Further rubidium-strontium age and isotope evidence for the nature of the late Archaean plutonic event in West Greenland. Nature Phys. Sci., 262, 124-126.

Miyashiro A. (1974) Metamorphism and Metamorphic Belts, George Allen & Unwin, London, 492 pages.

Newton R.C. and Goldsmith J.R. (1975) Stability of the scapolite meionite ($3CaAl_2Si_2O_8 \cdot CaCO_3$) at high pressures and storage of CO_2 in the deep crust. Contr. Min. Pet., 49, 49-62.

Nissen H.-U. (1971) End member compositions of the labradorite exsolution. Naturwiss., 58, 53-55.

Oliver R.L. (1969) Some observations on the distribution and nature of granulite-facies terrains. In: Geol. Soc. Australia, Sp. Publ. #2, 259-268.

Orville P.M. (1975) Stability of scapolite in the system Ab-An-NaCl-$CaCO_3$ at 4 kb and 750°C. Geochim. Cosmochim. Acta, 39, 1091-1105.

Pankhurst R.J., Moorbath S., Rex D.C., and Turner G. (1973) Mineral age patterns in ca. 3700 my old rocks from West Greenland. Earth Planet. Sci. Lett., 20, 157-170.

Poldervaart A. and Hess H.H. (1951) Pyroxenes in the crystallization of basaltic magma. J. Geol., 59, 472-489.

Raase P. (1974) Al and Ti contents of hornblende, indicators of pressure and temperature of regional metamorphism. Contr. Min. Pet., 45, 231-236.

Ray S. and Sen S.K. (1970) Partitioning of major exchangeable cations among orthopyroxene, calcic pyroxene, and hornblende. N. Jb. Miner. Abh., 114, 61-88.

Robinson P. and Jaffe H.W. (1969) Chemographic exploration of amphibole assemblages from central Massachusetts and southwestern New Hampshire. In: Sp. Publ. #2 Miner. Soc. Amer., 251-274.

Rumble D. (1973) Fe-Ti oxide minerals from regionally metamorphosed quartzites. Contr. Min. Pet., 42, 181-195.

Rumble D. (1976) Oxide minerals in metamorphic rocks. Ch. 3. In: Miner. Soc. Amer. Short Course Notes, Oxide Minerals, 3.

Shido F. and Miyashiro A. (1959) Hornblendes of basic metamorphic rocks. J. Fac. Sci. Univ. Tokyo II, 12, 85-102.

Smith J.V. (1974) Feldspar Minerals, 2, Chemical and Textural Properties, Springer-Verlag, New York, 690 pages.

Storre B. (1972) Dry melting of muscovite + quartz in the range P_s = 7 kb to P_s = 20 kb. Contr. Min. Pet., 37, 87-89.

Takeda H. and Ross M. (1975) Mica polytypism: Dissimilarities in the crystal structures of coexisting 1M and $2M_1$ biotite. Amer. Miner., 60, 1030-1040.

Thompson A.B. (1976) Mineral reactions in pelitic rocks: II. Calculations of some P-T-X (Fe-Mg) phase relations. Amer. J. Sci., 276, 425-454.

Thompson J.B., Jr. (1955) The thermodynamic basis for the mineral facies concept. Amer. J. Sci., 253, 65-103.

Thompson J.B., Jr. (1957) The graphical analysis of mineral assemblages in pelitic schists. Amer. Miner., 42, 842-858.

Touret J. (1971) Le facies granulite en Norvege Meridionale II. Les inclusions fluides. Lithos, 4, 423-436.

Tuttle O.F. and Bowen N.L. (1958) Origin of granite in the light of experimental studies in the system $NaAlSi_3O_8$ - $KAlSi_3O_8$ - SiO_2 - H_2O. Mem. Geol. Soc. Amer. #74, 153 pages.

Vernon R.H. (1972) Reactions involving hydration of cordierite and hypersthene. Contr. Min. Pet., 35, 125-137.

Weill D.F., McCallum I.S., Bottinga Y., Drake M.J., and McKay G.A. (1970) Mineralogy and petrology of some Apollo 11 igneous rocks. Proc. Apollo 11 Lunar Sci. Conf., Geochim. Cosmochim. Acta, Suppl. 1, 1, 937-955.

Wells P.R.A. (1976) Late Archaean metamorphism in the Buksefjorden Region, Southwest Greenland. Contr. Min. Pet., 56, 229-242.

Windley B.F. editor (1976) The Early History of the Earth, Wiley, New York, 550 pages.

Wiseman J.D.H. (1934) The central and southwest epidiorites: a study in progressive metamorphism. Quart. J. Geol. Soc. London, 90, 354-417.

Wood B.J. and Banno S. (1973) Garnet-orthopyroxene and orthopyroxene-clinopyroxene relationships in simple and complex systems. Contr. Min. Pet., 42, 109-124.

Wynne-Edwards H.R. and Hay P.W. (1963) Coexisting cordierite and garnet in regionally metamorphosed rocks from the Westport area, Ontario, Canada. Canad. Miner., 7, 453-478.

APPENDIX I. ESTIMATED MINERAL MODES AND PETROGRAPHIC CLASSIFICATION OF SAMPLES FROM LANGØ

	Qtz	Plag	Kf	Bio	Hbl	Opx	Cpx	Cdr	Gar	Sill	Ky	Fe-Ti Oxides	Zirc	Ap	White Mica	Others	Group
GREAT PYRIBOLITE																	
*39A	tr	35	--	tr	35	20	--	--	10	--	--	~1	--	--	--	--	3A
39B	tr	30	--	--	20	20	30	--	--	--	--	<1	--	tr	--	CC(tr)	3
39C	35	40	--	--	5	<1	20	--	--	--	--	tr	--	tr	tr	--	3
39D	tr	40	--	tr	15	25	5	--	10	--	--	5	--	--	tr	CC(tr),HERC(tr)	3A†
*39E	tr	40	--	--	25	15	20	--	--	--	--	~1	--	tr	--	--	3
2ND INTERMEDIATE LAYER																	
23A	--	5	--	5	5	40	45	--	--	--	--	<1	--	--	--	--	3
*23B	--	5	--	5	10	40	40	--	--	--	--	~1	tr	--	--	--	3
24A	25	60	15	<1	--	--	--	--	~1	--	tr	tr	tr	tr	tr	CHL(tr)	1
*24B	~1	40	--	10	10	--	40	--	--	--	--	--	tr	tr	--	--	4
*24C	30	35	10	10	--	--	--	~1	10	--	5	--	tr	--	tr	--	1
*24D	30	40	25	5	--	--	--	--	~1	1	tr	--	--	--	--	--	1
*24E	<1	40	--	5	33	15	2	--	--	--	--	5	tr	tr	--	--	3
24F	30	60	5	3	--	--	--	--	2	--	tr	tr	tr	--	--	--	1
25A	30	60	10	1	--	--	--	--	--	--	--	tr	--	--	--	--	1
25B	30	30	35	5	--	--	--	--	~1	--	--	tr	--	--	--	--	1
25C	35	55	tr	10	--	--	--	--	--	--	--	tr	--	--	tr	--	1
*25D	10	40	--	<1	35	--	15	--	--	--	--	2	--	tr	tr	CHL(tr),CC(tr)	3
*25E	45	40	10	5	--	--	--	--	--	--	--	tr	tr	--	--	--	1
26A	15	30	--	4	20	20	10	--	--	--	--	1	--	tr	--	--	3
*26B	--	--	--	--	35	50	8	--	--	--	--	5	--	--	--	DOL(tr),OL(2)	7
26C	--	--	--	20	20	50	10	--	--	--	--	~1	--	tr	--	--	7
*27	50	30	18	2	--	--	--	--	--	--	--	~1	tr	tr	tr	--	1
28A	20	20	--	30	--	30	--	--	--	--	--	tr	tr	--	--	CHL(tr)	2
*28B	15	20	--	30	--	30	--	5	--	--	tr	tr	tr	--	--	--	2
28C	<1	<1	--	50	--	30	--	20	--	<1	tr	<1	tr	--	--	--	2
*28D	15	60	--	5	--	20	--	--	--	--	--	--	tr	--	--	--	2
28E	10	65	--	5	--	20	--	--	--	--	--	tr	--	--	--	CC(tr)	2
28F	tr	~1	--	35	--	35	--	30	--	--	tr	tr	tr	--	--	--	2
28G	15	70	--	5	--	10	--	--	--	--	--	tr	tr	--	--	CHL(tr)	2
*28H	30	10	--	30	--	5	--	25	--	<1	tr	tr	tr	--	--	CHL(tr)	2
*28I	10	30	--	5	10	20	25	--	--	--	tr	tr	tr	--	--	SCAP(tr)	4
35817	15	35	--	5	15	25	5	--	--	--	tr	--	--	tr	--	SCAP(~1)	4

	Qtz	Plag	Kf	Bio	Hbl	Opx	Cpx	Cdr	Gar	Sill	Ky	Fe-Ti Oxides	Zirc	Ap	White Mica	Others	Group
*29	50	22	15	3	--	--	--	--	--	--	--	tr	tr	tr	tr	--	1
36A	50	40	2	5	--	3	--	--	--	--	--	tr	tr	tr	tr	CHL(tr)	1
*36B	30	35	30	5	--	--	--	--	--	--	--	tr	--	--	--	--	1
36C	50	30	15	5	--	tr	--	--	--	--	--	<1	tr	--	~1	CHL(tr)	1
36D	55	25	15	5	--	--	--	--	--	--	--	tr	tr	tr	tr	--	1
36E	60	25	15	5	--	--	--	--	--	--	--	tr	tr	tr	tr	--	1
36F	40	50	10	tr	--	--	--	--	--	--	--	tr	--	--	--	--	1
36G	30	35	--	5	15	15	--	--	--	--	--	tr	tr	--	--	--	3
*36H	50	30	10	5	--	--	--	--	5	~1	tr	tr	tr	tr	tr	CHL(tr)	1
*36I	tr	45	--	tr	tr	--	50	--	--	--	--	tr	--	--	--	SPH(~1), CC(tr), SCAP(5)	6
*36J	10	35	--	15	5	15	25	--	--	--	--	tr	tr	tr	--	CC(tr)	4
*36K	<1	55	--	3	40	tr	5	--	--	--	--	~1	--	--	tr	CC(<1)	3
*35861-1&2	50	40	tr	5	--	5	--	~1	--	tr	tr	tr	tr	--	tr	CHL(tr)	2
*35861-3	10	25	--	20	15	15	15	--	--	--	--	--	tr	tr	--	SCAP(<1)	4
PAS PYRIBOLITE																	
*30A	--	30	--	tr	40	25	5	--	--	--	--	tr	--	tr	--	--	3
30B	tr	20	--	--	30	30	20	--	--	--	--	tr	--	--	--	--	3
30C	tr	20	--	tr	60	tr	20	--	--	--	--	tr	--	tr	--	--	3
30D	--	30	--	tr	30	30	10	--	--	--	--	tr	--	--	--	--	3
31A	--	--	--	tr	30	70	--	--	--	--	--	~1	--	--	--	HERC(~1)	7
31B	60	15	tr	25	--	--	--	--	--	--	--	tr	tr	tr	--	--	1
32A	--	5	--	5	30	60	--	--	--	--	--	tr	tr	--	--	--	7
*32B	--	5	--	~1	35	60	--	--	--	--	--	tr	tr	--	--	--	7
32C	--	--	--	tr	30	70	--	--	--	--	--	tr	--	--	--	--	7
32D	--	25	--	tr	35	25	15	--	--	--	--	tr	tr	--	--	--	3
*33A	25	15	--	tr	5	--	50	--	--	--	--	tr	--	--	--	SPH(~1), CC(tr), SCAP(5)	
*33B	--	20	--	5	30	40	~1	--	5	--	--	tr	--	--	--	--	3A+
*33C	--	15	--	5	60	--	--	--	15	--	--	5	--	tr	--	HERC(5)	3A
33D	--	10	--	tr	45	45	--	--	--	--	--	--	--	--	--	--	3
*34A	25	65	--	tr	--	10	--	--	--	--	--	--	--	--	--	--	3
34B	--	5	--	10	30	45	10	--	--	--	--	--	--	--	--	--	3
35A	--	20	--	--	40	20	20	--	--	--	--	tr	--	--	--	--	3
*35B	--	20	--	5	40	35	~1	--	--	--	--	tr	tr	--	--	--	3
*35C	--	20	--	tr	30	30	20	--	--	--	--	tr	--	--	--	--	3
*35D	--	--	--	--	40	50	--	--	--	--	--	2	--	--	--	HERC(3),OL(5)	7

	Qtz	Plag	Kf	Bio	Hbl	Opx	Cpx	Cdr	Gar	Sill	Ky	Fe-Ti Oxides	Zirc	Ap	White Mica	Others	Group
NORDNOR DIORITE																	
*37	tr	50	--	5	25	15	2	--	--	--	--	3	--	--	--	CC(tr)	5
38A	tr	60	--	5	45	--	--	--	--	--	--	<1	--	--	--	--	5
*38B	tr	55	--	2	45	--	tr	--	--	--	--	tr	--	--	--	--	5
38C	--	5	--	tr	65	25	5	--	--	--	--	tr	--	--	--	--	3
38D	tr	50	--	2	48	--	tr	--	--	--	--	tr	--	--	--	--	5
38E	tr	40	--	2	55	5	<1	--	--	--	--	tr	--	--	--	--	5

† Gar-Cpx in different layers
* These samples used in electron microprobe study
1) Potassium feldspar gneisses
2) Orthopyroxene gneisses
3) Pyribolite gneisses
3A) Garnet pyribolite
4) Biotite-rich pyribolite
5) Diorite
6) Calc-silicate gneiss
7) Ultramafic

APPENDIX 2: ANALYTICAL TECHNIQUES

All of the data points plotted on the various diagrams represent complete analyses performed on a single spot consecutively for 5-14 elements in groups of three using a MAC-5-SA3 electron microprobe interfaced to a PDP-8/L computer for control and on-line data processing. Operating conditions were uniformly 15 KV accelerating voltage and 0.05 μA sample current (on brass), with beam current integration and pulse height selection. Spot size ranged from 1-30 μm depending on the nature of the phase being analyzed.

X-Ray intensities were converted to oxide weight percents according to the scheme outlined by Bence and Albee (1968) using correction factors modified from Albee and Ray (1970). The simple oxides and/or silicates that served as standards for the analyzed elements are listed in Table A2-1. A detailed discussion of the computer-controlled analytical procedure can be found in Chodos et al. (1973).

When F and Cl are determined, the appropriate corrections are made, and an oxygen equivalent is subtracted from the total of the analysis. In hydrous phases (e.g., micas), the difference between the oxide sum and 100% is assumed to be H_2O, and an iterative matrix correction for this "excess oxygen" is performed. In carbonates and scapolite, the difference between the analytical total and 100% is assumed to be CO_2, and the appropriate iterative matrix correction is applied there also.

TABLE A2-1: LIST OF STANDARDS USED FOR MICROPROBE ANALYSIS

	Element	Oxide Form	Standard	Crystal
1[1.]	Na	Na_2O	$NaAlSi_3O_8$ (P-103[2.]) Albite; Amelia, Virginia	KAP
2	Mg	MgO	MgO (P-85) Periclase; Synthetic	KAP
3	Al	Al_2O_3	Al_2SiO_5 (P-236) Kyanite; Locality unknown	KAP
4	Si	SiO_2	SiO_2 (P-213) Quartz; Brazil	PET
5	K	K_2O	$KAlSi_3O_8$ (P-102) Microcline; Asbestos, Quebec	PET LIF
6	Ca	CaO	$CaSiO_3$ (P-237) Wollastonite; Crestmore, Cal.	PET LIF
7	Ti	TiO_2	TiO_2 (P-530) Rutile; Synthetic	PET LIF
8	Cr	Cr_2O_3	Cr_2O_3 (P-585) Synthetic	LIF
9	Mn	MnO	$Mn_3Al_2Si_3O_{12}$ (P-130) Spessartine; Nuevo, Mexico	LIF
10	Fe	FeO[3.]	Fe_2SiO_4 (P-669) Fayalite; Synthetic	LIF
11	Ba	BaO	$BaTiSi_3O_9$ (P-372) Benitoite; San Diego Co., Cal.	LIF
12	Ni	NiO	NiO (P-634) Synthetic	LIF
13	S	SO_3	$CaSO_4$ (P-659) Anhydrite; Locality unknown	PET
14	P	P_2O_5	$Ca_5(PO_4)_3(F,Cl)$ (P-536) Apatite; Durango, New Mexico	LIF
15	Zr	ZrO_2	$ZrSiO_4$ (P-584) Zircon; Pacoima, Calif.	PET
16	Ce	CeO_2	Glass (P-649) Synthetic REE-2 glass	PET
17	Zn	ZnO	ZnO (P-471) Synthetic	LIF
19	F	F	$Ca_5(PO_4)_3(F,Cl)$ (P-536) Apatite; Durango, New Mexico	KAP
20	Cl	Cl		PET
25	Nb	Nb_2O_5	NbO (P-625) Synthetic	PET
26	Sr	SrO	Glass Synthetic Corning Glass "X"	LIF

1. Elements numbered according to the scheme used in the CIT microprobe.
2. P-numbers refer to CIT probe standard mount.
3. Total iron always analyzed as FeO.

Elements that yield X-Ray intensities with a peak to background ratio of greater than five (about 1 wt % of the oxide) are determined to a counting statistic precision of 1% or better, up to a maximum counting time of 90 seconds (120 for Fe). Minor elements, i.e., those present in the range 0.1-1.0 oxide wt %, are determined routinely to a counting statistic precision of better than 15%. The counting times that were selected represent a compromise between the shorter time needed to acquire analyses rapidly, and longer times required to achieve better counting statistics for elements present in small concentrations.

Subsequent to running standards, and prior to a sample run, routine analyses are performed on a garnet and feldspar. The use of such "internal standards" allows us to monitor the quality of our microprobe analyses by examining the stoichiometry of these minerals and, over an extended period of time, to judge such factors as reproducibility and operator bias (Champion et al, 1975).

Data for 66 microprobe analyses acquired for the garnet and feldspar are summarized in Table A2-2. These data include the average weight percent for each oxide, the standard deviation for each oxide ($\pm 1\sigma$), and the relative standard deviation for each oxide (% S.D.). Also illustrated are the average counting statistic relative standard deviation (% $\overline{\text{S.D.}}$) and ϕ, the ratio of the relative standard deviations.

In general, the standard deviation for each oxide increases and the relative standard deviation for each oxide decreases, as the oxide weight percent increases. These results are consistent with the constraints imposed by counting times in the computer programs that control

TABLE A2-2: SUMMARY OF ANALYSES OF INTERNAL STANDARDS

	Weight Percent			Counting Statistics	ϕ*
	Average	$\pm 1\sigma$	% S.D.	% $\overline{\text{S.D.}}$	
		Garnet (66 Analyses)			
MgO	20.255	0.212	1.05	0.34	3.12
Al_2O_3	22.594	0.313	1.38	0.40	3.45
SiO_2	42.276	0.337	0.80	0.38	2.09
CaO	4.716	0.078	1.66	0.72	2.29
TiO_2	0.177	0.030	17.19	8.12	2.12
Cr_2O_3	1.406	0.069	4.93	2.91	1.70
MnO	0.408	0.045	10.95	14.05	0.80
FeO	9.407	0.129	1.38	0.98	1.41
		Feldspar (66 Analyses)			
Na_2O	2.317	0.144	6.24	1.00	6.24
Al_2O_3	18.629	0.252	1.35	0.64	2.13
SiO_2	64.197	0.482	0.75	0.50	1.50
K_2O	13.052	0.235	1.80	0.49	3.67
FeO	0.160	0.019	11.99	12.30	0.98
BaO	1.179	0.134	11.37	12.68	0.90

*ϕ = Ratio of relative standard deviations.

the analytical procedure. The rather small standard deviations for each oxide indicate the excellent reproducibility attainable with the techniques used. The values of ϕ indicate that reproducibility of the analyses is 1½ to 3½ times the counting statistic standard deviation, except for Na, which is much larger. The "anomalous" result for Na may be a consequence of the difficulties inherent in the determination of this element, or more likely, an indication of slight heterogeneities in this natural sample.

Although the criteria for judging the precision of microprobe analyses can be inferred directly from the aforementioned tests for reproducibility, criteria for estimating their absolute accuracy can in general be obtained only indirectly from oxide summations and calculated mineral stoichiometry, or by direct comparison with analyses obtained independently on the same sample by other techniques. The latter test suffers somewhat from the possible inaccuracies in other analytical methods.

Accuracy of the analyses was monitored on the one hand by routine analysis of synthetic anorthite (An_{100}) and forsterite ($Fo_{92}Fa_{8}$). Agreement between the theoretical compositions and compositions as determined with the microprobe were found to be excellent.

In addition, accuracy of the analyses was monitored continuously during a run by scrutinizing carefully all oxide summations and calculated mineral stoichiometries, a process facilitated by on-line data processing. Any analysis that did not conform to the formulae as given in Chapter 4 was rejected and reanalyzed immediately.

PART II:

Evolution of Planetary Crusts As Inferred from Petrologic Studies of Regolith Breccias.

Introductory Statement

The results of imaging experiments of the terrestrial planets, together with earlier telescopic observation of the moon, have demonstrated that impact phenomena are an extremely important process in the evolution of planetary surfaces. The soil or regolith produced as a consequence of impact processes should, in theory, contain materials brought in and mixed together from a wide variety of source regions. Thus a regolith provides a sampling of rock types present over a rather large, albeit unspecified, area. This has certainly proven to be the case on the moon, where polymict lunar soils and soil breccias contain a greater variety (and number) of rock fragments than are represented among the large crystalline rock samples returned by the astronauts. Certain groups of meteorites, most notably the howardites, are polymict breccias that may represent samples of planetary regolith, and hence can provide a great amount of information on the nature of their parent bodies.

This part of the thesis presents the results of petrographic and mineralogic studies on two contrasting regolith samples - lunar soil breccia 15205 and the howardite Kapoeta.

Proceedings of the Fifth Lunar Conference
(Supplement 5, Geochimica et Cosmochimica Acta)
Vol. 1 pp. 235-260 (1974)
Printed in the United States of America

Glass-coated soil breccia 15205: Selenologic history and petrologic constraints on the nature of its source region

R. F. DYMEK, A. L. ALBEE, and A. A. CHODOS

Division of Geological and Planetary Sciences,* California Institute of Technology, Pasadena, California 91109

Abstract—Apollo sample 15205 is a layered, lithified soil breccia. The sample, and the boulder from which it was collected, are coated by dark, green-brown, vesicular glass and crosscut by glass-filled microfractures. Lithic clasts within the sample include feldspathic basalt and pyroxene-phyric basalt, and rare clasts resembling Apollo 15 olivine normative mare basalts. Glass fragments include typical Apollo 15 "green glass" and alkalic, high-alumina basalt glass. Fragments of ANT suite rocks were not observed, and glass of mare basalt composition and glass with $Al_2O_3 > 20\%$ are rare.

The inferred history of 15205 includes accumulation of the soil shortly after the formation of the Apollo 15 mare basalts, subsequent lithification and fracturing of the soil breccia, injection of the glass veins, formation of the glass coating, and excavation and deposition of the boulder at its present site on the lunar surface.

I. INTRODUCTION

STUDIES OF LUNAR SOIL SAMPLES have yielded important information on the nature and diversity of rock types present on the moon and on the processes involved in the evolution of the regolith. A greater variety of lithic fragments occurs in the soils than has been collected in the form of large samples. In addition, compositional groupings of glass fragments generally correspond to rock and soil compositions, and therefore provide further information on materials in the source areas.

Sample 15205 is a 337.3 g polymict breccia sample collected from a 1 m boulder at Apollo 15 Station 2. Though coherent, it is basically lithified soil that has been little modified by subsequent events. The lithic and glass fragments within this soil breccia provide a characterization of the source regions for the soil from which this breccia-boulder was derived. In addition, the observed structural and textural characteristics help to outline the selenologic history of sample 15205 and its parent boulder.

II. ANALYTICAL TECHNIQUES

Sample 15205 was an $8 \times 6 \times 4$ cm block. Six polished thin sections, separated by slabs, were cut from the 8 cm side. Four polished thin sections cut from the 6 cm side are also separated by slabs, and are oriented orthogonal to those from the 8 cm side. All ten thin sections and a slab from each side were studied microscopically prior to the initiation of analytical work. We feel certain that the clasts within the breccia that were selected for detailed analytical study are representative of the entire clast population.

---

*Contribution No: 2478.

Sample 15206, a 92.0 g rock from the same boulder, was not studied in detail. Although generally similar, study of several thin sections indicates that it has been more affected than 15205 by later impact events with resultant *in situ* vesiculation and possible melting.

All of the points plotted on the various diagrams represent analyses for 8–16 elements performed on a MAC-5 electron microprobe interfaced to a PDP-8/I computer for control and on-line data processing (Chodos *et al.*, 1973). Operating conditions were 15 kV and 0.05 μamps; beam diameter ranged from 1–20 μm depending on the phase analyzed. A computer output of all analyses can be obtained upon request from A. Albee.

III. Sample Description

Astronauts Scott and Irwin sampled a 1 m boulder at Apollo 15 Station 2 which they noted was partially covered by vesicular glass, with bubbles up to 1 cm across. This glass also penetrated the boulder along fractures and coated its underside (Apollo 15 Technical Air to Ground Voice Transcription). They noted that the boulder was anomalously large, had an opening beneath it, and appeared to have been emplaced recently. The boulder apparently impacted at a shallow angle from the N–NW and rolled up onto the rim of its own secondary crater (Swann *et al.*, 1971).

Sample 15205, broken from a top corner of the boulder, was nearly a parallelepiped, with surfaces apparently controlled by the conspicuous fractures visible in the boulder (Swann *et al.*, 1971). Five sides of the sample were partially covered by dark, green–brown, vesicular glass (Fig. 1A), while the sixth surface exposed the fresh interior of the rock (Fig. 1B). Three of the glass-coated surfaces were lunar exterior. These were covered with a thin film of dust, and contained a few microcraters. The other two glass-coated surfaces were along interior, glass-filled fractures in the boulder.

A set of subparallel microfractures occurs in 15205 that is not parallel to the fractures that form the surfaces of the sample. These microfractures offset, but do not rotate individual clasts, and are discontinuously filled by vesicular, brown glass. Even though these veins only rarely come into contact with the glass coating, it appears that they are truncated by it.

Sample 15205 is a polymict breccia formed by lithification, but not extensive modification, of lunar soil. It is comprised of about 75% clasts (~40% lithic, ~15% glass, and ~20% mineral fragments) set in a finer grained, clastic matrix that consists of glass and mineral particles. Modal percentages do not include the glass coating. Individual clasts range in size from 10 μm to ~1 cm. The mineral and lithic clasts are subangular to rounded, but many glass clasts are spheres. Reaction relations between clasts and matrix were not observed, and much of the glass shows no devitrification. This rock can be assigned to Group 2 of Warner's (1972) classification. The extent of devitrification varies markedly from clast to clast indicating that devitrification predates the accumulation of the soil. Lithic clasts exhibit a wide range of granulation and other shock effects such as glass rims. These effects must also predate accumulation.

Sample 15205 has a distinct depositional fabric as indicated by the consistent alignment of clasts in thin section (Fig. 2). Sharp contacts, parallel to the

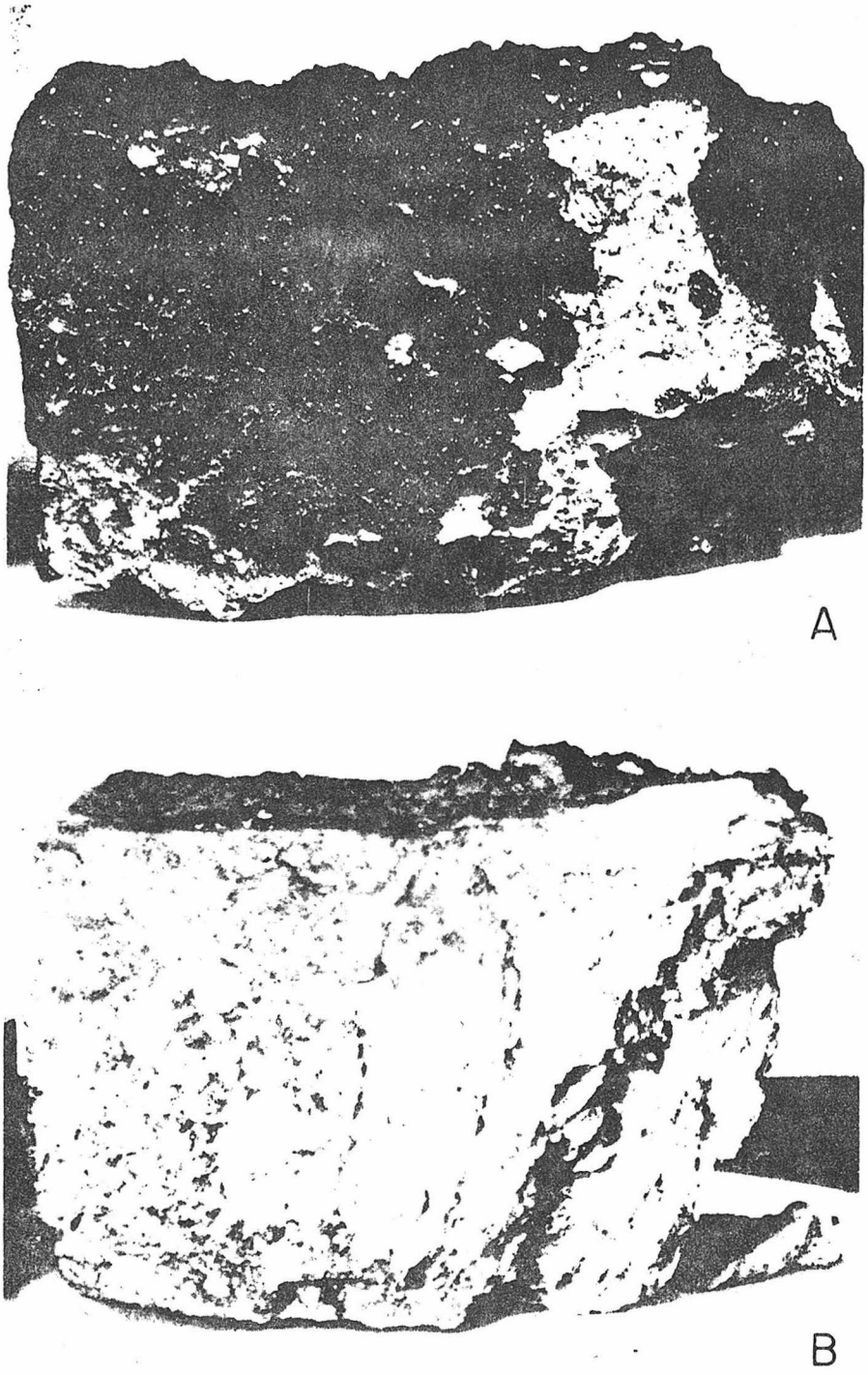

Fig. 1. Photographs of 15205 prior to sawing (horizontal field ~8 cm): (A) Fresh, green-brown glass coating on North surface (NASA photo S-71-42981). (B) Interior surface displaying individual clasts up to 1 cm across (NASA photo S-71-42986).

Fig. 2. Photomicrograph of polished thin section 15205,61, and corresponding map, showing nature and distribution of the largest clasts. Note the preferred orientation of fragments along a line from the lower right- to upper left-hand corners of the map.

alignment of the clasts, separate adjacent layers of contrasting lithology, color, and grain size. For example, layers of glass intercalated with mineral fragments (Fig. 6C) occur adjacent to layers dominated by rock fragments.

Since all of these observations are consistent with the interpretation that 15205 is a lithified lunar soil, detailed studies of the glass and lithic clasts were undertaken in order to characterize the source region of the soil.

IV. Characterization of Glass Types

Sample 15205 contains a remarkable variety of different types of glass, including the dark, green–brown glass coating, the brown-glass veins, glass layers of depositional origin, and glass fragments of many kinds. These petrographically distinct types also have distinctive chemical compositions, which are illustrated in Fig. 3.

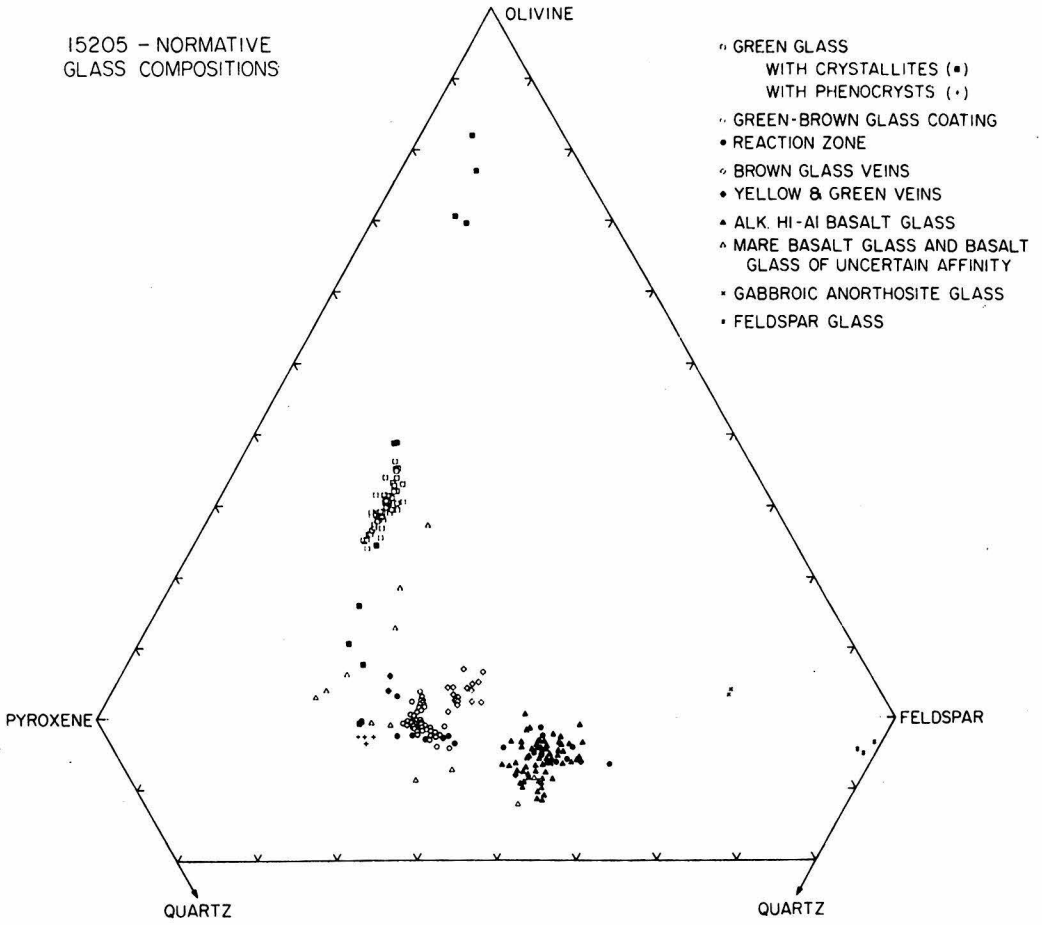

Fig. 3. Normative compositions of glass in sample 15205. Each data point represents catatom percent quartz, pyroxene (Wo + En + Fs), feldspar (An + Ab + Or + Cel), and olivine (Fo + Fa) normalized to 100%.

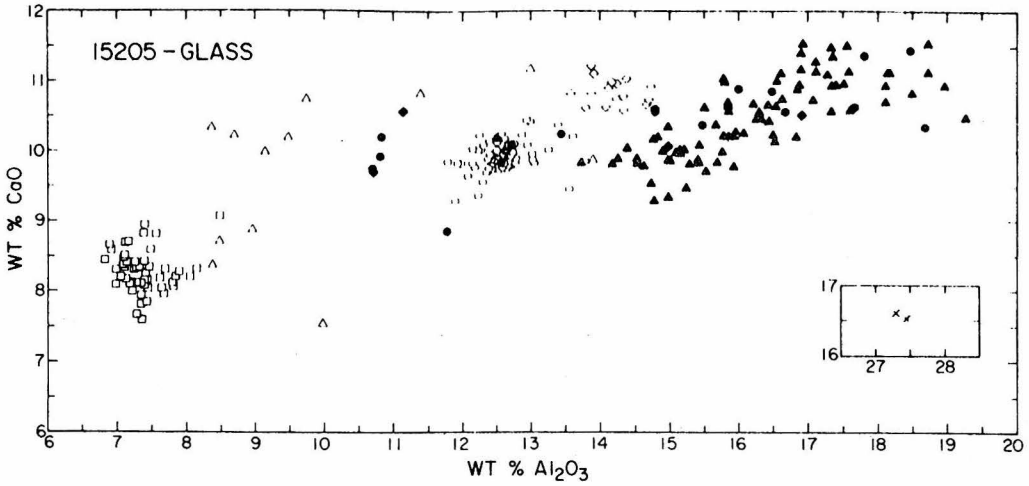

Fig. 4. CaO–Al_2O_3 variation diagram of glass in sample 15205. The symbols are explained in Fig. 3.

Oxide-variation diagrams (Figs. 4 and 5) show several distinct groups. In these diagrams the tight cluster near $CaO \sim 8\%$, $Al_2O_3 \sim 7\%$, $FeO \sim 20\%$, and $MgO \sim 18\%$ correspond to typical Apollo 15 "green glass" (Ridley *et al.*, 1973a). This glass type constitutes approximately 30% of the glass fragments in 15205. A second cluster near $CaO \sim 10\%$, $Al_2O_3 \sim 12.5\%$, $FeO \sim 15\%$ and $MgO \sim 10.5\%$ represents the glass coating. The brown-glass veins are represented by a slightly more diffuse group near $CaO \sim 11\%$, $Al_2O_3 \sim 14\%$, $FeO \sim 14\%$, and $MgO \sim 10\%$. The majority of the glass fragments in 15205 define a band near $CaO \sim 10$–12%, $Al_2O_3 \sim 14$–19%, $FeO \sim 8$–11%, and $MgO \sim 7$–10%. These correspond to the various types of Fra Mauro and "KREEP" basalt glass recognized in other Apollo 15 samples (Reid *et al.*, 1972).

Average chemical composition of the glass types and their corresponding catatom norms are presented in Table 1. The detailed petrography and discussion of each group is presented in the following sections.

1. *Glass coating*

The glass coating is dark green–brown and contains abundant spherical, smooth-walled vesicles up to 1 cm across. Flow-banding in the glass coating is marked by swirls of tiny (≤ 1 μm) beads of troilite (Fig. 6B). Rarely, the beads are as large as 20 μm and/or contain blebs of Fe metal.

The contact between the glass coating and breccia is sharp and is characterized by a distinct reaction zone (~ 100 μm wide) that is marked macroscopically by a zone of discoloration and in thin section is a narrow zone of clear, pale yellow glass (Figs. 6A and 6B). Locally, however, tiny apophyses of the glass coating project into the breccia without any visible effects. In addition, strings of 10–50 μm vesicles occur along the glass-breccia interface, both in the glass and in the breccia.

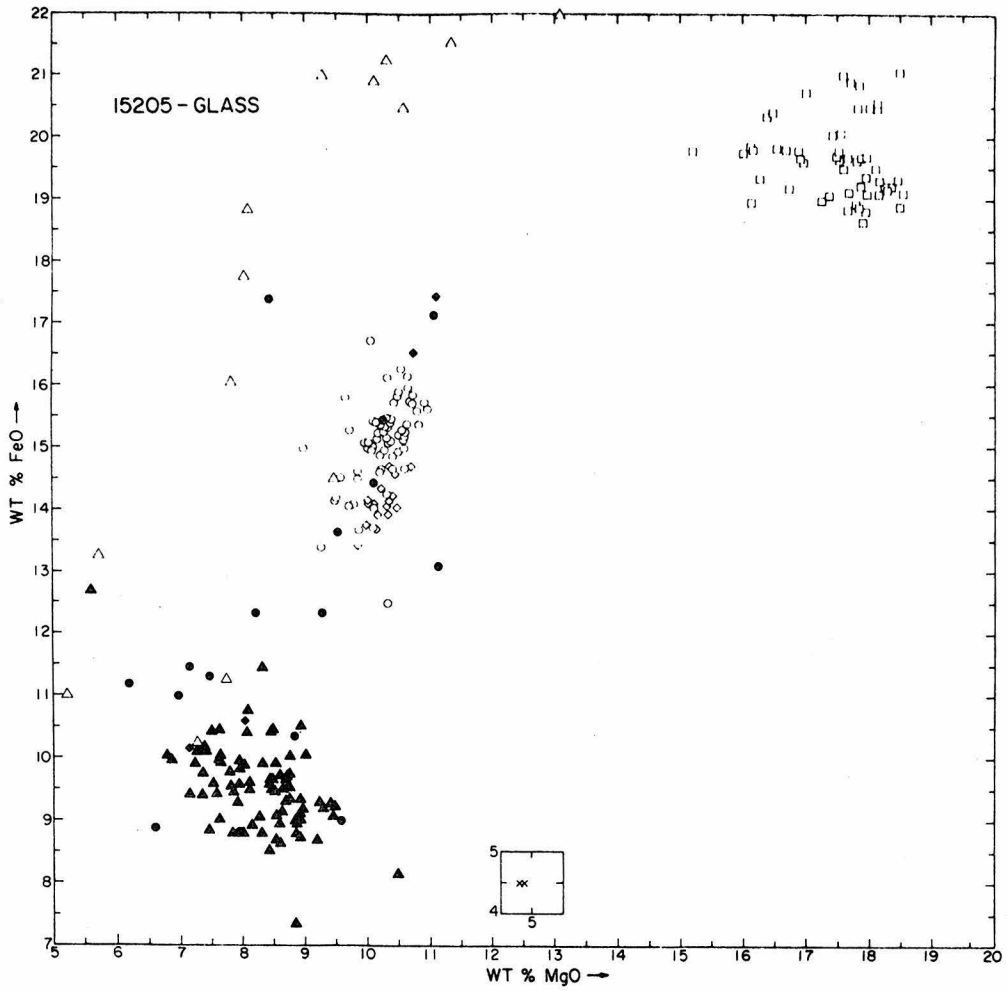

Fig. 5. FeO–MgO variation diagram of glass in sample 15205. The symbols are explained in Fig. 3.

The reaction zone is richer in SiO_2, Al_2O_3, K_2O, Na_2O, and P_2O_5 than the bulk of the glass coating. In one instance, however, the reaction zone which surrounds a pyroxene grain, is poorer in Al_2O_3 and richer in FeO. Both the chemical changes and the vesicles appear to reflect addition of material from the breccia during reaction between the glass coating and the breccia.

Exclusive of analyses of the reaction zone, the glass coating is chemically homogeneous despite the fact that it is in contact with a wide variety of materials. This demonstrates that the glass rind was not produced by *in situ* melting of the breccia.

The composition of the coating differs from the soil at Station 2, (Table 1, analyses 1 and 10). This fact, together with the observation that the glass covered the underside of the boulder, requires that the glass coating was emplaced prior to the deposition of the boulder at its present position on the lunar surface. The glass

Table 1. 15205—averaged glass compositions

No. of Analyses	1 65	2 17	3 2	4 2	5 50	6 83	7 2	8 4	9 —	10 —
Na_2O	0.54 ± .05	0.50 ± .03	0.47	0.88	0.15 ± .03	0.77 ± .13	0.24	0.36	0.73	0.39
MgO	10.28 ± .42	10.26 ± .22	10.94	7.72	17.50 ± .76	8.28 ± .80	4.84	9.78	8.23	10.36
Al_2O_3	12.58 ± .39	14.21 ± .37	10.92	15.91	7.36 ± .10	16.28 ± 1.26	27.37	9.39	14.92	17.38
SiO_2	48.38 ± .79	47.33 ± .42	47.47	51.39	45.59 ± .39	50.45 ± 1.19	44.61	47.71	51.03	45.95
K_2O	0.25 ± .05	0.22 ± .03	0.13	0.52	0.02 ± .02	0.61 ± .18	0.03	0.07	0.528	0.17
CaO	9.90 ± .22	10.83 ± .20	10.14	10.24	8.26 ± .30	10.47 ± .56	16.57	10.35	9.94	11.52
TiO_2	1.82 ± .09	1.60 ± .04	1.49	1.94	0.43 ± .10	1.77 ± .46	0.23	1.67	1.99	1.27
Cr_2O_3	0.44 ± .06	0.38 ± .06	0.45	0.13	0.55 ± .08	0.26 ± .06	0.11	0.56	0.34	N.R.
MnO	0.21 ± .05	0.18 ± .09	0.23	0.09	0.27 ± .06	0.14 ± .05	0.21	0.16	0.159	0.16
FeO	15.08 ± .72	14.11 ± .34	16.97	10.42	19.58 ± .64	9.62 ± .79	4.49	20.09	11.28	11.65
BaO	0.06 ± .07	0.09 ± .10	<0.01	0.12	0.03 ± .06	0.07 ± .06	<0.01	<0.01	N.R.	N.R.
NiO	0.03 ± .04	0.03 ± .03	<0.01	<0.01	0.03 ± .04	0.01 ± .02	0.07	0.02	N.R.	N.R.
P_2O_5	0.25 ± .06	0.24 ± .03	0.15	0.56	0.03 ± .02	0.52 ± .13	0.05	0.06	0.557	0.13
SO_3	0.20 ± .07	0.11 ± .02	0.04	0.06	0.20 ± .02	0.77 ± .13	0.06	0.08	0.080*	0.06*
SUM	100.03	100.09	99.40	99.96	99.82	100.01	98.88	100.30	99.784	99.04
					Catatom Percent Normative Minerals					
Q	.78	—	—	6.70	—	5.85	—	—	—	—
An	31.80	36.40	28.21	38.44	19.47	39.75	74.44	24.72	36.74	45.95
Ab	4.98	4.55	4.31	8.08	1.36	6.98	2.18	3.36	6.71	3.56
Or	1.53	1.33	0.81	3.13	0.14	3.63	0.18	0.43	3.19	1.02
Cel	0.12	0.17	—	0.22	0.06	0.13	<0.01	<0.01	—	—
En	29.07	25.95	27.64	21.74	24.45	23.23	21.74	26.57	23.26	21.40
Fs	21.04	17.85	22.14	13.66	15.04	11.59	13.66	28.07	14.94	12.30
Wo	6.75	6.70	9.08	3.85	8.68	3.82	3.85	11.28	4.01	4.52
Fo	—	2.18	2.66	—	18.25	—	2.53	1.10	—	5.77
Fa	—	1.50	2.13	—	11.23	—	1.29	1.16	—	3.32
Ap	0.53	0.51	0.33	1.19	0.06	1.11	0.11	0.13	1.19	0.28
Ilm	2.60	2.27	2.14	2.75	0.60	2.51	0.32	2.42	2.84	1.80
Chr	0.50	0.42	0.51	0.14	0.61	0.29	0.12	0.64	0.38	—
FeS	0.29	0.15	0.06	0.09	0.03	1.08	0.08	0.12	0.11	0.09
NiO	0.02	0.02	—	—	0.02	0.01	0.05	0.02	—	—

(1) Glass coating
(2) Brown-glass vein
(3) Pale green-glass vein
(4) Yellow green-glass vein
(5) "Green glass"
(6) Alkalic, high-alumina basalt glass
(7) Gabbroic anorthosite glass
(8) Mare basalt glass
(9) 15205,37 (Willis *et al.*, 1972)
(10) 15101, Apollo 15 Station 2 soil (Apollo 15—*Preliminary Science Report*, 1972)
N.R. = Not reported
* = Reported as S.

on all the surfaces of 15205 is physically and chemically identical, which suggests that the glass covering the boulder and filling the fractures in the boulder is the same.

The composition of the glass coating lies midway between that of the various glass fragments in 15205 (Figs. 4 and 5). This suggests that the glass coating represents a total melt of lunar soil similar to 15205, although the average composition of the glass coating and an analysis of 15203,37 (Willis *et al.*, 1972) are quite different (Table 1, analyses 1 and 9).

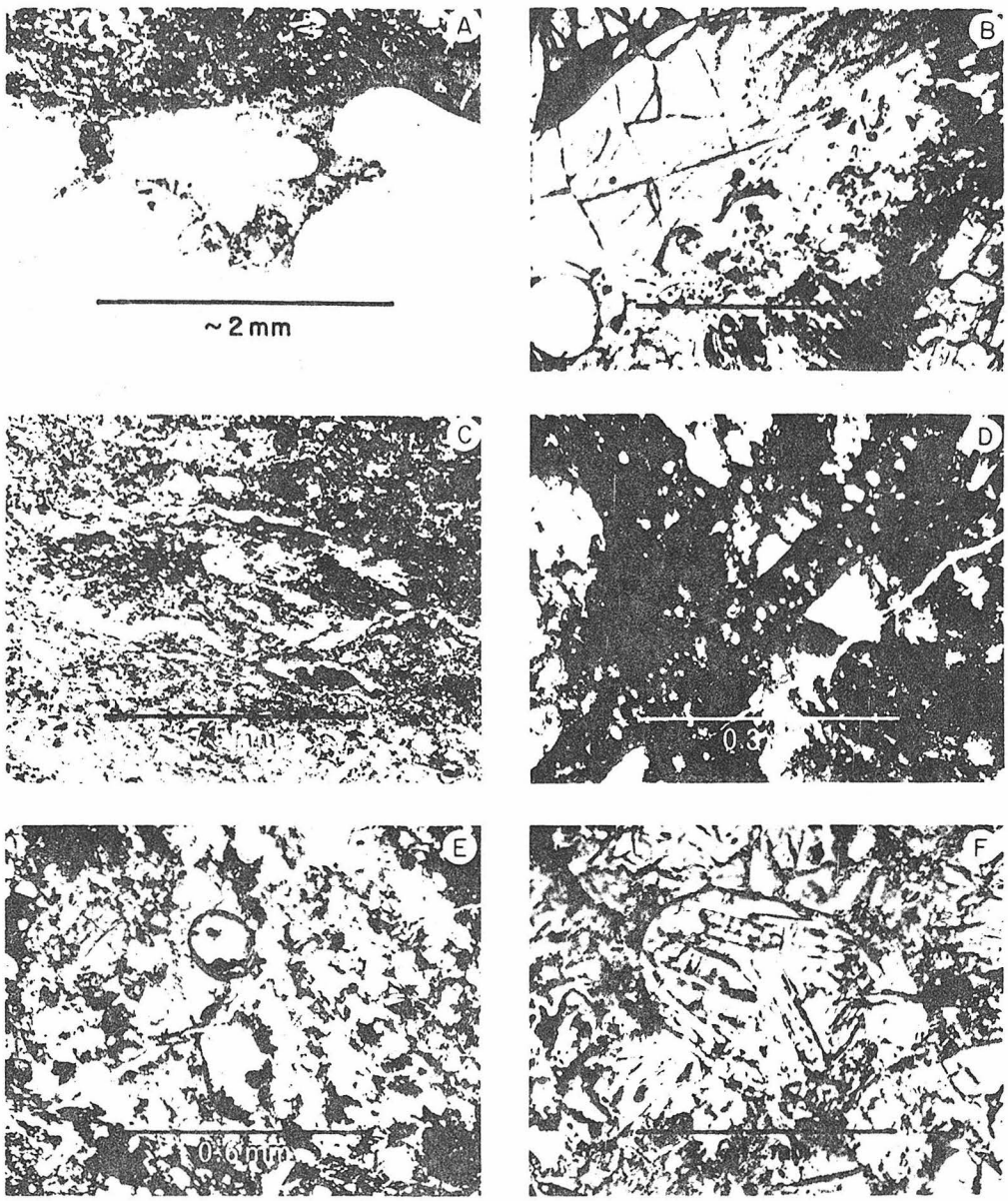

Fig. 6. (A) Photomicrograph of the sharp contact between the glass coating and the breccia. (B) Photomicrograph of the flow-banding in the glass coating (dark swirls in glass, upper left), and the reaction zone between the glass coating and the breccia. Note the vesicle in the lower left-hand corner. (C) Layers of alkalic, high-alumina basalt glass intercalated with fine-grained mineral debris. (D) Crosscutting, brown-glass vein. Note the offset grain of plagioclase (center), the vesicles in the vein, and the subparallel microfracture to the right of the vein. (E) An aggregate of green-glass spheres and fragments of spheres. Note the varied degrees of devitrification. (F) Olivine phenocrysts in a green-glass sphere. This photograph was taken from a different part of the aggregate shown in Fig. 6E.

2. *Glass veins*

Thin, 50–200 μm, brown-glass veins transect the sample at nearly right angles to the layering. They discontinuously fill a set of subparallel microfractures and are locally anastomosing. Such veins are at least 2 cm long and appear to be truncated by the glass coating, although the junctions are not displayed well in the thin sections. The veins are discordant and sharply bounded, and their internal structure varies as a function of the material with which they are in contact. In general, where they crosscut the breccia matrix, they contain numerous mineral particles and vesicles (Fig. 6D), and are surrounded by a narrow zone of discoloration, similar in appearance to the reaction zone associated with the glass coating. The vesicles occur as either small, rounded vesicles concentrated along the margins of the veins, or elongate vesicles nearly as wide as the veins themselves. Where the veins crosscut crystalline rock fragments, neither vesicles nor inclusions are present. However, in all places, the veins are layered parallel to their length.

These veins are uniform in composition, and, although their composition is within the range of the other glass in 15205, it is distinct from the other groups (Figs. 3, 4, 5; Table 1, analysis 2).

While these veins might be interpreted as an *in situ* melt of breccia matrix, their homogeneity suggests that they formed by injection of molten material along preexisting microfractures. As this melt was quenched, it incorporated gases from the breccia, that formed the vesicles that are concentrated along the margins. The elongate vesicles may represent a vapor phase in the melt.

In addition to the brown-glass veins, several irregularly shaped, yellow to pale green, glass veins occur. These differ from the brown-glass veins in form and composition (Table 1, analyses 3 and 4). Their boundaries with surrounding material range from sharp to diffuse. They are narrow (20–100 μm), can be either straight or meandering, and either transect the layering or are subparallel to it. However, they do crosscut clasts, and hence, are clearly post-accumulation.

3. *Green-glass fragments*

Glass spheres and fragments of spheres, which occur singly and in aggregates, are pale green to nearly white, whereas devitrified varieties are brown to pale gray. Certain of the spheres contain a network of dendritic to acicular olivine crystallites. Rarely, vesicles or euhedral phenocrysts of olivine (Fo_{79-82}) occur (Fig. 6F) within the spheres. The composition of these phenocrysts agrees well with that of the liquidus olivine (Fo_{81-83}) determined experimentally at low pressure by Stolper *et al.* (1974).

The green-glass fragments are characterized by a restricted composition differing from the other glass types in 15205. They have high FeO and MgO (Fig. 5) and high normative olivine content (Fig. 3). Their major element chemistry and physical characteristics are like similar objects in other Apollo 15 samples (Ridley *et al.*, 1973a). The average composition (Table 1, analysis 5) has the same

normative olivine content as that reported by Reid *et al.*, (1972). However, glass fragments that contain neither crystallites nor phenocrysts of olivine, do display a slight dispersion of their normative compositions along a line indicating either addition or subtraction of olivine (Fig. 3). This variation is outside the limits of analytical uncertainty, and calculations indicate that removal and addition of ~5% olivine (Fo_{80}) to the average composition of the green glass can account for this spread in the data.

In Fig. 7, those compositions more olivine-rich than the "glass without crystallites" represent analyses of mixtures of glass and crystallites in crystallite-bearing spheres. These plot along a mixing line connecting the "glass without crystallites" with the composition of olivine phenocrysts, indicating that the olivine crystallites are ~Fo_{80}.

Those compositions less olivine-rich than the "glass without crystallites" represent analyses of glass in green-glass spheres that contain crystallites. These plot along a fractionation curve connecting the "glass without crystallites" with the glass associated with olivine phenocrysts.

The fact that these trends connect the measured composition of olivine phenocrysts with the measured composition of glass in association with these phenocrysts, suggests that low-pressure fractional crystallization of liquidus olivine can explain the observed compositional variation within these Apollo 15 green glasses.

Olivine phenocrysts are rare in the green glass. If such phenocrysts represent crystals formed in communication with a large reservoir of green-glass composition, then the associated quench glass should lie close to the bulk composition of the glass. However, if these phenocrysts formed by crystallization after the

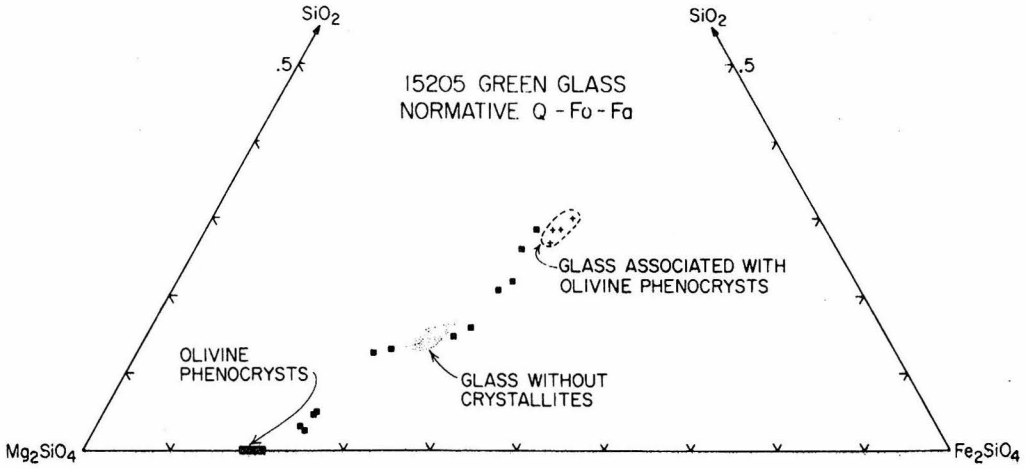

Fig. 7. Variation in the amounts of Q–Fo–Fa in green glass from sample 15205. The diagram was constructed by normalizing the sum of normative pyroxene (En and Fs, recalculated as olivine plus quartz) and olivine or quartz to 100%, in terms of catatom percent abundance. Points marked by the solid squares represent analyses of material in spheres that contain olivine crystallites, and are discussed in the text (Section IV-3). The stippled area corresponds to the open squares in Fig. 3.

spheres formed, then the residual glass should be extremely depleted in olivine, as is observed (Figs. 3 and 7). Hence, these olivine grains do not reflect processes occurring during the ascent and eruption of the magma, and the average composition of these green-glass spheres may very closely approximate a lunar magma type. The compositional variation in spheres that do not contain either phenocrysts or visible crystallites may require up to 10% olivine fractionation, although this variation may be due to the presence of submicroscopic olivine (~Fo_{80}) crystallites.

The sphere aggregates occur as clasts up to 1 cm long, and consist of spheres and fragments of spheres in a matrix of glass with identical composition (Fig. 6E). It is not clear whether this matrix is a quenched melt or whether it represents annealed, fine-grained glass particles. Similar objects have been reported by Agrell *et al.* (1973). These clasts contain 0–5% inclusions of plagioclase, pyroxene, and pyroxene–phyric basalt. Electron beam scans show no evidence of reaction between the glass and inclusions. A few spheres in the sphere aggregates and individual spheres within the rock have discontinuous crescent-shaped glass adhering to their surfaces; some spheres consist of devitrified cores surrounded by narrow (1–2 μm) rims of glass. Both features seem to be overgrowths of glass on glass. In addition, some spheres have concave indentations against adjacent spheres.

In the sphere aggregates, both spheres and fragments of spheres, display varied degrees of crystallization and devitrification. The juxtaposition of such a wide range of features requires that they formed prior to or during the aggregation of the spheres and not simply *in situ.*

These observations are consistent with the interpretation of McKay *et al.* (1973) that both in-flight collisions and recycling in a lava fountain have been important in the evolution of the Apollo 15 green glasses. Deposition and aggregation of the glass spheres as "ash layers" could have occurred during this activity; these layers were later disrupted by impact events that resulted in their incorporation into 15205 as clasts.

4. *Alkalic, high-alumina basalt glass fragments and layers*

The most abundant glass type in 15205 consists of white, yellow, brown, and purple fragments which are high in Na_2O, K_2O, and Al_2O_3 (Table 1, analysis 6). These glass fragments range from angular to subrounded, and from nondevitrified, homogeneous fragments to flow-banded, glass-agglutinate layers. Between these extremes are types displaying various stages of devitrification and containing different amounts of plagioclase and low-Ca pyroxene inclusions. These glass-agglutinate layers are parallel to, and help to define, the layering in the breccia (Fig. 6C). They appear to represent splashes of glass on the surface of the regolith. Rarely, yellow glass occurs as sheaths around feldspathic basalt clasts.

Chemically, this glass is distinct from the other glass types in 15205. The composition is similar to glass that has been variously termed Fra Mauro basalt glass (Kridelbaugh *et al.*, 1972; Reid *et al.*, 1972; Drake and Klein, 1973),

feldspathic basalt glass (Best and Minkin, 1972), or KREEP glass (Glass, 1972; Reid *et al.*, 1972) in other Apollo 15 samples. Such glass is quartz normative, and has a narrow range in normative pyroxene to plagioclase ratio (Fig. 3). Al_2O_3 ranges from 14–19% (Fig. 4), reflecting a variation in the normative feldspar composition and $(Na_2O + K_2O)/CaO$. The FeO/MgO ranges from ~1 to 1.5 (Fig. 5). The darker colored varieties are slightly richer in FeO, TiO_2, and K_2O and lower in MgO, CaO, and Al_2O_3 than the white and yellow ones.

Many groups have used average glass composition to infer the rock type from which the glass is derived. Feldspathic basalt clasts, identical in texture and mineral chemistry to "KREEP" basalt fragments present in Apollo 15 soils and breccias (Meyer, 1972; Cameron *et al.*, 1973; Drake *et al.*, 1973; Powell *et al.*, 1973), represent the dominant lithic type present in 15205. The major element chemistry of such rock clasts falls within the compositional range of the alkalic, high-alumina basalt glass in 15205. Hence, this argument suggests that the feldspathic basalt clasts and the alkalic, high-alumina basalt glass were formed from the same parental material.

5. *Less abundant fragments*

Glass with mare basalt compositions occurs as bright yellow to orange fragments and as pale green, shock-melted zones at the edges of some clasts of mare basalt (Table 1, analysis 8). Despite the fact that clasts of mare basalt are abundant in 15205, glass fragments with equivalent composition are rare.

A single, angular, white-glass fragment with the composition of gabbroic anorthosite has been identified. No true anorthosite glass fragments have been found, although rare plagioclase glass (An_{81-88}) is present. Although glass with $Al_2O_3 > 20\%$ forms a significant position of Apollo 15 soil sample (Reid *et al.*, 1972), only this single fragment has been identified in 15205. This probably reflects the character of the source region at the time of accumulation of the original soil.

In addition, a few rare glass fragments that have basaltic compositions occur, but do not fit into any of the aforementioned categories.

V. Characterization of Rock Fragments

Approximately 40% of sample 15205 consists of lithic clasts that include a number of distinctive volcanic rock types. Several textural varieties of feldspathic, orthopyroxene-bearing basalt make up about 20% of the rock and correspond mineralogically and texturally to fragments variously termed "KREEP" basalt (Meyer, 1972; Phinney *et al.*, 1972; Powell *et al.*, 1973; Cameron *et al.*, 1973; Drake *et al.*, 1973), highland basalt (Delano, 1972) and feldspathic basalt (Steele *et al.*, 1972) in other Apollo 15 samples. Pyroxene–phyric basalt clasts (Dowty *et al.*, 1974) constitute about 20% of the sample and are similar to large Apollo 15 samples such as 15486 (Albee *et al.*, 1972), 15499 (Bence and Papike, 1972) and 15597 (Wiegand and Hollister, 1973) and other quartz normative

Apollo 15 basalt samples. Several textural varieties of basalt that resemble the Apollo 15 olivine normative mare basalts make up an additional 1% of the rock.

No clasts of the ANT-suite have been recognized; and the fragments previously identified by us (Dymek *et al.*, 1974) as anorthosite/norite are in fact highly shocked feldspathic basalt. A few fragments of moderately recrystallized metaclastic rock are present, but have not been studied in detail.

1. *Feldspathic basalt fragments*

The feldspathic basalt clasts in 15205 have been divided into five textural groups which are as follows: subophitic to intersertal; intersertal; porphyritic intersertal; "ladder structure"; variolitic. The first four of these have primary igneous textures, while the fifth appears to be a recrystallized variety.

A. *Subophitic to intersertal.* Fragments with subophitic to intersertal texture are the most abundant variety of feldspathic basalt in 15205 (Fig. 8A). These are comprised of a network of subhedral plagioclase laths which are often curved. In general, pyroxene occurs as angular to subrounded, interstitial grains, but forms subhedral phenocrysts in some fragments. Plates of ilmenite, a glassy mesostasis, and grains of silica occur interstitially. Fe metal, troilite, Ca-phosphate, and a rare Zr-bearing phase are associated with the mesostasis areas.

Single grains of low-Ca pyroxene zone continously in composition from $Wo_2En_{80}Fs_{18}$ to $Wo_{15}En_{49}Fs_{36}$ (Fig. 9). Some of these zoned grains are overgrown by a narrow rim of high-Ca pyroxene ($Wo_{33}En_{38}Fs_{29}$). In some crystals, a core of low-Ca pyroxene ($Wo_3En_{77}Fs_{20}$) is surrounded by a relatively more-magnesian and less-aluminous pyroxene ($Wo_3En_{79}Fs_{18}$). The transition between the two is marked by a distinct optical discontinuity (Fig. 8B). Similar relationships have been described in feldspathic basalt 14310 by Hollister *et al.* (1972). High-Ca pyroxene is much less abundant and occurs in mesostasis areas. These grains have cores similar in composition to the high-Ca pyroxene rims on the low-Ca pyroxene and zone from $Wo_{33}En_{38}Fs_{29}$ to Fe-rich compositions near $Wo_{15}En_{20}Fs_{65}$ (Fig. 9A). Some fragments do not contain high-Ca pyroxene, but do have Fe-rich pyroxene ($Wo_{14}En_{29}Fs_{57}$) associated with the mesostasis.

Plagioclase ranges in composition from An_{72-88} (Fig. 9A). Complex zoning patterns are present but, in general, the cores are more calcic than the rims. Shock processes appear to have caused the development of a mosaic of zones with undulatory extinction, unrelated to compositional changes. Comparison of Figs. 9 and 12 shows that for a given An content, plagioclase in the feldspathic basalt is more potassic than in mare basalt.

Ilmenite is the only Fe–Ti–Cr oxide phase in the feldspathic basalt, in contrast to the mare basalt, which in addition contain chromite and ülvospinel. The mesostasis is comprised of K-rich glass, typically devitrified, in which abundant, tiny (1–2 μm) immiscible Fe-rich globules are present.

The inferred order of crystallization in these rocks is plagioclase, joined by low-Ca pyroxene; plagioclase and low-Ca pyroxene coprecipitated and, when the

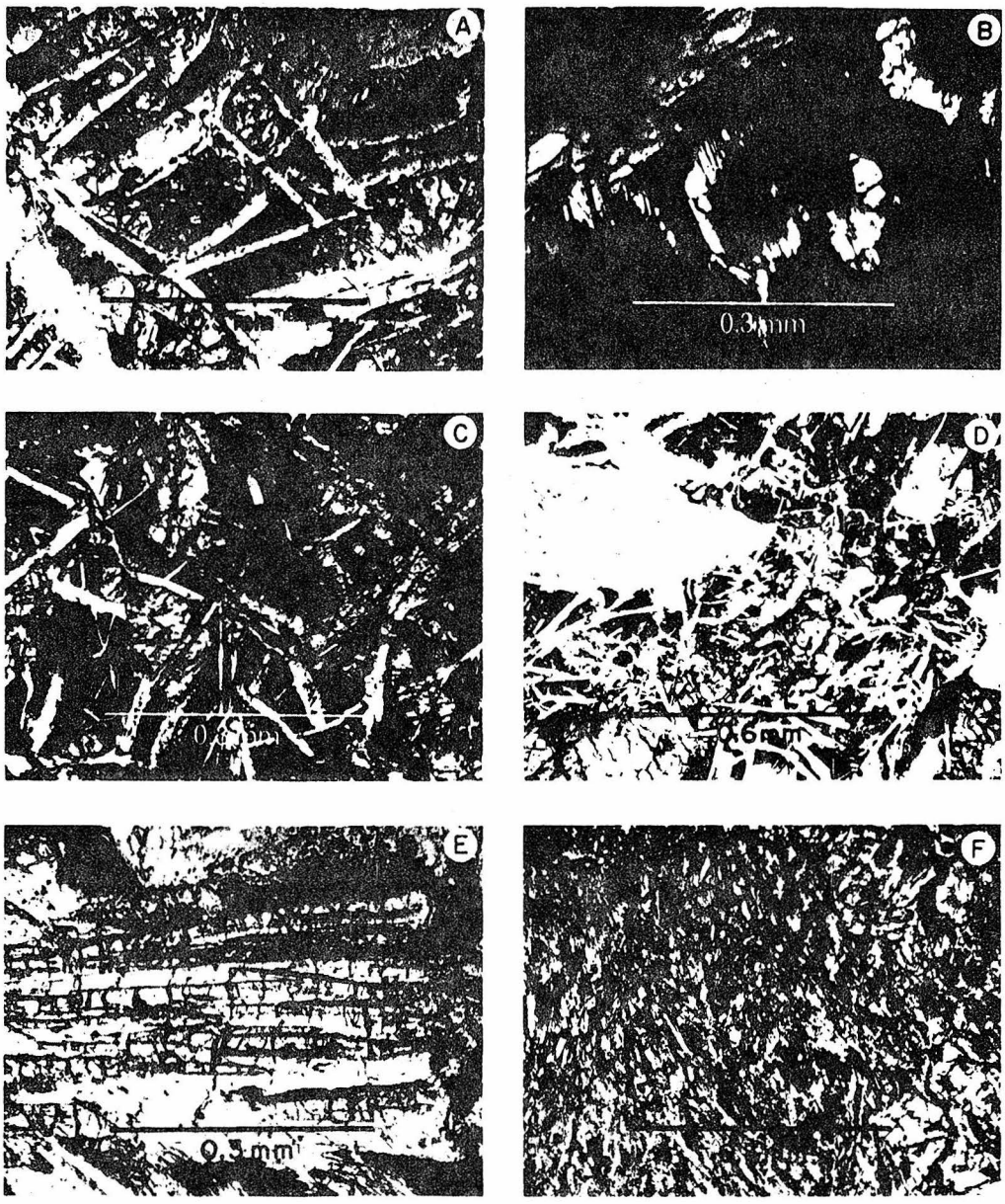

Fig. 8. Photomicrographs of textures exhibited in feldspathic basalt clasts: (A) Subophitic to intersertal feldspathic basalt (plane polarized light). (B) Complex pyroxene relationships in a subophitic feldspathic basalt clast. The center of this photograph shows a grain marked by an optical discontinuity that separates a core of low-Ca pyroxene ($Wo_3En_{77}Fs_{20}$) from a rim of low-Ca pyroxene ($Wo_3En_{79}Fs_{18}$). Locally, lamellae of what appear to be exsolved low-Ca and high-Ca pyroxene occur in the rim (crossed polarizers). (C) Intersertal feldspathic basalt (plane polarized light). (D) Porphyritic–intersertal feldspathic basalt (plane polarized light). (E) "Ladder Structure" (plane polarized light). (F) Porphyritic–variolitic feldspathic basalt. Note the large pyroxene grain in the lower right-hand corner of the photograph (plane polarized light).

pyroxene reached the composition of ~$Wo_{12}En_{46}Fs_{42}$, ilmenite began to crystallize, followed by high-Ca pyroxene. The early appearance of plagioclase and the crystallization of ilmenite before high-Ca pyroxene are indicated by the trend of minor elements in the pyroxene (Fig. 9A).

B. *Intersertal.* Intersertal feldspathic basalt is finer grained than the subophitic to intersertal variety and contains a greater amount of mesostasis material (Fig. 8C). Another distinction is that pyroxene is intergrown near its edges with plagioclase laths. Not only are there textural differences, but also there are differences in pyroxene zoning trends. The composition of the pyroxene does not extend beyond $Wo_{30}En_{35}Fs_{35}$ (Fig. 9B). These observations indicate that the

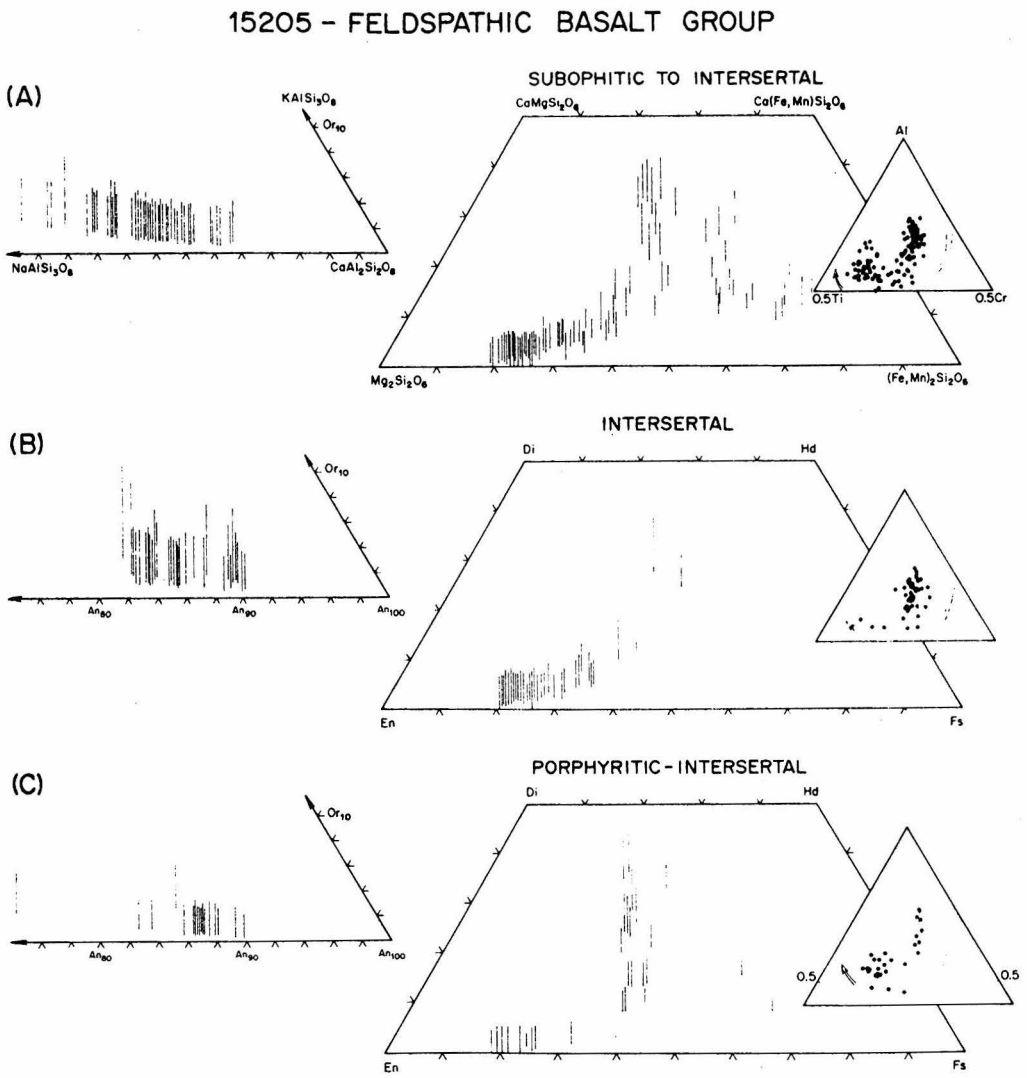

Fig. 9. Part I

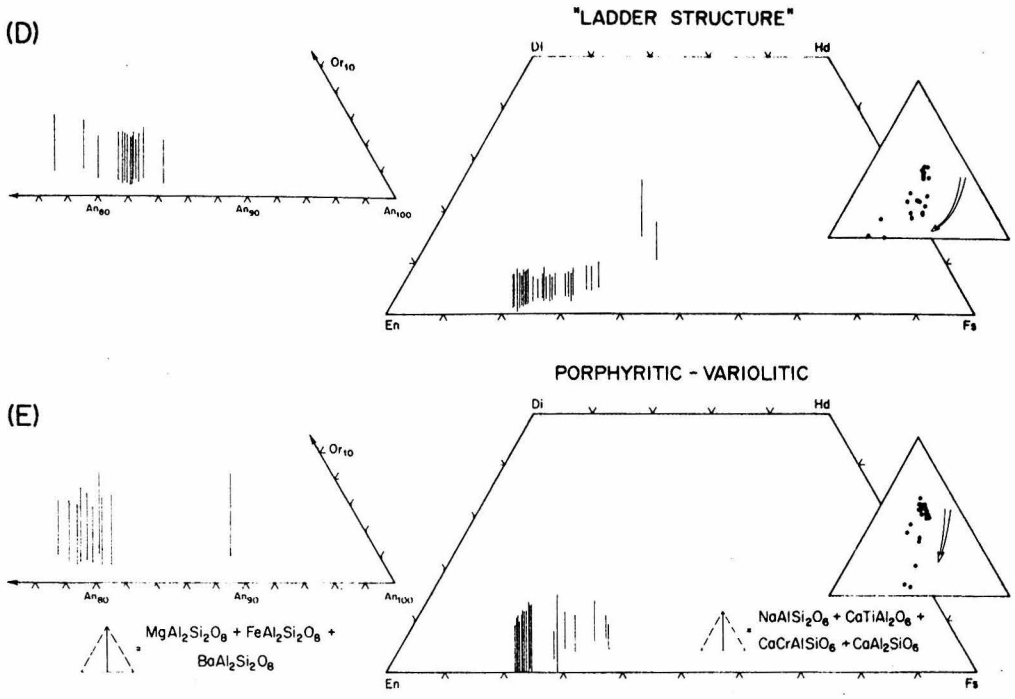

Fig. 9. Part II

Fig. 9. Compositions of the plagioclase and pyroxene in feldspathic basalts. The vertical lines represent the altitudes of triangles that correspond to the amount of minor element substitution, as indicated in the figure. The insets in the pyroxene quadrilaterals display the Al–Ti–Cr patterns in the pyroxene; the arrows depict the path of increasing Fe/Mg in pyroxene. A, B, C, D, and E refer to headings in the text.

intersertal feldspathic basalt clasts are less completely crystallized than the subophitic to intersertal feldspathic basalt clasts. In addition, one of these clasts contains olivine (Fo_{77-80}).

C. *Porphyritic–intersertal.* A single clast of porphyritic–intersertal feldspathic basalt was identified that has a texture basically similar to the subophitic to intersertal feldspathic basalt. However, plagioclase occurs as $.3 \times .5$ mm megacrysts (Fig. 8D). Pyroxene grains are continuously zoned from $Wo_2En_{80}Fs_{18}$ to $Wo_{38}En_{39}Fs_{23}$. Fe-rich, low-Ca pyroxene ($Wo_{10}En_{28}Fs_{62}$) is restricted to the mesostasis areas (Fig. 9C). Plagioclase megacrysts have composition An_{88-90}, and plagioclase laths in the groundmass range in composition from An_{88} to An_{82}.

D. "*Ladder structure.*" This group of feldspathic basalt clasts is comprised of intergrown, elongate crystals of plagioclase and low-Ca pyroxene which resemble the rungs of a ladder (Fig. 8E). Other phases include ilmenite, K-rich mesostasis, Fe metal, and troilite. Despite this textural distinction, the compositions of minerals are similar to those of the intersertal feldspathic basalt (Fig. 9D).

E. *Porphyritic–variolitic.* These clasts consist of plagioclase, low-Ca pyroxene, ilmenite, and K-rich mesostasis (Figs. 8F, 9E). Microprobe analyses of the finer grained clasts indicate that their bulk composition closely corresponds to the recrystallized, KREEP basalt fragment reported by Drake and Klein (1973) in sample 15086.

2. *Pyroxene–phyric basalt fragments*

Fragments of porphyritic, clinopyroxene basalt, termed pyroxene–phyric basalt by Dowty *et al.* (1974), are present in 15205. These form a coherent rock suite on the basis of the morphology and chemistry of the pyroxene phenocrysts. Consistent differences in the grain size of the groundmass distinguish three types which are: Type 1, aphanitic groundmass; Type II, ~10 μm groundmass; and Type III, ~25 μm groundmass. The increase in the grain size of the groundmass correlates with the increase in size of the phenocrysts as was pointed out by Dowty *et al.*, (1974) for similar rocks from Apollo 15. Photographs of the three types illustrating typical textures, are presented in Fig. 10.

Type I phyric basalt is pyroxene vitrophyre *sensu strictu,* and is comprised of tiny (10–150 μm) euhedral prismatic to skeletal grains of pyroxene set in an opaque, maroon, aphanitic groundmass (Fig. 10A). The groundmass ranges from undevitrified glass to an intergrowth of extremely fine-grained sheaves of plagioclase and pyroxene (?). However, the groundmass within any individual fragment appears homogeneous. In only a few fragments, tiny ($\leq$5 μm) rare grains of chromite or Fe metal occur.

The pyroxene is zoned continuously from $Wo_5En_{65}Fs_{30}$ to $Wo_{27}En_{40}Fs_{33}$ and the minor element content is greater for a given composition than in the other two types (Fig. 11I). The Al–Ti–Cr patterns reflect crystallization in the absence of plagioclase (Hollister, 1972).

Type II and Type III phyric basalts have similar mineral assemblages. Pyroxene, olivine, and chromite phenocrysts are set in a variolitic groundmass made up of acicular grains of plagioclase (An_{83-90}) and Fe-rich pyroxene with minor amounts of spinel, ilmenite, Fe metal, troilite and silica (Fig. 10B and 10C). In general, the groundmass crystals radiate from the borders of the phenocrysts (Fig. 10C).

The pyroxene phenocrysts range from subhedral prisms to acicular grains; many are hollow and contain groundmass material in their cores similar to that which surrounds them, although it is usually finer grained. The chromite occurs as euhedral inclusions in pyroxene (Fig. 10D) and in the groundmass as subrounded grains surrounded by ülvospinel. Aggregates of Fe metal and troilite are associated with the chromite phenocrysts. The olivine phenocrysts (Fo_{68-48} in Type II; Fo_{63-54} in Type III) are either partially resorbed, or mantled by low-Ca pyroxene (pigeonite).

Type II pyroxene phenocrysts consist of low-Ca pyroxene (pigeonite, $Wo_6En_{68}Fs_{26}$) overgrown by high-Ca pyroxene ($Wo_{30}En_{45}Fs_{25}$) that is zoned continuously to $Wo_{30}En_{32}Fs_{38}$. The edge of one phenocryst had composition

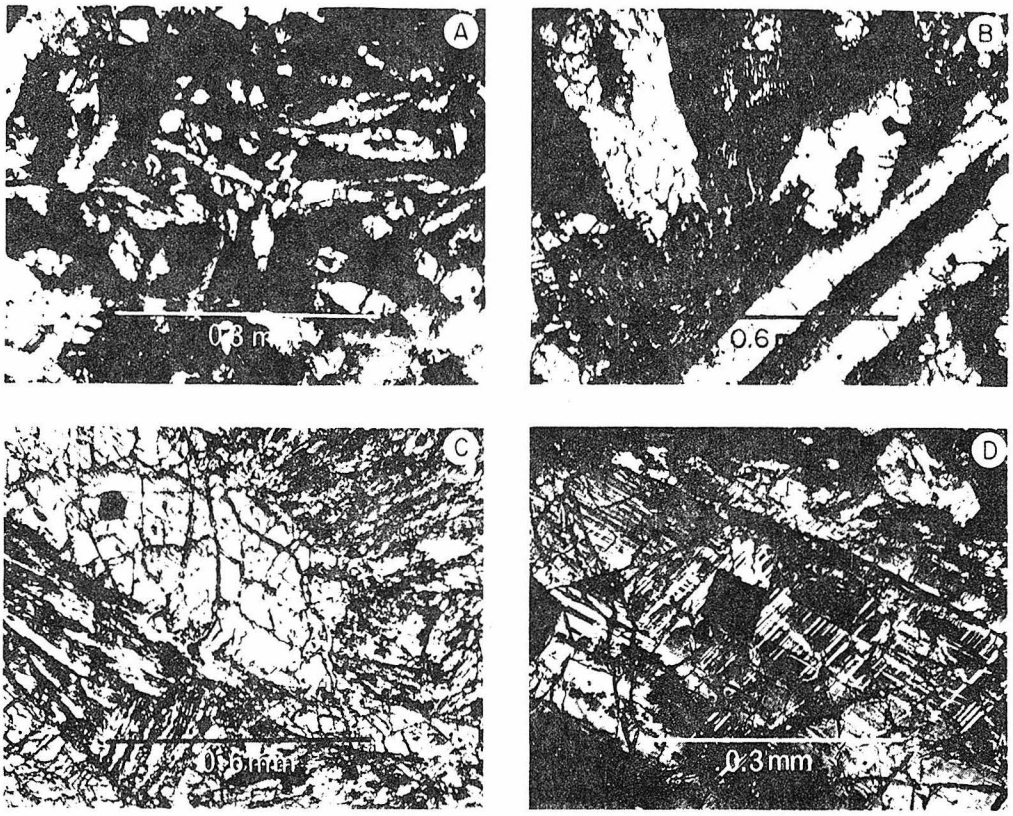

Fig. 10. Photomicrographs showing typical textures of the pyroxene–phyric basalts: (A) Pyroxene phenocrysts in an aphanitic groundmass, Type I (plane polarized light). (B) Pyroxene phenocrysts in ~10 μm variolitic groundmass, Type II (plane polarized light). (C) Pyroxene phenocryst in ~25 μm variolitic groundmass, Type III. Note that the groundmass crystals tend to radiate from the edge of the phenocryst (plane polarized light). (D) Lamellar structure in pyroxene phenocryst (crossed polarizers). Note the presence of euhedral chromite inclusions in the pyroxene phenocrysts in B, C, and D.

$Wo_{17}En_{23}Fs_{60}$. In some grains the low-Ca to high-Ca pyroxene transition is marked by a conspicuous optical discontinuity. Zoning patterns indicate that the phenocrysts grew both inward and outward into the melt.

Extremely fine lamellae (<1–2 μm) present in three crystallographic orientations, occur locally in these phenocrysts (Fig. 10D). No compositional differences were detected among them by electron beam scans although the small size of the lamellae makes a chemical distinction difficult.

The groundmass pyroxene ranges in composition from $Wo_{14}En_{29}Fs_{57}$ to $Wo_{14}En_{2}Fs_{84}$ and apparently overlaps in composition with the most Fe-rich phenocryst composition. This overlap, together with the fact that apophyses of the last pyroxene to form on the phenocrysts extend for 5–10 μm into the groundmass, suggests that crystallization of the groundmass immediately followed that of the larger grains. However, the strong bimodality in grain size and

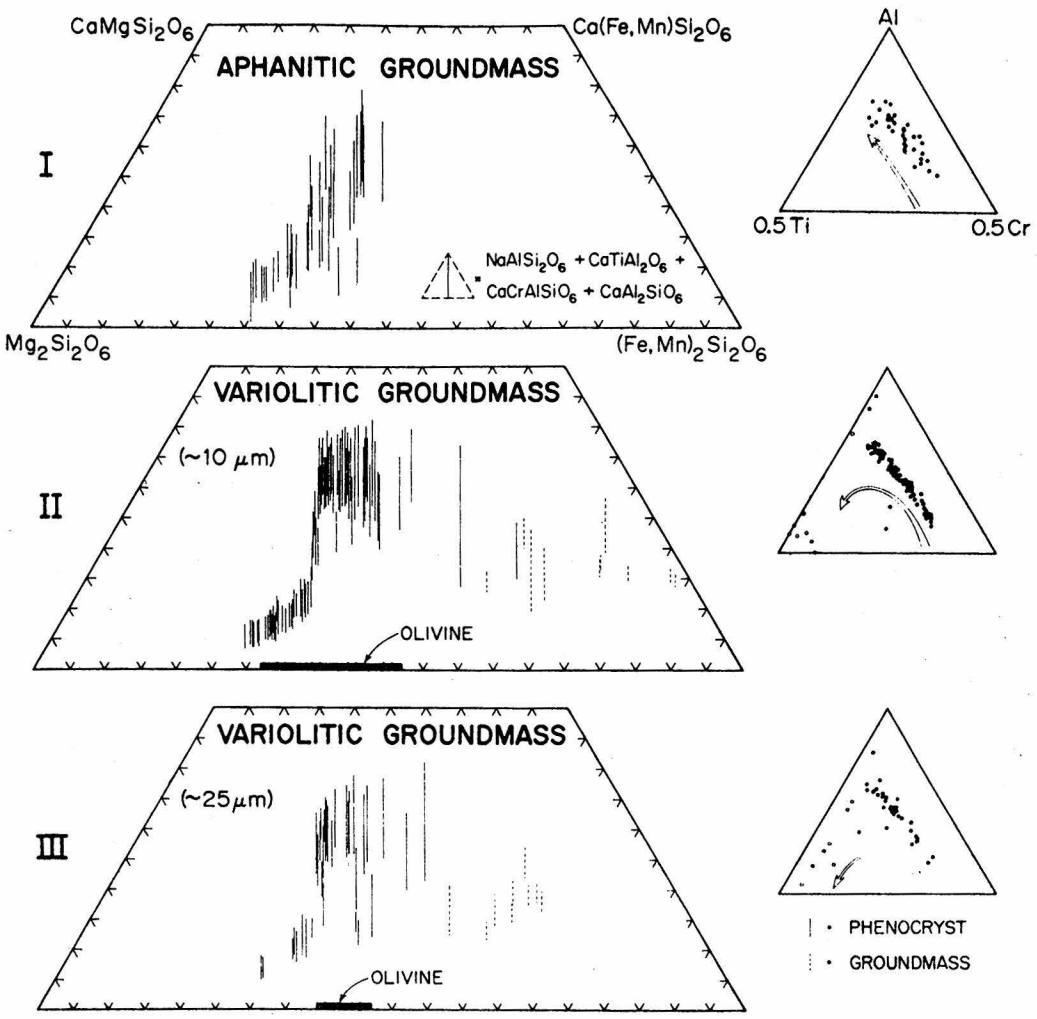

Fig. 11. Composition of the pyroxene in phyric basalt clasts. The arrows in the Al–Ti–Cr diagrams indicate the direction of increasing Fe/Mg in the pyroxene.

the large gap in the Al–Ti–Cr distribution (Fig. 11II) require that the bulk of the phenocryst growth was completed prior to the rapid co-precipitation of plagioclase and Fe pyroxene in the groundmass.

The pyroxene phenocrysts in Type III display essentially the same zoning patterns as in Type II except for an additional trend from $Wo_6En_{66}Fs_{28}$ to $Wo_{15}En_{45}Fs_{40}$ (Fig. 11III). The groundmass pyroxene, on the other hand, does not show the strong Fe enrichment and exhibits a continuous change in Al–Ti–Cr.

Wiegand and Hollister (1973) and Dowty *et al.* (1974) have argued that single-stage crystallization can produce the porphyritic textures of the Apollo 15

phyric basalts. Although it might appear that the three phyric basalt types in 15205 could represent different parts of a "single" flow unit, i.e. quenched-margin and interior, Type I does not appear to be related to Types II and III. The data, however, do permit Types II and III to be parts of similar flow units. There are two reasons for this. First, the pyroxene in Type I crystallized prior to the onset of chromite crystallization, whereas in Types II and III, chromite precedes or at least coincides with the crystallization of pyroxene. Second, olivine is absent in Type I, but occurs in Types II and III. Alternatively, the separation of early formed chromite and olivine by sinking or flow differentiation could explain the observations.

3. *Other mare basalt fragments*

A. *Olivine, granular-pyroxene basalt.* These basalt clasts are dominated by granular aggregates of pyroxene, some of which are poikilitically enclosed by plagioclase. Rounded, strongly zoned phenocrysts of olivine (Fo_{63-39}) are also present. Blocky grains of ilmenite, chromite, and ülvospinel occur together with Fe metal, troilite, and a K-poor, Ti- and Fe-rich mesostasis. The plagioclase has relatively homogeneous cores (An_{88-92}) with rims zoned to An_{82} (Fig. 12). Single grains of pyroxene are continuously zoned from $Wo_{12}En_{54}Fs_{34}$ to $Wo_{28}En_{47}Fs_{25}$ to $Wo_{24}En_{34}Fs_{42}$ or from $Wo_{12}En_{54}Fs_{34}$ to $Wo_{15}En_{25}Fs_{60}$. The trend of pyroxene compositions away from the Al apex of the Al–Ti–Cr diagram toward the Ti apex implies that the pyroxene crystallized with plagioclase, but before any Ti-bearing phase (Fig. 12). The textural relationships suggest that pyroxene preceded plagioclase, especially since the most Mg-rich pyroxene is included in the plagioclase. We interpret these relationships to indicate the following crystallization sequence: olivine + chromite; followed by pyroxene, followed rapidly by plagioclase. The bulk of the pyroxene formed together with plagioclase; ülvospinel and ilmenite formed late.

B. *Pyroxene, poikilitic–plagioclase basalt.* These basalt clasts are similar in overall texture to the olivine, granular-pyroxene basalt, but differ by the absence of chromite and magnesian–olivine, and by the presence of amoeboid grains of ülvospinel that are partly mantled by ilmenite. One ~20 μm grain of olivine (Fo_{34}) was found, included within plagioclase. The pyroxene is granular and is zoned from $Wo_{12}En_{53}Fs_{35}$ to $Wo_{18}En_{33}Fs_{49}$ (Fig. 12). The plagioclase shows a limited range in composition (An_{88-92}), and encloses grains of pyroxene. The inferred crystallization sequence is similar to that in the olivine, granular-pyroxene basalt.

C. *Ophitic microgabbro.* Several fragments of Fe-rich ophitic "microgabbro" occur, which are distinguished from all other basalt clasts in 15205 on the basis of the rectangular form of pyroxene, and the presence of hollow, elongate blades of silica. The zoning pattern of the pyroxene is likewise unique. These range continuously in composition from $Wo_8En_{44}Fs_{48}$ to $Wo_{31}En_{17}Fs_{52}$ to $Wo_{17}En_{02}Fs_{81}$ (Fig. 12). Both plagioclase (An_{85-91}) and ülvospinel mantled by ilmenite are present, much like some of the basalts from Apollo 11 and 17.

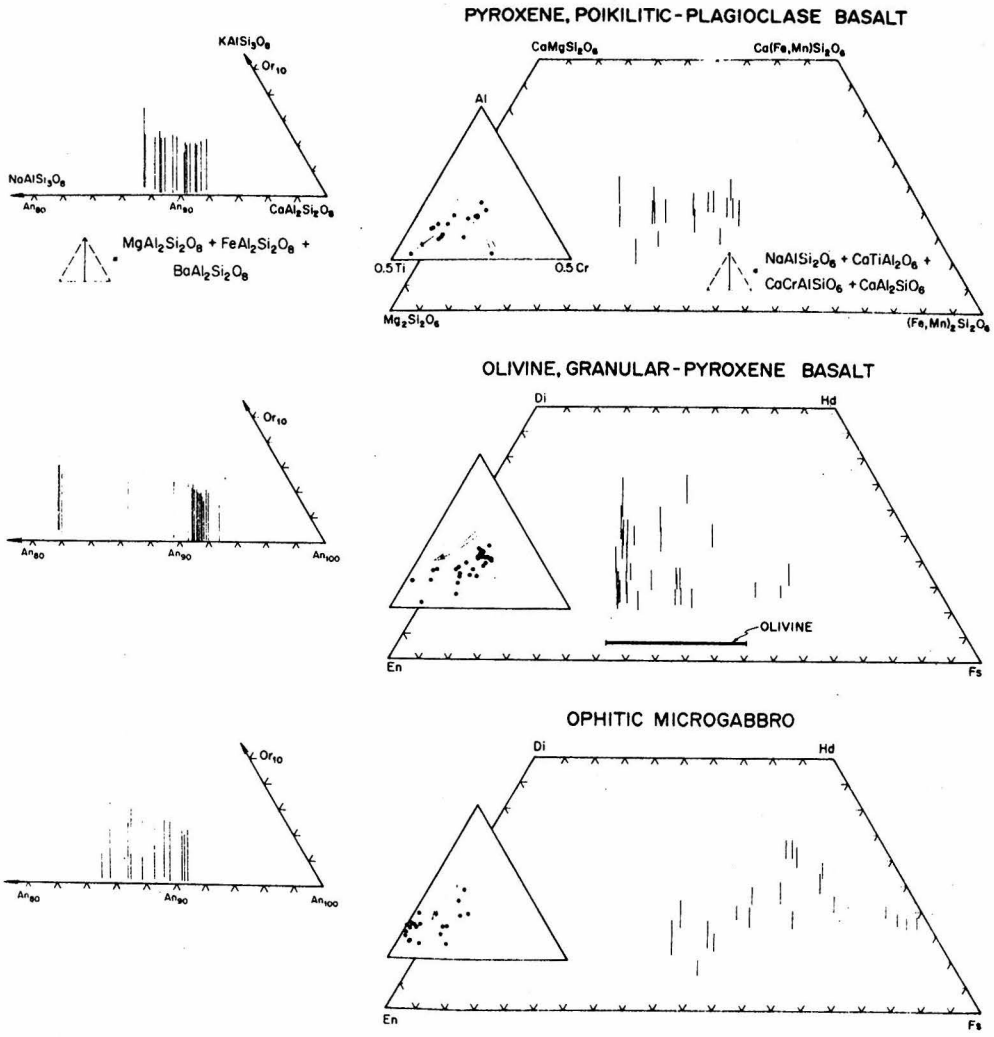

Fig. 12. Compositions of the plagioclase and pyroxene in mare basalt clasts. The arrows in the Al–Ti–Cr diagrams indicate the direction of increasing Fe/Mg in the pyroxene.

VI. Selenologic History

We have established the following chronology of events for lunar sample 15205 based on the large-scale features of the boulder, the textures and relationships observed microscopically, and the nature and compositions of glass and lithic fragments.

(1) The presence of materials with such a wide range of lithologies and textures, and the presence of compositionally and texturally distinct layers

suggest that multiple impact events deposited the soil from which 15205 and the boulder were derived. The observation that glass fragments with mare basalt composition are extremely rare in 15205—despite the fact that mare basalt clasts *are abundant*—together with the fact that impact glass is more easily formed in unconsolidated debris than in bedrock (Ahrens and O'Keefe, 1972), suggests that a mature mare regolith had not evolved during this accumulation interval. Hence, 15205 may preserve an ancient lunar soil which formed shortly after the eruption of the Apollo 15 mare basalts.

(2) The low porosity and coherent nature of this rock requires that post-accumulation impact events compacted the soil and lithified it by slight sintering of the fine-grained matrix material.

(3) Subsequent impact events fractured the now-lithified soil and injected shock-melted material into it to form the brown-glass veins.

(4) An impact event caused total melting of lunar soil and injected this melt into a series of fractures to form what is now observed as the glass coating on the boulder and sample 15205.

(5) During excavation of the boulder by a young Copernican age impact at ~.001 AE, it was emplaced at its present site on the lunar surface. This age, inferred from ^{22}Na–^{26}Al data, indicates surface exposure to cosmic rays for a period of less than 10^6 yr. (Keith *et al.*, 1972; Rancitelli *et al.*, 1972).

It is possible that (3), (4), and (5) are the same event, with only slight time intervals in between.

VII. Nature of the Source Region

The similarity between the soil from which 15205 was derived, and other Apollo 15 soils, is demonstrated by the presence in both of "green glass," alkalic, high-alumina basalt glass, feldspathic basalt fragments, and mare basalt fragments, in particular the characteristic pyroxene–phyric basalts. These similarities are consistent with the interpretation that 15205 was locally derived, even though it was collected from a boulder whose ultimate point of origin is unclear.

However, 15205 differs by the virtual absence of glass with mare basalt composition and glass with $Al_2O_3 > 20\%$—both of which are abundant in Apollo 15 soils (Best and Minkin, 1972; Glass, 1972; Reid *et al.*, 1973; von Engelhardt *et al.*, 1973). The near absence of glass with mare basalt composition has been discussed. The lack of glass with $Al_2O_3 > 20\%$ and the absence of ANT-suite fragments indicate that a typical highland region was not an important contributor to the 15205 soil.

Feldspathic basalt fragments and the alkalic, high-alumina basalt glass together comprise about 30% of sample 15205. These appear equivalent to KREEP, therefore the source region of the boulder must be KREEP-rich. In addition, reconnaissance petrographic observations of selected Apollo 15 breccias indicate that KREEP-rich fragments like those present in 15205 also occur in samples 15015 (see also Consortium, European and friends, 1974), 15059, 15265, 15299, 15459, 15465 (see also Delando and Cameron, 1973), and 15505. Hence, a source of

KREEP-rich basalt fragments must represent a prominent selenologic unit in and around the Apollo 15 site. Whether this KREEP material underlies the shallow mare cover at the Apollo 15 site or forms the nearby Apennine Mountains cannot be determined.

Acknowledgments—A. J. Gancarz and D. A. Papanastassiou supervised the original cutting of 15205. E. K. Jesseberger, J. C. Huneke, and G. J. Wasserburg assisted in the study of the slabs. Throughout the course of this project, discussions with J. C. Huneke, L. T. Silver, and G. J. Wasserburg have proven most instructive. We are especially endebted to L. T. Silver for his thoughts on Apollo 15 breccias, and to A. J. Gancarz for his instructive criticisms of earlier versions of the manuscript. In addition, the reviews of J. C. Huneke, G. J. Taylor, and one who chose to remain anonymous, are gratefully acknowledged. The 15205 project has been supported by NASA grants NGL-05-002-188 and NGL-05-002-338. The microprobe laboratory has been developed with the support of N.S.F., J.P.L., and the Union Pacific Foundation.

REFERENCES

Agrell S. O., Agrell J. E., and Arnold A. R. (1973) Observations on glass from 15425, 15426, 15427 (abstract). In *Lunar Science—IV*, pp. 12–14. The Lunar Science Institute, Houston.

Ahrens T. J. and O'Keefe J. D. (1972) Shock melting and vaporization of lunar rocks and minerals. *The Moon* **4**, 214–249.

Albee A. L., Chodos A. A., and Gancarz A. J. (1972) Petrology of Apollo 15 sample 15486. In *The Apollo 15 Lunar Samples*, pp. 20–25. The Lunar Science Institute, Houston.

Apollo 15 Technical Air to Ground Voice Transcription (1971) *NASA MSC-04558*. pp. 519–531, Houston.

Bence A. E. and Papike J. J. (1972) Pyroxenes as recorders of lunar basalt petrogenesis: Chemical trends due to crystal-liquid interaction. *Proc. Third Lunar Sci. Conf., Geochim. Cosmochim. Acta*, Suppl. 3, Vol. 1, pp. 431–470. MIT Press.

Best J. B. and Minkin J. A. (1972) Apollo 15 glasses of impact origin. In *The Apollo 15 Lunar Samples*, pp. 34–39. The Lunar Science Institute, Houston.

Cameron K. L., Delano J. W., Bence A. E., and Papike J. J. (1973) Petrology of the 2–4 mm soil fraction from the Hadley–Apennine region of the moon. *Earth Planet. Sci. Lett.* **19**, 9–21.

Carusi A., Cavarretta G., Cinotti F., Civitelli G., Coradini A., Funiciello R., Fulchignoni M., and Taddeucci A. (1972) Lunar glasses as an index of the impacted sites lithology: The source area of Apollo 15 "Green Glasses". *Geologica Romana* **11**, 137–151.

Chodos A. A., Albee A. L., Gancarz A. J., and Laird J. (1973) Optimization of computer-controlled quantitative analysis of minerals. *Proc. Eighth National Conference on Electron Probe Analysis*, 45A.

Consortium, European and friends (1974) The history of lunar breccia 15015 (abstract). In *Lunar Science—V*, pp. 217–219. The Lunar Science Institute, Houston.

Delano J. W. (1972) Petrologic examination of breccia 15465 and its implications as to the nature of the Apennine Front. In *The Apollo 15 Lunar Samples*, pp. 60–61. The Lunar Science Institute, Houston.

Delano J. W. and Cameron K. L. (1973) Petrology of Apollo 15 consortium breccia 15465. *Proc. Fourth Lunar Sci. Conf., Geochim. Cosmochim. Acta*, Suppl. 4, Vol. 1, pp. 461–466. Pergamon.

Dowty E., Prinz M., and Keil K. (1973) Composition, mineralogy, and petrology of 28 mare basalts from Apollo 15 rake samples. *Proc. Fourth Lunar Sci. Conf., Geochim. Cosmochim. Acta*, Suppl. 4, Vol. 1, pp. 423–444. Pergamon.

Dowty E., Keil K., and Prinz M. (1974) Lunar pyroxene–phyric basalts: Crystallization under supercooled conditions. *J. Petrol.* In press.

Drake J. C. and Klein C., Jr. (1973) Lithic fragments and glasses in microbreccia 15086: Their chemistry and occurrence. *Proc. Fourth Lunar Sci. Conf., Geochim. Cosmochim. Acta*, Suppl. 4, Vol. 1, pp. 467–480. Pergamon.

Drake M. J., Stoeser J. W., and Goles G. G. (1973) A unified approach to a fragmental problem: Petrological and geochemical studies of lithic fragments from Apollo 15 soils. *Earth Planet. Sci. Lett.* **20**, 425–439.

Dymek R. F., Albee A. L., and Chodos A. A. (1974) Petrology, clast characteristics, and selenologic history of glass-coated breccia 15205 (abstract). In *Lunar Science—V*, pp. 194–196. The Lunar Science Institute, Houston.

Gancarz A. J., Albee A. L., and Chodos A. A. (1971) Petrologic and mineralogic investigation of some crystalline rocks returned by the Apollo 14 mission. *Earth Planet. Sci. Lett.* **12**, 1–18.

Glass B. F. (1972) Major element composition of Apollo 15 glasses. In *The Apollo 15 Lunar Samples*, pp. 73–77. The Lunar Science Institute, Houston.

Hollister L. S. (1972) Implications of the relative concentrations of Al, Ti, and Cr in lunar pyroxenes (abstract). In *Lunar Science—III*, pp. 389–391. The Lunar Science Institute, Houston.

Hollister L., Trzcienski W., Jr., Dymek R., Kulick C., Wiegand P., and Hargraves R. (1972) Igneous fragment 14310,21 and the origin of the mare basalts (abstract). In *Lunar Science—III*, pp. 386–388. The Lunar Science Institute, Houston.

Keith J. E., Clark R. S., and Richardson K. A. (1972) Gamma-ray measurements of Apollo 12, 14, and 15 lunar samples. *Proc. Third Lunar Sci. Conf., Geochim. Cosmochim. Acta*, Suppl. 3, Vol. 2, pp. 1671–1680. MIT Press.

Kridelbaugh S. J., Grieve R. A. F., and Weill D. F. (1972) Glass compositions in breccias 15028 and 15059. In *The Apollo 15 Lunar Samples*, pp. 123–127. The Lunar Science Institute, Houston.

Lindsay J. F. (1972) Sedimentology of clastic rocks returned from the moon by Apollo 15. *Geol. Soc. Amer. Bull.* **83**, 2957–2970.

LSPET (Lunar Sample Preliminary Examination Team) (1972) The Apollo 15 lunar samples: A preliminary description. *Science* **175**, 363–375.

Mason B. (1972) Mineralogy and petrology of polymict breccia 15498. In *The Apollo 15 Lunar Samples*, pp. 137–139. The Lunar Science Institute, Houston.

Mason B., Jarosewich E., and Melson W. G. (1972) Mineralogy, petrology, and chemical composition of lunar samples 15085, 15256, 15271, 15471, 15475, 15476, 15535, 15555, and 15556. *Proc. Third Lunar Sci. Conf., Geochim. Cosmochim. Acta*, Suppl. 3, Vol. 1, pp. 785–796. MIT Press.

McKay D. S., Clanton U. S., and Ladle G. (1973) Scanning electron microscope study of Apollo 15 green glass. *Proc. Fourth Lunar Sci. Conf., Geochim. Cosmochim. Acta*, Suppl. 4, Vol. 1, pp. 225–238. Pergamon.

Meyer C., Jr. (1972) Mineral assemblages and the origin of non-mare lunar rock types (abstract). In *Lunar Science—III*, pp. 542–544. The Lunar Science Institute, Houston.

Nyquist L. E., Bansal B. M., Weismann H., and Jahn B. M. (1974) Taurus-Littrow chronology: Implications for early lunar crustal development (abstract). In *Lunar Science—V*, pp. 565–567. The Lunar Science Institute, Houston.

Phinney W. C., Warner J. L., Simonds C. H., and Lofgren G. E. (1972) Classification and distribution of rock types at Spur Crater. In *The Apollo 15 Lunar Samples*, pp. 149–153. The Lunar Science Institute, Houston.

Powell B. N., Aitken F. K., and Weiblen P. W. (1973) Classification, distribution, and origin of lithic fragments from the Hadley-Apennine region. *Proc. Fourth Lunar Sci. Conf., Geochim. Cosmochim. Acta*, Suppl. 4, Vol. 1, pp. 445–460. Pergamon.

Rancitelli L. A., Perkins R. W., Felix W. D., and Wogman N. A. (1972) Lunar surface processes and cosmic ray characterization from Apollo 12–15 lunar sample analyses. *Proc. Third Lunar Sci. Conf., Geochim. Cosmochim. Acta*, Suppl. 3, Vol. 2, pp. 1681–1691. MIT Press.

Reid A. M., Warner J. L., Ridley W. I., and Brown R. W. (1972) Major element composition of glasses in three Apollo 15 soils. *Meteoritics* **7**, 395–415.

Ridley W. I., Reid A. M., Warner J. L., and Brown R. W. (1973a) Apollo 15 green glass. *Phys. Earth Planet. Interiors* **7**, 133–136.

Ridley W. I., Reid A. M., Warner J. L., Brown R. W., Gooley R., and Donaldson C. (1973b) Glass compositions in Apollo 16 soils 60501 and 61221. *Proc. Fourth Lunar Sci. Conf., Geochim. Cosmochim. Acta*, Suppl. 4, Vol. 1, pp. 309–321. Pergamon.

Simonds C. H. (1973) Sintering and hot-pressing of Fra Mauro composition glass and the lithification of lunar breccias. *Amer. J. Sci.* **273**, 428–439.

Steele I. M., Smith J. V., and Grossman L. (1972) Mineralogy and petrology of Apollo 15 rake samples: II. Breccias. In *The Apollo 15 Lunar Samples*, pp. 161–164. The Lunar Science Institute, Houston.

Stolper E., Walker D., Longhi J., and Hays J. F. (1974) Compositional variation in lunar ultramafic glasses (abstract). In *Lunar Science—V*, pp. 749–751. The Lunar Science Institute, Houston.

Swann G. A., Hart M. H., Schaber G. G., Freeman V. L., Ulrich G. E., Wolge E. W., Reed V. S., and Sutton R. L. (1971) Preliminary description of Apollo 15 sample environments. *U.S.G.S. Interagency Report*: *36*, 219 pp.

Warner J. L. (1972) Metamorphism of Apollo 14 breccias. *Proc. Third Lunar Sci. Conf., Geochim. Cosmochim. Acta*, Suppl. 3, Vol. 1, pp. 623–644. MIT Press.

Wiegand P. W. and Hollister L. S. (1973) Basaltic vitrophyre 15597: An undifferentiated melt sample. *Earth Planet. Sci. Lett.* **19**, 61–74.

Willis J. P., Erlank A. J., Gurney J. J., and Ahrens L. H. (1972) Geochemical features of Apollo 15 materials. In *The Apollo 15 Lunar Samples*, pp. 268–271. The Lunar Science Institute, Houston.

Geochimica et Cosmochimica Acta, 1976, Vol. 40, pp. 1115 to 1130. Pergamon Press. Printed in Great Britain

Petrography of isotopically-dated clasts in the Kapoeta howardite and petrologic constraints on the evolution of its parent body

R. F. DYMEK, A. L. ALBEE, A. A. CHODOS and G. J. WASSERBURG
Divison of Geological and Planetary Sciences,* California Institute of Technology, Pasadena, California 91125, U.S.A.

(*Received* 5 *August* 1975; *accepted in revised form* 8 *March* 1976)

Abstract—Detailed mineralogic and petrographic data are presented for four isotopically-dated basaltic rock fragments separated from the howardite Kapoeta. Clasts C and ρ have been dated at ~4.55 AE and ~4.60 AE respectively, and Clast ρ contains ^{244}Pu and ^{129}I decay products. These are both igneous rocks that preserve all the features of their original crystallization from a melt. They thus provide good evidence that the Kapoeta parent body produced basaltic magmas shortly after its formation (<100 m.y.). Clast A has yielded a Rb–Sr age of ~3.89 AE and a similar ^{40}Ar/^{39}Ar age. This sample is extensively recrystallized, and we interpret the ages as a time of recrystallization, and not the time of original crystallization from a melt. Clast B has yielded a Rb–Sr age of ~3.63 AE, and an ^{40}Ar/^{39}Ar age of $\gtrsim$ 4.50 AE. This sample is moderately recrystallized, and the Rb–Sr age probably indicates a time of recrystallization, whereas the ^{40}Ar/^{39}Ar age more closely approaches the time of crystallization from a melt. Thus, there is no clearcut evidence for 'young' magmatism on the Kapoeta parent body.

Kapoeta is a 'regolith' meteorite, and mineral–chemical and petrographic data were obtained for numerous other rock and mineral fragments in order to characterize the surface and near-surface materials on its parent body. Rock clasts can be grouped into two broad lithologic types on the basis of modal mineralogy– basaltic (pyroxene- and plagioclase-bearing) and pyroxenitic (pyroxene-bearing). Variations in the compositions of pyroxenes in rock and mineral clasts are similar to those in terrestrial mafic plutons such as the Skaergaard, and indicate the existence of a continuous range in rock compositions from Mg-rich orthopyroxenites to very iron-rich basalts. The FeO and MnO contents of all pyroxenes in Kapoeta fall near a line with FeO/MnO ~ 35, suggesting that the source rocks are fundamentally related. We interpret these observations to indicate that the Kapoeta meteorite represents the comminuted remains of differentiated igneous complexes together with 'primary' undifferentiated basaltic rocks. The presently available isotopic data are compatible with the interpretation that this magmatism is related to primary differentiation of the Kapoeta parent body. In addition, our observations preclude the interpretation that the Kapoeta meteorite is a simple mixture of eucrites and diogenites.

The FeO/MnO value in lunar pyroxenes (~60) is distinct from that of the pyroxenes in Kapoeta. Anorthositic rocks were not observed in Kapoeta, suggesting that plagioclase was not important in the evolution of the Kapoeta parent body, in contrast to the Moon. Both objects appear to have originated in chemically-distinct portions of the solar system, and to have undergone differentiation on different time scales involving differing materials.

I. INTRODUCTION

CERTAIN types of meteorites, especially the gas-rich howardites, strongly resemble lunar soil breccias. This suggests that impact processes such as fragmentation, gardening, and lithification by sintering of regolith materials occurred on the surfaces of the parent bodies of these meteorites. The howardite Kapoeta is highly representative of this group of regolith meteorites, and has been extensively studied. Kapoeta is a polymict breccia (WAHL, 1952; DUKE and SILVER, 1967), which contains various types of mineral and lithic clasts (FREDRIKSSON and KEIL, 1963; DYMEK *et al.*, 1975a), maskelynitized plagioclase, a few impact glass fragments with a range in composition (NOONAN *et al.*, 1974)—some of which possess 'zap pits' on their surfaces (BROWNLEE and RAJAN, 1973), and rare fragments of carbonaceous chondrites (WILKENING, 1973), set in an aphanitic matrix comprised of very fine-grained, comminuted mineral particles.

Macroscopically, Kapoeta exhibits a characteristic 'light–dark' structure (FREDRIKSSON and KEIL, 1963). In thin section, local alignment of clasts suggests an accumulation fabric. In addition, regions of slightly-different grain size, color, and mineralogy are separated by sharp lithologic contacts. These features indicate a complex evolutionary history, probably involving multiple impact events.

Despite this apparent complex history, most textural relationships in lithic clasts predate the formation of the breccia from which this meteorite was derived. The presence of discrete glass particles, the presence of large amounts of noble gases (SIGNER and SUESS, 1963), the preservation of solar flare tracks

* Contribution No. 2653.

(LAL and RAJAN, 1969; PELLAS *et al.*, 1969; WILKENING, 1971; WILKENING *et al.*, 1971; RAJAN, 1974), and the non-recrystallized nature of the matrix indicates that the Kapoeta meteorite was not subjected to strong thermal metamorphism. These observations support the contention that features observed in lithic clasts are 'primary'. Therefore, it is exceedingly important to characterize these clasts chemically, petrographically, and isotopically to understand the chemical nature and time scale for differentiation of the Kapoeta parent body.

Four basaltic rock fragments, affectionately named A, B, C, and ρ, were separated from the Kapoeta meteorite. Rb-Sr and $^{40}Ar/^{39}Ar$ isotopic analyses have been obtained on these clasts (PAPANASTASSIOU *et al.*, 1974; PAPANASTASSIOU and WASSERBURG, 1976; RAJAN *et al.*, in preparation) and ρ contains ^{244}Pu and ^{129}I decay products (ROWE, 1970). In this paper, we present the results of petrographic and electron-microprobe studies of these isotopically-dated rock fragments.

In addition, we have studied several other lithic clasts and numerous mineral fragments in thin sections of Kapoeta in order to outline the range in lithology and chemistry of the source materials from which the Kapoeta meteorite was derived. We compare our data to data from other meteorite and lunar samples, and discuss the consequences of our observations for the evolution of the Kapoeta parent body, *assuming that the source for the regolith from which the Kapoeta meteorite was derived was representative of the Kapoeta parent body.*

II. ANALYTICAL TECHNIQUES

All of the data points plotted on the various diagrams represent analyses performed on a single spot consecutively for 8–16 elements in groups of three using a MAC-5-SA3 electron microprobe interfaced to a PDP-8/L computer for control and on-line data processing. Operating conditions were uniformly 15 kV accelerating voltage and 0.05 μA sample current (on brass), with beam current integration and pulse height selection. Elements with peak to background ratios greater than five (about 1 wt % of the oxide) are determined to a counting statistic precision of 1% or better. Minor elements (< 1 wt %) are usually counted for 90 sec, which yields a counting statistic precision of better than 10% for elements present in amounts greater than ~0.1 wt %. Reproducibility on two 'known unknowns' (a garnet and feldspar) over a period of 13 months ranges from 1½% (for elements with abundances greater than 1%) to 3% of the amount present (for elements with abundances of 0.1–1.0%) (CHAMPION *et al.*, 1975). The analytical procedure is described in detail by CHODOS *et al.* (1973).

All mineral compositions reported in the text are in terms of molecular proportions based on the following scheme: plagioclase, % An = 100 [Ca/(Ca + Na + K + Ba + Fe + Mg)]; pyroxene, % Wo = 100 [Ca/(Ca + Mg + Fe + Mn)], % En = 100 [Mg/(Ca + Mg + Fe + Mn)], % Fs = 100 [(Fe + Mn)/(Ca + Mg + Fe + Mn)]; and olivine, % Fo = 100 [Mg + Fe + Mn)].

Microprobe point counts, 'average' mineral compositions, and calculated bulk-chemical compositions (Tables 1, 3 and 4) were obtained using techniques modified from those of GANCARZ and ALBEE (1973). The mineral compositions reported in these tables are analyses of individual sample points that correspond as closely as possible to the 'average' as determined by the point count.

III. SAMPLING PROCEDURE

Four fragments of pyroxene plagioclase rock were extracted from portions of the Kapoeta meteorite with tungsten tweezers. Three of these (A, B, C) were sharply-bounded, cm-sized clasts that were removed from material held in the Caltech meteorite collection. The fourth fragment (ρ) was provided by M. W. Rowe (Texas A & M University) who described it as an "...angular gram-sized pebble... Kapoeta extra dark" (ROWE, 1970, p. 1020). Polished micro thin-sections were prepared from tiny chips of each fragment and the remainder reserved for isotopic studies. Grain mounts were prepared of the mineral separates used in the isotopic analyses. In addition, several pieces of the Kapoeta meteorite were examined with a binocular microscope and polished micro thin-sections were subsequently prepared from selected chips.

IV. PETROGRAPHY AND MINERALOGY OF ISOTOPICALLY-DATED BASALTIC ROCK FRAGMENTS

A. *Basalt Clast A*

Clast A is a fragment of a fine-grained, granulitic-textured basaltic rock comprised of plagioclase (47%), pyroxene (47%), and tridymite (5%), with minor amounts of ilmenite, Ti-rich chromite, Fe-metal, and troilite. Phase abundances, 'average' phase compositions, and a calculated bulk composition, based on a computer-controlled electron microprobe point count of thin section FQM-316 (area ≈ 12 mm^2), are listed in Table 1.

The plagioclase and pyroxene are anhedral and subequant, range in size from ~0.2 to 1 mm, and form a partially-annealed, granular texture that is characterized by straight to slightly-curved grain boundaries, and 120° triple junctions (Fig. 1A). Some of the plagioclase and pyroxene grains appear to be recrystallized remnants of larger, mm-sized single crystals. In general, these phases are clear, and remarkably free of inclusions. However, a few plagioclase grains enclose rounded granules of pyroxene and/or opaque minerals. The latter occur predominantly in interstitial positions.

Tridymite is pale brown and slightly turbid, and forms polygonal grains up to ~0.5 mm that contain inclusions of rounded plagioclase and angular pyroxene. In addition, scattered grains of tridymite (10–50 μm) occur along pyroxene-plagioclase boundaries.

Clast A shows some evidence of shock such as undulose extinction in a few grains, and very minor cataclasis. In addition, it is partly mantled by the meteorite fusion crust. Despite these secondary effects, the original form of the grains, and their mutual relationships, are well-preserved.

There is no evidence of compositional zoning in any of the minerals. The plagioclase has a measured range in composition from An_{88} to An_{90}, and contains only small amounts of minor elements (Fig. 2). The pyroxene is dark brown, relatively Fe-rich, and consists of alternating lamellae of hypersthene (~ $Wo_2En_{36}Fs_{62}$; $2V_x$ ~ 56) and augite (~ $Wo_{40}En_{30}Fs_{30}$; $2V_z$ ~ 49) (e.g. Fig. 1B) in exsolution relationship. In addition, some hypersthene lamellae have a second set of lamellae normal to the direction of the first set. This suggests two episodes of exsolution.

The relations among the pyroxenes in Clast A strongly resemble those of inverted pigeonite in terrestrial plutonic rocks (HESS, 1941), and in certain lunar samples (PAPIKE and BENCE, 1972). Hence we infer that the pyroxene in Clast A evolved from homogeneous pigeonite with composition near $Wo_{12}En_{33}Fs_{55}$ that underwent extensive post-crystallization, subsolidus exsolution and inversion at a relatively high-temperature due to prolonged slow cooling.

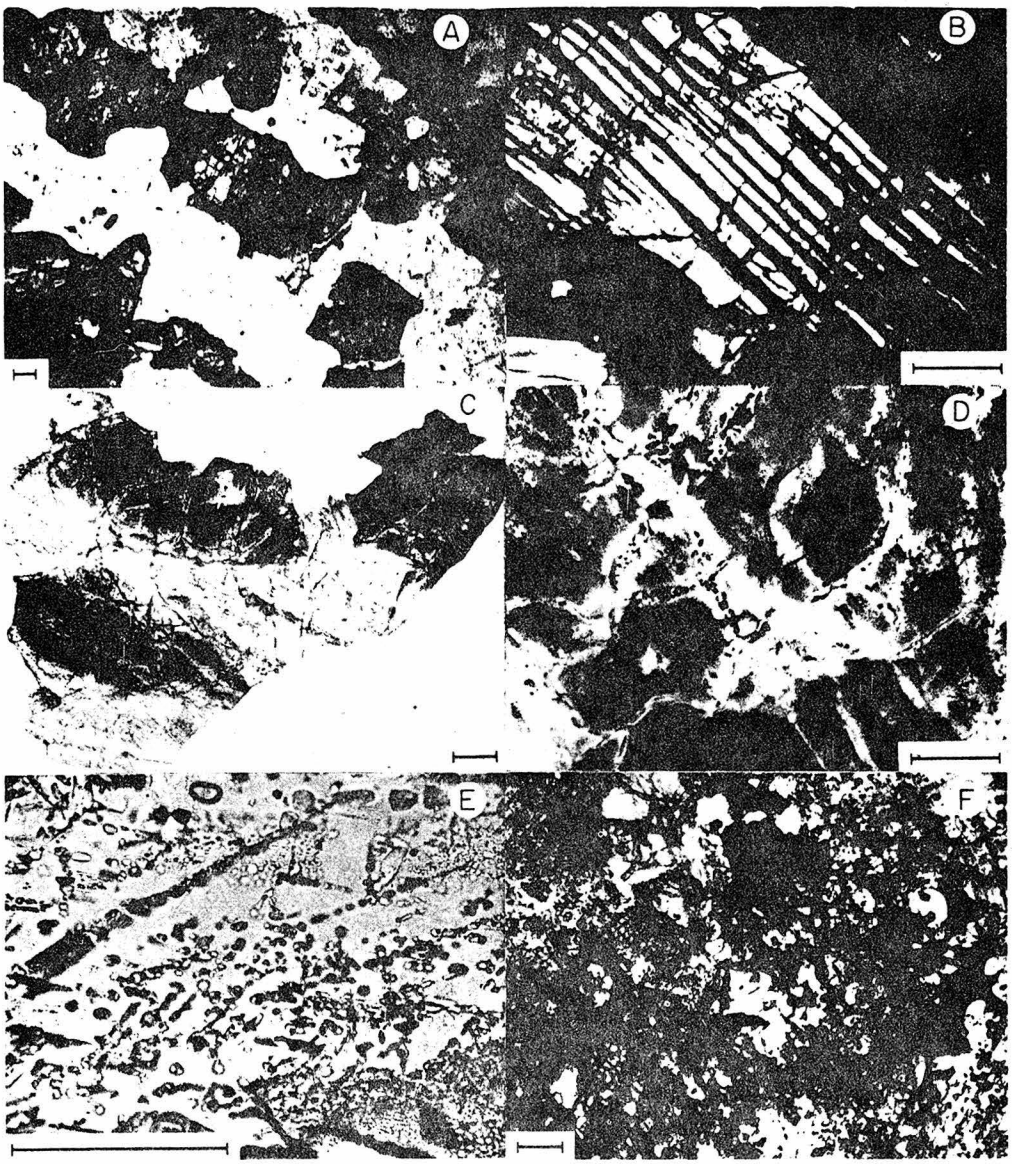

Fig. 1. Photomicrographs of textural relations in Basalt Clasts A and B. (All bar scales = 50 μm.) (A) Plane-polarized light; anhedral plagioclase (light) and pyroxene (dark) grains forming granulite-like texture in Clast A. (B) Cross-polarized light; an example of coarse exsolution in pyroxene grain in Clast A (light lamellae are hypersthene, dark lamellae are augite). (C) Plane-polarized light; anhedral pyroxene (dark) and plagioclase (light) grains in small fragments of Clast B. Note the abundant inclusions in these phases, and the conspicuous fractures that transect grain boundaries. (D) Plane-polarized light, conoscopic illumination; close-up of ilmenite inclusions in pyroxene grain, Clast B. The dark specks along the bleach zones (healed fractures?) are also ilmenite. (E) Plane-polarized light; close-up of inclusions in plagioclase grain in Clast B, most appear to be pyroxene. (F) Plane-polarized light; opaque-rich region in Clast B. SiO_2, Ca-phosphate and a K-rich phase occur here, and these are termed mesostasis areas (see text).

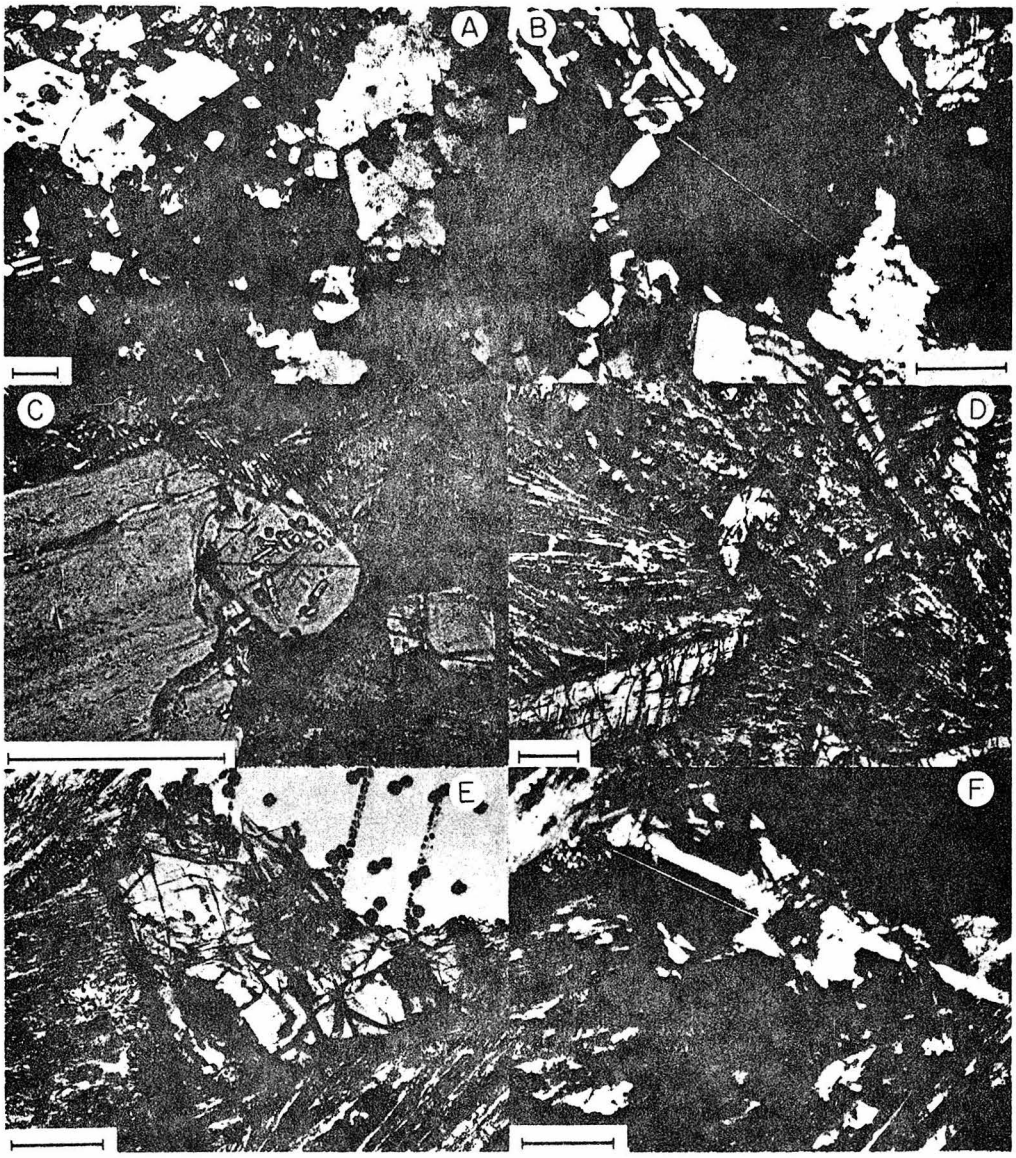

Fig. 5. Photomicrographs of textural relations in Basalt Clasts C and ρ. (All bar scales = 100 μm.) (A) Plane-polarized light; poikilitic textured portion of Clast C. Note the tiny plagioclase inclusions in pyroxene, and the euhedral form of much of the plagioclase. (B) Cross-polarized light, conoscopic illumination; strongly zoned plagioclase grain in Clast C. Note the optical discontinuity separating the core (dark gray) from rim (light gray), note also that the extreme margin of this grain is darker than the rest of the rim indicating a zoning reversal. The white line shows the location of the microprobe traverse illustrated in Fig. 6 (Plag. Grain no. 1, top). (C) Plane-polarized light; zoned plagioclase grain in Clast C; note the ring of pyroxene inclusions that separate core from rim. The black line indicates the location of the microprobe traverse shown in Fig. 6 (Plag. Grain no. 2, bottom). (D) Plane-polarized light; porphyritic texture of Clast ρ. Note bladed and skeletal form of pyroxene phenocrysts. (E) Plane-polarized light; pyroxene phenocryst with hollow core, Clast ρ. Note the textural similarity between groundmass material surrounding the phenocryst, and the core material. Black dots in upper right corner are burn marks in epoxy. (F) Cross-polarized light view of pyroxene phenocryst illustrated in Fig. 5E. Note the optical discontinuity between core (bright) and rim (dark). The thin white line shows the location of the microprobe traverse illustrated in Fig. 7. The thick white bar parallel to this traverse line is a twin lamella.

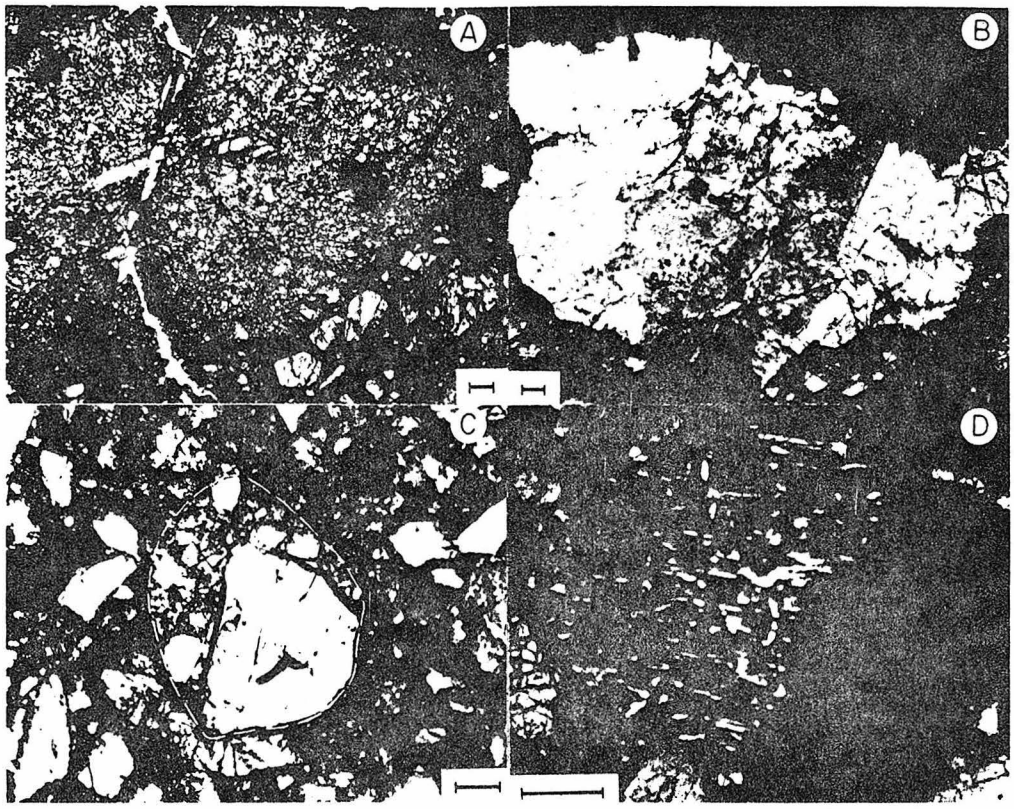

Fig. 9. Photomicrographs of various clasts in Kapoeta. (All bar scales = 100 μm). (A) 'Basaltic' clast with thermally-metamorphosed (hornfels) texture. (B) 'Pyroxenite' clast comprised of a coherent polycrystalline aggregate of pyroxene with composition $Wo_1En_{76}Fs_{24}$. (C) 'Pyroxenite' clast comprised of brecciated pyroxene fragments with composition $Wo_3En_{69}Fs_{28}$ (dashed line indicates boundary of clast). (D) Vermicular exsolution in pyroxene grain from 'pyroxenite' clast.

Table 1. Kapoeta-Basalt Clast A—phase abundances, 'average' phase compositions, and bulk-chemical composition

	PLAGIOCLASE	HYPERSTHENE	AUGITE	ILMENITE	CHROMITE	METAL*	TRIDYMITE	BULK COMPOSITION
Vol %	47.4_1	35.5_7	10.7_6	0.2_6	0.1_0	$< 0.0_1$	5.8_8	(Calculated-953
± 1σ	2.2_3	1.9_3	1.0_6	0.1_6	0.1_0	-	0.7_9	points)
Wt %	41.5_7	41.6_1	12.0_4	0.3_9	0.1_6	< 0.01	4.2_4	
SiO_2	46.04	49.92	51.53	0.13	0.20	n.a.	98.30	50.26
TiO_2	0.06	0.17	0.39	51.82	10.86	n.a.	0.16	0.37
Al_2O_3	34.65	0.09	0.64	0.21	4.92	n.a.	0.17	14.53
Cr_2O_3	n.a.	0.05	0.20	0.17	38.87	n.a.	n.a.	0.11
MgO	< 0.01	12.56	10.34	0.44	0.43	n.a.	0.02	6.48
CaO	18.22	2.44	19.51	n.a.	n.a.	n.a.	0.03	10.94
FeO	0.28	33.87	16.55	45.47	40.57	97.00	0.17	16.45
MnO	n.a.	1.06	0.55	0.88	1.04	n.a.	n.a.	0.53
BaO	0.05	n.a.	n.a.	n.a.	n.a.	n.a.	0.07	0.02
Na_2O	1.15	< 0.01	0.12	n.a.	n.a.	n.a.	0.02	0.49
K O	0.07	n.a.	n.a.	n.a.	n.a.	n.a.	0.11	0.03
ZrO_2	n.a.	n.a.	n.a.	0.03	< 0.01	n.a.	n.a.	< 0.01
V_2O_3	n.a.	n.a.	n.a.	n.a.	0.58	n.a.	n.a.	< 0.01
Nb_2O_5	n.a.	n.a.	n.a.	< 0.01	< 0.01	n.a.	n.a.	< 0.01
Ni	n.a.	n.a.	n.a.	n.a.	n.a.	< 0.01	n.a.	< 0.01
Co	n.a.	n.a.	n.a.	n.a.	n.a.	0.20	n.a.	< 0.01
SUM	100.52	100.17	99.82	99.15	97.46	97.20	99.05	100.21
An	89.1	Wo 5.0	Wo 40.0					
Ab	9.9	En 36.8	En 30.0					
Or	0.4	Fs 57.5	Fs 27.8					
Others	0.6	0.7	2.2					

* Elemental abundances.
n.a. = not analyzed.
$[(Fe/Fe + Mg)]_{Molar} = 0.587$ (total rock).

The range in pyroxene compositions shown in Fig. 2 may be caused by inability to resolve the exact composition of the lamellae due to their small size (2–20 μm), or it may represent a range in composition caused by continuous down-temperature equilibration. The presence of exsolution in two directions is consistent with the latter interpretation.

The ilmenite and chromite are Mg-poor, and the chromite is TiO_2-rich (up to 12 wt %). Troilite and Fe-metal occur separately. The metal has a very low nickel content (<0.1 wt % Ni), and we infer that it crystallized from the melt, and did not form by reduction of the sulfide. The low Ni-content may indicate that Ni was stripped from the melt by fractionation of olivine or an earlier metal phase.

Clast A is characterized by both textural and chemical equilibrium, as evidenced by the granulite-like texture, the lack of zoning in the plagioclase, and the extensive subsolidus reactions in the pyroxene. These observations suggest prolonged slow cooling in a plutonic or hypabyssal environment. The parental rock unit from which Clast A was derived could have been a ferrobasalt that formed via crystallization–differentiation from a more-magnesian magma but it could also have formed from a melt of its own composition. The preservation of tridymite limits the maximum pressure to <3 kbar.

B. *Basalt Clast B*

Clast B is a fragment of fine-grained granular basaltic rock comprised of pyroxene (~50%) and plagioclase (~45%), and ~1% each of ilmenite, troilite, and Fe-metal. Small amounts of Ti-rich chromite, SiO_2, Ca-phosphate, and a rare K-rich phase are also present. The mode presented here is an optical estimate. A point count was not performed because one of the two thin sections studied is unusually enriched in opaque phases and not representative of the clast in general, and the other is a grain mount of binary and multi-mineral aggregates (e.g. Fig. 1C) which may also not be representative of the clast in general. Analyses of the various phases in Clast B are listed in Table 2.

Most of the pyroxene grains are pale-green to pale-brown in color (≤1 mm), and contain numerous oriented needles and platelets of an Fe–Ti oxide phase (Fig. 1C). Locally, the pyroxene is crosscut by 'bleached zones' along which tiny grains (<10 μm) of ilmenite, plagioclase, and rarely troilite occur. This 'bleaching' is also present at the margins of many of the pyroxene crystals. Here, some of the pyroxene has recrystallized into colorless aggregates of 10–20 μm polygonal grains. Grains of ilmenite and SiO_2 (up to 100 μm) are associated with this polygonal pyroxene. Since the pyroxene adjacent to these 'bleach' zones is free of oxide inclusions we infer that the ilmenite in this association formed via granular exsolution from the pyroxene, but the origin of the plagioclase, SiO_2, and troilite is unclear.

As in Clast A, the pyroxene is iron-rich, and shows almost no variation in Fe/Mg (Fig. 3). The pyroxene was originally pigenoite, some of which is still preserved ($\sim Wo_{11}En_{35}Fs_{54}$; $2V_z \sim 5°$). However, the majority of the pyroxene now consists of grains comprised of alternating lamellae of augite ($\sim Wo_{38}En_{31}Fs_{31}$; $2V_z \sim 48°$) and hypersthene ($\sim Wo_5En_{37}Fs_{58}$; $2V_x \sim 55°$). Many of these exsolved pyroxene grains show a characteristic herringbone texture. In addition, some of the low-Ca pyroxene has not inverted to the orthorhombic form and occurs as 'clinohypersthene' ($2V_z \sim 14°$). A few discrete grains of augite and hypersthene also occur, with compositions not unlike those in the exsolved grains.

The plagioclase ranges from pale-brown and translucent, to colorless or pale-green and transparent, with coloration caused by numerous, irregularly-distributed inclusions of two types. The first are tiny (~1 μm) rounded granules that tend to be concentrated in the central portions of the grains, and are of unknown composition. The second are acicular to ovoid to amoeboid blebs of a pale-green, transparent phase (Fig. 1E). The larger ones are pyroxene with compositions similar to the pyroxene elsewhere in the sample; the smaller ones are inferred to be pyroxene

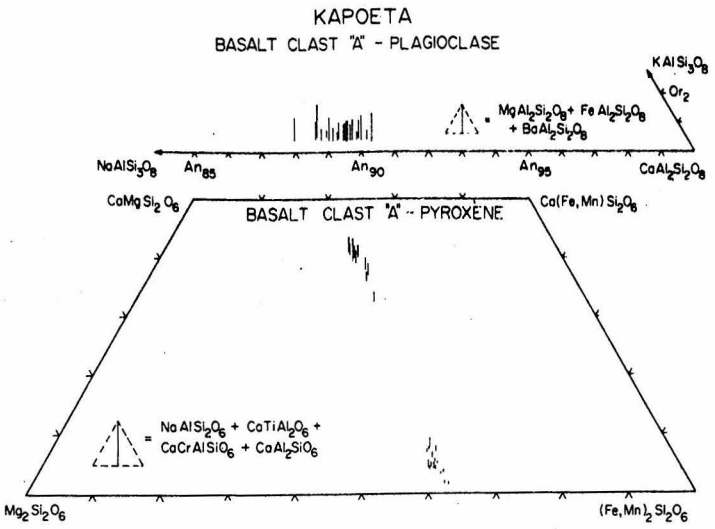

Fig. 2. Compositions of the pyroxene and plagioclase in Clast A. The vertical lines represent the altitudes of triangles that correspond to the amount of minor element substitution as indicated in the figure.

also. Locally, these have orientations that appear to be crystallographically-controlled; some form a curvilinear array like a string of sausages.

These inclusions in the plagioclase could be tiny grains of pyroxene that were occluded during growth of the plagioclase, or they may be melt inclusions, with only the pyroxene remaining after crystallization of plagioclase on to the 'walls' of the inclusion. Alternatively, these may have formed by exsolution from the plagioclase during cooling (or later heating). A few rare inclusions of SiO_2 were also found in the plagioclase.

The plagioclase is optically and chemically zoned (An_{73}–An_{95}; Fig. 3). In general, the zoning within individual grains is normal (up to 8 mole % An), but some grains also show irregular variations in An-content. The zoning is symmetric about grain boundaries, and there is nothing to suggest that it is not a primary feature, i.e. there are no phases with which the plagioclase could react to change its composition. The large variation in the minor element content of the plagioclase shown in Fig. 3 is due in part to contribution of Fe and Mg from the inclusions.

Portions of the rock are unusually rich in opaque phases (Fig. 1F). Grains of troilite, Fe-metal (<0.1 wt % Ni), and ilmenite (up to 300 μm across) are intergrown with pyroxene. A few grains of chromite and SiO_2 (quartz and tridymite), and rarely Ca-phosphate (fluoroapatite and REE-

Table 2. Kapoeta–Basalt Clast B—representative mineral analyses

	PLAGIOCLASE	HYPERSTHENE	PIGEONITE	AUGITE	ILMENITE	CHROMITE	SiO_2	MESOSTASIS	METAL*	WHITLOCKITE	APATITE
P_2O_5	n.a.	n.a.	n.a.	n.a.	n.a.	n.a.	n.a.	n.a.	n.a.	43.23	40.78
SiO_2	47.14	49.24	48.67	50.33	0.07	0.12	99.21	51.24	n.a.	0.20	0.15
TiO_2	< 0.01	0.13	0.36	0.41	52.46	11.01	0.03	0.03	n.a.	n.a.	n.a.
Al_2O_3	33.75	0.12	0.14	0.46	< 0.01	5.33	0.02	29.83	n.a.	0.20	< 0.01
Cr_2O_3	n.a.	0.06	0.54	0.52	0.09	40.25	n.a.	n.a.	n.a.	n.a.	n.a.
MgO	0.02	12.92	11.55	10.63	0.97	0.71	< 0.01	< 0.01	n.a.	2.49	0.04
CaO	17.15	1.24	5.28	19.00	n.a.	n.a.	0.01	14.55	n.a.	43.01	56.50
FeO	0.11	35.43	32.30	17.63	45.72	41.45	0.41	0.07	98.83	1.82	0.12
MnO	n.a.	1.00	0.98	0.54	1.02	0.95	n.a.	n.a.	n.a.	n.a.	n.a.
BaO	< 0.01	n.a.	n.a.	n.a.	n.a.	n.a.	0.02	0.10	n.a.	n.a.	n.a.
Na_2O	1.64	0.01	0.06	0.06	n.a.	n.a.	0.01	2.04	n.a.	0.76	< 0.01
K_2O	0.14	n.a.	n.a.	n.a.	n.a.	n.a.	0.01	2.96	n.a.	n.a.	n.a.
ZrO_2	n.a.	n.a.	n.a.	n.a.	< 0.01	< 0.01	n.a.	n.a.	n.a.	n.a.	n.a.
V_2O_3	n.a.	n.a.	n.a.	n.a.	< 0.01	0.38	n.a.	n.a.	n.a.	n.a.	n.a.
Nb_2O_5	n.a.	n.a.	n.a.	n.a.	< 0.01	< 0.01	n.a.	n.a.	n.a.	n.a.	n.a.
Ni	n.a.	n.a.	n.a.	n.a.	n.a.	n.a.	n.a.	n.a.	0.03	n.a.	n.a.
Co	n.a.	n.a.	n.a.	n.a.	n.a.	n.a.	n.a.	n.a.	0.20	n.a.	n.a.
F	n.a.	n.a.	n.a.	n.a.	n.a.	n.a.	n.a.	n.a.	n.a.	< 0.01	4.11
Cl	n.a.	n.a.	n.a.	n.a.	n.a.	n.a.	n.a.	n.a.	n.a.	0.01	0.09
Y_2O_3	n.a.	n.a.	n.a.	n.a.	n.a.	n.a.	n.a.	n.a.	n.a.	1.86	0.02
RE_2O_3	n.a.	n.a.	n.a.	n.a.	n.a.	n.a.	n.a.	n.a.	n.a.	4.92†	0.33†
SUM	99.95	100.15	99.88	99.58	100.33	100.20	99.72	100.82	99.06	98.49‡	100.32‡
	An 84.1	Wo 2.4	Wo 10.6	Wo 37.9							
	Ab 14.5	En 37.6	En 33.6	En 30.1							
	Or 0.8	Fs 59.5	Fs 54.4	Fs 28.9							
	Others 0.6	0.5	1.4	3.1							

* Elemental abundances.

† Calculated based on measured abundances of La_2O_3, Ce_2O_3, and Nd_2O_3 assuming $(REE_{mineral}/REE_{chondrite})$ = constant for all REE.

‡ Minus oxygen for F, Cl; n.a. = not analyzed.

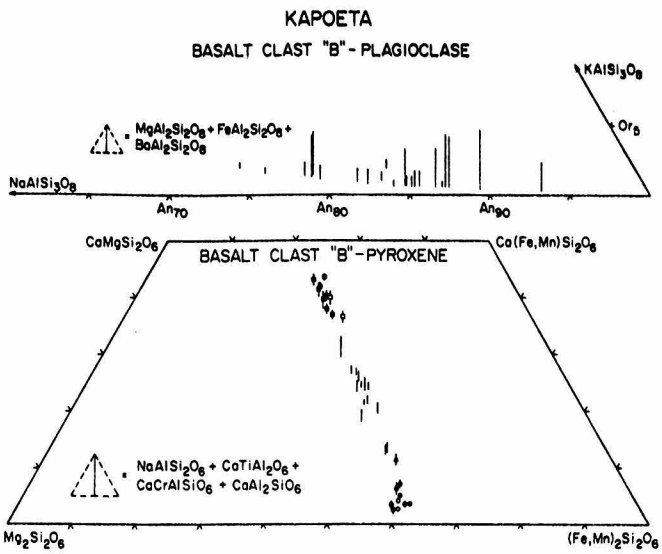

Fig. 3. Compositions of the pyroxene and plagioclase in Clast B. Open symbols represent the compositions of discrete pyroxene grains (○ □) the triangle represents the composition of unexsolved pigeonite (▲); the filled symbols (● ■) represent the compositions of the high- and low-Ca lamellae in exsolved pyroxene grains; the lines without symbols represent compositions of pyroxene that are inferred to represent mixtures of augite and hypersthene.

bearing whitlockite) and a K-rich phase, are also present. The pyroxene in this association occurs both as the typical exsolved grains similar to its occurrence elsewhere in the rock, and as discrete separate grains of hypersthene and augite. The latter have compositions similar to the pyroxenes that occur in exsolution relationship, and we infer that they represent totally unmixed pigeonite. These areas probably represent a type of late-crystallizing 'mesostasis' as indicated by the presence of SiO_2, Ca-phosphate, and K-rich material. In addition, the abundance of troilite may indicate that a late-stage sulfur-rich fluid was present. However, the fact that some of the pyroxene is totally unmixed, in contrast to its occurrence elsewhere in the rock, suggests that there has been some secondary heating perhaps caused by a small degree of thermal metamorphism, or related to introduction of hot sulfur-rich solutions.

The textural and chemical features displayed by the pyroxene and plagioclase suggest a complex history that we infer to be the following. (1) Original crystallization as a pigeonite–bytownite rock with small amounts of residual (trapped?) melt from which the minor phases formed. The relationships among the phases are consistent with an origin as either a differentiated (cumulate) ferrobasalt or by crystallization from a melt of the same composition. (2) A period of annealing during which the pyroxene underwent partial exsolution and inversion, the oxide rods and plates exsolved from the pyroxene, and some tridymite inverted to quartz. (3) Further recrystallization occurred that resulted in granular exsolution of ilmenite from pyroxene, and caused the development of the fine-grained polygonal pyroxene aggregates.

The fact that the plagioclase has not been homogenized, nor has the pyroxene undergone *complete* exsolution and inversion indicates that Clast B has not been as extensively annealed as Clast A. Whether the areas of the rock that are enriched in opaque phases resulted from introduction of material at a later time, are related to redistribution of material during subsequent thermal metamorphism, or are related to primary crystallization, is not clear. In addition, whether the complexities in the rock are the result of prolonged slow cooling or caused by a combination of cooling and later thermal events is not known. However, the original texture of Clast B indicates that it, like Clast A, formed under hypabyssal or plutonic conditions.

C. *Clast C*

Basalt Clast C is a fragment of fine-grained, subophitic-textured basaltic rock comprised of pyroxene (~60%) and plagioclase (~40%), with minor amounts of tridymite, chromite, ilmenite, Ca-phosphate, and Fe-metal. No troilite was observed. Phase abundances, 'average' phase compositions, and a calculated bulk composition, based on a computer-controlled electron microprobe point count of thin section FQM-316 (area ≈ 20 mm^2), are listed in Table 3.

Plagioclase in Clast C occurs in two ways. Small (up to 50 μm), tabular to equant grains occur as scattered inclusions within pyroxene (Fig. 5A). These are unzoned, and relatively constant in composition (~ An_{80}). The remainder of the plagioclase occurs as euhedral prismatic to polygonal grains up to 250 μm across. Some occur as inclusions within pyroxene (Fig. 5A), but most occur at boundaries between adjacent pyroxene grains. Many contain rounded (1–10 μm) inclusions of pyroxene. These plagioclase grains have a measured range in composition from An_{82} to An_{95} and are strongly zoned (up to 10 mole % An in a single grain). Many contain cores (often clouded) that are separated from clear rims by a conspicuous optical discontinuity in most cases (Fig. 5B). In addition, the boundary between core and rim is sometimes marked by a ring of pyroxene inclusions (Fig. 5C).

Detailed microprobe traverses were performed on several grains to investigate the nature of the zoning. Results of traverses across the large plagioclase grains in Fig. 5B (Grain no. 1) and Fig. 5C (Grain no. 2) are illustrated in Fig. 6, and demonstrate that the zoning is quite complex, yet symmetric and systematic. Traverses across the plagioclase grains enclosed in poikilitic SiO_2, reveal reverse zoning from An_{85} (core) to An_{90} (rim); the extreme outer edge shows a sharp decrease in An-content to ~ An_{84}. This drop in An-content at the margins of the plagioclase grains is a pervasive feature (c.f., Fig. 6), and is marked by a slight optical discontinuity. As mentioned

Table 3. Kapoeta–Basalt Clast C—phase abundances, 'average' phase compositions, and bulk-chemical composition

	PLAGIOCLASE	HYPERSTHENE	PIGEONITE	AUGITE	CRISTOBALITE	CHROMITE	WHITLOCKITE	BULK COMPOSITION	LUNAR MARE BASALT 15486
Vol %	38.6_6	0.4_0	58.0_1	1.4_1	1.3_0	0.1_1	0.1_1	(Calculated-	(Cuttitta et al.,
± 1σ	1.4_5	0.1_3	1.8_1	0.2_8	0.2_7	$.0_8$	$.0_8$	1772 Points)	1973)
Wt %	33.4_9	0.4_6	63.2_7*	1.5_6	0.9_6	0.1_8	0.1_1		
P_2O_5	n.a.	n.a.	n.a.	n.a.	n.a.	n.a.	43.60	0.05	0.13
SiO_2	46.40	49.18	50.05	49.97	98.96	0.07	0.24	49.16	48.25
TiO_2	< 0.01	0.34	0.44	1.02	0.19	3.12	n.a.	0.31	1.81
Al_2O_3	34.17	0.32	0.73	1.11	0.57	7.49	0.20	11.94	10.00
Cr_2O_3	n.a.	0.40	0.35	0.37	n.a.	47.35	n.a.	0.31	0.50
MgO	< 0.01	13.47	13.66	11.45	< 0.01	2.78	2.57	8.89	8.80
CaO	17.48	1.57	5.85	15.44	0.11	n.a.	43.18	9.85	10.25
FeO	0.14	32.96	28.52	19.85	0.03	36.04	1.99	18.61	19.85
MnO	n.a.	1.11	0.96	0.64	n.a.	1.06	n.a.	0.62	0.29
BaO	0.05	n.a.	n.a.	n.a.	< 0.01	n.a.	n.a.	0.01	n.r.
Na_2O	1.51	0.06	0.03	0.07	0.03	n.a.	0.83	0.53	0.37
K_2O	0.12	n.a.	n.a.	n.a.	0.26	n.a.	n.a.	0.04	0.08
ZrO_2	n.a.	n.a.	n.a.	n.a.	n.a.	0.66	n.a.	< 0.01	n.r.
V_2O_3	n.a.	n.a.	n.a.	n.a.	n.a.	0.34	n.a.	< 0.01	n.r.
Nb_2O_5	n.a.	n.a.	n.a.	n.a.	n.a.	< 0.01	n.a.	< 0.01	n.r.
F	n.a.	n.a.	n.a.	n.a.	n.a.	n.a.	< 0.01	< 0.01	n.r.
Cl	n.a.	n.a.	n.a.	n.a.	n.a.	n.a.	0.01	< 0.01	n.r.
Y_2O_3	n.a.	n.a.	n.a.	n.a.	n.a.	n.a.	1.41	< 0.01	n.r.
RE_2O_3	n.a.	n.a.	n.a.	n.a.	n.a.	n.a.	6.80*	< 0.01	n.r.
SUM	99.85	99.61	100.58	99.93	100.18	98.89	100.84†	100.32	100.33
An	85.4	Wo 2.7	Wo 11.0	Wo 30.5					
Ab	13.3	En 39.5	En 39.2	En 33.0					
Or	0.7	Fs 56.1	Fs 47.5	Fs 33.1					
Others	0.6	1.7	2.3	3.4					

* Calculated based on measured abundances of La_2O_3, Ce_2O_3, and Nd_2O_3 by assuming $(REE_{mineral}/REE_{chondrite})$ = constant for all REE.

† less oxygen for F, Cl.

n.a. = not analyzed.

n.r. = not reported.

$[(Fe/Fe + Mg)]_{Molar} = 0.540$ (total rock).

above, the smaller plagioclase inclusions in pyroxene are unzoned.

The presence of well-formed plagioclase inclusions in pyroxene suggests that some of the plagioclase crystallized before pyroxene. These inclusions, together with the cores in the larger grains may represent early-formed cumulate crystals, whereas the rims on the larger plagioclase grains may represent adcumulus overgrowths.

Pyroxene occurs as anhedral grains up to ~1 mm, and consists predominantly of pale, red-brown, relative iron-rich pigeonite (~$Wo_{13}En_{37}Fs_{50}$). These grains are crosscut by numerous curved fractures (Fig. 5A), and many contain abundant (001) polysynthetic twins. As shown in Fig. 4, there is a range in the Ca-content of the pigeonite. This variation is consistent with the observed range in optic axial angle ($2V_z$ = 0–14°), and does not appear to be a result of exsolution.

However, a few pigeonite grains do contain exsolution lamellae. Analyses of the high- and low-Ca end-members yield compositions ~$Wo_{23}En_{37}Fs_{40}$ and ~$Wo_3En_{41}Fs_{56}$,

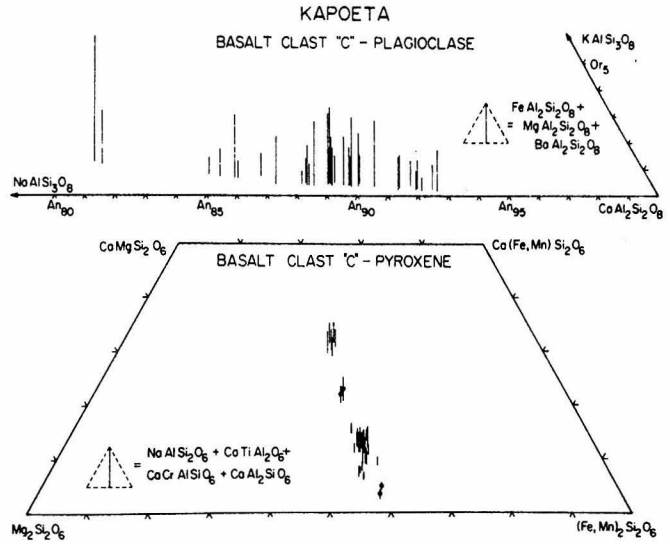

Fig. 4. Compositions of the pyroxene and plagioclase in Clast C. The data points with the filled circles (●) represent the compositions of high- and low-Ca lamellae in an exsolved pigeonite grain.

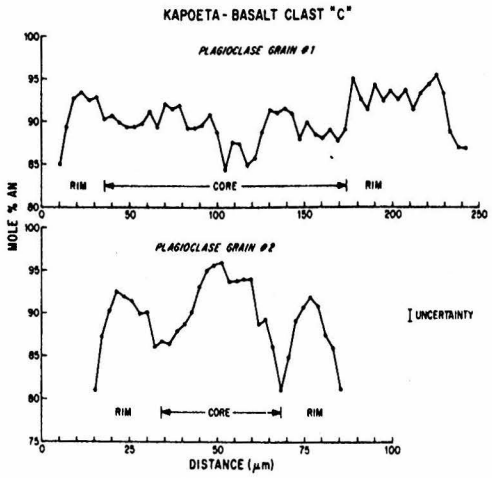

Fig. 6. Radial variation in plagioclase composition from grains depicted in Fig. 5B (Plag. Grain no. 1) and 5C (Plag. Grain no. 2). Each point on this diagram represents 15 sec of accumulated counts for Ca, K, and Na corrected for background and dead time converted to % An by comparison to complete microprobe analyses on the same grains.

and are distinguished by a special symbol (♦) in Fig. 4. The small size of these lamellae prevented reliable determination of optical properties. A few rare grains of homogeneous pale-pink augite ($\sim Wo_{33}En_{34}Fs_{33}$; $2V_z = 44°$) are also present. As in Clast A and B, there is very little variation in Fe/Mg in the pyroxene here.

Tridymite occurs as tiny ($\leq 10\,\mu m$) anhedral grains at boundaries between plagioclase and pyroxene, as rare inclusions in pyroxene, and as large poikilitic grains up to 100 μm across. Rare grains of chromite, ilmenite, REE-bearing whitlockite, and Fe-metal occur along plagioclase–pyroxene grain boundaries, but the Fe-metal also occurs as inclusions in plagioclase. Energy dispersive analyses indicate that the metal is very poor in nickel ($\lesssim 0.1$ wt % Ni).

The coexistence of pigeonite and augite, the general lack of exsolution in the pigeonite, the preservation of pronounced zoning in the plagioclase, and the preservation of tridymite indicate that the Clast C crystallized originally at a high temperature, cooled relatively rapidly, and was not modified by subsequent thermal events. As with Clast A and B, it is not clear whether Clast C crystallized from a melt of the same composition, or is a differentiate from a more-magnesium parent magma. However, we prefer the interpretation that Clast C is partly cumulate in origin, and does not represent a primary magma composition.

D. *Basalt Clast ρ*

This sample is a fragment of fine-grained porphyritic basalt (Fig. 5D) that consists of pale-brown pyroxene microphenocrysts (~40%) set in a holocrystalline, variolitic-textured groundmass comprised of acicular plagioclase (~25%) and subequant to acicular brown pyroxene (~35%). Minor amounts of SiO_2, chromite, ilmenite, Ca-phosphate, Fe-metal, and troilite are also present. The minor phases occur intergrown with plagioclase and pyroxene in the groundmass but chromite also occurs as phenocrysts. Phase abundances, 'average' phase compositions, and a calculated bulk-chemical composition of this clast, based on a computer-controlled electron microprobe point count of thin section FQM-354 (area ≈ 15 mm^2), are presented in Table 4. Texturally, this clast strongly resembles some Apollo 12 and 15 pyroxene-phyric basalts (Dowty *et al.*, 1974), but the composition of the phenocrysts is very different.

These pyroxene phenocrysts range up to 2 mm in length. Some are skeletal and hollow, some have swallow-tail form, whereas others have an euhedral outline. They all contain material in their cores that resembles the surrounding groundmass (Fig. 5E). Rare inclusions of chromite are present in a few phenocrysts.

Many of the phenocrysts display lamellar structures 1–25 μm in width (e.g. Fig. 5F). Detailed microprobe traverses across these features did not resolve compositional

Table 4. Kapoeta–Basalt Clast ρ—phase abundances, 'average' phase compositions, and bulk-chemical composition

	PLAG.	LOW-CA PYROX.	MED-CA PYROX.	HIGH-CA PYROX.	SiO_2	ILMENITE	CHROMITE	CA-PHOS.†	METAL*	BULK COMPOSITION
Vol %	31.2_0	23.4_5	19.0_6	21.3_0	3.8_7	0.6_0	0.2_2	0.2_2	0.0_7	(Calculated-
± 1σ	1.5_2	1.3_2	1.1_9	1.2_6	0.5_4	0.2_1	0.1_3	0.1_3	0.0_7	1343 Points)
Wt %	26.4_3	26.2_7	20.1_1	22.8_0	2.7_9	0.8_8	0.3_5	0.2_1	0.1_7	
P_2O_5	n.a.	n.a.	n.a.	n.a.	n.a.	n.a.	n.a.	43.15	-	0.09
SiO_2	47.36	49.95	49.33	48.92	98.63	0.20	0.07	-	-	49.47
TiO_2	< 0.01	0.21	0.35	0.83	< 0.01	51.22	5.57	-	-	0.78
Al_2O_3	32.82	0.73	1.56	2.92	< 0.01	1.00	9.19	-	-	9.88
Cr_2O_3	n.a.	0.95	1.13	1.10	n.a.	0.91	46.18	-	-	0.90
MgO	0.27	16.29	15.05	11.90	0.05	0.92	1.02	-	-	10.10
CaO	16.69	1.66	4.48	15.24	0.20	n.a.	n.a.	54.54	-	9.34
FeO	0.85	29.64	27.67	19.44	0.50	45.70	36.61	-	100.00	18.77
MnO	n.a.	0.91	0.81	0.54	n.a.	0.92	0.98	-	-	0.54
BaO	0.05	n.a.	n.a.	n.a.	0.11	n.a.	n.a.	-	-	0.01
Na_2O	1.71	0.04	< 0.01	0.01	< 0.01	n.a.	n.a.	-	-	0.47
K_2O	0.14	n.a.	n.a.	n.a.	0.02	n.a.	n.a.	-	-	0.04
ZrO_2	n.a.	n.a.	n.a.	n.a.	n.a.	< 0.01	< 0.01	-	-	< 0.01
V_2O_3	n.a.	n.a.	n.a.	n.a.	n.a.	< 0.01	0.24	-	-	< 0.01
Nb_2O_5	n.a.	n.a.	n.a.	n.a.	n.a.	< 0.01	< 0.01	-	-	< 0.01
F	n.a.	n.a.	n.a.	n.a.	n.a.	n.a.	n.a.	2.31	-	< 0.01
SUM	99.89	100.38	100.37	100.89	99.52	100.86	99.86	100.00	100.00	100.39
An	79.4	Wo 1.9	Wo 6.6	Wo 26.8						
Ab	14.7	En 46.2	En 42.8	En 33.5						
Or	0.8	Fs 48.6	Fs 45.5	Fs 31.6						
Others	5.1	3.3	5.1	8.1						

* Elemental abundances; assumed pure Fe-metal based on energy dispersive analysis. $[(Fe/Fe + Mg)]_{Molar} = 0.510$ (total rock).

† Assumed 1:1 mixture of fluorapatite and 'whitlockite'.

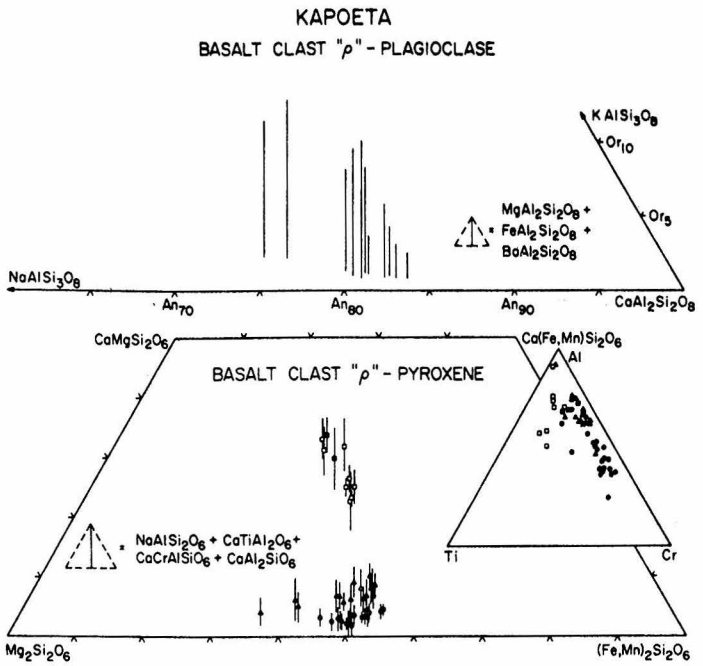

Fig. 7. Compositions of pyroxene and plagioclase in Basalt Clast ρ. Open symbols represent groundmass compositions, closed symbols represent phenocryst compositions. (● = low-Ca pyroxene; ▲ △ = medium-Ca pyroxene; □ ■ = high-Ca pyroxene; see text for discussion). Inset illustrates variation in Al, Ti, and Cr in pyroxene.

differences between adjacent lamellae, although the small size of some would make chemical distinction difficult. These may be multiple (001) twins, but exsolution cannot be ruled out. In addition, a few simple (100) twins are present.

The groundmass crystals tend to radiate from the margins of the phenocrysts, and in general, the boundary between the groundmass and phenocrysts is distinct (Fig. 5D). Locally, however, the phenocrysts are optically continuous with adjacent pyroxene grains that extend into the groundmass. This suggests that the growth of the pyroxene phenocrysts was in part coincident with the crystallization of the groundmass.

The pyroxene in this sample shows a considerable range in Fe/(Fe + Mg) and Ca-content that appears to have resulted from melt–crystal interaction. Three groups have been recognized that are distinguished primarily on the basis of calcium content. These compositional differences can be correlated with petrographic occurrence, and the pyroxene types are distinguished by special symbols in Fig. 7.

Low-Ca pyroxene ($Wo_2En_{55}Fs_{43}$–$Wo_4En_{42}Fs_{54}$) occurs only in phenocrysts; medium-Ca pyroxene ($Wo_4En_{55}Fs_{41}$–$Wo_{10}En_{40}Fs_{50}$) occurs predominantly in phenocrysts, but a few grains were identified in the groundmass. Both types appear to be pigeonite ($2V_z \sim 0$–$15°$). The high-Ca pyroxene ($Wo_{25}En_{35}Fs_{40}$–$Wo_{33}En_{35}Fs_{32}$) is the predominant groundmass pyroxene, and is also present at the margins of some phenocrysts. It is an augite with $2V_z \sim 30$–$40°$. High-Ca pyroxene occurs as overgrowths on both low- and medium-Ca, but low- and medium-Ca pyroxene are only rarely present in the same grain.

Some phenocrysts are complexly zoned, as demonstrated by the presence of marked undulose or wavy extinction. A microprobe traverse across the grain shown in Fig. 5E,F is illustrated in Fig. 8. The data shown in the figure demonstrate that there is a significant change in Fe/(Fe + Mg), with only a slight gradual variation in Ca. Assuming that Fe/(Fe + Mg) increases with progressive crystallization, we can infer from the profile in Fig. 8 that this grain grew

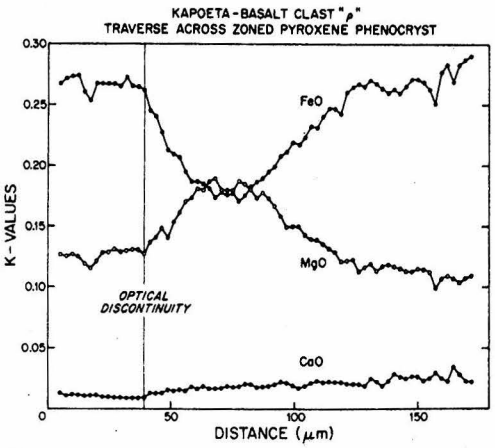

Fig. 8. Radial variation in composition of zoned pyroxene phenocryst illustrated in Fig. 5E and 5F. Each point represents 15 sec of accumulated counts corrected for background and dead time; K-values are the ratios of counts per sec per unit of beam current for each oxide in the sample to the same oxide in the appropriate standard, and are approximately equal to wt %. Left-hand portion of the traverse begins in the center of the pyroxene phenocryst, right-hand portion terminates at the edge of the pyroxene phenocryst, i.e. traverse data is reversed from orientation of photograph. Note that Fe/Fe + Mg increases in both directions suggesting that the phenocryst grew both inward and outward into the melt.

both inward and outward into the melt, as is suggested by the hollow core. The nature of the pronounced optical discontinuity in the center of the grain shown in Fig. 5F is not known.

Variations in the relative amounts of Al–Ti–Cr in the pyroxene in this clast are illustrated in Fig. 7 (inset). There is an increase in the relative amount of Al (and also the absolute amount) from low- to medium- to high-Ca pyroxene in phenocrysts. This trend towards Al-enrichment is consistent with crystallization of pyroxene in the absence of plagioclase caused by metastable incorporation of Al into pyroxene during quenching. Most of the groundmass pyroxene, which crystallized with plagioclase, is depleted in Al, as shown by the trend away from the Al-corner of this diagram. Similar patterns are known from studies of pyroxene in the Apollo 15 pyroxene-phyric basalts (cf. WIEGAND and HOLLISTER, 1973).

The plagioclase ranges in composition from An_{76} to An_{84}, and is anomalously iron-rich. The small size of the plagioclase, and its fine intergrowth with pyroxene makes analysis difficult; the iron content may be enhanced due to secondary fluorescence from the adjacent pyroxene.

Chromite occurs as 20–50 μm inclusions in pyroxene, and ilmenite is present as irregularly distributed 1–10 μm granules throughout the groundmass. The SiO_2 has the characteristic mosaic fracture pattern suggestive of cristobalite. Metal and troilite occur separately; energy dispersive analysis showed the metal to be extremely poor in nickel ($\lesssim$0.1 wt % Ni). A few tiny (<5 μm) grains of Ca-phosphate are also present.

The texture and mineralogy of this sample suggest the following crystallization sequence: chromite and low-calcium pigeonite formed first, with the pigeonite increasing in Fe/(Fe + Mg) as crystallization progressed; the pyroxene reacted with the melt to form augite, and a final quenching resulted in the precipitation of augite, plagioclase and the other minor phases during the formation of the groundmass. The variation in the Ca-content of the pigeonite may be a result of submicroscopic exsolution, caused by nucleation and growth of certain grains at different times, or controlled by sector-growth phenomena. However, since we could not verify the presence of exsolution with the microprobe, and since no hourglass structures were observed, the cause of this phenomena is not clear.

We conclude from the texture (Fig. 5D) that Clast ρ is derived from a quenched surface flow. The skeletal form of the pyroxene phenocrysts, the apparent overlap in the time of crystallization of some phenocrysts with the groundmass, the anomalous pyroxene compositions, and the major and minor element zoning of the phenocrysts are consistent with *in situ* quench crystallization of a melt of approximately the same composition, as has been shown for lunar basalts with similar textures (c.f. DOWTY *et al.*, 1974). Alternatively, if Clast ρ formed via fractional crystallization, the crystallization sequence of the minerals in this sample indicate that such fractionation could have involved only an Mg-rich, low-Ca pyroxene. In either case, this suggests that the Kapoeta parent body was capable of generating lavas of a highly differentiated character [i.e. relatively high Fe/(Fe + Mg)].

Stolper (written communication, 1975) has indicated that, from an experimental viewpoint, a lava with the bulk composition of Clast ρ, would be in equilibrium with a low-Ca pyroxene that is more-magnesian than the most Mg-rich identified by us. If this observation is meaningful, then it permits the interpretation that a portion of the pyroxene phenocrysts are cumulate in origin, and that the melt composition from which Clast ρ formed would have a higher Fe/(Fe + Mg) than is actually observed.

There does not seem to be any textural evidence for crystal settling in this sample, and the disparity between the observed pyroxene composition and that inferred from experimental work could be due to pronounced undercooling of the melt. Alternatively, we may not have analyzed the most Mg-rich low-Ca pyroxene.

A comparison of the bulk compositions of Clast A, C, and ρ (Tables 1, 3 and 4), and of the pyroxene compositions in Clasts A, B, C, ρ (Fig. 2, 3, 4, and 7) indicates that although ρ is relatively iron-rich, it is more-magnesian than the others. Hence, it is possible that a magma with the composition of ρ could by fractional crystallization accompanied by slower cooling, yield rocks like A, B, and C.

V. PETROGRAPHY AND MINERALOGY OF OTHER LITHIC CLASTS

A. *Basaltic clasts*

Twenty-four rock fragments identified in thin sections of Kapoeta are comprised predominantly of subequal amounts of pyroxene and plagioclase. These are termed 'basaltic', and can be divided into two principal textural types. (1) Clasts that have porphyritic–variolitic and intergranular to subophitic textures (some of which resemble Clasts C and ρ) are inferred to be volcanic in origin.

(2) Clasts that have granular, recrystallized textures (some of which resemble Clast A and B) have a range in grain size ($\sim$10 μm to $\sim$2 mm), and are inferred to be hypabyssal/plutonic rocks, and thermally-metamorphosed volcanic rocks. Some of the latter resemble terrestrial hornfels (e.g. Fig. 9A).

The basaltic rock fragments all contain relatively iron-rich pyroxene [Fe/(Fe + Mg) $\gtrsim$ 0.4], not unlike that in Clasts A, B, C, and ρ. The range in $Fe/(Fe + Mg)_{pyx}$ in each fragment is small ($\sim$0.1), and the total range from fragment to fragment is only slightly larger. As is shown in Fig. 10, the range in pyroxene composition is similar in both recrystallized-granular and in volcanic-textured clasts.

Pyroxene grains in the recrystallized-granular fragments are not zoned, and consist of pigeonite or its exsolved counterpart—augite and hypersthene. Pyroxene in the igneous-textured clasts consists of pigeonite, augite, and hypersthene (?). Some grains are zoned, and the zoning resembles that of the pyroxene in Clast ρ.

Plagioclase in these basaltic fragments has a total range in measured composition from An_{78} to An_{95}, but the range in any given fragment is only 2–10 mole % An. Some clasts contain zoned plagioclase (up to $\sim$6 mole % An), but most are relatively homogeneous. The K-content of the plagioclase is uniformly low ($<$0.3 wt % K_2O). Many plagioclase grains in the coarser-grained recrystallized-granular clasts contain rounded to irregularly-shaped blebs of pyroxene.

Minor phases in the basaltic fragments include ilmenite, titanium-rich and titanium-poor chromite, SiO_2, Ca-phosphate, troilite, and Fe-metal ($\lesssim$0.1 wt % Ni). No potassium-rich mesostasis was found in any of the fragments studied.

B. *Pyroxenitic fragments*

Seven rock fragments were identified in thin sections of Kapoeta that are comprised almost exclusively of Mg-rich pyroxene. Although these clasts may represent fragments of relatively coarse-grained noritic or gabbroic rocks, they are termed 'pyroxenitic', because they contain no plagioclase. These clasts are either coherent polycrystalline aggregates (Fig. 9B) or monomict-breccias (Fig. 9C). In addition, there are many single crystal fragments of Mg-rich, low-Ca pyroxene that are as large as many of the rock fragments (up to 1 mm). These are discussed below with mineral fragments.

The pyroxene in these fragments is homogeneous with Fe/(Fe + Mg) $\lesssim$ 0.4, but there is a considerable variation from fragment to fragment (Fig. 10). Four contain only

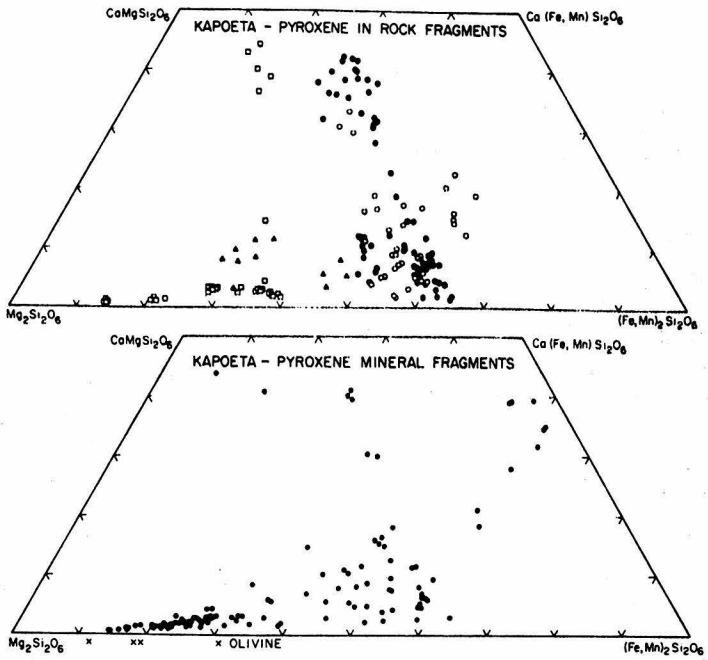

Fig. 10. Composition of pyroxene in rock fragments and mineral fragments in Kapoeta. Note that although the compositional range is large, the overlap is almost total. (□ = pyroxenite fragments; ▲ = vitric breccia fragments; ○ = basaltic fragments with igneous textures; ● = basaltic fragments with recrystallized textures.)

bronzite, two contain hypersthene and diopside, and one fragment consists of diopside and magnesian pigeonite. Part of this pigeonite has undergone vermicular exsolution to hypersthene and diopside (Fig. 9D). Minor phases in these pyroxenitic fragments include chromite, SiO_2, Fe-metal (5–40 wt % Ni), and troilite. No plagioclase or olivine was found.

The coarse grain size of the pyroxene in these fragments (up to a few mm), and the magnesium-rich composition of the pyroxene suggests that the rock units from which they were derived may have been plutonic cumulates.

C. *Vitric breccia fragments*

Part of the evidence that supports a complex, multiple-impact evolution for the regolith from which the Kapoeta meteorite-breccia was derived is the presence of vitric breccia fragments. Four of these fragments are characterized by a dense, dark-brown, aphanitic matrix. This matrix appears to be a combination of a very-fine grained mineral debris and (devitrified) glass. The compositions of this matrix material resembles the glass fragments that occur in Kapoeta.

The vitric breccia clasts contain inclusions of basaltic rock fragments, single-crystal fragments of pyroxene and (maskelynitized) plagioclase, and crushed granular aggregates of pyroxene. The compositions of pyroxene in the vitric breccia clasts, exclusive of that in the basaltic inclusions, are illustrated in Fig. 10. The vitric breccia fragments are inferred to represent shocked, melted, and lithified regolith.

D. *Other clasts*

WILKENING (1973) reported the occurrence of rare carbonaceous chondrite fragments in Kapoeta. We have likewise observed these, and interpret them to be the result of meteoritic infall on the Kapoeta parent body.

VI. MINERAL FRAGMENTS

Rock fragments form only a small portion of the Kapoeta meteorite ($\lesssim 10\%$), and the vast majority of this object is comprised of a variety of mineral fragments. These are predominantly pyroxene and plagioclase (pyroxene/plagioclase ~ 2/1), with small amounts of ilmenite, chromite, SiO_2, olivine, Ca-phosphate, Fe Ni metal, and troilite. The relative abundances of these phases are consistent with derivation from material not unlike the observed rock fragments.

FREDRICKSSON and KEIL (1963, Figs. 7 and 8) reported a large variation in the composition of the pyroxene mineral fragments in Kapoeta. Our analyses of pyroxene grains overlap those reported by them, but extend the range in compositions from Mg-bronzite to ferrohedenbergite (Fig. 10). The compositions and textures displayed in pyroxene mineral fragments correspond very closely to those which occurs in the rock fragments, except that the source of the ferrohedenbergite is not known.

The composition of plagioclase grains ranges from An_{75} to An_{96}, and corresponds closely to that in the basaltic fragments. The olivine ranges in composition from Fo_{88} to Fo_{69}. WILKENING (1973) has shown that some of the carbonaceous chondrite fragments in Kapoeta contain olivine-bearing chondrules. Hence, some of the olivine identified by us may be a condritic component.

VII. DISCUSSION

Many workers have contributed data and observations that establish the basic similarities between howardite meteorites and lunar soil breccias (WILKENING *et al.*, 1971; JEROME and MICHEL-LEVY, 1972; REID, 1974; BUNCH, 1975; DYMEK *et al.*, 1975a; PRINZ

et al., 1975). Howardites are inferred to have originated in an impact-derived regolith on their parent bodies, and our observations on Kapoeta support such a model.

However, it should be emphasized that howardites are not strictly analogous to lunar soil breccias. This is especially true with respect to the low abundance of glass particles in howardites. Whether this difference reflects contrasting residence times in the regoliths on their respective parent bodies, or is related to the mechanics of impact processes (e.g. differing gravitational attraction) is not known. Lunar soils and soil breccias provide a good statistical sampling of lithologic units at each landing site, from which important conclusions have been deduced regarding local and regional lunar geology (c.f. BENCE *et al.*, 1974; DYMEK *et al.*, 1974). It seems logical then to extend this approach developed in the study of clastic lunar samples to howardites.

In this section, we summarize our data on mineral and lithic clasts in an attempt to outline and understand: (a) the petrologic makeup of the Kapoeta meteorite; (b) the isotopic constraints on the evolution of the Kapoeta parent body; (c) the relationship between materials in Kapoeta and other achondrites; (d) the similarities and/or differences between the Kapoeta parent body and the Earth's Moon; (e) the relationships among the materials in the Kapoeta meteorite, and (f) inferences regarding the evolution of the Kapoeta parent body.

A. *Petrologic characteristics of the Kapoeta meteorite*

Our study of rock fragments in the Kapoeta meteorite indicates that two major lithologies predominate. (1) Pyroxene- and plagioclase-bearing 'basaltic' rocks with Fe/(Fe + Mg) $\lesssim$ 0.4. These show a remarkable range in texture suggesting origins both in volcanic and in hypabyssal/plutonic environments. (2) Pyroxene-bearing, plagioclase-free 'pyroxenitic' rocks with Fe/(Fe + Mg) $\lesssim$ 0.4. These are coarse-grained and appear to have originated in plutonic-hypabyssal environments. This dual classification scheme does not imply two compositionally distinct source lithologies, but rather, as can be seen in the range in pyroxene compositions in Fig. 10, a continuum in source rock composition.

These compositions, textures and relative abundances of individual mineral fragments indicates their derivation from source materials similar to the rock fragments. We have not identified the source of olivine and ferrohedenbergite among rock fragments, but these constitute only an extremely small portion of the mineral fragments. In summary, the overwhelming majority of fragments in the Kapoeta meteorite can be related to derivation from a relatively-few recognizable rock types that are considered to be representative of the surface and near-surface lithologies of the Kapoeta parent body.

B. *Isotopic constraints on the evolution of the Kapoeta parent body*

Isotopic studies have been completed on each of the four basaltic clasts that have been studied in detail petrographically (PAPANASTASSIOU *et al.*, 1974; PAPANASTASSIOU and WASSERBURG, 1976; RAJAN *et al.*, in preparation). The correlation of petrographic observations with isotopic data places constraints on the origin of these fragments, and sets limits on any model for the evolution of the Kapoeta parent body.

Clast C has yielded a Rb-Sr internal isochron age of 4.54 $\pm$ 0.12 AE and an initial $^{87}Sr/^{86}Sr$ isotopic composition (I-value) of 0.69885 $\mp$ 4 (PAPANASTASSIOU and WASSERBURG, 1976). This I-value is very low, and indicates the primitive nature of the source region from which Clast C was derived. In addition, a plagioclase separate from Clast C provides a $^{40}Ar/^{39}Ar$ age that is consistent with the Rb-Sr age (RAJAN *et al.*, in preparation).

The textural and mineralogical characteristics of Clast C indicate that this fragment has the features of an igneous rock. There is no petrographic evidence to suggest that it has been modified by subsequent metamorphism. We interpret these observations to indicate that Clast C resulted from magmatism, perhaps related to planetary differentiation, and that the isotopic ages represent the time of primary igneous crystallization. The I-value for Clast C indicates that the initial Sr-isotopic composition of the Kapoeta parent body was distinctly less than BABI (=0.69898). It thus appears that the parent bodies of at least two meteorites [Kapoeta and Angra dos Reis (PAPANASTASSIOU, 1970)] produced igneous differentiates that preserved primitive I-values over the time scale of early planetary differentiation.

Basalt Clast ρ is a fragment of a quenched surface flow. All mineralogic and petrographic evidence indicates that this sample has not experienced any recognizable metamorphism since its original crystallization. This clast contains ^{244}Pu fission xenon and ^{129}Xe produced from the decay of ^{129}I (ROWE, 1970). The presence of decay products of these extinct radionuclides is very important, and indicates that the Kapoeta parent body formed very early in the history of the solar system, and suggests, but does not prove, that Clast ρ formed on a time scale of a few tens of millions of years thereafter. We emphasize that these decay products are associated with a discrete fragment of igneous rock, and not with a nondescript mineral aggregate. Hence, it is plausible that the excess xenon observed by ROWE (1970) was generated by *in situ* decay and not implanted at a later time, although this contention cannot be proven.

An $^{40}Ar/^{39}Ar$ release spectrum indicates an age of $\gtrsim$4.6 AE for Clast ρ (RAJAN *et al.*, in preparation). A total rock Rb–Sr analysis yielded a measured $^{87}Sr/^{86}Sr$ = 0.69937 $\pm$ 14, which, when extrapolated back to 4.6 AE, provides an I-value = 0.69903 $\pm$ 14 (PAPANASTASSIOU and WASSERBURG, 1976). This

I-value is primitive, but slightly higher than the *I*-value for Clast C. However, the errors are too large to infer the existence of a magma reservoir with a different isotopic composition from that of Clast C.

We conclude from our petrographic observations, taken in conjunction with all the isotopic studies, that Clast ρ formed as a result of planetary magmatic processes, and that such magmatism occurred within a time scale of <100 my after the formation of the Kapoeta parent body.

Clasts A and B have yielded Rb Sr internal isochron ages of 3.89 ± 0.05 AE and 3.63 ± 0.08 AE, and *I*-values of 0.69888 ∓ 5 and 0.69905 ∓ 6, respectively (PAPANASTASSIOU *et al.*, 1974). These ages are distinctly younger than the Rb Sr age for Clast C, yet the *I*-values are very low and similar to the *I*-value for Clast C. These low *I*-values indicate that the source regions from which these samples were derived had very primitive Sr, and an extremely low Rb/Sr ratio.

An $^{40}Ar/^{39}Ar$ study of a plagioclase separate from Clast A provided a gas retention age greater than 3.9 AE, with evidence for extensive argon loss ~3.5 AE ago (RAJAN *et al.*, in preparation). A plagioclase separate from Clast B yielded a complex $^{40}Ar/^{39}Ar$ release pattern suggesting an age greater than 4.5 AE, much older than the age determined by the Rb–Sr method. In no part of the argon release spectrum of the Clast B plagioclase were the apparent ages less than 4.37 AE. The discrepancies between the two isotopic methods are discussed extensively by RAJAN *et al.* (in preparation).

Based on our petrographic observations, basalt Clast A is highly recrystallized, whereas basalt Clast B shows moderate recrystallization. Hence, it appears that the Rb–Sr age for Clast A is most plausibly interpreted as the time of recrystallization, and not the time of primary crystallization from a melt. The Rb Sr age for Clast B is also most plausibly interpreted as the time of recrystallization, while the $^{40}Ar/^{39}Ar$ systematics may reflect the time of primary crystallization.

These interpretations are compatible with the low *I*-values, but require that Clasts A and B have very low Rb/Sr as total rock systems, if they formed originally at 4.6 AE and were 'metamorphosed' at 3.9 and 3.6 AE respectively. Since the Rb–Sr ages are highly dependent on the phases most enriched in Rb, which in all clasts are silica phases, it is possible that the recrystallization affected these low abundance phases in such a way that their radiogenic strontium was redistributed without enhancing $^{87}Sr/^{86}Sr$ of the rock. Since the $^{40}Ar/^{39}Ar$ ages of the plagioclase are dependent on the K–Ar in a major abundance mineral phase, then we must argue that the plagioclase is less susceptible to redistribution. Alternatively, Clasts A and B could have formed originally in an environment that was essentially free of Rb, such that the Rb–Sr ages for them mark a time at which Rb was added to each system.

There are no petrographic observations on Clast A that either support or reject these possibilities. However, in Clast B, the areas that are enriched in opaque phases are associated with silica and a K-rich phase, and, as indicated in our description of that fragment, the textural features in these portions of the clast could have resulted from late addition of material.

As has become evident from studies of lunar and terrestrial materials, there are, in general, no clear-cut petrographic criteria that can be used to determine whether a given parent–daughter isotopic system has been disturbed. Nor are there any *a priori* criteria to determine the relative sensitivity of different parent–daughter systems to processes of recrystallization. By identifying significant changes in mineralogy brought about by recrystallization, we may reasonably argue that the resulting isotopic systematics reflect recrystallization. Whether or not the recrystallization was separated in time significantly from the original igneous process must depend on an adequate understanding of the isotopic data.

In summary, the correlation of petrologic and isotopic data for these four basaltic fragments indicates that the Kapoeta parent body underwent differentiation very early in its history (~4.5–4.6 AE), and that 'basaltic' magmas preserved in Clasts C and ρ were among the products of this differentiation. The young Rb–Sr ages of Clasts A and B may not represent times of magmatic activity, but rather times of recrystallization at 3.6–3.9 AE or younger. At present, there is no strong evidence that magmatic activity on the Kapoeta parent body occurred at times later than ~4.5 AE, although such younger magmatic processes have clearly been documented for the Earth, Moon, Mars, Mercury, and the meteorites Kodaikanal (BURNETT and WASSERBURG, 1967) and Nakhla (PAPANASTASSIOU and WASSERBURG, 1974).

C. *Relationship between Kapoeta and other achondritic meteorites*

JEROME and GOLES (1971) and MCCARTHY *et al.* (1972, 1973), on the basis of bulk-chemical and trace element data, have proposed that howardites are physical mixtures of eucrites (basaltic achondrites) and diogenites (hypersthene achondrites). The presence of both basaltic and pyroxenitic rock fragments in the Kapoeta howardite permits constraints to be placed on such a mixing model.

The basaltic rock fragments in Kapoeta have textures and mineral compositions that are similar to those in many of the eucrites described by DUKE and SILVER (1967). The bulk-chemical compositions of Clasts C and ρ are similar to eucrites as outlined by MASON (1967). In addition, the composition and subsolidus exsolution of the pigeonite in many of the basaltic fragments (e.g. Clast A) is similar to that reported for the Moore County (HESS and HENDERSON, 1949) and Juvinas eucrites (TAKEDA *et al.*, 1974).

Hence, there is little doubt that the basaltic fragments in Kapoeta have many strong affinities with eucrites.

The pyroxenite fragments in Kapoeta have a much wider range in Fe/(Fe + Mg) than that reported for diogenites by MASON (1963). In addition, we have examined three diogenites – Shalka, Tatahouine, and Johnstown – and our microprobe analyses indicate that the pyroxene in these do indeed have a very narrow range in composition ($Wo_{1-3}En_{72-76}Fs_{22-26}$). Hence, there is only a slight similarity between these diogenites and the pyroxenitic fragments in Kapoeta (see Fig. 10).

Although Kapoeta can be interpreted as a simple physical mixture of materials with 'basaltic' and 'pyroxenitic' bulk compositions, such mixing would involve materials not presently recognized as meteorites, and more than two simple end-member lithologies. Similar conclusions were reached by REID (1974) based on a study of the Macibini meteorite and by BUNCH (1975) based on a survey of several howardites.

D. *Comparison with the Earth's Moon*

The nature of rock fragments in the Kapoeta meteorite suggests that the Kapoeta parent body is petrologically unlike the Moon. Plagioclase-rich anorthositic rocks, feldspathic basalts, and high-titanium basalts, so characteristic of many lunar soils and soil breccias, are not present in Kapoeta. Moreover, coarse-grained pyroxenitic rocks, which are inferred to be abundant on the Kapoeta parent body, have not been recognized among the returned lunar samples. Fragments of Mg-rich orthopyroxene do occur in some soils, but the source for these are probably coarse-grained norites like 78235 (IRVING *et al.*, 1974).

MASON and MELSON (1970) and MELSON and MASON (1971) have shown that lunar mare basalts bear some textural and chemical affinities to eucritic meteorites. This comparison may be extended to the basaltic fragments in Kapoeta. The fact that these fragments are iron-rich, and contain relatively iron-rich pyroxene suggests that they are highly-evolved chemically, and are analogous to some lunar mare basalts, in particular the low-TiO_2 basalts from Apollo 12 and 15. A comparison of the bulk compositions of Clast A, C, and ρ with lunar sample 15486 (Table 3 and 4) demonstrates this similarity, except that the Kapoeta basalt fragments are lower in TiO_2. Another significant similarity is the low alkali content reflected in the low-Ab content of the plagioclase in both lunar mare basalts and Kapoeta basaltic fragments.

The presence of nickel-poor, Fe-metal phase in both lunar mare basalts and basaltic fragments in Kapoeta suggests that both rock types crystallized under conditions of very low oxygen fugacity. Most of the Kapoeta basaltic rock fragments contain late-stage SiO_2, analogous to lunar mare basalts; however, K-rich mesostasis is only rarely present in contrast to the lunar samples.

A major distinction between the basaltic fragments in Kapoeta and lunar mare basalts is their inferred environments of formation, and/or post-crystallization histories. Lunar basalts appear to have formed rapidly from surface flows or in very shallow intrusions and preserve most features of their primary crystallization, especially mineral zoning. A general lack of coarse exsolution in pyroxene in mare basalts is also a significant feature. In contrast, the basaltic rocks in Kapoeta appear to have evolved in surface, near-surface, and 'deep-seated' environments. Many show features suggesting prolonged slow cooling, i.e. phase homogeneity and exsolution.

SCHMITT and LAUL (1973) have demonstrated a strong linear correlation for the oxide pair FeO–MnO in lunar rocks, soil and breccias. The FeO/MnO value (~80) differs markedly from that in meteoritic or terrestrial silicate material. They found that the total rock values for achondrites scattered considerably, but WÄNKE *et al.* (1973) showed that the eucrite Juvinas, the howardite Kapoeta, and the diogenite Johnstown lie along a line with an FeO/MnO value near 35.

Figure 11 illustrates the FeO and MnO contents of pyroxenes in samples from all Apollo and Luna missions utilizing microprobe analyses from our own laboratory. These data scatter about a line with FeO/MnO near 60, slightly lower than the total rock value of 80.* The FeO and MnO contents of pyroxene in Kapoeta are also illustrated in Fig. 11. These also show a linear correlation with an FeO/MnO value identical to that of the total meteorite (~35), but quite different from that of the Moon. The FeO/MnO value for pyroxene in diogenites (Shalka, Tatahouine, and Johnstown) is identical to that in Kapoeta.

Clearly, these data indicate constant fractionation of FeO and MnO between pyroxene and rock. In Kapoeta, FeO and MnO occur almost exclusively in pyroxene (also true for diogenites), hence the fact that the pyroxene value is identical to the total rock value is expected. In lunar samples, various amounts of FeO and MnO occur in olivine and ilmenite, which have a higher FeO/MnO value than pyroxene. Hence the pyroxene value should be less than the total rock value, as is observed.

The difference between the FeO/MnO value in lunar samples and Kapoeta deserves some comment. WÄNKE *et al.* (1973) suggested that this number is strongly dependent on oxidation. Our observations indicate that the difference is not caused solely by differing oxidation states during crystallization of the rocks. Since both Kapoeta and lunar rocks contain Fe-metal, these rocks must have formed under conditions of similar and low f_{O_2}.

* In a previous paper, we reported incorrectly that the FeO/MnO value in lunar pyroxenes was the same as that in the rocks (DYMEK *et al.*, 1975a).

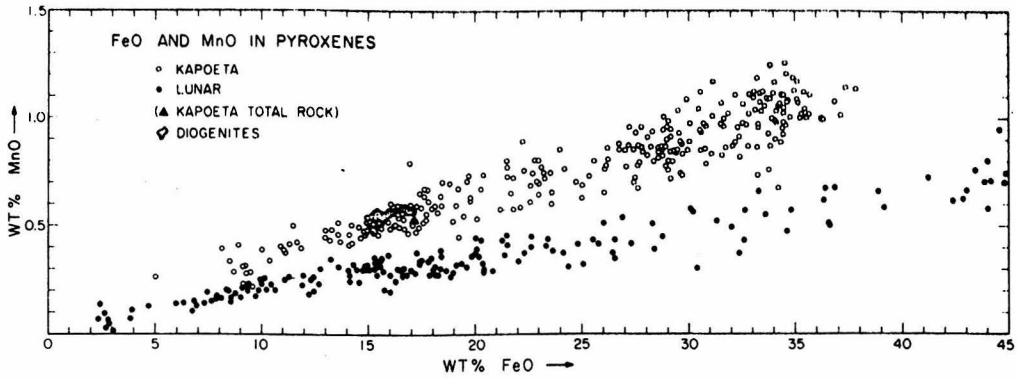

Fig. 11. Comparison of FeO and MnO contents of pyroxenes in Kapoeta and lunar samples. The Kapoeta total rock point is from MASON and WIIK (1966); field of diogenites are from our own analyses of Johnstown, Shalka and Tatahouine.

This difference indicates that the Kapoeta parent body accumulated in a different physical-chemical environment from the Moon, as suggested by SCHMITT and LAUL (1973), and that this difference results from varying initial oxide–metal proportions in primordial material. The oxygen isotope compositions of eucrites (TAYLOR *et al.*, 1965) are markedly different from lunar samples, and also support origins in differing chemical systems (TAYLOR and EPSTEIN, 1970), but additional isotopic data is required on the howardites proper.

SCHMITT and LAUL (1973) have interpreted the lunar data to indicate that the Moon underwent homogeneous accretion. Alternatively, these data could indicate that the lunar rocks are all derived from source regions that are fundamentally related by a primary planetary differentiation that yielded this homogeneity in FeO and MnO. The coherence of the pair FeO–MnO in Kapoeta pyroxenes suggests that the source regions of the rocks from which these rock and mineral fragments were derived are fundamentally related also.

Isotopic ages provide an additional basis for comparison. The ancient ages of Clast C and ρ provide good evidence that the Kapoeta parent body produced magmas with affinities to lunar mare basalts very shortly after its formation, in contrast to the Moon where such magmatism appears to have occurred during the interval 3–4 AE. In addition, we interpret this basaltic magmatism to be a consequence of primary planetary differentiation of the Kapoeta parent body. This is in marked contrast to the Moon where primary planetary differentiation produced rocks such as dunite, troctolite, norite, and anorthosite (DYMEK *et al.*, 1975b).

E. *Evolution of the Kapoeta parent body*

The range in the composition of pyroxene in Kapoeta (Fig. 10) is similar to the range observed in many terrestrial layered mafic plutons such as the Skaergaard (BROWN, 1957; BROWN and VINCENT, 1963). Thus it is possible that the Kapoeta meteorite represents the remains of differentiated igneous complexes that were comminuted and mixed by multiple impact events. Although restriction of plagioclase to those rocks with $Fe/(Fe + Mg)_{pyx} \gtrsim 0.4$ may be an accident, it seems more likely that this has important petrogenetic significance.

These observations, together with the occurrence of a rock fragment (Clast ρ) that may represent a quenched melt of appropriate composition, allows us to propose the following model for the evolution of the Kapoeta parent body: magmas with a bulk composition similar to that of Clast ρ were formed by partial melting in the interior of the Kapoeta parent body as a result of planetary differentiation (suggested by the 'old ages' of Clasts C and ρ). These magmas were either erupted at the surface to yield rocks with volcanic textures (e.g. Clast ρ) or emplaced at various depths to yield rocks with hypabyssal/plutonic textures (e.g. Clast A). Crystallization of such a magma would commence with the formation of Mg-rich orthopyroxene (and olivine?), with some Ni-rich Fe-metal. Bronzite orthopyroxenites would form at this time. Diopside joins the crystallization sequence and bronzite–diopside rocks accumulate. Orthopyroxene reacts with the melt to form Mg-rich pigeonite, and the separation of pigeonite and diopside yielded rocks from which the observed diopside–pigeonite clasts were derived. When the $Fe/(Fe + Mg)_{pyx}$ is about 0.4, plagioclase commences crystallization. The accumulation of plagioclase, pigeonite (continually increasing Fe/Fe + Mg), and minor augite produce the basaltic clasts. When the $Fe/(Fe + Mg)_{pyx}$ reached about 0.70, a two-pyroxene crystallization trend was replaced by a single pyroxene that changed composition towards ferrohedenbergite.

Whether augite formed together with pigeonite during the accumulation of the 'basaltic' fragments was probably controlled by slight differences in bulk composition of the magmas. The fact that we have not found the ferrohedenbergite in rock clasts may indicate that plagioclase ceased crystallization at an earlier time. Metamorphism (in ejecta blankets?) could

account for the secondary thermal effects observed in some clasts (e.g. hornfels texture). In addition, impact melting of regolith materials could produce other rocks of mixed compositions and volcanic textures.

In this model, the homogeneity of FeO MnO is explained by derivation of the parent magmas from similar source regions, coupled with fractional crystallization from separate magmas. The early appearance of an Ni-rich metal phase could account for the near absence of nickel in the metal phase in the 'basaltic' rocks, although olivine separation could accomplish the same effect. Although we have found little evidence for olivine fractionation, JEROME and MICHEL-LEVY (1972) reported a dunite fragment comprised of Mg-rich olivine in the howardite Washougal.

This model for the evolution of the Kapoeta parent planet is similar in many respects to that proposed by MASON (1967) for the achondrites in general. Our model differs from Mason's in that we relate specific rock fragments in a single meteorite rather than various meteorites that may or may not come from a single parent body. He invoked the fractionation of pyroxene to account for the sequence pallasite hypersthene achondrite howardite-eucrite. However, MASON (1967) invoked a magma with chondritic composition that does not satisfy some important chemical constraints, particularly the low abundance of alkalis in achondrites.

VII. SUMMARY AND CONCLUSIONS

The Kapoeta meteorite represents a lithified, polymict soil breccia that evolved in an impact-derived regolith on another planetary body, separate from the Earth and Moon. Detailed petrographic study reveals that two lithologic types are represented among rock fragments. One is 'basaltic' in composition and resembles eucrites, the other is 'pyroxenitic' in composition and slightly resembles diogenites. Although Kapoeta is a mixture of these two types of materials, no specific end members emerge. Instead there is a continuum in rock compositions.

In contrast to the Moon, a source of anorthositic rocks does not appear to have been present on the Kapoeta parent body. Thus, the petrologic evolution of the Kapoeta parent body, as indicated by the Kapoeta meteorite, involved chiefly pyroxene, whereas plagioclase played an important role in lunar evolution.

Microprobe analyses reveal that the basaltic fragments in Kapoeta contain relatively iron-rich pyroxene. Thus, they are highly-differentiated and analogous to some lunar mare basalts, but lower in TiO_2.

The FeO–MnO relationships suggest that the source of the materials in the Kapoeta parent planet are fundamentally related. This relationship may result from fractional crystallization of 'basaltic' magmas with Fe/(Fe + Mg) ~ 0.5, producing early-formed Mg-rich pyroxenites, and later-formed iron-rich basalts. Such magmas may be formed by partial melting of similar materials in which this FeO–MnO relationship already existed, or the materials in Kapoeta may be related to a primary planetary differentiation and subsequent modification by impact events.

Magmatic activity on the Kapoeta parent planet occurred very early in its history (4.5–4.6 AE), but, as yet, no unequivocal evidence exists for magmatism at later times.

Acknowledgements—We wish to thank Dr. A. H. ISHAG and Dr. A. WIDATALLA, Geological Survey of the Sudan, for their kind and generous cooperation in allowing us access to samples of Kapoeta. In addition, we wish to thank Dr. R. S. RAJAN for arranging the transfer of Basalt Clast ρ to this laboratory, and Dr. M. W. ROWE for providing us with this very important sample. We have benefited from discussions with M. DAILY, D. A. PAPANASTASSIOU, R. S. RAJAN, S. P. SMITH, and E. M. STOLPER. We would especially like to thank J. C. HUNEKE for extremely helpful discussions and encouragement throughout the course of this study. Our research on Kapoeta has been supported by NSF Grant GP-28027 and NASA Grant NGL-05-002-338. The microprobe laboratory has been developed with the support of the National Science Foundation, the Jet Propulsion Laboratory, and the Union Pacific Foundation. This paper has benefited from thorough reviews by A. M. REID and J. L. WARNER, and comments on the manuscript by R. BRETT and O. JAMES.

REFERENCES

BENCE A. E., DELANO J. W., PAPIKE J. J. and CAMERON K. L. (1974) Petrology of the highlands massifs at Taurus–Littrow: an analysis of the 2–4 mm soil fraction. *Proc. 5th Lunar Sci. Conf., Geochim. Cosmochim. Acta Suppl.* **5**, Vol. 1, pp. 785–827. Pergamon Press.

BROWN G. M. (1957) Pyroxenes from the early and middle stages of fractionation of the Skaergaard intrusion, East Greenland. *Mineral. Mag.* **31**, 511–543.

BROWN G. M. and VINCENT E. A. (1963) Pyroxenes from late stages of fractionation of the Skaergaard intrusion, East Greenland. *J. Petrol.* **4**, 175–197.

BROWNLEE D. E. and RAJAN R. S. (1973) Micrometeorite craters discovered on chondrule-like objects from Kapoeta. *Science* **182**, 1341–1344.

BUNCH T. E. (1975) Petrography and petrology of basaltic achondrite polymict breccias (howardites). *Proc. 6th Lunar Sci. Conf., Geochim. Cosmochim. Acta Suppl.* **6**, Vol. 1, pp. 469–492. Pergamon Press.

BURNETT D. S. and WASSERBURG G. J. (1967) Evidence for the formation of an iron meteorite at 3.8×10^9 years. *Earth Planet. Sci. Lett.* **2**, 137–147.

CHAMPION D. E., ALBEE A. L. and CHODOS A. A. (1975) Reproducibility and operator bias in a computer-controlled system for quantitative electron microprobe analysis. *Proc. 10th Natl Conf. Electron Probe Analyses*, 55A.

CHODOS A. A., ALBEE A. L., GANCARZ A. J. and LAIRD J. (1973) Optimization of computer-controlled quantitative analyses of minerals. *Proc. 8th Natl Conf. Electron Probe Analysis*, 45A.

CUTTITTA F., ROSE N. J., JR., ANNELL C. S., CARRON H. K., CHRISTIAN R. P., LIGON D. T., JR., DWORNIK E. J., WRIGHT T. L. and GREENLAND L. P. (1973) Chemistry of twenty-one igneous rocks and soils returned by the Apollo 15 mission. *Proc. 4th Lunar Sci. Conf., Geochim. Cosmochim. Acta Suppl.* **4**, Vol. 2, pp. 1081–1096. Pergamon Press.

DOWTY E., KEIL K. and PRINZ M. (1974) Lunar pyroxene-phyric basalts: crystallization under supercooled conditions. *J. Petrol.* **15**, 419–453.

DUKE M. B. and SILVER L. T. (1967) Petrology of eucrites, howardites, and mesosiderites. *Geochim. Cosmochim. Acta* **31**, 1637–1665.

DYMEK R. F., ALBEE A. L. and CHODOS A. A. (1974) Glass-coated soil breccia 15205: selenologic history and petrologic constraints on the nature of its source region. *Proc. 5th Lunar Sci. Conf., Geochim. Cosmochim. Acta Suppl.* **5**, Vol. 1, pp. 235–260. Pergamon Press.

DYMEK R. F., ALBEE A. L. and WASSERBURG G. J. (1975a) A petrologic comparison of the Kapoeta parent planet with the moon. (Abstract). In *Lunar Science* VI, pp. 227–229. The Lunar Science Institute, Houston.

DYMEK R. F., ALBEE A. L. and CHODOS A. A. (1975b) Comparative petrology of lunar cumulate rocks of possible primary origin: dunite 72415, troctolite 76535, norite 78235, and anorthosite 62237. *Proc. 6th Lunar Sci. Conf., Geochim. Cosmochim. Acta Suppl.* **6**, Vol. 1, pp. 301–341. Pergamon Press.

FREDRIKSSON K. and KEIL K. (1963) The light–dark structure in the Pantar and Kapoeta stone meteorites. *Geochim. Cosmochim. Acta* **27**, 717–739.

GANCARZ A. J. and ALBEE A. L. (1973) Microprobe analyses of the bulk composition of phase aggregates. *Proc. 8th Natl Conf. Electron Probe Analysis*, 77A.

HESS H. H. (1941) Pyroxenes of common mafic magmas, Parts I and II. *Amer. Mineral.* **26**, 515–535, 537–594.

HESS H. H. and HENDERSON E. P. (1949) The Moore County meteorite: a further study with comment on its primordial environment. *Amer. Mineral.* **34**, 494–507.

IRVING A. J., STEELE I. M. and SMITH J. V. (1974) Lunar noritic fragments and associated diopside veins. *Amer. Mineral.* **59**, 1062–1068.

JEROME D. Y. and GOLES G. G. (1971) A re-examination of relationships among pyroxene–plagioclase achondrites. In *Activation Analysis in Geochemistry and Cosmochemistry*, pp. 261–266. Universitetforlaget.

JEROME D. Y. and MICHEL-LEVY M. C. (1972) The Washougal meteorite. *Meteoritics* **7**, 449–461.

LAL D. and RAJAN R. S. (1969) Observations on space irradiation of individual crystals of gas-rich meteorites. *Nature* **223**, 269–271.

MCCARTHY T. S., AHRENS L. H. and ERLANK A. J. (1972) Further evidence in support of the mixing model for howardite origin. *Earth Planet. Sci. Lett.* **15**, 86–93.

MCCARTHY T. S., ERLANK A. J. and WILLIS J. D. (1973) On the origin of eucrites and diogenites. *Earth Planet. Sci. Lett.* **18**, 433–442.

MASON B. (1963) The hypersthene achondrites. *Amer. Museum Novitates*, No. 2155.

MASON B. (1967) The Bununu meteorite, and a discussion of the pyroxene–plagioclase achondrites. *Geochim. Cosmochim. Acta* **31**, 107–115.

MASON B. and MELSON W. G. (1970) Comparison of lunar rocks with basalts and stony meteorites. *Proc. Apollo 11 Lunar Sci. Conf., Geochim. Cosmochim. Acta Suppl.* **1**, Vol. 1, pp. 661–671. Pergamon Press.

MASON B. and WIIK H. B. (1966) The composition of the Barratta, Carraweena, Kapoeta, Morrestort, and Ngawi meteorites. *Amer. Museum Novitates*, No. 2273.

MELSON W. G. and MASON B. (1971) Lunar "basalts": some comparisons with terrestrial and meteoritic analogs, and a proposed classification and nomenclature. *Proc. 2nd Lunar Sci. Conf., Geochim. Cosmochim. Acta Suppl.* **2**, Vol. 1, pp. 459–467.

NOONAN A. F., RAJAN R. S. and CHODOS A. A. (1974) Microprobe analyses of glassy particles from howardites. (Abstract). In *Meteoritics* **9**, 385–386.

PAPANASTASSIOU D. A. (1970) The determination of small time differences in the formation of planetary objects. Ph.D. Thesis, California Institute of Technology.

PAPANASTASSIOU D. A. and WASSERBURG G. J. (1974) Evidence for late formation and young metamorphism in the achondrite Nakhla. *Geophys. Res. Lett.* **1**, 23–26.

PAPANASTASSIOU D. A. and WASSERBURG G. J. (1976) Early lunar differentiates and lunar initial $^{87}Sr/^{86}Sr$. (Abstract.) In *Lunar Science* VII, pp. 665–667. The Lunar Science Institute, Houston.

PAPANASTASSIOU D. A., RAJAN R. S., HUNEKE J. C. and WASSERBURG G. J. (1974) Rb–Sr ages and lunar analogs in a basaltic achondrite; implications for early solar system chronologies. (Abstract.) In *Lunar Science* V, pp. 583–585. The Lunar Science Institute, Houston.

PAPIKE J. J. and BENCE A. E. (1972) Apollo 14 inverted pigeonites. Possible samples of lunar plutonic rocks. *Earth Planet. Sci. Lett.* **14**, 176–182.

PELLAS P., POUPEAU G., LORIN J. C., REEVES H. and AUDOUZE J. (1969) Primitive low-energy particle irradiation of meteorite crystals. *Nature* **223**, 272–274.

PRINZ H., FODOR R. V. and KEIL K. (in press) Comparison of lunar rocks and meteorites: implication to histories of the moon and parent meteorite bodies. In *Proc. Soviet–American Conf. on Cosmochemistry of Moon and Planets*. Lunar Science Institute, Houston.

RAJAN R. S. (1974) On the irradiation history and origin of gas-rich meteorites. *Geochim. Cosmochim. Acta* **38**, 777–788.

RAJAN R. S., HUNEKE J. C., SMITH S. P. and WASSERBURG G. J. (in preparation) ^{40}Ar–^{39}Ar chronology of individual clasts from the Kapoeta howardite.

REID A. M. (1974) The Macibini meteorite and some thoughts on the origin of basaltic achondrites. (Abstract.) *Meteoritics* **9**, 398–399.

ROWE M. W. (1970) Evidence for decay of extinct ^{244}Pu and ^{129}I in the Kapoeta meteorite. *Geochim. Cosmochim. Acta* **34**, 1019–1025.

SCHMITT R. and LAUL J. C. (1973) A survey of the selenochemistry of major, minor, and trace elements. *The Moon* **8**, 182–209.

SIGNER P. and SUESS H. E. (1963) Rare gases in the sun, in the atmosphere, and in meteorites. *Earth Sci. Meteoritics* (Houterman Vol.), 241–272.

TAKEDA H., MIYAMOTO M. and REID A. M. (1974) Host clinopyroxene with exsolved augite and the thermal history of the Juvinas eucrite. (Abstract.) *Meteoritics* **9**, 410–411.

TAYLOR H. P., JR., DUKE M. B., SILVER L. T. and EPSTEIN S. (1965) Oxygen isotope studies of minerals in stony meteorites. *Geochim. Cosmochim. Acta* **29**, 489–512.

TAYLOR H. P., JR. and EPSTEIN S. (1970) O^{18}/O^{16} ratios of Apollo 11 lunar rocks and minerals. *Proc. Apollo 11 Lunar Sci. Conf., Geochim. Cosmochim. Acta Suppl.* **1**, Vol. 2, pp. 1613–1626. Pergamon Press.

WÄNKE H., BADDENHAUSEN H., DREBIUS G., JAGOUTZ E., KRUSE H., PALME H., SPETTEL B. and TESCHKE F. (1973) Multielement analyses of Apollo 15, 16 and 17 samples and the bulk composition of the moon. *Proc. 4th Lunar Sci. Conf., Geochim. Cosmochim. Acta Suppl.* **4**, Vol. 2, pp. 1461–1481. Pergamon Press.

WAHL W. (1952) The brecciated stoney meteorites and meteorites containing foreign fragments. *Geochim. Cosmochim. Acta* **2**, 91–117.

WIEGAND P. W. and HOLLISTER L. S. (1973) Basaltic vitrophyre 15597: an undifferentiated melt sample. *Earth Planet. Sci. Lett.* **19**, 61–71.

WILKENING L. L. (1971) Particle track studies and the origin of gas-rich meteorites. Nininger Meteorite Award Paper, Arizona State University Tempe, 36 pp.

WILKENING L. L. (1973) Foreign inclusions in stony meteorites—I. Chondritic xenoliths in the Kapoeta howardite. *Geochim. Cosmochim. Acta* **37**, 1985–1989.

WILKENING L., LAL D. and REID A. M. (1971) The evolution of the Kapoeta howardite based on fossil track studies. *Earth Planet. Sci. Lett.* **10**, 334–340.

PART III:

Characterization and Evolution of the Lunar Crust as Inferred from Petrologic Studies of Apollo 16 and 17 Crystalline Rock Samples.

Introductory Statement

A synthesis of the currently-available knowledge of the state of the moon suggests that lunar evolution can be described in terms of three major episodes or phases. The first or earliest phase involved large scale melting and differentiation that resulted in the formation of a feldspathic crust and associated cumulate rock types between about 4.4 and 4.6 AE. The second phase involved the modification of the lunar surface by intense meteorite bombardment that culminated in the formation of the major basins at ca. 3.95 AE. The third phase involved the filling of these basins by mare basalt lavas between about 2.5 and 3.9 AE. Although simplified, such a model for lunar evolution explains much, if not most, of the data obtained from investigations of the returned samples and from examination of photographs of the lunar surface (c.f., Taylor, 1975).

This part of the thesis presents mineralogic and petrologic studies of isotopically-dated lunar samples that are characteristic of each of the three phases of lunar evolution. The first paper is a study of ancient cumulate rocks from the Apollo 16 and 17 sites. The second paper is a study of samples that formed from impact melts related to the Serenetatis basin-forming event. The third paper is a study of high-titanium mare basalt samples from the Taurus-Littrow Valley at the Apollo 17 site.

Reference

Taylor S.R. (1975) Lunar Science: A Post-Apollo View, Pergamon Press, New York, 373 pages.

Proc. Lunar Sci. Conf. 6th (1975), p. 301–341
Printed in the United States of America

Comparative petrology of lunar cumulate rocks of possible primary origin: Dunite 72415, troctolite 76535, norite 78235, and anorthosite 62237

R. F. DYMEK, A. L. ALBEE, and A. A. CHODOS

Division of Geological and Planetary Sciences,* California Institute of Technology, Pasadena, California 91125

Abstract—The mineralogy, petrology, and crystallization history of four coarse-grained lunar rocks of cumulate origin—dunite 72415-8, troctolite 76535, norite 78235, and ferroan anorthosite 62237—are discussed in detail. All four samples have undergone long annealing at temperatures of 810°C or less, and probably originate from greater depths than most of the returned highland samples. The dunite is almost certainly, and the other samples are probably, relicts of a primary lunar differentiation and crustal formation. The dunite, troctolite, and norite can all be related by simple fractional crystallization of olivine, plagioclase, and orthopyroxene coupled with interaction with trapped intercumulus melt. The ferroan anorthosite is a plagioclase–olivine cumulate that cannot have such a simple relationship with the others, but may have formed by convective mixing of plagioclase and olivine and subsequent loss of intercumulus melt.

1. INTRODUCTION

CURRENT, WIDELY ACCEPTED MODELS for early lunar history suggest that the oldest rocks to be found on the lunar surface will have an igneous cumulate origin. Such models have evolved to explain a wide variety of petrologic, geochemical, isotopic, and geophysical constraints and, in general, invoke early extensive melting of at least the outer 100–200 km of the moon at ~4.5 AE, with the resultant formation of a layered crust comprised of a variety of cumulate rocks (cf. Taylor and Jakeš, 1974). This primary differentiation produced upper regions enriched in plagioclase and lower regions enriched in olivine, spinel, and pyroxene. The content of trapped residual melt varied from layer to layer, but such KREEP-rich liquid was most abundant at intermediate levels. The various models do differ in many details, such as the assumed vertical and horizontal scale of the layering and in the inferred extent of disruption of such simple gravity separation by impacts or by convective magmatic processes.

These models were in part stimulated by the discovery of anorthositic fragments in the Apollo 11 soils (Wood *et al.*, 1970; Smith *et al.*, 1970) and supported by the subsequent realization that the lunar highlands are highly enriched in plagioclase (Adler *et al.*, 1973). Isotopic data provide evidence for early lunar differentiation (cf. Albee *et al.*, 1970; Albee and Gancarz, 1975) but the models of early lunar history would be greatly strengthened if petrologic, isotopic, and geochemical evidence can show that some of the supposed cumulate rocks are comagmatic and are in fact relicts of a primary lunar differentiation.

*Contribution No. 2617.

Many of the cumulate rock types that have been described were found among small soil and rake samples, or as clasts in breccias. However, the Apollo 17 collection included several unique cumulate rocks that are large enough to provide material for integrated studies by a variety of techniques. This paper describes the petrology of the lunar dunite 72415-8, and compares it with that of several other cumulate rocks of possible primary origin—troctolite 76535, norite 78235, and ferroan anorthosite 62237.

II. Analytical Techniques

All of the data points plotted on the various diagrams represent analyses performed consecutively on a single spot for 8–16 elements in groups of three using a MAC-5-SA3 electron microprobe interfaced to a PDP-8/L computer for control and on-line data processing. Operating conditions were uniformly 15-kV accelerating voltage and 0.5-μA sample current (on brass) with beam current integration and pulse height selection. Elements with peak to background ratios greater than five (about 1 wt.% of the oxide) are determined to a counting statistic precision of 1% or better. Minor elements ($\lesssim$ 1% abundances) are usually counted for 90 sec, which yields a counting statistic precision of better than 10% for elements present in amounts greater than $\sim$0.1 wt.%. Reproducibility (1 σ) on two "known unknowns" over a 13-month period ranges from 1½% (for elements with abundances >1%) to 3% of the amount present (for elements with abundances 0.1–1.0%) (Champion *et al.*, 1975). The analytical procedure is described in detail by Chodos *et al.* (1973).

Microprobe point counts, "average" mineral compositions, and calculated bulk-chemical compositions were performed using techniques modified from those described by Gancarz and Albee (1973). On any point where a positive mineral identification cannot be made using only the triad Fe–Ca–Si, the identification is confirmed by driving one or more spectrometers to analyze for Ti, K, and F. The addition of a determination of Ti permits the computer to discriminate between ilmenite, armalcolite, rutile, ulvöspinel, chromite, Fe-metal, and troilite, K permits discrimination between SiO_2 and silica-rich mesostasis and F permits discrimination between apatite and whitlockite.

Each of the "average" mineral compositions given in Tables 1 and 5 is an actual analysis of a single point that was selected from all of the analyses as the best fit to the average values obtained by the point count. A computer print out of all the analyses may be obtained from A. Albee. All formula compositions and elemental ratios used in the text are in molecular proportions: olivine compositions are reported as % Fo = 100 × [Mg/(Mg + Fe + Mn)]; pyroxene compositions are reported as % Wo = 100 × [Ca/(Ca + Mg + Fe + Mn)], % En = 100 × [Mg/(Ca + Mg + Fe + Mn)], % Fs = 100 × [(Fe + Mn)/(Ca + Mg + Fe + Mn)]; plagioclase compositions are reported as % An = 100 × [Ca/(Na + Ca + K + Ba + Fe + Mg)].

III. Dunite (72415-8)

A. *Sample description, preparation, and distribution*

Five fragments, that were collected from a 10 × 20-cm clast in boulder # 3 at Apollo 17 Station 2, represent the only "large" samples of dunite returned from the moon. The boulder ($\sim$0.5 m diameter), a metaclastic blue–gray breccia represented by sample 72435 (see PSR, Fig. 6-11), contained several smaller centimeter-sized greenish-white clasts that were inferred to be dunite also. Sample 72435 does in fact contain a few millimeter-sized clasts of dunite that resemble 72415-8 both in texture and mineralogy. Thus, despite the rarity of dunite among the returned lunar samples, its abundance in this boulder has provided an opportunity to study this significant lunar rock type.

In hand specimen, all five fragments were comprised of pale-green, translucent grains of olivine (up to 10 mm, approximately 50%) set in a coherent fine-grained white matrix. It was concluded after preliminary examination that the five samples were virtually identical (Fig. 1). They all had lunar exterior on one surface, indicated by a greenish-brown patina and microcraters, bore tool marks, and had adhering particles of lunar soil. It now appears that the fragments were chipped from the boulder with a tool, and then recovered from the lunar surface by astronauts Cernan and Schmitt. Samples 72415A (16.7 g) and 72415B (12.4 g) were so numbered because they could be matched (Fig. 1); the others were numbered consecutively: 72416 (11.5 g); 72417 (11.3 g); and 72418 (3.5 g). PET thin sections (,11 and ,12) were made from a chip taken from one end of sample 72415A; preliminary chemical data were obtained from this same chip.

Subsequently, 72415A was sawn to produce a cube for various geophysical measurements, and polished thin sections (,52 ,53 and ,54) were made parallel to the faces of the cube. Sample 72417 was transferred to the Lunatic Asylum to be subdivided with minimal contamination for geochemical studies. The prime geochemical sample (72417,1) was prepared by removing adhering soil particles, and by chiseling away all exterior surfaces and tool smear marks with a tungsten carbide microchisel. Our petrographic study was performed on the above-mentioned five polished thin sections, and on one polished thin section and several polished grain mounts of 72417.

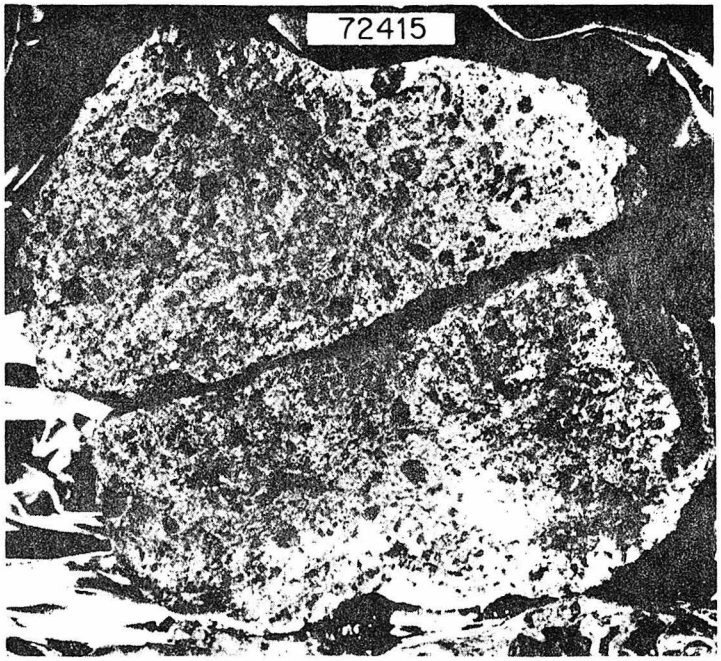

Fig. 1. Hand specimen photograph of sample 72415 (A–bottom, B–top) illustrating cataclastic texture. The horizontal dimensions of the two fragments are approximately 4 cm. (NASA photo S-73-27576.)

Preliminary studies of the dunite have been reported by LSPET (1973), Albee *et al.* (1974, 1975), Bell and Mao (1975), Brecher (1975), Clayton and Mayeda (1975), Gibson and Moore (1974), Higuchi and Morgan (1975), Laul and Schmitt (1974, 1975a), Papanastassiou and Wasserburg (1975a), Pearce *et al.* (1974), and Snee and Ahrens (1975a). In addition to this paper, these volumes contain papers that report other studies on the dunite: chemistry (Laul and Schmitt, 1975b), Rb–Sr isotope systematics (Papanastassiou and Wasserburg, 1975b), and shock features in olivine (Snee and Ahrens, 1975b).

B. Petrography

The lunar dunite is comprised of angular to sub-rounded clasts (~ 60%) that are predominantly deformed single crystals of very pale-green olivine (up to 10 mm), set in a fine-grained (1–50 μm), granulated matrix that is also predominantly olivine (Fig. 2). This sample is a cataclasite, and its present state resulted from simple crushing that was not accompanied by recrystallization.

The mineralogy of the dunite is quite simple. It consists of olivine (93%), plagioclase (4%), low-Ca pyroxene (2%), and high-Ca pyroxene (1%), with minor amounts of Cr-spinel and Fe–Ni–Co–Cr metal alloy. Rare grains of troilite,

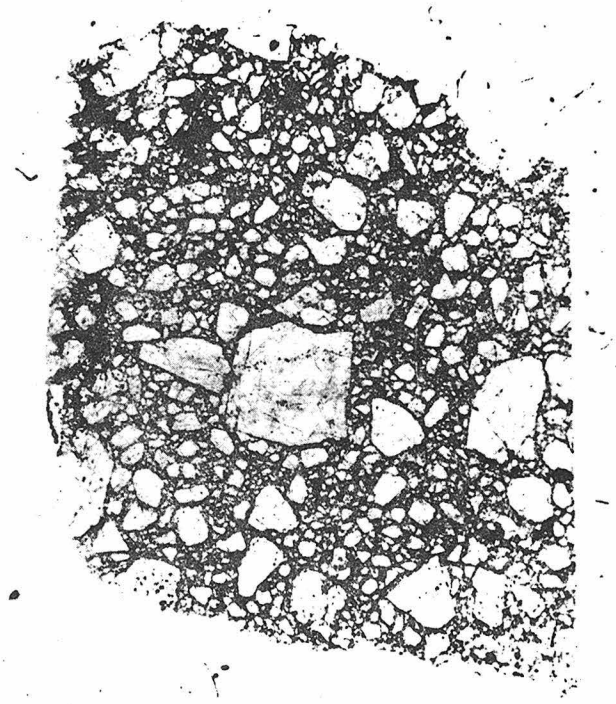

Fig. 2. Photomicrograph of polished thin section 72415,54. Note the large, subangular clasts in a finer-grained matrix. (Vertical dimension of thin section is approximately 9 mm.)

whitlockite, and Zr–Cr armalcolite also occur. Table 1 gives the measured mode, a mineral analysis corresponding to the average composition of each phase, and a calculated bulk-chemical composition. These data are based on an average of electron microprobe point counts of thin sections 72415,11-12-53-54 and PQM-306 (from 72417). The total area point-counted was ≈ 325 mm^2, and the average was calculated by weighting each point count by the area of the particular section studied.

Plagioclase content varied significantly in the various thin sections (1.4–5.2 vol.%). Laul and Schmitt (1975a; 1975b) chemically analyzed ten 69–135-mg chips from 72417,1 and calculated that the plagioclase content ranged from 0.6 to 11 wt.%. The CaO and Al_2O_3 contents, as determined from our point count, are nearly the same as the weighted average reported by them, and only slightly less than those reported in the PET analysis.

Table 1. Dunite 74215 and 74217: Phase abundances, "average" phase compositions and bulk-chemical composition.

	Plag.	Low-Ca pyx	High-Ca pyx	Olivine	Cr-spinel	Metal*	Bulk composition	
Vol.%	4.0$_3$	2.1$_8$	1.0$_2$	92.5$_2$	0.1$_9$	0.0$_7$	Calculated LSPET,	
Wt.%	3.3$_5$	2.1$_7$	1.0$_0$	93.0$_4$	0.2$_6$	0.1$_7$	(4641 Points) 1973	
SiO_2	44.79	56.05	54.13	40.24	0.04	0.05	40.70	39.93
TiO_2	< 0.01	0.28	0.11	0.02	1.05	< 0.01	0.03	0.03
Al_2O_3	35.00	0.96	1.22	< 0.01	16.71	n.a.	1.25	1.53
Cr_2O_3	n.a.	0.26	1.11	0.04	51.81	0.54	0.19	0.34
MgO	0.23	32.29	18.40	47.65	10.60	0.01	45.24	43.61
FeO	0.14	6.94	2.71	12.29	19.27	67.65	11.82	11.34
MnO	n.a.	0.15	0.11	0.13	0.58	0.02	0.13	0.13
CaO	19.25	2.24	22.50	0.13	n.a.	0.01	1.04	1.14
Na_2O	0.62	0.01	0.05	n.a.	n.a.	n.a.	0.02	< 0.02
K_2O	0.09	n.a.	n.a.	n.a.	n.a.	n.a.	0.00$_3$	0.00
BaO	0.04	n.a.	n.a.	n.a.	n.a.	n.a.	< 0.01	—
ZrO_2	n.a.	n.a.	n.a.	n.a.	< 0.01	n.a.	< 0.01	< 0.01
V_2O_3	n.a.	n.a.	n.a.	n.a.	0.37	n.a.	< 0.01	—
Nb_2O_5	n.a.	n.a.	n.a.	n.a.	0.05	n.a.	< 0.01	< 0.01
NiO	n.a.	n.a.	n.a.	< 0.01	n.a.	30.42	0.07	0.02
Co	n.a.	n.a.	n.a.	n.a.	n.a.	1.42	< 0.01	—
Total	100.16	99.18	100.34	100.50	100.48	100.14†	100.49	98.07
	An 92.0	Wo 3.0	Wo 41.7	Fo 87.2				
	Ab 5.4	En 84.2	En 49.7	Fa 21.8				
	Or 0.5	Fs 10.4	Fs 4.3					
	Others 2.1	2.4	4.3					

*Elemental abundances, converted to oxides for bulk-composition calculation.
†Includes 0.02 wt.% P.
n.a. = not analyzed.

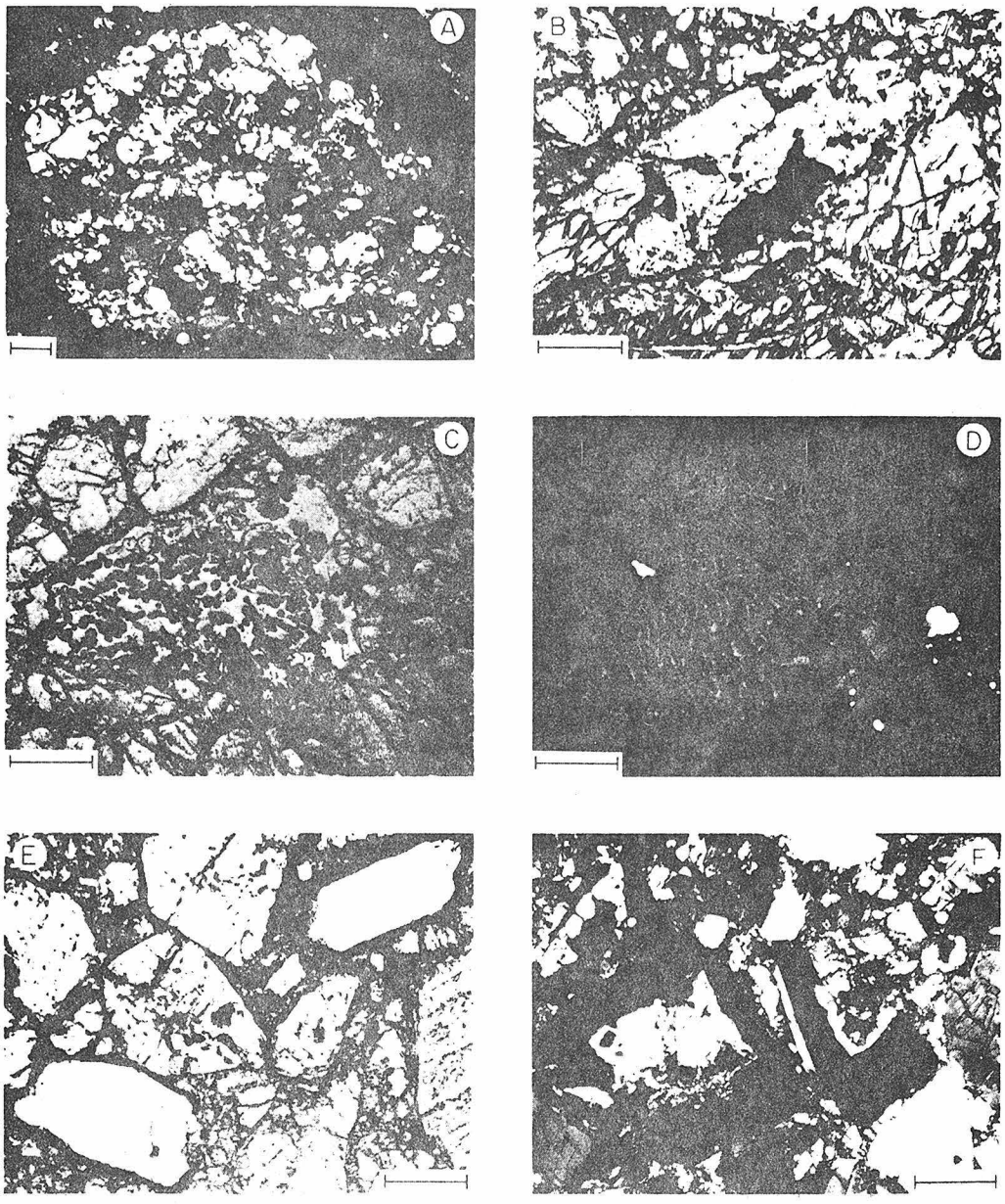
A
B
C
D
E
F

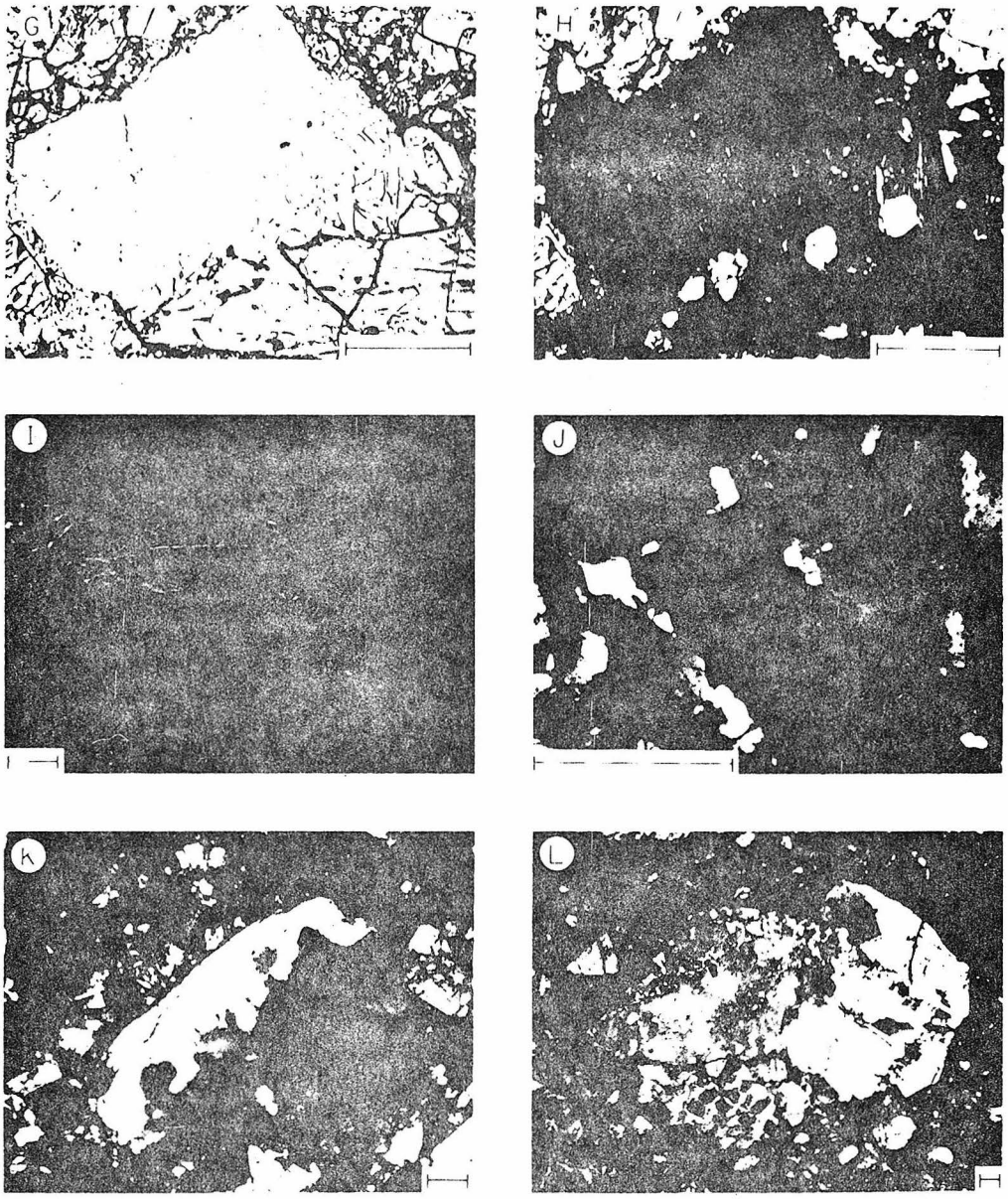
G
H
I
J
K
L

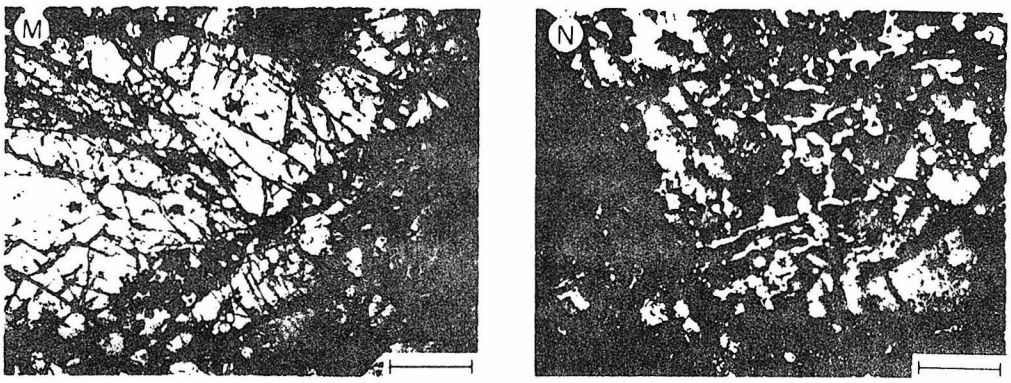

Fig. 3. Photomicrographs illustrating various textural features in lunar dunite samples 72415 and 72417. All bar scales = 100 μm except 3I (= 10 μm). (A) Clast of polygonal-textured olivine. Small amounts of plagioclase occur interstitial to the olivine here (transmitted cross-polarized light). (B) Clast comprised of blocky Cr-spinel, pyroxene, and olivine (transmitted plane-polarized light). (C) Clast comprised of intergrown Cr-spinel, olivine, and plagioclase. The olivine (e.g. arrow) encloses tiny Cr-spinel granules. These are all included in plagioclase (white) that contains larger inclusions of Cr-spinel (black) (transmitted plane-polarized light). (D) Symplectic intergrowth comprised of vermicular Cr-spinel (light gray), high-Ca and low-Ca pyroxene (dark gray), and metal (white). A small amount of olivine occurs to the left of the symplectite (reflected light). (E) Closeup view of the cataclastic texture of the dunite. The two white clasts are recrystallized maskelynite. Note abundant dark inclusions in olivine (transmitted plane-polarized light). (F) Lath-shaped plagioclase clasts in granulated matrix of the dunite. Note the twinning in plagioclase (transmitted cross-polarized light). (G) Complex plagioclase-rich clast. The grain attached to the plagioclase is olivine. Note the abundant high-index granules included in plagioclase. Both the granules and plagioclase coarsen from left to right. Analyses of the larger, angular inclusions at the plagioclase–olivine contact indicate that these inclusions are high-Ca and low-Ca pyroxene (transmitted plane-polarized light). (H) The same field of view as in 3G in transmitted cross-polarized light. Note the "felty-textured" plagioclase in left-hand portion of clast (= recrystallized maskelynite), and the development of lath-shaped plagioclase forming a distinctive intergranular texture along the contact with olivine. We infer from textural relationships such as illustrated here that the development of lath-shaped plagioclase occurred by crystallization of small amounts of impact melt along plagioclase–olivine grain boundaries. (I) Microsymplectite inclusion in olivine. Note the extensive plagioclase–olivine contacts (horizontal elongate grain indicated by arrow is plagioclase). The tiny inclusions dispersed throughout the olivine are inferred to be predominantly plagioclase (transmitted plane-polarized light). (J) Multiple fractures and strain bands in olivine. Note the tiny recrystallized, polygonal grains aligned along the fractures (transmitted cross-polarized light). (K) Clast illustrating cuspate grain boundaries between adjacent olivine grains (transmitted cross-polarized light). (L) Clast illustrating complex grain boundaries between adjacent olivine grains. Note recrystallized polygonal olivine within clast (lower left) (transmitted cross-polarized light). (M) Aggregate of granular spinel (black) and plagioclase (white) along relic grain boundary between adjacent olivine grains in clast (transmitted plane-polarized light). (N) Anastamosing plagioclase-rich veinlet. Note abundant twinning and lathlike form of plagioclase (transmitted cross-polarized light).

Most clasts are single crystals of olivine, but the occurrence of several other types is critical to understanding the primary features and history of this rock. These clasts include:

(1) aggregates of recrystallized polygonal olivine (Fig. 3A) with small amounts of interstitial plagioclase and rarely pyroxene or metal;
(2) blocky Cr-spinel surrounded in part by pyroxene (Fig. 3B);
(3) intergrowths of Cr-spinel ± olivine ± plagioclase ± high-Ca pyroxene ± low-Ca pyroxene ± metal, with the form of the Cr-spinel in such clasts ranging from granular to vermicular. The intergrowth illustrated in Fig. 3C consists of small grains of olivine, with abundant inclusions of Cr-spinel, that are in turn all included in lath-shaped plagioclase which itself has inclusions of Cr-spinel. These relationships point to a complex formational history.

The principal occurrence of "symplectite" in the dunite resembles Fig. 3D. These consist of Cr-spinel + high-Ca pyroxene ± low-Ca pyroxene ± olivine ± plagioclase ± metal. In one instance, the spinel was intergrown with a single crystal of high-Ca pyroxene. The lack of a constant phase assemblage, together with the lack of constant phase proportions in each case, precludes the formation of such intergrowths by a specific mechanism such as a solid state reaction between olivine and plagioclase; and

(4) plagioclase-rich clasts that typically consist of aggregates of 5–20 μm granules of felty-textured plagioclase that are inferred to be devitrified maskelynite. Some are 100% plagioclase (Fig. 3E), whereas others contain abundant micrometer-sized blebs of a mafic silicate mineral at the junctions of the plagioclase grains (Fig. 3G). Some of the latter have intergranular-textured zones at their margins, consisting of a network of interlocking plagioclase laths with interstitial 1–15 μm grains of low- and high-Ca pyroxene (Figs. 3G, 3H). Such lath-like plagioclase is always developed at a boundary with adjacent olivine grain, and at this contact the olivine appears recrystallized. Note that in Figs. 3G and 3H, the transition from felty-texture to intergranular-texture involves a gradational coarsening, and clearly occurs within the sharply bounded clasts. In addition, a few clasts consist of lath-like plagioclase that occur as either broken single crystals, or intergrown with pyroxene and olivine within a clast (Fig. 3F). Plagioclase in this occurrence is well-twinned, strongly zoned, and occasionally contains micrometer-sized inclusions of mafic silicate mineral in their cores.

The olivine clasts show a number of complex petrographic features that consist of the following:

(1) *Inclusions.* Many grains are locally clouded (Fig. 3E), in part caused by concentrations of abundant transparent, micrometer-sized and smaller inclusions that have a refractive index lower than the host olivine. The larger ones are always plagioclase (Fig. 3I), and we infer that many of the smaller ones are plagioclase also. P. M. Bell (written communication, 1975) has indicated that some inclusions

are Mg-, Ca-, and Si-rich glass. Tiny inclusions of metal, Cr-spinel, and possibly troilite also contribute to this clouding. Larger inclusions (up to 50 μm) of angular Cr-spinel, and rectagular to ovoid aggregates of felty-textured plagioclase are also present within olivine. The latter resemble the plagioclase-rich clasts (e.g. Figs. 3E, 3G) and are interpreted to be recrystallized maskelynite that formed from shocked plagioclase inclusions. E. Roedder (oral communication, 1975) has suggested that some might represent recrystallized plagioclase-rich melt inclusions in addition.

(2) *Microsymplectites.* Many of the olivine grains contain a few tiny ($\lesssim$ 25 μm) intergrowths of Cr-spinel + pyroxene (Fig. 3I). These microsymplectites are somewhat similar texturally to those figured by Roedder and Weiblen (1971; Fig. 17) in olivine from mare basalt 12018. Bell and Mao (1975) interpreted these as pseudomorphs of high-pressure Cr-garnet based on the fact that analyses of the microsymplectites yield an Si/O ratio ~ 4. Our analyses confirm this discovery, but indicate that the microsymplectites have excess divalent (Mg, Fe, Ca) and deficient trivalent (Cr, Al) cations relative to a garnet formula. P. M. Bell (written communication, 1975) has indicated that this discrepancy can be resolved by assuming that the original Cr-garnet reacted with the surrounding olivine to yield the assemblage Cr-spinel + pyroxene. Hence, the deviation of microsymplectite composition from that of a garnet is an indication of the amount of olivine "admixed." However, an Si/O ratio of 4 is not unique to garnet, but is characteristic of olivine and anorthite as well. Hence, the Si/O criterion is also satisfied by assuming that the microsymplectites were formed by reaction between olivine and plagioclase. In many cases (e.g. Fig. 3I), the microsymplectites occur adjacent to inclusions of plagioclase. In addition, the presence of abundant plagioclase–olivine contacts in the immediate vicinity of the microsymplectites (Fig. 3I), without any evidence for reaction between the olivine and plagioclase, casts doubt on an origin for the microsymplectites by olivine–plagioclase reaction. We prefer to interpret the microsymplectites as the products of slow crystallization of melt or melt–crystal inclusions trapped within the growing olivine crystals. The fact that the microsymplectites are Cr-rich suggests that they represent trapped inclusions of melt + Cr-rich spinel.

(3) *Shock and recrystallization features.* Most large olivine crystals possess parallel zones of undulatory extinction (20–40 μm wide) that are separated by planar partings and inferred to be shock-induced strain bands. Small (5–15 μm) oval or equant olivine grains with uniform extinction are aligned along some of these bands (Fig. 3J). In addition, some of the planar partings are decorated with some minute beads, which are apparently metal, and some partings terminate with strings of these beads present along the projected continuation. Only a few olivine clasts are relatively strain-free. These consist of several crystals that meet at cuspate boundaries (Fig. 3K); other clasts contain granular, polygonalized grains that meet at 120° triple junctions (Fig. 3L).

Snee and Ahrens (1975a, 1975b) compared the populations of fracture orientations in olivine from the dunite with those produced in experimentally shocked olivine single crystals. They concluded that the dunite experienced a peak shock

pressure between 330 and 440 kbar, which agrees well with our earlier estimate of 350–450 kbar (Albee *et al.*, 1974), based on a comparison of various petrographic features in the dunite with the data presented by Stöffler (1972).

Some olivine clasts are crosscut by irregularly shaped to linear "veinlets" that are predominantly lath-shaped plagioclase (Fig. 3N). Some contain high-Ca pyroxene, low-Ca pyroxene, and granular Cr-spinel. The formation of these "veinlets" appears to post-date the main shock event since they crosscut the planar shock features. Olivine included within them, and the olivine which immediately surrounds them, are recrystallized. We infer that these "veinlets" formed by shock-melting of interstitial, relatively late-stage plagioclase with a low-An content.

(4) *Relic grain boundaries.* A few of the olivine clasts consist of two olivine grains separated by a zone of granular to vermicular Cr-spinel, high-Ca pyroxene, low-Ca pyroxene, and lath-shaped plagioclase (Fig. 3M). This feature is interpreted to represent aggregates of intercumulus phases along relic olivine grain boundaries.

These textural features, discussed in the preceding few paragraphs, are in all cases truncated at clast margins. This indicates that they were produced prior to the most recent shock event, and that this latest event involved merely crushing and granulation, without any associated recrystallization and coarsening. These complex clasts are rare, since most clasts contain only olivine. However, we feel that these rare textural features provide insight into the nature of the intercumulus material that was interstial to the coarse-grained olivine.

C. *Mineral chemistry*

The compositions of the various minerals in the dunite are illustrated in Fig. 4A. Olivine has a very restricted range in composition (Fo_{86-89}), and there is no systematic difference in composition between olivine that occurs in clasts and matrix, or among the various types of clasts. The olivine is low in Ca, Ti, Mn, and Cr compared to that in mare basalts, but similar to the olivine in 76535 and 62237 (cf. Tables 1, 2, 5).

Pyroxene also has a very restricted Fe/Mg ratio, but the composition differs slightly in different petrographic associations. The pyroxene occurring with lath-shaped plagioclase has compositions that fall into two groups ($\sim Wo_2En_{87}Fs_{11}$ and $\sim Wo_{44}En_{50}Fs_6$). The intermediate compositions shown in Fig. 4A are believed to be mixtures. The high-Ca pyroxene in symplectites is $\sim Wo_{43}En_{51}Fs_6$, but the low-Ca pyroxene shows an apparent range in composition and averages $\sim Wo_9En_{80}Fs_{11}$. The composition of low-Ca pyroxene associated with polygonal olivine resembles that of the low-Ca pyroxene in symplectites. Finally, the pyroxene that surrounds blocky Cr-spinel ranges from $Wo_2En_{87}Fs_{11}$ to $Wo_{22}En_{66}Fs_{12}$. The higher-Ca compositions do not fall along a mixing line defined by the other pyroxene types, and are believed to be real.

The composition of plagioclase also differs in various petrographic associa-

tions. Felty-textured plagioclase, both the discrete clasts and the inclusions in olivine, are the most calcic in the rock and have the same narrow range in composition (An_{94-97}; Fig. 4A). We infer that these represent recrystallized grains of maskelynitized plagioclase, and that their compositions represent that of the primary plagioclase that first began to coprecipitate with olivine and Cr-spinel. Lath-shaped plagioclase grains are zoned (up to 5 mole% An), and show a rather wide range in composition (An_{85-94}). This range overlaps the composition of plagioclase that occurs in symplectites (An_{89-91}). Plagioclase found with recrystallized polygonal olivine ranges from An_{89} to An_{95}.

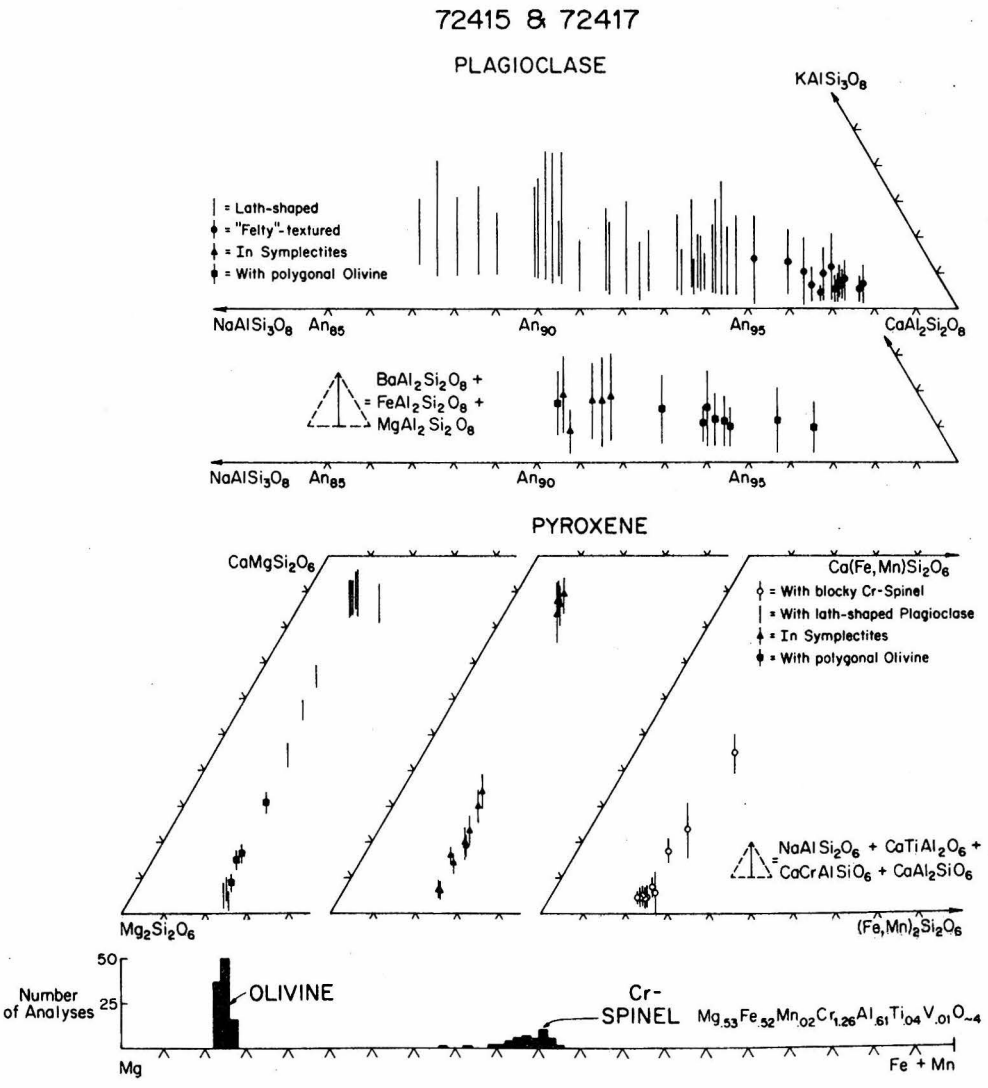

Fig. 4 A.

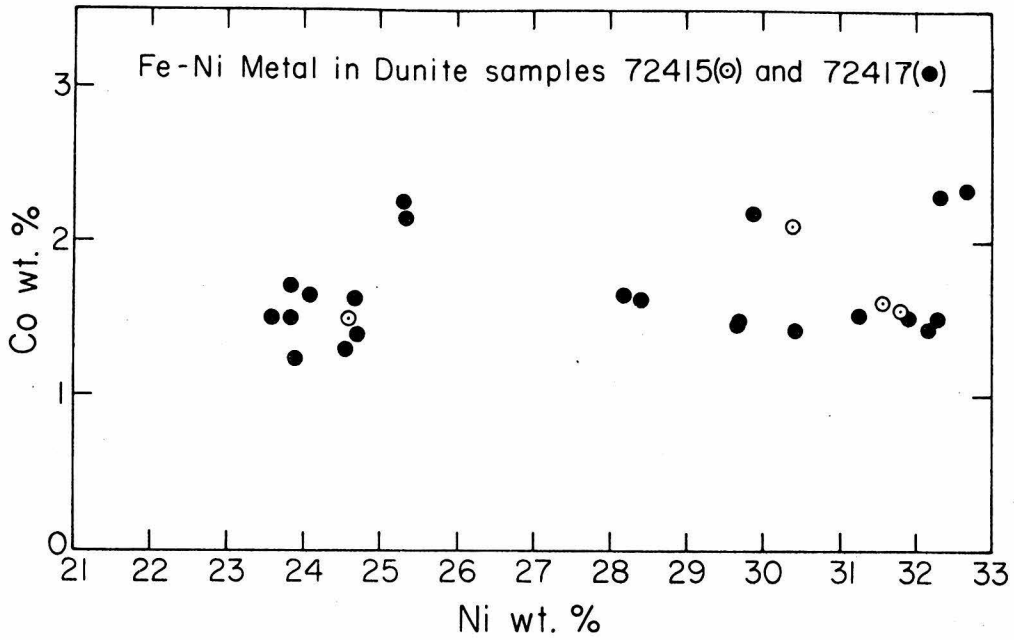

Fig. 4. (A) Compositions of the principal phases in lunar dunite samples 72415 and 72417. Compositions of the plagioclase and pyroxene are separated according to their petrographic occurrence, as discussed in the text. (B) Ni and Co contents of the metal phase in dunite samples 72415 and 72417.

The Cr-spinel has a restricted range in composition. However, the spinel in symplectites is more Fe-rich, and has a slightly lower Cr/(Cr + Al) than the blocky spinel grains, the spinel inclusions in olivine, or the granular spinel occurring with plagioclase.

Metal grains that are large enough to analyze yield compositions that are high in Ni (24.5–31.8 wt.%) and Co (1.3–2.2 wt.%) (Fig. 4B). These compositions are well outside the range of meteoritic Ni–Fe metal, and Fe metal in lunar mare basalts. In addition, the Cr content is notably large (0.4–0.6 wt.%). The composition of the metal, and its occurrence in the rock, suggest that it subtracted Ni and Co from the melt during crystallization, rather than forming by a late-stage reduction process.

A single grain of Cr–Zr "armalcolite," together with rare grains of whitlockite and troilite associated with the metal, was identified, but accurate analyses were not obtained because of the small grain size ($< 5\ \mu m$). Ilmenite (0.4–2.4 wt.% MgO) was recovered from a heavy liquid mineral separate of sample 72417. However, it was not found in any of the thin sections studied.

D. Inferred history

Despite the great amount of shock-induced deformation, recrystallization, and crushing, Rb and Sr in the dunite have undergone little apparent redistribution. The isotopic data indicate that the primary age of 72417 is 4.55 ± 0.10 AE

(Papanastassiou and Wasserburg, 1975b), and the dunite is inferred to be a product of the primary lunar differentiation. It seems logical then, to expect this rock to provide some insight into the early history of the moon, and in particular, the sequence of crystallization of the phases in the dunite should have important implications for the nature of the early lunar differentiation. However, such insights may be obfuscated by the exceedingly complex history experienced by this sample as indicated by petrographic relationships discussed in the previous section.

Although important it is difficult to distinguish between the primary and the deformational features of this sample. The size of single-crystal olivine clasts indicates that the dunite was originally a coarse-grained plutonic rock. However, it is highly unlikely that it crystallized from a melt of the same composition, and it is more probable that it formed as a cumulate from a more "gabbroic" magma. Textural evidence indicates that olivine and Cr-spinel began crystallizing first and were followed by plagioclase. Cr-spinel, plagioclase, low-Ca pyroxene, high-Ca pyroxene, and metal continued to crystallize from small amounts of trapped intercumulus liquid interstitial to the cumulate olivine grains. Olivine and Cr-spinel are most assuredly cumulate phases, whereas very little if any of the plagioclase in the rock is cumulate in origin.

The fact that plagioclase and pyroxene follow olivine allows for the possibility that rocks such as troctolites, norites, and anorthosites are comagmatic with the dunite. The compositional homogeneity displayed by the olivine suggests that the olivine re-equilibrated with its intercumulus melt for an extended period of time, or that original growth of the olivine was slow enough to allow diffusive equilibrium to be achieved during crystallization.

We infer that the symplectic intergrowths formed by coprecipitation of several phases from intercumulus melt. Hodges and Kushiro (1974) have demonstrated experimentally that, for a model moon composition, the five phases: olivine, plagioclase, low-Ca pyroxene, high-Ca pyroxene, and Cr-spinel, crystallize together for an extended pressure range at temperatures just above the solidus. The variability in texture, phase assemblage, and phase abundances displayed by the symplectic and other Cr-spinel-bearing intergrowths was probably governed by local variations in the composition of the trapped melt, and a peculiar balance between nucleation and growth rates prompted by slow crystallization in an anhydrous environment. However, it seems likely that much of this intercumulus material underwent later modification as discussed below.

Subsequent to complete crystallization, the dunite was shocked to pressures in excess of 330 kbar and excavated, perhaps in a basin-forming event. Snee and Ahrens (1975b) esimate that the maximum depth of origin of the dunite for such an event was *ca.* 50–150 km. However, Head *et al.* (1975) indicate that the maximum depth of excavation for the major lunar basins was only about 20 km. This intense shock event produced the strain bands in the olivine, and transformed the plagioclase into maskelynite. In addition, there is evidence that suggests that this event also produced some silicate melt in the intercumulus material along olivine grain boundaries.

At the shock pressures involved (> 330 kbar), all plagioclase in the rock should have been transformed into maskelynite (Gibbons and Ahrens, 1975a). However, most of the plagioclase in the dunite occurs as well-twinned laths with a texture that suggests crystallization from a melt. In addition, pyroxene should show abundant (001) polysynthetic mechanical twins (Gibbons and Ahrens, 1975b). However, most of the pyroxene occurs as clear, pristine crystals, although a few possess lamellar structure and undulose extinction that may be shock-induced features. In an X-ray study of some pyroxene from the dunite, S. Ghose (University of Washington, oral communication) has identified anomalous reflections that may be shock-induced disorientations. In general, most of the pyroxene and plagioclase appear visually unshocked.

Thus, we infer that the lath-shaped plagioclase found in grain boundary aggregates, the composite lath-shaped plagioclase–pyroxene clasts (Fig. 3F), and in particular, the anastamosing "veinlets" of lath-shaped plagioclase (Fig. 3N) formed from small amounts of silicate melt that was shock-produced from intercumulus material, locally mobilized, and injected into some olivine grains along fractures. Whether this melting was intense enough to involve Cr-spinel is not clear, but the recrystallized appearance of olivine near lath-shaped plagioclase may be a result of "reaction" with the melt. None of our observations precludes the possibility that some of the symplectic intergrowths formed at this time by a similar mechanism. The observed intermediate compositions of pyroxene in symplectites (Fig. 4) may be a result of partial equilibration with some secondary silicate melt.

After this shock event there was a period of limited recrystallization, during which the granules formed along strain bands in olivine (Fig. 3J), the maskelynite recrystallized (Figs. 3G, 3H), the polygonal-textured olivine formed (Fig. 3A, 3L), and the shock-produced melt crystallized (Fig. 3N). Subsequently, a second impact event occurred that shattered the dunite mass, caused extensive crushing and granulation, and incorporated it into the metaclastic blue–gray breccia (72435). The crushing must have preceded incorporation into the breccia (at least slightly) as there is no evidence for admixture of breccia into the dunite along shear planes. Petrographic study of 72435 indicates that it contains abundant clasts ($\sim 25\ \mu m$ to a few centimeters) of various lithologies that have not equilibrated with the very fine-grained, subophitic to micropoikilitic "melt rock" matrix. Rb–Sr-isotopic studies indicate that the matrix of 72435 only partially equilibrated at a time more recent than 4.1 AE and a Rb–Sr internal isochron on a clast, which had not equilibrated with the matrix yields an age of 3.85 ± 0.15 AE (Papanastassiou and Wasserburg, 1975a, 1975b). The $^{40}Ar/^{39}Ar$ release pattern for 72417 is complicated, but indicates argon loss at about 3.95 ± 0.1 AE (J. C. Huneke, oral communication).

Despite the complex history described here, Rb and Sr appear to have remained relatively undisturbed at the scale of the size of the samples used to establish the isochron. This indicates that the redistribution of Rb and Sr between phases during the post-shock recrystallization was limited to 1 mm or less. It would seem that such behavior might only be possible in a rock made up largely of

olivine, a phase that does not contain appreciable Rb or Sr, and thus behaves like an inert container.

An alternative possibility is that the first, highly intense shock event actually occurred very early in lunar history, shortly after the original formation of the dunite, and that the isochron age obtained is in fact determined by post-shock recrystallization at 4.55 ± 0.10 AE. This possibility is considered less likely because it then becomes necessary to store and protect the dunite through the ~ 3.95 AE lunar cataclysm (Tera *et al.*, 1974).

IV. TROCTOLITE (76535)

A. Introduction

Lunar rock 76535 was a 155.5-g rake sample collected at Apollo 17 Station 6. It is a coarse-grained troctolite with a granulite-like texture comprised of plagioclase (35%), olivine (60%), and low-Ca pyroxene (5%). Small amounts of a remarkable number of minor phases occur that include: Cr-spinel, high-Ca pyroxene, Fe–Co–Ni metal alloy, whitlockite (2 compositional types), apatite (2 compositional types), baddeleyite, K–Ba feldspar, and "pyrochlore." Although a very good discussion of the petrography (Gooley *et al.*, 1974) and chemistry (Haskin *et al.*, 1974) of the rock, and the problems attendant upon its origin as an olivine–plagioclase cumulate, have been presented, a discussion of this sample is included here because the overall similarity in the compositions of the phases in 76535 and the dunite suggest a common origin. In addition, some of the petrographic features and mineral relationships in 76535 have recently been questioned (Albee *et al.*, 1975).

Compositions of the principal phases are illustrated in Fig. 7, and selected mineral analyses are listed in Tables 2 and 3. The results reported here are based on a petrographic study of polished thin sections 76535,46 and 76535,56. It should be noted that all the polished thin sections of 76535 in existence are in fact mounts of very small fragments of the sample, since the rock disintegrated upon sawing (P. Butler, JSC, written communication). Hence, the fragmentary nature of the thin sections make textural interpretation at times difficult. For the same reason we have not performed electron microprobe point counts on this sample.

B. Petrography and mineral chemistry

76535 is characterized by relatively coarse grains of olivine and plagioclase (up to 5 mm), grain boundaries that are straight to slightly curved, and abundant 120° triple junctions (Fig. 5A). A few smaller, tabular to rounded plagioclase grains occur as inclusions in the olivine, and at boundaries between adjacent olivine grains (e.g. Fig. 5F). Both the olivine and plagioclase contain abundant acicular to rounded opaque inclusions. Their orientations in many cases appear to be crystallographically controlled; in general, the margins of the olivine and plagioclase grains are devoid of these inclusions. Gooley *et al.* (1974) reported that the

Table 2. 76535: Selected mineral compositions.

	Plag.	Olivine	Low-Ca pyx*	Low-Ca pyx†	High-Ca pyx†	Cr-spinel
SiO_2	44.21	40.30	55.89	56.43	53.48	0.14
TiO_2	0.03	0.01	0.42	0.27	0.53	0.78
Cr_2O_3	n.a.	0.02	0.80	0.72	0.72	50.72
Al_2O_3	35.89	< 0.01	1.26	1.07	1.00	16.02
MgO	0.07	47.96	32.23	33.47	18.11	9.24
CaO	19.60	0.03	1.44	0.66	23.44	n.a.
FeO	0.10	12.30	7.55	8.14	2.87	20.84
MnO	n.a.	0.16	0.17	0.16	0.06	0.76
BaO	< 0.01	n.a.	n.a.	n.a.	n.a.	n.a.
Na_2O	0.29	n.a.	0.02	0.03	0.02	n.a.
K_2O	0.05	n.a.	n.a.	n.a.	n.a.	n.a.
ZrO_2	n.a.	n.a.	n.a.	n.a.	n.a.	0.06
V_2O_3	n.a.	n.a.	n.a.	n.a.	n.a.	0.72
Nb_2O_5	n.a.	n.a.	n.a.	n.a.	n.a.	< 0.01
NiO	n.a.	< 0.01	n.a.	n.a.	n.a.	n.a.
Total	100.26	100.78	99.77	100.95	100.24	99.30
	An 96.2	Fo 87.3	Wo 0.9	Wo 0.0	Wo 43.6	
	Ab 2.6	Fa 12.7	En 84.1	En 85.2	En 48.5	
	Or 0.3		Fs 11.3	Fs 11.9	Fs 4.4	
	Others 0.9		3.7	2.9	4.5	

*Discrete coarse pyroxene.
†Pyroxene in symplectites.
n.a. = not analyzed.

inclusions in plagioclase are predominantly metal particles, whereas those in the olivine are Cr-spinel–pyroxene intergrowths. Anhedral grains of coarse low-Ca pyroxene (up to 3 mm) occur interstitial to olivine and plagioclase, and in one case this low-Ca pyroxene formed a rim on a rounded (resorbed?) grain of olivine (Fig. 5B). In addition, a few anhedral Cr-spinel grains are present at grain boundaries. As can be seen in Fig. 7, the olivine (Fo_{86-88}), plagioclase (An_{95-97}), and coarse low-Ca pyroxene ($Wo_2En_{86}Fs_{12}$) show an extremely narrow range in composition; these contain only small amounts of minor elements (Table 2).

A small portion of 76535 consists of curious vermicular intergrowths of Cr-spinel + high-Ca pyroxene ± low-Ca pyroxene and rarely metal that were termed "symplectic assemblages" by Gooley *et al.* (1974). These have a variety of occurrences and textures. The vast majority of these symplectites occur along olivine–plagioclase grain boundaries, (Figs. 5C, 5F), but some occur at olivine–low-Ca pyroxene grain boundaries (Fig. 5B). In addition, one symplectite appears to be entirely enclosed by plagioclase.

The symplectites range in size from ~25 to 250 μm across, and are generally uniform in texture. However, as can be seen in Fig. 5C, texturally inhomogenous varieties also occur. The boundary between the symplectite and plagioclase is

Table 3. 76535: Minor phases in "mesostasis" areas.

	(1)	(2)	(3)	(4)	(5)	(6)	(7)	(8)	(9)
P_2O_5	n.a.	41.45 ± 0.18	43.39 ± 0.69	n.a.	n.a.	n.a.	41.67	45.47	tr.
SiO_2	0.01	0.35 ± 0.06	0.33 ± 0.28	56.99	55.02	65.25	0.34	0.14	n.d.
TiO_2	2.03	n.a.	n.a.	0.05	0.06	0.05	n.a.	n.a.	10.0
Cr_2O_3	0.09	n.a.	n.a.	< 0.01	0.15	n.a.	n.a.	n.a.	< 0.01
Al_2O_3	n.a.	0.05 ± 0.07	0.01	0.12	0.21	17.28	< 0.01	< 0.01	< 0.01
MgO	0.37	0.09 ± 0.01	3.77 ± 0.64	33.46	18.21	0.79	0.13	3.54	< 0.01
CaO	n.a.	55.57 ± 0.54	40.97 ± 0.39	0.39	24.47	0.20	55.29	47.51	6.7
FeO	0.15	0.08 ± 0.05	0.30 ± 0.09	7.89	2.11	0.57	0.24	0.65	0.9
MnO	< 0.01	n.a.	n.a.	0.16	0.04	n.a.	n.a.	n.a.	n.d.
BaO	n.a.	n.a.	n.a.	n.a.	n.a.	0.98	n.a.	n.a.	n.d.
Na_2O	n.a.	< 0.01	0.06 ± 0.01	< 0.01	0.12	< 0.01	< 0.01	0.31	n.d.
K_2O	n.a.	n.a.	n.a.	n.a.	n.a.	12.37	n.a.	n.a.	n.d.
ZrO_2	93.47	n.a.	n.a.	n.a.	n.a.	n.a.	n.a.	n.a.	n.a.
V_2O_3	0.35	n.a.	n.a.	n.a.	n.a.	n.a.	n.a.	n.a.	n.a.
Nb_2O_5	1.22	n.a.	n.a.	n.a.	n.a.	n.a.	n.a.	n.a.	50.1
Y_2O_3	n.a.	0.09 ± 0.03	4.25 ± 0.07	n.a.	n.a.	n.a.	0.03	2.12	4.4
RE_2O_3	n.a.	0.29 ± 0.03*	5.81 ± 0.73*	n.a.	n.a.	n.a.	0.24*	0.37*	n.d.
HfO_2	2.19	n.a.	n.a.	n.a.	n.a.	n.a.	n.a.	n.a.	n.d.
ThO_2	n.a.	n.a.	n.a.	n.a.	n.a.	n.a.	n.a.	n.a.	16.2
UO_2	n.a.	n.a.	n.a.	n.a.	n.a.	n.a.	n.a.	n.a.	2.3
PbO	n.a.	n.a.	n.a.	n.a.	n.a.	n.a.	n.a.	n.a.	6.8
F	n.a.	2.95 ± 0.13	0.04 ± 0.06	n.a.	n.a.	n.a.	2.83	< 0.01	n.d.
Cl	n.a.	1.18 ± 0.16	0.01 ± 0.01	n.a.	n.a.	n.a.	1.00	0.01	n.d.
Total	99.88	100.60†	98.90†	99.08	100.38	97.49	100.35†	100.10†	97.4

(1) Baddeleyite.
(2) Apatite (avg. and std. dev. of 5 analyses of single ~300 μm grain).
(3) Whitlockite (avg. and std. dev. of 4 analyses of single ~200 μm grain).
(4) Low-Ca pyroxene, (5) High-Ca pyroxene, (6) K-Ba feldspar } phases illustrated in Fig. 6.
(7) Apatite. (8) Whitlockite. (9) "Pyrochlore" (see text).
*Calculated based on measured abundances of La_2O_3, Ce_2O_3, and Nd_2O_3 by assuming (REE mineral/REE chondrite) = constant for all REE.
†minus oxygen for F, Cl.
n.a. = not analyzed; n.d. = not detected in λ-scan.
tr. = detected in beam scan.

sometimes "interdigitating," whereas the symplectite–olivine boundary is usually sharp (Fig. 5F). However, the reverse also occurs, and in some cases, both boundaries are sharp (Fig. 5C). As in the dunite, the variation in the texture of the symplectites points to a complex formational history.

The composition of the pyroxenes in the symplectites are illustrated in Fig. 7. It should be noted that the low-Ca pyroxene in the symplectites has a lower Ca content than the low-Ca pyroxene that occurs as discrete coarse grains. The composition of the Cr-spinel that occurs in symplectites overlaps the composition of Cr-spinel that occurs along grain boundaries. There is a considerable variation

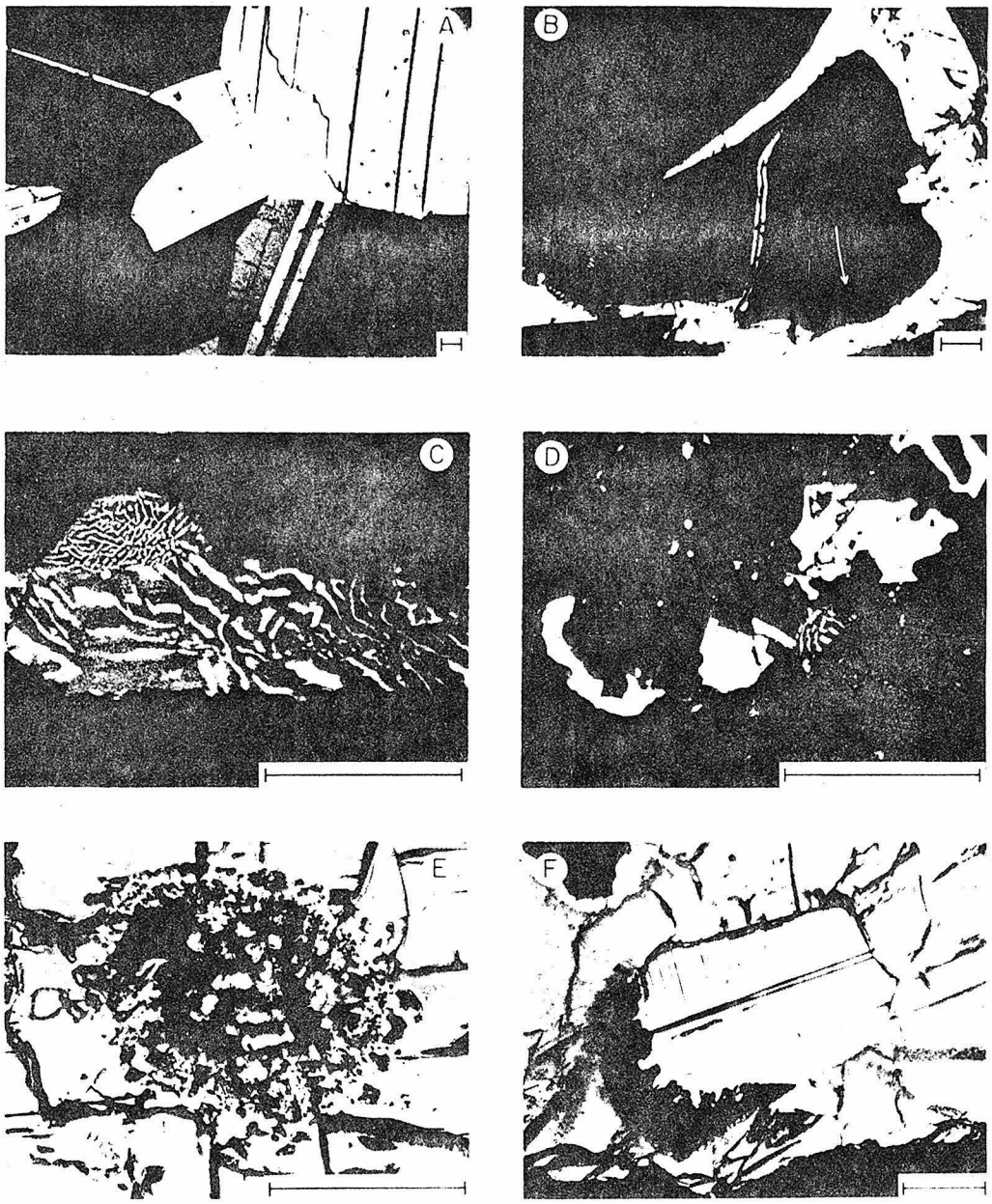

Fig. 5. Photomicrographs illustrating various textures in lunar troctolite sample 76535. All bar scales = 100 μm. (A) Granulite-like texture of troctolite characterized by straight to slightly curved grain boundaries and 120° triple junctions. The contacts between olivine (gray, lower-left and lower-right) and plagioclase do not have symplectic intergrowths developed along them. This is characteristic of the vast majority of olivine–plagioclase contacts in this sample (transmitted cross-polarized light). (B) Rounded [resorbed (?)] olivine grain (center, dark) mantled by low-Ca pyroxene (= discrete coarse-grained type). A twinned plagioclase lath is present in the lower left-hand corner. Note how the symplectic intergrowth (triangular, dark patch) invades

in spinel composition in the rock (Fig. 7); however, as noted by Gooley *et al.* (1974), there is no systematic relationship between the composition of Cr-spinel and its occurrence.

These symplectites are inferred by Gooley *et al.* (1974) to result from a solid-state reaction between olivine and plagioclase at high pressure, thus indicating a deep origin for the rock. Since most olivine–plagioclase contacts *do not* have symplectite developed along them, we infer that the stability field of olivine and plagioclase was not exceeded. In addition because the symplectites do not have the same phase assemblage everywhere, and occur in a variety of petrographic positions, we infer that they did not form by a specific reaction such as: An + 2Fo → Di + 2En + Cr-spinel. We interpret the symplectites to be the result of coprecipitation of all the phases involved from trapped intercumulus melt. Such a model is supported by the relationships displayed in Fig. 5B. Here, a demonstrably magmatic reaction texture is displayed between olivine and low-Ca pyroxene. In addition, a symplectite is developed between the olivine and low-Ca pyroxene, and along the extension of the olivine–low-Ca pyroxene reaction boundary. These relationships suggest that formation of the olivine–pyroxene reaction and the symplectite were contemporaneous, and that the symplectites formed during the primary crystallization of 76535. An example of a similar pyroxene–spinel symplectite from the Skaergaard Intrusion is figured by Wager and Brown (1967; Fig. 42) who interpreted these to represent crystallization from "... only very late dregs of the trapped liquid..." (Wager and Brown, 1967, p. 73).

In principle, a pressure calculated for the reaction mentioned above would represent the conditions under which coprecipitation occurred. However, as we have previously pointed out (Albee *et al.*, 1975), the uncertainties involved in the application of thermodynamic data to this problem are great, and a resultant pressure should in no way be considered a meaningful pressure, and hence depth, of formation of the rock.

---

olivine. In addition, note the second symplectic intergrowth at the low-Ca pyroxene–olivine grain boundary (arrow). The relationships in this photograph suggest a magmatic reaction between olivine and melt to form low-Ca pyroxene. The position of the symplectite along the extension of the olivine–low-Ca pyroxene contact suggests that the symplectite formed contemporaneously with the low-Ca pyroxene, perhaps by crystallization from melt trapped at this grain junction (transmitted cross-polarized light). (C) Symplectite developed along grain boundary between olivine (top) and plagioclase (bottom). Note the bimodal grain size of the Cr-spinel (bright gray) which clearly indicates a complex formational history. This biomodality is atypical of the symplectic intergrowths (reflected light). (D) Multiphase inclusion in olivine grain. This is a portion of the "mosaic assemblage" figured by Gooley *et al.* (1974). Note the variation in the form of the Cr-spinel from skeletal and embayed to vermicular (bright gray), and the irregular shape of the curved metal grain (white) (reflected light). (E) Multiphase inclusion in olivine; additional data on this inclusion are presented in Fig. 6 (transmitted plane-polarized light). (F) Symplectic intergrowth developed between olivine and plagioclase. A large portion of the grain boundary does not show the intervening symplectite. Note the contrast in the nature of the contact between the symplectite and olivine (sharp) and symplectite and plagioclase (interdigitating) (transmitted cross-polarized light).

76535 also contains polyphase aggregates that occur either as inclusions in olivine, or, in one case, along a plagioclase–plagioclase grain boundary. These were termed "mosaic assemblages" by Gooley *et al.* (1974), and consist of all or some of the following phases: low-Ca pyroxene, high-Ca pyroxene, apatite, whitlockite, Cr-spinel, metal, baddeleyite, K-Ba feldspar, and "pyrochlore." Due to the presence of these abundant late-crystallizing phases, we prefer to call these aggregates "mesostasis" areas. In fact, one contains a semi-opaque material that appears to be K- and Si-rich devitrified glass. As shown in Fig. 5D, the form of the spinel ranges from anhedral and embayed to vermicular. The vermicular spinel is intergrown with pyroxene to form a symplectite identical in texture to those present at grain boundaries. The embayed habit of the Cr-spinel resembles the form of ilmenite in many mare basalt samples. We interpret the "mesostasis" areas as the result of crystallization of residual trapped melt.

Compositions of the pyroxene in the "mesostasis" areas are illustrated in Fig. 7; and analyses of other phases in these areas are listed in Table 3. The distribution of phases in one of these inclusions (Fig. 5E) is illustrated in Fig. 6. The composition of the "pyrochlore" listed in Table 3 is unusual in that it contains several percent of U, Th, and Pb. A model age calculated from our microprobe analysis, assuming no initial Pb, yields an "age" of ~4.4 AE. Hinthorne *et al.*, (1975) determined the abundances of U–Th–Pb with an ion microprobe and reported a Pb–Pb model age for this grain of 4.27 AE. However, the grain is extremely small (~ 5 μm) and the analysis in Table 3 is not of very high quality.

C. Inferred history

Gooley *et al.* (1974) have suggested that 76535 represents an olivine–plagioclase cumulate. None of our observations contradicts such a conclusion and we also support this interpretation. Haskin *et al.* (1974) estimated the amount of trapped liquid to be 8–16%. In our model for the origin of 76535, this trapped melt crystallized to form olivine and plagioclase, perhaps represented by the inclusion-free rims of some grains (= adcumulus overgrowths), coarse grains of low-Ca pyroxene, the symplectic intergrowths, and the "mesostasis" areas. The development of a symplectic texture may result from the fact that 76535 was held at a temperature just above the solidus for an extended period of time. Subsequently, the sample was annealed during slow cooling to produce the equilibrated, granulite-like texture.

Despite the difference in interpretation of the origin of the symplectic intergrowths in 76535, which we feel should not be used as *prima facie* evidence for deep formation of this, or any other lunar rock, we agree with the general conclusion of Gooley *et al.* (1974) that 76535 formed at a depth greater than most of the returned lunar samples. The texture of the rock, the phase homogeneity, X-ray data on plagioclase (Smyth, 1975) and equilibration of high-Ca and low-Ca pyroxene and metal to temperatures below 810°C (Lindsley *et al.*, 1974; Hewins and Goldstein, 1975), are all consistent with a deep origin of this sample.

The compositions of the plagioclase, olivine, pyroxene, and Cr-spinel in 76535

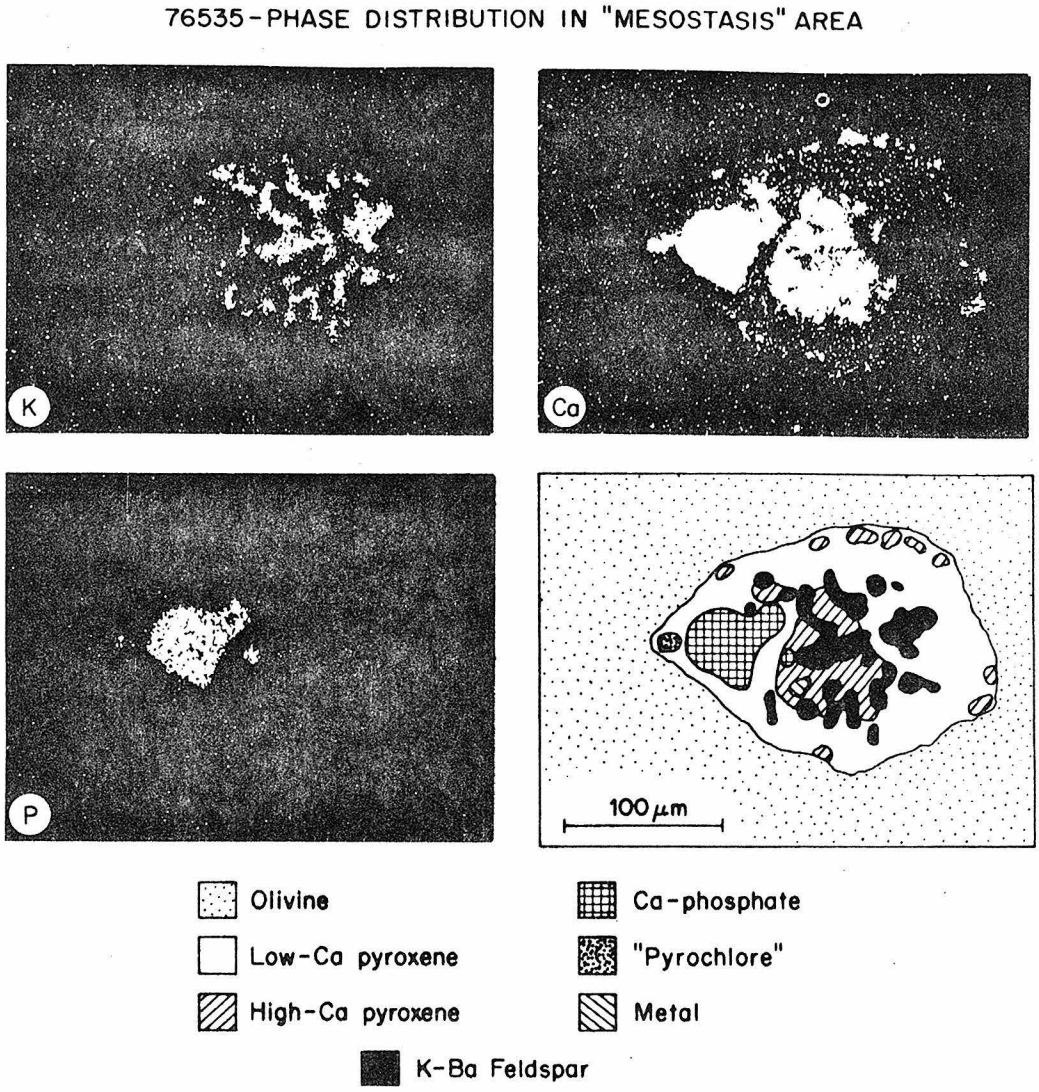

Fig. 6. X-ray scans for K, Ca, and P across the inclusion in olivine illustrated in Fig. 5E. The map showing phase distribution was drawn from these and other element X-ray scans. Compositions of the phases in this inclusion are listed in Table 3.

(compare Figures 4A and 7) are such that it could be related to 72415-8 by fractional crystallization of olivine and Cr-spinel, with the troctolite representing a cumulate rock formed after the plagioclase–olivine cotectic was intersected. However, in order to prove such a relationship, it must be demonstrated that the ages of 76535 and 72415-8 are the same.

Although the troctolite appears "pristine" compared to the dunite; i.e. 76535 shows no obvious evidence of having been affected by a shock event as intense as the one that transformed the dunite, no unequivocal primary or recrystallization

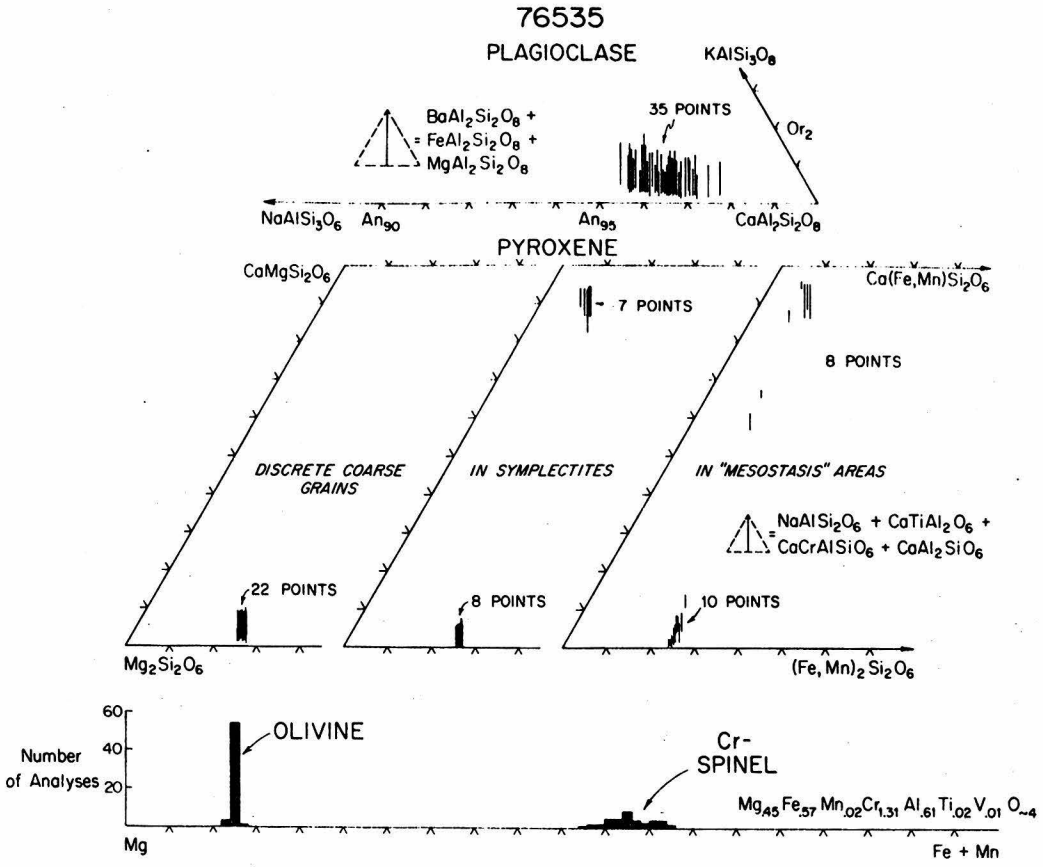

Fig. 7. Compositions of the principal phases in lunar troctolite sample 76535. Pyroxene compositions are separated according to petrographic occurrence as discussed in the text.

age has yet been obtained on it. The U–Pb systematics are disturbed, but suggest that the rock was last equilibrated at ~4.0 AE (Tera and Wasserburg, 1974). Bogard *et al.* (1974) showed that the Rb–Sr systematics have been disturbed, and that their data did not uniquely define an isochron. In addition, Bogard *et al.* (1974) reported an age of 4.34 AE for a plagioclase separate, and 4.14 AE for the total rock, by the K–Ar method after correction for trapped excess ^{40}Ar. A detailed $^{40}Ar/^{39}Ar$ study (Huneke and Wasserburg, 1975) yielded complex release patterns consistent with the presence of excess ^{40}Ar. These experiments were interpreted to indicate that a disturbance occurred more recently than 4.08 AE, and that an age of formation could not be determined reliably. Husain and Schaeffer (1975) reported $^{40}Ar/^{39}Ar$ data for 76535 and no excess ^{40}Ar. They interpreted a ~4.26-AE plateau to represent the age of excavation by the Serenetatis basin-forming event. Hinthorne *et al.* (1975) reported a Pb–Pb model age of 4.27 AE for our "pyrochlore" grain based on an ion microprobe study. The constraints of the presently available isotopic data regarding the origin of 76535 as a cumulate rock

related to the primary lunar differentiation can perhaps best be met by assuming that 76535 was an open system isotopically between ~4.55 AE and the time of excavation—4.25 according to Husain and Schaeffer (1975) or younger than 4.08 according to Huneke and Wasserburg (1975). However, the constraints can also be met by a scenario in which the rock is not assumed to be an isotopically open system for the entire period between the two events.

V. NORITE (78235)

A. Sample description

Sample 78235 (199.0 g) was one of five fragments collected from a glass-coated $\frac{2}{3}$-m boulder at Apollo 17 Station 8. It was described in the sample catalog as a coarse-grained, grayish-green, "gabbroic" rock with cumulate (?) layering. Jackson *et al.* (1975) presented a detailed study of the five hand specimens, together with an analysis of fabric orientations in the boulder, and emphasized the clear-cut evidence for these rocks as cumulates. Study of polished thin section 78235,51 (area $\approx 120\ mm^2$) indicates that this sample is a shocked and melted norite comprised of plagioclase (~40%), low-Ca pyroxene (~40%), and glass (~20%), with rare grains of high-Ca pyroxene, troilite, SiO_2, chromite, and whitlockite. In 78235,49, McCallum *et al.* (1975a) have reported a similar suite of accessory minerals that also includes fluorapatite, chromian rutile, Fe–Co–Ni metal, and baddeleyite. Thus the minor phases in 78235 are remarkably similar to those found in 76535. Analyses of the principal phases in 78235 are listed in Table 4, and mineral compositions are illustrated in Fig. 8.

B. Petrography and mineral chemistry

Sample 78235 shows the effects of extensive shock-induced deformation. Nearly half of the plagioclase has been transformed into maskelynite, whereas the remainder displays marked undulose extinction and is in part devitrified maskelynite. Crystalline plagioclase is only rarely preserved as well-twinned, rhomb-shaped zones in a few grains. Likewise, the pyroxene has been altered to brown, partly isotropic material that locally possesses multiple (shock-induced?) twinning. Most pyroxene grains show a mosaic or undulose extinction. However, despite these extreme shock effects in the minerals, original grain shapes and grain boundaries have been preserved. No obvious planar fabric is present in our thin section, in contrast to that figured by McCallum *et al.* (1975a).

Individual crystals of plagioclase and low-Ca pyroxene (up to 5 mm long) are present in subequal amounts, and form what was originally an equigranular, coarse-grained rock with straight to smoothly curved grain boundaries. Several smaller grains of low-Ca pyroxene occur at junctions of adjacent plagioclase crystals. High-Ca pyroxene occurs as inclusions in plagioclase and along grain boundaries; troilite occurs as inclusions in both plagioclase and pyroxene; SiO_2 and whitlockite occur along grain boundaries; and a single grain of chromite was

Table 4. 78235: Selected phase compositions.

	Plag.	Low-Ca pyx	High-Ca pyx	Glass-coating (1)	Glass veins (2)	Calculated composition (3)
P_2O_5	n.a.	n.a.	n.a.	0.05 ± 0.05	0.10 ± 0.10	
SiO_2	44.79	55.08	51.33	49.42 ± 1.19	48.41 ± 0.32	49.8
TiO_2	0.01	0.17	1.01	0.16 ± 0.04	0.15 ± 0.01	0.08
Cr_2O_3	n.a.	0.63	1.11	0.35 ± 0.10	0.34 ± 0.06	0.31
Al_2O_3	34.79	1.08	2.86	17.86 ± 4.64	18.52 ± 0.72	18.4
MgO	0.06	29.65	15.77	14.25 ± 3.52	12.96 ± 0.66	14.5
CaO	19.09	1.47	22.49	10.24 ± 1.76	10.52 ± 0.21	10.5
FeO	0.13	12.17	4.90	6.97 ± 1.83	7.67 ± 0.68	6.02
MnO	n.a.	0.19	0.12	0.10 ± 0.03	0.12 ± 0.04	0.10
BaO	< 0.01	n.a.	n.a.	0.02 ± 0.03	0.02 ± 0.02	—
Na_2O	0.60	0.01	0.09	0.25 ± 0.12	0.39 ± 0.03	0.30
K_2O	0.10	n.a.	n.a.	0.06 ± 0.04	0.08 ± 0.03	0.05
ZrO_2	n.a.	n.a.	n.a.	< 0.01	< 0.01	—
NiO	n.a.	n.a.	n.a.	0.05 ± 0.05	0.16 ± 0.13	—
SO_3	n.a.	n.a.	n.a.	0.07 ± 0.04	0.30 ± 0.05	—
Total	99.57	100.44	99.70	98.82	99.74	99.96
	An 93.2	Wo 1.2	Wo 40.7			
	Ab 5.3	En 77.5	En 43.4			
	Or 0.6	Fs 18.1	Fs 7.7			
	Others 0.9	3.2	8.2			

(1) Avg. and std. dev. for 8 analyses.

(2) Avg. and std. dev. for 10 analyses.

(3) Based on 51% plagioclase and 49% low-Ca pyroxene. It was assumed that the glass veins represent a bulk analysis of the rock. Then, by comparing mixing ratios for various oxide pairs, it was found that the "best fit" to the composition of the glass veins was obtained using these phase abundances.

n.a. = not analyzed.

found included in low-Ca pyroxene. Our thin section does not appear to contain the metal–diopside–chromite–silica intergrowths within low-Ca pyroxene that were reported by Schlar and Bauer (1975).

The plagioclase, low-Ca pyroxene, and high-Ca pyroxene show almost no compositional variation (An_{92-94}; $Wo_{2-3}En_{77-78}Fs_{18-19}$; $Wo_{47}En_{45}Fs_8$; Fig. 8). Both the plagioclase and low-Ca pyroxene contain only small amounts of minor elements, but the high-Ca pyroxene contains ~2 wt.% Al_2O_3, and ~1 wt.% each of TiO_2 and Cr_2O_3, (Fig. 8; Table 4). Compositions of the spinel and whitlockite could not be accurately determined, but qualitative analysis indicates that the spinel is an aluminous Mg–Fe chromite, and that the whitlockite contains ~3 wt.% Ce_2O_3, and ~1 wt.% each of Y_2O_3 and Nd_2O_3.

The thin section is crosscut by veinlets of dark-brown, vesicular glass up to ~1 mm wide. These contain inclusions of plagioclase, plagioclase glass, and low-Ca pyroxene that are identical in composition to those that form the rock. Some of the inclusions are shaped like teardrops or lozenges, appear to have been

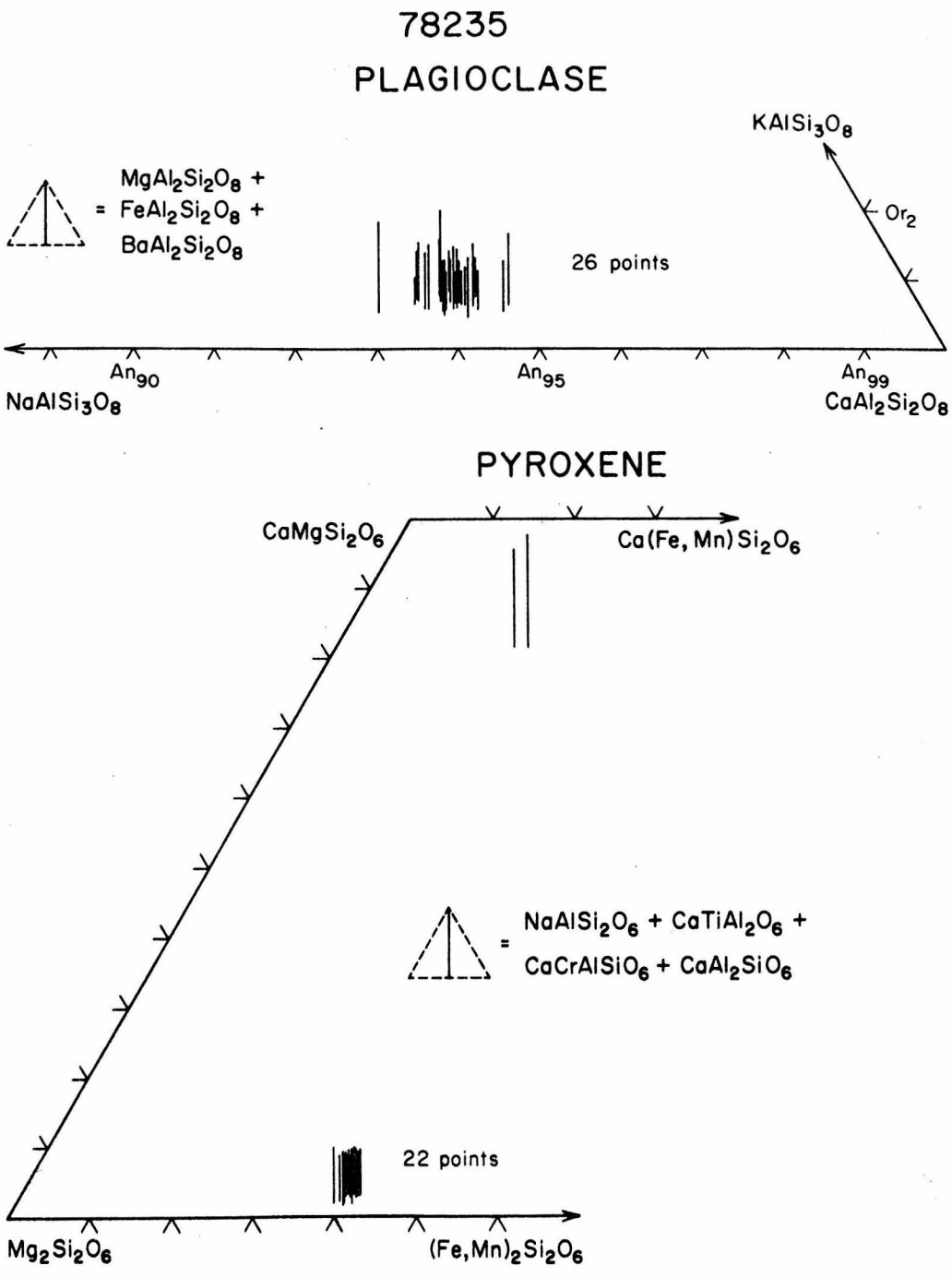

Fig. 8. Compositions of the pyroxene and plagioclase in lunar norite sample 78235.

partly assimilated by the glass, and have their long axes aligned parallel to the walls of the veins. The glass veins contain abundant opaque beads. The larger ones are troilite, one of which contains an inclusion of Fe metal. The composition of this metal (≤ 0.5 wt.% Ni and Co) is distinct from the metal compositions reported in 78235 by McCallum *et al.* (1975a), and suggests an origin by reduction of the sulfide. The glass veins are flow-banded, and clearly crosscut and intrude the rock.

These veins are relatively homogenous in composition throughout, and contain subequal amounts of normative pyroxene (En_{76}) and plagioclase (An_{93}) (Fig. 9A). When plotted on oxide variation diagrams such as CaO–FeO, CaO–MgO, FeO–Al_2O_3, and MgO–Al_2O_3 (e.g. Fig. 9B), the compositions of the veins fall on a mixing line between the measured composition of the plagioclase and low-Ca pyroxene. The fact that the glass composition is slightly displaced from this mixing line indicates that a small amount of other phases contribute chemically to the glass. These relationships suggest that the glass veins represent a total melt of the norite that has been mobilized and injected into the sample along fractures.

One exterior portion of the thin section contains a portion of the glass-coating. It is flow-banded, and consists of alternating layers of light- and pale-brown glass. Swirls of tiny opaque beads (≤ 1 μm) parallel this banding. The boundary between the glass-coating and the rock is marked by a pale zone containing glassy spherulites and inclusions of low-Ca pyroxene and plagioclase that also are identical in composition to those phases in the rock. The glass-coating is chemically inhomogenous, but its composition lies along the same mixing line as the veinlets (Fig. 9B). This suggests that the glass-coating is also a melt of the norite, but is not as well-mixed as the veins. In some of the hand specimens from this boulder, Jackson *et al.* (1975) report continuity between the glass-coating and the glass veins.

C. Inferred history

The coarse grain size of 78235 indicates that this sample evolved in a plutonic environment. This observation, together with the presence of a well-documented cumulate texture (Jackson *et al.*, 1975), suggests that 78235 could be a product of crystallization–differentiation in a large magma body. The composition of the plagioclase ($\sim An_{93}$) and low-Ca pyroxene ($\sim En_{78}$) are such that it is possible that noritic rocks like 78235 are related via crystal fractionation and liquid line of descent to dunitic and troctolitic rocks like 72415-8 and 76535. The principal requirement for such an origin is that 78235 be an ancient rock. Isotopic studies have helped to establish the old age of both 76535 and 72415-8. However, 78235 has been so strongly modified by later impact melting, that it seems unlikely that similar isotopic studies will establish an unequivocal age for the formation of the cumulate texture. Hence, our petrographic study is consistent with the formation of 78235 by the accumulation of plagioclase and orthopyroxene during the primary lunar differentiation, but an origin in a separate and younger magmatic event cannot be precluded on the basis of available data.

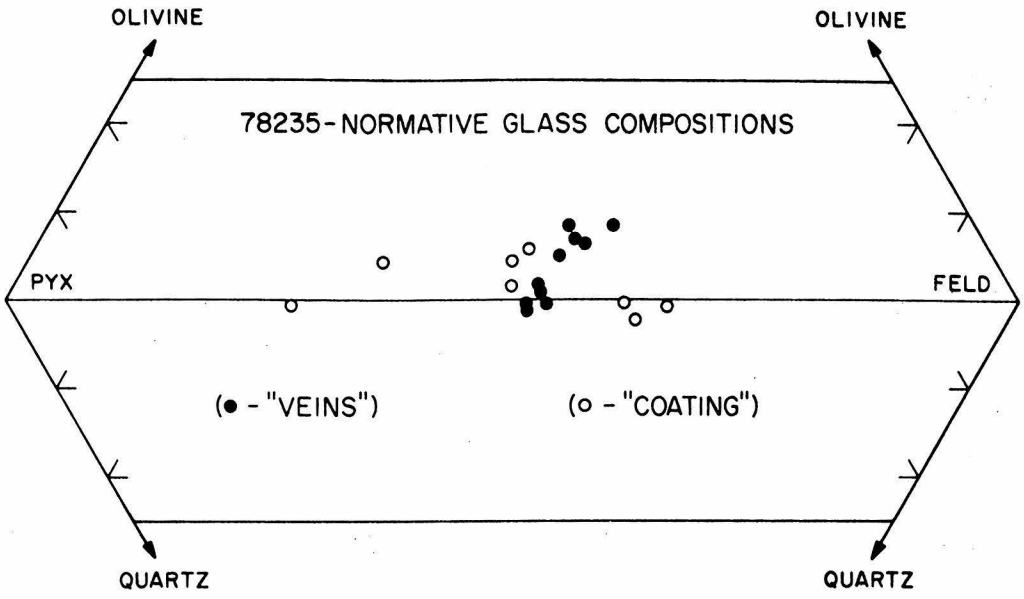

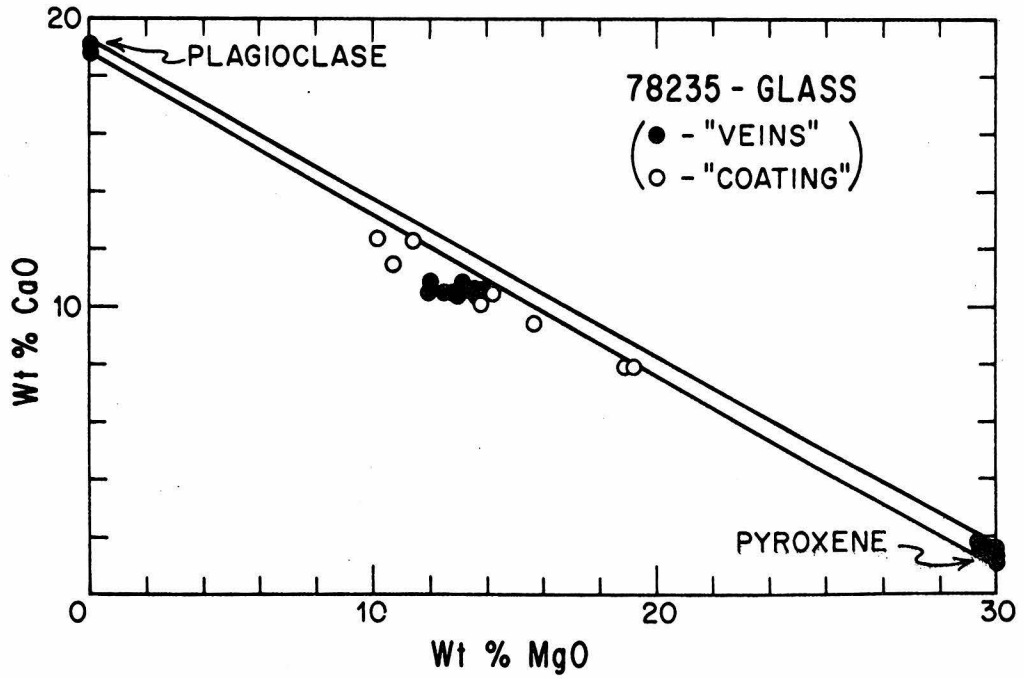

Fig. 9. (A) Normative compositions of the glass veins and glass-coating in sample 78235. (B) Compositions of the glass in sample 78235 plotted on a CaO–MgO variation diagram.

VI. Anorthosite (62237)

A. Sample description

Sample 62237 was a 62.4-g rock (5 × 4 × 3 cm) that was found perched on the lunar surface at Apollo 16 Station 2. The hand specimen was very light gray in color, subangular to blocky, and moderately friable. It was described in the sample catalog as a monomict anorthosite microbreccia, comprised of shattered and broken plagioclase (~80%), with clots of mafic minerals (~20%). LSPET (1972) subsequently classified 62237 as a cataclastic anorthosite (Type II rock). Our study indicates that 62237 is a monomict-brecciated troctolitic anorthosite comprised of plagioclase (83%) and olivine (16%), with minor amounts of pyroxene (1%), Cr-spinel, ilmenite, and troilite.

The measured mode, an analysis corresponding to the average composition of each phase, and a calculated bulk-chemical composition based on an electron microprobe point count of polished thin section 62237,10 (≈ 150 mm^2) are presented in Table 5; mineral compositions are illustrated in Fig. 12. In general, 62237 strongly resembles other Apollo 16 anorthositic rocks such as 67075 (McCallum *et al.*, 1975b).

B. Petrography and mineral chemistry

As can be seen in Fig. 10, 62237 is marked by extreme textural inhomogeneity. However, although this sample has been extensively modified by later crushing, the original coarse grain size is locally preserved. Large grains of fractured plagioclase and olivine (up to 3 mm) form what appears to be a primary igneous cumulate texture. The plagioclase in this portion of the thin section is well-twinned and transected by numerous microfaults (Fig. 11A). The original large olivine grains have been transformed into numerous optically continuous subgrains separated by very fine-grained crush zones.

This "coarse" portion of the thin section grades rapidly into a zone comprised predominantly of fine-grained mineral debris. A few clasts of polygonally textured "microanorthosite" (Fig. 11B) and "microdunite," together with three glass fragments (15, 50, and 100 μm, respectively) occur in this area. The compositions of the glass fragment are highly feldspathic, and consistent with derivation from the enclosing sample by shock-melting. The remainder of the thin section consists of angular fragments of plagioclase, olivine, pyroxene, Cr-spinel, and troilite. Many of these plagioclase grains are characterized by very fine, shock-induced (?), polysynthetic twin lamellae. In addition, about $\frac{1}{4}$–$\frac{1}{3}$ of the plagioclase in the disaggregated portion of the thin section has been transformed into a pale-brown, nearly isotropic material that is probably devitrified maskelynite. Despite the pervasive evidence for shock, none of the olivine shows strain features like those present in the dunite olivine.

The plagioclase has a measured range in composition from An_{95} to An_{99}, and contains only small amounts of minor elements. Some grains contain rounded inclusions of Cr-spinel (10–50 μm), and rounded to elongate blebs of pyroxene

Table 5. 62237: Phase abundances, "average" phase compositions, and bulk-chemical composition.

	Plag.	Olivine	Low-Ca pyx	Low-Ca pyx†	High-Ca pyx	Cr-spinel	Ilmenite	Troilite*	Bulk composition calculated
Vol.%	$82.6_7 \pm 1.7_2$	$16.1_2 \pm 0.7_6$	$0.6_8 \pm 0.1_6$	$0.2_0 \pm 0.0_9$	$0.1_6 \pm 0.0_8$	$0.1_8 \pm 0.0_8$	< 0.01	< 0.01	(2807 points)
Wt.%	78.4_1	20.0_5	0.8_1	0.2_4	0.1_9	0.3_0	< 0.01	< 0.01	
SiO_2	43.56	35.59	53.20	51.24	50.88	0.03	0.01	0.01	41.94
TiO_2	0.01	0.01	0.35	0.28	0.61	2.82	53.24	< 0.01	0.02
Al_2O_3	35.94	< 0.01	0.72	0.72	1.50	13.14	< 0.01	n.a.	28.23
Cr_2O_3	n.a.	0.05	0.33	0.27	0.37	48.66	0.33	< 0.01	0.16
MgO	0.03	30.11	24.37	19.89	13.04	3.08	3.27	< 0.01	6.34
FeO	0.17	34.58	19.72	24.49	11.98	31.77	42.24	63.84	7.40
MnO	n.a.	0.42	0.35	0.41	0.37	0.74	0.50	< 0.01	0.09
CaO	20.00	0.03	1.10	1.69	21.22	n.a.	n.a.	0.03	15.74
BaO	< 0.01	n.a.	n.a.	n.a.	n.a.	n.a.	n.a.	n.a.	< 0.01
Na_2O	0.26	n.a.	0.01	< 0.01	0.01	n.a.	n.a.	n.a.	0.20
K_2O	0.01	n.a.	n.a.	n.a.	n.a.	n.a.	n.a.	n.a.	0.01
ZrO_2	n.a.	n.a.	n.a.	n.a	n.a.	0.08	< 0.01	n.a.	< 0.01
V_2O_3	n.a.	n.a.	n.a.	n.a.	n.a.	0.55	< 0.01	n.a.	< 0.01
Nb_2O_5	n.a.	n.a.	n.a.	n.a.	n.a.	< 0.01	< 0.01	n.a.	< 0.01
NiO	n.a.	0.03	n.a.	n.a.	n.a.	n.a.	n.a.	< 0.01	0.01
Co	n.a.	n.a.	n.a.	n.a.	n.a.	n.a.	n.a.	< 0.01	< 0.01
S	n.a.	n.a.	n.a.	n.a.	n.a.	n.a.	n.a.	37.76	< 0.01
Total	99.98	100.82	100.15	99.00	99.98	100.87	99.59	101.64	100.14
	An 96.8	Fo 60.5	Wo 1.1	Wo 2.4	Wo 40.5				
	Ab 2.3	Fa 39.5	En 66.2	En 56.1	En 36.3				
	Or 0.0		Fs 30.6	Fs 39.4	Fs 19.3				
	Others 0.9		2.1	2.1	3.9				

*Elemental abundances.
†Low-Ca pyroxene in exsolution relationship (e.g. Fig. 11D).
n.a. = not analyzed.

(1–20 μm). The compositions of these inclusions are the same as in larger grains that occur outside of plagioclase, thus making an origin by exsolution for all the inclusions unlikely (Steele and Smith, 1974).

Olivine also has a very restricted compositional range (Fo_{59-61}; Fig. 12). It contains small amounts of minor elements compared to mare basalt olivine (Smith, 1971), and even smaller amounts than the dunite olivine. In particular, this olivine is exceptionally depleted in Ca. The olivine contains rare inclusions of Cr-spinel (1–10 μm).

Pyroxene has a range in composition and a variety of occurrences. Low-Ca pyroxene with composition $Wo_2En_{67}Fs_{31}$, the tight cluster in Fig. 12, occurs as rare inclusions in plagioclase, as small grains interstitial to plagioclase crystals, as rims on olivine (Fig. 11C), and as fragments in the granulated matrix. One of these grains contained an inclusion of Cr-spinel. A single grain of homogenous high-Ca pyroxene ($\sim Wo_{43}En_{38}Fs_{19}$) was found in the granulated matrix. Pyroxene also occurs in complex grains such as illustrated in Fig. 11D. These consist of lamellar

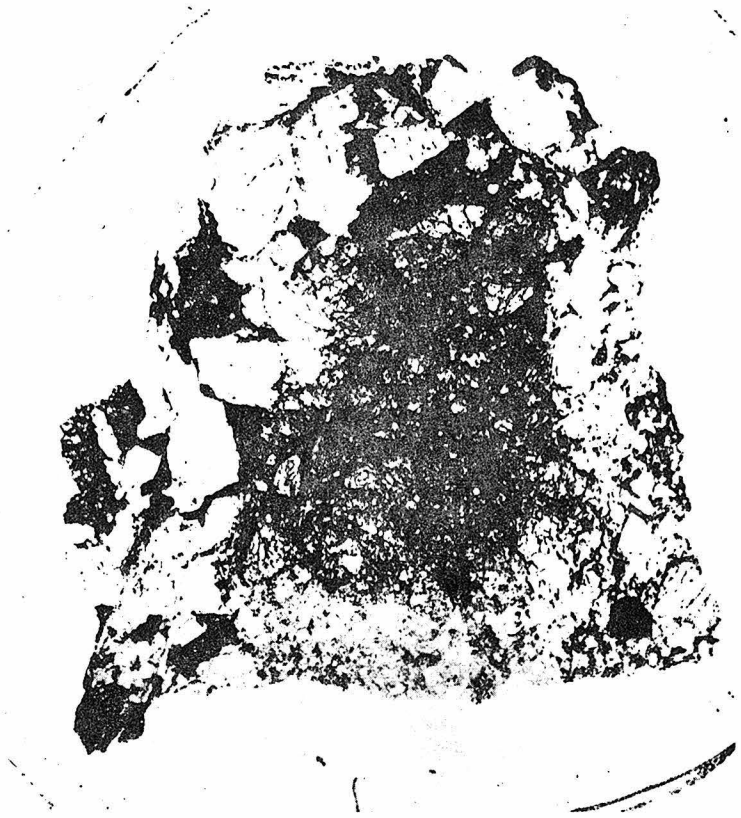

Fig. 10. Photomicrograph of polished thin section 62237,10. Note the similar and coarse grain size of olivine (dark) and plagioclase (light) in the bottom portion of the photo (horizontal dimension of thin section is approximately 12 mm).

to vermicular intergrowths of low-Ca pyroxene ($Wo_{2-4}En_{40-48}Fs_{41-48}$) and high-Ca pyroxene ($Wo_{43}En_{37-39}Fs_{20-22}$). Compositions of these exsolved pyroxenes are distinguished by a special symbol in Fig. 12. These probably represent an exsolved pigeonite, as analyses of these grains yield bulk compositions near $Wo_{12}En_{37}Fs_{51}$. The pyroxene in 62237 is particularly low in minor-element content (Fig. 12; Table 5). The compositional data on the pyroxene in this rock suggests that, at the time of original crystallization, three pyroxenes coexisted: an augite ($Wo_{43}En_{38}Fs_{19}$); a pigeonite ($Wo_{12}En_{37}Fs_{54}$); and an "orthopyroxene" ($Wo_2En_{67}Fs_{31}$). The presence of exsolution textures in the pyroxene in 62237 suggests that the sample underwent extended subsolidus equilibration, although we have not confirmed whether the low-Ca portion of these grains has inverted to the orthorhombic form. The compositions of the coexisting pairs in such grains suggest equilibration to temperatures near 800°C as in 67075 (McCallum *et al.*, 1975b).

The Cr-spinel [Mg/(Mg + Fe) = .12–.16] and ilmenite [Mg/(Mg + Fe) = .11] have a narrow range in composition (Fig. 12), and typically occur between olivine and plagioclase, although the spinel also occurs as inclusions in other phases as mentioned above. The spinel in 62237 is more iron-rich, and more Ti-rich than the

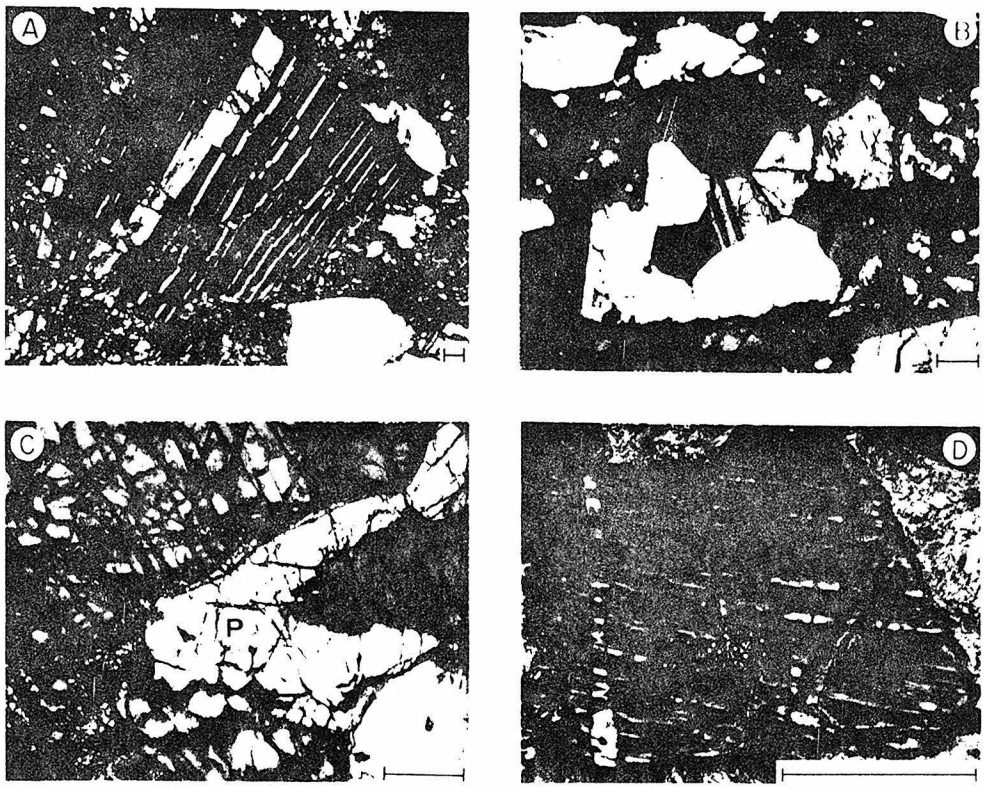

Fig. 11. Photomicrographs illustrating various textural features in lunar anorthosite 62237. All bar scales = 100 μm. All photographs with transmitted cross-polarized light. (A) Microfaults in plagioclase clast. (B) Clast of polygonally-textured plagioclase (= microanorthosite). (C) Lobate grain of homogenous low-Ca pyroxene (center, light gray) that appears to partly mantle olivine (dark gray, upper left). (D) Exsolution textures in pyroxene clast. Lamellae (all low-Ca pyroxene) occur in two directions and suggest two periods of exsolution.

spinel in the dunite or troctolite (cf. Tables 1, 2, 5). Some of the spinel grains are crosscut by tiny "veinlets" of troilite (≤ 5 μm wide). Troilite also occurs as fragments in the granulated matrix and as tiny micron-sized inclusions in plagioclase.

C. Inferred history

The coarse grain size of the plagioclase and olivine indicates that 62237 originated in a plutonic environment. This sample may have crystallized from a melt of the same composition, but the fact that the bulk composition is highly enriched in plagioclase suggests that it is much more likely a plutonic cumulate. Moreover, if 62237 is, in fact, a rock of cumulate origin, then the similar grain size of the olivine and plagioclase (Fig. 10) suggests that they are both cumulate phases. Spinel occurs as inclusions in both olivine and plagioclase, and along grain

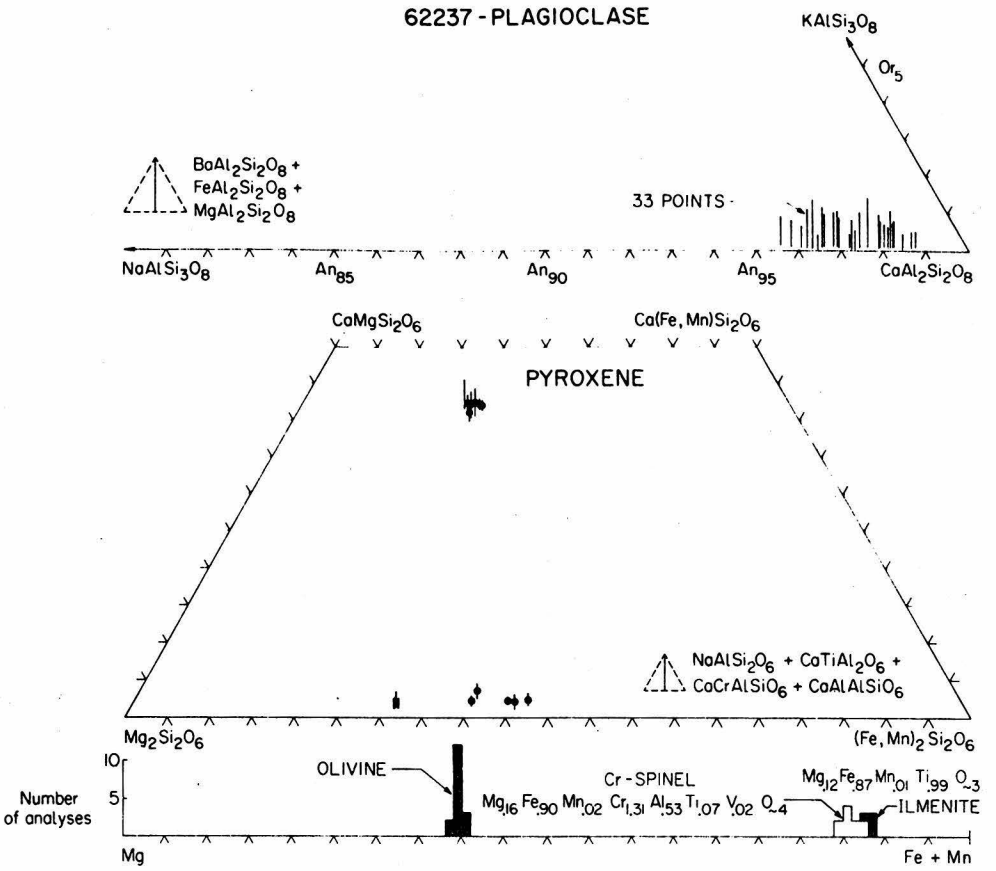

Fig. 12. Compositions of the principal phases in lunar ferroan anorthosite sample 62237. Pyroxenes with the special symbol (●) occur in exsolution relationship, such as are illustrated in Fig. 11D.

boundaries, indicating that it began crystallizing early, and continued to crystallize for an extended period of time. The pyroxene appears to have formed after olivine, and the occurrence of compositionally similar pyroxene as inclusions in plagioclase and along plagioclase–olivine grain boundaries suggests that pyroxene and plagioclase co-crystallized in part. Our interpretation of the crystallization sequence of 62237 is that spinel formed first and was followed by olivine. Olivine and spinel coprecipitated and were joined by plagioclase. Olivine reacted with the melt to form pyroxene, with plagioclase, pyroxene and spinel continuing to crystallize together. Ilmenite and troilite were the last phases to form.

Subsequent to complete solidification, 62237 underwent prolonged slow cooling during which the pigeonite exsolved and the polygonally textured plagioclase formed. A later impact event excavated this sample and produced the presently observed cataclastic texture.

62237 is characterized by very calcic plagioclase and Mg–Fe silicates with relatively low Mg/(Mg + Fe) ratios (Fig. 12). Such distinctive chemical charac-

teristics indicate that 62237 is a member of the unique lunar rock group termed "ferroan anorthosite" by Dowty *et al.* (1974). The petrographic and mineral–chemical features of 62237 also resemble those of the large rock samples 15415, 60015, 60025, 60215, 61016, and 67075 (Brown *et al.*, 1973; Dixon and Papike, 1975; Hargraves and Hollister, 1972; James, 1972; McCallum *et al.*, 1975b). Both Dowty *et al.* (1974) and McCallum *et al.* (1975b) have recognized and discussed the enigma presented by the compositions of the plagioclase and Mg–Fe silicates; i.e. the very high-An content of the plagioclase suggests "early" precipitation of plagioclase, whereas the low Mg/(Mg + Fe) of the Mg–Fe silicates suggests "late" precipitation of olivine and pyroxene, in any rational model of crystallization–differentiation. McCallum *et al.* (1975b) and Wood (1975) suggested that convective interaction might result in early-formed plagioclase trapping relatively differentiated liquid from which small amounts of "Fe-rich" olivine and pyroxene would precipitate. However, 62237 appears to be the only sample that preserves its original texture from which an origin as an *olivine–plagioclase* cumulate can be inferred. The amount of olivine in 62237, and its grain size, seem to preclude an origin simply via crystallization from trapped intercumulus melt. Moreover, crystallization of a relatively differentiated Fe-rich liquid would almost certainly involve the precipitation of abundant ilmenite as well as other less-abundant phases. A cumulate rock with phase compositions like 62237 cannot have a simple subtractive relationship with the other cumulate rocks with Mg-rich olivine and pyroxene and less-calcic plagioclase. However, one explanation would be that 62237 does represent a recrystallized plagioclase–olivine cumulate, which was formed by mixing of early plagioclase and later olivine, but one which subsequently lost any residual intercumulus melt before any substantial amount crystallized. This is supported by the lack of mesostasis in this sample.

Isotopic work on 62237 has not yet been completed. However, initial $^{87}Sr/^{86}Sr$-isotopic compositions of other lunar ferroan anorthosites are very low, and similar to the dunite I value (= 0.69900 ± 5; Papanastassiou and Wasserburg, 1975b). Such low-I values are most simply interpreted to indicate that ferroan anorthosites were isolated from a Rb-rich environment not long after ~4.6 AE and are compatible with their original formation during the early lunar differentiation.

VII. Discussion

Since the Apollo 11 mission there has been a mounting array of evidence indicating that the moon underwent a differentiation early in its history resulting in the formation of a feldspathic crust. Part of this evidence has been the recognition of possible cumulate igneous rocks among soil and rake samples and as clasts in breccias that may have formed during this early differentiation. However, since cumulate rocks also could have been formed during later, more local, magmatic activity, it is important to:

(1) establish whether any cumulate rocks are in fact relicts from such a primary differentiation;

(2) establish the characteristics of such cumulate rocks in order to distinguish primary differentiates from later ones; and,
(3) use the characteristics of such cumulate rocks to place constraints on how such samples may be related to each other in order to better understand the process of lunar differentiation and crustal formation.

The four rocks described in this paper have many similar characteristics and some marked differences. One common characteristic is the preservation of evidence for a deep-seated origin despite the varied effects of a later shock event, one which is probably related to the impact that excavated the rock. In this section we will compare and discuss the evidence that we presented in the detailed descriptions of these four rocks which has a bearing on: (A) the nature and age of the later shock event, (B) the origin and age of the primary deep-seated rock, and (C) their possible genetic relationships.

A. *Nature and age of the later shock events*

Intense shock effects characterize three of these samples and only troctolite 76535 displays no obvious major shock effects. However, 76535 is very friable and resembles sample 76536, which is a crushed equivalent (J. Warner, written communication, 1975). Hence, there is some evidence to suggest that 76535 has been shocked, although the effects are very minor compared to the other samples. Almost no recrystallization of shock-produced maskelynite or melt (glass) has occurred in norite 78325 or anorthosite 62237, but in dunite 72415-8, post-shock recrystallization has occurred along strain bands in olivine, in maskelynite, and in shock-produced melt. This post-shock recrystallization was followed by a still-later shock event, that resulted in the crushing of the rock without recrystallization or other mineralogic effects.

Isotopic studies on the dunite and the troctolite indicate that the later shock event was probably part of the *ca.* 3.9–4.0 lunar cataclysm (Tera *et al.*, 1974). It is logical to relate this event to the excavation of these relatively deep-seated rocks during the major basin-forming events. This chronologic control provides evidence that these cumulate rocks are not directly related to the mare basalts and that, in particular, they cannot represent a residua from which the mare basalts were derived by partial melting. They provide substantial evidence that the upper portions of the moon were "layered" and differentiated prior to the eruption of the mare basalts.

B. *Origin and age of the primary rocks*

All four rocks are exceedingly coarse-grained—by lunar standards—and grain sizes up to 5–10 mm have been preserved despite the later shock event. Both the norite 78235 and the anorthosite 62237 preserve a coarse cumulate texture and the other two samples also appear to be cumulate in origin, although their primary textures have been modified.

All four samples provide evidence for a long period of subsolidus annealing. The compositions of coexisting pyroxenes indicate that pyroxene equilibration occurred at less than 810°C in all four rocks (Lindsley *et al.*, 1974). Features indicative of long annealing, such as phase homogeneity, 120° triple junctions, phase relations of metal phases, X-ray crystallographic study of plagioclase etc. are best developed in the troctolite 76535 (Gooley *et al.*, 1974). Such features are least well developed in dunite 72415-8 in which post-shock recrystallization has been most extensive. Collectively these samples provide good evidence that they are cumulate igneous rocks that have undergone a long period of annealing. We can also infer that they therefore formed (and remained for some time) at a greater depth than most known samples of lunar rocks.

The single most important clue to the origin of these rocks is the 4.55 AE age determined by a Rb–Sr internal isochron on dunite 72417. This primary age has been preserved despite the complex shock history experienced by this rock, whereas troctolite 76535, which shows little evidence of a later shock event, has not yet yielded an unequivocal age. It seems most likely to us that the discrepancies between the textural evidence and the various isotopic studies will fall to further isotopic work. Nevertheless it is intriguing to note that these discrepancies can be resolved by assuming: (1) that the Rb–Sr isochron in 72417 dates the intense shock event at a time very shortly after the formation of the rock rather than the primary age, and that the later crushing marks the excavation event; and (2) that the troctolite 76535 was annealed with continued extensive recrystallization for about 0.5 AE before being excavated (Husain and Schaeffer, 1975; Stewart, 1975).

As mentioned previously, the extensive shock-melting superimposed on the primary cumulate texture in norite 78235 probably precludes a reliable determination of its original crystallization age.

Isotopic work on anorthosite 62237 has not yet been completed. However, the relatively well-preserved original texture suggests that meaningful isotopic data can be obtained on this sample. We emphasize that the initial $^{87}Sr/^{86}Sr$ isotopic compositions of other lunar ferroan anorthosites are very low, and consistent with their derivation during the early lunar differentiation. At this time, the isotopic chronological evidence is not incompatible with the concept that such cumulate rocks are relicts of primary lunar differentiation, and the data on the dunite strongly supports this concept.

Evidence from the phase relations and mineral chemistry as well as the textural evidence also supports an origin as igneous cumulates rather than simply as deep-seated metamorphic rocks. In the dunite, troctolite, and norite, calcic plagioclase coexists with Mg-rich olivine and pyroxene. These compositions appear to be compatible with each other in magmatic processes on the basis of experimental work and mineral pairs in terrestrial layered mafic plutons. Despite the evidence for a long annealing time and recrystallization of the pyroxenes, the Fe/Mg ratio of the pyroxenes and olivine in general must reflect the primary magmatic Fe/Mg because these rocks contain almost no other Fe- or Mg-bearing phases with which they could react and substantially change their compositions.

Each of these rocks could form by accumulation of the appropriate minerals with relatively small amounts of trapped residual liquid. The troctolite and the norite contain mesostasis areas such as might be related to late-stage crystallization of a residual melt—the concept of a cumulate origin for these three rocks is also supported by trace-element studies on the dunite by Laul and Schmitt (1975a,b), on the troctolite by Haskin *et al.* (1974), and on the norite by Winzer *et al.* (1975). The latter also note that the cumulate plagioclase and pyroxene in the norite could not have been in equilibrium with the same liquid.

The anorthosite 62237 contains unusually Fe-rich olivine and pyroxene relative to the An content of its plagioclase. This association can be explained by convective mixing of early plagioclase with later olivine and pyroxene, with subsequent loss rather than retention of most of the residual melt, in accord with its lack of mesostasis. Such a model is supported by the textural evidence, which indicates that in 62237, both the olivine and plagioclase are cumulate phases.

The mineral chemistry provides additional evidence on possible relationships of these cumulate rocks with mare basalts—even avoiding the controversy over plagioclase saturation of the melt. The mafic phases in the dunite, troctolite, and norite are too Mg-rich, and those in the anorthosite are too Fe-rich, to have coexisted with residual melts with the composition of the mare basalts (Green *et al.*, 1975).

C. *Petrogenetic considerations*

Models for the mineral crystallization sequence that accompanied the primary lunar differentiation generally invoke the settling of olivine and pyroxene, and the "flotation" of plagioclase, resulting in an upper "crustal" portion enriched in anorthositic rocks, and a lower "mantle" portion enriched in mafic minerals (Hodges and Kushiro, 1974; Taylor and Jakeš, 1974; Wood, 1975). Walker *et al.* (1975) have emphasized the problems that emerge from pressure and thermal gradients in a magma chamber hundreds of kilometers thick, and their possible effects on crystallization sequence. Lunar seismic data require that the "crust"–"mantle" boundary occur at $\simeq 60$ km (Toksöz *et al.*, 1974). Hence, if the gravitative separation of early-formed, Mg-rich olivine was carried out effectively, then a major problem is encountered regarding the depth of origin of the dunite.

Cratering models indicate that the maximum depth of excavation by the major basin-forming events may be as low as 20 km (Head *et al.*, 1975). Hence, it is possible, within the realm of presently available data and models, that the lunar dunite was not excavated from a depth near the "crust"–"mantle" boundary where olivine-rich rocks are likely to be an important constituent.

On the basis of plagioclase, pyroxene, and olivine compositions, the dunite 72415-8, troctolite 76535, and norite 78235 can be related by simple fractional crystallization: initial crystallization and accumulation of olivine to form the dunite; co-crystallization of olivine and plagioclase to yield the troctolite; reaction between olivine and melt to form orthopyroxene; and co-crystallization of

plagioclase and orthopyroxene to form the norite. This model breaks down, however, because of the very high-An content of the ferroan anorthosite 62237. The latter problem is enhanced by the negative correlation between the An content of plagioclase and Mg/(Mg + Fe) in mafic minerals noted by Steele and Smith (1973) in Apollo 16 soil fragments that is contrary to the trend predicted from terrestrial igneous complexes.

McCallum *et al.* (1975b) have suggested that crystallization in the lunar system might be best modeled by considering the Upper Border Group of the Skaergaard Intrusion where "inverted" mineral stratigraphy is present (Wager and Brown, 1967). Morse (1969) noted a similar situation in the Upper Border Zone (UBZ) of the Kiglapait Intrusion. He interprets this to indicate that "... crystals which formed the UBZ and bottom cumulates differed only in their direction of motion after nucleation." (Morse, 1969; p. 42). Such a mechanism may be important in the petrogenesis of the lunar highland crust. We propose that the dunite, troctolite, and norite may represent "cumulate" rocks that formed during crystallization downward from the "roof" of the lunar "magma chamber." Below this zone, turbulent mixing of later olivine with plagioclase would form the ferroan anorthosites (Wood, 1975). An increase in An content of plagioclase with depth could be brought about by steep temperature gradients in the magma. Such a model can account for the apparent incompatibility of ferroan anorthosite with dunite, troctolite, and norite. It also bypasses what appears at present to be an unreasonable depth of excavation of the dunite 72415-8.

VIII. CONCLUSION

We conclude that certainly the dunite 72415-8 and almost certainly the troctolite 76535, norite 78235, and anorthosite 62237 samples described in this paper are relicts of primary lunar differentiation and crustal formation. They can be distinguished from localized cumulates related to mare basalts by chronological relations and by the compositions of their mafic phases. Furthermore, the nature of these rocks indicates that primary lunar differentiation did not just involve simple gravitative separation; it must have involved considerable convective or impact mixing of cumulate phases and interaction with and removal of residual melt. The concept of crystallization of these rocks downward from the "roof" of the moonwide magma chamber must also be considered (McCallum *et al.*, 1975b).

Acknowledgments—We wish to thank A. J. Gancarz for assistance in the analysis of the "pyrochlore" phase in sample 76535. D. S. Goldman performed some preliminary petrographic work on the dunite, and D. J. DePaolo provided us with a very thorough analysis of the thermodynamics of olivine–plagioclase reactions. We thank D. A. Papanastassiou, J. Warner, P. M. Bell, and S. Haggerty for their comments on the manuscript. We have also benefited from discussions with G. J. Wasserburg and D. A. Papanastassiou. This study has been supported by NASA grant NGL-05-002-338. The microprobe laboratory has been developed with the support of the Jet Propulsion Laboratory, the National Science Foundation, and the Union Pacific Foundation.

REFERENCES

Adler I., Trombka J. I., Schmadebeck R., Lowman P., Blodget H., Yin L., Eller E., Podwysocki M., Weidner J. R., Bickel A. L., Lum R. K. L., Gerard J., Gorenstein P., Rjorkholm P., and Harris B. (1973). Results of the Apollo 15 and 16 x-ray experiment. *Proc. Lunar Sci. Conf. 4th*, p. 2783–2791.

Albee A. L., Burnett D. S., Chodos A. A., Eugster O. J., Huneke J. C., Papanastassiou D. A., Podosek F. A., Russ G. P., III, Sanz H. G., Tera F., and Wasserburg G. J., (1970) Ages, irradiation history, and chemical composition of lunar rocks from the Sea of Tranquillity. Science **167**, 463–466.

Albee A. L., Chodos A. A., Dymek R. F., Gancarz A. J., Goldman D. S. Papanastassiou D. A., and Wasserburg G. J. (1974) Dunite from the lunar highlands: Petrography, deformational history, Rb–Sr age (abstract). In *Lunar Science V*, p. 3–5. The Lunar Science Institute, Houston.

Albee A. L., Dymek R. F., and DePaolo D. J. (1975) Spinel symplectites: High-pressure solid-state reactions or late-stage magmatic crystallization? (abstract). In *Lunar Science VI*, p. 1–3. The Lunar Science Institute, Houston.

Albee A. L. and Gancarz A. J. (1975) Petrogenesis of lunar rocks: Rb–Sr constraints and lack of H_2O (preprint). *Proc. Soviet–American Conf. Cosmochemistry of the Moon and Planet (Moscow)*. The Lunar Science Institute, Houston.

Bell P. M. and Mao H. K. (1975) Cataclastic plutonites: Possible keys to the evolutionary history of the early moon (abstract). In *Lunar Science VI*, p. 34–35. The Lunar Science Institute, Houston.

Bogard D. D., Nyquist L. E., Bansal B. M., and Wiesmann H. (1974) 76535: An old lunar rock? (abstract). In *Lunar Science V*, p. 70–72. The Lunar Science Institute, Houston.

Brecher A. (1975) Textural remanence: A new model for lunar rock magnetism (abstract). In *Lunar Science VI*, p. 83–85. The Lunar Science Institute, Houston.

Brown G. M., Peckett A., Phillips R., and Emeleus C. H. (1973) Mineral-chemical variations in the Apollo 16 magnesio-feldspathic highland rocks. *Proc. Lunar Science Conf. 4th*, p. 505–518.

Champion D. E., Albee A. L., and Chodos A. A. (1975) Reproducibility and operator bias in a computer-controlled system for quantitative electron microprobe analysis. Proc 10th Nat. Conf. on Electron Probe Analyses. Las Vegas, Nevada.

Chodos A. A., Albee A. L., Gancarz A. J., and Laird J. (1973) Optimization of computer-controlled quantitative analysis of minerals. Proc. 8th Nat. Conf. on Electron Probe Analyses. New Orleans, La.

Dixon J. R. and Papike J. J. (1975) Petrology of cataclastic anorthosites from the Descarates region of the moon: Apollo 16 (abstract). In *Lunar Science VI*, p. 190–192. The Lunar Science Institute, Houston.

Dowty E., Prinz M., and Keil K. (1974) Ferroan anorthosite: a widespread and distinctive lunar rock type. *Earth Planet. Sci. Lett.* **24**, 15–25.

Gancarz A. J. and Albee A. L. (1973) Microprobe analysis of the bulk composition of phase aggregates. Proc. 8th Nat. Conf. on Electron Probe Analyses. New Orleans, La.

Gibbons R. V. and Ahrens T. J. (1975a) Effects of shock pressures on calcic plagioclase. *Amer. Mineral.* In press.

Gibbons R. V. and Ahrens T. J. (1975b) Effects of shock pressures on orthopyroxene. *Amer. Mineral.* In press.

Gibson E. K., Jr. and Moore G. W. (1974) Sulfur abundance and distribution in the valley of Taurus-Littrow. *Proc. Lunar Sci. Conf. 5th*, p. 1823–1837.

Gooley R., Brett R., Warner J., and Smyth J. R. (1974) A lunar rock of deep crustal origin: sample 76535. *Geochim. Cosmochim. Acta.* **38**, 1329–1340.

Green D. H., Ringwood A. E., Hibberson W. O., and Ware N. G. (1975) Experimental petrology of Apollo 17 mare basalts. *Proc. Lunar Sci. Conf. 6th.* This volume.

Hargraves R. B. and Hollister L. S. (1972) Mineralogic and petrologic study of lunar anorthosite slide 15415,18. *Science* **175**, 430–432.

Haskin L. A., Shih C. Y., Bansal B. M., Rhodes J. M., Weismann H., and Nyquist L. E. (1974) Chemical evidence for the origin of 76535 as a cumulate. *Proc. Lunar Sci. Conf. 5th*, p. 1213–1225.

Head J. W., Settle M., and Stein R. (1975) Volume of material ejected from major lunar basins:

Implications for the depth of excavation of lunar samples (abstract). In *Lunar Science VI*, p. 352–354. The Lunar Science Institute, Houston.

Hewins R. H. and Goldstein J. I. (1975) Comparison of silicate and metal geothermometers for lunar rocks (abstract). In *Lunar Science VI*, p. 365–357. The Lunar Science Institute, Houston.

Hinthorne J. R., Conrad R., and Anderson C. A. (1975) Lead–lead age and trace element abundances in lunar troctolite, 76535 (abstract). In *Lunar Science VI*, p. 373–375. The Lunar Science Institute, Houston.

Hodges F. N. and Kushiro I. (1974) Apollo 17 petrology and experimental determination of differentiation sequences in model moon compositions. *Proc. Lunar Sci. Conf. 5th*, p. 505–520.

Huneke J. C. and Wasserburg G. J. (1975) Trapeed ^{40}Ar in troctolite 76535 and evidence for enhanced ^{40}Ar–^{39}Ar age plateaus (abstract). In *Lunar Science VI*, p. 417–419. The Lunar Science Institute, Houston.

Husain L. and Schaeffer O. (1975) Lunar evolution: The first 600 million years. *Geophys. Res. Lett.* **2**, 29–32.

Jackson E. D., Sutton R. L., and Wilshire H. G. (1975) Structure and petrology of a cumulus norite boulder sampled by Apollo 17 in Taurus Littrow Valley, the Moon. *Bull. Geol. Soc. Amer.* **86**, 433–442.

James D. B. (1972) Lunar anorthosite 15415: texture, mineralogy, and metamorphic history. *Science* **175**, 432–436.

Laul J. C. and Schmitt R. A. (1975a) Dunite 72417: A chemical study (abstract). In *Lunar Science VI*, p. 495–497. The Lunar Science Institute, Houston.

Laul J. C. and Schmitt R. A. (1975b) Dunite 72417: A chemical study and interpretation. *Proc. Lunar Sci. Conf. 6th.* Vol. 2.

Lindsley D. H., King H. E., Jr., and Turnock A. C. (1974) Compositions of synthetic augite and hypersthene coexisting at 810°C. Application to pyroxenes from lunar highland rocks. *Geophys. Res. Lett.* **1**, 134–136.

LSPET (1972) The Apollo 16 lunar samples: Petrographic and chemical description. *Science* **179**, 23–34.

LSPET (1973) Apollo 17 lunar samples: Chemical and petrographic description. *Science* **182**, 659–672.

Lunar Sample Information Catalogue—Apollo 16 (1972) NASA MSC-03210. 372 pp.

Lunar Sample Information Catalogue—Apollo 17 (1973) NASA MSC-03211. 447 pp.

McCallum I. S., Mathez E. A., Okamura F. P., and Ghose S. (1975a) Petrology of noritic cumulates: Samples 78235 and 78238 (abstract). In *Lunar Science VI*, p. 534–536. The Lunar Science Institute, Houston.

McCallum I. S., Okamura F. P., and Ghose S. (1975b) Mineralogy and petrology of sample 67075 and the origin of lunar anorthosites. *Earth Planet. Sci. Lett.*, In press.

Morse S. A. (1969) The Kiglapait Layerd Intrusion, Labrador. *Geol. Soc. Amer.* **112**, 146 *pp.*

Papanastassiou D. A. and Wasserburg G. J. (1975a) A Rb–Sr study of Apollo 17 Boulder 3: Dunite clast, microclasts, and matrix (abstract). In *Lunar Science VI*, p. 631–633. The Lunar Science Institute, Houston.

Papanastassiou D. A. and Wasserburg G. J. (1975b) Rb–Sr study of a lunar dunite and evidence for early lunar differentiates. *Proc. Lunar Sci. Conf. 6th.* Vol. 2.

Pearce G. W., Strangway D. W., and Gose W. A. (1974) Magnetic properties of Apollo samples and implications for regolith formation. *Proc. Lunar Sci. Conf. 5th*, p. 2815–2826.

PSR (Apollo 17 Preliminary Science Report) (1973) NASA publication SP-330.

Roedder E. and Weiblen P. W. (1971) Petrology of silicate melt inclusions, Apollo 11 and Apollo 12 terrestrial equivalents. *Proc. Lunar Sci. Conf. 2nd*, p. 507–528.

Sclar C. B. and Bauer J. F. (1975) Shock-induced subsolidus reduction-decomposition of orthopyroxene and shock-induced melting in norite 78235 (abstract). In *Lunar Science VI*, p. 727–729. The Lunar Science Institute, Houston.

Smith J. V. (1971) Minor elements in Apollo 11 and Apollo 12 olivine and plagioclase. *Proc. Lunar Sci. Conf. 2nd*, p. 143–150.

Smith J. V. and Steele I. M. (1974) Intergrowths in lunar and terrestrial anorthosites with implications for lunar differentiation. *Amer. Mineral.* **59**, 673–680.

Smith J. V., Anderson A. T., Newton R. C., Olsen E. J., Wyllie P. J., Crewe A. V., Isaacson M. S., and Johnson D. (1970) Petrologic history of the moon inferred from petrography, mineralogy and petrogenesis of Apollo 11 rocks. *Proc. Apollo 11 Lunar Sci. Conf.*, p. 897–925.

Smyth J. R. (1975) A crystal structural refinement of an anomalous lunar anorthite (abstract). In *Lunar Science VI*, p. 756–758. The Lunar Science Institute, Houston.

Snee L. W. and Ahrens T. J. (1975a) Shock-induced deformation features in terrestrial olivine and lunar dunite (abstract). In *Lunar Science VI*, p. 759–761. The Lunar Science Institute, Houston.

Snee L. W. and Ahrens T. J. (1975b) Shock-induced deformation in terrestrial peridot and lunar dunite. *Proc. Lunar Sci. Conf. 6th*. This volume.

Steele I. M. and Smith J. V. (1973) Mineralogy and petrology of some Apollo 16 rocks and fines: General petrologic model of the moon. *Proc. Lunar Sci. Conf. 5th*, p. 519–536.

Stewart D. B. (1975) Apollonian metamorphic rocks (abstract). In *Lunar Science VI*, p. 774–776. The Lunar Science Institute, Houston.

Stöffler D. (1972) Deformation and transformation of rock-forming minerals by natural and experimental shock processes. *Fortschr. Miner.* **49**, 50–113.

Taylor S. R. and Jakeš P. (1974) The geochemical evolution for the moon. *Proc. Lunar Sci. Conf. 5th*, p. 1287–1305.

Tera F. and Wasserburg G. J. (1974) U–Th–Pb systematics on lunar rocks and inferences about lunar evolution and the age of the moon. *Proc. Lunar Sci. Conf. 5th*, p. 1571–1599.

Tera F., Papanastassiou D. A. and Wasserburg G. J. (1974) Isotopic evidence for a terminal lunar cataclysm. *Earth Planet. Sci. Lett.* **22**, 1–21.

Toksöz M. N., Dainty A. N., Solomon S. C., and Anderson K. R. (1974) Structure of the Moon. *Rev. Geophys.* **12**, 539–567.

Wager L. R. and Brown G. M. (1967) *Layered Igneous Rocks*. Freeman. 588 pp.

Walker D., Grove T. L., Longhi J., Stolper E. M., and Hays J. F. (1973) Origin of lunar feldspathic rocks. *Earth Planet. Sci. Lett* **20**, 335–336.

Walker D., Longhi J., and Hays J. F. (1975) Differentiation of a very thick magma body (abstract). In *Lunar Science VI*, p. 838–840. The Lunar Science Institute, Houston.

Winzer S. R., Lum R. K. L., Schuhmann S., and Philpotts J. A. (1975) Large ion lithophile trace element abundances in phases from 78235,34, a lunar norite cumulate (abstract). In *Lunar Science VI*, p. 872–874. The Lunar Science Institute, Houston.

Wood J. A. (1975) Lunar petrogenesis in a well-stirred magma ocean (abstract). In *Lunar Science VI*, p. 881–883. The Lunar Science Institute, Houston.

Wood J. A., Dickey J. S. Jr., Marvin U. B., and Powell B. N. (1970) Lunar anorthosites and a geophysical model of the moon. *Proc. Apollo 11 Lunar Sci. Conf.*, p. 965–988.

Proc. Lunar Sci. Conf. 7th (1976), p. 2335-2378.
Printed in the United States of America

Petrology and origin of Boulders # 2 and # 3, Apollo 17 Station 2

R. F. DYMEK, A. L. ALBEE, and A. A. CHODOS

Division of Geological and Planetary Sciences,* California Institute of Technology, Pasadena, California 91125

Abstract—Detailed petrographic descriptions and mineralogic data are presented for five samples from Boulder # 2 (72315, 72335, 72355, 72375, and 72395), and sample 72435 from Boulder # 3 at Apollo 17 Station 2. All these samples consist of a few percent megaclasts set in a fine-grained matrix; the matrix is comprised of microclasts and a poikilitic to subophitic-textured groundmass that crystallized from a melt. Clasts display textures indicative of origin in a variety of environments, but are exclusively members of the DANT-suite. The samples all have similar modal mineralogies, mineral compositions, and bulk-chemical compositions, and resemble other Apollo 17 "noritic breccias."

Boulders # 2 and # 3 are interpreted to be igneous rocks that crystallized from clast-laden impact melts probably related to the Serenitatis basin-forming event. Our observations are consistent with the models of James (1975) and Simonds (1975) and indicate that these samples formed by mixing of molten material with predominantly unshocked, cold clasts. Rapid dissipation of heat into the cold clasts resulted in undercooling of the melt. Consequently, there occurred a sudden, massive amount of homogeneous nucleation of plagioclase, which accounts for the unique textures of these samples. The groundmass that crystallized from this melt appears to differ chemically from the clast assemblage. This implies that clasts and melt originated in different source areas.

I. INTRODUCTION AND GEOLOGICAL SETTING

ONE OF THE UNIQUE OPPORTUNITIES afforded the astronauts during the Apollo 17 mission was the chance to sample selectively and describe several large boulders encountered at three stations. Boulders were sampled at the foot of the South Massif at Station 2, and at the foot of the North Massif at Stations 6 and 7. At Stations 6 and 7 three breccia types occur within individual boulders, with light-gray breccia enclosed within blue-gray breccia that is enclosed within green-gray breccia. Each of the three boulders sampled within 30 m of each other at Station 2 represents a different breccia type. Boulder # 1 is a light-gray breccia, Boulder # 2 is a green-gray breccia, and Boulder # 3 is a blue-gray breccia. Boulder # 1 is layered and foliated, whereas Boulders # 2 and # 3 are generally more massive and uniform in appearance.

Schmitt (in AFGIT, 1975), based upon his field observations, suggested that the three boulders at Station 2 originated in the upper part of the South Massif, an area where he saw subtle color variations in a linear pattern suggestive of different stratigraphic units. Reed and Wolfe (1975) have synthesized the evidence on the nature of the massifs, including the astronauts' observations, photographic data, and sample data. They conclude that the massifs consist of discontinuous pods and lenses rather than subhorizontal continuous layers of ejecta from

*Contribution No. 2754.

several basins. They also concluded that the breccias that form both massifs were derived from a single source—the southern Serenitatis impact.

Detailed studies of the boulders are necessary to characterize the lithologies that comprise the Taurus-Littrow massifs, and to understand the rock-forming processes that occur during a major impact event. The samples from the Station 6 boulder have been described by Simonds *et al.* (1974) and Simonds (1975), and the Station 7 boulder is being studied by Chao *et al.* (1974, 1975).

Extensive reports by the Consortium Indomitabile (1974a,b, 1975) have been presented on samples from Boulder # 1 at Station 2; detailed petrologic studies by Stoeser *et al.* (1974) and Ryder *et al.* (1975) are particularly relevant. This paper describes the petrology of the samples from Boulders # 2 and # 3 at Apollo 17 Station 2.

II. SAMPLE OCCURRENCE

Boulder #2 was an approximately 2 m high, rounded, tan-gray block with an overall massive appearance. It was, however, transected by poorly-developed sets of fractures. Five samples [72315 (131 g), 72335 (109 g), 72355 (367 g), 72375 (18 g), and 72395 (536 g)] were all collected from one face of this boulder.

The surface of the boulder was rough and rubbly, and gave the impression that the boulder was locally friable. During the sampling of the boulder, Schmitt (in AFGIT, 1975) observed a distinctive half-meter patch on its surface that he interpreted as a clast of material quite similar to the rest of the boulder. The astronauts collected sample 72315 to represent this "clast," 72335 at the contact of the "clast," and 72355, 72375, and 72395 to represent normal boulder "matrix." Subsequent study has shown that all five samples are virtually identical, and it seems probable that the distinctive patch was caused by the spalling-off of a circular slab, exposing fresher surface. Each sample has an exterior side marked by numerous "zap pits," and is coated with a brownish patina so that its color is quite different from the green-gray color of the fresh rock. Hence, such a spall would have produced a distinctive patch on the boulder surface.

A number of other prominent rounded areas that impart a spheroidal aspect to the surface of the boulder can be seen in photographs. In addition, Schmitt (in AFGIT, 1975) observed "a lot of flake fractures" on Boulder #2, and suggested that they may have been caused by moderate-sized impacts resulting in incomplete spalling of the broken rock around the spall. Sample 72315 was a remnant of such a spall. It occurred as a small projecting slab attached along only one edge. Thus, although it was originally inferred that Boulder #2 contained large clasts in a breccia matrix, it now appears that these features are related to the intersection of fractures and spalled areas.

Boulder #3 was an approximately 0.5 m equant, subangular block with an overall dull blue-gray color. No well-developed fracture sets occur, but a few irregular fractures are present. Several 2–4 cm clasts and a larger 10 cm light-colored clast are visible in the photographs of Boulder #3. Sample 72435 (161 g) was collected to represent the matrix of the boulder, and samples 72415–18 (55 g) were collected from the 10 cm clast. This latter sample proved to be a cataclastic dunite, and has been studied in great detail (Dymek *et al.*, 1975).

The relative positions of Boulders #2 and #3 at Station 2, and the locations and orientations of the seven samples in these two boulders, are well documented on photographs in the Apollo 17 Preliminary Science Report (p. 6–9 to 6–15), and are not reproduced here.

III. SAMPLE PROCESSING AND CONSORTIUM STUDIES

Investigations of samples from the Station 2 Boulders #2 and #3 have been conducted by various members of a loosely-knit consortium. Preliminary petrographic and isotopic data for all samples were presented by Albee *et al.* (1974a) and Tera *et al.* (1974), and additional petrographic data by Dymek *et*

al. (1976a,b). Chemical data for all samples were presented by Laul and Schmitt (1974, 1975a), and a particle track study of sample 72315 was presented by Hutcheon *et al.* (1974a,b). Papanastassiou and Wasserburg (1975) reported additional isotopic work on sample 72335.

Lunar dunite samples 72415 and 72417 have been the subject of extensive study. These include: preliminary petrographic and isotopic data (Albee *et al.*, 1974b); petrography (Bell *et al.*, 1975); magnetics (Brecher, 1975); oxygen isotopes (Clayton and Mayeda, 1975); petrography (Dymek *et al.*, 1975); carbon and sulfur chemistry (Gibson and Moore, 1974); siderophile elements (Higuchi and Morgan, 1975); deformation, recrystallization, and recovery features (Lally *et al.*, 1976); chemistry (Laul and Schmitt, 1975b); Rb–Sr isotype systematics (Papanastassiou and Wasserburg, 1975); magnetics (Pearce *et al.*, 1974); microcracks (Richter *et al.*, 1976); and deformation features in olivine (Snee and Ahrens, 1975).

LSPET had described all the samples from Boulders #2 and #3. Thin sections were available for 72315, 72355, 72415, and 72435, chemical analyses were made of 72415 and 72435, and γ-ray analyses were made of 72355 and 72415 (Apollo 17 *PSR*, 1973). These data and our binocular microscope observations indicated that the five Boulder #2 samples were relatively homogeneous "metaclastic" rocks and were very similar to each other. They contained relatively few mappable clasts, lithic boundaries, or planar features. Preliminary chemical and petrographic studies (Albee *et al.*, 1974a; Laul and Schmitt, 1974) were performed on small chips from each of these samples to test the apparent similarity.

Subsequently, all five samples were mapped in detail on colored photographs. Extensive sawing and sampling was initiated on sample 72395 as a representative sample of Boulder #2, and on 72315 because its peculiar geometry held important consequences for track investigations (Hutcheon *et al.*, 1974a,b). Sample 72435 was also mapped on colored photographs and sawn for distribution; the distribution of 72415-17 is described by Dymek *et al.* (1975).

Mapping of the samples and of the sawn surfaces provided relatively little new information on Boulder #2 because of the homogeneous nature of the matrix, and the lack of large clasts of apparent interest for special study. Sample 72435 contains large clasts, and these are predominantly anorthosite and dunite. Although no detailed chemical studies have been performed on them, isotopic data on selected clasts in 72435 are reported by Papanastassiou and Wasserburg (1975), and we have studied each one petrographically.

Samples 72395 and 72415-17 have been widely allocated; samples 72315 and 72435 have not been widely allocated, and sawn material should be available for study. Details of the sampling and allocation, including our mapping, are well-documented in the data packs of the Curator's office and will not be reproduced here.

IV. Sample Description

Sample 72395 is typical of the samples from Boulder #2, and is a sugary-textured, light greenish-gray "metaclastic" rock with only a few clasts larger than a few mm (Fig. 1A). The most abundant clasts are clear white plagioclase and pale-green olivine, although shocked, glassy plagioclase is also present. Each type occurs as subangular to rounded fragments 1–3 mm across. The few large lithic clasts are typically fine-grained "felsites", probably shocked anorthosite. The sample is highly vesicular (Fig. 1B), containing very small spherical vesicles ($< 50\ \mu$m), irregular vesicles, and "slit" vesicles. The porous mass of blocky pyroxene and plagioclase crystals in the center of Fig. 1A and B is unique and probably represents a partially-assimilated lithic clast, although it may be some type of a vesicle filling.

In comparison, sample 72435 is also a "metaclastite" but is finer-grained, and has a dark blue-gray color. As illustrated in Fig. 1C, it contains abundant large clasts (< 15 mm), and isolated, spherical, smooth-walled vesicles (≤ 8 mm). The large clasts are predominantly anorthosite, but include dunite and troctolite(?). Distinctive large (1–3 mm) clasts of olivine, pyroxene, and plagioclase also occur. The smooth-walled spherical vesicles occur in a wide range of sizes (Fig. 1D), but slit vesicles with crystal coatings predominate locally.

Although the two boulders differ in color, abundance of clasts and large vesicles, and grain size of

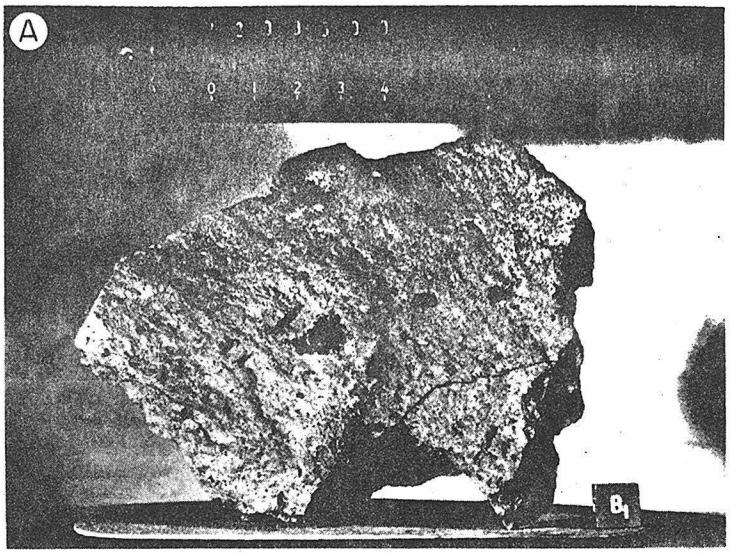
A
0 1 2 3 4
B1

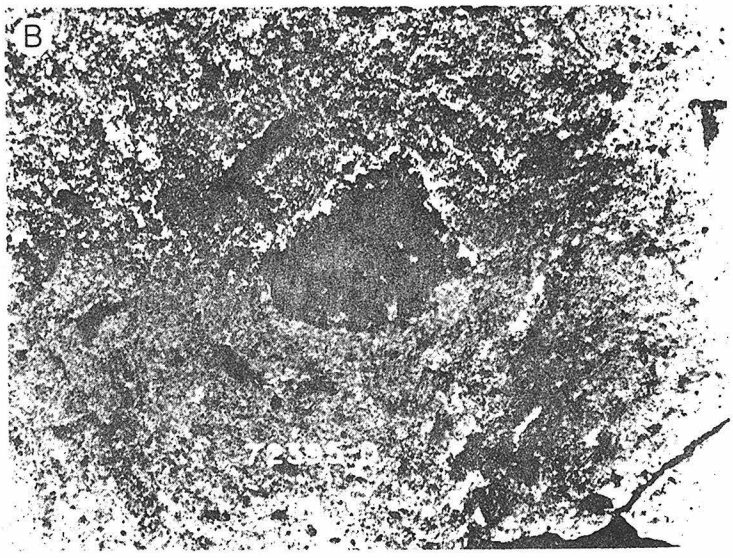
B

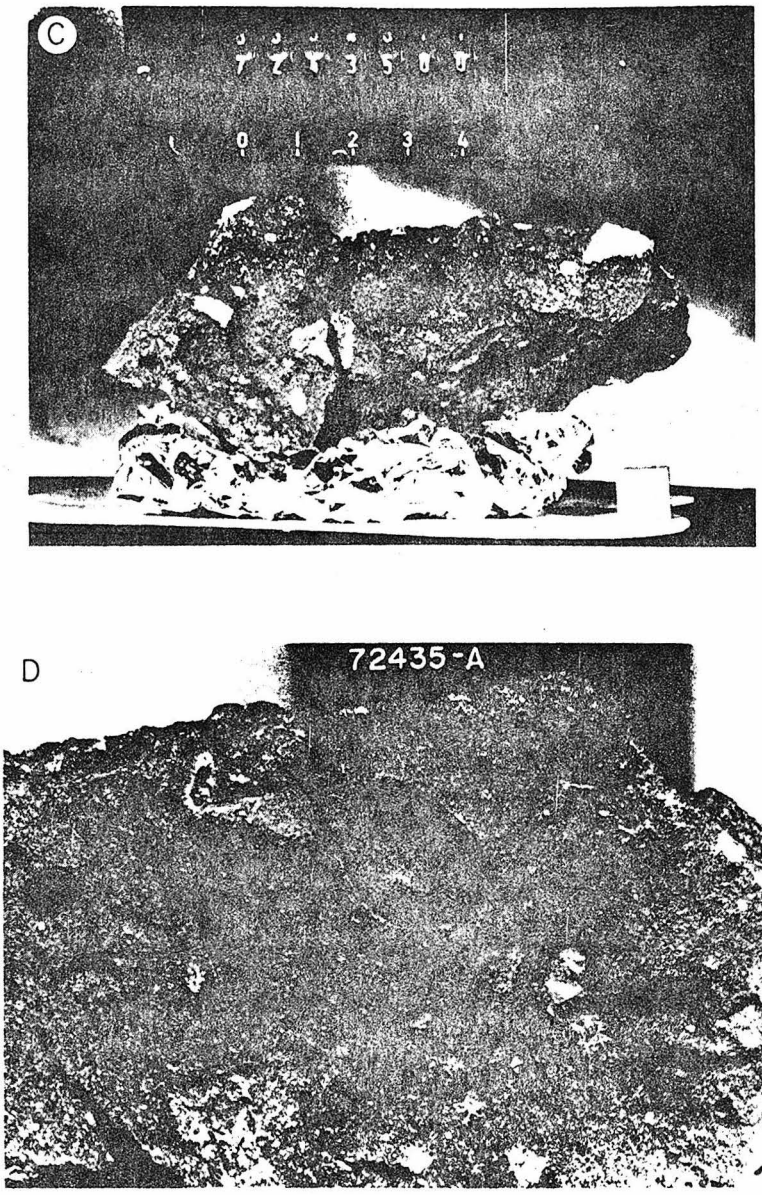

Fig. 1. (A) Hand specimen photograph of sample 72395 illustrating the fresh surface where it was broken away from Boulder #2. The sample is dense and structureless, and contains only a few recognizable clasts at this scale. Note prominent slit vesicles and vuggy area in center of sample (scale interval = 1 cm; NASA photo S-73-16052). (B) Close-up photograph of dark, vuggy area in sample 72395. This feature appears to be a partially-assimilated pyroxene- and plagioclase-bearing clast. Note the abundance of tiny vesicles in the matrix and the concentric arrangement of slit vesicles around the clast (NASA photo S-73-27575). (C) Hand specimen photograph of sample 72435 illustrating the fresh surface where it was broken away from Boulder #3. The prominent pale-colored clasts are anorthositic rocks. Like 72395, the matrix appears dense and structureless at this scale. (Scale interval = 1 cm; NASA photo S-73-16187). (D) Close-up photograph of sample 72435 illustrating scattered smooth-walled spherical vesicles with a range in size. The largest one in the center is approximately 1 cm across. (NASA photo S-73-27572).

the matrix, it should be emphasized that they are similar to each other, being dense crystalline rocks very similar to samples collected from the boulders at Station 6 and 7. However, we note that Boulders #2 and #3 are different from Boulder #1 at Station 2 (c.f. Ryder *et al.*, 1975).

V. ANALYTICAL TECHNIQUES

All of the data points plotted on the various diagrams represent complete analyses for 8–16 elements obtained with a MAC-5-SA3 electron microprobe interfaced to a PDP-8/L computer for control and on-line data processing. Analytical procedures and a discussion of precision and error are given by Dymek *et al.* (1975). A computer printout of all the analyses can be obtained from A. L. Albee.

Microprobe point counts, "average" mineral compositions, and calculated bulk-chemical compositions for samples from Boulder #2 were obtained using techniques described by Dymek *et al.* (1975). In addition, a new point count method, that utilizes an ORTEC Si(Li) solid state detector interfaced to a NS-880 multichannel analyzer, has been developed. It is particularly useful on very fine-grained rocks like 72435. Details of this procedure are discussed by Chodos *et al.* (in preparation). Each of the "average" mineral compositions listed in Tables 2 and 4 is an actual analysis of a single point that was selected from all of the analyses of that sample as the best fit to the average value, as determined by the point count.

All formula compositions and elemental ratios used in the text are in atomic proportions. Olivine compositions are reported as % Fo = 100 × [Mg/(Mg + Fe + Mn)]. We have used a simpler graphical representation of plagioclase and pyroxene compositions than in our previous papers. This simplification was necessitated by the large number of data points, and because of the lack of appreciable systematic variations in the minor element content of the pyroxene and plagioclase in these samples. Here, we have represented plagioclase compositions in the following way: % An = [Ca/(Ca + Na + K)]; % Ab = [Na/(Ca + Na + K)]; % Or = [K/(Ca + Na + K)]. For pyroxene compositions formula proportions are normalized to 4 cations; Na, Ti, Cr, and Al are successively calculated as $NaCrSi_2O_6$, $NaAlSi_2O_6$, $CaTiAl_2O_6$, $CaCrAlSiO_6$, and $CaAl_2SiO_6$; Mg, Fe + Mn, and the remaining Ca are calculated as $Mg_2Si_2O_6$, $(Fe, Mn)_2Si_2O_6$, and $Ca_2Si_2O_6$. The data points in the figures are located at the center of the triangle that is formed by plotting Wo-En-Fs.

Broad beam analyses, using a 200-μm diameter defocused spot, were performed with an ORTEC Si(Li) solid state detector interfaced to an NS-880 multichannel analyzer. Operating conditions were 15 kV accelerating voltage and 0.005 μA sample current (on brass) in beam current regulation mode.

Normal correction procedures for elemental interactions cannot be used since they assume a homogeneous sample. Inter-element correction factors were calculated for each element by iteration, using correction factors for each phase weighted by the relative proportions of that element in each phase, which was itself based on a mineral norm calculated from the chemical composition (Gancarz and Albee, 1973).

VI. CHEMICAL AND MODAL ANALYSES

A. *Boulder #2*

Multi-element analyses for major and minor elements in the five samples from Boulder #2 have been reported and discussed by Laul and Schmitt (1974, 1975a) and Wänke *et al.* (1975). We have performed electron microprobe point counts on thin sections made from chips adjacent to most of those samples used for the chemical analyses.

The resultant modal abundances are illustrated in Fig. 2; with a single exception (3′ in Fig. 2), the modal compositions are remarkably similar to each other, and the slight differences that occur reflect a range in the abundance of plagioclase.

Table 1 compares the Al_2O_3-content obtained by chemical analyses on chips of Boulder #2 samples (Laul and Schmitt, 1974, 1975a) with those calculated from point counts on the corresponding

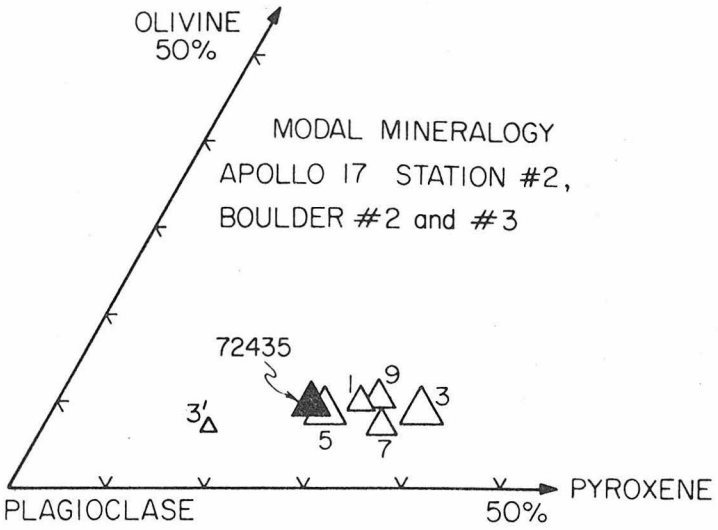

Fig. 2. Diagram illustrating the volume percent of olivine, plagioclase, and pyroxene in samples from Boulders # 2 and # 3 as determined by electron microprobe point count techniques. The altitude of each triangle corresponds to the amount of other phases. Data are in volume percent. The numbers adjacent to the symbols corresponds to the sample (e.g., 9 = 72395).

Table 1. Weight percent Al_2O_3—comparison of values obtained by chemical analysis of documented small chips with values calculated from modal abundance in thin sections made from adjacent chips.

Sample	Calculated		Chemical analysis	
72335	,12 ,14	16.6 wt.%	,6 ,7	18.2† wt.% 18.3†
72395	,5	17.5	,3	18.7*
72375	,4	18.2	,2	18.2*
72315	,12	18.5	,4 ,3	19.2* 19.8*
72355§	,5	19.3	,7	18.8*
72335	,4	25.6	,2	27.3*
72435§	,39	20.7		19.23‡

*INAA, Laul and Schmitt (1974).

†INAA, LSPET (1973).

‡XRFA, LSPET (1973).

§Non-adjacent chips used for chemical analysis and for thin section.

thin section. Despite the small size of the thin sections, there is reasonable agreement between the two methods of analysis. The Al_2O_3-contents of the five samples are similar, with one exception again (point 3').

The anomalous composition (27.3 wt. % Al_2O_3) was obtained on a chip from the preliminary allocation, which was designed to test the similarity of these samples (Albee *et al.*, 1974a; Laul and Schmitt, 1974). Chemical and modal analyses of two additional chips (72335,6,7) and corresponding thin sections (72335,12,14) differ from the original results and are similar to those for the other four samples. It is now apparent that the original chip from the edge of 72335 was inadvertently plucked from a cm-sized clast of granulitic-textured anorthositic norite with about 75% plagioclase (Fig. 1; see Fig. 5B). Thin section 72335,4 contains a portion of the clast contact with typical Boulder #2 matrix along one edge.

The results of a microprobe point count on thin section 72395,5, which is a typical thin section of Boulder #2 sample, are given in Table 2, and include an an analysis for each phase which corresponds to the average composition of that phase, and a calculated bulk composition. Also listed is the average modal composition for Boulder #2, which represents the weighted average of point counts performed on all five samples. A bulk-chemical composition for Boulder #2, calculated from this average mode is presented in Table 3.

Our calculated bulk composition is similar to the mass-weighted, average composition determined for Boulder #2 by Laul and Schmitt (1974). The only oxide for which a discrepancy exists is K_2O, which has a lower calculated value. This can be accounted for by two facts. Most of the K in these samples occurs in tiny (≤ 5 μm), irregularly-distributed interstitial areas that are difficult to detect by the point count method. More importantly, a correct bulk K_2O-content in a rock with 50% plagioclase would require a fortunate estimate of the average K_2O-content in a very heterogeneous collection of plagioclase.

Finally, we note the close similarity between the composition of Boulder #2 and the average composition of Apollo 17 noritic breccias (Rhodes *et al.*, 1974).

B. *Boulder #3*

The results of a microprobe point count on thin section 72435,39 are presented in Table 4. This sample, like those from Boulder #2, has the modal composition of a norite (Fig. 2). The bulk-chemical composition of 72435 determined from the point count is in good agreement with the XRF-analysis reported by LSPET (compare Table 3 with Table 4). In addition, 72435 has a bulk composition similar to the samples from Boulder #2, and to the average composition of Apollo 17 noritic breccias (Rhodes *et al.*, 1974).

Data on the modal mineralogy and chemistry of samples 72415 and 72417 from the dunite clast have been reported by Albee *et al.* (1974b), Dymek *et al.* (1975), and Laul and Schmitt (1975b).

VII. PETROGRAPHY AND MINERAL CHEMISTRY

A. *Boulder #2*

1. *General Description.* We have examined 4 thin sections from 72315, 3 from 72335, 1 each from 72355 and 72375, and 9 from 72395. The five samples are very similar petrographically; consequently separate descriptions will not be given. Each of the samples appears to consist of several percent megaclasts ($\sim$ 1 mm to 1 cm) set in a fine-grained, partially-clastic, crystalline matrix (Fig. 3A). This $<$1 mm portion of the rocks is comprised of abundant microclasts and a groundmass that crystallized from a melt. Simonds *et al.* (1974) have referred to these samples from Boulder #2 as "matrix-supported breccias" to emphasize the abundance of aphanitic material.

Table 2. 72395,5: Phase abundances, "average" phase compositions, and bulk-chemical composition.

	Plag.	Low-Ca pyx	High-Ca pyx	Olivine	Ilmenite	Troilite*	Metal*	Ca-Phos.†	Mesostasis	Bulk-composition
Vol.%	56.2_1	25.4_0	5.9_8	8.8_5	1.3_4	0.1_5	0.0_8	0.9_6	1.0_3	Calculated
$\pm 1\sigma$	2.0_8	1.4_1	0.6_8	0.8_2	0.3_2	0.1_0	0.0_8	0.2_7	0.2_8	(1307
Wt.%	50.4_3	28.4_4	6.5_6	10.2_3	2.0_0	0.2_3	0.2_1	1.0_1	0.8_9	points)
P_2O_5	n.a.	n.a.	n.a.	n.a.	n.a.	n.a.	n.a.	43.15	0.08	0.44
SiO_2	46.67	53.53	50.81	37.66	0.21	n.a.	n.a.	—	57.98	46.47
TiO_2	0.02	0.90	1.87	0.09	54.16	0.01	<0.01	—	1.82	1.50
Al_2O_3	33.51	0.99	1.95	0.02	<0.01	n.a.	n.a.	—	23.14	17.52
Cr_2O_3	n.a.	0.50	0.64	0.15	0.44	n.a.	n.a.	—	0.03	0.20
CaO	17.78	2.43	18.74	0.16	n.a.	0.08	0.01	54.54	5.29	11.50
MgO	0.09	26.36	17.08	35.76	6.56	0.03	<0.01	—	0.76	12.46
FeO	0.25	15.42	8.65	26.24	37.38	63.17	92.58	—	1.40	8.96
MnO	n.a.	0.19	0.21	0.32	0.46	n.a.	n.a.	—	<0.01	0.11
BaO	<0.01	n.a.	n.a.	n.a.	n.a.	n.a.	n.a.	—	0.90	0.01
Na_2O	1.51	0.06	0.17	n.a.	n.a.	n.a.	n.a.	—	0.53	0.79
K_2O	0.13	n.a.	n.a.	n.a.	n.a.	n.a.	n.a.	—	7.21	0.13
ZrO_2	n.a.	n.a.	n.a.	n.a.	0.01	n.a.	n.a.	—	0.07	<0.01
V_2O_3	n.a.	n.a.	n.a.	n.a.	<0.01	n.a.	n.a.	—	n.a.	<0.01
Nb_2O_5	n.a.	n.a.	n.a.	n.a.	0.13	n.a.	n.a.	—	n.a.	<0.01
NiO	n.a.	n.a.	n.a.	<0.01	n.a.	0.04	6.99	—	n.a.	0.02
Co	n.a.	n.a.	n.a.	n.a.	n.a.	<0.01	0.37	—	n.a.	<0.01
S	n.a.	n.a.	n.a.	n.a.	n.a.	38.52	<0.01	—	<0.01	0.09
F	n.a.	n.a.	n.a.	n.a.	n.a.	n.a.	n.a.	2.31	n.a.	0.02
Total	99.94	100.39	100.13	100.40	99.35	101.85	99.96	100.00	99.22	100.22
	An 86.1	Wo 3.3	Wo 33.5	Fo 70.6						
	Ab 13.2	En 69.4	En 45.2	Fa 29.4						
	Or 0.7	Fs 23.1								
	Others	4.2	8.1							
				Average—boulder #2–5 samples						
Vol.%	59.9	22.9	5.8	7.7	1.6	0.1	0.1	0.8	0.9	
Wt.%	54.1	25.8	6.4	9.0	2.5	0.1	0.4	0.9	0.8	

*Elemental abundances; converted to oxides for calculating bulk composition.
†Assumed 1:1 mixture of fluorapatite and whitlockite.
n.a. = Not analyzed.

Table 3. Boulders 2 and 3, selected analyses.

	1	2	3	4	5	6	7	8
P_2O_5	0.38	N.R.	0.28	0.27	0.47 ± 0.31	0.56 ± 0.11	0.20	N.A.
SiO_2	45.9	N.R.	46.15	45.76	48.4 ± 2.3	48.4 ± 1.1	75.21	50.74
TiO_2	1.80	1.6	1.50	1.54	1.96 ± 2.48	1.43 ± 0.51	1.50	0.12
Al_2O_3	18.7	18.8	18.01	19.23	17.8 ± 3.1	16.6 ± 1.2	12.60	34.73
Cr_2O_3	0.18	0.19	0.20	0.20	0.18 ± 0.09	0.18 ± 0.07	0.01	N.A.
CaO	11.1	11.1	11.16	11.72	11.8 ± 2.0	11.6 ± 0.6	0.47	0.06
MgO	12.0	12	12.33	11.63	9.92 ± 2.04	11.8 ± 1.1	0.04	12.11
FeO	8.6	8.8	9.16	8.70	7.89 ± 2.09	8.48 ± 0.54	1.32	3.94
MnO	0.10	0.113	0.12	0.11	0.10 ± 0.10	0.11 ± 0.07	<0.01	0.05
Na_2O	0.79	0.67	0.65	0.52	0.69 ± 0.17	0.61 ± 0.12	0.27	0.08
K_2O	0.17	0.31	0.26	0.23	0.66 ± 0.19	0.31 ± 0.09	7.37	0.06
S	0.05	N.R.	0.08	0.08	0.08 ± 0.15	0.07 ± 0.07	0.25	N.A.

1 Calculated from weighted average of point counts. } Bulk composition
2 Weighted average of INAA measurements (Laul & Schmitt, 1974). } of Boulder # 2
3 Average composition of Apollo 17 noritic breccias (Rhodes *et al.*, 1974).
4 Bulk composition of 72435 (XRF-analysis; Apollo 17-PSR, p. 7-18).
5 Boulder # 2 groundmass (72395) } Each represents the average and standard
6 Boulder # 3 groundmass (72435) } deviation of 30 defocussed beam microprobe analyses performed with an energy dispersive analyzer.
7 72395: Glass in "vug" (see Fig. 4A).
8 72435: Cordierite (formula proportions in text).
N.R. = Not reported. N.A. = Not analyzed.

Further inspection reveals that there is a seriate clast size distribution from the largest ones to those as small as grains in the groundmass. We place an important distinction on the difference between the partially-clastic, megascopic *matrix* and the igneous *groundmass* interstitial to the clasts, in a fashion similar to that of James (1975, 1976).

The distinction between clasts and groundmass has been drawn at 100 μm. A small and variable proportion of the groundmass ($\leq$ 10%) consists of rounded to ragged grains of plagioclase and olivine that may represent partially-resorbed mineral clasts. Hence, in some cases, it is difficult to distinguish microclasts from groundmass. Simonds *et al.* (1975), in their survey on Apollo 17 non-mare rocks, have noted that the samples from Boulder # 2 comprise a unique textural group among the collection of Apollo 17 highland material, and have classified them as "clast-rich ophitic" breccias.

When viewed in transmitted light, the thin sections have a grayish cast due to the abundance of fine-grained pyroxene in the matrix. Slight variations in the grain size of the groundmass, and irregularities in the distribution of clasts and vesicles lend an inhomogeneous, mottled appearance to the rocks.

Void space constitutes approximately 10% of each thin section, but locally comprises up to 30% of the sample. The most common voids are 1–25 μm angular pores dispersed throughout the matrix. Irregularly-shaped slit vesicles (up to 250 μm long) are also present, which may wrap around the margins of the larger

Table 4. 72435,39: Phase abundances, "average" phase compositions, and calculated bulk-chemical composition.

	Plag.	Low-Ca pyx	High-Ca pyx	Olivine	Ilmenite	Troilite*	Metal*	Ca-Phos.†	Meso-stasis	SiO_2	Bulk comp.
Vol.%	63.0_0	21.0_4	3.8_0	8.1_7	1.9_3	0.0_6	0.1_3	0.3_2	0.9_0	0.6_4	
$\pm 1\,\sigma$	2.8_5	1.6_5	0.7_0	1.0_3	0.5_0	0.0_6	0.1_3	0.1_0	0.3_4	0.2_9	Calculated
Wt.%	57.5_6	23.9_1	4.2_3	9.5_3	2.7_1	0.0_9	0.3_5	0.3_4	0.7_9	0.5_0	(777 points)
P_2O_5	n.a.	n.a.	n.a.	n.a.	n.a.	n.a.	n.a.	43.15	0.09	n.a.	0.15
SiO_2	45.46	52.77	51.96	37.71	0.31	<0.1	<0.01	—	64.10	99.93	45.59
TiO_2	0.09	1.03	1.85	0.10	53.53	n.a.	<0.01	—	1.92	<0.01	1.85
Al_2O_3	34.98	1.39	2.53	<0.01	0.08	n.a.	n.a.	—	16.79	0.48	20.71
Cr_2O_3	n.a.	0.40	0.67	0.10	0.40	n.a.	n.a.	—	<0.01	n.a.	0.14
MgO	0.07	25.33	17.38	36.65	5.98	n.a.	<0.01	—	0.11	0.03	10.49
FeO	0.12	14.87	8.01	26.12	39.12	63.12	91.26	—	1.19	0.04	8.01
MnO	n.a.	0.20	0.19	0.21	0.39	0.05	n.a.	—	0.01	n.a.	0.09
CaO	18.48	3.83	17.88	0.11	n.a.	n.a.	n.a.	54.54	1.28	0.03	12.51
Na_2O	1.12	0.02	0.13	n.a.	n.a.	n.a.	n.a.	—	0.26	<0.01	0.66
K_2O	0.21	n.a.	n.a.	n.a.	n.a.	n.a.	n.a.	—	13.31	0.25	0.23
BaO	0.11	n.a.	n.a.	n.a.	n.a.	n.a.	n.a.	—	1.29	0.24	0.07
ZrO_2	n.a.	n.a.	n.a.	n.a.	<0.01	n.a.	n.a.	—	<0.01	n.a.	<0.01
V_2O_3	n.a.	n.a.	n.a.	n.a.	<0.01	n.a.	n.a.	—	n.a.	n.a.	<0.01
Nb_2O_5	n.a.	n.a.	n.a.	n.a.	0.19	n.a.	n.a.	—	n.a.	n.a.	<0.01
NiO	n.a.	n.a.	n.a.	<0.01	n.a.	<0.01	7.18	—	n.a.	n.a.	0.03
Co	n.a.	n.a.	n.a.	n.a.	n.a.	<0.01	0.58	—	n.a.	n.a.	<0.01
S	n.a.	n.a.	n.a.	n.a.	n.a.	37.25	<0.01	—	n.a.	n.a.	0.03
F	n.a.	n.a.	n.a.	n.a.	n.a.	n.a.	n.a.	2.31	n.a.	n.a.	<0.01
Total	100.63	99.85	100.61	101.01	100.00	100.42	99.02	100.00	100.37	101.01	
	An 89.0	Wo 5.6	Wo 32.4	Fo 71.3							
	Ab 9.8	En 67.8	En 47.9	Fa 28.7							
	Or 1.2	Fs 22.6	Fs 12.7								
	Others	4.0	7.0								

*Elemental abundances; converted to oxides for calculating bulk composition.
†Assumed 1:1 mixture of fluorapatite and whitlockite.
n.a. = Not analyzed.

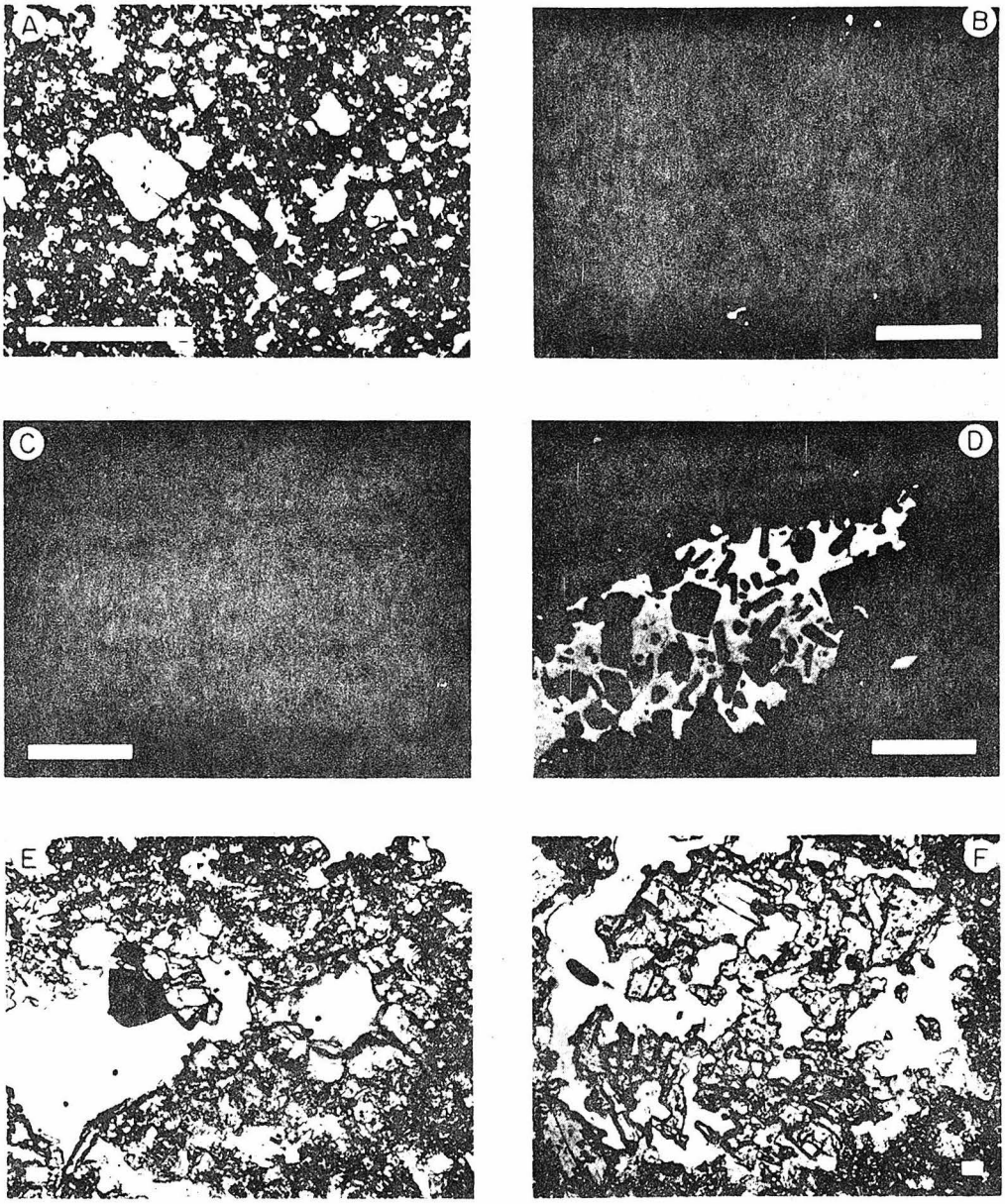
A
B
C
D
E
F

clasts, or crosscut clast-matrix contacts. Locally, there is a slight alignment of clasts and/or void space. However, the samples are generally structureless.

Vugs, lined by euhedral crystals of pyroxene and plagioclase, and rarely troilite, ilmenite, and Ca-phosphate, are common (Fig. 3E). Spherical to globular-shaped, smooth-walled vesicles also occur. These are typically 25–100 μm across, and are most abundant in thin sections from sample 72395.

"Vesicular pods" (up to 2 mm) consist of porous aggregates of intergrown high- and low-Ca pyroxene and plagioclase (Figs. 1B and 3F). The plagioclase in some contains dark melt inclusions. In some pods, plagioclase occurs only as tabular inclusions in pyroxene. Some of these "vesicular pods" contain bladed plagioclase crystals that project from the matrix into the void, and probably formed as some type of vesicle-filling during the crystallization of the melt. However, most are sharply-bounded objects that we interpret to be partially-assimilated lithic clasts.

In sample 72395, a few areas consist of a "shell" of euhedral high- and low-Ca pyroxene filled by glass of granitic composition (Fig. 4A). The glass contains euhedral pyroxene crystals and tiny (≤ 1 μm wide) needles of ilmenite, which probably accounts for the high-TiO_2 content of the analyses (Table 3).

The composition of the glass is appropriate for an origin by liquid immiscibility (Roedder and Weiblen, 1971; Hess *et al.*, 1976), but the pyroxene compositions are no more Fe-rich than other analyses from the groundmass. The lack of extensive iron enrichment in these pyroxenes argues against an origin by liquid immiscibility.

Although these areas could represent melted granite clasts, the similarity among the two dozen or so objects observed in thin sections suggests a more simple interpretation. At present, we prefer the interpretation that these features represent a granitic residue formed as the end product of crystallization of the groundmass melt.

2. *Groundmass.* The groundmass of Boulder #2 samples consists predominantly of an interlocking network of tiny pyroxene oikocrysts that enclose

Fig. 3. Photomicrographs illustrating various textural features in samples from Boulder #2. (Bar scale in A = 1 mm, all others = 50 μm). (A) 72395—Large scale view of fragmental aspect of a Boulder #2 sample. Note the apparent seriate size distribution among clasts. Scattered black grains in matrix are ilmenite. Gray areas are intergrown pyroxene and plagioclase in the groundmass (transmitted plane polarized light). (B) 72395—Subophitic texture typical of the groundmass in a Boulder #2 sample consisting of plagioclase (dark gray) and pyroxene (light gray) (reflected light). (C) 72315—Well-developed poikilitic texture in groundmass of a Boulder #2 sample consisting of subhedral plagioclase chadacrysts (dark gray) enclosed by a single pyroxene oikocryst (light gray) (reflected light). (D) 72375—Sieve-texture typical of ilmenite (bright) in the groundmass of Boulder #2. Dark silicate inclusions are plagioclase and pyroxene (reflected light). (E) 72315—Circular vug lined with euhedral pyroxene crystals (right of center) and euhedral troilite crystal (black) projecting into irregularly-shaped vug (left of center) (transmitted plane polarized light). (F) 72395—Vesicular pod consisting of intergrown pyroxene and plagioclase. This feature probably represents a partially-assimilated clast (transmitted, plane-polarized light).

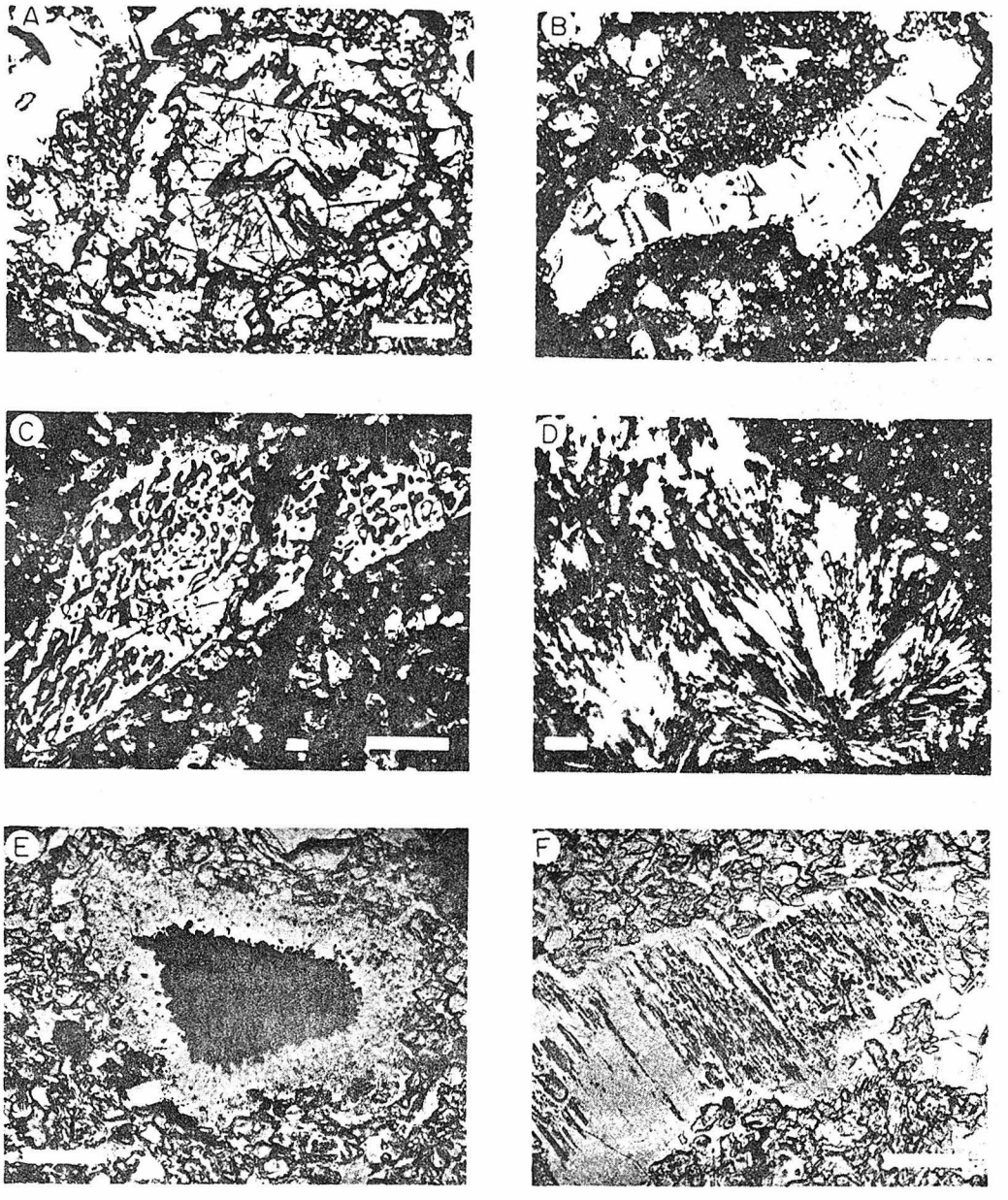

Fig. 4. Photomicrographs illustrating various features in samples from Boulder #2 (all bar scales = 100 μm). (A) 72395—Glass-filled vug surrounded by shell of pyroxene. Euhedral inclusions in glass are pyroxene, acicular inclusions are ilmenite (transmitted plane-polarized light). (B) 72315—Partially-assimilated plagioclase clast ($An_{88}Ab_4Or_1$) (transmitted plane-polarized light). (C) 72395—Vermicular exsolution in pyroxene clast. Blebs have composition $Wo_{39}En_{47}Fs_{14}$; host has composition $Wo_4En_{70}Fs_{26}$ (transmitted, cross-polarized light). (D) 72315—Plagioclase clast ($An_{94.9}Ab_{4.7}Or_{0.4}$) with spherulitic texture that is inferred to be devitrified maskelynite (transmitted cross-polarized light). (E) 72355—Clast of pink to red spinel (dark gray, center) surrounded by granular ilmenite (black), all are in turn overgrown by plagioclase that zones from An_{96} at the contact with ilmenite to An_{88} near the groundmass (transmitted plane-polarized light). (F) 72355—Inclusion-rich plagioclase clast ($An_{63}Ab_{31}Or_6$) overgrown by a rim of clear plagioclase ($An_{85}Ab_{14}Or_1$) (transmitted plane-polarized light).

abundant chadacrysts of plagioclase (Fig. 3B). The texture of the groundmass in these samples is reminiscent of the Apollo 16 poikilitic rocks such as 60315, 61156, 65015, and 67955 (Albee *et al.*, 1973; Bence *et al.*, 1973; Hollister, 1973; Simonds *et al.*, 1973). However, in samples from Boulder # 2, the oikocrysts are smaller, and not as well-developed as in the Apollo 16 rocks. The majority of the oikocrysts are low-Ca pyroxene ($Wo_2En_{75}Fs_{23}$ to $Wo_{10}En_{65}Fs_{25}$), but high-Ca types also occur ($Wo_{28}En_{54}Fs_{18}$ to $Wo_{40}En_{45}Fs_{15}$). The oikocrysts are typically 25–100 μm across, but ones as large as 500 μm have been observed (Fig. 3C). Chadacrysts are randomly oriented and typically uniformly distributed, and can form up to 50% of the area of an individual oikocryst. However, some oikocrysts have chadacryst-free cores and chadacryst-rich rims. This feature is more common in high-Ca than in low-Ca pyroxene.

Chadacrysts have a limited range in composition (An_{85} to An_{92}), are 1–20 μm in width, and are tabular to equant with rounded corners (Fig. 3C). Euhedral plagioclase laths (10–25 μm across; An_{79} to An_{85}) and blocky plagioclase grains (up to 50 μm across; An_{85} to An_{95}) occur in the regions between oikocrysts. In some places, alignment of these laths gives the groundmass a trachytic appearance.

Olivine in the groundmass (Fo_{68} to Fo_{72}) does not appear to form well-developed oikocrysts like pyroxene, but occurs as angular irregularly-shaped to somewhat rounded grains between pyroxene oikocrysts or between pyroxene and plagioclase grains. The margins of some olivine grains are intergrown with plagioclase, or contain tiny plagioclase inclusions, but typically they are sharply bounded and inclusion-free. Some low-Ca pyroxene grains contain rounded cores of olivine. The ragged form of some of the olivine grains suggests that these may represent partially resorbed microclasts.

Ilmenite forms large irregularly shaped grains with a striking sieve-texture (Fig. 3D). These typically contain chromite and rutile lamellae, and may have grains of baddeleyite at their margins. Inclusions in ilmenite are predominantly equant to tabular single crystals of plagioclase and pyroxene, but blebs of K-rich material also occur. In general, K-rich mesostasis occurs between pyroxene and plagioclase, but it is also present at the margins of the ilmenite grains.

Troilite forms only a small portion of the samples, but certain portions of the groundmass are enriched in that phase. Typically, this enrichment takes the form of an approximately 100 μm wide region in which abundant 1–5 μm granules of troilite are scattered. Angular grains of Fe–Co–Ni metal ($\lesssim$ 1–5 μm) occur with troilite in this association. Their compositions were not determined.

The paragenetic sequence in the groundmass appears to be the following: plagioclase formed first, followed by olivine. Low-Ca pyroxene formed next followed by high-Ca pyroxene. Olivine appears to have ceased crystallization either just before high-Ca pyroxene, or slightly thereafter. The occurrence of rounded olivine grains as "resorbed" cores in some low-Ca pyroxene suggests that there was a reaction relation between olivine and melt to produce low-Ca pyroxene. Ilmenite formed next, followed by the other minor phases at the end. This crystallization sequence is consistent with the experimental work of Walker *et al.* (1972) on rocks with similar composition.

3. *Mineral Clasts.* The majority of clasts in Boulder #2 samples are single mineral crystals. Plagioclase is the most abundant, but olivine, low- and high-Ca pyroxene, ilmenite, Fe–Co–Ni metal, and pink spinel clasts are also present. These are typically rounded to subangular in form, but a few display delicate angular forms (Fig. 4B). Grain shapes like the latter are interpreted to represent assimilation of the clasts by the groundmass melt.

A few mineral clasts display shock effects. These include undulose extinction, fractures, strain bands, and partial anisotropy. In addition, some plagioclase clasts consist of feathery aggregates that appear to be devitrified maskelynite (Fig. 4D).

Some, but not all, mineral clasts possess conspicuous rims, either overgrowths of the same phase locally marked by optical discontinuities, or a mantle of another phase. Pink spinel grains display the most spectacular coronas (Fig. 4E). They have a rim of ilmenite and/or ulvospinel and are mantled by plagioclase in which the individual feldspar grains radiate away from the spinel-plagioclase interface. Plagioclase at the contact of each is usually $\sim An_{95}$ and zones outward to $\sim An_{88}$. Chao (1974) has figured a similar occurrence in sample 76055.

Olivine clasts range from rounded to angular, and are typically sharply bounded, but a few are mantled by low-Ca pyroxene. Some olivine clasts are zoned from Fo_{80} in the core to Fo_{70} on the rim, suggesting partial equilibration with the groundmass. Most of the olivine is bright and clear, and free of inclusions but a few grains are clouded by numerous tiny inclusions.

Both high- and low-Ca pyroxene occur as clasts. These are typically rounded and have overgrowth rims (25–100 μm wide) that consist of an intergrowth of pyroxene and plagioclase. The pyroxene in these rims tends to be optically continuous with that in the clast, and in many cases is a single crystal surrounding the clast. The rim pyroxene has the texture typical of oikocrysts in the groundmass, in that it contains numerous plagioclase inclusions.

In general, there is little measurable difference between the composition of pyroxene in the clast and in the rim. Some clasts are strongly zoned (up to 20 mole % En), but the edge of these clasts have compositions similar to the rim. Rim compositions are in turn similar to the composition of pyroxene that forms the groundmass. The rounded form of most pyroxene clasts suggests that some resorption has occurred, and the presence of zoning indicates that there has been some equilibration between clasts and the groundmass melt.

Many pyroxene fragments are dark and clouded by Fe–Ti oxide platelets. Several pyroxene clasts, inferred to be exsolved pigeonite, consist of vermicular intergrowths of high- and low-Ca pyroxene (Fig. 4C). A single large clast (~ 500 μm across) in 72395 displayed lamellar exsolution with a herringbone texture characteristic of inverted pigeonite (cf. Papike and Bence, 1972).

Plagioclase clasts are typically clear and well-twinned, but clouded or untwinned varieties also occur. In addition, a few plagioclase clasts are antiperthitic. The majority of plagioclase clasts are unzoned, but many show conspicuous reaction rims. The extent to which a reaction rim develops appears to be controlled by the An-content of the clast. If the clast has an An-content less than the groundmass ($\lesssim An_{85}$), a prominent overgrowth rim develops. Many of these grains with low-An

contents have dark clouded cores that contain glassy melt inclusions and are overgrown by clear, inclusion-free plagioclase (Fig. 4F). If the clast has an An-content similar to or greater than the groundmass, a reaction rim is typically not present but some slight zoning may occur.

Ilmenite and metal clasts typically occur with rounded to amoeboid forms. The ilmenite clasts are very interesting because they contain tiny (< 15 μm) globules of metal, troilite, plagioclase, and pyroxene. No lithic clast seen in Boulder # 2 contains ilmenite with this texture. The borders of the metal clasts range from smooth to serrated. The serrated borders may indicate that the metal was in reaction relation with the matrix.

4. *Lithic Clasts.* Lithic clasts in Boulder # 2 samples are almost exclusively DANT-type* materials that display a variety of textures, grain sizes, and compositions. These clasts can be correlated reasonably well with fragments described in the Apollo 17 2–4 mm soil fraction by Bence *et al.* (1974).

Anorthositic rocks. Anorthosites are the most abundant type of rock fragment in the Boulder # 2 samples. These grade by an increase in olivine or low-Ca pyroxene content into anorthositic troctolites and anorthositic norites. Opaque minerals only rarely occur in the clasts, and are invariably ilmenite, although intergrowths of ilmenite with Zr-armalcolite and rutile were found in one clast in addition.

The anorthositic rocks are typically fine-grained (25–250 μm), and the clasts themselves are usually smaller than many single mineral fragments. Igneous-looking textures occur in a few, but most are moderately to extensively recrystallized. Textures range from hornfelsic (finest-grained and equigranular) to granulitic (coarser-grained and somewhat inequigranular) with 120° triple junctions, and smooth grain boundaries. The small amounts of olivine and low-Ca pyroxene that are present typically occur at interstices between adjacent plagioclase grains or as inclusions in plagioclase. In a few cases, the mafic minerals form oikocrysts that enclose chadacrysts of rounded plagioclase.

Many of these textures are complicated by later cataclasis. However, fractures and microfaults are truncated at clast margins and hence, these features were induced prior to the incorporation of the clasts into the melt.

Another type of anorthositic rock has been distinguished on the basis of color, and the presence of abundant (up to 10%) ilmenite. These clasts consist of brown, shocked and partly-devitrified plagioclase and sieve-textured ilmenite, with smaller amounts of rounded pyroxene and/or olivine grains (Fig. 5A). An additional distinguishing feature is the occurrence of tiny (< 5 μm) blebs of K-rich material dispersed throughout the plagioclase. Ilmenite grains in these clasts locally protrude into the groundmass, and have compositions similar to ilmenite grains in the interior of the clasts. The significance of this feature is not clear, but it may be an indication of partial assimilation by the melt.

*DANT = *Dunite*-anorthosite-norite-troctolite.

A fine-grained, granulitic-textured noritic anorthosite clast is illustrated in Fig. 5B. This is the original chip of 72335 that yielded a chemical composition different from the other samples. Comparison of Fig. 5B with photographs of typical boulder matrix demonstrates the petrographic distinction. This clast has yielded a Rb–Sr model age of 4.39 AE (Tera *et al.*, 1974).

Poikilitic rocks. Several granulitic-textured troctolitic and noritic clasts are characterized by large poikilitic grains of olivine or pyroxene (Fig. 5C). These poikilitic grains do not have a well-defined form like the oikocrysts in the groundmass of these samples, but seem to fill the interstices between plagioclase crystals. In a few clasts, such poikilitic grains range up to 3 mm across. One 2 mm clast consisted of numerous rounded plagioclase grains enclosed by a single olivine crystal. Most of the clasts contain both olivine and low-Ca pyroxene, but are dominated by poikilitic grains of one or the other phase.

Gabbro. Clasts that contain plagioclase and high-Ca pyroxene range from igneous-textured to recrystallized. In some, the pyroxene and plagioclase are similar in size, whereas in others the plagioclase is much smaller than pyroxene, and tends to occur as tabular grains enclosed by the pyroxene.

Troctolite and dunite. Clasts of pink spinel troctolite range from igneous-appearing rocks with an intergranular texture (Fig. 5D) to recrystallized types. The spinel in these may occur as tiny, rounded inclusions in plagioclase, or angular grains between plagioclase laths. Troctolite clasts range from equigranular recrystallized types (Fig. 5E) to ones with igneous textures. One of the igneous-textured troctolites contains discrete grains of ilmenite and Zr-armalcolite.

A large (2 cm) clast in 72395 is a coarse-grained, recrystallized and cataclastic troctolite that resembles sample 76535 (Gooley *et al.*, 1974; Dymek *et al.*, 1975). The original, coarse-grained, annealed, granulitic texture is locally preserved although much of the clast has undergone granulation and recrystallization resulting in a much finer grain size (Fig. 5F). As in 76535, this clast contains symplectic intergrowths of high-Ca pyroxene and Cr-spinel. However, in marked contrast to 76535, the symplectites in this clast contain Zr-armalcolite in addition to the other phases.

Dunite fragments also occur in this sample. They are fine-grained, granulitic-textured rocks comprised of green-brown, clouded olivine (Fo_{70-77}). Some olivine grains contain prominent strain bands marked by undulose extinction.

5. *Mineral Chemistry.* Compositions of the principal phases in samples from Boulder #2 separated by sample number, are illustrated in Figs. 6–10. In this section, unless noted, no distinction is made between phases in lithic clasts, mineral clasts, or groundmass. It can be seen that, with few exceptions (e.g., plagioclase in 72355 and olivine in 72395), the range in phase composition in each sample is quite similar.

Plagioclase has a total range in composition from $An_{64}Ab_{28}Or_8$ to $An_{97.5}Ab_{2.4}Or_{0.1}$. The range in An-content is similar to that found in samples from boulders at Apollo 17 Stations 6 and 7 (Simonds *et al.*, 1974; Chao *et al.*, 1974), but

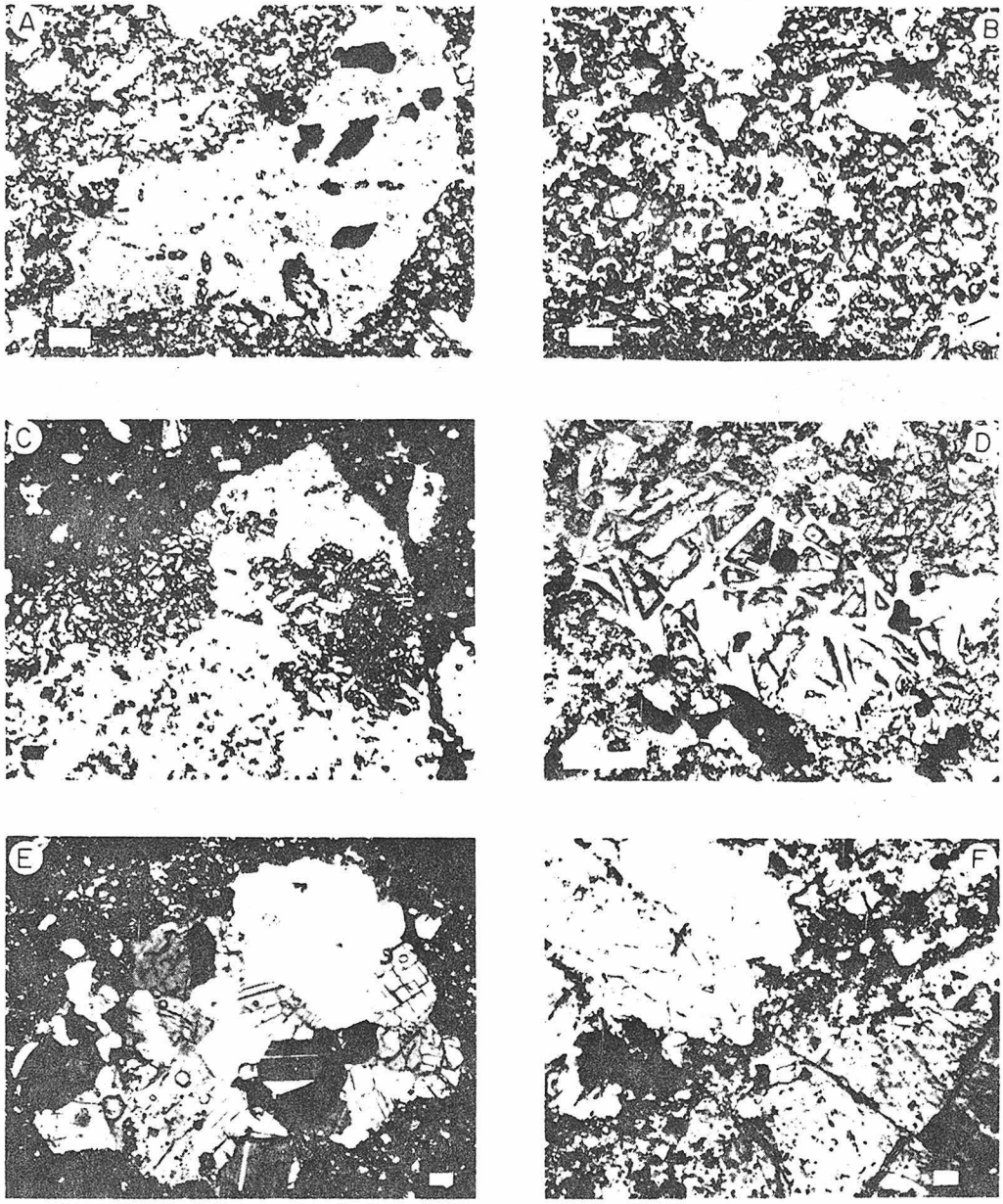

Fig. 5. Photomicrographs illustrating various textures of lithic clasts in samples from Boulder #2 (all bar scales = 100 μm). (A) 72315—Clast of "brown anorthosite" comprised of plagioclase (speckled), ilmenite (black) and olivine (high relief) (transmitted plane-polarized light). (B) 72335—Recrystallized noritic anorthosite breccia with a fine-grained granulitic texture. This is the "anomalous" piece of 72335 (transmitted plane-polarized light). (C) 72315—Poikilitic troctolitic anorthosite. The two high-relief areas on the left and right margins of the clast are each single crystals of olivine (transmitted plane-polarized light). (D) 72395—Igneous-textured pink spinel troctolite clast (transmitted plane-polarized light). (E) 72395—Troctolite clast with annealed granulitic texture (transmitted cross-polarized light). (F) 72395—Portion of a granulated, coarse-grained troctolite clast texturally similar to sample 76535. Fractured single crystals of plagioclase ($\sim An_{96}$, upper left) and olivine ($\sim Fo_{78}$, lower right) are displayed here (transmitted cross-polarized light).

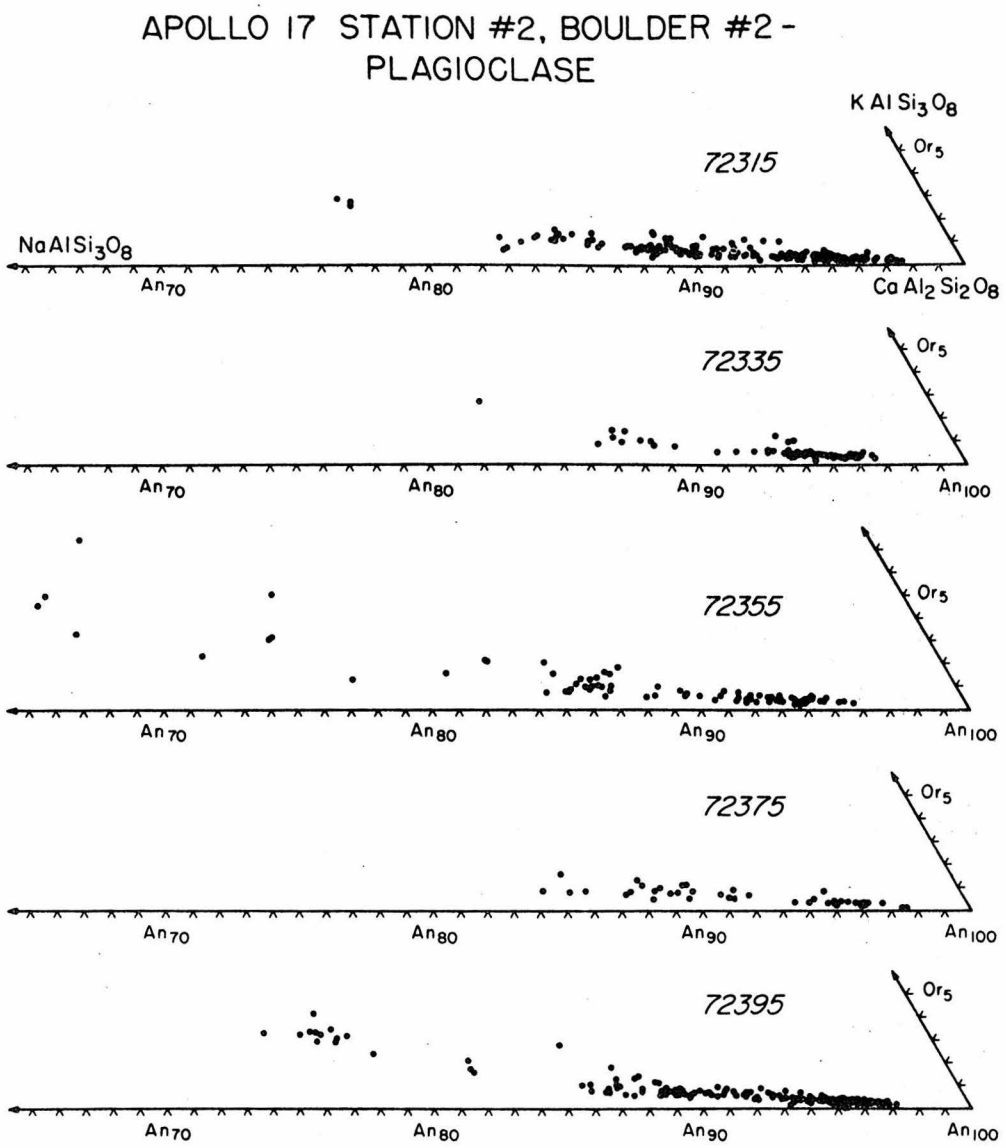

Fig. 6. Compositions of the plagioclase feldspar in samples from Boulder # 2.

trends to more sodic compositions than those reported for Boulder # 1 at Station 2 (Ryder *et al.*, 1975).

As can be seen in Fig. 6, the K_2O-content increases with decreasing An-content, a feature common to most lunar samples. The FeO- and MgO-contents of plagioclase do not vary systematically with An-content. However, there is a general increase in total FeO and MgO as the An-content decreases. The lack of detailed correlation, in contrast to mare basalts, is probably due to the fact that plagioclase in the boulder samples originated in a variety of sources.

Low-Ca pyroxene has a considerable range in composition (~ $Wo_2En_{90}Fs_8$ to

~ $Wo_{11}En_{63}Fs_{26}$, Fig. 7). Some of the more magnesian grains have been identified optically as orthopyroxene, and some of the more Fe- and Ca-rich types are optically pigeonite. *High-Ca pyroxene* ranges in composition from $Wo_{28}En_{49}Fs_{25}$ to $Wo_{43}En_{47}Fs_{10}$ (Fig. 7), and has the optical properties of augite. No X-ray data have been obtained on the pyroxene in these samples.

The relative amounts of Al, Ti, and Cr in pyroxene do not show any systematic variation with Fe/(Fe + Mg). High-Ca pyroxenes contain more Al, Ti, and Cr than low-Ca pyroxenes (e.g., Table 2). Plots of Al vs. Ti indicate that the $CaTiAl_2O_6$ coupled substitution is important in these pyroxenes. In low-Ca pyroxene, most of the Al is in four-fold coordination, whereas high-Ca pyroxene contains substantial Al^{VI} in addition. The range in Ca, Fe, and Mg variation in the pyroxene in these samples is similar to those in the Station 6 boulder samples, except that the latter show slightly more iron-enrichment (Simonds *et al.*, 1974; Simonds, 1975). Pyroxenes from Boulder # 1 at Station 2 show considerably more iron-enrichment than those reported here (Stoeser *et al.*, 1974; Ryder *et al.*, 1975).

Olivine ranges in composition from Fo_{88} to Fo_{66} (Fig. 8). The range in olivine compositions in our samples is considerably less than that reported by Stoeser *et al.* (1974) and Ryder *et al.* (1975) for Boulder # 1 at Station 2, but only slightly less than that in samples from the boulders at Stations 6 and 7 (Chao *et al.*, 1974; Simonds *et al.*, 1974). Minor element contents are small (Table 2), and similar to the data reported by Steele and Smith (1975). In particular, the CaO-content of the olivines are similar to those in DANT-types reported in the literature.

Ilmenite has a measured variation in Fe/(Fe + Mg) of .65 to .79 (Fig. 8), and tends to be more Mg-rich than ilmenite typical of lunar mare basalts. *Armalcolite* also tends to be more Mg-rich than armalcolite in mare basalts [Fig. 8; (Fe/(Fe + Mg) = .43–.57)]. The armalcolite is also enriched in ZrO_2 relative to mare basalts (2.3–3.9 wt.% vs. < 0.4 wt.%). These data are similar to analyses of "Zr-armalcolite" reported in other Apollo 17 breccias by Steele (1974).

The *spinels* in Boulder # 2 samples show a wide range in composition similar to those in other lunar highland samples (Fig. 9). There is a correlation between the petrographic association of a particular spinel type and its composition. Pink spinels are Mg- and Al-rich and Cr-poor, but zone to more Cr-rich red spinel. Some of these pink to red spinels have blebs of Ti-rich ulvospinel at their margins. Chromite that occurs as lamellae in ilmenite all have similar compositions, and these in turn are similar to Cr-rich spinel grains in lithic clasts. As can be seen in Fig. 9, Cr/(Cr + Al) increases as Mg/(Mg + Fe) decreases.

The compositions of the *metal* clasts in Boulder # 2 samples are illustrated in Fig. 10; compositions of the tiny metal grains in the groundmass were not determined. The Ni-(2–16 wt.%) and Co-contents (0.2–1.0 wt.%) show a large variation, similar to the metal in samples from the Station 6 boulder (Misra *et al.*, 1976), and generally fall within the range of "meteoritic" metal (Goldstein and Yakowitz, 1971). This could be used to infer that the metal in these samples originated in iron meteorites. However, as pointed out by Misra and Taylor (1975), the Ni–Co distribution in the metal may not be a valid criterion for identifying its meteoritic origin.

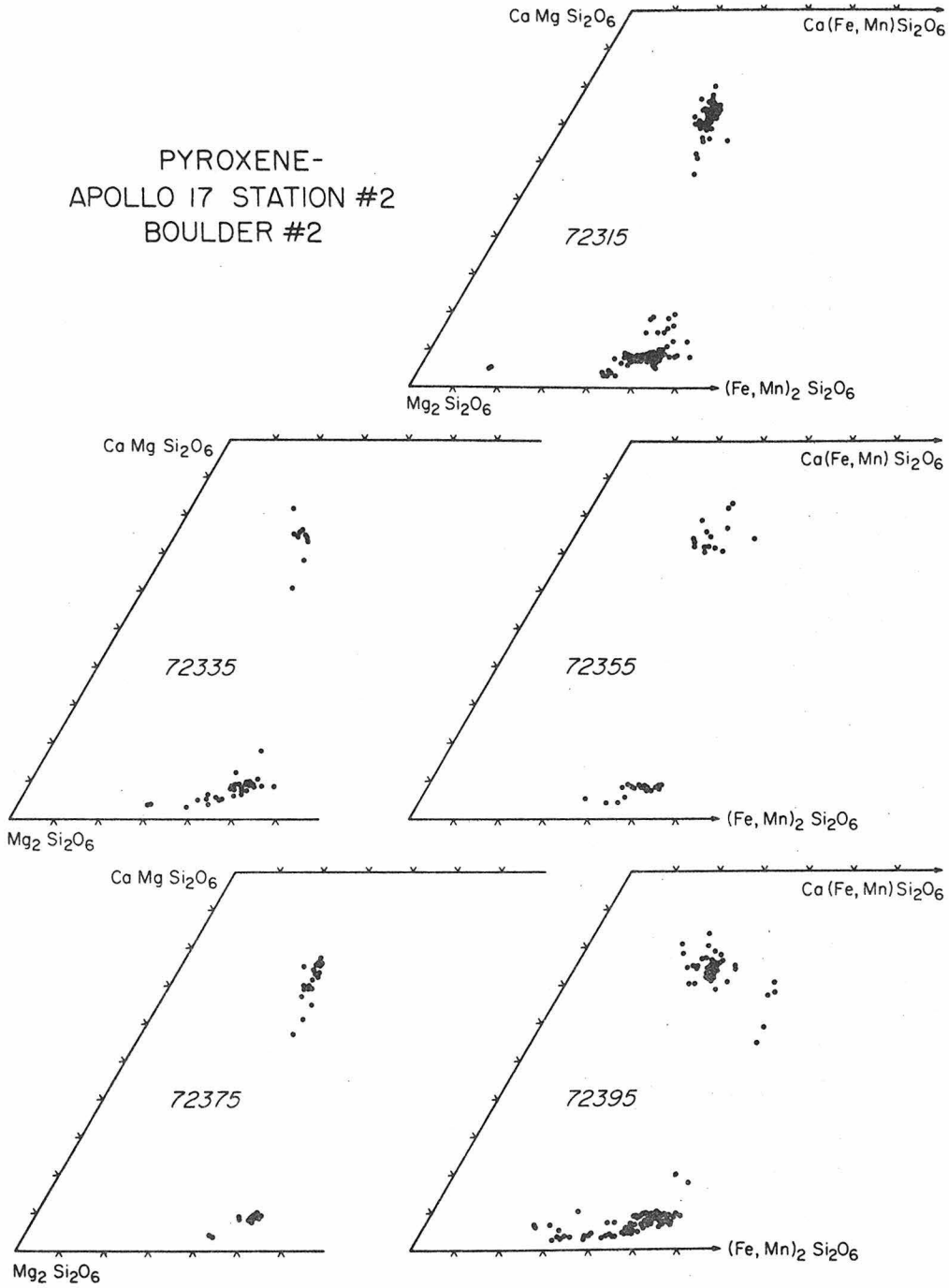

Fig. 7. Compositions of the pyroxene in samples from Boulder #2.

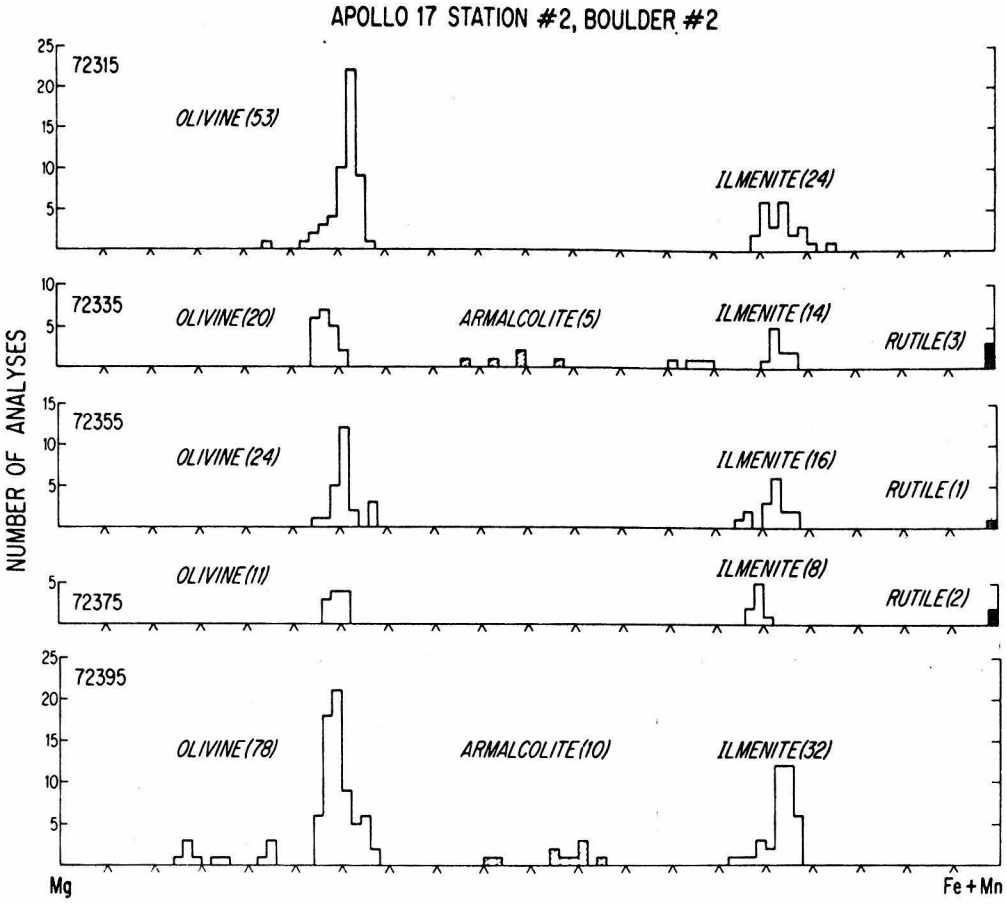

Fig. 8. Compositions of the olivine and Fe–Ti oxide phases in samples from Boulder # 2.

6. *Comparison of mineral chemistry in clasts and groundmass.* The principal phases were divided according to their occurrence in clasts or in the groundmass (the latter includes reaction rims on clasts). As can be seen in Fig. 11, there are slight systematic differences between the compositions of pyroxene, plagioclase, and olivine in clasts and groundmass; ilmenite compositions are the same, whereas armalcolite occurs only in clasts.

The groundmass pyroxene falls into two rather tight clusters in the pyroxene quadrilateral compared to the pyroxene in clasts. In addition, pyroxene in clasts, especially low-Ca pyroxene, trends towards more Mg-rich compositions.

Plagioclase in clasts shows a much greater compositional range than groundmass plagioclase. In addition, the bulk of the plagioclase in clasts is more calcic than the plagioclase in the groundmass. The latter observation was also made by Simonds *et al.* (1974) for the Station 6 boulder samples.

Olivine in clasts shows a greater compositional range than groundmass olivine. Although the bulk of the olivine in clasts is similar in composition to olivine in the

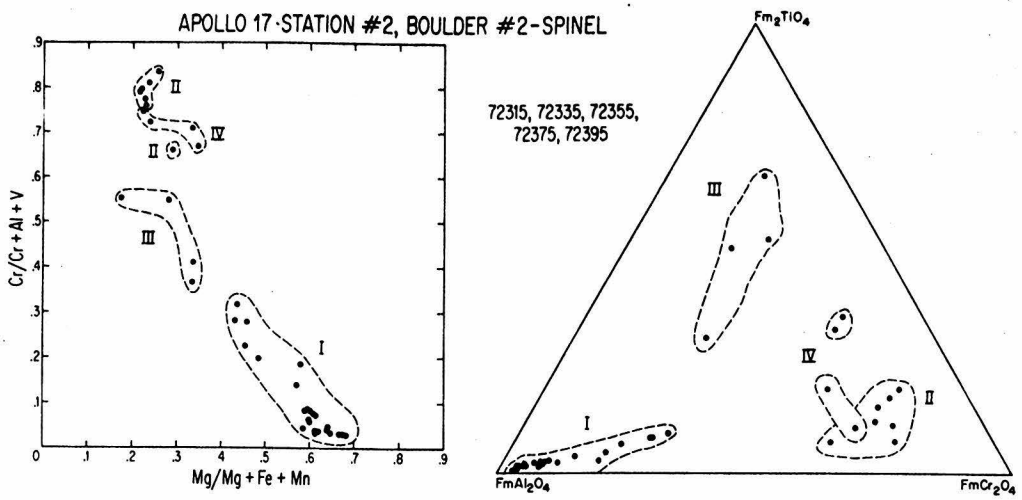

Fig. 9. Compositions of the spinels in samples from Boulder #2. Data points in the outlined areas correspond to analyses of petrographically similar types of spinels: I, Al-rich pink to red spinel; II, Cr-rich lamellae in ilmenite; III, Ti-rich rims on pink to red spinels; IV, Cr-rich spinels in lithic clasts.

groundmass, the olivine in clasts trends towards more Mg-rich compositions.

Relatively clast-free areas of the matrix have been chemically-analyzed using broad beam microprobe techniques. The average of 30 such analyses which represent our best estimate of the composition of the groundmass, is presented in Table 3. These data indicate that the groundmass has a somewhat different composition from that of the boulder as a whole, reflected in a lower content of Al_2O_3 and MgO, and higher SiO_2. This chemical difference, together with the observed difference in mineral composition between clasts and groundmass (Fig. 11) indicates that the groundmass of Boulder #2 cannot be produced by simple crushing, grinding, and recrystallization of the observed clast lithologies.

B. *Boulder #3*

1. *General Description.* Petrographic study of thirteen thin sections from sample 72435, the "matrix" of Boulder #3, indicates that it is comprised of 5–10% megaclasts (1 mm–2 cm) set in an extremely fine-grained, partially-clastic matrix (Fig. 12A). The < 1 mm portion of the sample consists of microclasts with a seriate grain size distribution, and an igneous groundmass with an average grain size of $\lesssim 50\ \mu$m. In general appearance, 72435 resembles the samples from Boulder #2, and it likewise has been classified as a "matrix-supported breccia" by Simonds *et al.* (1974).

In transmitted light, the thin sections all have a dark gray appearance due to the color of the aphanitic matrix (Fig. 12A). The groundmass portion of the matrix is extremely homogeneous with only slight variations in grain size. There are, however, a few 200–300 μm areas in the groundmass that are much finer-grained

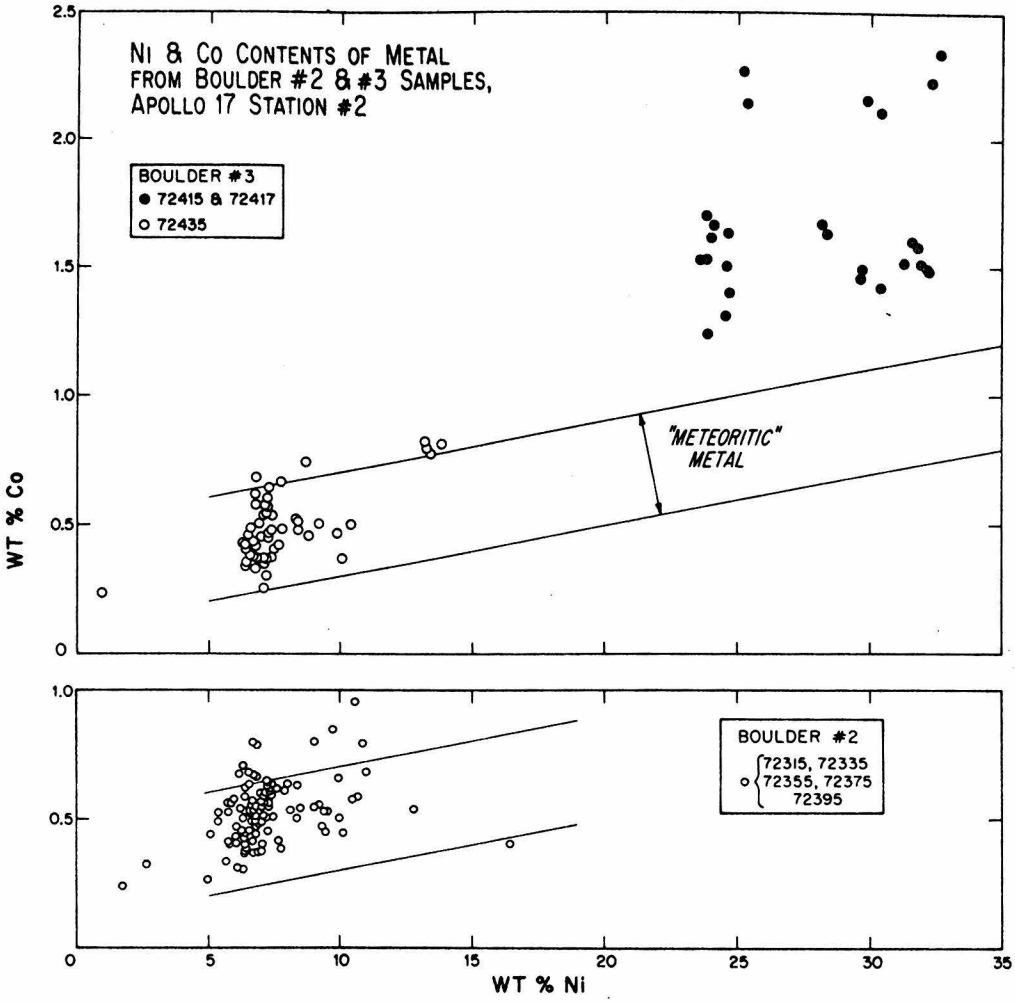

Fig. 10. Diagram illustrating the variation of Ni and Co in metal clasts in samples from Boulders # 2 and # 3.

than their surroundings. In one instance, the adjacent groundmass appeared to flow around the finer-grained area as if it were a clast. This texture may represent a type of early-formed igneous microblock disrupted by later motion of the melt. A second type of anomalous groundmass area is represented by aggregates of randomly oriented plagioclase laths in regions up to approximately 500 μm across (Fig. 12B). Although these areas may be clasts, it is possible that they represent a type of "synneusis" texture formed by the accumulation of early-formed plagioclase since the material between plagioclase laths is identical to the surrounding groundmass. It is important to emphasize that "chilled-zones" do not occur around clasts, in contrast to those observed in Station 7 boulder sample 77115, which 72435 resembles (Chao *et al.*, 1975).

Locally the sample has a distinct foliation caused by the alignment of clasts

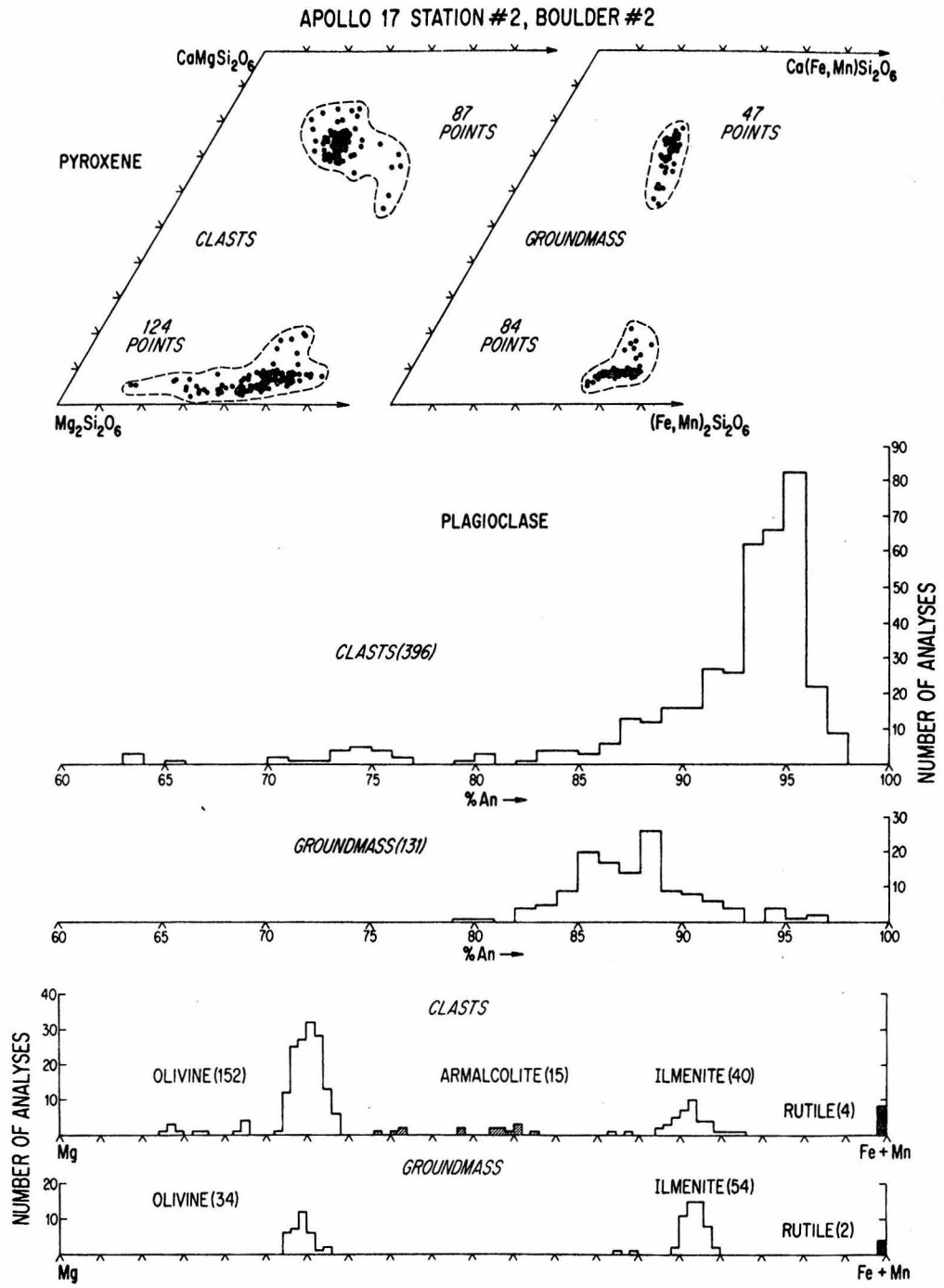

Fig. 11. Summary diagram for the principal phases in Boulder # 2 samples illustrating the distinction between the composition of minerals in clasts vs. groundmass.

and slit vesicles. The groundmass appears to be unaffected by this alignment. Since this foliation is not a pervasive feature, the areas may represent local flow planes formed during consolidation of the melt.

Voids comprise approximately 10% of each thin section, and include elongate slit vesicles, isolated smooth-walled spherical vesicles as large as 15 mm (Figs. 1B and 12D), smaller, more evenly distributed smooth-walled spherical vesicles (25–100 μm), and angular vesicles dispersed throughout the matrix. Crystal-lined vugs are rare, and the pyroxene-plagioclase "vesicular pods", which are so prominent in Boulder # 2 samples, were not observed in 72435.

Sample 72435 does however contain porous aggregates of plagioclase, K-rich "glass," SiO_2, small amounts of ilmenite, troilite, and metal, and in one case zircon (Fig. 13A). The K-rich "glass" is actually an intergrowth of ~ 1–2 μm wide rods of SiO_2 and K-feldspar(?); this SiO_2 in the intergrowths is distinct from the separate grains of SiO_2. Every interface with the surrounding groundmass, as well as interfaces with the pores in the aggregate, is lined with a thin $\leq$10 μm layer of pyroxene. This pyroxene is similar to a vesicle coating, but instead of projecting into the void, crystal terminations project into the silicate phase. Some of these aggregates appear to resemble granitic clasts described in Boulder # 1 from Station 2 (Ryder *et al.*, 1975).

2. *Groundmass.* The groundmass of 72435 consists of very fine-grained, intergrown grains of pyroxene, plagioclase, olivine, and ilmenite that has been termed "micropoikilitic" by Simonds *et al.* (1974). The mafic silicate minerals form tiny oikocrysts (~ 10–50 μm across) that enclose abundant grains of plagioclase (Fig. 12C). The majority of the oikocrysts appear to be low-Ca pyroxene with measured composition $Wo_2En_{73}Fs_{25}$ to $Wo_{14}En_{62}Fs_{24}$. Minor amounts of high-Ca pyroxene also form oikocrysts, but no reliable analyses were obtained.

Olivine oikocrysts range in composition from Fo_{70} to Fo_{72}. Olivine also occurs at oikocryst boundaries and forms subrounded, locally ragged grains ($\leq$ 25 μm) with compositions that are similar to the composition of the olivine oikocrysts. The ragged form of these olivine grains may indicate that they are partially resorbed microclasts. No pyroxene reaction rims were observed around these olivine grains. Some low-Ca pyroxene oikocrysts have rounded olivine inclusions in them.

The enclosed plagioclase chadacrysts generally form euhedral laths less than 10 μm across, but angular, irregularly shaped grains also occur (Fig. 12C). Chadacrysts comprise up to a third of the area of an individual oikocryst, and are typically randomly oriented and evenly distributed. The few analyses of the chadacrysts yield compositions of An_{85} to An_{91}. Plagioclase (An_{80} to An_{95}) also forms twinned and apparently unzoned lathlike to blocky grains ($\leq$ 25 μm) between oikocrysts.

Ilmenite in the matrix occurs as bladed to angular grains, 1–10 μm wide, with a skeletal form. Although these contain occasional silicate inclusions, they do not have a sieve-texture like the ilmenite in Boulder # 2 samples. Ilmenite also occurs

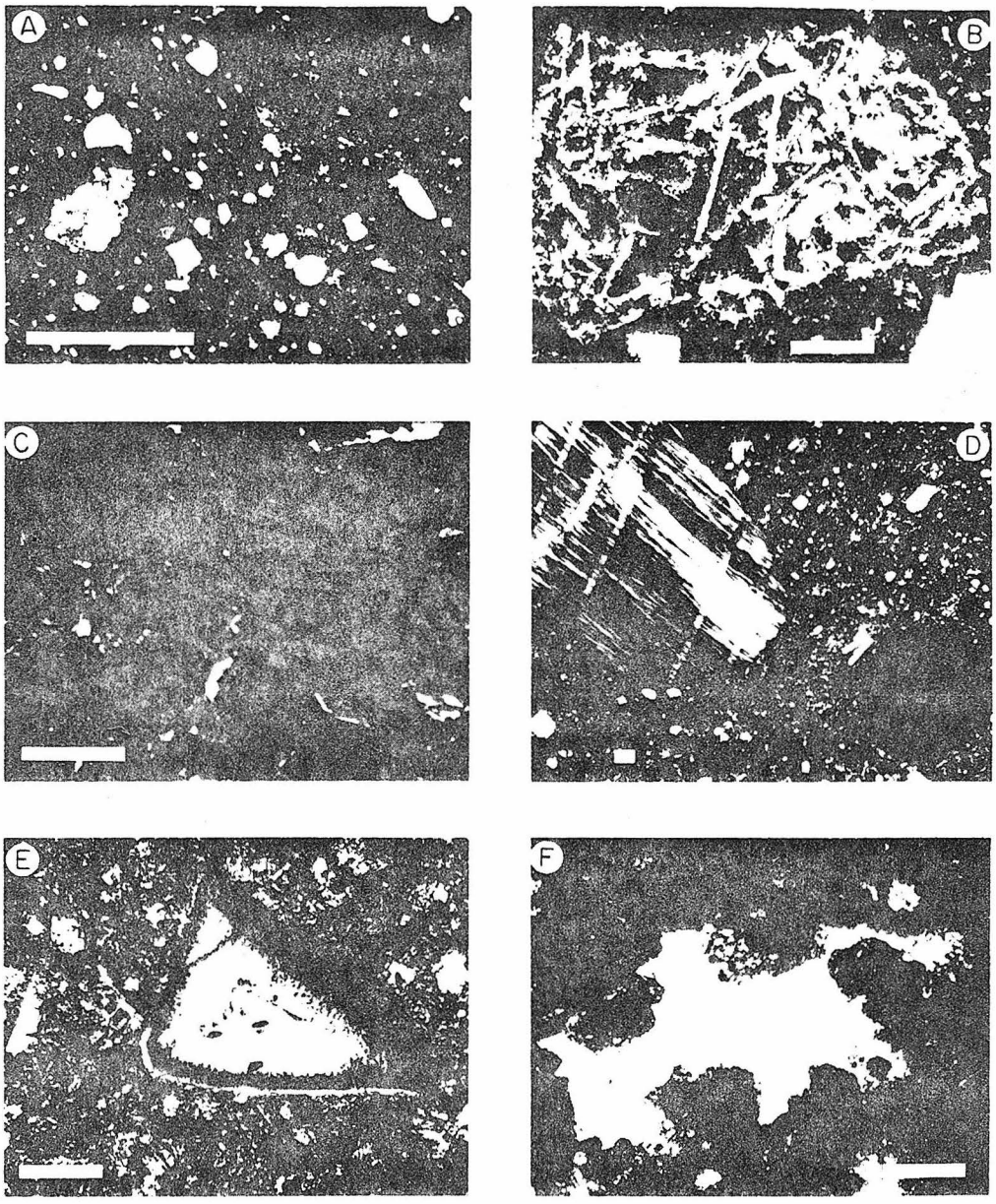
A
B
C
D
E
F

as $\leq 5\ \mu m$ blebs that are more or less uniformly dispersed throughout the groundmass. These occur within pyroxene oikocrysts, at the boundaries between plagioclase chadacrysts and oikocrysts, and rarely within olivine. However, they do not appear to occur as inclusions within plagioclase chadacrysts. Ilmenite also occurs at the edges of large metal clasts.

Troilite occurs in a habit similar to ilmenite, i.e., as interstitial grains, as tiny dispersed blebs, and at the edges of large metal clasts. Tiny ($\leq 5\ \mu m$) grains of metal are also dispersed throughout the matrix, typically associated with similarly-sized troilite.

Tiny interstitial areas of K-rich mesostasis ($\leq 10\ \mu m$) are also dispersed throughout the matrix. Analyses yield up to 13.5 wt.% K_2O. Ca-phosphate occurs as $\leq 5\ \mu m$ interstitial grains but no analyses were obtained.

As in the case of the samples from Boulder # 2, the paragenetic sequence in the groundmass of 72435 is plagioclase, olivine, pyroxene, ilmenite, and minor phases. This sequence matches that expected for crystallization from a melt, and that predicted by the experimental work of Walker *et al.* (1972) for rocks of similar composition.

3. *Mineral Clasts.* Most of the clasts in 72435 are mineral fragments. These include plagioclase, olivine, high- and low-Ca pyroxene, metal, ilmenite, and spinel. These are apparently derived from a variety of sources since they show differences in grain size, angularity, and degree of shock, and have a wide range in composition.

Plagioclase clasts include untwinned to twinned types that range from subrounded to subangular, and from subequant to elongate in shape. These clasts are unshocked and clear, or clouded and shocked types with undulose extinction. Clasts comprised of feathery to spherulitic aggregates are inferred to represent devitrified maskelynite. An unusual type of plagioclase clast (An_{95}) with wavy extinction is comprised of elongated spindles arranged parallel to (010) (Fig. 12D). James (personal communication) has indicated that this texture is a result of shock. Zoning is only rarely present in plagioclase clasts, but the range in measured compositions is extremely large ($An_{55}Ab_{30}Or_{15}$ to $An_{98}Ab_2Or_{<1}$). Reac-

Fig. 12. Photomicrographs illustrating various textural features in Boulder # 3 sample 72435 (bar scales: A = 1 mm; C = 50 μm; all others = 100 μm). (A) Large-scale view of fragmental aspect of 72435. Note the very fine-grained, dark appearance of the groundmass (compare with Fig. 3A) (transmitted plane-polarized light). (B) Region of synneusis texture comprised of acicular plagioclase grains ($An_{90.4}Ab_{8.0}Or_{1.6}$) enclosing fine-grained material indistinguishable from the surrounding groundmass (transmitted plane-polarized light). (C) Micropoikilitic texture in groundmass of 72435. Note lathlike form of plagioclase (dark gray) and fine-grained, bladed ilmenite (compare with Fig. 3B and 3D) (reflected light). (D) Sharply-bounded plagioclase clast ($An_{96}Ab_4Or_{<1}$) with "spindle" (shocked) texture and adjacent spherical vesicle (transmitted cross-polarized light). (E) Clear plagioclase clast ($An_{53}Ab_{32}Or_{15}$) surrounded by a fine-grained dark reaction zone and mantled by a rim of clear plagioclase ($An_{86.3}Ab_{11.9}Or_{1.7}$) (transmitted plane-polarized light). (F) Extensively assimilated single crystal of plagioclase ($An_{90.8}Ab_{8.8}Or_{0.4}$) (transmitted, plane-polarized light).

tion rims are prominent on some clasts (Fig. 12E), but the extent to which an overgrowth is developed depends on the An-content of the clast. Rare, extensively-resorbed, irregularly-shaped grains of plagioclase, also occur (Fig. 12F). These relationships in 72435 are similar to those described in Boulder #2 samples.

Pyroxene clasts range from green to pale brown to those with a dark brown, mottled appearance that is probably related to shock. Elongate grains are rare, and most grains are subangular to subrounded and subequant. Homogeneous low-Ca ($\sim Wo_1En_{81}Fs_{18}$ to $\sim Wo_{10}En_{65}Fs_{25}$) and high-Ca ($\sim Wo_{30}En_{50}Fs_{20}$ to $\sim Wo_{43}En_9Fs_{48}$) types occur as well as a few grains that display vermicular to lamellar exsolution. The latter are probably exsolved pigeonite. Reaction rims are rare.

Olivine clasts (Fo_{92}–Fo_{70}) range from strain-free, pale green to colorless, clear grains, to grains with abundant strain bands and planar partings. Reaction rims are not present, but zoning does occur. Edge compositions are similar to the composition of olivine in the groundmass.

Spinel clasts are typically rounded, and range from pale pink to orange to red. The spectacular reaction rims observed around pink spinel grains in Boulder #2 samples are not present in 72435.

Metal clasts are typically globular to rounded. Most have smooth margins but ones with jagged edges also occur (Fig. 13B). Most metal clasts have a narrow range in composition (5–11 wt.% Ni; 0.3–0.7 wt.% Co; Fig. 10) and lie within the field of "meteoritic" metal. However, a few analyses fall outside the cluster. The few analyses with 13% Ni are from petrographically similar metal grains, but the lone analysis with approximately 1 wt.% Ni is from a metal grain in a lithic clast. All of the metals in 72435 have compositions that are markedly different from the composition of the metal in dunite samples 72415 and 72417 (Fig. 10).

4. *Lithic Clasts.* Lithic clasts in 72435, like those in Boulder #2, are exclusively DANT-type material, and comprise several percent of the sample. These range from fine-grained varieties with grain sizes smaller than most mineral clasts, to coarse-grained types in megaclasts up to 15 mm across. Clast lithologies include: recrystallized anorthositic, noritic, and troctolitic rocks (some of which appear to be recrystallized breccias); poikilitic-textured norite; dunite; and pink spinel cataclasite. There seems to be less of a variety of clast types in 72435 than in Boulder #2 samples, but fewer thin sections were studied.

Plagioclase in the lithic clasts generally is more calcic than An_{90}. Pyroxene and olivine compositions are similar to those for the mineral clasts. The petrographic features of the clasts are virtually identical to those described for lithic clasts in Boulder #2 samples, and only the dunite and the unique spinel cataclasite will be discussed here.

The dunite clasts in 72435 resemble 72415 and 72417 in part (Fig. 13C and 13D). The clasts are typically coarse-grained, although a few fine-grained types occur. They preserve polygonally recrystallized textures, and are not cataclasites like 72415 and 72417. Olivine grains are clouded by numerous inclusions and display

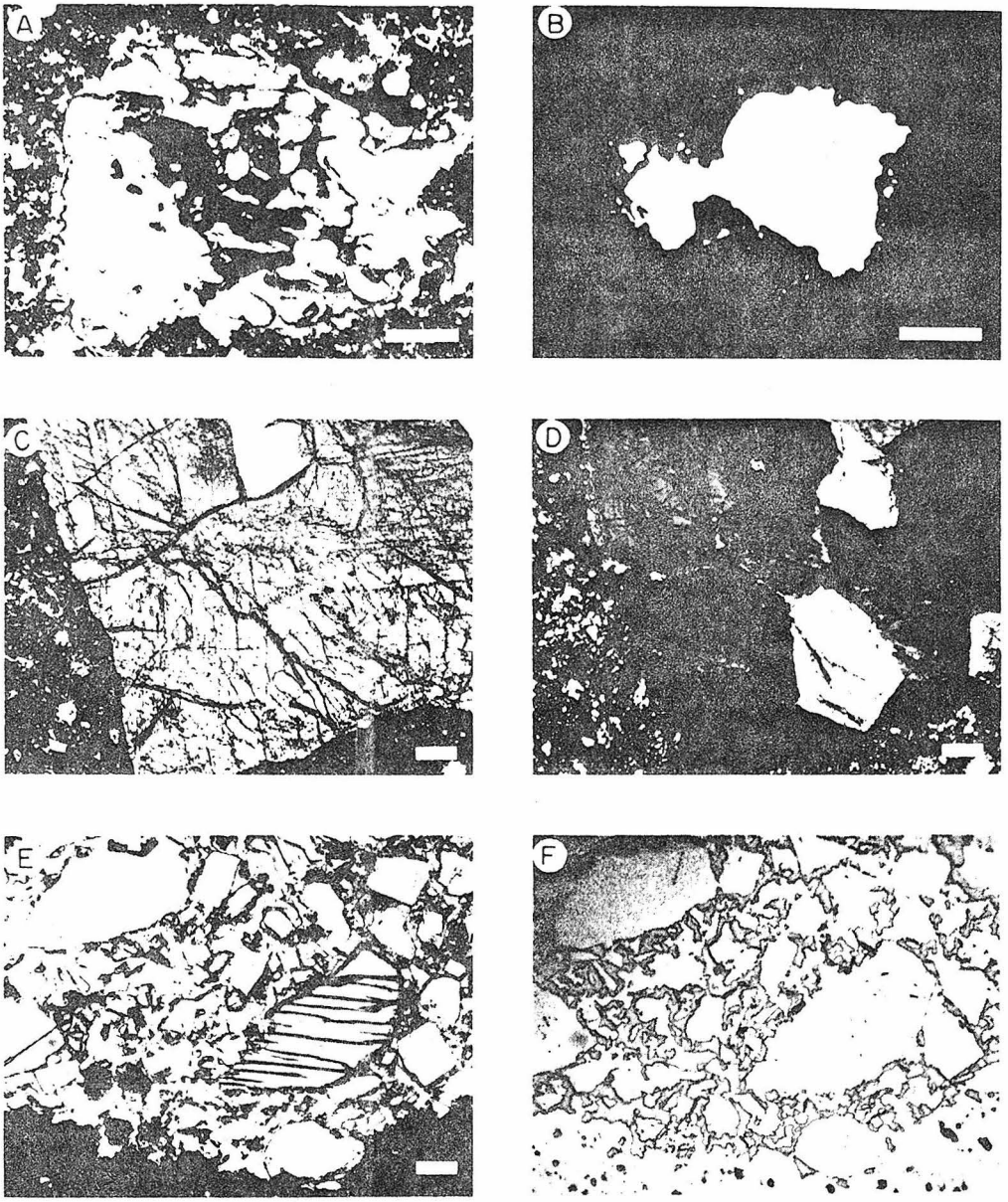

Fig. 13. Photomicrographs illustrating various textural features in Boulder # 3 sample 72435 (all bar scales = 100 μm). (A) Vesicular aggregate comprised of SiO_2 (clear-left side), K- and Si-rich "glass" (dark center, upper and lower right side), and zircon (arrow) (transmitted plane-polarized light). (B) Irregularly-shaped metal globule. Note serrated edges (reflected light). (C) Dunite clast. Note abundant inclusions in olivine (transmitted plane-polarized light). (D) Dunite clast. Note coarse polygonal texture (transmitted cross-polarized light). (E) Spinel cataclasite clast. Note the sharpness of the contact between clast (light) and groundmass (dark), and the disrupted cataclastic texture of the clast (transmitted plane-polarized light). (F) Spinel cataclasite clast. Note the vuggy nature of the clast and the contrast between the type of porosity displayed by the clast compared with the groundmass (reflected light).

strain bands and planar partings. Interior olivine compositions range up to Fo_{90}, but the grains are zoned to compositions as Fe-rich Fo_{75} near the border with the groundmass suggesting some chemical equilibration therewith. The largest dunite clast studied contained a symplectic intergrowth of Cr-spinel and high-Ca pyroxene. Rounded grains of Cr-spinel occur as inclusions in a few of the olivine grains.

Spinel cataclasite (Fig. 13E and F) is the most distinctive clast observed in 72435 and two clasts occur in the thin sections studied. The best documented clast was highly friable, and the thin sections contain only "rims" attached to matrix material. Nearby mineral clasts and slit vesicles are oriented parallel to the margin of this clast. This suggests that the clast responded to the motion of the clast-laden melt. Hence, it must have been a "coherent" aggregate of grains prior to its incorporation into the melt. Preservation of such a friable rock as a collectable sample would be difficult, and spinel cataclasite may be a much more common lunar highland rock type than indicated by its apparent abundance.

Spinel cataclasite has been recognized by Bence *et al.* (1974) in the Apollo 17 2–4 mm soil fraction. Like the soil fragment figured by them, the clasts in 72435 are comprised of a vuggy aggregate of broken, angular mineral fragments (10–500 μm). Plagioclase (An_{94}–An_{98}) comprises approximately 70% of the clast. These grains are unshocked, contain only rare inclusions, and have complex multiple twinning. Olivine is very uniform in composition (Fo_{72}), comprises approximately 20% of the clast, and is also free of any visual shock effects. A great number of the large clear green olivine and translucent white plagioclase grains in 72435 and Boulder #2 samples could have been derived from spinel cataclasite, and could not have been derived from other observed DANT lithologies.

Pink to red spinel accounts for approximately 5% of the clast. These grains are zoned with Fe/(Fe + Mg) (= .31 – .56), and Cr/(Cr + Al) (= .03 – .21) increasing from core to rim. Most spinel grains are mantled by plagioclase, but μm-sized ilmenite blebs may occur at the plagioclase-spinel interface. A few of the spinel grains contain 10–20 μm inclusions of low-Ca pyroxene, and one contains a single 30 μm inclusion of cordierite in addition ($K_{.00}Na_{.02}Ca_{.00}Mg_{1.75}Mn_{.00}Fe_{.32}Ti_{.00}Al_{3.97}Si_{4.92}O_{\sim 18}$; Table 3). A few μm-sized blebs of ilmenite are present at the spinel-cordierite contact.

Low-Ca pyroxene comprises approximately 1% of the clasts, and, although individual grains are homogeneous, a range of compositions are present ($Wo_2En_{87}Fs_{20}$ to $Wo_2En_{65}Fs_{33}$). High-Ca pyroxene has not been observed. A few rare individual grains of ilmenite [Fe/(Fe + Mg) = 0.23], troilite, and Fe-metal (0.8 wt.% Ni; 0.25 wt.% Co) are also present. The ilmenite in spinel cataclasite contains silicate and metal inclusions and may represent the source of the large ilmenite grains in 72435 and Boulder #2 samples.

Anderson (1973) has described a lunar peridotite (15445,10) that consists of the assemblage enstatite-anorthite-spinel-forsterite, similar to spinel cataclasite, and estimated that such an assemblage could indicate a high pressure origin for the rock (~ 40 km depth). Bence *et al.* (1974) reached a similar conclusion (~ 60 km

depth) based on their study of spinel cataclasite fragments found in Apollo 17 2–4 mm soil fraction. The overall coarse grain size of the spinel cataclasite clast in 72435, although somewhat reduced by granulation, is consistent with a plutonic origin. It should be noted that the olivine in the clasts described by Anderson (1973) and Bence *et al.* (1974) has composition ~ Fo_{90}, in contrast to the Fo_{72} in the clast from 72435.

Anderson (1973) has speculated that the assemblage observed in 15445,10 could have been derived from a magmatic assemblage that included cordierite. Phase relations in the system $CaO–Al_2O_3–MgO–SiO_2$ indicate that a reaction of the type Fo + Cd → En + Sp could eliminate cordierite. Since one of the spinel grains in the spinel cataclasite clasts in 72435 contains a relic inclusion of cordierite, the suggestion of Anderson (1973) should be examined seriously.

For example, does the plutonic aspect of spinel cataclasite imply that cordierite-bearing rocks are important in the lower lunar crust? A major problem remains, however, in that if samples like peridotite 15445,10 and spinel cataclasite are cogenetic and complementary differentiates from a melt with cordierite as a liquidus or near-liquidus phase, what was the composition of that magma, and what is the relationship between that and other lunar magma types?

5. *Mineral Chemistry.* Compositions of the principal phases in samples 72415, 72417, and 72435 are illustrated in Figs. 10, 14–17. Except for slight differences in compositional range, the chemistry of the minerals in sample 72435 is virtually identical to that of the minerals from samples in Boulder # 2. Hence, no detailed discussion will be given. The phases in 72415 and 72417 have been described in detail elsewhere (Dymek *et al.*, 1975), and will not be repeated.

6. *Clast-Groundmass Comparison.* The compositions of the phases in 72435 have been divided according to their occurrence in clasts or in the groundmass. As illustrated in Figs. 14–16, the minerals in the groundmass have a more restricted range in composition than those in the clasts. The clustering of data points in Fig. 14 indicates that the bulk of the plagioclase clasts are more calcic than the groundmass plagioclase. Olivine in clasts overlaps in composition with that of the groundmass olivine, but trends towards more Mg-rich compositions. Although there are only a few analyses of low-Ca pyroxene from the groundmass of 72435, it appears that the low-Ca pyroxene in clasts tends to be more magnesian than in the groundmass. Ilmenite compositions in clasts and groundmass are similar.

The average composition of the groundmass of 72435, as determined by broad beam microprobe analysis, is different from the whole rock (Table 3). This observation, together with the mineralogical evidence, indicates that the groundmass of Boulder # 3, like Boulder # 2, cannot be produced by crushing, grinding, and recrystallization of the observed clast lithologies.

The olivine and pyroxene in dunite samples 72415 and 72417 are distinctly more magnesian than those in 72435 (Figs. 15 and 16). Metal compositions are likewise very different (Fig. 10). Plagioclase compositions overlap in part, but trend towards higher An-contents (Fig. 14). These data support our earlier contention that the dunite has not been contaminated by its host rock (Dymek *et*

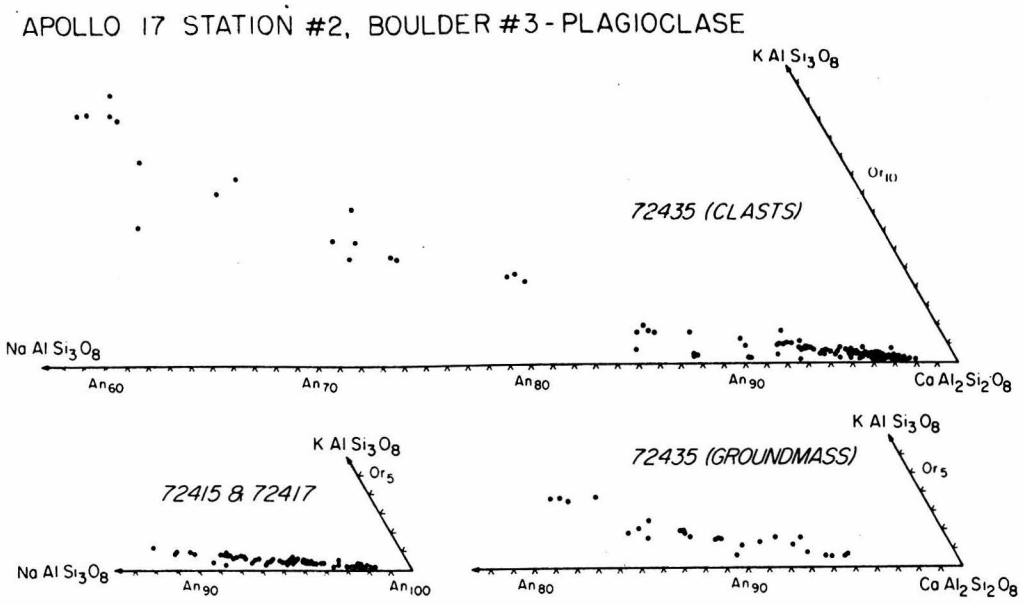

Fig. 14. Composition of the plagioclase in samples from Boulder # 3. Samples 72415 and 72417 are depicted separately, but these data can be grouped with 72435 (clasts).

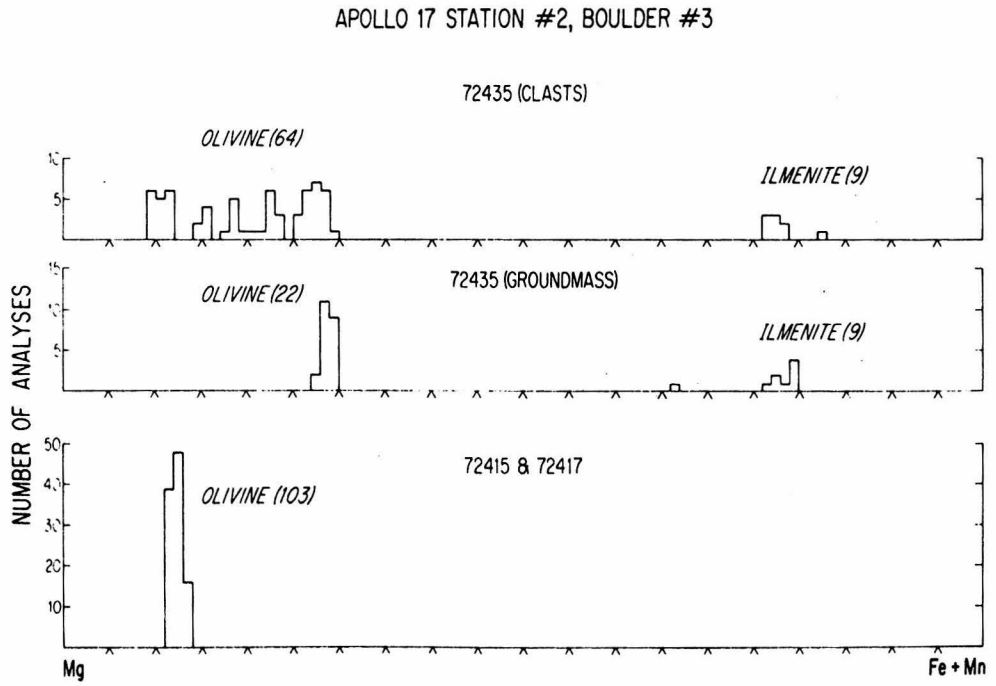

Fig. 15. Composition of the olivine and ilmenite in samples from Boulder # 3. The olivine in 72415 and 72417 can be grouped with 72435 (clasts).

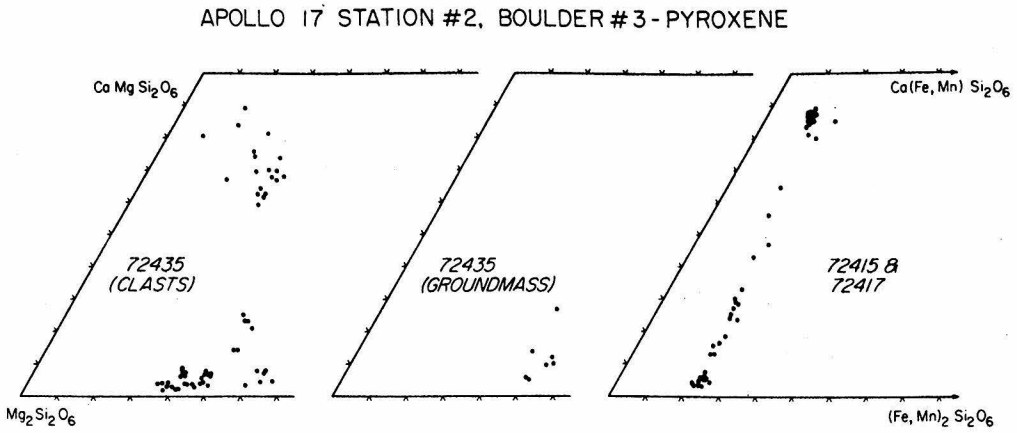

Fig. 16. Composition of the pyroxene in samples from Boulder # 3. The pyroxene in 72415 and 72417 can be grouped with 72435 (clasts).

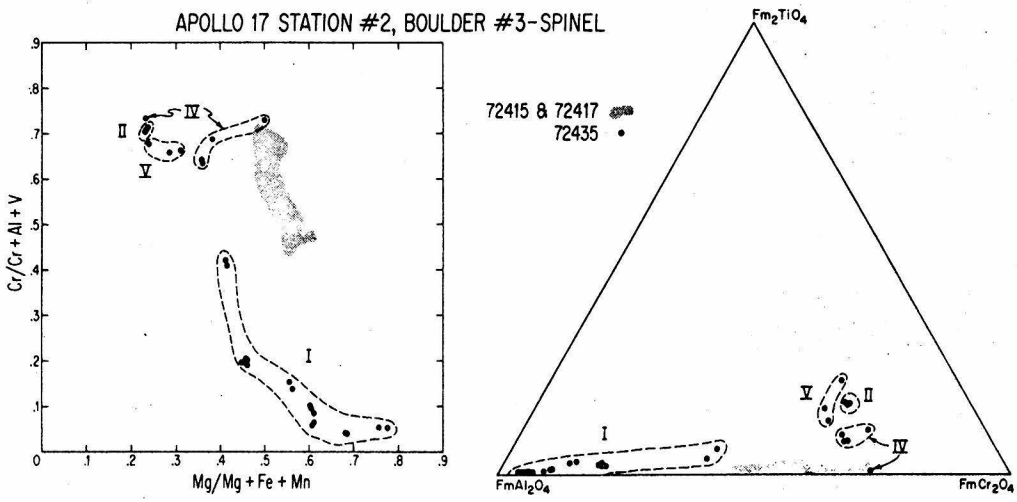

Fig. 17. Composition of the spinels in samples from Boulder # 3. Data points in the outlined areas correspond to analyses of petrographically similar types of spinels: I, Al-rich pink to red spinel; II, Cr-rich spinel associated with ilmenite; IV, Cr-rich spinels in lithic clasts; V, Cr-rich spinel clasts in matrix. Note that the composition of the spinels in dunite samples 72415 and 72417 appear distinct from the others.

al., 1975). Isotopic data also support such a conclusion (Papanastassiou and Wasserburg, 1975).

VIII. Discussion

Samples from Boulders # 2 and # 3 consist of a variety of mineral and lithic clasts set in a very fine-grained groundmass that we interpret to be igneous in origin. These types of rocks appear to be the dominant lithologies in the North and

South Massifs at the Apollo 17 site. The massifs and their constituent lithologies appear to have formed as a consequence of, and in response to, the Serenitatis basin-forming event. By inference then, such "metaclastic" rocks should be an extremely important and widespread lunar rock type associated with the large impact basins. Hence, a characterization of these samples, and an understanding of their origin, is critical to our interpretation of the pre-3.95 AE history of the moon.

In this section, we summarize our observations as they relate to an eclectic model for the origins of Boulders #2 and #3. We consider the relationships between Boulders #2 and #3, and their clast lithologies, and some petrologic implications of these results.

A. *Origin of the groundmass as a melt*

Several lines of evidence indicate that the groundmass in each boulder formed by crystallization of a melt rather than by metamorphism or sintering of fine-grained clastic debris. These include the sequence of crystallization of the phases, the texture, and the presence of vesicles. First, the paragenetic sequence of the groundmass minerals certainly matches that expected for crystallization from a melt of feldspathic basalt composition (i.e., plagioclase → olivine → pyroxene → ilmenite → minor phases, including a K-rich mesostasis). Such a crystallization sequence is also predicted by the experimental data of Walker *et al.* (1972).

Although textural criteria can be ambiguous, the common euhedral lathlike form of the plagioclase suggests that they crystallized from a melt. Moreover, certain portions of the groundmass in the boulder samples (best displayed in 72355) have a coarser, intersertal texture somewhat similar to sample 14310. Such a texture, we feel, results only from crystallization from a melt.

The extremely fine grain size of the matrix is consistent with an origin by quenching of a melt, although such small particles might also be produced by devitrification or recrystallization of a glass. However, Simonds (1975) points out that sintering and annealing experiments performed at temperatures below 1000°C on glassy material yield spherulitic to granulitic textures, rather than the subophitic to poikilitic textures observed in our boulder samples.

The occurrence of spherical vesicles is most logically interpreted to indicate the former presence of a fluid-fluid contact. The large smooth-walled spherical vesicles, as in 72435, suggest that exsolution of a vapor phase from the melt occurred prior to extensive crystallization. (Such "boiling" may be responsible for the finer grain size of the groundmass in 72435.) The slit vesicles and other more irregular vugs probably formed by separation of vapor later in the crystallization sequence when newly-formed crystals (and clasts) would interfere with the formation of spherical bubbles, and when movement of the crystal- and clast-laden melt would be recorded in the parallel alignment and deformation of vesicles into slit vesicles.

B. *Relationships between mineral clasts and melt*

The distribution of clasts in thin sections of the boulder samples indicates that clasts and matrix are everywhere well-mixed. It is rare to find a 1 mm^2 area devoid of clasts in these samples, as was pointed out by Simonds (1975) for the Station 6 boulder samples. Hence, whatever process generated the boulder melt simultaneously mixed it with its clast component down to the smallest scale.

Clast compositions are biased towards more anorthitic plagioclase and more Mg-rich olivine and pyroxene than those found in the groundmass. Such a relationship is consistent with the interpretation that these phases represent early-formed crystals that precipitated from the melt. However, the tremendous range in clast textures, grain sizes, clast shapes, and compositions indicate that the clasts originated in a variety of environments. We conclude from these relationships that the clasts do not represent a phenocryst assemblage, but rather are more appropriately termed "xenocrysts," as suggested by Chao *et al.* (1975).

Lunar highland "metaclastic" rocks characteristically contain a high siderophile element content which has been used to indicate extensive meteoritic contamination (Morgan *et al.*, 1974). Analyses of Boulder # 2 samples demonstrate that they also have a high siderophile element content, likewise suggesting some meteoritic contamination (Laul and Schmitt, 1974, 1975a).

The question of whether the igneous matrix in these highland "metaclastites" originated via impact processes or by endogeneous magmatism has been discussed by Chao *et al.* (1975), Crawford and Hollister (1974), Simonds *et al* (1974), Simonds (1975) and others. Chao *et al.* (1975) observed that nearly all clasts in 77115 appeared unshocked, and suggested that such an observation is consistent with an internal origin for the melt. Crawford and Hollister (1974) argued that the volcanic liquid parental to sample 62235 was intruded into a fragmental regolith, partly assimilating it, thereby accounting for the high siderophile element content.

Several geologic observations seem pertinent. First, mare basalts, which must have been emplaced through fragmental regolith materials, show no similar meteoritic contamination. Yet we can think of no *a priori* reason why one magma type should become contaminated and another not contaminated during extrusion. Moreover, it is rare to find terrestrial lavas contaminated with foreign material to the extent observed and inferred in lunar metaclastic rocks (see Simonds, 1975, for an extended discussion).

We conclude that the features displayed in samples from Boulders # 2 and # 3 are best interpreted in terms of mixing in a violent, turbulent impact event. It is interesting to note that fragmental debris in the melt sheet from the Manicouagan impact structure is dominated by unshocked clasts, and that the melt sheet illustrates mixing similar to that observed in the lunar samples (Simonds *et al.*, 1976).

The mineralogical and chemical data on Boulder # 2 and # 3 samples indicate that clasts and groundmass are chemically different. This observation precludes the derivation of the matrix directly from the observed clast assemblages by crushing, grinding, melting, and/or recrystallization. Several possibilities could account for this apparent dichotomy.

The first possibility involves *in situ* chemical fractionation brought about by selective shock melting in a debris pile, with the clasts representing the refractory residue formed during this process (Warner *et al.*, 1974). However, the vast majority of clasts in Boulder #2 and #3 samples are visually unshocked. Moreover, the passage of a transient shock wave through a debris pile that results in selective melting, would selectively melt plagioclase (Gibbons *et al.*, 1975). Since plagioclase is the most abundant clast type, we regard this possibility as untenable.

Assuming that these samples represent an extensively reworked regolith that was laid down as a hot, glass-rich ejecta blanket, we can explore the possibility that this chemical difference between clasts and matrix was inherited from the protolith. If insulated, such a debris pile could heat up with the result that the glass-rich matrix portion undergoes partial melting (Albee *et al.*, 1973). Such a process is probably important in the genesis of many lunar rocks such as the Apollo 14 breccias (Warner, 1972). However, in the case of the samples from Boulders #2 and #3, it seems difficult to envision such a process producing up to 70% melt and remaining well-mixed. In addition, such heating would probably be slow, and it is not clear why slow heating should be followed by extremely rapid cooling, as required by the fine grain size of our samples. Therefore, we conclude that Boulders #2 and #3 did not form by "metamorphism" in ejecta blankets.

The model that we consider the most likely possibility involves mixing of impact melt (groundmass) with additional cold fragmental debris (clasts). The details of such a mechanism have been discussed by James (1975) and Simonds (1975), and we endorse most of their conclusions. An important corollary is that clasts and melt may have originated in different source areas.

Simonds (1975) has proposed that the melt that was involved in the formation of the Station 6 boulder was superheated. Several petrographic features in our boulder samples permit constraints to be placed on such a model. These include: (1) some plagioclase clasts appear to be partly melted by the groundmass; (2) prominent overgrowth rims occur only on plagioclase clasts with an An-content less than the An-content of the groundmass ($\lesssim An_{85}$); (3) plagioclase clasts with an An-content greater than that of the groundmass do not have overgrowths; and (4) an extremely large number of tiny plagioclase crystals occur in the groundmass, indicating a sudden, massive amount of homogeneous nucleation.

Impact melting, a process that is not buffered by crystal-liquid equilibria like partial melting, can result in total melting, and should be capable of generating abundant superheat in the melt. The presence of melting of clasts by the groundmass in Boulders #2 and #3 (Figs. 3F, 4B, and 12F), is consistent with some superheat in the melt.

Bowen (1928) has discussed the problems of assimilation and superheat in silicate melts. He noted that reaction will proceed between a melt and a "foreign inclusion" whether the melt is superheated or not, provided the temperature of the inclusions is near the solidus. Otherwise, the melt must heat up the inclusions, thereby limiting the extent of reaction.

Bowen (1928) outlined the effects of a "basaltic" melt, which does not contain

any superheat, on "foreign inclusions" of plagioclase that are at approximately the same temperature as the melt. If the plagioclase inclusion has an An-content less than that in equilibrium with the melt, under conditions of slow cooling, the melt will tend to dissolve the inclusion. If the melt were quenched, overgrowth rims will develop. If the An-content of the plagioclase inclusion is greater than that in equilibrium with the melt, under conditions of slow cooling, the inclusion would be made over to a composition compatible with the melt. If the melt were quenched, essentially nothing would happen.

The situation in the samples from Boulders # 2 and # 3 more closely resembles Bowen's case of quenching. In addition, by analogy with Bowen's examples, it is clear from the petrographic relationships that the melt in the boulders need not have been superheated if the clasts were hot when they came into contact with the melt.

Simonds (1975) has summarized the evidence for cold clasts in the Station 6 boulder, and our observations on Boulder # 2 and # 3 samples are in agreement with his. Thus, the initial thermal event consequent upon mixing impact melt with cold clasts would involve heating the clasts. Hence, any superheat that is present would be rapidly dissipated, and it is not obvious how one can quantitatively evaluate the initial temperature of the melt.

The great abundance of individual plagioclase grains in the groundmass indicates that a massive amount of homogeneous nucleation occurred during the initial stages of crystallization. Such a feature might be expected to result during crystallization from an undercooled melt. The undercooling may have resulted from the rapid dissipation of heat into the cold clasts.

In summary then, Boulders # 2 and # 3 both crystallized from clast-laden impact melts. These resulted from the thorough mixing of cold clastic debris with molten material that may have possessed some superheat. The melt became undercooled due to a rapid loss of heat into the cold clasts causing sudden homogeneous nucleation of plagioclase.

C. *Significance of lithic clast types*

Lithic clasts in samples from Boulders # 2 and # 3 are similar to each other and are exclusively members of the DANT-suite. Clasts of FeTi-mare basalts, aluminous mare basalts, and intersertal-feldspathic pigeonite ("KREEP"-type) basalts were not observed. Either the protolith of the boulder samples formed prior to the extrusion of these lava types, or else the absence of these rocks as clasts represents derivation from a limited source area. There is little chronologic control on this since no crystallization ages have been determined for the groundmass of Boulders # 2 and # 3. It thus appears that the source region of the clastic component in Boulders # 2 and # 3 were similar.

An important feature regarding the clasts in Boulder # 3 is the 4.55 ± 0.10 AE age of dunite sample 72417 (Papanastassiou and Wasserburg, 1975). This sample has been inferred to be a product of the primary lunar differentiation (Dymek *et al.*, 1975; Papanastassiou and Wasserburg, 1975), and it is conceivable that other

clasts in this boulder might also be products of the primary lunar differentiation. Rb–Sr isotopic studies have been performed on selected samples of 72435 (Papanastassiou and Wasserburg, 1975). These data indicate only partial isotopic equilibration in the matrix of 72435 on a scale of approximately 1 mm at a time more recent than 4.1 AE (Papanastassiou and Wasserburg, 1975). In addition, a Rb–Sr internal isochron on an anorthositic clast in 72435 yielded an age of 3.85 ± 0.10 AE (Papanastassiou and Wasserburg, 1975). The $^{40}Ar/^{39}Ar$ release pattern for 72417 is complicated, but indicates argon loss at about 3.95 ± 0.1 AE (J. C. Huneke, pers. comm.). This may represent the time when this clast was incorporated into the impact melt.

Steele and Smith (1973), in their study of Apollo 16 soil fragments, discovered an apparent anticorrelation between the anorthite content of plagioclase and the forsterite content of olivine, in contrast to terrestrial samples. Roedder and Weiblen (1974) presented data suggesting the existence of two trends from their study of clasts in sample 67915. This discovery was extended by Warner *et al.*

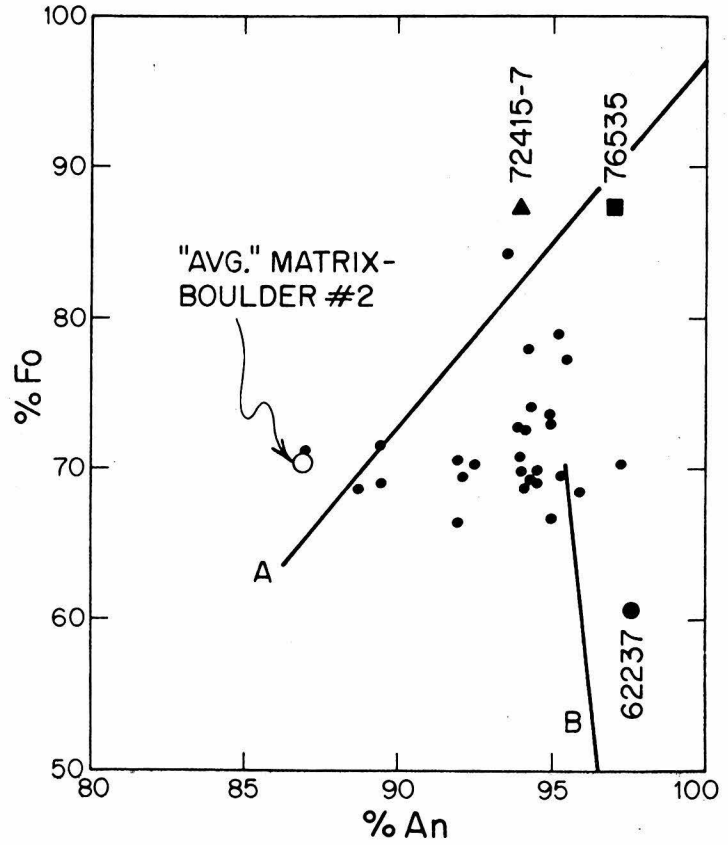

Fig. 18. Diagram illustrating olivine and plagioclase compositions in clasts from Boulder #2. The data for dunite 72415-7, troctolite 76535, and anorthosite 62237 are from Dymek *et al.* (1975). Lines A and B correspond to the Mg-rich plutonic rock series (A) and anorthositic series (B) of Warner *et al.* (1976). The average matrix composition of Boulder #2 was calculated from our point count data.

(1976) who showed convincingly the existence of two trends based on data from "large" lunar plutonic rock samples, and clasts of plutonic rocks in sample 76255—an anorthositic trend with an An–Fo anticorrelation, and a Mg-rich plutonic rock trend with a positive An–Fo correlation.

The compositions of olivine and plagioclase in clasts from Boulders # 2 and # 3 are illustrated in Fig. 18, on which the trends of Warner *et al.* (1976) are reproduced. Dunite 72415 and troctolite 76535 lie along the Mg-rich plutonic rock trend (line A) whereas troctolitic anorthosite 62237 lies near the anorthosite trend (line B). However, our data from Boulders # 2 and # 3 do not fall on these two lunar rock trends, but rather along trends that appear to represent mixing between anorthosite with dunite-troctolite and the composition of boulder # 2 groundmass. The data points that lie between the anorthosite point and dunite-troctolite points may represent a real continuation of the trend. However, the data may indicate that interaction with the molten boulder groundmass may have modified the "original" chemistry of these clasts.

Most clasts in Boulders # 2 and # 3 have textures indicating that they have undergone some recrystallization, and only a very few clasts preserve igneous textures. However, Rb–Sr data on clasts from 72435 demonstrate that Rb and Sr did not undergo extensive redistribution (Papanastassiou and Wasserburg, 1975). The isotopic data suggest that the trend for clasts in Boulders # 2 and # 3 may be valid, although it is difficult to evaluate this fully.

Acknowledgments—We wish to express our appreciation to the staff of the Curator's office at the Johnson Space Center, in particular to J. Annexstad and P. Butler for their assistance and cooperation during the study, sampling, and sawing of the samples described in this paper.

A. J. Gancarz assisted in the mapping of the samples, and D. S. Goldman discovered the cordierite in sample 72435. We wish to thank them for their assistance with the preliminary petrographic study of these samples. The manuscript has benefitted from reviews by A. J. Gancarz, O. B. James, U. B. Marvin, C. H. Simonds, G. J. Taylor, and J. L. Warner.

The microprobe laboratory has been developed through the support of the Jet Propulsion Laboratory, the National Science Foundation, and the Union Pacific Foundation. Our research has been sponsored by NASA grant NGL-05-002-338.

References

AFGIT (Apollo Field Geology Investigation Team) (1975) Documentation and environments of the Apollo 17 samples. In *Astrogeology # 73, Apollo 17 Landing Site Geology*, Part I, p. 1–316. NASA-JSC, Houston.

Albee A. L., Chodos A. A., Dymek R. F., Gancarz A. J., Goldman D. S., Papanastassiou D. A., and Wasserburg G. J. (1974a) Dunite from the lunar highlands: Petrography, deformational history, and Rb–Sr age (abstract). In *Lunar Science V*, p. 3–5. The Lunar Science Institute, Houston.

Albee A. L., Chodos, A. A., Dymek R. F., Gancarz A. J., and Goldman D. S. (1974b) Preliminary investigation of Boulders 2 and 3, Apollo 17, Station 2: Petrology and Rb–Sr model ages (abstract). In *Lunar Science V*, p. 6–8. The Lunar Science Institute, Houston.

Albee A. L., Gancarz A. J., and Chodos A. A. (1973) Metamorphism of Apollo 16 and 17 and Luna 20 metaclastic rocks at about 3.95 AE: Samples 61156, 64423,14-2, 65015, 67483,15-2, 76055, 22006, and 22007. *Proc. Lunar Sci. Conf. 3rd*, p. 569–595.

Anderson A. T. (1973) The texture and mineralogy of lunar peridotite, 15445,10. *J. Geol.* **81**, 219–226.

Apollo 17 Prelim. Sci. Rep. (PSR) (1973) NASA publication SP-330. NASA, Washington, D.C.

Bell P. M., Mao H. K., Roedder E., and Weiblen P. W. (1975) The problem of the origin of symplectites in olivine-bearing lunar rocks. *Proc. Lunar Sci. Conf. 6th*, p. 231–248.

Bence A. E., Delano J. W., Papike J. J., and Cameron K. L. (1974) Petrology of the highlands massifs at Taurus-Littrow: An analysis of the 2–4 mm soil fraction. *Proc. Lunar Sci. Conf. 5th*, p. 785–827.

Bence A. E., Papike J. J., Sueno S., and Delano J. W. (1973) Pyroxene poikiloblastic rocks from the lunar highlands. *Proc. Lunar Sci. Conf. 3rd*, p. 597–611.

Bowen N. L. (1928) *The Evolution of the Igneous Rocks*. Dover, New York. 332 pp.

Brecher A. (1975) Textural remanence: A new model of lunar rock magnetism (abstract). In *Lunar Science VI*, p. 83–85. The Lunar Science Institute, Houston.

Chao E. C. T. (1973) The petrology of 76055,10, a thermally metamorphosed fragment-laden olivine micronorite hornfels. *Proc. Lunar Sci. Conf. 4th*, p. 719–732.

Chao E. C. T., Minkin J. A., and Thompson C. L. (1974) Preliminary petrographic description and geologic implications of the Apollo 17 Station 7 boulder consortium samples. *Earth Planet. Sci. Lett.* **23**, 413–428.

Chao E. C. T., Minkin J. A., Thompson C. L., and Huebner J. S. (1975) The petrogenesis of 77115 and its xenocrysts: Description and preliminary interpretation. *Proc. Lunar Sci. Conf. 6th*, p. 493–515.

Clayton R. N. and Mayeda T. K. (1975) Genetic relations between the moon and meteorites (abstract). In *Lunar Science VI*, p. 155–157. The Lunar Science Institute, Houston.

Consortium Indomitabile (1974a) Interdisciplinary studies of samples from Boulder 1, Station 2, Apollo 17, vol. 1, L.S.I. Contr. No. 210D, Smithsonian Astrophys. Observ. Cambridge, Massachusetts.

Consortium Indomitabile (1974b) Interdisciplinary studies of samples from Boulder 1, Station 2, Apollo 17, vol. 2, L.S.I. Contr. No. 211D. Smithsonian Astrophy. Observ. Cambridge, Massachusetts.

Consortium Indomitabile (1975) Final consortium report. *The Moon* **18**, 303–517.

Crawford M. L. and Hollister L. S. (1974) KREEP Basalt: A possible partial melt from the lunar interior. *Proc. Lunar Sci. Conf. 5th*, p. 399–419.

Dymek R. F., Albee A. L., and Chodos A. A. (1975) Comparative petrology of lunar cumulate rocks of possible primary origin: Dunite 72415, troctolite 76535, norite 78235, and anorthosite 62237. *Proc. Lunar Sci. Conf. 6th*, p. 301–341.

Dymek R. F., Albee A. L., and Chodos A. A. (1976a) Petrographic investigation of lunar sample 72435 with emphasis on the nature of its clasts (abstract). In *Lunar Science VII*, p. 227–229. The Lunar Science Institute, Houston.

Dymek R. F., Albee A. L., and Chodos A. A. (1976b) Chemical and mineralogical homogeneity of Boulder #2, Apollo 17 Station #2 (abstract). In *Lunar Science VII*, p. 230–232. The Lunar Science Institute, Houston.

Gancarz A. J. and Albee A. L. (1973) Microprobe analysis of the bulk composition of phase aggregates. In *Proc. 8th Nat. Conf. on Electron Probe Analyses*, New Orleans.

Gibbons R. V., Morris R. V., Hörz F., and Thompson T. D. (1975) Petrographic and ferromagnetic resonance studies of experimentally shocked regolith analogs. *Proc. Lunar Sci. Conf. 6th*, p. 3143–3171.

Gibson E. K., Jr. and Moore G. W. (1974) Total sulfur abundances and distributions in the valley of Taurus-Littrow: Evidence of mixing (abstract). In *Lunar Science V*, p. 267–269. The Lunar Science Institute, Houston.

Goldstein J. I. and Yakowitz H. (1971) Metallic inclusions and metal particles in the Apollo 12 Lunar soil. *Proc. Lunar Sci. Conf. 2nd*, p. 177–191.

Gooley R., Brett R., Warner J., and Smyth J. R. (1974) A lunar rock of deep crustal origin: Sample 76535. *Geochim. Cosmochim. Acta* **38**, 1329–1340.

Hess P. C., Rutherford M. J., and Ryerson F. J. (1976) Lunar granites: A discussion (abstract). In *Lunar Science VII*, p. 364–366. The Lunar Science Institute, Houston.

Higuchi H. and Morgan J. W. (1975) Ancient meteoritic component in Apollo 17 boulders (abstract). In *Lunar Science VI*, p. 364–366. The Lunar Science Institute, Houston.

Hollister L. S. (1973) Sample 67955: A description and a problem. *Proc. Lunar Sci. Conf. 4th*, p. 633–641.

Hutcheon I. D., Macdougall D., and Price P. B. (1974a) Improved determination of the long-term average Fe spectrum from ~1 to ~460 MeV/amu. *Proc. Lunar Sci. Conf. 5th*, p. 2561–2576.

Hutcheon I. D., Macdougall D., and Stevensen J. (1974b) Apollo 17 particle track studies: Surface residence times and fission track ages for orange glass and large boulders. *Proc. Lunar Sci. Conf. 5th*, p. 2597–2608.

James O. B. (1975) Petrography of the matrix of light gray (consortium) breccia 73215 (abstract). In *Lunar Science VI*, p. 438–440. The Lunar Science Institute, Houston.

James O. B. (1976) Petrology of aphanitic lithologies in consortium breccia 73215 (abstract). In *Lunar Science VII*, p. 420–422. The Lunar Science Institute, Houston.

Lally J. S., Christie J. M., Heuer A. H., and Nord G. L., Jr. (1976) Electron microscopy of lunar dunite 72417 (abstract). In *Lunar Science VII*, p. 468–470. The Lunar Science Institute, Houston.

Laul J. C. and Schmitt R. A. (1974) Chemical composition of Boulder-2 rocks and soils, Apollo 17, Station 2. *Earth Planet. Sci. Lett.* **23**, 206–217.

Laul J. C. and Schmitt R. A. (1975a) Chemical composition of Apollo 17 samples: Boulder breccias (2), rake breccias (8), and others (abstract). In *Lunar Science VI*, p. 489–491. The Lunar Science Institute, Houston.

Laul J. C. and Schmitt R. A. (1975b) Dunite 72417: A chemical study and interpretation. *Proc. Lunar Sci. Conf. 6th*, p. 1231–1254.

Misra K. C. and Taylor L. A. (1975) Characteristics of metal particles in Apollo 16 rocks. *Proc. Lunar Sci. Conf. 6th*, p. 615–639.

Misra K. C., Walker B. M., and Taylor L. A. (1976) Native FeNi metal particles in Apollo 17 Station 6 Boulder (abstract). In *Lunar Science VII*, p. 565–567. The Lunar Science Institute, Houston.

Morgan J. W., Ganapathy R., Higuchi H., Krähenbühl U., and Anders E. (1974) Lunar basins: Tentative characterization of projectiles, from meteoritic elements in Apollo 17 boulders. *Proc. Lunar Sci. Conf. 5th*, p. 1703–1736.

Papanastassiou D. A. and Wasserburg G. J. (1975) Rb–Sr study of a lunar dunite and evidence for early lunar differentiates. *Proc. Lunar Sci. Conf. 6th*, p. 1467–1489.

Papike J. J. and Bence A. E. (1972) Apollo 14 inverted pigeonites: Possible samples of lunar plutonic rocks. *Earth Planet. Sci. Lett.* **14**, 176–182.

Pearce G. W., Gose W. A., and Strangway D. W. (1974) Magnetism of Apollo 17 samples (abstract). In *Lunar Science V*, p. 590–592. The Lunar Science Institute, Houston.

Reed V. S. and Wolfe E. W. (1975) Origin of the Taurus-Littrow massifs. *Proc. Lunar Sci. Conf. 6th*, p. 2443–2461.

Rhodes J. M., Rodgers K. V., Shih C., Bansal B. M., Nyquist L. E., Wiesmann H., and Hubbard N. J. (1974) The relationship between geology and soil chemistry at the Apollo 17 landing site. *Proc. Lunar Sci. Conf. 5th*, p. 1097–1117.

Richter D., Siegfried R., and Simmons G. (1976) Unusual cracks and pores in breccia 15418 and lunar dunite 72415 (abstract). In *Lunar Science VII*, p. 736–738. The Lunar Science Institute, Houston.

Roedder E. and Weiblen P. W. (1971) Petrology of silicate melt inclusions, Apollo 11 and Apollo 12 and terrestrial equivalents. *Proc. Lunar Sci. Conf. 2nd*, p. 507–528.

Roedder E. and Weiblen P. W. (1974) Petrology of clasts in lunar breccia 67915. *Proc. Lunar Sci. Conf. 5th*, p. 303–318.

Ryder G., Stoeser D. B., Marvin U. B., Bower J. F., and Wood J. A. (1975) Boulder 1, Station 2, Apollo 17. Petrology and petrogenesis. *The Moon* **14**, 327–357.

Simonds C. H. (1975) Thermal regimes in impact melts and the petrology of the Apollo 17 Station 6 boulder. *Proc. Lunar Sci. Conf. 6th*, p. 641–672.

Simonds C. H., Phinney W. C., and Warner J. L. (1974) Petrography and classification of Apollo 17 non-mare rocks with emphasis on samples from the Station 6 boulder. *Proc. Lunar Sci. Conf. 5th*, p. 337–353.

Simonds C. H., Warner J. L., and Phinney W. C. (1973) Petrology of Apollo 16 poikilitic rocks. *Proc. Lunar Sci. Conf. 4th*, p. 613–632.

Simonds C. H., Warner J. L., and Phinney W. C. (1976) Clast-melt interactions in lunar and terrestrial impact melts (abstract). In *Lunar Science VII*, p. 812–814. The Lunar Science Institute, Houston.

Snee L. W. and Ahrens T. J. (1975) Shock induced deformation features in terrestrial peridot and lunar dunite. *Proc. Lunar Sci. Conf. 6th*, p. 833–842.

Steele I. M. (1974) Ilmenite and armalcolite in Apollo 17 breccias. *Amer. Mineral.* **59**, 681–689.

Steele I. M. and Smith J. V. (1973) Mineralogy and petrology of some Apollo 16 rocks and fines: General petrologic model of the moon. *Proc. Lunar Sci. Conf. 4th*, p. 519–536.

Steele I. M. and Smith J. V. (1975) Minor elements in lunar olivine as a petrologic indicator. *Proc. Lunar Sci. Conf. 6th*, p. 451–468.

Stoeser D. B., Marvin U. B., Wood J. A., Wolfe R. W., and Bower J. F. (1974) Petrology of a stratified boulder from South Massif, Taurus-Littrow. *Proc. Lunar Sci. Conf. 5th*, p. 355–377.

Tera F., Papanastassiou D. A., and Wasserburg G. J. (1974) Isotopic evidence for a terminal lunar cataclysm. *Earth Planet. Sci. Lett.* **22**, 1–21.

Wänke H., Palme H., Baddenhausen H., Dreibus G., Jagoutz E., Kruse H., Palme C., Spettel B., Teschke F., and Thacker R. (1975) New data on the chemistry of lunar samples: Primary matter in the lunar highlands and the bulk composition of the moon. *Proc. Lunar Sci. Conf. 6th*, p. 1313–1340.

Walker D., Longhi J., and Hays J. F. (1972) Experimental petrology and origin of Fra Mauro rocks and soils. *Proc. Lunar Sci. Conf. 3rd*, p. 797–817.

Warner J. L. (1972) Metamorphism of Apollo 14 breccias. *Proc. Lunar Sci. Conf. 3rd*, p. 623–644.

Warner J. L., Simonds C. H., and Phinney W. C. (1974) Impact-induced fractionation in the lunar highlands. *Proc. Lunar Sci. Conf. 5th*, p. 379–397.

Warner J. L., Simonds C. H., and Phinney W. C. (1976) Genetic distinction between anorthosites and Mg-rich plutonic rocks: New data from 76255 (abstract). In *Lunar Science VII*, p. 915–917. The Lunar Science Institute, Houston.

Wood J. A. (1975) The nature and origin of Boulder 1, Station 2, Apollo 17. *The Moon* **18**, 505–517.

Proc. Lunar Sci. Conf. 6th (1975), p. 49–77.
Printed in the United States of America

Comparative mineralogy and petrology of Apollo 17 mare basalts: Samples 70215, 71055, 74255, and 75055

R. F. DYMEK, A. L. ALBEE, and A. A. CHODOS

Division of Geological and Planetary Sciences,* California Institute of Technology, Pasadena, California 91125

Abstract—Detailed petrographic descriptions are presented for four Apollo 17 mare basalts—70215, 71055, 74255, and 75055—that are representative of the textural types reported in the literature, and were allocated to the Lunatic Asylum for isotopic age dating. Microprobe data are presented for all the principal silicate and oxide phases in each sample. In addition, we report the results of an automated electron microprobe point-count method that permits the determination of modes and average mineral compositions for such complex rocks. Bulk-chemical compositions calculated from these parameters match well with those determined by more standard analytical techniques.

An examination of mineral–chemical, bulk-chemical, and isotopic data indicates that 70215, 74255, and 75055 are samples of three separate lava flows; 71055 may represent a fourth flow, or it may be a derivative of 74255. The available data on these and other Apollo 17 mare basalts indicates that the Taurus-Littrow Valley was filled by a variety of lava flows related in time and space to a common source region in the lunar interior.

1. INTRODUCTION

THE APOLLO 17 MISSION returned a great number of mare basalt samples from the Taurus-Littrow Valley. During preliminary examination by the Apollo 17 geology team, these were divided into five groups on the basis of vesicularity, grain size, and porphyritic character (Apollo 17 PSR, 1973, p. 6–39). Subsequent studies on comprehensive suites of these basalts have led to the recognition of two chemical types: (1) a relatively rare suite of quartz-normative, ilmenite-rich basalts with predominantly subophitic textures; and (2) an olivine-normative ilmenite basalt suite ranging in texture from vitrophyric to microgabbroic.

Petrographic studies have resulted in several three-fold classifications. Brown *et al.* (1974, 1975) presented preliminary results on the extensive collection of large Apollo 17 basalt samples allocated to them. Papike *et al.* (1974) investigated one large sample and 91 basalt fragments in the 2–4-mm size range from soil samples at all Apollo 17 stations. Warner *et al.* (1975) and Laul and Schmitt (1975) have reported both petrographic and chemical data on 26 basalt fragments from rake samples at Apollo 17, Stations 1A, 7, and 8. These classifications are:

Papike *et al.* (1974)	Brown *et al.* (1975)	Warner *et al.* (1975)
olivine–porphyritic ilmenite basalt	(1A) quenched, olivine rich	(1A) microporphyritic ilmenite basalt
plagioclase–poikilitic ilmenite basalt	(1B) slower-cooled, olivine poor	(1B) poikilitic ilmenite basalt
Apollo 11, low-K-type basalt	(II) olivine-free	(II) low-Mg ilmenite basalt

*Contribution No. 2608.

This paper presents the results of our mineralogic and petrologic studies of four Apollo 17 mare basalt samples that are representative of the three-fold classifications and were allocated to the Lunatic Asylum for isotopic age dating. On sample 75055, a Rb–Sr internal isochron yielded an age of 3.77 ± 0.06 AE, an initial $^{87}Sr/^{86}Sr$ of 0.69919 ∓ 3, and model age (T_{BABI}) of 4.98 ± 0.35 AE (Tera *et al.*, 1974a). Tatsumoto *et al.* (1973) obtained a similar age (3.83 ± 0.10 AE) by the Rb–Sr method. Huneke *et al.* (1973) reported a $^{40}Ar/^{39}Ar$ age of 3.78 ± 0.04 AE, and Turner *et al.* (1973) reported $^{40}Ar/^{39}Ar$ age of 3.75 ± 0.05 AE. In addition, Tera and Wasserburg (1975) reported a U–Pb internal isochron age of 3.8 AE.

On sample 71055, a Rb–Sr internal isochron gives an age of 3.64 ± 0.09 AE, an initial $^{87}Sr/^{86}Sr$ composition of 0.69910 ∓ 4, and a model age (T_{BABI}) of 4.50 ± 0.04 AE (Tera *et al.*, 1974b).

A Rb–Sr model age of 5.8 ± 1.0 AE has been obtained on sample 70215 (D. A. Papanastassiou, CIT, oral communication), but isotopic measurements have not yet been completed by the Lunatic Asylum on this sample or on sample 74255. However, Kirsten and Horn (1974) report a $^{40}Ar/^{39}Ar$ age of 3.84 ± 0.04 AE for 70215.

Similar ages of crystallization and initial $^{87}Sr/^{86}Sr$ isotopic compositions have been obtained from Rb–Sr internal isochron measurements on a number of other Apollo 17 basalt samples by Nyquist *et al.* (1974, 1975) and Evensen *et al.* (1973). In addition, Schaeffer and Husain (1975) and Papike *et al.* (1974) have reported a number of similar ages based on the $^{40}Ar/^{39}Ar$ technique.

II. Analytical Techniques

All of the data points plotted on the various diagrams represent analyses performed consecutively on a single spot for 8–16 elements in groups of three using a MAC-5-SA3 electron microprobe interfaced to a PDP-8/L computer for control and on-line data processing. Operating conditions were uniformly 15-kV accelerating voltage and 0.5-μA sample current (on brass) with beam current integration and pulse height selection. Elements with peak to background ratios greater than five (about 1 wt.% of the oxide) are determined to a counting statistic precision of 1% or better. Minor elements ($\lesssim$1% abundances) are usually counted for 90 sec, which yields a counting statistic precision of better than 10% for elements present in amounts greater than ~0.1 wt.%. Reproducibility (1 σ) on two "known unknowns" over a 13-month period ranges from 1½% (for elements with abundances >1%) to 3% of the amount present (for elements with abundances 0.1–1.0%) (Champion *et al.*, 1975). The analytical procedure is described in detail by Chodos *et al.* (1973).

Microprobe point counts, "average" mineral compositions, and calculated bulk-chemical compositions were performed using techniques modified from those described by Gancarz and Albee (1973). On any point where a positive mineral identification cannot be made using only the triad Fe–Ca–Si, the identification is confirmed by driving one or more spectrometers to analyze for Ti, K, and F. The addition of a determination of Ti permits the computer to descriminate between ilmenite, armalcolite, rutile, ulvöspinel, chromite, Fe metal, and troilite, K permits discrimination between SiO_2 and silica-rich mesostasis and F permits discrimination between apatite and whitlockite. Comparison with standard bulk-chemical analyses (see Tables 1–4) demonstrates that our calculated bulk compositions are very similar.

Each of the "average" mineral compositions given in the tables is an actual analysis of a single point that was selected from all of the analyses as the best fit to the average values obtained by the point count. A computer print-out of all the analyses may be obtained from A. Albee. All formula compositions and elemental ratios used in the text are in molecular proportions: olivine compositions

are reported as % Fo = 100 × [Mg/(Mg + Fe + Mn)]; pyroxene compositions are reported as % Wo = 100 × [Ca/(Ca + Mg + Fe + Mn)], % En = 100 × [Mg/(Ca + Mg + Fe + Mn)], % Fs = 100 × [(Fe + Mn)/(Ca + Mg + Fe + Mn)]; plagioclase compositions are reported as % An = 100 × [Ca/(Na + Ca + K + Ba + Fe + Mg)].

III. Petrography and Mineral Chemistry

A. *Sample* 70215

Lunar rock 70215, the largest sample returned by the Apollo 17 mission (8110 g), was collected from the lunar surface approximately 50 m east of the lunar module site. Muehlberger *et al.* (in Apollo 17 PSR, 1973; p. 6–39) classified 70215 as a dense aphanitic basalt; it was described in the sample catalog as a subangular block (10.5 × 13 × 23 cm) of dense, fine-grained, medium gray basalt. All surfaces of the hand-sample contained zap-pits, and one side (*T*) has a slickensided crust. Papike *et al.* (1974) designated 70215 as a large rock equivalent to rake basalts termed "olivine–porphyritic ilmenite basalts," whereas Brown *et al.* (1975) described 70215 as a "quenched olivine-rich basalt" (Type 1A). In addition, Longhi *et al.* (1974) have summarized the petrography of 70215.

Our study of polished thin section 70215,158 (area ≈ 125 mm^2) indicates that this sample is a fine-grained, porphyritic basalt comprised of clinopyroxene (58%), plagioclase (18%), ilmenite (13%), olivine (6%), and SiO_2 (4%) with minor amounts of armalcolite, Cr-ulvöspinel, rutile, troilite, and Fe metal. An exceedingly small amount of a K-rich mesostasis is also present (≤0.05 vol.%). Table 1 gives the phase abundances, "average" phase compositions and a calculated bulk-chemical composition of this sample based on a computer-controlled electron microprobe point count. It should be noted that the mode presented here differs significantly from that given by Longhi *et al.* (1974), and suggests that the sample is not homogenous. Compositions of the principle phases in 70215 are illustrated in Fig. 1.

70215 is characterized petrographically by abundant phenocrysts (~50%) of olivine, ilmenite, and clinopyroxene set in a texturally-variable groundmass. Approximately three-fourths of the groundmass portion of our thin section consists of a variolitic intergrowth of acicular grains of plagioclase, SiO_2, and ilmenite with blocky to acicular clinopyroxene. The remainder consists of tiny needles of ilmenite that alternate with fan spherulites of plagioclase and clinopyroxene (*cf.* Longhi *et al.*, 1974). A small portion of the groundmass contains abundant pore space, but no spherical vesicles are present.

All of the olivine phenocrysts show the effects of extremely rapid crystallization, being poorly formed, hollow, and skeletal in habit (Fig. 2A). Many are intergrown with ilmenite, whereas others have a unique, box-like cross section. The phenocrysts range from equant to elongate (up to 2 mm), and locally have a "swallow-tail" form. Most of the olivine phenocrysts are mantled by pyroxene, which, in some cases, is also present as an overgrowth in the hollow interiors. Olivine phenocrysts in the spherulitic groundmass do not have pyroxene rims. A few contain small (10–50 μm) euhedral inclusions of Cr ulvöspinel (Fig. 2B).

Table 1. 70215 phase abundances, "average" phase compositions, and bulk-chemical composition.

	Plag.	Med-Ca pyx	High-Ca pyx	Fe pyx	Olivine	Ilmenite	Armal.	Rutile	Cr Ulvöspinel	SiO_2	Troilite*	Bulk Composition†	
vol.%	$18.0_5 \pm 0.9_6$	$23\ 1_7 \pm 1.0_9$	$29.0_0 \pm 1.2_2$	$5.7_5 \pm 0.5_4$	$6.1_6 \pm 0.5_6$	$13.4_7 \pm 0.8_3$	$0.2_0 \pm 0.1_0$	< 0.01 —	$0.1_5 \pm 0.0_9$	$3.9_5 \pm 0.4_5$	$0.1_0 \pm 0.07$	Calc. (1964 Pts.)	LSPET. 1973
Wt.%	14.4_5	23.0_3	28.7_4	5.8_0	6.3_8	18.3_2	0.2_7	< 0.01	0.2_0	2.7_0	0.1_4		
SiO_2	50.40	48.17	43.26	48.74	37.60	0.04	0.09	0.04	0.05	98.58	—	38.71	37.19
TiO_2	0.26	2.90	6.07	1.42	0.12	53.48	73.66	98.94	20.97	0.44	—	12.59	13.14
Cr_2O_3	n.a.	0.28	0.69	0.28	0.19	0.75	1.80	0.42	21.41	n.a.	—	0.48	0.42
Al_2O_3	30.57	3.93	8.49	1.75	0.02	< 0.01	2.01	< 0.01	7.28	0.50	—	7.90	8.67
CaO	16.35	14.76	20.01	12.29	0.33	n.a.	n.a.	n.a.	n.a.	0.04	—	12.25	10.43
MgO	0.23	13.16	10.38	7.88	34.66	3.48	6.81	< 0.01	6.46	0.06	—	9.39	8.52
FeO	0.92	15.83	10.23	27.66	28.44	41.31	15.88	0.34	41.84	0.46	63.60	17.96	19.62
MnO	n.a.	0.35	0.21	0.55	0.31	0.42	0.01	0.04	0.60	n.a.	—	0.27	0.28
BaO	0.01	n.a.	n.a.	n.a.	n.a.	n.a.	n.a.	n.a.	n.a.	< 0.01	—	< 0.01	—
Na_2O	1.66	0.07	0.18	0.01	n.a.	n.a.	n.a.	n.a.	n.a.	0.01	—	0.31	0.32
K_2O	0.05	n.a.	n.a.	n.a.	n.a.	n.a.	n.a.	n.a.	n.a.	0.01	—	0.01	0.04
ZrO_2	n.a.	n.a.	n.a.	n.a.	n.a.	< 0.01	0.03	0.07	< 0.01	n.a.	—	< 0.01	0.02
V_2O_3	n.a.	n.a.	n.a.	n.a.	n.a.	< 0.01	0.06	< 0.01	0.29	n.a.	—	< 0.01	—
Nb_2O_5	n.a.	n.a.	n.a.	n.a.	n.a.	0.01	< 0.01	< 0.01	< 0.01	n.a.	—	< 0.01	< 0.01
NiO	n.a.	n.a.	n.a.	n.a.	< 0.01	n.a.	n.a.	n.a.	n.a.	n.a.	—	< 0.01	< 0.01
S	n.a.	n.a.	n.a.	n.a.	n.a.	n.a.	n.a.	n.a.	n.a.	n.a.	36.40	0.06	0.18
Total	100.45	99.45	99.52	100.58	101.67	99.49	100.35	99.86	98.90	100.11	100.00	99.93	98.81
An 79.9	Wo 26.1	Wo 31.8	Wo 24.1	Fo 68.2							$\frac{Fe}{Fe+Mg} =$	.518	.564
Ab 14.7	En 38.0	En 30.0	En 23.5	Fa 31.8									
Or 0.3	Fs 26.3	Fs 17.0	Fs 47.2										
Others 5.1	9.6	21.2	5.2										

*Assumed stoichiometric FeS; converted to oxides for calculation of bulk composition.
†Ca phosphate and K-rich mesotasis present but not detected by point count.
n.a. = not analyzed.

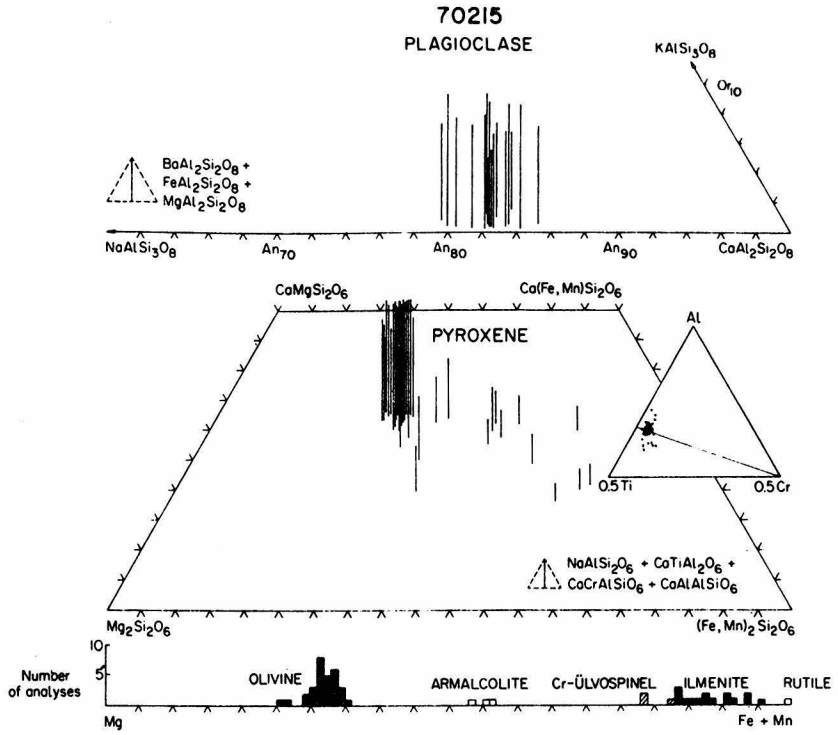

Fig. 1. Compositions of the principal silicate and oxide phases in mare basalt 70215. The vertical lines represent the altitudes of triangles that correspond to the amount of minor-element substitution, as indicated in the figure. The triangular inset in the pyroxene quadrilateral displays the relative amounts of Al–Ti–Cr in pyroxene; the diagonal line therein is line "*b*" of Hollister *et al.* (1971).

The olivine has a measured range in composition from Fo_{75-65}, with a maximum variation in a single grain being 4 mole% Fo. The most-magnesian composition occurs adjacent to an inclusion of the spinel phase, suggesting early precipitation of the latter. The olivine contains only small amounts of minor elements (e.g. Table 1 and Fig. 5). Although the data in Fig. 5 scatter considerably, it appears that, as the forsterite content decreases, CaO increases slightly, TiO_2 remains relatively constant, and Cr_2O_3 decreases slightly (cf. Smyth, 1971). The decrease of Cr is consistent with the prior (or simultaneous) crystallization of the spinel phase; and the increase in Ca is consistent with the delayed appearance of Ca-rich pyroxene and plagioclase.

The ilmenite phenocrysts also display a variety of forms. Most occur as skeletal needles [up to 3 mm long; $Fe/(Fe+Mg) \cong .84–.89$] that have jagged, sawtooth margins. Grains with a subhedral, blocky habit [50–200 μm; $Fe/(Fe+Mg) \cong .88–.93$] have margins that resemble the larger acicular grains, but these also have rounded embayments and protrusions against olivine and/or pyroxene. The groundmass ilmenite (5–50 μm) has compositions with $Fe/(Fe+Mg) \cong .95$. In general $Fe/(Fe+Mg)$ in ilmenite increases with decreasing grain size.

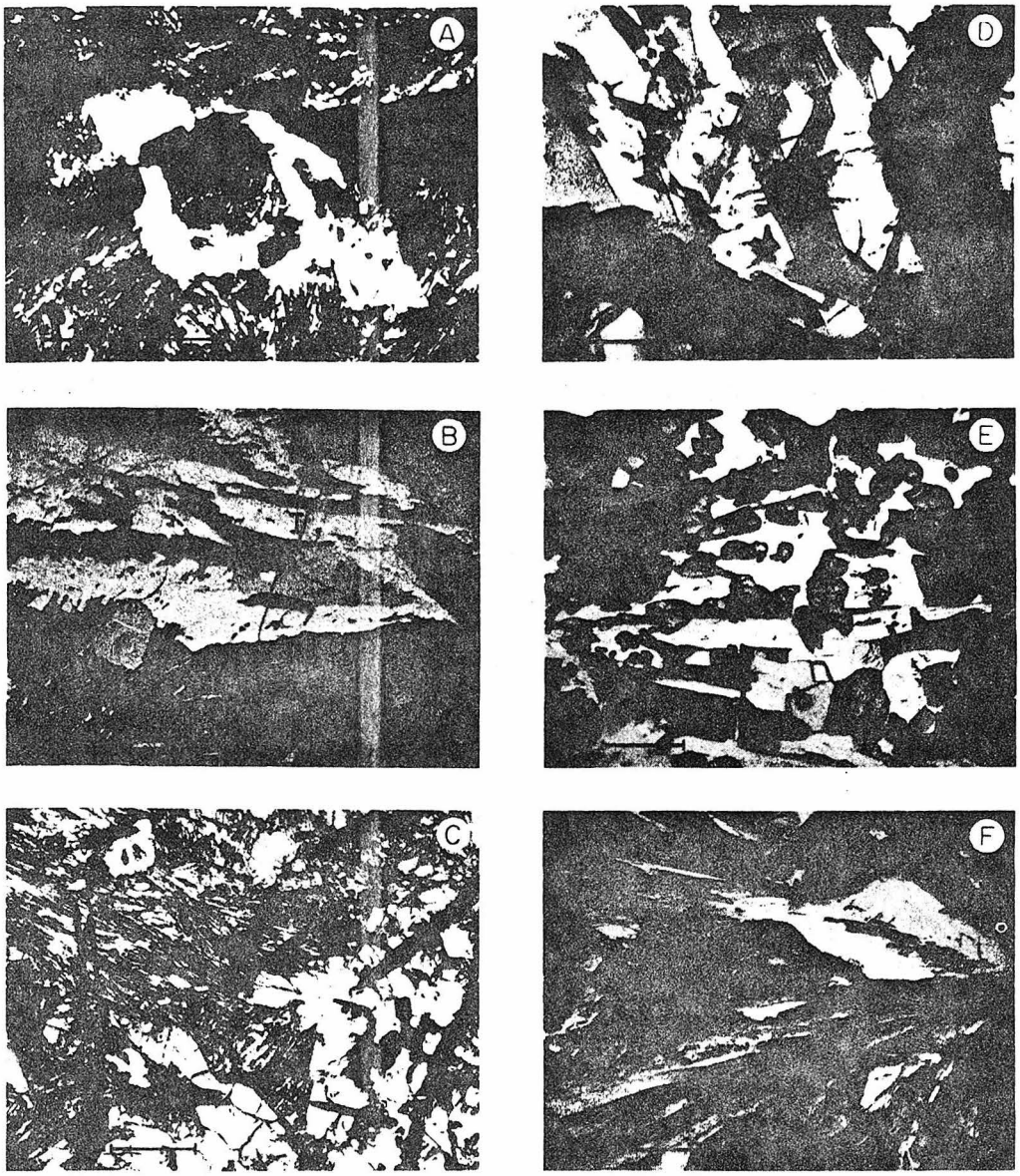

Fig. 2. (A) 70215—skeletal olivine phenocryst in spherultic groundmass (transmitted plane-polarized light); (B) 70215—complex oxide association including dark armalcolite (A) mantled by rutile-bearing ilmenite. (I), equant Cr ulvöspinel with ilmenite lamellae (S, above bar scale), and euhedral Cr ulvöspinel inclusion in olivine (S, lower right). Note sawtooth margins of ilmenite (reflected light). (C) 70215—abundant ilmenite and sharply bounded pyroxene phenocrysts in variolitic groundmass. Note olivine cores (transparent) in pyroxene (gray) (transmitted plane-polarized light). (D) 71055—alternating bands of light (Al, Ti-poor) and dark (Al, Ti-rich) pyroxene in complexly zoned augite (transmitted plane-polarized light). (E) 71055—granular pyroxene enclosed in poikilitic plagioclase (transmitted plane-polarized light). (F) 71055—acicular plagioclase and pyroxene intergrown in the form of "fan spherulites." Note glassy inclusions in large-plagioclase grain and skeletal form of ilmenite (transmitted plane polarized light). (All bar scales = 200 μm.)

Rare grains of armalcolite occur [Fe/(Fe + Mg) ≅ .48–.51; up to 200 μm] that are mantled by rutile-bearing ilmenite [Fe/(Fe + Mg) ≅ .83]. In addition, microphenocrysts of Cr ulvöspinel (up to 100 μm) are present, the larger, containing oriented lamellae of ilmenite (Fig. 2B).

Plagioclase occurs as elongate untwinned grains scattered throughout the groundmass (≈ 20-μm maximum width). The measured range in composition is An_{75-81}. The measured minor-element content is large (0.2–0.8 wt.% MgO, 0.8–1.5 wt.% FeO) and does not appear to vary systematically with An content (Fig. 3). Because the plagioclase grains are small, these measured values may be enhanced by secondary fluorescense from adjacent pyroxene and ilmenite.

Clinopyroxene typically occurs as reaction rims around olivine phenocrysts and as irregularly shaped composite grains forming complex intergrowths with olivine and illmenite (up to ~1 mm across; Fig. 2C). This pyroxene is deep pink in color, has a restricted range in composition (≈$Wo_{37}En_{47}Fs_{16}$–$Wo_{44}En_{34}Fs_{22}$; represented by the high-Ca cluster in Fig. 1), and contains large amounts of minor elements (4.8–8.8 wt.% Al_2O_3; 3.6–6.6 wt.% TiO_2; 0.4–0.9 wt.% Cr_2O_3). Discrete phenocrysts of pale- to dark-pink pyroxene range in form from elongate and subrounded to subequant; skeletal varieties are also present. These have a range in composition from (~$Wo_{43}En_{38}Fs_{18}$–~$Wo_{36}En_{34}Fs_{30}$) and have minor-element contents similar to those quoted above. These are also represented by the cluster of high-Ca compositions in Fig. 1. Groundmass pyroxene is pale pink to pale brown, ranges in composition from $Wo_{33}En_{41}Fs_{26}$–$Wo_{22}En_{20}Fs_{58}$, contains smaller amounts of minor elements, and in Fig. 1 is represented by the trend towards Fe-rich compositions.

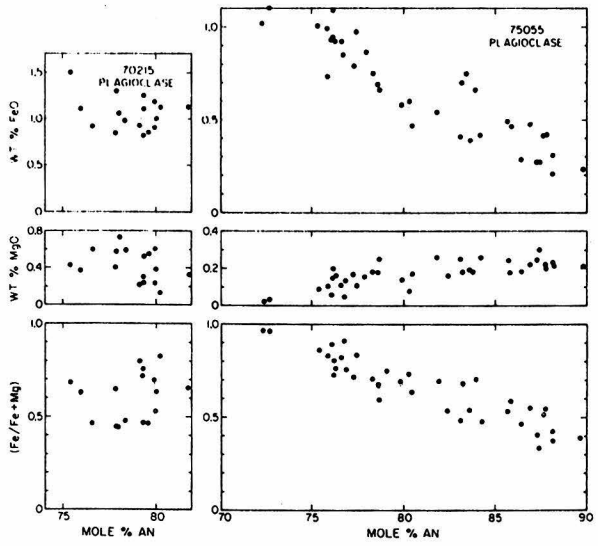

Fig. 3. Diagrams illustrating the FeO and MgO contents, and Fe/(Fe + Mg), in plagioclase in mare basalt samples 70215 and 75055.

The Ti, Al, and Cr contents of the pyroxene in 70215 are illustrated in Fig. 4. In general, their abundances decrease with increasing Fe/Mg. Despite the great range in the absolute amounts of Al and Ti, the Ti/Al ratio approaches 1 : 2 over much of the compositional range, suggesting R^{2+} $TiAl_2O_6$ as the principal coupled substitution. However, many of the deep-pink aluminous titanaugites have Ti/Al < 1 : 2, suggesting the presence of Al^{VI} as the component R^{2+} Al_2SiO_6.

The inset in Fig. 1 illustrates the relative proportions of Ti, *total* Al, and Cr in pyroxene, and it can be seen that most data cluster near the diagonal line (line "*b*" of Hollister *et al.*, 1971). If all the Ti in the pyroxene exists as Ti^{4+}, then no data points should plot below this line. The presence of Ti^{3+} can be inferred from the position of the data between the baseline and the diagonal. Many analyses of the aluminous titanaugites plot above the diagonal, suggesting Al–Al substitution, consistent with the interpretation inferred from the Ti–Al plot. Finally, all pyroxene with Fe/(Fe + Mg) $\geq$ 0.35 (edges of larger grains and groundmass) fall below the diagonal. These are relatively depleted in Al, consistent with the simultaneous crystallization of plagioclase.

The crystallization sequence of 70215, as inferred from our observations begins with the precipitation of spinel followed by olivine. The rarity of armalcolite precludes a definitive statement regarding its paragenesis; it may have formed prior to, or after olivine. Armalcolite reacted with the melt to form ilmenite, and clinopyroxene formed after olivine. Clinopyroxene and ilmenite coprecipitated, the latter increasing in Fe/(Fe + Mg) as crystallization proceeded. The pyroxene changed decomposition only slightly until plagioclase formed. The onset of plagioclase crystallization was marked by a decrease in Al_2O_3 content in clinopyroxene. Fe-enriched pyroxene, plagioclase, and ilmenite, together with SiO_2, coprecipitated during the formation of the groundmass.

The porphyritic texture of this sample, the skeletal form of the phenocrysts, and the observation of armalcolite indicate that 70215 cooled rapidly from near-liquidus temperatures. The fact that the composition of the most-magnesian olivine ($\sim Fo_{75}$) and armalcolite [Fe/(Fe + Mg) $\sim$ .53] match closely with the equilibrium compositions of the experimentally determined 1 atm. liquidus phases suggests that the 70215 lava contained little, if any, solid phases related to intratelluric crystallization at the time of extrusion (Green *et al.*, 1975). However, the order of appearance of plagioclase and pyroxene, as observed in the rock, is at variance with that determined experimentally (Green *et al.*, 1975; Kesson, 1975; Longhi *et al.*, 1974). We find no evidence which contradicts the interpretation that 70215 was liquid at the time of eruption and was thereafter rapidly quenched.

B. Sample 71055

Lunar rock 71055 was a 670 g sample chipped from a 1-m boulder, along with samples 71035, 71036, and 71037, at Apollo 17, Station 1A. Muehlberger *et al.* (in Apollo 17 PSR, 1973, p. 6–39) classified 71055 as a vesicular, fine-grained basalt; it was then described in the sample catalog as an angular to rounded block of light,

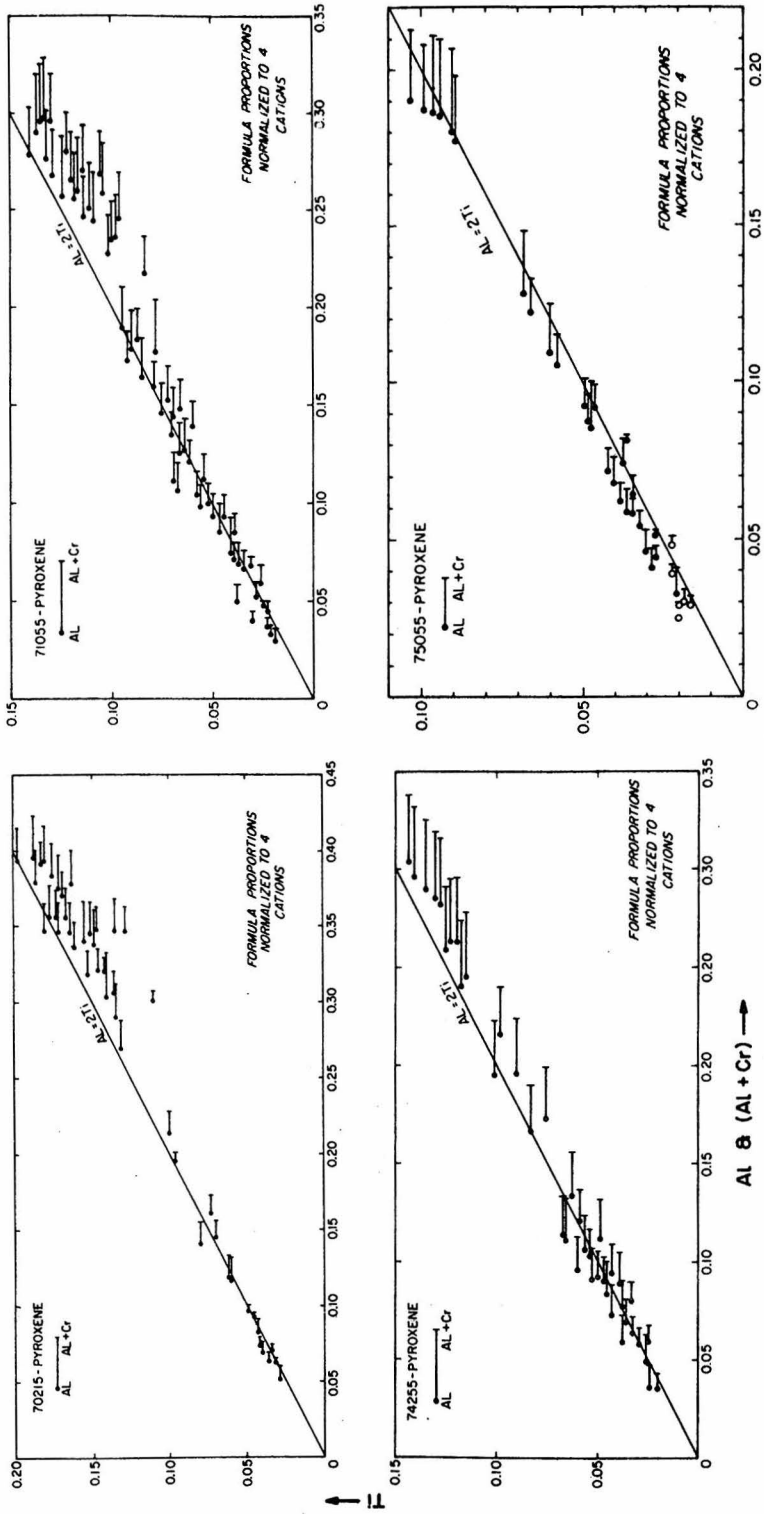

Fig. 4. Diagram illustrating the absolute amounts of Al, Ti, and Cr in pyroxene in samples 70215, 71055, 74255, and 75055. The open circles among the 75055 data represent pyroxferroite (cf. Fig. 10). Note that much of the data closely approach the lines labeled Al = 2 Ti suggesting $R^{2+}Ti\,Al_2O_6$ as the principal coupled substitution.

brownish-gray basalt (17.5 × 9.5 × 2.5 cm). The hand specimen contained abundant vugs (20–25%, 1–12 mm) and a few milimeter-sized, smooth-walled vesicles.

Our work indicates that 71055 is a vesicular, fine- to medium-grained olivine-bearing ilmenite basalt with a seriate grain size distribution. On the basis of texture, 71055 can be grouped with the "plagioclase–poikilitic ilmenite basalts" of Papike *et al.* (1974). Brown *et al.* (1975) have classified 71055 as Type 1B, a "slowly cooled, olivine-poor" ilmenite basalt.

The sample is comprised of plagioclase (27%), pyroxene (46%), ilmenite (17%), olivine (3%), and SiO_2 (2%), with minor amounts of Cr ulvöspinel, troilite, Fe metal, Ca phospate, and mesostasis. The results of a microprobe point count on polished thin section 71055,75 ($\approx$130 mm^2) are listed in Table 2, and the compositions of the phases in this sample are depicted in Fig. 6.

Olivine occurs as rounded (10–200 μm) cores in pyroxene, and rarely as subhedral grains up to ~1 mm that have only thin pyroxene rims. Rare inclusions of ilmenite were observed in the olivine. The measured range in composition is Fo_{75-65}, the maximum variation in a single grain being 5 mole% Fo. The most Mg-rich composition occurs in the core of the largest grain. The minor-element contents are small (Fig. 5) and comparable to those in 70215.

Ilmenite occurs predominantly as subequant, skeletal grains (~20 μm–1 mm) with pronounced embayments along their margins. These form inclusions in pyroxene and are also intergrown with pyroxene and plagioclase. Grains with a rectangular outline (up to 100 μm long), and elongate bladed crystals with sawtooth margins (up to 5 mm), are also present. The latter consist of multiple subgrains with differing optical orientations suggesting that the large grains formed by coalescence of smaller ones. Papike *et al.* (1974) suggest that this phenomenon is related to the replacement of preexisting armalcolite by ilmenite. Most ilmenite contains tiny ($\lesssim$5 μm wide) oriented lamellae of rutile and chromite. The ilmenite has a measured range in composition from Fe/(Fe + Mg) $\cong$ .87–.96. The most-magnesian ilmenite forms a rim around Cr ulvöspinel. The latter have a restricted range in composition [Fe/(Fe + Mg) $\cong$ 0.90; up to ~0·5 mm]. No armalcolite was identified in our section.

The pyroxene in 71055 is highly complex, both chemically and texturally. The largest grains (up to 2 mm), typically composite, are comprised of pale-pink (Al- and Ti-poor) to dark-pink (Al- and Ti-rich) regions arranged in parallel bands, in a radiating spherulitic pattern, or forming an hourglass structure. These may have olivine cores, and contain abundant inclusions of ilmenite, with which they sometimes form a "graphic" intergrowth. Plagioclase occurs only at the margins. One hourglass grain partially surrounds a vesicle, suggesting that exsolution of a vapor phase occured prior to the cessation of growth of these large pyroxene grains.

Almost all portions of these large grains have compositions that fall in the range ~$Wo_{28}En_{52}Fs_{20}$ to ~$WO_{40}En_{45}Fs_{15}$ to ~$Wo_{35}En_{45}Fs_{20}$, the high-Ca cluster in Fig. 6. Continuous and oscillatory zoning occurs with respect to both major and minor elements. For example, the adjacent dark and light bands, illustrated in Fig. 2D have Al_2O_3 contents of ~5.7 and ~2.5 wt.%, and TiO_2 contents of ~4.4 and

Table 2. 71055: phase abundances, "average" phase compositions, and bulk-chemical composition.

	Plag.	Low-Ca pyx	Med-Ca pyx	High-Ca pyx	Fe pyx	Olivine	Ilmenite	Cr Ulvöspinel	Fe Metal*	Troilite*	Ca phosphate†	SiO_2	Mesostasis	Bulk composition	
vol.%	$27.3_7 \pm 1.0_4$	$5.1_6 \pm 0.4_5$	$21.35 \pm 0.9_1$	$16.41_1 \pm 0.8_0$	$2.8_4 \pm 0.3_3$	$2.67 \pm 0.3_2$	$16.57 \pm 0.8_1$	$0.2_7 \pm 0.1_0$	$0.1_6 \pm 0.0_8$	$0.3_7 \pm 0.1_3$	$0.1_6 \pm 0.0_8$	$2.0_0 \pm 0.2_8$	$0.75 \pm 0.1_7$	Calc. (2550 Pts.)	Rose *et al.* (1974)
wt.%	22.7_4	5.3_6	22.0_3	16.8_3	2.9_8	2.9_0	23.7_0	0.3_8	0.3_9	0.5_4	0.1_6	1.4_2	0.5_7		
P_2O_5	n.a.	n.a.	n.a.	n.a.	n.a.	n.a.	n.a.	n.a.	n.a.	n.a.	43.15	n.a.	n.a.	0.07	0.08
SiO_2	48.39	51.35	50.27	47.82	48.93	37.53	0.09	0.08	n.a.	n.a.	—	98.03	57.59	37.17	38.14
TiO_2	0.12	1.24	1.66	3.23	1.02	0.11	52.44	22.19	0.55	0.33	—	0.39	0.44	13.56	13.41
Al_2O_3	31.59	1.31	1.92	4.16	1.41	0.01	< 0.01	5.63	n.a.	n.a.	—	0.94	11.05	8.52	8.62
Cr_2O_3	n.a.	0.33	0.30	0.68	0.31	0.13	0.62	23.69	n.a.	n.a.	—	n.a.	n.a.	0.45	0.41
MgO	0.31	19.30	15.85	13.22	7.07	35.93	2.59	2.87	< 0.01	< 0.01	—	0.01	4.10	8.61	9.04
CaO	16.78	6.42	11.81	18.20	13.01	0.29	n.a.	n.a.	< 0.01	0.01	54.54	0.22	12.26	10.38	10.77
FeO	0.54	19.92	17.23	11.27	28.64	27.44	44.18	45.52	98.02	63.84	—	0.14	3.59	20.13	19.20
MnO	n.a.	0.37	0.39	0.29	0.55	0.28	0.44	0.52	n.a.	n.a.	—	n.a.	n.a.	0.29	0.26
BaO	0.05	n.a.	n.a.	n.a.	n.a.	n.a.	n.a.	n.a.	n.a.	n.a.	—	0.04	2.31	0.03	0.03
Na_2O	1.56	0.07	0.06	0.16	< 0.01	n.a.	n.a.	n.a.	n.a.	n.a.	—	0.02	1.02	0.40	0.31
K_2O	0.06	n.a.	n.a.	n.a.	n.a.	n.a.	n.a.	n.a.	n.a.	n.a.	—	< 0.01	5.19	0.04	0.06
ZrO_2	n.a.	n.a.	n.a.	n.a.	n.a.	n.a.	0.02	0.01	n.a.	n.a.	—	n.a.	n.a.	0.01	0.02
V_2O_3	n.a.	n.a.	n.a.	n.a.	n.a.	n.a.	0.01	0.35	n.a.	n.a.	—	n.a.	n.a.	< 0.01	< 0.01
Nb_2O_5	n.a.	n.a.	n.a.	n.a.	n.a.	n.a.	< 0.01	< 0.01	n.a.	n.a.	—	n.a.	n.a.	< 0.01	< 0.01
NiO	n.a.	n.a.	n.a.	n.a.	n.a.	< 0.01	n.a.	n.a.	0.09	< 0.01	—	n.a.	n.a.	< 0.01	< 0.01
S	n.a.	n.a.	n.a.	n.a.	n.a.	n.a.	n.a.	n.a.	0.03	36.32	—	n.a.	n.a.	0.20	—
F	n.a.	n.a.	n.a.	n.a.	n.a.	n.a.	n.a.	n.a.	n.a.	n.a.	2.31	n.a.	n.a.	< 0.01	—
Co	n.a.	n.a.	n.a.	n.a.	n.a.	n.a.	n.a.	n.a.	0.53	< 0.01	—	n.a.	n.a.	< 0.01	< 0.01
Total	99.40	100.31	99.49	99.03	100.94	101.72	100.39	100.86	99.22	100.50	100.00	99.78	97.55	99.86	100.35
An 81.7		Wo 11.1	Wo 21.7	Wo 32.4	Wo 26.0	Fo 69.8						$\frac{Fe}{Fe+Mg} =$	.56	.544	
Ab 13.7		En 53.1	En 44.8	En 37.7	En 21.1	Fa 30.2									
Or 0.3		Fs 31.3	Fs 27.9	Fs 18.5	Fs 48.9										
Others 4.3		4.5	5.6	11.4	4.0										

*Elemental abundances; converted to oxides for calculation of bulk composition.

†Assumed 1:1 mix of fluorapatite and whitlockite.

n.a. = not analyzed.

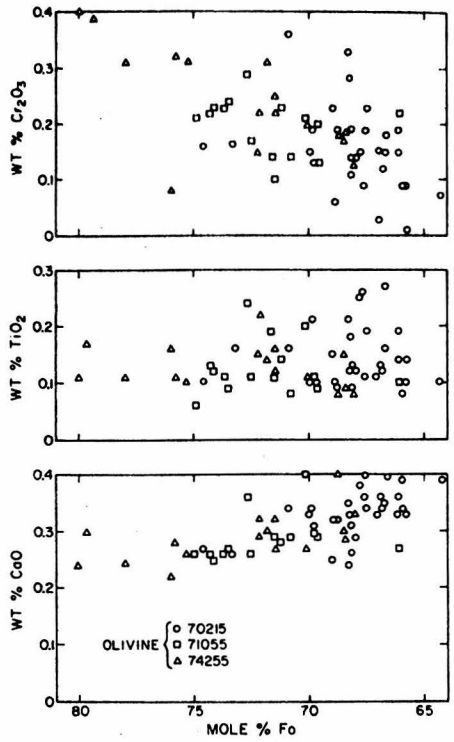

Fig. 5. Diagram illustrating Cr_2O_3, TiO_2, and CaO contents of olivine.

~2.4 wt.%, respectively. The margins of many grains zone continuously toward lower Ca contents and have edge compositions near $Wo_{10}En_{60}Fs_{30}$.

A second textural type of pyroxene occurs as equant to stubby granules (20–200 μm) that in most cases are enclosed poikilitically by plagioclase (Fig. 2E). These have compositions that fall into general linear trends on Fig. 6, a low-Ca trend from ~$Wo_{10}En_{60}Fs_{30}$ to ~$Wo_{15}En_{40}Fs_{45}$, and an intermediate-Ca trend from ~$Wo_{10}En_{60}Fs_{30}$ to ~$Wo_{32}En_{25}Fs_{43}$.

The third type of pyroxene is elongate in form, and ranges from stubby and tabular to acicular. The latter are typically intergrown with needles of plagioclase in the form of fan spherulites (Fig. 2F). The composition of this pyroxene is similar to that of the intermediate-Ga trend (above), except that these display a greater degree of Fe enrichment, reaching compositions near $Wo_{12}En_{18}Fs_{70}$. The latter two pyroxene types appear to have formed later than the large, complex grains, and simultaneously with plagioclase.

The Ti/Al ratio in pyroxene closely approaches 1:2 throughout the entire compositional range (Fig. 4). However, the most aluminous augite grains have Ti/Al < 1:2, suggesting octahedrally coordinated Al. The variation in the relative amounts of Al–Ti–Cr (Fig. 6, inset) is small, and is not consistently related to the Fe/Mg ratio. However, those analyses which suggest the presence of Al^{VI} on the Ti–Al diagram, fall above the diagonal, and provide an internally consistent case

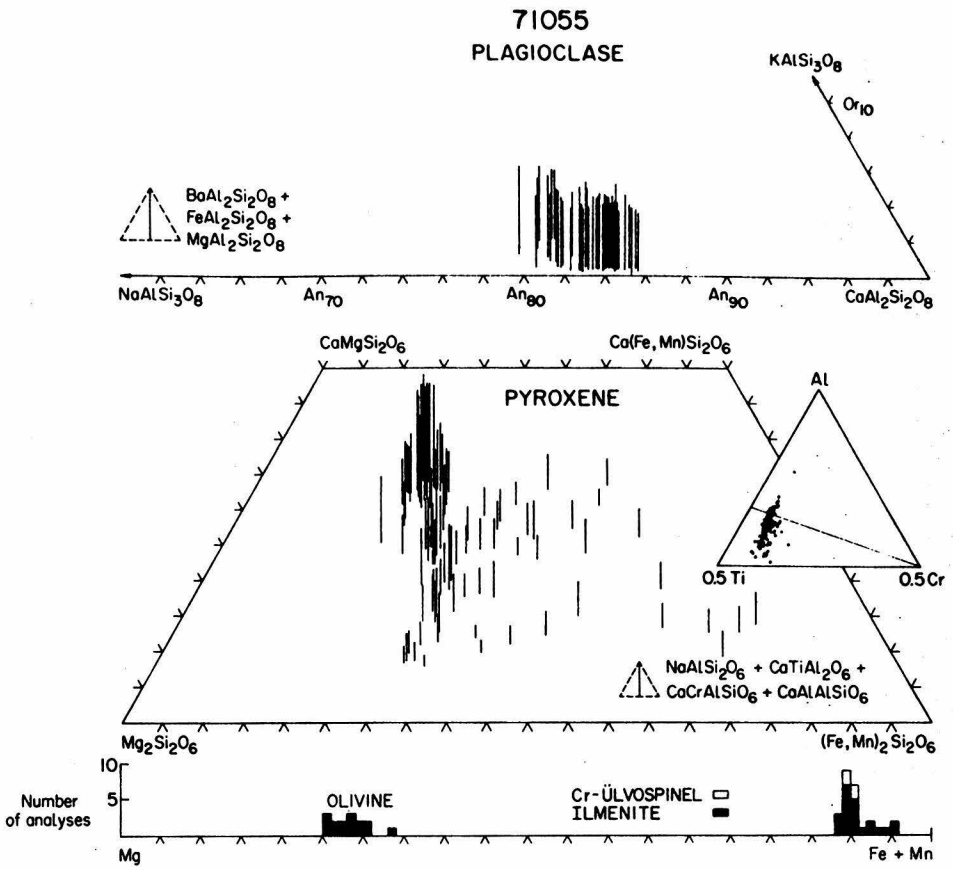

Fig. 6. Compositions of the principal silicate and oxide phases in mare basalt 71055. (Triangular inset as in Fig. 1.)

for octahedrally coordinated aluminum in the pyroxene. Note that Ti^{3+} may be present in 71055 pyroxene, as inferred from the position of the analyses on the Al–Ti–Cr diagram. Spectral measurements on the pyroxene in 71055 suggest the presence of a substantial content of Ti^{3+} (Sung *et al.*, 1974).

Plagioclase occurs in three general habits, although gradations certainly exist between these. It forms large grains (up to 1.5 mm) that poikilitically enclose pyroxene (Fig. 2E), discrete lath-like subequant grains (.05–0.5 mm), and elongate sheaves intergrown with pyroxene (Fig. 2F). A few tiny (~25 μm) grains are intergrown with SiO_2. Twinning is well developed, and many of the larger grains have glassy inclusions in their cores (Fig. 2F). The measured compositional range of the plagioclase is An_{77-84}, and there is no direct correlation between petrographic type and composition, although the most-sodic variety occurs with SiO_2. The presence of pronounced normal zoning indicates that the earliest-formed plagioclase (cores) is also the most calcic.

The minor-element contents of the plagioclase are illustrated in Fig. 7. As can be seen in the figure, FeO and Fe/(Fe + Mg) increase with decreasing An content,

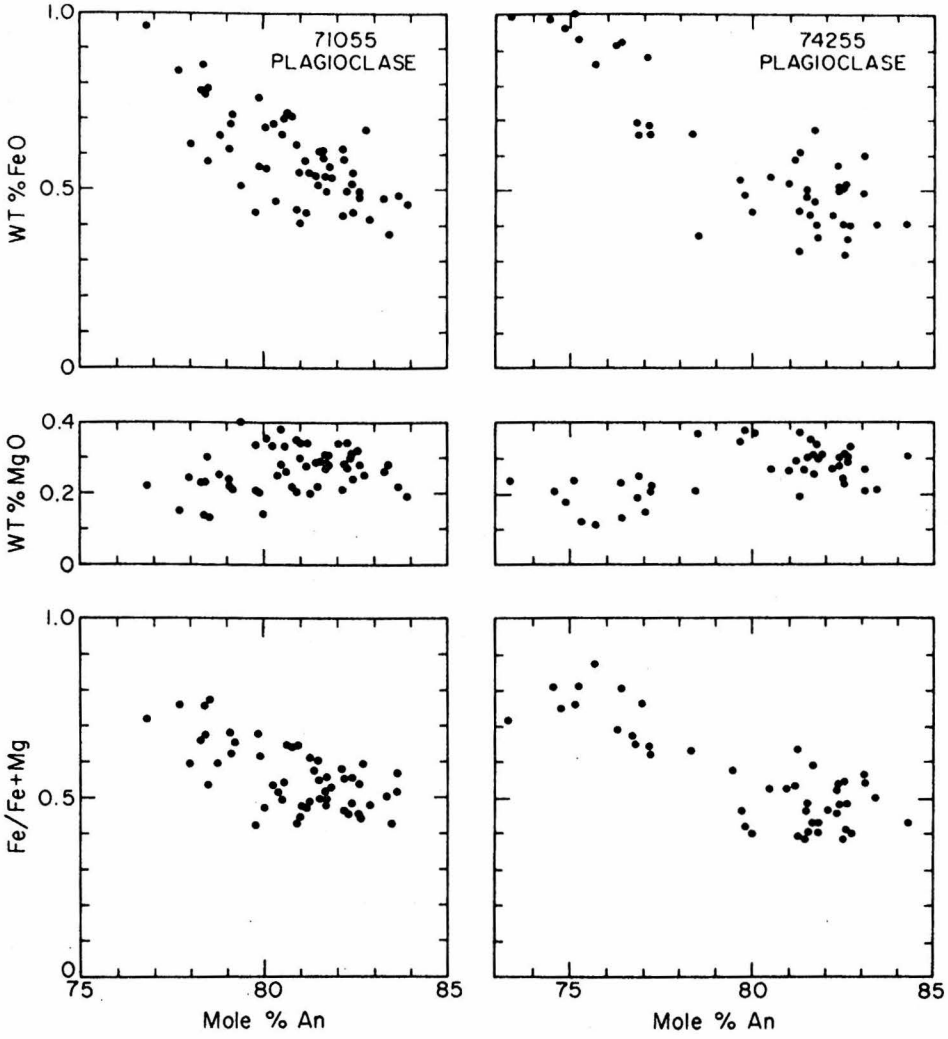

Fig. 7. FeO, MgO, and Fe/(Fe + Mg) in plagioclase in samples 71055 and 74255.

whereas MgO remains relatively constant, or decreases slightly. These relations are consistent with those reported by Smyth (1971). Crawford (1973) has suggested that variations in the Fe/(Fe + Mg) in plagioclase reflect changes in the chemistry of the lava which can in turn be related to the composition of the pyroxene at the onset of plagioclase crystallization. For certain Apollo 12 and 15 mare basalts, Crawford found that the $Fe/(Fe+Mg)_{pyx} \cong Fe/(Fe+Mg)_{plag}$. In 71055, the Fe/(Fe + Mg) of the earliest-formed plagioclase is ≅0.4 (Fig. 7). However, petrographically it can be shown that pyroxene with Fe/(Fe + Mg) at least as low as 0.35 is intergrown with plagioclase. Hence, in 71055, the $Fe/(Fe+Mg)_{plag}$ cannot be simply equated to the composition of the pyroxene, as pointed out by Longhi *et al.* (1974) in other Apollo 17 mare basalts.

The crystallization history of 71055 can be summarized as follows: olivine,

ilmenite, and spinel formed first, but their relative order of crystallization is difficult to ascertain. Olivine and spinel reacted out, but ilmenite continued to crystallize with pyroxene and plagioclase throughout most of the history of the rock. The petrographic character of the pyroxene indicates that the large aluminous titanaugite grains formed next, in part by reaction between olivine and melt. The zoning trends in such grains show that an initial increase in Ca content and Fe/(Fe + Mg) was followed by an abrupt decrease in Ca content and local overgrowth by pigeonite. The granular pyroxene nucleated at the onset of pigeonite growth, and was followed by growth of tabular to acicular pyroxene. The compositional data for these pyroxenes (Fig. 6) suggest the precipitation of a pigeonite series and an augite series as in 70035 (Wiegand, 1973). The abrupt drop in Ca content of the early formed pyroxene may be due to the first appearance of plagioclase, but the Al–Ti–Cr variations in pyroxene do not clearly mark the appearance of plagioclase in the crystallization sequence. Pyroxene, plagioclase, and ilmenite continued to coprecipitate, with the pyroxene increasing in Fe/(Fe + Mg), and the plagioclase becoming more sodic. Crystallization ceased with the formation of SiO_2 and other minor phases along with a residual potassic mesostasis.

C. Sample 74255

Lunar rock 74255 was a 737.3-g sample chipped from a partially buried and severely fractured 5-m boulder at Apollo 17, Station 4, near the south rim of Shorty Crater. Muehlberger *et al.* (in Apollo 17 PSR, 1973; p. 6–39) tentatively classified 74255 as a vesicular porphyritic coarse-grained basalt; it was described in the sample catalog as an angular block ($13 \times 7 \times 6$ cm) of homogeneous, medium dark-gray basalt with abundant vugs (~10%). The hand specimen was crosscut by a penetrative fracture, and only one surface contained zap-pits. The data presented here are an extension of preliminary work on 74255 published previously (Dymek *et al.*, 1975).

Our study indicates that sample 74255 is a medium- to coarse-grained vesicular porphyritic basalt comprised of plagioclase (28%), pyroxene (51%), ilmenite (15%), olivine (4%), and SiO_2 (1%) with minor amounts of armalcolite, troilite, Fe metal, Cr ulvöspinel, Ca phosphate, and mesostasis. It strongly resembles 71055 in texture and mineralogy except that 74255 is distinctly porphyritic and less vesicular. Therefore, 74255 is a variant of the "plagioclase–poikilitic ilmenite basalts" of Papike *et al.* (1974) and Type IB of Brown *et al.* (1975). The results of a microprobe point count of polished thin section 74255,61 (area $\approx 120\ mm^2$) are presented in Table 3. The compositions of the principal phases are illustrated in Fig. 8.

Olivine in 74255 occurs principally as tiny (20–100 μm) cores within pyroxene. A few large grains (up to 0.7 mm) have only a narrow pyroxene rim. In addition, two of these grains (~Fo_{70}) without any pyroxene overgrowth, project into a vug (Fig. 9B). A similar observation was reported during preliminary macroscopic examination of 74255. This relationship suggests exsolution of a vapor phase very

Table 3. 74255: phase abundances, "average" phase compositions and bulk-chemical composition.

	Plag.	Low-Ca pyx	Med-Ca pyx	High-Ca pyx	Fe pyx	Olivine	Ilmenite	Armal.	Cr Ulvöspinel	Fe metal*	Troilite*	Ca phosphate†	SiO_2	Mesostasis	Bulk Composition	
vol.%	$27.6_1 \pm 1.2_8$	$12.3_9 \pm 0.8_5$	$26.1_9 \pm 1.2_4$	$12.3_0 \pm 0.8_5$	$0.9_4 \pm 0.2_4$	$3.2_1 \pm 0.4_4$	$14.5_7 \pm 0.9_3$	$0.5_9 \pm 0.1_9$	$0.1_2 \pm 0.0_8$	$0.0_9 \pm 0.0_7$	$0.1_5 \pm 0.0_9$	$0.0_6 \pm 0.0_6$	$1.0_6 \pm 0.2_5$	$0.7_1 \pm 0.2_0$	Calc. (1695 Pts.)	Rose *et al.* (1975)
wt.%	22.2_3	12.4_6	26.1_8	12.2_2	0.9_6	3.3_5	19.8_9	0.8_1	0.1_6	0.2_1	0.2_1	0.0_6	0.7_3	0.5_2		
P_2O_5	n.a.	n.a.	n.a.	n.a.	n.a.	n.a.	n.a.	n.a.	n.a.	n.a.	n.a.	43.15	n.a.	0.37	0.03	0.06
SiO_2	47.49	51.70	49.93	47.84	49.39	37.36	0.01	0.07	0.11	n.a.	n.a.	—	97.20	68.27	38.71	38.40
TiO_2	0.32	1.34	2.35	3.46	1.15	0.11	53.58	73.15	20.40	< 0.01	0.04	—	0.34	0.90	12.58	12.76
Al_2O_3	32.70	1.76	3.04	4.90	1.22	< 0.01	0.07	2.12	8.43	n.a.	n.a.	—	0.95	13.77	9.02	8.84
Cr_2O_3	n.a.	0.46	0.75	0.80	0.29	0.20	1.08	1.59	25.00	n.a.	n.a.	—	n.a.	0.02	0.63	0.60
MgO	0.27	19.82	17.59	14.88	11.08	35.80	2.04	6.20	7.93	0.01	< 0.01	—	n.a.	0.27	10.73	0.72
CaO	17.03	6.24	12.22	18.56	9.77	0.27	n.a.	n.a.	n.a.	< 0.01	0.02	54.54	0.26	3.98	10.19	10.20
FeO	0.43	19.27	13.78	8.97	27.01	27.00	42.88	17.35	37.48	99.42	63.65	—	0.38	4.85	17.56	17.98
MnO	n.a.	0.33	0.26	0.25	0.37	0.22	0.40	0.16	0.56	n.a.	n.a.	—	n.a.	0.08	0.23	0.28
BaO	< 0.01	n.a.	n.a.	n.a.	n.a.	n.a.	n.a.	n.a.	n.a.	n.a.	n.a.	—	< 0.01	0.81	< 0.01	—
Na_2O	1.60	0.03	0.07	0.07	0.02	n.a.	n.a.	n.a.	n.a.	n.a.	n.a.	—	0.02	0.62	0.39	0.37
K_2O	0.08	n.a.	n.a.	n.a.	n.a.	n.a.	n.a.	n.a.	n.a.	n.a.	n.a.	—	0.02	5.17	0.05	0.10
ZrO_2	n.a.	n.a.	n.a.	n.a.	n.a.	n.a.	0.08	0.09	< 0.01	n.a.	n.a.	—	n.a.	0.34	0.02	—
V_2O_3	n.a.	n.a.	n.a.	n.a.	n.a.	n.a.	0.01	0.14	0.27	n.a.	n.a.	—	n.a.	n.a.	< 0.01	
Nb_2O_5	n.a.	n.a.	n.a.	n.a.	n.a.	n.a.	< 0.01	< 0.01	0.01	n.a.	n.a.	—	n.a.	n.a.	< 0.01	—
NiO	n.a.	n.a.	n.a.	n.a.	n.a.	< 0.01	n.a.	n.a.	n.a.	0.14	0.07	—	n.a.	< 0.01	< 0.01	—
S	n.a.	n.a.	n.a.	n.a.	n.a.	n.a.	n.a.	n.a.	n.a.	< 0.01	37.85	—	n.a.	0.06	0.08	—
F	n.a.	n.a.	n.a.	n.a.	n.a.	n.a.	n.a.	n.a.	n.a.	n.a.	n.a.	2.31	n.a.	n.a.	< 0.01	—
Co	n.a.	n.a.	n.a.	n.a.	n.a.	n.a.	n.a.	n.a.	n.a.	0.81	< 0.01	—	n.a.	n.a.	< 0.01	—
Total	99.92	100.95	99.99	99.73	100.30	100.96	100.15	100.87	100.19	100.38	101.63	100.00	99.17	99.51	100.22	100.31

An 82.1	Wo 10.1	Wo 20.6	Wo 31.5	Wo 18.3	Fo 70.1	$\frac{Fe}{Fe + Mg} = .478$ .484
Ab 14.0	En 54.5	En 48.8	En 41.7	En 32.3	Fa 29.9	
Or 0.5	Fs 30.3	Fs 21.9	Fs 14.5	Fs 44.7		
Others 3.4	5.1	8.7	12.3	4.7		

*Elemental abundances; converted to oxides for calculation of bulk composition.
†Assumed 1:1 mix of fluorapatite and whitlockite.
n.a. = not analyzed.

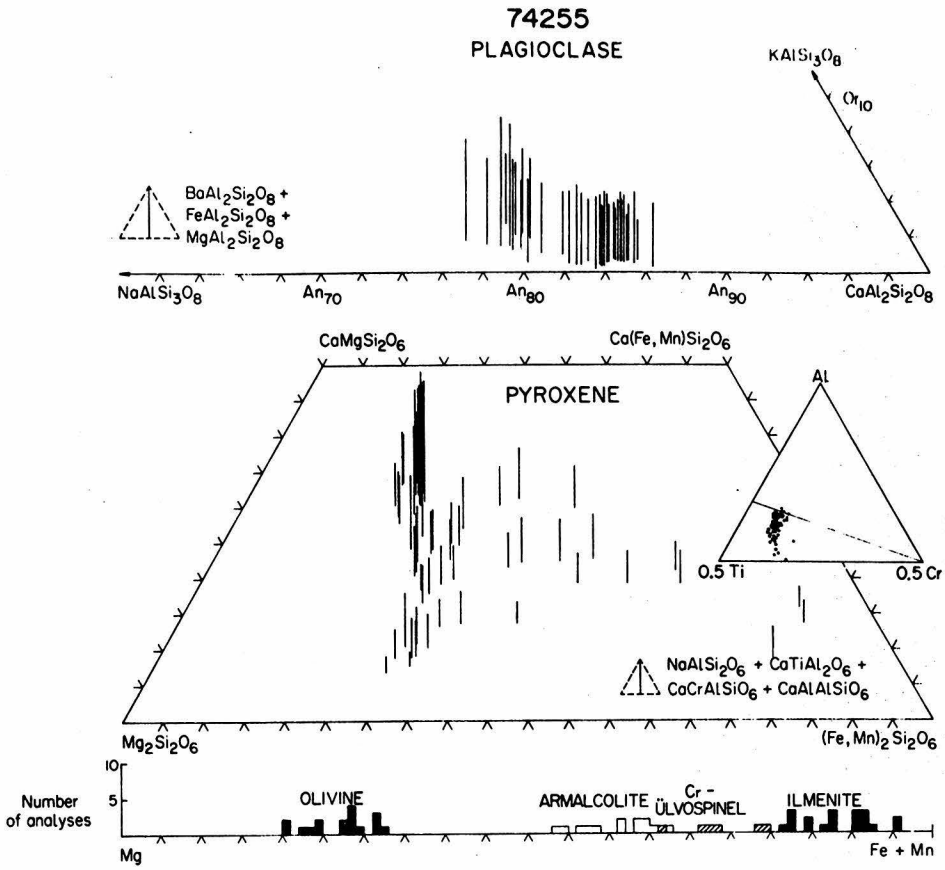

Fig. 8. Compositions of the principal silicate and oxide phases in mare basalt 74255. (Triangular inset as in Fig. 1.)

early in the crystallization history of this rock. A few rare inclusions of ilmenite and Cr ulvöspinel occur in olivine. The measured range in the composition of the olivine is Fo_{80-67}. The minor-element abundances and patterns resemble those in 70215 and 71055 (Fig. 5).

The most striking occurrence of pyroxene is as coarse, commonly composite, complexly zoned phenocrysts (up to 4 mm across). These range from pale-pink to dark-pink, and strongly resemble the large pyroxene grains in 71055. Abundant inclusions of ilmenite, together with rare grains of armalcolite and euhedral Cr ulvöspinel are present. These have measured compositions that range from $\sim Wo_{30}En_{52}Fs_{18}$ to $\sim Wo_{44}En_{40}Fs_{16}$, represented by the high-Ca cluster in Fig. 8. Thus, the principal variation is in Ca content, with only a slight change in Fe/Mg. The outer portions of some phenocrysts are pigeonite with compositions near $Wo_{10}En_{60}Fs_{30}$. These can be seen to zone continuously to augite ($\sim Wo_{25}En_{50}Fs_{25}$).

Hourglass structures are well developed in some grains, and microprobe traverses demonstrate the presence of sector zoning. The (010) sector of the grain illustrated in Fig. 9A has a composition that deviates only slightly from

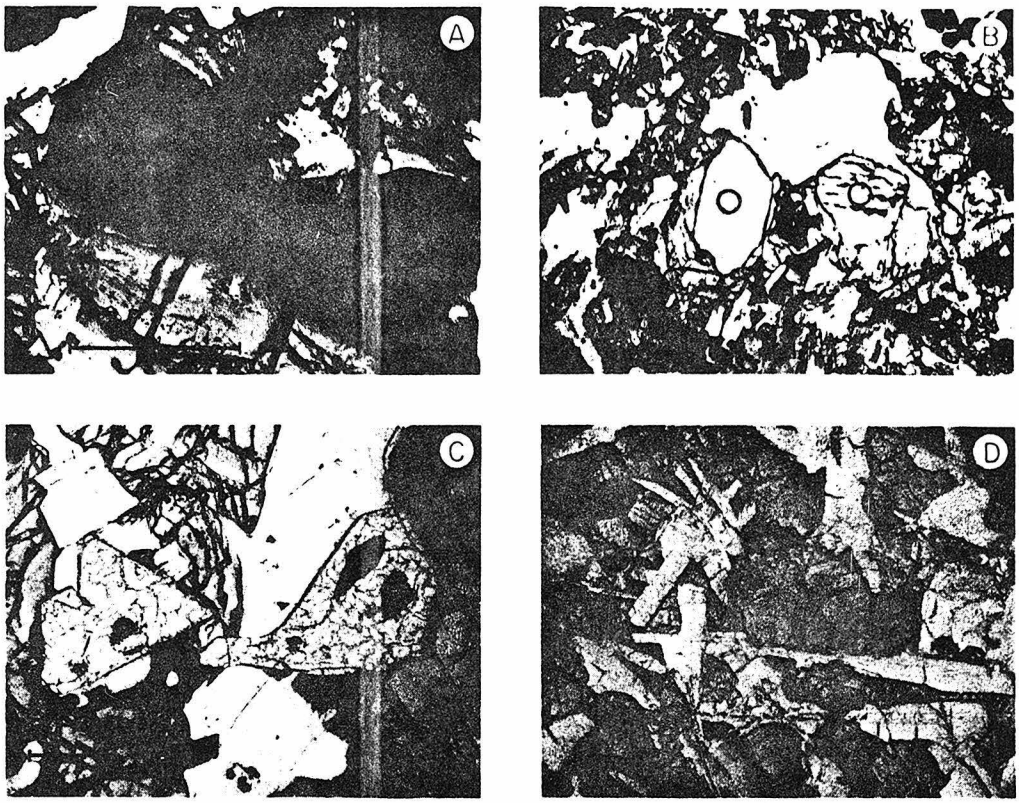

Fig. 9. (A) 74255—hourglass structure in pyroxene. This grain, cut nearly parallel to (100) beautifully displays the (010) sector (dark core), an augite with average composition: $(Na_{.00}Ca_{.77}Mg_{.79}Fe_{.27}Mn_{.00}Cr_{.03}Ti_{.12}Al_{.25}Si_{1.76}O_6)$, and (001) sector (light rim), an augite with approximate composition: $(Na_{.00}Ca_{.61}Mg_{.97}Fe_{.34}Mn_{.01}Cr_{.02}Ti_{.05}Al_{.11}Si_{1.89}O_6)$. The outer portions of the (001) sector are pigeonite with average composition: $(Na_{.00}Ca_{.25}Mg_{1.10}Fe_{.59}Mn_{.01}Cr_{.01}Ti_{.03}Al_{.06}Si_{1.93}O_6)$ (transmitted plane-polarized light). (B) 74255—photomicrograph illustrating two grains of olivine (O, center) that protrude into a vug. Note intergrown plagioclase–pyroxene–ilmenite surrounding the vug (transmitted plane-polarized light). (C) 75055—photomicrograph illustrating two grains of cristobalite (center, mosaic fracture pattern) with dark-brown glassy inclusion of K- and Si-rich "mesostasis" (transmitted plane-polarized light). (D) 75055—photomicrograph illustrating intergranular-subophitic texture of this sample. Note plagioclase laths (white), angular clinopyroxene (gray) and anhedral ilmenite (black) (transmitted plane-polarized light). All bar scales = 200 μm.)

$Wo_{43}En_{42}Fs_{15}$ (~4% TiO_2, ~6% Al_2O_3), whereas the (001) sector has a composition near $Wo_{32}En_{50}Fs_{18}$ (~2%TiO_2, ~3%Al_2O_3). The outermost rim on the (001) sector is pigeonite (~$Wo_{12}En_{56}Fs_{32}$), in contrast to Apollo 11 sector-zoned clinopyroxene where pyroxferroite is present (c.f., Albee and Chodos, 1970).

Pyroxene also occurs as colorless to pale-pink blocky grains (5–50 μm) that are poikilitically enclosed by plagioclase. These grade to elongate pyroxene bladed that are intergrown with plagioclase and ilmenite. Intergrowths of acicular pyroxene and plagioclase also occur. As shown on Fig. 8, the compositions

of these pyroxene types fall along an intermediate-Ca trend ($Wo_{10}En_{60}Fs_{30}$–$Wo_{30}En_{43}Fs_{27}$–$Wo_{25}En_{32}Fs_{43}$) and a low-Ca trend ($Wo_{10}En_{60}Fs_{30}$–$Wo_{15}En_{44}Fs_{41}$). Some pyroxene shows extensive Fe enrichment, and one grain has measured compositions that zone continuously from $Wo_{35}En_{33}Fs_{32}$ to $Wo_{11}En_{14}Fs_{75}$.

The minor-element content of the pyroxene is shown in Fig. 4. The Ti/Al ratio closely approaches 1 : 2 except for aluminous titanaugite which has excess Al. The relative amounts of Al–Ti–Cr (inset Fig. 8) are consistent with the presence of some Al^{VI} and Ti^{3+}, based on arguments outlined earlier in the text.

Rare grains of armalcolite [Fe/(Fe + Mg) ≅ .53–.67], in part mantled by ilmenite, occur as equant to elongate inclusions (20–50 μm) in the pyroxene phenocrysts. Euhedral Cr ulvöspinel [~5–25 μm; Fe/(Fe + Mg) ≅ .66–.80] occurs as inclusions in olivine and also in the pyroxene that surrounds the olivine. Ilmenite occurs both as inclusions in pyroxene phenocrysts (and rarely olivine), and also intergrown with pyroxene and plagioclase. There is a correlation between the Fe/(Fe + Mg) ratio of ilmenite and its occurrence: rims on armalcolite ~0.82; inclusions in pyroxene phenocrysts, ~0.84–0.87; intergrown with plagioclase and pyroxene, 0.86–0.96. These data indicate increasing Fe/(Fe + Mg) in ilmenite with progressive crystallization.

Plagioclase ranges in composition from An_{73-85}, and occurs as elongate laths intergrown with pyroxene and ilmenite (up to 200 μm wide), and as larger irregularly shaped poikilitic grains enveloping pyroxene. Normal zoning (up to 6 mole% An) was observed in several grains. 74255 contains curious intergrowths of plagioclase and SiO_2. This plagioclase is the most-sodic in the rock (An_{73-76}; 0.19–0.33 wt.% K_2O). Such an assemblage may be the crystalline equivalent of the "anamalous low-K melt inclusions" identified by Roedder and Weiblen (1975) in other Apollo 17 mare basalts. FeO and Fe/(Fe + Mg) increase, and MgO decreases, with decreasing An content in the plagioclase (Fig. 7). As in 71055, the Fe/(Fe + Mg) of the earliest-formed plagioclase (~0.4) is slightly higher than that of the pyroxene that crystallized at this time [i.e. a pigeonite with Fe/(Fe + Mg) ~0.30–0.35].

The presence of armalcolite and spinel only within pyroxene phenocrysts and olivine suggests that these phases formed earliest in the crystallization sequence. Olivine crystallized next, reacting with the melt to form augite before armalcolite ceased crystallization. The presence of euhedral, unreacted armalcolite within a pyroxene phenocryst that mantles olivine demonstrates this fact. This also suggests that pyroxene began to crystallize slightly before ilmenite. Augite phenocrysts continued to grow with ilmenite, and, with the onset of plagioclase crystallization, pigeonite nucleated. As in 71055, an augite-series and a pigeonite-series coprecipitated with plagioclase and ilmenite to the final stages. Fe-rich pyroxene, SiO_2, sodic plagioclase, and potassic mesostasis formed last.

D. Sample 75055

Lunar rock 75055 was a 949.4 g tetrahedron-shaped block (1.8 × 14 × 21 cm) collected from a 1-m boulder near the southwest rim of Camelot Crater at Apollo

17, Station 5. Muehlberger *et al.* (in Apollo 17 PSR, 1973; p. 6–39) classified this sample as a vesicular, coarse-grained basalt; it was described in the sample catalog as a homogenous white medium-brownish-gray basalt with few vugs ($\leq 5\%$). The hand specimen contained some planar partings, perhaps related to vesicle concentrations, and all exposed surfaces contained a few zap-pits. Papike *et al.* (1974) have designated 75055 as the large rock equivalent to Apollo 17 rake basalt samples termed "Apollo 11 low-K-type," and Brown *et al.* (1975) grouped 75055 with their "olivine-free" (Type 2) basalts. In addition, a petrographic description of 75055 has been presented by Kridelbaugh and Weill (1973).

Our study indicates that 75055 is a medium- to fine-grained intergranular to subophitic ilmenite basalt. It is comprised of plagioclase (33%), clinopyroxene (50%), ilmenite (12%), and SiO_2 (3%), with minor amounts of troilite, Fe metal, ulvöspinel, Ca phospate, "tranquilityite," and mesostasis. Sample 75055 is virtually identical in texture and mineralogy to 10044, a coarse-grained Apollo 11 low-K-type B basalt (Albee and Chodos, 1970). Hence, the close similarity between 75055, and other similar Apollo 17 mare basalts, and Apollo 11 low-K mare basalts, is supported by our observations (c.f. Papike *et al.*, 1974).

The results of an electron microprobe point count on polished thin section 75055,14 (area $\approx 200\ mm^2$) are presented in Table 4 and compositions of the principal phases are illustrated in Fig. 10. The results of an electron microprobe point count on polished thin section 10044,33 (area $\approx 200\ mm^2$) are presented in Table 5 for comparison. The mode, "average" mineral compositions, and bulk-chemical composition of 75055 and 10044 are remarkably similar. It should also be pointed out that the Rb–Sr crystallization age of 10044 ($=3.71 \pm 0.11$ AE) and the initial $^{87}Sr/^{86}Sr$ isotopic composition ($=0.69909 \pm 7$) are virtually indistinguishable from those of 75055, although the Rb–Sr model age ($T_{BABI} = 4.52$ AE) is slightly younger (Papanastassiou and Wasserburg, 1971).

Plagioclase forms a discontinuous, interlocking network of stubby tablets to elongate laths (~0.1–3.5 mm in length) enclosing pyroxene and ilmenite (Fig. 9D). Several grains contain numerous aligned glassy inclusions and rare inclusions of pyroxene and ilmenite. However, most of the plagioclase is remarkably free of inclusions of other phases. The margins of the larger plagioclase grains tend to be rounded and irregular, and are intergrown with pyroxene and ilmenite. The plagioclase has a measured range in composition of An_{72-90}. Microprobe analyses indicate zoning of up to 15 mole% An in a single grain, with the most-calcic compositions occurring in cores. As shown in Fig. 3, FeO and Fe/(Fe + Mg) increase uniformly with decreasing An content. However, MgO shows a slight but steady depletion from An_{90} to $\sim An_{80}$, with the decrease becoming more rapid at lower An contents.

The Fe/(Fe + Mg) of the most-calcic (i.e. earliest-formed) plagioclase is ~0.4, whereas the Fe/(Fe + Mg) of the earliest-formed pyroxene is ~0.28. From textural considerations, it appears that plagioclase began to crystallize before pyroxene, and therefore, the Fe/(Mg + Mg) in plagioclase at the onset of pyroxene crystallization must be higher. Hence, in sample 75055, as in the other rocks, the

Table 4. 75055: phase abundances, "average" phase compositions, and bulk-chemical composition.

	Plag.	Augite I	Autite II	Fe pyx	Ilmenite	Ulvöspinel	SiO_2	Mesostasis	Ca Phosphate†	Metal*	Troilite*	Bulk composition	
vol.%	$32.6_2 \pm 1.4_1$	$36.7_1 \pm 1.5_0$	$7.4_5 \pm 0.6_7$	$5.9_3 \pm 0.6_2$	$12.1_6 \pm 0.8_6$	< 0.1 —	$3.4_2 \pm 0.4_6$	$1.5_3 \pm 0.3_1$	$0.1_2 \pm 0.0_8$	< 0.01 —	$0.0_6 \pm 0.0_6$	Calc. (1637 Pts.)	LSPET, 1973
wt.%	27.0_0	37.4_9	7.8_8	6.7_4	17.2_6	< 0.01	2.4_1	1.0_2	0.1_2	< 0.01	0.0_8		
P_2O_5	n.a.	n.a.	n.a.	n.a.	n.a.	n.a.	< 0.01	0.12	43.15	< 0.01	0.01	0.05	0.07
SiO_2	49.15	47.77	49.48	48.00	0.10	0.31	98.84	78.31	—	0.12	0.07	41.51	41.27
TiO_2	0.03	3.12	1.07	0.69	52.87	32.31	0.12	0.44	—	< 0.01	0.02	10.48	10.17
Al_2O_3	31.61	3.92	1.17	0.74	0.05	0.35	0.64	11.10	—	n.a.	n.a.	10.28	9.75
Cr_2O_3	n.a.	0.71	0.17	0.15	0.55	1.95	0.06	< 0.01	—	< 0.01	< 0.01	0.39	0.27
MgO	0.14	12.02	9.08	4.61	1.01	0.07	< 0.01	0.01	—	< 0.01	< 0.01	5.75	6.84
FeO	0.58	14.15	26.97	36.38	45.02	63.51	0.09	0.78	—	98.42	63.23	17.86	18.24
MnO	n.a.	0.24	0.54	0.62	0.45	0.41	< 0.01	< 0.01	—	0.02	0.01	0.25	0.29
CaO	16.63	17.85	12.29	8.74	n.a.	n.a.	0.17	1.69	54.54	0.02	0.02	12.83	12.30
BaO	< 0.01	n.a.	n.a.	n.a.	n.a.	n.a.	< 0.01	0.03	—	n.a.	n.a.	< 0.01	—
Na_2O	1.90	0.13	0.08	0.06	n.a.	n.a.	0.01	0.34	—	n.a.	n.a.	0.58	0.44
K_2O	0.08	n.a.	n.a.	n.a.	n.a.	n.a.	0.02	4.50	—	n.a.	n.a.	0.07	0.09
Zr_2O_2	n.a.	n.a.	n.a.	n.a.	0.10	0.19	< 0.01	0.23	—	n.a.	n.a.	0.02	0.03
V_2O_3	n.a.	n.a.	n.a.	n.a.	< 0.01	0.02	n.a.	n.a.	—	n.a.	n.a.	< 0.01	—
Ni	n.a.	n.a.	n.a.	n.a.	n.a.	n.a.	n.a.	n.a.	—	< 0.01	< 0.01	< 0.01	< 0.01
Ca	n.a.	n.a.	n.a.	n.a.	n.a.	n.a.	n.a.	n.a.	—	0.56	< 0.01	< 0.01	< 0.01
S	n.a.	n.a.	n.a.	n.a.	n.a.	n.a.	n.a.	n.a.	—	0.08	36.35	0.03	0.19
F	n.a.	n.a.	n.a.	n.a.	n.a.	n.a.	n.a.	n.a.	2.31	n.a.	n.a.	< 0.01	—
Total	100.12	99.91	100.85	99.99	100.16	99.12	99.95	97.55	100.00	99.22	99.71	100.10	99.95
	An 79.9	Wo 31.8	Wo 24.5	Wo 18.6							$\frac{Fe}{Fe+Mg}$ = .635		.599
	Ab 16.5	En 34.2	En 26.6	En 14.3									
	Or 0.5	Fs 23.0	Fs 45.2	Fs 64.5									
	Others 3.1	11.0	3.7	2.6									

†Assumed 1:1 mix of fluorapatite and whitlockite.
*Elemental abundances; converted to oxides for calculation of bulk composition.
n.a. = not analyzed.

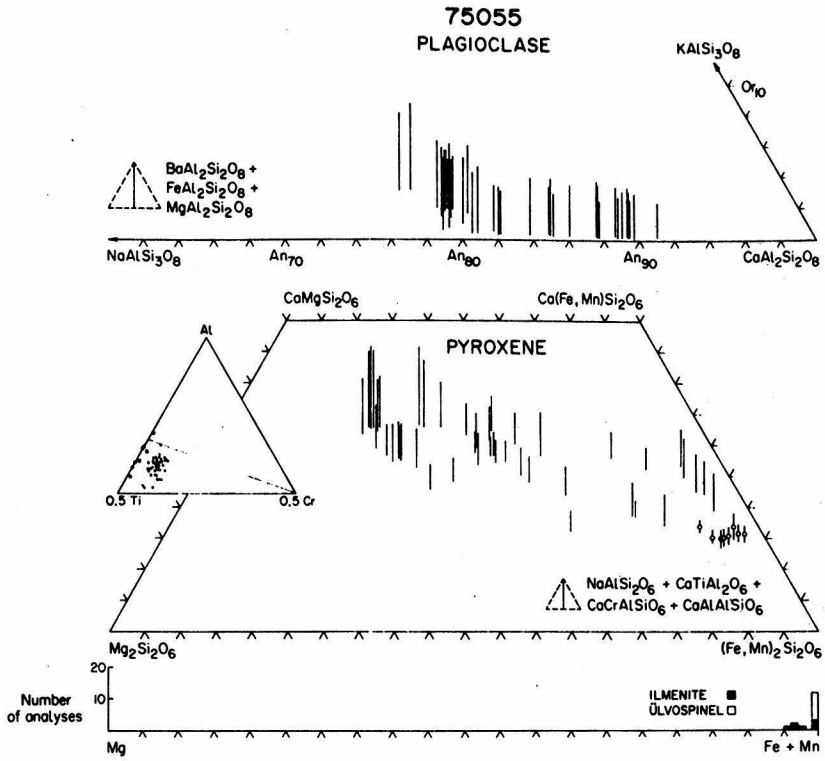

Fig. 10. Compositions of the principal silicate and oxide phases in mare basalt 75055. (Triangular inset as in Fig. 1.) The pyroxene compositions marked by the open circles are presumed to be pyroxferroite.

Fe/(Fe + Mg) in plagioclase is not a reliable indicator of the composition of the first formed pyroxene.

Pyroxene occurs as pale-pink to pale-yellow-brown to nearly colorless, subhedral to anhedral grains (~0.1–1.0 mm) that fill interstices between plagioclase laths. Many grains include and are intergrown with ilmenite and plagioclase. Optical zoning is pronounced, but hourglass structures are poorly developed. The measured range in composition is $\sim Wo_{40}En_{44}Fs_{16}$—$Wo_{16}En_3Fs_{81}$, with the variation in many grains spanning almost the entire compositional range (Fig. 10). The most Fe-rich compositions have extremely low-Cr contents, and are distinguished by a special symbol on Figs. 4 and 10. These probably represent pyroxferroite; similar depletion in Cr occurs in the most iron-rich "pyroxene" in 10044 (Albee and Chodos, 1970). Both the Ti/Al ratio (= 1:2; Fig. 4), and the Al–Ti–Cr abundance (inset, Fig. 10) indicate the presence of some Ti^{3+} and no Al^{VI}. Both relationships are consistent with pyroxene–plagioclase coprecipitation or crystallization of (some) plagioclase prior to the growth of pyroxene.

Ilmenite tends to form elongate grains (up to 2 mm) with subhedral and lobate outlines. Most contain abundant subrounded melt and pyroxene inclusions and rarely plagioclase. The vast majority of the ilmenite grains in this sample are

Table 5. 10044: Phase abundances, "average" phase compositions, and bulk-chemical composition.

	Plag.	Augite I	Augite II	Fe pyx	Ilmenite	SiO_2	Mesostasis	Ca Phosphate	Troilite*	Bulk composition	
vol.%	$36.9_2 \pm 1.4_7$	$32.3_8 \pm 1.3_7$	$7.2_7 \pm 0.6_5$	$5.4_1 \pm 0.5_6$	$12.2_7 \pm 0.8_4$	$4.2_4 \pm 0.5_0$	$1.2_2 \pm 0.2_7$	$0.1_7 \pm 0.1_0$	$0.1_2 \pm 0.0_8$	Calc.	Engel and
wt.%	30.8_7	33.3_9	7.7_6	6.2_1	17.6_0	3.0_1	0.8_2	0.1_7	0.1_7	(1720 Pts.)	Engel (1970)
P_2O_5	n.a.	n.a.	n.a.	n.a.	n.a.	n.a.	n.a.	39.3	—	0.07	0.08
SiO_2	47.23	49.93	49.43	47.08	0.08	98.32	76.76	1.2	—	41.61	42.01
TiO_2	n.a.	1.96	1.32	0.76	52.48	0.35	0.19	n.a.	—	10.05	8.81
Al_2O_3	32.57	2.22	1.48	0.79	0.06	0.91	11.90	n.a.	—	11.10	11.67
Cr_2O_3	n.a.	0.38	0.26	0.14	0.45	n.a.	n.a.	n.a.	—	0.23	n.a.
MgO	0.09	13.44	9.94	3.51	0.40	0.02	0.02	n.a.	—	5.58	6.25
CaO	16.93	17.01	12.63	8.06	n.a.	0.17	1.39	52.2	—	12.33	12.18
FeO	0.64	14.81	25.60	38.89	45.66	0.04	1.03	1.9	63.60	17.73	17.98
MnO	n.a.	0.32	0.48	0.66	0.48	n.a.	n.a.	n.a.	—	0.27	0.24
Na_2O	1.59	0.01	0.06	0.03	n.a.	0.14	0.23	n.a.	—	0.51	0.48
K_2O	0.30	n.a.	n.a.	n.a.	n.a.	0.03	7.50	n.a.	—	0.16	0.11
S	n.a.	n.a.	n.a.	n.a.	n.a.	n.a.	n.a.	n.a.	36.40	0.06	n.a.
F	n.a.	n.a.	n.a.	n.a.	n.a.	n.a.	n.a.	3.4	—	<0.01	n.a.
Total	99.35	100.08	101.20	99.92	99.61	99.98	99.02	98.0	100.00	99.71	99.81
An 81.4	Wo 31.6	Wo 24.4	Wo 17.0						$\frac{Fe}{Fe+Mg} = .641$		.618
Ab 13.9	En 37.8	En 28.7	En 10.9								
Or 1.7	Fs 23.9	Fs 42.3	Fs 69.2								
Others 3.1	6.7	4.6	2.9								

*Elemental abundances assuming stoichiometric FeS; converted to oxides for calculation of bulk composition.
n.a. = not analyzed.

either intergrown with or included in pyroxene. "Graphic" intergrowths of ilmenite and pyroxene are quite common. Occasionally, ilmenite is intergrown with plagioclase. The ilmenite is more Fe rich than that in any of the basalts studied [Fe/(Fe + Mg) = .95–.99], and in one instance was overgrown and appeared to have been resorbed by ulvöspinel [Fe/(Fe + Mg) = .99]. No armalcolite or Cr spinel were observed.

The SiO_2 phase in 75055 occurs predominantly as subhedral to euhedral interstitial grains (up to ~0.3 mm across) with the characteristic mosaic fracture pattern of lunar cristobalite (Fig. 9C). A few grains occur as needles (up to ~1 mm long) intergrown with plagioclase and pyroxene, and are probably tridymite. Both types contain infrequent tiny (10–50 μm) inclusions of a dark-brown K- and Si-rich, devitrified glass (Fig. 9C). The SiO_2 needles are uniformly higher in K content than the angular grains; a similar relationship was reported for the SiO_2 in mare basalt 12064 (Klein *et al.*, 1971).

In comparison with 70215, 71055, and 74255, 75055 appears to have had a much simpler crystallization history. Ilmenite and plagioclase were the first phases to form. Although these phases are occasionally intergrown at their margins, they only rarely occur as inclusions within each other, hence their relative order of crystallization is not clear. In a few cases, well-formed laths of plagioclase appear to have interfered with the growth of some ilmenite grains. Therefore, we suggest that plagioclase may have appeared very slightly before ilmenite. These coprecipitated and were joined by pyroxene. Ilmenite, plagioclase, and pyroxene cocrystallized and were joined by tridymite. Solidification was completed with the "replacement" of ilmenite by ulvöspinel, and the formation of cristobalite and mesostasis in the interstices.

The REE abundance patterns in 75055 indicate that it has a pronounced negative Eu anomaly, analogous to all other lunar mare basalts (Shih *et al.*, 1975). However, our petrographic observations suggest that 75055 may have been plagioclase-saturated at the time of eruption. Hence, the possibility exists that any Eu anomaly present in 75055 could have been enhanced by accumulation of plagioclase. However, this could only be caused by low-pressure, near-surface fractionation. The bulk composition of 75055 lies near the olivine–plagioclase–pyroxene–ilmenite saturation surface at low pressure (Longhi *et al.*, 1974). The stability field of plagioclase disappears at higher pressure for this composition, indicating that plagioclase would not be a liquidus phase at pressures above about 1–2 kbar (J. Longhi, Harvard University, written communication, 1975).

IV. Discussion

We have attempted, in this study, to correlate detailed changes in mineral chemistry with the crystallization sequence in each of four Apollo 17 mare basalts. Here, we shall summarize these observations, and discuss how these rocks may or may not be related to each other.

A. Mineral chemistry

Olivine occurs in three samples and has a compositional range from Fo_{80} to Fo_{64}. The data in Fig. 5 suggest decreasing-Cr, increasing-Ca, and constant-Ti with decreasing-Mg content, consistent with prior or simultaneous crystallization of Cr spinel, and delayed crystallization of Ca-rich phases. Ti apparently does not vary in olivine in any meaningful way.

The *pyroxene* in all four samples shows a wide range in composition, but augite forms first in each. We note that the Fe/(Fe + Mg) of the first-formed clinopyroxene in 71055 and 74255 are the same (~0.25), but slightly more-magnesian than in 75055 (~0.28) and distinctly more-magnesian than 70215 (~0.35; cf. Figs. 1, 6, 8, and 10).

In 70215, 71055, and 74255, where plagioclase began to crystallize after pyroxene, the augite became excessively enriched in Al_2O_3, with some Al entering octahedral coordination as R^{2+} Al Al SiO_6. The pyroxene in 75055, where plagioclase began to crystallize before pyroxene, contains only moderate amounts of Al_2O_3, and no R^{2+} Al Al SiO_6. These relationships suggest that the anomalously high-Al contents of the earliest-formed pyroxenes are related to metastable crystallization; the onset of plagioclase crystallization was delayed due to supercooling of the melt, and Al_2O_3 was metastably incorporated in the pyroxene.

The pyroxene contains abundant Ti, despite the fact that Fe–Ti oxides coprecipitated with pyroxene. The tendency of the Ti/Al ratio to approach 1:2 indicates that Ti^{4+} enters pyroxene to maintain charge balance with Al^{3+} as R^{2+} Ti Al_2O_6, but the chemical data suggest the presence of some Ti^{3+} in addition.

In 71055 and 74255 a two-pyroxene crystallization sequence developed after plagioclase formed, whereas in 70215, only augite continued to form. Since these rocks have similar bulk compositions, we suggest that the extremely rapid quenching of 70215 "overstepped" the onset of pigeonite crystallization, and this feature is attributable to differences in cooling rate.

The pyroxene in all samples show Fe enrichment during the late stages of crystallization. However, Fe pyroxene is present in only small amounts (c.f. Tables 1–4), suggesting that the crystallization of abundant Fe–Ti oxide phases served to restrict Fe enrichment in the pyroxene (c.f. Papike *et al.*, 1974). We have not observed the assemblage ferrohedenbergite–fayalite–SiO_2, attesting to the stability of the metastable pyroxenoid in 75055.

In 71055, 74255, and 75055, the FeO and Fe/(Fe + Mg) in *plagioclase* increased uniformly during crystallization. The Fe/(Fe + Mg) in plagioclase is greater than the Fe/(Fe + Mg) in pyroxene at the onset of pyroxene crystallization.

Ilmenite shows a wide range in Fe/(Fe + Mg) and progressive increase in Fe/(Fe + Mg) with extent of crystallization in 70215, 71055, and 74255. In 75055, the ilmenite is very Fe rich and has a narrow range in Fe/(Fe + Mg).

All samples contain late-stage SiO_2, and silica- and potassium-enriched mesostasis. Thus, even for those rocks that begin crystallizing olivine, *in situ* differentiation produces silica-oversaturated residua. In summary, all four rocks are characterized by mineralogic features, particularly in their pyroxenes, that suggest metastable and disequilibrium crystallization during solidification. The

extent to which these features are developed was probably controlled predominantly by cooling rate.

B. Petrogenesis

To a first approximation, the four basalt samples examined by us could be related to each other by fractional crystallization or accumulation of olivine, spinel, armalcolite, ilmenite, and plagioclase, and differences in cooling rate. Longhi *et al.* (1974) have shown the bulk compositions of most Apollo 17 basalt fall along a liquid line of descent governed by differential removal of these phases. The textures in the rocks, their bulk-chemical compositions, and the compositions of their minerals place constraints on such relationships.

If these samples are related to a common parent magma by olivine fractionation, then the Fe/(Fe + Mg) of the rocks should reflect this. Based on the chemical analyses in Tables 1–4, the predicted sequence is: 74255 → 70215 ≃ 71055 → 75055. The TiO_2 content should be an indicator of ilmenite (and armalcolite) fractionation. Based on TiO_2, the predicted sequence is 71055 → 70215 ≃ 74255 → 75055. In addition, the Cr_2O_3 content, although small, should be a sensitive indicator of spinel fractionation. The sequence predicted from Cr_2O_3 is: 74255 → 70215 ≃ 71055 → 75055. These data all indicate that 75055 is the most "differentiated" of the four samples, but no consistent pattern emerges for the other three.

The textures of the rocks are probably the best indicator of cooling rate. The predicted sequence, based on textural relationships, is: 70215 (quenched liquid) → 74255 (slowly cooled, porphyritic) → 71055 (more slowly cooled, non-porphyritic) → 75055 (slowest cooled). The features in the four samples could be related by progressive down-temperature equilibration between crystals and melt in a single lava flow or lava lake. However, the differences in bulk composition among the four samples, although slight, indicate that they cannot be related to the same magma merely by differences in cooling rate unless there was accompanying fractional crystallization. The fact that all the rocks show the effects of very rapid crystallization suggests that crystal fractionation, if it occurred, was probably insignificant.

In 70215, the most-magnesian olivine (Fo_{75}) and spinel [Fe/(Fe + Mg) = 0.78] are more Fe rich than in 74255 [olivine-Fo_{80}; spinel—Fe/(Fe + Mg) = 0.67]. If 70215 represents a quenched liquid, as seems likely, than that liquid was more evolved than the one that gave rise to 74255, as indicated by the bulk-chemical data. In addition, 74255 cannot have resulted from accumulation of olivine from a magma with 70215 composition, because the composition of the liquidus olivine in 70215 is more Fe rich than that in 74255. Hence, we feel that the petrologic evidence indicates the likelihood of a separate origin for each.

The most-magnesian olivine and spinel in 71055 are more Fe rich than those in both 70215 and 74255. Hence, 71055 could be a derivative of either. The similarity in pyroxene and plagioclase compositions, and textures, between 71055 and 74255 suggests a close connection between the two. However, 71055 is the most TiO_2 rich of the three samples, and if it is a derivative of 70215 or 74255, it must also be

an ilmenite (or armalcolite) accumulate at the same time. However, we have not found any armalcolite in 71055 (armalcolite is present in 70215 and 74255), and the ilmenite in 71055 is more Fe rich than in 70215 and 74255, and does not support the addition of early formed ilmenite simultaneously with the subtraction of early formed spinel and olvine.

Basalt 75055 does not resemble the others in either texture or paragenesis. In addition, it is lower in TiO_2 (cf. Tables 1–4), and is quartz-normative (cf. Papike *et al.*, 1974). Petrographically, 75055 could, in principle, have resulted by fractionation of olivine, armalcolite, spinel, and ilmenite from a lava with composition not unlike 70215. The fact that the ages of the two samples are identical is consistent with this interpretation. However, the extensive trace element enrichment of 75055 relative to 70215, which requires fractionation of nearly 40% of the latter, is not supported by the major-element data (Rhodes, 1973).

Shih *et al.*, (1975) suggested that 75055 could be derived from a liquid with composition resembling 70017, a rock that is similar petrographically to 71055 and 74255. However, the composition of the most-magnesian olivine in 70017 (Fo_{69}; Longhi *et al.*, 1974) is more Fe rich than either 71055 ($\sim Fo_{75}$; Fig. 6) or 74255 ($\sim Fo_{80}$; Fig. 8) suggesting that 70017 may itself be somewhat removed from a primary-magma composition, or may represent a sample of yet another lava flow.

The older ages of 75055 and 70215, versus ~3.64 AE for 71055 might seem to preclude their derivation from the same lava. However, except for this one age on 71055, the isotopic data suggest that mare volcanism at Taurus-Littrow occurred during a limited time period around 3.8 AE, and are not incompatible with derivation from related volcanic events. However, the large differences in Rb–Sr model ages for samples 70215, 71055, and 75055 precludes their derivation from the same lava flow, although the close similarity in the initial $^{87}Sr/^{86}Sr$ isotopic compositions suggests that the source regions were chemically similar, and similar to the source of some Apollo 11 mare basalts such as 10044.

In conclusion, our petrographic study indicates that 70215, 74255, and 75055 formed from three separate lava flows; 71055 may be derived from 74255 or in a separate event. Volcanic activity at Taurus-Littrow produced a variable suite of basalts with a rather limited range in chemistry that appear to be related both in space and time to a common source.

Acknowledgments—This study has been supported by NASA grant NGL-05-002-338. J. Quick assisted with microprobe analyses on sample 74255. We wish to thank J. Longhi and T. Usselman for very helpful reviews of this manuscript. Discussions with D. H. Green have assisted us in our work on these basalt samples. The microprobe laboratory has been developed with the support of the National Science Foundation, the Jet Propulsion Laboratory and the Union Pacific Foundation.

References

Albee A. L. and Chodos A. A. (1970) Microprobe investigations on Apollo 11 samples. *Proc. Apollo 11 Lunar Sci. Conf.*, p. 135–157.

ALGIT (Apollo Lunar Geology Investigation Team) (1973) Documentation and environment of the Apollo 17 samples: A preliminary report. *U.S. Geological Survey Interagency Report: Astrogeology* **71**. 332 pp.

Apollo 17 *Preliminary Sci. Report* (1973) NASA publication SP-330.

Brown G. M., Peckett A., Emeleus C. H., and Phillips R. (1974) Mineral–chemical properties of Apollo 17 mare basalts and terra fragments (abstract). In *Lunar Science V*, p. 89–91. The Lunar Science Institute, Houston.

Brown G. M., Peckett A., Phillips R., and Emeleus C. H. (1975) Mineralogy and petrology of Apollo 17 basalts (abstract). In *Lunar Science VI*, p. 95–97. The Lunar Science Institute, Houston.

Champion D. E., Albee A. L., and Chodos A. A. (1975) Reproducibility and operator bias in a computer controlled system for quantitative electron microprobe analysis. *Proc. 10th Nat. Conf. on Electron Probe Analyses.* Las Vegas, Nevada.

Chodos, A. A., Albee A. L., Gancarz A. J., and Laird J. (1973) Optimization of computer controlled quantitative analysis of minerals. *Proc. 8th Nat. Conf. on Electron Probe Analyses.* New Orleans, La.

Crawford M. L. (1973) Crystallization of plagioclase in mare basalts. *Proc. Lunar Sci. Conf. 4th*, p. 705–717.

Dymek R. F., Albee A. L., and Chodos A. A. (1975) Petrology of Apollo 17 mare basalt 74255 (abstract). In *Lunar Science VI*, p. 230–232. The Lunar Science Institute, Houston.

Engel A. E. J. and Engel C. G. (1970) Lunar rock compositions and some interpretations. *Proc. Apollo* 11 *Lunar Sci. Conf.*, p. 1081–1084.

Evensen N. M., Murthy V. R., and Coscio M. R., Jr. (1973) Rb–Sr ages of some mare basalts and the isotopic and trace element systematics in lunar fines. *Proc. Lunar Sci. Conf. 4th*, p. 1707–1724.

Gancarz A. J. and Albee A. L. (1973) Microprobe analysis of the bulk composition of phase aggregates. *Proc. 8th Nat. Conf. on Electron Probe Analyses.* New Orleans, La.

Green D. H., Ringwood A. E., Ware N. G., and Hibberson W. O. (1975) Experimental petrology and petrogenesis of Apollo 17 mare basalts (abstract). In *Lunar Science VI*, p. 311–313. The Lunar Science Institute, Houston.

Hollister L. S., Trzcienski W. E., Jr., Hargraves R. B., and Kulick C. G. (1971) Petrogenetic significance of pyroxenes in two Apollo 12 samples. *Proc. Lunar Sci. Conf. 2nd*, p. 529–557.

Huneke J. C., Jessberger E. K., Podosek F. A., and Wasserburg G. J. (1973) $^{40}Ar/^{39}Ar$ measurements in Apollo 16 and 17 samples and the chronology of metamorphic and volcanic activity in the Taurus-Littrow region. *Proc. Lunar Sci. Conf. 3rd*, p. 1725–1757.

Kesson S. E. (1975) Melting experiments on synthetic mare basalts and their petrogenetic implications (abstract). In *Lunar Science VI*, p. 475–477. The Lunar Science Institute, Houston.

Kirsten T. and Horn P. (1974) Chronology of the Taurus-Littrow region III: Ages of mare basalts and highland breccias and some remarks about the interpretation of lunar highland rock ages. *Proc. Lunar Sci. Conf. 5th*, p. 1451–1475.

Klein C., Jr., Drake J. C., and Frondel C. (1971) Mineralogical, petrological, and chemical features of four Apollo 12 lunar microgabbros. *Proc. Apollo* 11 *Lunar Sci. Conf.*, p. 265–284.

Krindelbaugh S. J. and Weill D. F. (1973) The mineralogy and petrology of ilmenite basalt 75055 (abstract). *EOS* (*Trans. Amer. Geophys. Union*) **54**, 597–598.

Laul J. C. and Schmitt R. A. (1975) Chemical composition of 18 Apollo 17 rake basalts and one basalt-breccia (abstract). In *Lunar Science VI*, p. 492–494. The Lunar Science Institute, Houston.

Longhi J., Walker D., Grove T. L., Stopler E. M., and Hays J. F. (1974) The petrology of the Apollo 17 mare basalts. *Proc. Lunar Sci. Conf. 5th*, p. 447–469.

LSPET (1973) Apollo 17 lunar samples: Chemical and petrographic description. *Science* **182**, 659–672.

Lunar Sample Information Catalog—Apollo 17 (1973) *NASA MSC*-03211. 477 pp.

Nyquist L. E., Bansal B. M., Wiesmann H., and Jahn B.-M. (1974) Taurus-Littrow chronology: Some constraints on early lunar crustal development. *Proc. Lunar Sci. Conf. 4th*, p. 1515–1539.

Nyquist L. E., Bansal B. M., and Wiesmann H. (1975) Rb–Sr ages and initial $^{87}Sr/^{86}Sr$ for Apollo 17 basalts and KREEP basalt 15386 (abstract). In *Lunar Science VI*, p. 610–612. The Lunar Science Institute, Houston.

Papanastassiou D. A., and Wasserburg G. J. (1971) Lunar chronology and evolution from Rb–Sr studies of Apollo 11 and 12 samples. *Earth Planet. Sci. Lett.* **11**, 37–62.

Papike J. J., Bence A. E., and Lindsley D. H. (1974) Mare basalts from the Taurus Littrow region of the moon. *Proc. Lunar Sci. Conf. 5th*, p. 471–504.

Rhodes J. M. (1973) Major and trace element chemistry of Apollo 17 samples (abstract). *EOS (Trans. Amer. Geophys. Union)* **54**, 609–610.

Roedder E. and Weiblen P. W. (1975) Anomalous low-K silicate melt inclusions in ilmenite from Apollo 17 basalts (abstract). In *Lunar Science VI*, p. 683–685. The Lunar Science Institute, Houston.

Rose H. J., Jr., Cuttitta F., Berman S., Brown F. W., Carron M. K., Christian R. P., Dwornik E. J., and Greenland L. P. (1974) Chemical composition of rocks and soils at Taurus-Littrow. *Proc. Lunar Sci. Conf. 5th*, p. 1119–1133.

Rose H. J., Jr., Christian R. P., Dwornik E. J., and Schnepfe M. M. (1975) Major elemental analysis of Apollo 15, 16, and 17 samples (abstract). In *Lunar Science VI*, p. 686–688. The Lunar Science Institute, Houston.

Schaeffer O. A. and Husain L. (1975) The duration of volcanism in the Taurus-Littrow region and ages of highland rocks returned by Apollo 17 (abstract). In *Lunar Science VI*, p. 707–709. The Lunar Science Institute, Houston.

Shih C.-Y., Wiesmann H. W., and Haskin L. (1975) On the origin of high-Ti mare basalts (abstract). In *Lunar Science VI*, p. 735–737. The Lunar Science Institute, Houston.

Smyth J. V. (1971) Minor elements in Apollo 11 and Apollo 12 olivine and plagioclase. *Proc. Lunar Sci. Conf. 2nd*, p. 143–150.

Sung C.-M., Abu-Eid R. M., and Burns R. G. (1974) Ti^{3+}/Ti^{4+} ratios in lunar pyroxenes: Implications to depth of origin of mare basalt magmas. *Proc. Lunar Sci. Conf. 5th*, p. 717–726.

Tatsumoto M., Nunes P. D., Knight R. J., Hedge C. E., and Unruh D. M. (1973) U–Th–Pb, Rb–Sr, and K measurements of Apollo 17 samples (abstract). *EOS (Trans. Amer. Geophys. Union)* **54**, 614–615.

Tera F. and Wasserburg G. J. (1975) The evolution and history of mare basalts as inferred from U–Th–Pb systematics (abstract). In *Lunar Science VI*, p. 807–809. The Lunar Science Institute, Houston.

Tera F., Papanastassiou D. A., and Wasserburg G. J. (1974a) Isotopic evidence for a terminal lunar cataclysm. *Earth Planet. Sci. Lett.* **22**, 1–21.

Tera F., Papanastassiou D. A., and Wasserburg G. J. (1974b) The lunar time scale and a summary of isotopic evidence for a terminal lunar cataclysm (abstract). In *Lunar Science V*, p. 792–794. The Lunar Science Institute, Houston.

Turner G., Cadogan P. H., and Yonge C. J. (1973) Argon selenochronology. *Proc. Lunar Sci. Conf. 3rd*, p. 1889–1915.

Warner R., Prinz M., and Keil K. (1975) Mineralogy and petrology of mare basalts from Apollo 17 rake samples (abstract). In *Lunar Science VI*, p. 850–852. The Lunar Science Institute, Houston.

Wiegand P. W. (1973) Petrology of coarse-grained Apollo 17 ilmenite basalt 70035 (abstract). *EOS (Trans. Amer. Geophys. Union)* **54**, 621–622.